U.S.NRC
United States Nuclear Regulatory Commission
Protecting People and the Environment

State-of-the-Art Reactor Consequence Analyses (SOARCA) Project

Sequoyah Integrated Deterministic and Uncertainty Analyses

Draft Technical Report

[redacted]

Office of Nuclear Regulatory Research

TABLE OF CONTENTS

LIST OF FIGURES

LIST OF TABLES

EXECUTIVE SUMMARY

The U.S. Nuclear Regulatory Commission (NRC), the nuclear power industry, and the domestic and international nuclear energy research community have devoted considerable research over the last several decades to examining severe reactor accident phenomena and offsite consequences. Following the terrorist attacks of 2001 in the United States (U.S.), an NRC initiative reassessed severe accident progression and offsite consequences in response to security-related events. An insight gained from these security assessments was that the NRC needed updated analyses of severe reactor accidents to reflect realistic estimates of the more likely outcomes, considering the current state of plant design and operation and the advances in understanding of severe accident behavior.

The NRC initiated the State-of-the-Art Reactor Consequence Analyses (SOARCA) project to develop best estimates of the offsite radiological health consequences for potential severe reactor accidents. The initial SOARCA work considered two pilot plants: the Peach Bottom Atomic Power Station in Pennsylvania and the Surry Power Station in Virginia. Peach Bottom is generally representative of U.S. operating reactors using the General Electric boiling-water reactor (BWR) design with a Mark I containment. Surry is generally representative of U.S. operating reactors using the Westinghouse pressurized-water reactor (PWR) design with a large, dry (subatmospheric) containment. The SOARCA project evaluates plant improvements and changes not reflected in earlier NRC publications such as NUREG/CR-2239, "Technical Guidance for Siting Criteria Development, NUREG-1150, "Severe Accident Risks: An Assessment for Five U.S. Nuclear Power Plants," and WASH-1400, "Reactor Safety Study: An Assessment of Accident Risks in U.S. Commercial Nuclear Power Plants". SOARCA includes system improvements, improvements in training and emergency procedures, offsite emergency response, and security-related improvements, as well as plant changes such as power uprates and higher core burnup. The collection of SOARCA reports helps the NRC to communicate its current understanding of severe-accident-related aspects of nuclear safety to Federal, State, and local authorities, licensees, international counterparts, and the general public. Quantitative SOARCA results are specific to the plants and accident sequences evaluated in these studies. The insights derived from the SOARCA analyses may be generally applicable to plants with similar designs, but additional work would be needed to confirm this because differences exist in plant-specific designs, procedures, and emergency response characteristics.

After completing the Peach Bottom and Surry SOARCA analyses, the Commission approved the staff's recommendations to complete an analysis of station blackouts at the third pilot plant, Sequoyah, a PWR with an ice condenser containment. Staff recommended this study because ice condenser containments have a lower design pressure than other U.S. nuclear power plant containment types and are therefore potentially more susceptible to early failure from hydrogen combustion during a severe accident. Ice condensers are pressure suppression containments and use ice to absorb heat in a severe accident. Unlike the BWR Mark I and Mark II pressure suppression containments, ice condensers are not inerted with nitrogen. Therefore they use alternating current (AC) powered igniters to introduce sparks to burn hydrogen in a controlled manner before the hydrogen can accumulate to levels that could result in a highly energetic deflagration or detonation that could challenge the containment, should the postulated accident occur. The SOARCA project sought to focus its resources on the more important severe accident scenarios for Sequoyah, and in particular focused on issues associated with containment response for ice condenser containments.

The staff used updated and benchmarked standardized plant analysis risk (SPAR) models and available plant-specific external events information to identify the most probable of the very low probability station blackout (SBO) scenario variations for analysis. Similar to the Peach Bottom and Surry analyses, this group of scenarios includes the short-term station blackout (STSBO) and the long term station blackout (LTSBO). Both types of SBOs involve a loss of all AC power. SBO scenarios can be initiated by external events such as a fire, flood, or earthquake. The Sequoyah SOARCA analysis assumes that an SBO is initiated by a low probability severe seismic event because this is an extreme case in terms of timing and equipment failure. For the LTSBO, AC power is lost but the turbine-driven auxiliary feedwater pump (TDAFW) is available until batteries deplete. The contribution to core damage frequency for the LTSBO was estimated at one event per approximately 100,000 years of reactor operation. For the STSBO, AC power is lost and the turbine-driven auxiliary feedwater pump is not available, and therefore the postulated scenario proceeds to core damage more rapidly (hence "short term"). The contribution to core damage frequency for the STSBO is lower, and was estimated at one event per approximately 500,000 years of reactor operation.

SOARCA analyses were performed primarily with two computer codes, MELCOR for accident progression and MACCS for offsite consequences. MELCOR models the thermal-hydraulic response in the reactor coolant system, reactor cavity, containment, and confinement buildings; core heatup, degradation, and relocation; core-concrete attack; hydrogen production, transport, and combustion; fission product transport and release to the environment. MACCS models the atmospheric transport and deposition of radionuclides released to the environment as well as emergency response and long-term protective actions, exposure pathways, dosimetry, and health effects for the affected population. The Peach Bottom and Surry SOARCA studies were comprised of deterministic base case analyses using point estimates for input parameter values, followed by probabilistic uncertainty analyses (UAs) which sampled distributions representing input uncertainty to generate multiple results to represent the range of potential outcomes. For the Sequoyah SOARCA analysis, staff integrated probabilistic consideration of uncertainty into accident progression and offsite consequence analyses in parallel with deterministic calculations.

The Sequoyah containment is a free-standing steel containment consisting of a cylinder topped by a hemispherical dome. The vessel has been determined as nominally capable of resisting an internal pressure of 67 psig before rupturing. Upon overpressure failure, a tear in the containment (estimated to be on the order of a few square feet in area) is envisioned to open in the cylindrical portion, resulting in the potential for release of radioactive material to the atmosphere. Understanding the impact of the igniters as well as random sources of ignition on accident progression was a primary focus of the Sequoyah SOARCA analysis. As illustrated in Figure ES-1, Sequoyah SOARCA analyses continue to confirm that successful use of igniters can control hydrogen accumulation through earlier deflagrations resulting in smaller pressure spikes that avert early containment failure (long-term containment over-pressurization from ongoing steam production, unabated fission product decay heating and noncondensable gas generation associated with core-concrete interaction can still lead to containment failure).

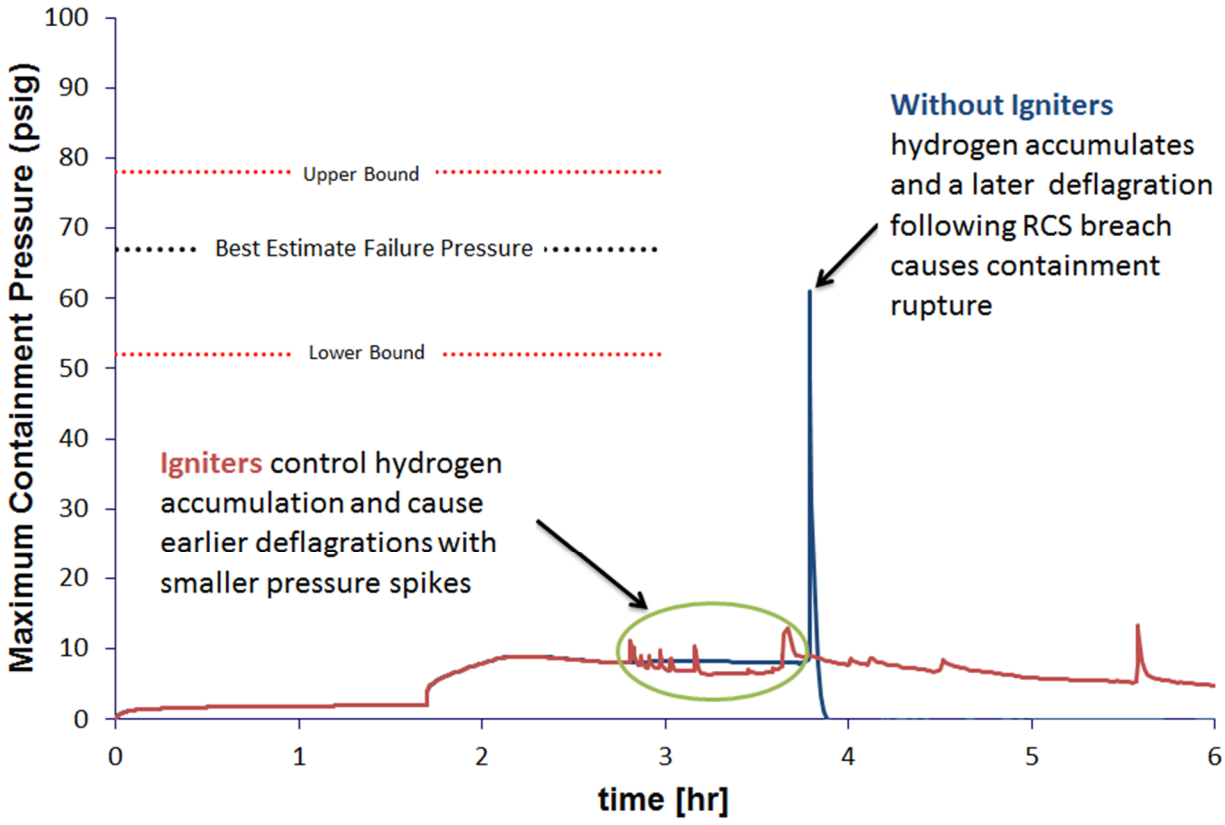

Figure ES-1 Illustration of the effect of hydrogen igniters in a typical Sequoyah SOARCA unmitigated STSBO accident progression

The critical time frame for igniter operation is prior to the accumulation of hydrogen in the containment (e.g., < 3 hours for the STSBO and 10-14 hours after direct current (DC) battery failure for the LTSBO). Igniters can be useful until the containment oxygen concentration falls below the flammability limit (i.e., >18 hours for the STSBO and >30 hours for the LTSBO) due to burning of hydrogen by the igniters and gas generation from core concrete interaction, at which point igniters are no longer needed.

Several variations of the STSBO were evaluated. The base case scenario was an evaluation of an unmitigated (i.e., without igniters) STSBO scenario. A sensitivity case of a mitigated STSBO was evaluated in which hydrogen igniters are modeled as operable. Two unmitigated (i.e., igniters are assumed inoperable) STSBO variations were run probabilistically with and without the presence of random ignition sources. Random ignition sources refer to the potential of the accident to lead to sparks possibly caused by structural materials sliding against or falling on other materials, static discharge, etc., but the timing and location of the spark(s) is inherently unknown. The staff modeled hundreds of variations of the STSBO with and without random ignition sources, each of which used different values of important input parameters[1] selected from distributions that account for parameter uncertainty in both accident progression (MELCOR) and offsite consequences (MACCS). For the LTSBO scenario, staff has

[1] Because the unmitigated STSBO does not credit human actions, the UA also does not address human actions.

deterministically analyzed accident progression for a scenario without igniters or random ignition sources, and performed a number of deterministic sensitivity calculations to assess the impact of features including battery duration, hydrogen ignition criteria, and safety valve (SV) behavior. A sensitivity case of a mitigated LTSBO was also evaluated in which hydrogen igniters are modeled as operable. The scenario variations and approach are listed in Table ES-1.

Table ES-1 SBO scenario variations and modeling approach

SBO	Mitigation	Variation	Approach
STSBO	Mitigated (igniters available)		Deterministic sensitivity analysis
	Unmitigated (igniters not available)	No random ignition sources modeled	Integrated UA (Deterministic and probabilistic analyses)
		Random ignition sources modeled	Integrated UA (Probabilistic analyses)
LTSBO	Mitigated (igniters available)		Deterministic sensitivity analysis
	Unmitigated (igniters not available)	Hydrogen ignition criteria	
		Battery duration	
		Safety valve behavior	

Based on the results of the previous Peach Bottom and Surry uncertainty analyses, several MELCOR parameters that were shown to be important were selected for sampling in the integrated UA for the Sequoyah unmitigated (i.e., igniters inoperable) STSBO scenarios. In addition, new parameters were added specific to the ice condenser containment. The uncertain MELCOR input parameters affecting accident progression are identified in Table ES-2.

Table ES-2 Uncertain MELCOR parameters used in unmitigated STSBO UA

Sequence Issues	• Number of primary SV cycles to failure • Failed SV flow area
In-Vessel Accident Progression	• Melting temperature of the eutectic formed between ZrO_2 and UO_2
Ex-vessel Accident Progression and Containment behavior	• Containment fragility (failure pressure) • Ice condenser inlet door response • Containment barrier seal failure pressure and area
Hydrogen Combustion	• Flammability (flame propagation and direction) • Ignition source
Aerosol transport and deposition	• Dynamic shape factor

For the unmitigated STSBO (i.e., igniters inoperable), there are two potential containment outcomes: early failure (~3-12 hours from initiating event) due to hydrogen combustion or late failure (> 30 hours) from more gradual overpressure. If igniters are not available because of the loss of power, containment can fail soon after hot leg rupture or at the time of lower head failure

due to hydrogen deflagration. However, if a random spark triggers ignition prior to reactor coolant system breach, the accident is less likely to proceed to early containment failure. An early containment failure can result in the potential for radionuclide release to the environment before the 0-10 mile EPZ population has time to complete evacuation; however, the consequence analysis shows that even under such conditions, health risk to the public is low. The uncertainty in the release magnitude and timing is illustrated in Figure ES-2 for iodine and Figure ES-3 for cesium. These are the results assuming that an unmitigated SBO accident has occurred (in other words, the conditional results). Each gray curve represents an individual scenario simulation of an unmitigated STSBO and each black curve represents a deterministic variation of the unmitigated LTSBO. These figures show that there is a large variation in release timing and magnitude for the unmitigated STSBO. With respect to release timing, a bifurcation is observed between simulations leading to early failure (~ 3-12 hrs) and simulations leading to late overpressure failure (> 30 hrs). The unmitigated LTSBO variations fall within the unmitigated STSBO variations, however for the unmitigated LTSBO, there are no cases of early containment failure. The use of TDAFW to extend core cooling in the unmitigated LTSBO delays containment failure to greater than about 18 hours following the initiating event.

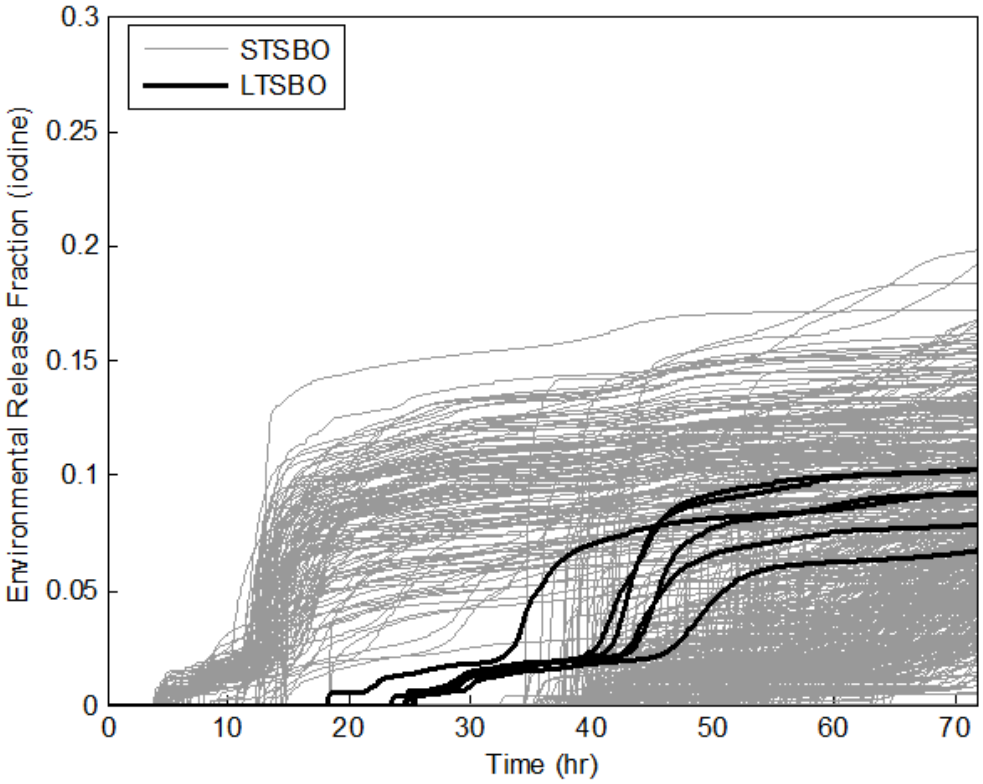

Figure ES-2 Iodine release to the environment for variations of unmitigated STSBO and LTSBO

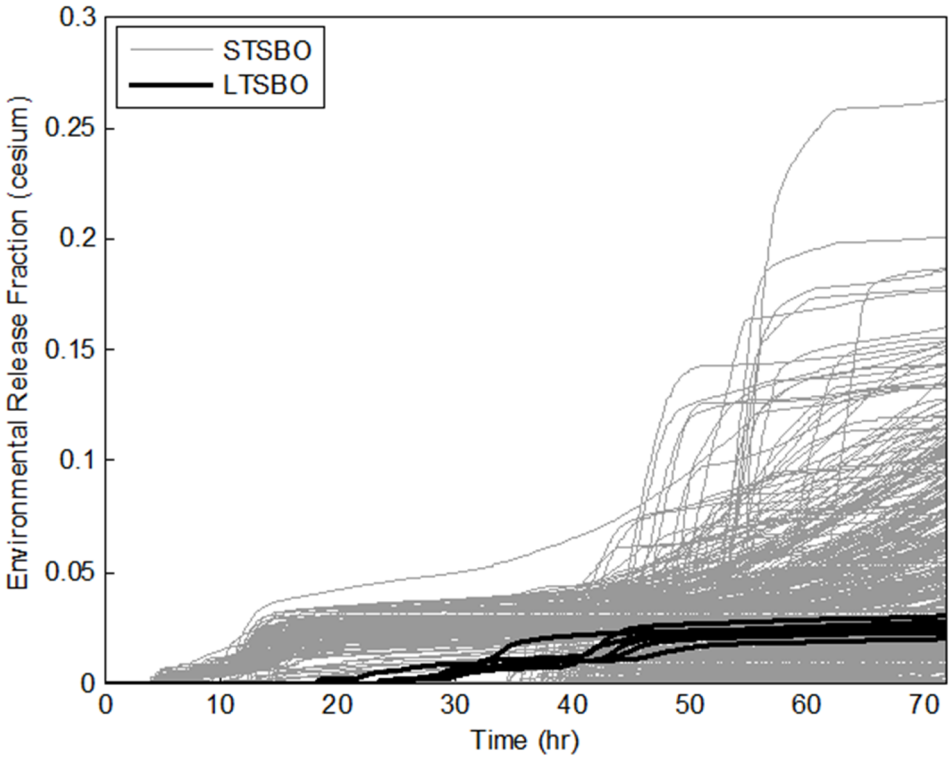

Figure ES-3 Cesium release to the environment for variations of unmitigated STSBO and LTSBO

The base case STSBO and LTSBO analyses indicate that a near complete melting of ice can occur as a result of flow of steam and hot gases following the failure of the reactor coolant system pressure boundaries. Complete melting of the ice has the beneficial effect of lowering containment pressure in the long term however it can make hydrogen combustion more likely in some situations. Igniters would delay but not alleviate potential containment overpressure failure following lower head failure if no other mitigation systems are available.

Regression and single-realization analysis results show that uncertain accident progression parameters (of those included in the analysis) most important to release timing are those affecting the timing of the containment failure, which naturally included the containment rupture pressure. An early containment failure was most likely if the hydrogen was distributed throughout the containment prior to the development of a strong ignition source, which was influenced by an early failure of the pressurizer safety valve (low number of safety valve cycles) and a large flow area for failed safety valve. Uncertain accident progression parameters most important to release magnitude (cesium and iodine release fraction) are the ones that affect the timing of the containment failure and events that contribute to fission product revaporization, which included the number of safety valve cycles and the failed safety valve flow area. Uncertain accident progression parameters most important to hydrogen production include the melting temperature of the eutectic formed from fuel (UO_2) and oxidized cladding (ZrO_2), and the parameters that lead to reactor coolant system depressurization (i.e., few pressurizer safety valve cycles before failure and the subsequent flow area of the failed safety valve).

For the LTSBO, sensitivity calculations show that hydrogen combustion-induced failure occurs ~18-24 hours after accident initiation. The TDAFW system is very important in extending core cooling and allowing more time for implementation of additional mitigation.

The MACCS model was developed using information from the site-specific emergency preparedness programs and State emergency response plans to reflect timing of offsite protective action decisions. Scenarios that are assumed to be initiated by a seismic event consider the earthquake's impact on infrastructure (i.e., loss of bridges). As with the accident progression analyses, key uncertain parameters were varied as part of the integrated MACCS uncertainty analyses. There were over three hundred individual parameters that were varied, within the parameter groups[2] identified in Table ES-3.

Table ES-3 Uncertain MACCS parameter groups used in unmitigated STSBO UA

Atmospheric Dispersion	• Crosswind Dispersion Linear Coefficient • Vertical Dispersion Linear Coefficient • Time-Based Crosswind Dispersion Coefficient
Deposition	• Wet Deposition • Dry Deposition Velocities
Emergency Response	• Evacuation Delay • Evacuation Speed • Hotspot Relocation Time and Dose Criterion • Normal Relocation Time and Dose Criterion
Shielding Factors	• Groundshine Shielding Factors • Inhalation Protection Factors
Early Health Effects	• Lethal dose to 50% of the population (LD_{50}) • Shape factor in hazard function • Threshold dose
Latent Health Effects	• Dose and Dose Rate Effectiveness Factor • Lifetime Cancer Fatality Risk Factors • Long Term Inhalation Dose Coefficients
Aleatory Uncertainty	• Weather Trials

Similar to the results from the Peach Bottom and Surry SOARCA analyses, the Sequoyah analyses show essentially zero individual early fatality risk and a very low individual risk of fatal cancer for the population close to the plant. The relatively slow releases allow effective protective actions to limit exposures to offsite populations. Even for STSBO variations leading to early containment failure in which the release to the environment begins prior to the completion of the 0-10 mile emergency planning zone (EPZ) evacuation, there is essentially zero individual early fatality risk and the individual cancer fatality risk to residents within ten miles of the plant is very low – a lifetime risk of fatal cancer following an accident of approximately 0.07 percent. When the very low likelihood of the accident occurring is also considered, which has been estimated to be on the order of one per several hundred thousand

[2] Some parameter groups represent multiple individual parameters. For example, latent health effects parameters are radionuclide-specific and organ-specific.

years of reactor operation, the overall risk is much lower. For comparison, the average lifetime risk of fatal cancer to a member of the US population is approximately 20 percent.

Figure ES-4 shows for selected deterministic cases of the unmitigated STSBO, conditional (on the occurrence of the core damage scenario) scenario-specific probabilities of a latent cancer fatality (LCF) for an individual located within the EPZ (0-10 miles from the plant), an individual residing outside the EPZ (10-20 miles from the plant), and within the local region (i.e., within 50 miles of the plant). Calculations illustrated in this figure use the linear no threshold (LNT) dose response model that assumes all dose, no matter how small, results in health risk. In Figure ES-4, the cross-hatched sections of the bars represent the individual LCF risk due to emergency phase exposures (in the first week of the accident) while the solid sections represent the individual LCF risk due to doses experienced in the intermediate and long-term phases of the accident (from one week to potentially decades). This figure shows that individual LCF risk calculations are generally dominated by long-term exposure to small annual doses (below 2 rem in the year of the accident and below 500 mrem per year in subsequent years corresponding to the habitability criterion) for evacuees and relocated populations returning to their homes after the accident and being exposed to residual radiation over a long period of time. The use of dose response models that truncate annual doses below certain levels results in a further reduction to the individual LCF risks.

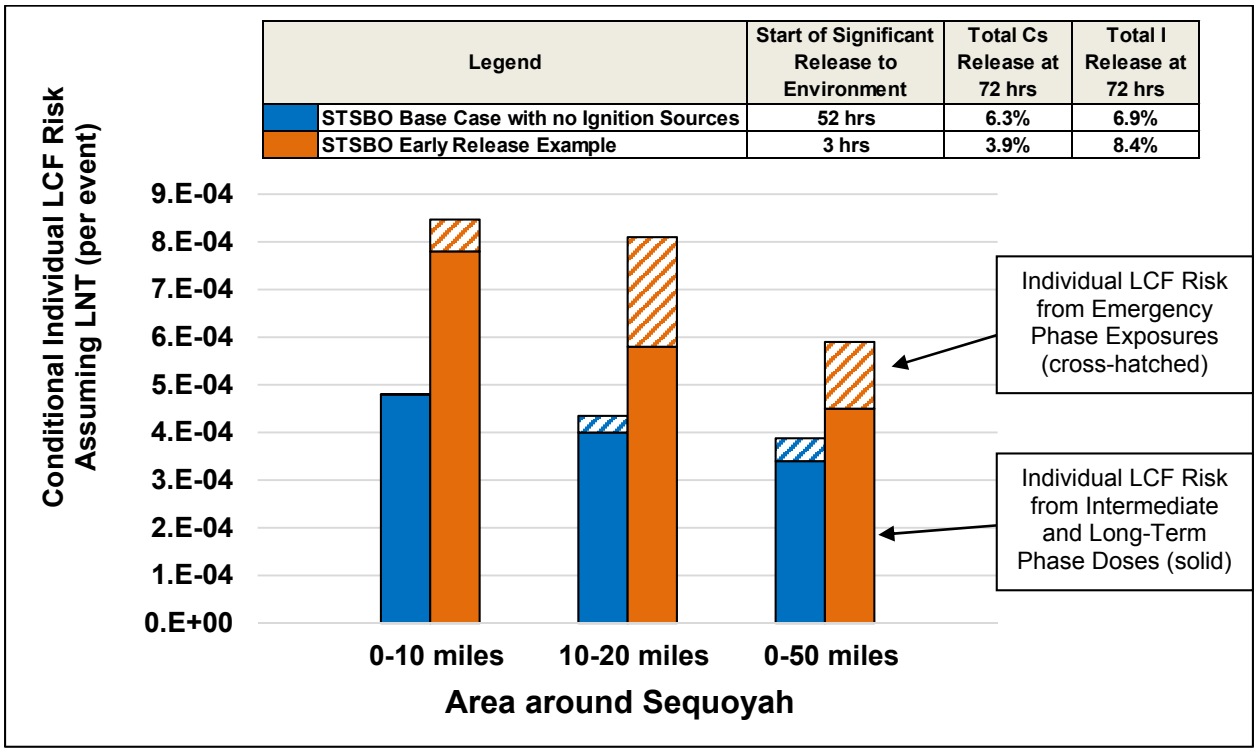

Figure ES-4 Individual latent cancer fatality risk conditional on unmitigated STSBO (per event)

Regression analysis results show that uncertain input parameters (of those included in the analysis) that show importance to individual LCF risk in the STSBO cases include: failed safety

valve flow area (and number of safety valve cycles experienced, in some cases), the cancer fatality risk factor for the "residual" organ[3] (and sometimes other organs), dose and dose rate effectiveness factor for the "residual" organ, the groundshine shielding factors, and the containment rupture pressure.

Figure ES-5 shows conditional (per event) individual LCF risk calculations for the 0-10 mile EPZ population for unmitigated SOARCA scenarios for Peach Bottom, Surry, and Sequoyah. This figure provides deterministic base case results as well as UA results for scenarios analyzed (Sequoyah unmitigated STSBO in this report, Peach Bottom unmitigated LTSBO in NUREG/CR-7155, and Surry unmitigated STSBO and STSBO with thermally induced steam generator tube rupture (TISGTR) in a forthcoming NUREG/CR). While there are differences in the modeling of each scenario, this shows that Sequoyah results in terms of individual LCF risk are comparable to those calculated for the other SOARCA pilot plants. The individual LCF risk is often in the range of 1E-4 to 1E-3 which can be considered small given that the severe accidents have a contribution to core damage frequency typically on the order of 1E-5 per year of reactor operation or lower. Sequoyah SOARCA unmitigated STSBO results show that the range in individual LCF risk due to uncertainty in the selected MELCOR and MACCS input parameters is not very large—approximately one order of magnitude separates the 5th and 95th percentile values.

[3] MACCS uses eight cancer sites (organs), seven of which are specific (lung, red bone marrow, bone, breast, thyroid, liver, and colon) and the last of which ("residual") is used as a surrogate for the remaining soft tissues not explicitly modeled.

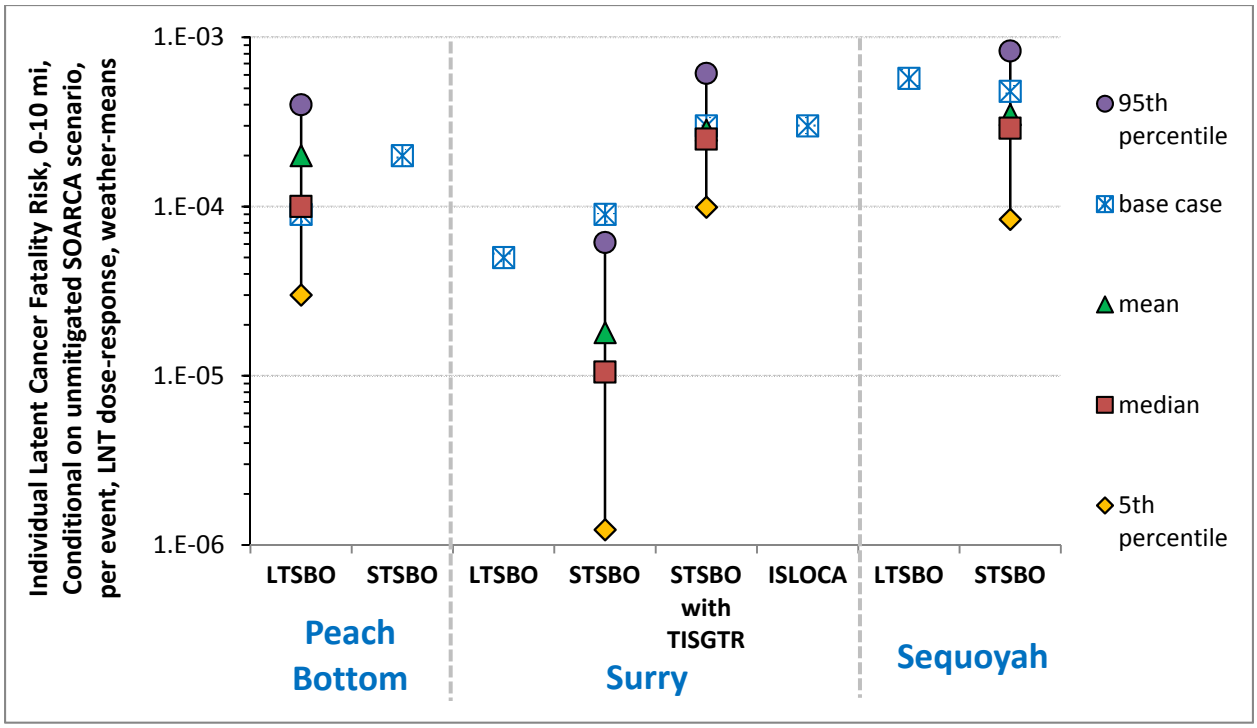

Figure ES-5 Comparison of Peach Bottom, Surry, and Sequoyah SOARCA unmitigated scenarios in terms of conditional (per event) individual latent cancer fatality risk within 10 mile radius using LNT dose-response and mean values over weather variations

In summary, this analysis reinforces the results of past analyses of ice condenser containments showing that successful use of igniters is effective in averting early containment failure. The relatively slow releases allow effective protective actions to limit exposures to offsite populations. Even for scenarios resulting in early containment failure (radioactive release to the environment prior to completion of evacuation for the 0-10 mile EPZ), resulting individual fatal cancer risks are very small. Although early releases were calculated, under these specific conditions, for the Sequoyah SOARCA STSBO, health risks are projected to be low, with essentially zero individual early fatality risk. Quantitative Sequoyah SOARCA results are specific to Sequoyah and the scenarios evaluated herein. The insights derived from these analyses may be generally applicable for other PWRs with ice condenser containments, but additional work would be needed to confirm this because differences exist in plant-specific designs, procedures, and emergency response.

ACKNOWLEDGMENTS

Numerous NRC and Sandia National Laboratories (Sandia) managers and technical staff contributed to the production of the Sequoyah SOARCA deterministic and uncertainty analyses. The NRC manager, Patricia Santiago, and project managers, Jonathan Barr, Salman Haq, and AJ Nosek provided the leadership to ensure this project met the objectives of the program and ensured sufficient resources were available. Tina Ghosh served as the NRC technical lead for the uncertainty applications. Additional NRC staff developed computer code models, conducted accident progression and offsite consequence simulations, and analyzed and documented results. Sandia technical staff, including Kyle Ross, Nathan Bixler, Joseph Jones, Matt Denmen, Aubrey Eckert, Dusty Brooks, Doug Osborn, and Jeff Cardoni performed research in developing technical bases for parameters, enhanced the state of the MELCOR model, and advanced the regression techniques used in the analysis. Mr. KC Wagner of dycoda, Inc. supported model development and analysis of results. The Sequoyah SOARCA project team also acknowledges the feedback and guidance provided by the project's technical advisory group consisting of senior level experts throughout NRC. The project team also acknowledges the participation of Tennessee Valley Authority Sequoyah staff who supported site visits, provided information to NRC staff, and who have reviewed the report and provided a "fact check" of the project's modeling of Sequoyah.

ABBREVIATIONS AND ACRONYMS

ACRS	Advisory Committee on Reactor Safeguards
AFW	auxiliary feedwater
ANS	American Nuclear Society
atm	atmosphere
ARV	atmospheric relief valve
BEIR	Biological Effects of Ionizing Radiation
BWR	boiling water reactor
CCP	centrifugal charging pump
CCDF	complementary cumulative distribution function
CCI	core-concrete interaction
CDF	cumulative distribution function
CFC	containment fragility curve
CMTR	certified material property test reports
CPI	Consumer Price Index
CPI-U-RS	Consumer Price Index for urban consumers
CST	condensate storage tank
CV	control volume
CVH	control volume hydrodynamics
CVCS	chemical and volume control systems
DCF	dose conversion factor
DDREF	dose and dose rate effectiveness factor
DF	decontamination factor
EAB	exclusion area boundary
EAL	emergency action level
EAS	emergency alert system
EF	early fatality
ECCS	emergency core cooling systems
ECST	emergency condensate storage tank
EDG	emergency diesel generator
ELAP	extended loss of AC power
EOP	emergency operating procedure
EPA	Environmental Protection Agency
EPZ	emergency planning zone
ETE	evacuation time estimate
FGR	Federal Guidance Report
FP	flow path
FSAR	final safety analysis report
FSI	FLEX support instructions
FTC	failure to close
FTO	failure to open
GE	general emergency
gpm	gallons per minute
GSDE	ground shine deposited energy
GSI	generic safety issue
Gy	gray
HMS	hydrogen mitigation system
HPS	Health Physics Society
HTC	heat transfer coefficient

IPE	individual plant examination
IPEEE	Individual Plant Examination for External Events
LCF	latent cancer fatality
LD_{50}	lethal dose to 50% of population
LHS	Latin hypercube sampling
LET	linear energy transfer
LOOP	loss of offsite power
LNT	linear no threshold
LTSBO	long-term station blackout
LWR	light water reactor
m	meter
MACCS	MELCOR Accident Consequence Code System
MARS	Multivariate Adaptive Regression Splines
MCCI	molten core concrete interactions
MD-AFW	motor-driven auxiliary feedwater
mph	miles per hour
MSIV	main steam isolation valve
MSL	main steam line
MSS	main steam system
NRC	Nuclear Regulatory Commission
NTTF	Near Term Task Force
NWS	National Weather Service
ORO	offsite response organization
PAG	protective action guideline
PAR	protective action recommendation
PDF	probability density function
PGA	peak ground acceleration
PORV	power operated relief valve
PRA	probabilistic risk assessment
PRT	pressure relief tank
PRY	per reactor year
PWR	pressurized water reactor
QHO	quantitative health objective
RCP	reactor coolant pump
RCS	reactor coolant system
RPV	reactor pressure vessel
SAE	Site Area Emergency
SBO	station blackout
scfh	standard cubic feet per hour
SG	steam generator
SGTR	steam generator tube rupture
SME	subject matter expert
SNL	Sandia National Laboratories
SOARCA	State-of-the-Art Reactor Consequence Analyses
SPAR	Standardized Plant Analysis Risk
SPAR-AHZ	SPAR All Hazards
SRRC	standardized rank regression coefficients
SRS	simple random sampling
SSC	systems, structures, and components
STSBO	short-term station blackout
SV	safety valve

TDAFW	turbine driven auxiliary feedwater
TVA	Tennessee Valley Authority
UA	uncertainty analysis
USBGR	U.S. background

1. INTRODUCTION

This document describes the severe accident analyses performed for the Sequoyah Nuclear Plant (Sequoyah) as part of the U.S. Nuclear Regulatory Commission's (NRC's) State-of-the-Art Reactor Consequence Analyses (SOARCA) project.

1.1 Background

The NRC initiated the SOARCA project to develop best estimates of the offsite radiological health consequences for potential severe reactor accidents. The project initially envisioned analyzing all U.S. nuclear power plants but then chose to analyze pilot plants generally representative of the major plant and containment design types. The first two pilot plants are the Peach Bottom Atomic Power Station (Peach Bottom) in Pennsylvania and the Surry Power Station (Surry) in Virginia. Peach Bottom is generally representative of U.S. operating reactors using the General Electric boiling-water reactor (BWR) design with a Mark I containment. Surry is generally representative of U.S. operating reactors using the Westinghouse pressurized-water reactor (PWR) design with a large, dry (subatmospheric) containment. The third pilot plant, Sequoyah, was selected as a representative of the ice condenser containment design and is the subject of this report.

The Peach Bottom and Surry SOARCA analyses evaluated plant improvements and changes that were not reflected in earlier NRC publications. SOARCA included system improvements; improvements in training and emergency procedures; offsite emergency response; improvements codified in 10 CFR 50.54(hh)(2) [1]; and plant changes, such as power uprates and higher core burnup. To provide a perspective between SOARCA results and more conservative offsite consequence estimates, SOARCA results were compared to NUREG/CR-2239 (December 1982), "Technical Guidance for Siting Criteria Development" (also referred to as the 1982 Siting Study) [2]. The SOARCA analysis and reports help the NRC communicate its current understanding of severe-accident-related aspects of nuclear safety to stakeholders, including Federal, State, and local authorities; licensees; and the general public.

A systematic approach was implemented in SOARCA to calculate the potential consequences of the analyzed severe accidents. The project team first decided it could learn more by rigorously and realistically analyzing a relatively small number of important accident scenarios instead of carrying out less detailed modeling of many scenarios. Therefore, the team selected a core damage frequency threshold to help select scenarios to analyze (greater than 1E-7 per operating year for bypass accidents and greater than 1E-6 per operating year for non-bypass accidents). Accident progression calculations used the MELCOR computer code. For scenarios leading to an offsite release of radioactive material, SOARCA analyzed atmospheric dispersion, emergency response, and potential health consequences using the MELCOR Accident Consequence Code System (MACCS) computer code.

SOARCA's key results for Peach Bottom and Surry include the following:

- When operators are successful in using available onsite equipment during the accidents analyzed in SOARCA, they can prevent the reactor from melting or can delay or reduce releases of radioactive material to the environment.

- SOARCA analyses indicate that all modeled accident scenarios, even if operators are unsuccessful in stopping the accident, progress more slowly and release much smaller

amounts of radioactive material than calculated in earlier studies such as the 1982 Siting Study [2].

- As a result, public health consequences from severe nuclear power plant accidents modeled in SOARCA are smaller than previously calculated.

- The delayed releases calculated provide more time for emergency response actions, such as evacuating or sheltering for affected populations. For the scenarios analyzed, SOARCA shows that emergency response programs, if implemented as planned and practiced, reduce the risk of public health consequences.

- Both mitigated (operator actions are successful) and unmitigated (operator actions are unsuccessful) cases of all modeled severe accident scenarios in SOARCA cause essentially no risk of death to the public from ionizing radiation during or shortly after the accident.

- SOARCA's calculated longer term cancer fatality risks for the accident scenarios analyzed are millions of times lower than the general U.S. cancer fatality risk from all causes.

The SOARCA analysis of Peach Bottom and Surry is documented in a series of NUREG reports. NUREG-1935, "State-of-the-Art Reactor Consequence Analyses (SOARCA) Report," was published in 2012 and provides a summary of the project's objectives, methods, results, and conclusions [3]. NUREG/CR-7110, "State-of-the-Art Reactor Consequence Analyses Project," Volume 1, "Peach Bottom Integrated Analysis," and Volume 2, "Surry Integrated Analysis," provide additional technical details on the analyses conducted for each of the pilot plants [4][5]. In addition, the staff developed an information brochure, NUREG/BR-0359, "Modeling Potential Reactor Accident Consequences," to facilitate communication with stakeholders, including the public [6]. The staff documented best modeling practices as applied in SOARCA for the MELCOR and MACCS codes in NUREG/CR-7008 and NUREG/CR-7009, respectively [7][8].

NRC staff completed an uncertainty analysis (UA) of the SOARCA unmitigated long term station blackout (LTSBO) at Peach Bottom to develop insights into the overall sensitivity of SOARCA results to uncertainty in inputs; to identify the most influential input parameters for releases and consequences; and to demonstrate a UA methodology that could be used in future source term, consequence, and site level 3 probabilistic risk assessment (PRA) studies. Integrated analyses using about 40 independent MELCOR and MACCS parameter groups corroborate the overall SOARCA results and conclusions for the selected accident scenario. The Peach Bottom UA is documented in NUREG/CR-7155 [9].

Following the completion of the SOARCA analyses of the first two pilot plants, the NRC staff issued a memorandum to the Commission, SECY-12-0092 [10], recommending completion of SOARCA analyses of the third pilot plant, Sequoyah, a PWR with an ice condenser containment. This analysis, as well as a UA of a SOARCA Surry scenario, was recommended to

inform agency activities such as implementation of the Fukushima[4] Near Term Task Force (NTTF) Tier 3 recommendations related to hydrogen control and reliable hardened vents for containment designs other than BWR Mark I and Mark II and the site level 3 PRA project for Vogtle Units 1 and 2. Both analyses were also recommended to expand on the body of knowledge on severe accident progression and consequences developed in the SOARCA pilot plant analyses. The SOARCA analysis of an ice condenser plant was recommended because its relatively low design pressure and reliance on hydrogen igniters makes it potentially susceptible to early failure from hydrogen combustion during a severe accident.

In December 2012, the Commission approved the staff's recommendations. Prior to this recommendation, Sequoyah had been the third SOARCA pilot plant after Peach Bottom and Surry. Plant and site information had been gathered and the MELCOR plant model was being updated. These Sequoyah activities were paused in 2009 in order to focus on completion of the Peach Bottom and Surry analyses. Because the staff had already started the process of analyzing Sequoyah, it was the logical candidate for the follow-on analyses recommended in SECY-12-0092. Sequoyah is generally representative of the fleet of ice condenser containment plants in the U.S. although there are differences from unit to unit and site to site. With ten units[5], nine of which are operational[6], the PWR ice condenser design is the third most prevalent after the PWR large dry containment and the BWR Mark I containment.

Figure 1-1 shows that the typical design pressure of a PWR ice condenser containment is the lowest among U.S. nuclear power plant containment types, around 12 psig (83 kPa), slightly below that of the BWR Mark III containment. Ice condensers are pressure suppression containments and use ice to absorb heat in a severe accident. Unlike the BWR Mark I and Mark II pressure suppression containments, ice condensers are not inerted with nitrogen. Therefore they use alternating current (AC) powered igniters to introduce sparks that burn hydrogen in a gradual, controlled manner before it can rise to levels that could result in a highly energetic deflagration or detonation that could challenge the containment. The susceptibility of ice condenser (and Mark III) containments to early failure from hydrogen combustion during a severe accident was analyzed in the NRC's generic safety issues (GSI) program as GSI-189. The GSI-189 technical assessment led staff to recommend the addition of a backup power supply for the igniters for plants with an ice condenser or Mark III containment. Licensees of these plants committed to voluntarily develop and maintain the capability to provide backup power to the containment hydrogen igniters during severe accidents and certain security scenarios. The staff accepted these commitments and verified acceptable implementation of the commitments as of January 2013 [11].

---

[4] On March 11, 2011, a 9.0-magnitude earthquake struck Japan and was followed by a 45-foot tsunami, resulting in extensive damage to the nuclear power reactors at the Fukushima Dai-ichi facility. The NRC has taken significant action to enhance the safety of reactors in the United States based on the lessons learned from this accident. NRC has developed a webpage (http://www.nrc.gov/reactors/operating/ops-experience/japan-dashboard.html) to serve as a navigation hub to follow the NRC's progress in implementing the many different lessons-learned activities.

[5] There are 10 reactors at five sites with ice condenser containments: Catawba Units 1 & 2 in South Carolina, DC Cook Units 1 & 2 in Michigan, McGuire Units 1 & 2 in North Carolina, and Sequoyah Units 1 & 2 and Watts Bar Units 1 & 2 in Tennessee.

[6] Watts Bar Unit 2 is scheduled to start commercial operation in 2016 [16].

The ice condenser containment design was also analyzed in NUREG-1150 in which the staff conducted a level 3 PRA of five plants representing different design types [12]. The Sequoyah analysis was documented in greater detail in NUREG/CR-4551, Volume 5 [13].

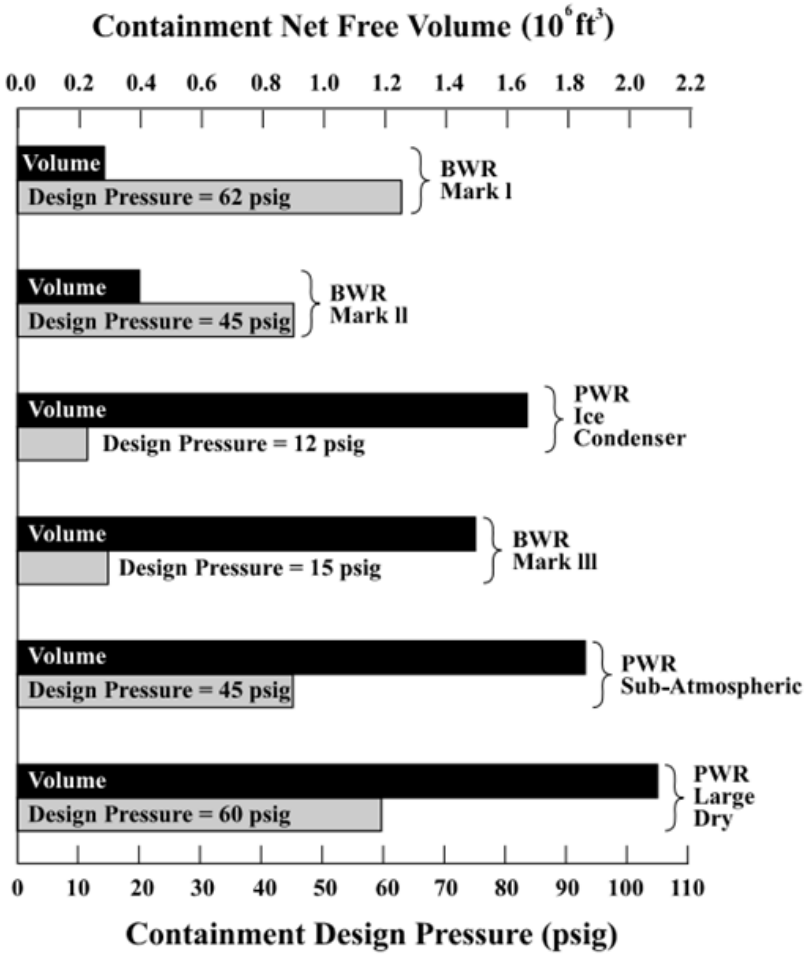

Figure 1-1 Typical Containment Volumes and Design Pressures *(Figure 4.1-1 from NUREG/CR-6042, Rev. 2 [14]*)

1.2 General Sequoyah Plant and Site Information

Sequoyah is located near Soddy-Daisy in Hamilton County, Tennessee, about 18 mi (29 km) northeast of Chattanooga along the Tennessee River. Sequoyah is owned and operated by Tennessee Valley Authority (TVA). Sequoyah has two Westinghouse 4-loop PWRs with ice condenser containments. Units 1 and 2 received their operating license in 1980 and 1981, began commercial operation in 1981 and 1982, and received their renewed licenses in 2015 to operate until 2040 and 2041, respectively. Both units are licensed at 3455 MW_{th} and have operated at a 92% (Unit 1) and 89% (Unit 2) average annual capacity factor for years 2008-2014 [15]. Spent fuel is kept at Sequoyah in a spent fuel pool and in dry cask storage. An aerial view of Sequoyah is shown in Figure 1-2 looking from the north to the south.

Figure 1-2 View of Sequoyah from the north

1.3 Sequoyah SOARCA Scope

Similar to the Peach Bottom and Surry SOARCA analyses [4][5], the priority of the Sequoyah analysis is on detailed analytical modeling of a set of important severe accident scenarios considering both likelihood and potential consequences. Like Peach Bottom and Surry, the scope is on single unit reactor accident scenarios postulated to be caused by seismic events. The Sequoyah analysis does not consider multiunit accidents, spent fuel pool or dry cask storage accidents, accidents during shutdown or low-power modes, extreme seismic events that lead directly to gross containment failure with simultaneous reactor core damage, or accidents caused by malevolent acts[7]. The Sequoyah SOARCA analysis is not a PRA, and it does not attempt to quantify the frequency of each modeled variation in the accidents analyzed. While the Peach Bottom and Surry SOARCA analyses [4][5] considered a variety of scenarios including station blackouts (SBOs), steam generator tube ruptures (SGTRs), and interfacing systems loss of cooling accidents (ISLOCAs), the Sequoyah SOARCA analysis is focusing specifically on short-term SBO (STSBO) and long-term SBO (LTSBO). These scenarios involve an immediate loss of offsite and onsite AC power. In the STSBO variation, early failure of the

---

[7] The NRC's Site Level 3 PRA of Vogtle Units 1 & 2 includes within its scope multiunit accidents, spent fuel pool and dry cask accidents, and accidents during shutdown and low-power modes. Information on the objectives and status of the Site Level 3 PRA is available on the NRC's website from the 2015 Regulatory Information Conference: http://www.nrc.gov/public-involve/conference-symposia/ric/past/2015/docs/abstracts/sessionabstract-10.html

turbine driven auxiliary feedwater (TDAFW) is assumed and direct current (DC) power is also immediately unavailable; thus, the accident can progress to core damage in the "short term". In the LTSBO variation, DC power is available until station batteries deplete and thus the accident can progress to core damage in the "long term". These are important scenarios for an ice condenser plant because of its reliance on AC-powered igniters for hydrogen control. The Surry SOARCA analyses revealed insights on SGTRs and ISLOCAs and because those are not expected to progress much differently in an ice condenser containment plant, they are excluded from the Sequoyah analysis.

1.4 Approach for Uncertainty Considerations

The initial SOARCA studies were comprised of a deterministic base case or "best estimate" analysis (documented in NUREG-1935 and NUREG/CR-7110 Volumes 1 and 2) for the Peach Bottom and Surry plants. An integrated uncertainty analysis[8] for one of the Peach Bottom accident scenarios was begun before the conclusion of the initial SOARCA project, and subsequently completed and documented in NUREG/CR-7155. A second uncertainty analysis for a Surry accident scenario, the unmitigated STSBO, was also subsequently completed and will be documented as a NUREG/CR report [17]. At the conclusion of the original SOARCA project, one of the recommendations of the NRC's Advisory Committee on Reactor Safeguards (ACRS) was to conduct future deterministic "best estimate" studies and associated uncertainty analyses in parallel.

For the Sequoyah SOARCA analysis, staff integrated consideration of uncertainty into accident progression and offsite consequence analyses from the beginning of the project. The approach used to consider uncertainty varied by accident scenario. Because this study had a particular focus on the potential for early containment failure, and ice condenser containment-specific issues, an integrated uncertainty analysis was included for the two scenarios with highest likelihood of early containment failure: the unmitigated STSBO[9] cases with, and then without, the presence of random ignition sources. The analysis of remaining scenarios applied sensitivity analyses to examine variations in system response and results. The different scenarios, their variations, and the approach to considering uncertainty are listed in Table 1-1.

---

[8] The original SOARCA study did not include a formal human reliability analysis within its scope. The Peach Bottom Uncertainty Analysis also did not include human actions within the scope of its integrated assessment. It did, however, document the results of a sensitivity analysis varying the timing of the two operator actions that are credited in the unmitigated LTSBO.

[9] Because the unmitigated STSBO does not credit human actions, the UA also does not address human actions.

Table 1-1 Sequoyah SOARCA scenarios, variations, and approach for considering uncertainty

SBO Type	Variation	Approach
STSBO	• Unmitigated (igniters not available and no random ignition sources modeled)	Integrated UA (Deterministic and probabilistic analyses)
	• Unmitigated (igniters not available but random ignition sources modeled)	Integrated UA (Probabilistic analyses)
	• Mitigated (igniters available)	Deterministic sensitivity analysis
LTSBO	• Igniters	Deterministic sensitivity analysis
	• Hydrogen ignition criteria	Deterministic sensitivity analysis
	• Battery duration	Deterministic sensitivity analysis
	• Safety valve behavior	Deterministic sensitivity analysis

For the MELCOR accident progression analysis, the parameters selected for sampling in the integrated UA were based on insights from previous UAs, and new ice condenser containment-specific and hydrogen-specific considerations. Insights from the Surry SOARCA UA [17] were leveraged heavily to identify a reduced set of parameters to include in the Sequoyah integrated UA. Ice condenser containment-specific and hydrogen-specific considerations added new parameters to the list, resulting in the selection of 11 MELCOR parameters to vary in the integrated UA. These parameters are further described in Chapter 3.

For the MACCS offsite consequence analysis, the set of uncertain parameters was selected based on insights from previous UAs and based on a review to identify any new site-specific considerations. Parameters varied as part of the Sequoyah integrated UA are the same as those in the Surry SOARCA UA, with the addition of a time-based crosswind dispersion coefficient in Sequoyah. The selected parameter groups are further described in Chapter 5.

For a more complete discussion of the UA methodology used in this study, the reader is directed to Chapter 3 of the Surry SOARCA UA [17] and Appendix A of the Peach Bottom SOARCA UA [9] which describe the probabilistic methodology in even more detail. The reader is also referred to the “Glossary of Uncertainty Analysis Terms” that is contained as an appendix to both of these earlier SOARCA UAs.

The Sequoyah integrated UA for the two variations of unmitigated STSBO (with and without random ignition sources) again employed a Monte Carlo approach as described in Appendix A of this report. Uncertainty in chosen MELCOR and MACCS parameters was described by assigning distributions of possible values. The uncertainty in these input parameters was then propagated to results of interest using Monte Carlo simulation with simple random sampling in both the MELCOR uncertainty engine and WinMACCS, the Windows-based user interface for MACCS. The Monte Carlo results were post-processed and analyzed using four regression techniques – linear rank regression, quadratic regression, recursive partitioning, and multivariate adaptive regression splines (MARS) – as well as scatter plots and investigation of interesting single realizations (the outcome of one vector of sampled input values of the ‘n’ successful Monte Carlo realizations). The purpose of the regression analysis and scatter plots is to determine the contributions of uncertain inputs to the uncertainty in the analysis results. The single realization analyses further help construct phenomenological explanations of

interesting variations in system behavior (e.g., variations in containment failure time) that are dependent on uncertain inputs.

MELCOR, MelMACCS, and MACCS are the three primary codes used in the integrated UA. These codes are continually enhanced, updated, and maintained as part of the NRC research program. As improvements or fixes are implemented, the codes are updated. The codes were designed for outputs from one code to become inputs for the next code to support deterministic analyses. The codes have been integrated for use in analyzing uncertainty in the same manner as implemented for the Peach Bottom UA [9] and Surry UA [17], as illustrated in Figure 1-3.

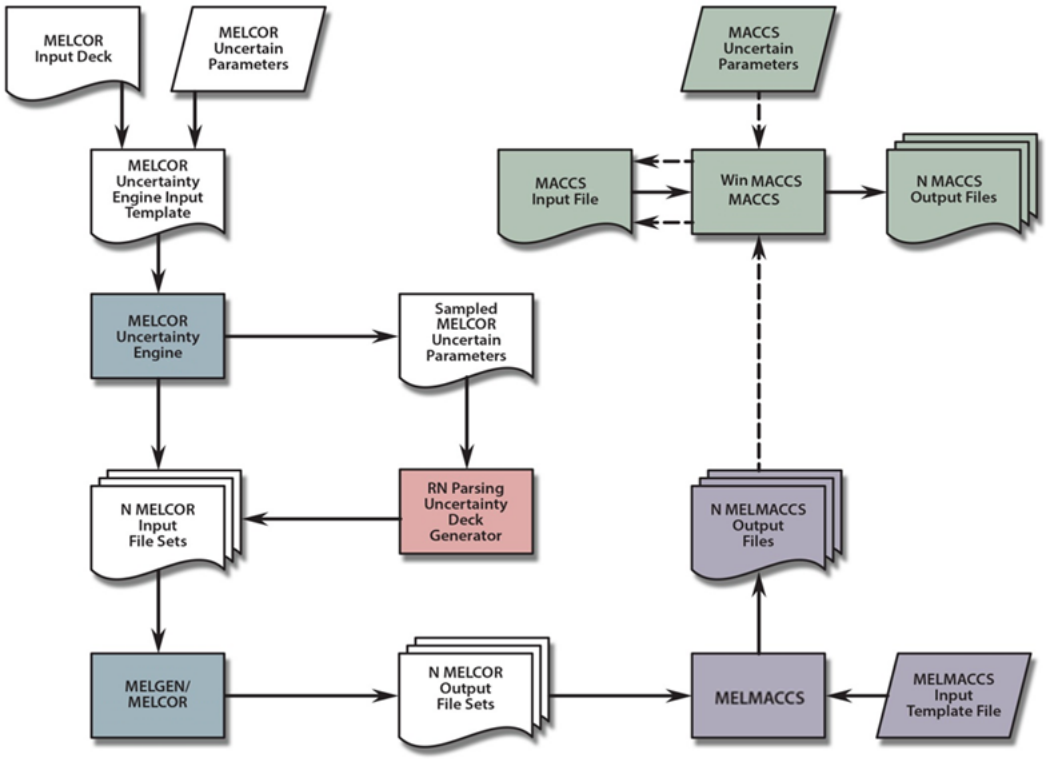

Figure 1-3 Diagram of code information flow for uncertainty analysis

1.5 Outline of Report

Chapter 2 of this report describes the severe accident scenarios modeled, their estimated frequency, and the seismic event postulated to initiate them. Chapter 3 describes the MELCOR model of Sequoyah used in the analyses and the approach used to develop it. Chapter 3 also discusses the MELCOR input parameters which are modeled using a distribution of values to account for epistemic model uncertainty. Chapter 4 describes the results of MELCOR accident progression calculations. Chapter 5 describes the MACCS model of Sequoyah, the approach used to develop it, and the uncertain MACCS input parameters. Chapter 6 describes the offsite consequence results in terms of individual early and latent cancer fatality risks along with the regression analysis used to assess the importance of MELCOR and MACCS uncertain input parameters on the results. Chapter 7 provides a brief conclusion of the study's results and insights gained. References are listed in Chapter 8. Three appendices provide additional detail

on UA methodology (Appendix A), MACCS input parameters (Appendix B), and an evacuation roadway capacity analysis (Appendix C).

2. ACCIDENT SCENARIO DEVELOPMENT

2.1 Background

Ice condenser plants such as Sequoyah are unique because of low containment design pressure (12 psig for Sequoyah) and a relatively small volume containing a four loop PWR reactor coolant system (RCS) having a power rating of 3455 MWt. A severe accident in such a plant can generate high concentrations of hydrogen which can potentially lead to early containment failure during an SBO. The scope of this study is limited to SBO scenarios [10].

2.2 Scenario Selection

Information from the NRC's Standardized Plant Analysis Risk (SPAR) model for Sequoyah was used to assist the selection of SBO scenarios as candidates to be studied in this project. Loss of offsite power (LOOP) events contribute significantly to plant core damage frequency. A further examination of the failure combinations that lead to core damage shows that SBO contributions are dominant.

SBO events may arise from different hazards, such as internal events, seismic events, internal fire events, external flooding events, etc. Moreover, their occurrence frequencies are plant and site specific. Based on insights from available studies, high-pga seismic events (0.5g pga and above) are chosen as the representative initiators for the severe accident SBO scenarios to be analyzed in this study. SBO events stemming from other hazard categories would provide different additional event frequencies, recovery and mitigation opportunities. The two selected SBO scenario variations are (1) an early failure of TDAFW (STSBO) which includes loss of DC power systems and (2) a late failure of TDAFW (LTSBO).

Directly below is a description of the initiating event for both scenarios. Sections 2.2.1 and 2.2.2 define the STSBO and LTSBO accident scenarios, respectively. Section 2.3 discusses mitigation measures for the LTSBO scenario.

The initiating event for both accident scenarios in this study is a beyond design basis earthquake resulting in a LOOP due to a damaged transmission line or switchyard components. The initiating event is similar to that in Surry and Peach Bottom SOARCA analyses. The emergency diesel generators (EDGs) also fail to start or the emergency AC power system becomes inoperable, and the event is classified as an SBO, i.e., loss of all onsite and offsite AC power. In PWRs this can lead to loss of cooling water in the steam generators (SGs) and loss of water inventory in the RCS that covers and cools the core.

2.2.1 Short-term Station Blackout (STSBO)

A seismically initiated STSBO has an estimated contribution to the CDF of approximately one in 500,000 years of reactor operation. For Sequoyah, STSBO scenarios include AFW unavailable due to a loss of DC power, failure of a TDAFW[10] system component, or loss of the water supply

[10] The authors note that TVA has upgraded and performed modifications to the TDAFW system to better cope with external events such as earthquakes. However, the NRC had not finished a review of these upgrades at the time of this report and thus a discussion of this new capability is not included.

due to the seismic initiating event. The TDAFW uses DC power to open the motor-driven trip/throttle valve that supplies steam to the turbine and to the control governor valve. However, the plant emergency procedures include actions to manually perform those functions. The normal supply of water to the TDAFW is the two non-seismically-qualified condensate storage tanks (CSTs). The CSTs are assumed to fail in a large seismic event. There are two backup (seismic Category I) essential raw cooling water (ERCW) system header feeds to each AFW electric pump as an alternate water supply. The AFW turbine pump can be remote-manually aligned to receive water from the ERCW header. However, the AFW is unavailable in the STSBO due to (a) component failure (e.g., batteries/DC power), (b) failure to manually open the steam valve to the TDAFW, or (c) failure to establish a water supply.

A review of the survivability of systems, structures, and components (SSCs) of interest for the accident progression analysis permits an assessment of the assumptions made in that analysis.

Ice Condenser – The Individual Plant Examination for External Events (IPEEE) report for Sequoyah reports a high confidence in low probability of failure (HCLPF) of 0.3 g for the ice condenser using design allowable stresses as acceptance criteria for the estimation. Such criteria are judged to be a conservative indicator of the condenser functionality. A walkdown of the ice condenser for a plant with similar characteristics recently completed in 2014 confirms that the structure of the ice condenser would undergo some structural damage and some ice might drop for the seismic event. It was considered that this damage would not significantly prevent the ice condenser from performing its function. The large number of doors in the ice condenser and its open internal structure is assumed to provide redundancy to establish cooling and condensing pathways.

Auxiliary Feedwater Systems – The natural sources of water for the TDAFW are the two CSTs which were not designed and built as safety-related structures. Using the seismic fragility derived by Nie (2011) for similar steel CST tanks designed for a safe-shutdown earthquake (SSE) similar to that used in the design of Sequoyah, the HCLFPF and median fragility for these tanks are about 0.4g and 0.9g, respectively. This means that there is high confidence that the CST tanks would survive a seismic event with a PGA of 0.4 g and about a 50% likelihood that they would survive a seismic event with a PGA of 0.9 g. According to the Sequoyah final safety analysis report (FSAR), water loss from CST would accumulate in the sump of the turbine building and in the plant holding pond. The plant operator upgraded the auxiliary feedwater (AFW) system and the CST tanks to better cope with external events such as earthquakes but details of that upgrade were not yet reviewed by the NRC at the time of the Sequoyah SOARCA study. Review of those details or related additional information from the plant operator will permit confirmation or revision of this survivability review.

Containment structure and containment isolation system – The IPEEE report for Sequoyah confirms that the steel containment structure has a high seismic capacity and there is high confidence that it would survive the seismic event. Fragility estimates of the isolation systems for one other ice condenser plant with similar characteristics, assuming that the systems for that plant are adequate surrogates for the systems in the Sequoyah plant, indicates that there is high confidence that the isolation systems would survive the seismic event.

The following list shows the key events at the plant for the STSBO scenario, with unavailability of the AFW due to a beyond design basis earthquake. These define the boundary conditions for the unmitigated STSBO base case MELCOR analyses.

- LOOP initiating event, a beyond design basis earthquake, occurs.

- The reactor protection system will automatically actuate upon a LOOP and terminate the fission power reaction – reactor is tripped.
- The EDG, emergency AC, will receive a start signal but will fail.
- The reactor coolant pumps (RCPs) will coast down to stop within few minutes and all other pumps normally running (e.g., chemical and volume control system (CVCS) charging pumps) stop due to loss of AC power.
- Valves designed to fail-close, close to isolate systems and the containment (e.g., Main Steam Isolation Valves (MSIVs)).
- Emergency AC power is not available due to SBO, therefore Motor-Driven AFW (MD-AFW) pumps fail to start.
- TDAFW is inoperable.
- Fission product decay heat continues to heat the water in the reactor vessel.
- The safety valves (SVs) on primary and secondary system open to control the pressure, which decreases the RCS and SG water inventory, respectively.
- The RCP seals start to leak initially at a nominal rate of 21 gpm per pump due to the failure of the pump seal cooling injection.
- AC power recovery prior to core damage is unsuccessful (both offsite and onsite).

2.2.2 Long-term Station Blackout (LTSBO)

A seismically initiated LTSBO has an estimated contribution to core damage frequency of one in approximately 100,000 years of reactor operation. The system availabilities following the seismic initiating event are the same as those noted for STSBO, with one exception – the TDAFW is initially operable in the LTSBO due to the initial availabilities of DC power and one of the AFW water supplies discussed in Section 2.2.1 above.

The following list shows the key events at the plant for LTSBO, due to a beyond design basis earthquake. These define the boundary conditions for the unmitigated LTSBO base case MELCOR analyses.

- LOOP initiating event, a beyond design basis earthquake, occurs.
- The reactor protection system will automatically actuate upon a LOOP and terminate the fission power reaction – reactor is tripped.
- The EDG, emergency AC, will receive a start signal but will fail.
- The RCPs will coast down to stop within few minutes and all other pumps normally running (e.g., CVCS charging pumps) stop due to loss of AC power.

- Valves designed to fail-close, close to isolate systems and the containment (e.g., MSIVs).
- Because DC power is available, the AFW system automatically receives a start signal.
- Emergency AC power is not available due to SBO, therefore MD-AFW pumps fail to start.
- Fission product decay heat continues to heat the water in the reactor vessel.
- The SVs on primary and secondary system are available to control the pressure.
- The RCP seals start to leak initially at a nominal rate of 21 gpm per pump due to the failure of the pump seal cooling injection.
- The supply valve to the AFW steam turbine automatically opens and DC power is available, which starts AFW injection into steam generators.
- The TDAFW pump will automatically maintain the water level in the steam generators, which will remove decay heat from the core using natural convection heat transfer and prevent core damage as long as water inventory is available. The operators will simultaneously attempt to mitigate the accident by restoring AC power or aligning diesel-driven portable pumps.
- Manual DC deep load shedding and secondary depressurization is successful. The secondary depressurization stops at 160 psig to maintain adequate steam pressure for the TDAFW.
- Battery runs out after 8 hours (i.e., nominally with successful load shedding) and all attempts to restore AC power restoration is unsuccessful (both offsite and onsite).
- The AFW steam turbine control valve fully opens following the loss of battery power and increases AFW injection. The AFW steam turbine fails when the SG overfills. No credit is given for local operator actions to keep the AFW pump running, although it is considered in the NRC's SPAR model.
- The atmospheric relief valve closes following the loss of battery power and the SVs open to control pressure.

2.3 Mitigative Measures

Sequoyah operators are expected to follow the emergency procedures, such as ECA-0.0, "LOSS OF ALL AC POWER" during an SBO event. For example, if the TDAFW is inoperable due to failure of DC power, then the operators can start the system by manually opening the steam line valve to start the turbine and control it manually to avoid a STSBO. Recently added FLEX equipment provide many additional options to the operators to restore power, or add components like pumps, alternate sources of water, and piping connections to steam generators or the RCS. Following confirmation of the LOOP and failure of the EDGs, which can take about 15 minutes, the declaration of extended loss of AC power (ELAP) is made typically within one

hour of the SBO. If cooling water level in SG or RCS is not restored, then the peak core temperature can reach 1200 °F within two to three hours and a technical support center becomes operational to start implementation of severe accident mitigation guidelines (SAMGs) and FLEX support instructions (FSIs). Using the plant specific SAMGs and FSIs, the recommended mitigating actions are identified for plant operators. If these actions are successful in time, then the RCS breach can be prevented or containment failures can be delayed long enough to allow emergency evacuation plans to be implemented.

For this project, the SAMGs and recently developed FSIs were reviewed for mitigating actions. The actions identified in the FSIs and the supporting document including time duration for adding mitigating equipment, have been recently submitted by TVA in response to the NRC order EA-12-049 [ML14064A295]. As in past studies, the significance of operable igniters, using backup power generators, was identified. If these igniters have power prior to a significant accumulation of hydrogen into the containment, then early containment failure during an STSBO can be avoided, which allows time to implement emergency protective actions. The generation of a significant amount of hydrogen can be prevented if operators can successfully complete mitigating actions, e.g., maintaining the SG water level and maintaining the water level in the reactor above the top of active fuel.

An unmitigated STSBO will progress quickly, to fuel failure within a few hours, resulting in steam and hydrogen blowdown into containment. This can ultimately lead to containment failure if operator mitigating actions are unsuccessful. Two variations of the unmitigated STSBO are analyzed in this study – one without the presence of random ignition sources, and one with the presence of random ignition sources. An integrated uncertainty analysis is performed for both of these unmitigated STSBO cases. The only potential mitigation that is modeled for the STSBO scenario is successfully supplying power to the igniters. Chapter 4 discusses further details of these STSBO cases.

The LTSBO progresses more slowly and RCS failure is delayed as long as the AFW maintains the steam generator water level. The LTSBO benefits from the initial cooling provided by TDAFW. In the unmitigated[11] LTSBO base case scenario, two emergency operating procedure (EOP)-based operator actions are credited. First, the operators must complete load shedding to extend DC battery life to 8 hrs. Second, the operators can use the steam generator atmospheric relief valves and with the TDAFW injection, perform feed and bleed steps that cool down the RCS and lower pressure to about 160 psig. This will allow accumulators to passively inject water into the RCS. These operator actions of cooling the RCS and adding water from accumulators further delay the failure of the RCS and potential containment failure. Except for the time delay, the unmitigated LTSBO accident progression is similar to the STSBO. Additional mitigation is examined for the LTSBO scenario in sensitivity cases, including examination of the benefits of timely restoration of power to the igniters to mitigate against early failure of the containment due to hydrogen burns. Chapter 4 discusses further details of these LTSBO cases.

[11] “Unimitigated” here is used in the same way as the original SOARCA study [3], meaning SAMGs, FLEX, 10 CFR 50.54(hh)(2) measures are not credited, but EOPs are credited.

3. SEQUOYAH MELCOR MODEL

3.1 Sequoyah MELCOR Model

The Sequoyah MELCOR model is equally representative of the two functionally identical units at TVA's Sequoyah Nuclear Plant. Both Sequoyah units comprise a Westinghouse 4-loop PWR in an ice-condenser containment. The reactors each have an operating power of 3,455 MW_{th}. The Sequoyah model is current with respect to the steam generator replacements accomplished at the plant.

During multiple site visits, substantial information was obtained for updating the model including detailed characteristics of replacement steam generators. The model description below identifies the activities in building the Sequoyah MELCOR input deck.

The Sequoyah model was modified primarily in three areas. The first area was the reactor core where the core representation was upgraded to be consistent with MELCOR 1.8.6 and 2.1. This upgrade included the following:

1. Replacing the cylindrically-walled flat-bottomed geometry of the lower head with a hemispherical geometry;

2. Adding core former and core baffle structures that become fully integrated into core degradation modeling which includes treatment of debris in the bypass region between the core barrel and the core shroud;

3. Activating logic for simulating the formation of molten pools in the lower plenum and the core, crust formation, convection in molten pools, stratification of molten pools into metallic and oxide layers, and partitioning of radionuclides between stratified molten pools;

4. Making use of a reflood quench model that separately tracks the component quench front, quench temperature, and unquenched temperatures;

5. Activating a control rod silver release model;

6. Applying the CORSOR-Booth fission product release model; and

7. Updating core degradation modeling practices.

The second area included numerous plant design features and safety systems while updating and converting the model from MELCOR Version 1.8.6 to MELCOR Version 2.1. Existing modeling was enhanced and new modeling was added to broaden the capabilities of the Sequoyah model in addressing a wide range of severe accident sequences. These enhancements included:

1. Largely redefining the SG representations using data supplied by the plant;

2. Revising containment overpressure failure modeling;

3. Revising the operation of the pressurizer and secondary system pressure relief valves such that they fail open after a certain number of cycles based on the Surry UA [17];

4. Revising containment floor areas to better predict flooding of the lower compartments;

5. Accounting for heat loss from the reactor to the containment;

6. Adding motor and TDAFW models with control logic representing both automatic and manual operation;

7. Accounting for steam draw by the TSAFW, flooding failure of the pump's drive turbine, and variable performance of the pump with changing steam pressure;

8. Accounting for nitrogen discharge from the accumulators as they empty;

9. Updating core fission product inventory, decay heat, and axial and radial peaking factors;

10. Adding fission product tracking;

11. Adding better representation of natural circulation in the hot legs and steam generators and associated prediction of creep rupture;

12. Adding gaps around the inlet and exit doors of the ice condenser for better representation of flow leakage through the ice condenser;

13. Managing the ignition of hydrogen deflagrations with additional mechanistic considerations;

14. Adding a representation of the auxiliary building (although this enhancement was not used in the subject SBO calculations);

15. Updating the ice condenser door modeling (including lower and upper plenum door, and the intermediate deck doors) based on the information provided in [18]; and

16. Revising the characteristics of RCP seal leakage to be consistent with current best modeling practice and Surry UA [17].

The third area of enhancements was representation of operator and mitigative actions. Logic was added to manage the following activities:

1. The planned operator action at Sequoyah in the case of a LTSBO where the RCS will be cooled and depressurized by venting one of the four steam generators to 300 psig, is represented in the MELCOR model.

2. The only identified mitigative actions in STSBO and LTSBO scenarios involved activation of the igniters by the time hydrogen is generated and released to the containment.

Lastly, modifications to the Surry model in support of the Surry UA [17] were made to the Sequoyah model, where appropriate, and some final items specific to Sequoyah were added or modified. The additions and modifications involved:

- Adding multiple control volumes (both axially and radially) to better represent the ice chests, and inlet and outlet plenum compartments;
- Adding detailed SG nodalization;
- Updating drains with check valves;
- Updating all control function initial conditions;
- Adding and updating sensitivity coefficients per current Sandia National Laboratories (SNL) best practices;
- Adding the hot leg creep rupture modeling (two-part criteria) as applied in the Surry UA;
- Adding the latest MELCOR CAV package heat transfer modeling practices that capture better heat transfer from core-concrete debris to an overlying pool of water;
- Updating the fuel failure and eutectic temperature;
- Adding changes to containment condensation per accepted historical work accomplished with the CONTAIN code [19];
- Updating the aerosol shape factors;
- Limiting maximum time step size to 100 ms;
- Adding pressurizer relief valve stochastic failures to open/close after a variable number of cycles as configured in the Surry UA model;
- Added the same for MSL relief valves;
- Implementing a variable Zr breakout temperature and a variable melting temperature for the eutectic formed between UO_2 and ZrO_2; and
- Disabling mechanistic pump seal failure modeling and instead applying discrete leakage values per Westinghouse Owners Group.

For convenience, many of the enhancements cited above were made to the MELCOR 1.8.6 version of the Sequoyah SOARCA model. The model was then converted to MELCOR Version 2.1 and improvements remaining to be made were accomplished. Because multiple modelers had contributed over a significant period to the enhancements, the model was compared electronically (applying the MELCOR differences function) to a converted version of the original 1.8.6 Sequoyah SOARCA model. This process was implemented to identify all enhancements made in the current Sequoyah work. Important model design parameters for Sequoyah are identified in Table 3-1.

Table 3-1 Important design parameters for Sequoyah.

Parameter	Value	Units
Rated core power	3,455	MW_{th}
Number of fuel assemblies	193	-
Fuel rod array size	17 x 17	-
Fuel rods per assembly	264	-
Fuel (UO_2) mass	102,130	kg
Zircaloy mass as fuel cladding	23,127	kg
RPV inner diameter	2.202	m
RPV inner height	12.294	m
Pressurizer PORV capacity	2 x 22.55 @ 16.20	kg/s @ MPa(g)
Pressurizer safety valve capacity	3 x 52.92 @ 17.13	kg/s @ MPa(g)
PRT volume	52.13	kL
PRT initial inventory	25.60	kL
PRT burst disk rupture pressure	6.90	bar(g)
Reactor inlet/outlet temperature	289/325	°C
RCS coolant flow	16,907	kg/s
Nominal RCS pressure	15.41	Mpa(g)
Number of steam generators	4	-
Steam generator recirculation ratio*	11.2	-
Steam generator heat transfer area	5,139	m^2
Secondary pressure	5.890	MPa(g)
Steam generator secondary water mass	192,512	kg
Steam generator secondary side volume	710	kL
CST water volume	908.50	kL
RWST inventory	1,341.49	kL
TDAFW capacity	55.52 @ 6.932	L/s @ MPa(g)
Motor-driven AFW capacity	2 x 27.8	L/s
Containment design pressure	0.745	bar(g)
Containment free volume	33,613	kL
Containment operating pressure	0	bar(g)
Containment operating temperature	30.0 upper 38.1 lower 1.9 ice	°C
Accumulator combined water volume	124.8	kL
Accumulator pressure	4.302	MPa(g)
High head safety injection max flow	41.0	L/s
Low head safety injection max flow	378.5	L/s
Ice mass	1,165,760	kg
* Ratio of riser flow to steam flow		

3.1.1 Reactor Core and Vessel

The active height of the reactor core was represented with five concentric rings and 12 axial levels. An additional six levels were included to represent core lower support structure and a single level was included to represent the fuel assembly upper tie plate (for a COR nodalization comprised of a total 19 axial levels). A control volume hydrodynamics (CVH) nodalization which is axially coarser than the COR nodalization was employed where a single control volume was

used to represent several axial core cells. The MELCOR COR and CVH nodalizations for the active fuel and lower plenum regions of the reactor vessel are shown in Figure 3-1. Reactor operating power was assumed to be 3,455 MW_{th}. Fission product inventories and decay powers were defined per a mid-time in cycle ORIGEN calculation made for a representative Sequoyah core comprised of 193 total 17 x 17 fuel assembles. Representative radial and axial power shapes were applied.

The core support structures are modeled as distinct structures in the MELCOR COR package, and failure is calculated based on temperature and stress criteria, as specified in the MELCOR COR User's Guide and Reference Manual [20][21]. The core support and diffuser plates of a Westinghouse reactor are column-supported, and the assemblies load the plates between the columns. These plates are modeled as grid supported plates per SNL MELCOR modeling best practice. The lower core plate (also known as the lower forging) is modeled as an edge-supported plate. Self-supporting column structures are located between the plates.

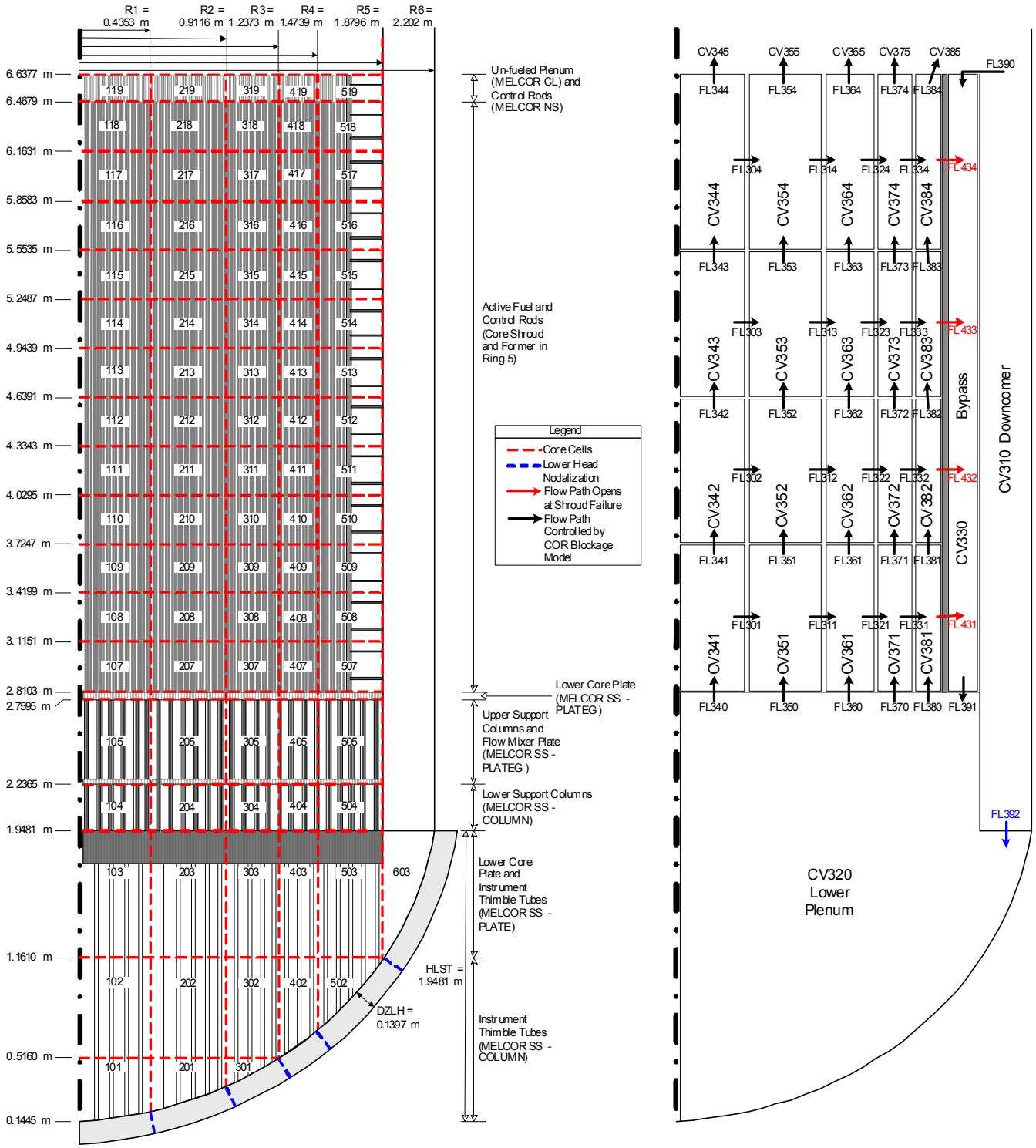

Westinghouse 4-Loop PWR with Ice Condenser Containment Core Nodalization

Westinghouse 4-Loop PWR with Ice Condenser Containment CVH/FL Nodalization

Figure 3-1 MELCOR COR/CVH nodalization

The lower head is modeled as a hemispherical carbon steel structure. A one-dimensional model of the stress and strain distribution in the lower head was used to determine failure, or alternatively, the lower head can fail without stress when the melting temperature of steel is reached. When the failure criterion is met, a vessel breach of variable size opens between the reactor lower plenum volume and the reactor cavity below the RPV.

Twenty control volumes are coupled to the fueled cells of the COR nodalization with four vertically stacked volumes associated with each of the five concentric rings. A parallel control volume represents the bypass region of the core. A single control volume represents the lower plenum and is coupled to the six lower axial levels of the COR nodalization. The remaining control volumes in the RPV represent the upper plenum as illustrated in Figure 3-2. At each axial level of the core, coolant cross-flow between channels and the bypass region (if indicated) are accommodated by horizontal flow paths. Structures making up the RPV not accounted for in the COR nodalization were modeled with a collection of heat structures representing the RPV wall, thermal shield, core barrel and upper plenum internals.

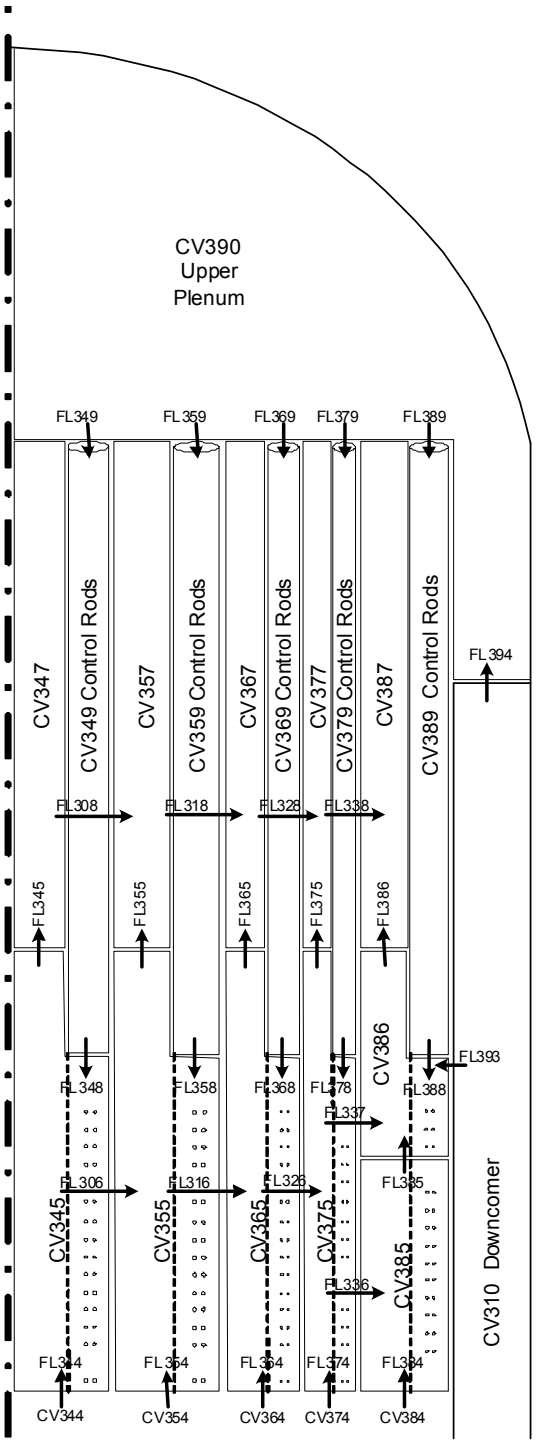

Westinghouse 4-Loop PWR
with Ice Condenser Containment
Upper RPV CVH/FL Nodalization

Figure 3-2 Upper RPV CVH/FL nodalization

The active core region is discretized into 60 nodes, which includes 5 axisymmetric rings and 12 axial levels. Above the active core there is one (unfueled) level to represent the upper core structures and axial cladding. Below the core, 6 levels are used to represent the core support plate and lower plenum region. In total, 97 COR nodes are used to model the core and lower plenum of the reactor. The use of several core nodes permits spatially resolved calculations of heat transfer, oxidation reactions, and material relocation.

The fuel assemblies are allocated over the 5 active core rings according to Table 3-2 and shown in Figure 3-3. This nodalization scheme captures the radial decay power distribution over the core, which can be important for the core degradation calculations performed by MELCOR. The outer two rings have relatively low power density compared to the inner three rings.

Table 3-2 MELCOR rings and number of fuel assemblies.

MELCOR Ring	Number of Assemblies
1	13
2	44
3	44
4	48
5	44
Total	193

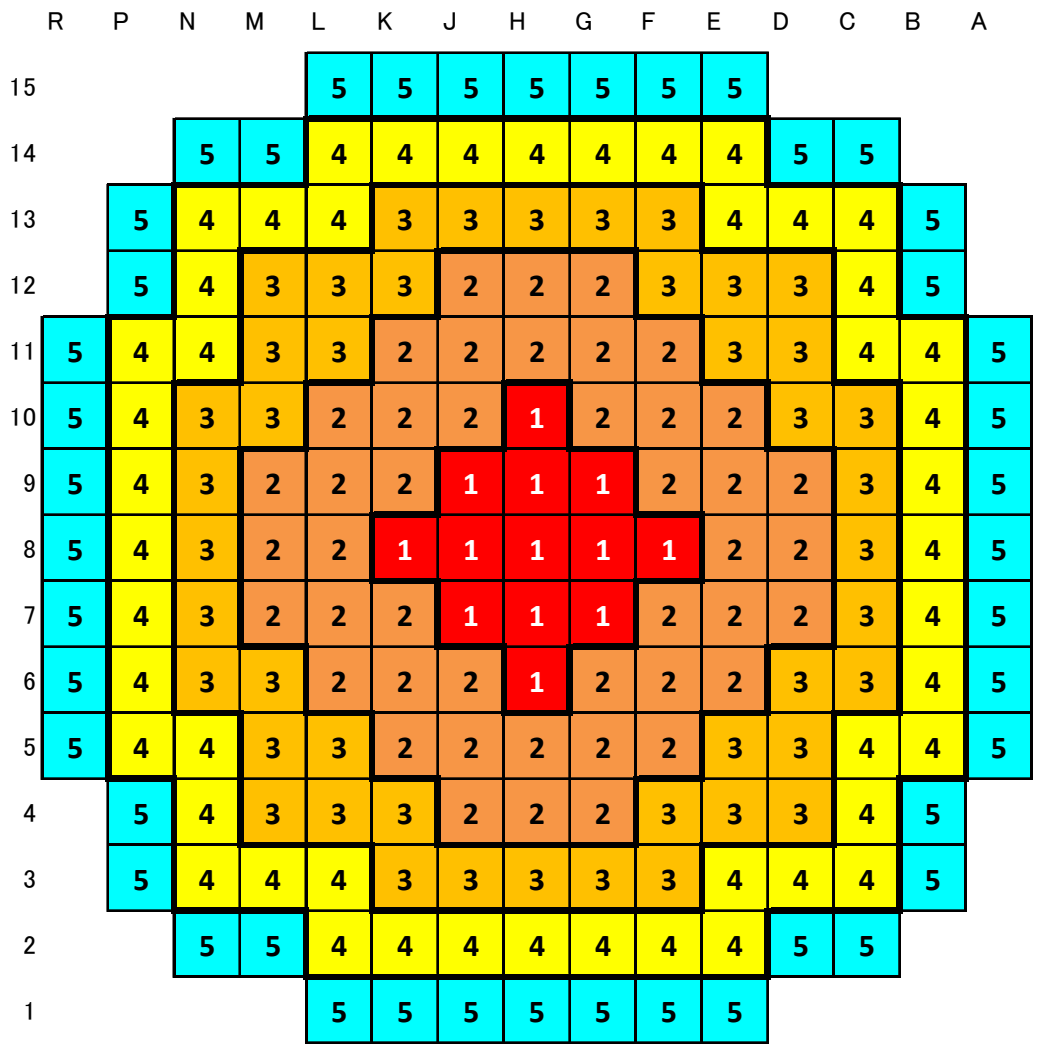

Figure 3-3 MELCOR radial nodalization of Sequoyah core

Consistent decay heat and fission product inventories inputs were created for the MELCOR and MACCS models of Sequoyah. SCALE6 calculations are performed to generate this information in conjunction with post-processing scripts (using Perl programming language) that directly create the MELCOR and MACCS input records in an automated fashion. Radionuclide class inventories, class decay powers, total core decay power information are derived for MELCOR, along with a corresponding nuclide-level inventory for MELMACCS input. The methodologies used to generate the MELCOR and MACCS inputs for Sequoyah are consistent with past best-estimate severe accident research for SOARCA uncertainty analysis efforts, and recent Fukushima research [22].

The SCALE6 calculations make use of proprietary plant operating data from cycles 12-14 at Sequoyah. The severe accident initiator and subsequent reactor shutdown is defined to occur during cycle 14. Reactor shutdown is assumed to occur near middle of cycle (MOC) for the MELCOR and MACCS analyses. The fuel assemblies in the Sequoyah core during cycle 14 include fresh fuel and previously irradiated fuel that is largely from cycles 12 and 13. Thus the

burnup calculations infer radionuclide inventories and decay heat information from known reactor operation for cycles 12 through 14.

The ORIGEN-S/ARP cross section libraries used in this work are generated using the TRITON sequence in SCALE6, and the data libraries reflect the 17x17 fuel lattice used in Sequoyah. Since burnup calculations are to be executed for each assembly and for a variety of burnup conditions, it is desirable to perform standalone ORIGEN-S/ARP calculations in order to expedite CPU time and facilitate subsequent sensitivity studies. The decay heat and inventory inputs for MELCOR and MACCS are integral quantities (e.g. lumped radionuclide classes and whole-core nuclide inventories). Therefore, standalone depletion calculations with reasonably representative cross section libraries are sufficient for severe accident and consequence simulations, especially when taking into account the rather large uncertainties associated with severe accidents such as boundary condition and modeling uncertainties. Figure 3-4 provides the decay heat curve developed for the Sequoyah MOC for cycle 12-14 data. The radionuclide grouping and curie content used for MACCS are presented in Appendix B.

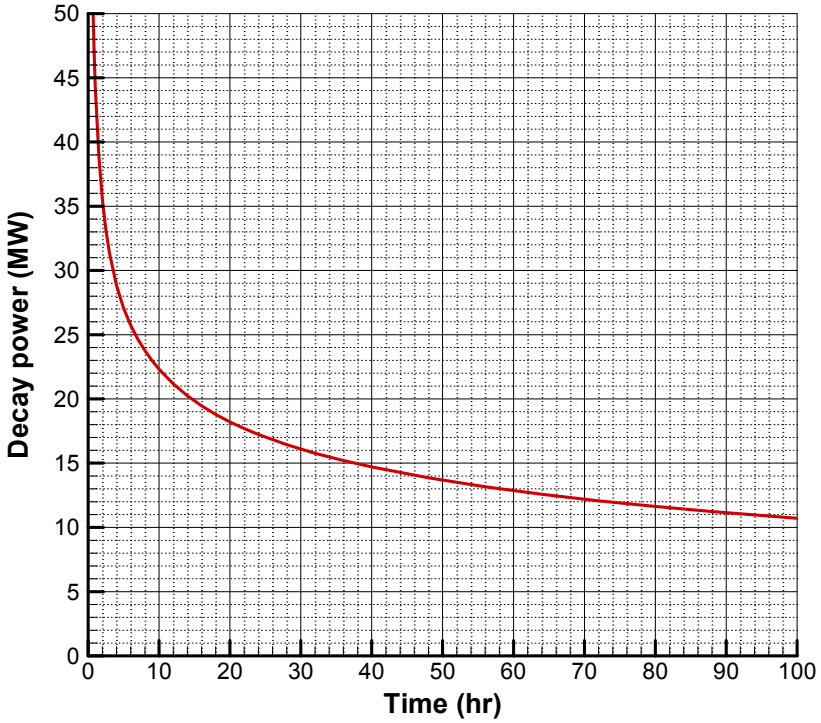

Figure 3-4 Sequoyah middle of cycle decay heat curve

The principal severe accident inputs are lumped radionuclide class inventories, decay power curves, and whole-core nuclide inventories. Within the domain of LWRs, these quantities are mainly functions of the integral fuel burnups and the most recent power history; integral burnup has the most influence on key nuclide inventories that are important for consequences (primarily ^{137}Cs), and the most recent operating power level largely determines the decay power soon after shutdown. The decay heat soon after shutdown is dominated by many short-lived nuclides that quickly reach equilibrium/saturation concentrations due to short half-life (and in some cases, significant neutron absorption cross section). For longer decay time (i.e. after 10^3 sec), the overall burnup has a significant effect on decay heat due to differing quantities of longer-lived nuclides that tend to drive decay power hours after shutdown; the shorter-lived nuclide.

3.1.2 Reactor Coolant System

The reactor coolant loops, including the steam generators (SGs), pressurizer, hot- and cold-leg piping, and recirculation pumps, are modeled. The model of the SGs was based on the Westinghouse inverted U-tube design. When the secondary side of these SGs is water-filled, primary coolant system full-loop natural circulation can sustain primary-to-secondary system heat rejection following a loss of pumping power. Additionally, when the void fraction in the primary coolant system hot legs and SG becomes large, vapor-phase, hot-leg, countercurrent, natural circulation patterns can form, which have important heating effects on the hot legs, surge line, and SG tubes. These two types of circulation behavior are illustrated in Figure 3-5. The Sequoyah MELCOR model incorporates special modeling and hot-leg nodalization to manage hot-leg natural circulation.

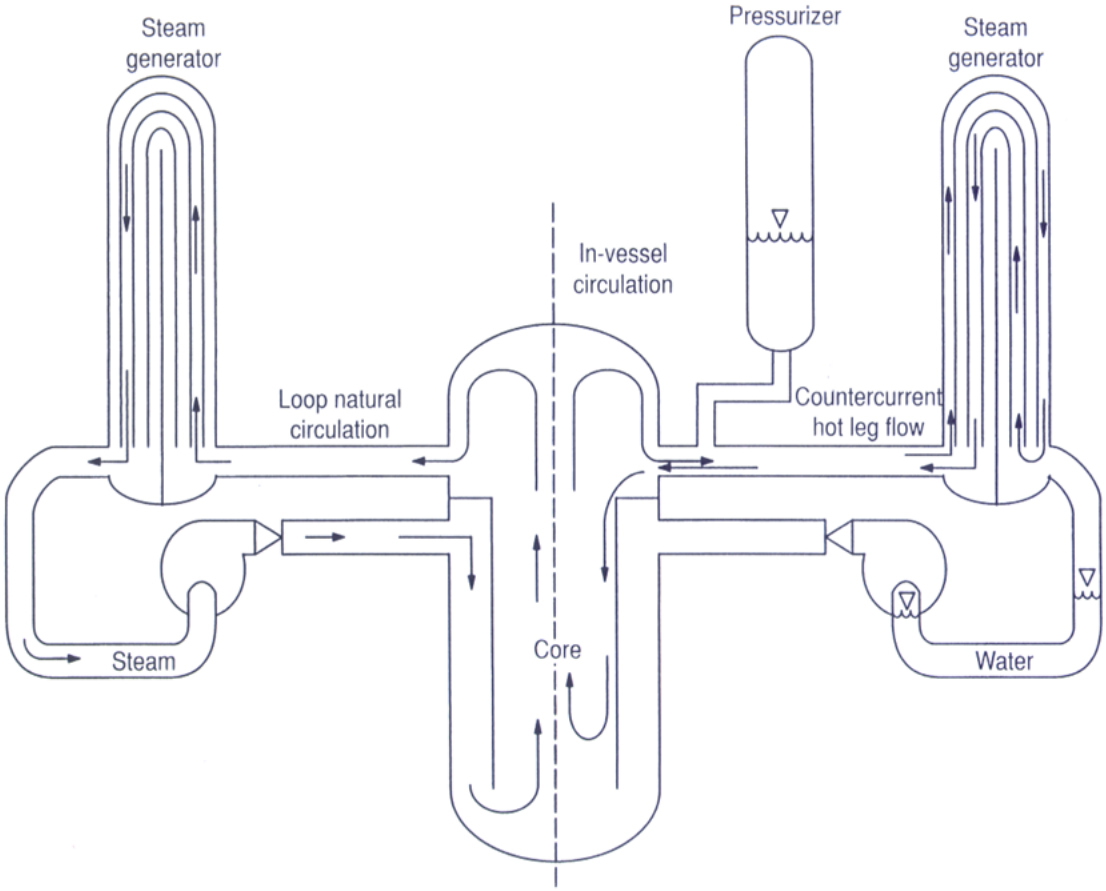

Figure 3-5 Natural circulation flow patterns in a PWR

Natural Circulation Flow Patterns in a PWR

One of the four circulation loops (loop 2 accommodating the pressurizer) in a Sequoyah unit is modeled separately and the remaining three loops are lumped together on the assumption that these loops would behave similarly. Each cold leg is represented using four control volumes with two volumes on either side of the recirculation pump. Heat structures are included to represent the walls of the hot and cold leg piping, as illustrated in Figure 3-6.

The primary sides of the SGs are modeled using multiple volumes to represent the tube bundle and the inlet and outlet plena. The inlet plenum of each SG is represented using three volumes to simulate a range of mixing and countercurrent flow conditions. The outlet plenum of each SG is represented using a single volume.

The pressurizer and surge line are each modeled as one CV in the Sequoyah MELCOR model as illustrated in **Error! Reference source not found.**. The surge line is connected to the single-loop hot leg.

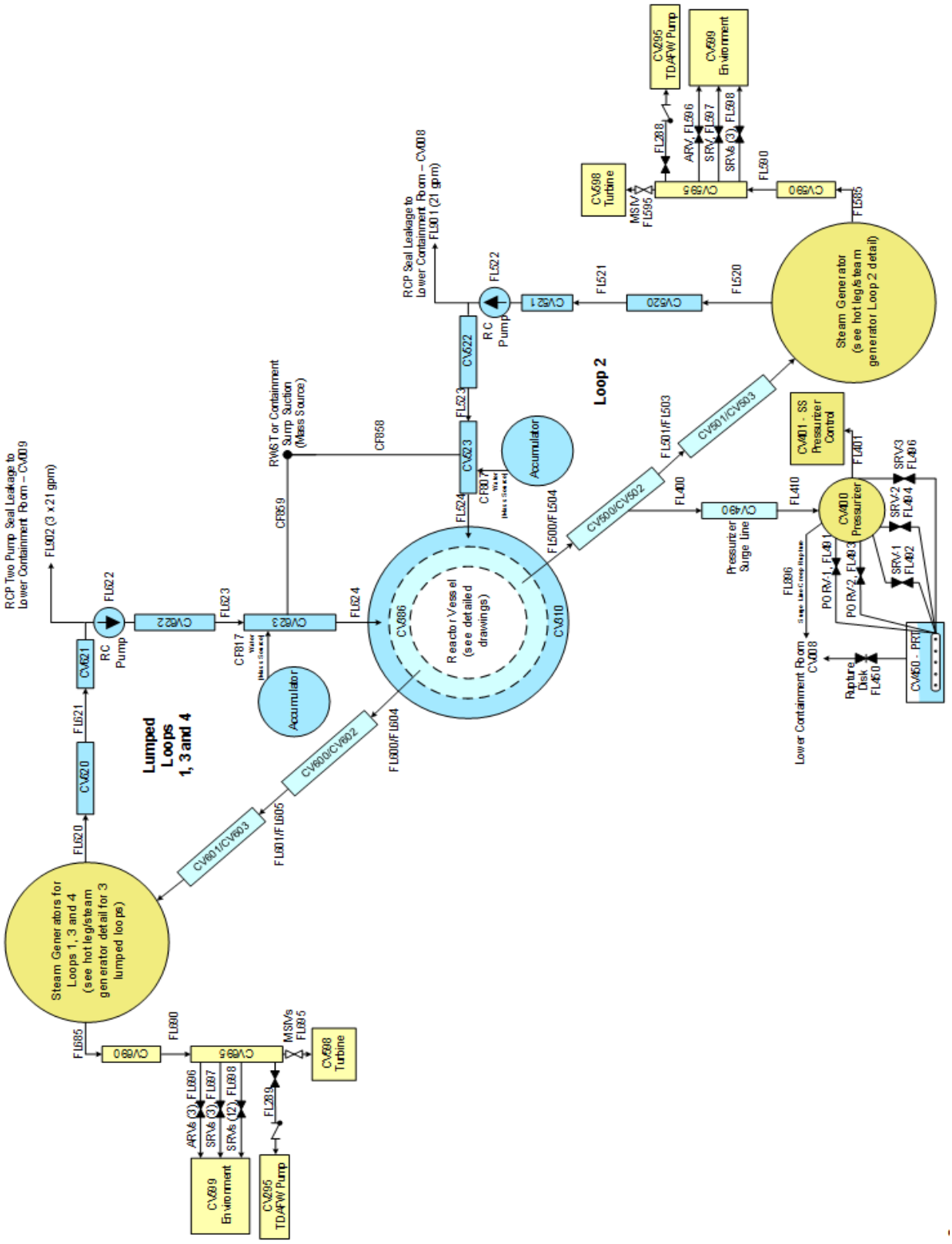

Figure 3-6 Sequoyah reactor coolant system hydrodynamic nodalization

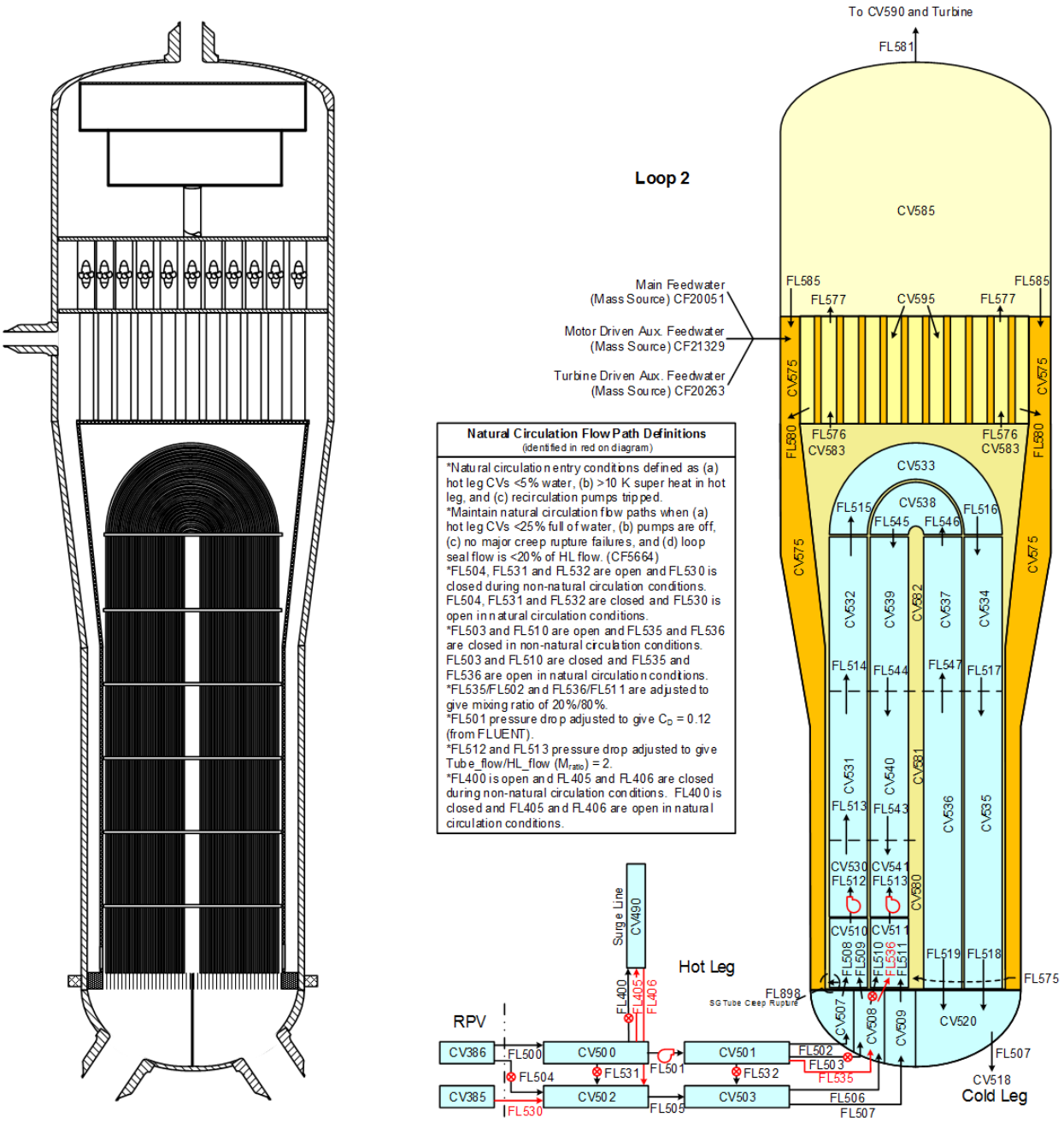

Figure 3-7 Sequoyah steam generator lumped Loop 2

3.1.3 Secondary System

The nodalization is configured with the minimum number of CVs and flow paths needed to accomplish reasonably accurate conditions in the model at rated power and to support hot leg countercurrent natural circulation (see **Error! Reference source not found.**). MSL SVs are epresented with the lowest set-point valve on each MSL accounted for individually, and all other valves accounted for jointly. Stochastic (over-cycling) failure of the lowest set-point valves to

reseat is modeled with failure in the fully open position imposed on the 45th cycle which is the best-estimate cycles to failure based on the Surry UA [17]. Atmospheric relief valves are represented as are MSIVs. Turbine bypass is not represented (and is not needed for the subject calculations on account of being unavailable in a SBO). Leakage past the MSIVs was included only in the LTSBO calculations due to a logic error undiscovered until after the STSBO calculations had completed. The error is thought to be inconsequential primarily because investigating the contribution to risk of SGTRs was not a goal in the Sequoyah work[12] and a detailed SGTR model (see Surry UA [17]) was not developed.

3.1.4 Emergency Core Cooling System

A working model of the emergency core cooling system (ECCS) is included in the Sequoyah model but, with the exception of accumulator actuation, was dormant in the SBO calculations. The accumulators are represented complete with nitrogen introduction to the cold legs upon their water inventory being exhausted.

3.1.5 Natural Circulation Modeling

The Sequoyah model is configured the same as the Surry model with respect to accommodating hot leg countercurrent natural circulation. See Appendix A of the Surry UA [17] for a detailed discussion on modeling natural circulation.

3.1.6 Containment

The containment in the Sequoyah model is made up of a collection of CVs representing the upper dome, lower compartments, annulus, reactor cavity, ice condenser, and the SG and pressurizer cubicles. Bypass flow areas between upper and lower containment are accounted for including the refueling canal drain. Figure 3-8 illustrates the containment nodalization showing the ice condenser CVs immediately below the upper plenum and upper dome.

[12] MSIV leakage would aggravate the stress in steam generator tubing by reducing secondary pressure. It would also provide a release pathway for fission products given an SGTR. The contribution to risk of SGTRs was studied in depth in the Surry UA [17].

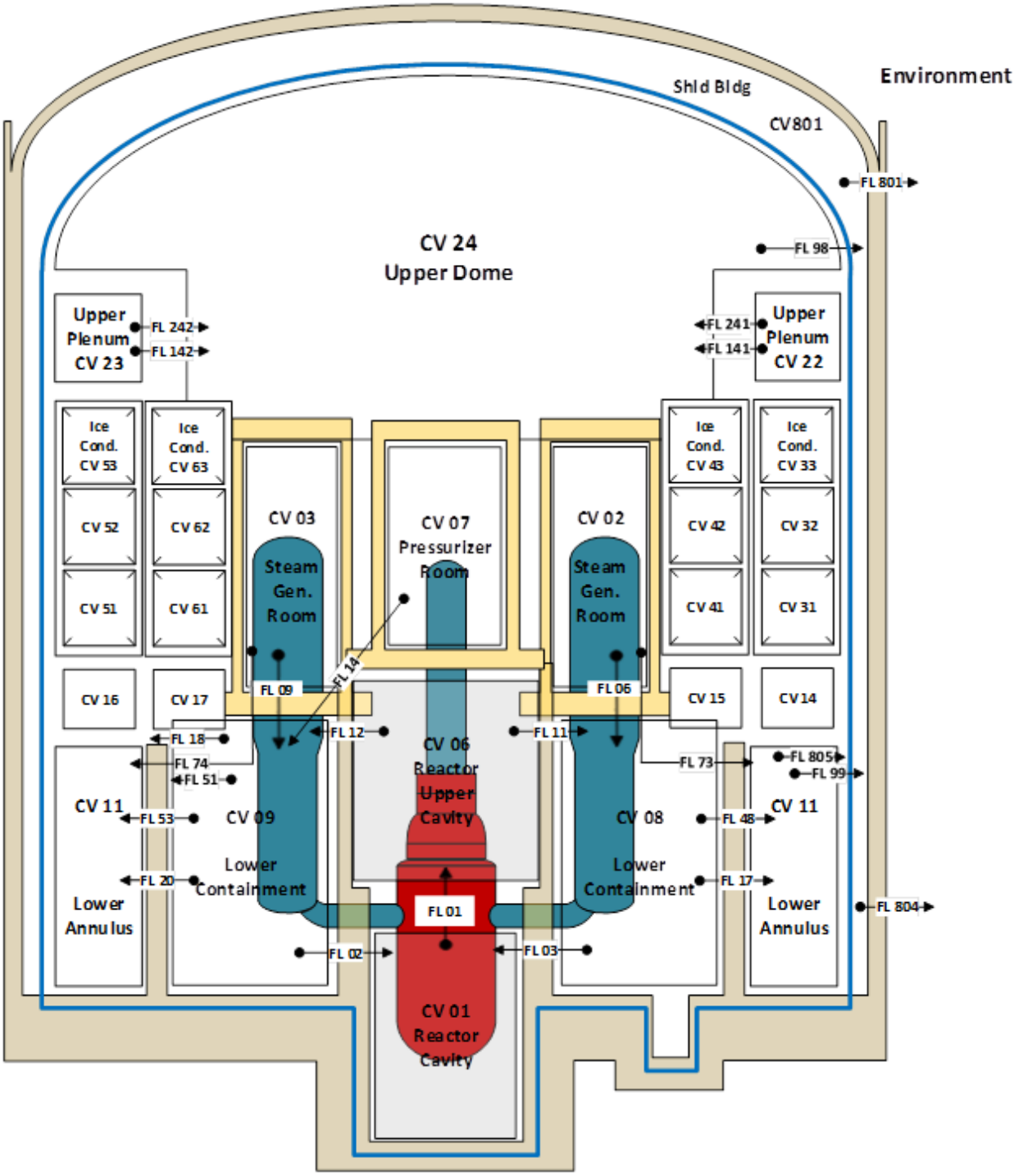

Figure 3-8 Containment nodalization

The ice condenser is an important accident mitigation feature limiting containment pressurization by condensing steam. It is important to consider potential ice condenser bypass flow paths, because any bypass flow will reduce the effectiveness of the ice condenser. The ice condenser is comprised of a lower plenum, ice chest, and upper plenum as seen in Figure 3-9. Lower plenum Inlet doors connect the lower compartment of containment to the lower plenum of

the ice condenser. The lower plenum represents the volume directly beneath the ice baskets. The ice chest, representing the region from the base of the ice baskets to the intermediate deck doors, includes the heat structure representation of the ice stored within the ice baskets. The lower plenum and ice chest regions are divided azimuthally into four sections with an additional axial subdivision of the ice chest into three levels. Above the ice baskets, intermediate deck doors connect the ice chest to the upper plenum region, which is divided azimuthally into two control volumes. Finally, upper plenum doors connect the upper plenum control volumes to the upper containment.

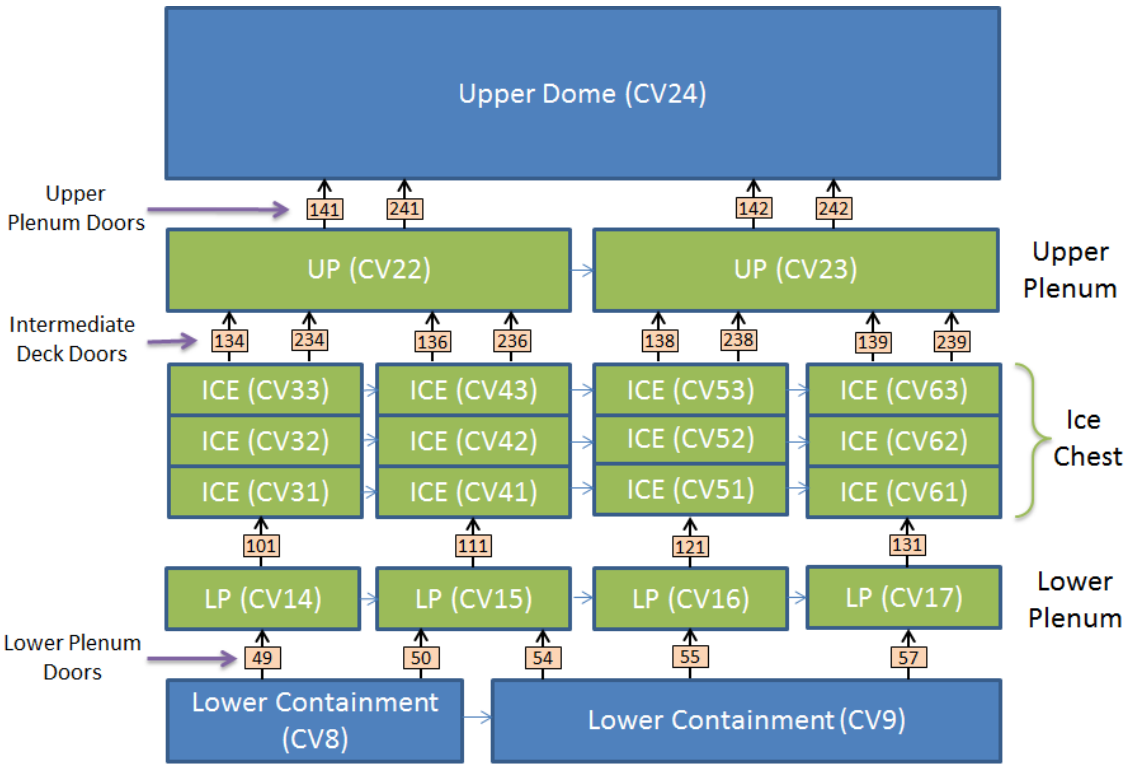

Figure 3-9 Sequoyah ice condenser nodalization

The lower plenum, intermediate deck, and upper plenum ice condenser doors' operations are modeled as presented in Reference [23] consistent with the early MELCOR modeling and calculations in support of GSI-189 [11]. Each door set functions differently, based on design and orientation; therefore, different modeling methods were used. Each door set, at a minimum, uses a flow path which operates from fully-closed to fully-open as a function of the forward differential pressure. If the forward differential decreases, the represented door area fraction is permitted to decrease and is referred to as "reversible." The intermediate deck and upper plenum door models apply a second flow path to model doors which may not return to their closed position once opened. For example, the intermediate deck doors, which use a horizontal-fixed hinge, close under the force of gravity; therefore, these doors may open beyond ninety degrees and may not return to a closed position even though the forward differential pressure decreases. This operation is referred to as "irreversible" and is modeled using a second flow path which maintains its maximum open fraction. The forward differential pressure range of the "reversible" flow path terminates at the start of the opening range of the "irreversible" flow path. In Figure 3-9, flow paths 134, 136, 138, 139, 141, and 142 are reversible and flow paths 234, 236, 238, 239, 241, and 242 are irreversible.

The lower plenum doors are modeled using only the reversible flow path; however, in the event the doors are fully-opened, the doors are modeled to remain fully-open to represent hinge deformation. An operation of the lower plenum doors to fully-open is taken as sufficient to deform the hinges given the relatively small amount of pressure necessary to operate the doors. Reversible and irreversible flow paths are used to represent the intermediate deck and upper plenum doors. Leakage through the doors is taken from "NUREG/CR-6427, "Assessment of the DCH Issue for Plants with Ice Condenser Containment," [23] and is applied to the reversible door flow paths. The ice condenser is perfectly insulated in the MELCOR model.

Within the ice chest, ice melting is modeled by activating the "degassing" ice model. The degassing model determines the associated mass generation in response to energy transfer to a heat structure. Concrete degassing provided the namesake of the model; however, a modification was implemented in an early MELCOR version to use the degassing model for ice melting in ice condenser containment designs. As energy is transferred to the ice heat structure, liquid water mass generation is determined and sourced to the control volume. Drain lines connecting the lower plenum to the lower compartment allow accumulated water, due to melting of ice, condensation, and film flow drainage, to be drained from the ice condenser. Selected ice condenser parameters are provided in Table 3-3.

Table 3-3 Sequoyah ice condenser input parameters.

Parameter	Value	Comments
Ice mass	2.65×10^6 lbm (1.20×10^6 kg)	Average ice mass from 12 measurements
Ice baskets	486 baskets per bank 4 banks	1944 total baskets
Initial ice temperature	19°F (-7.2°C)	The sensible heat from the initial temperature to the melting temperature is included in the heat of fusion
Effective density	584 kg/m^3	Effective density of the ice in the baskets is calculated from the total mass divided by the ice basket volume
Surface area	6200 m^2	Plant data

Additionally, the Sequoyah MELCOR model includes representations of containment spray and air-return fan operation, residual heat removal, and switchover to recirculation through the emergency sump. The SBO scenarios documented here, however, do not involve these systems or actions.

3.1.7 Containment Leakage and Rupture

Containment Description

The Sequoyah containment is a free-standing steel containment consisting of a cylinder topped by a hemispherical dome as shown with the finite element model in Figure 3-10. The internal radius of the cylinder is 57.5 feet and its height to the intersection with the dome (springline) is 115 feet. The thickness of the steel shell in the cylindrical portion varies along the height. This thickness is 1-3/8 inches at the bottom and decreases to ½-inch at the springline. The dome

wall thickness also varies and ranges from 7/16-inch at the springline to 15/16-inch at the apex. The containment cylinder wall has a set of outside vertical stringers at a 4-degree circumferential spacing that extend partially into the dome. This wall also has a set of outside horizontal circumferential stiffeners and platforms. The steel for the containment structure is A516 Grade 60 steel. The design pressure for the containment is 10.8 psig.

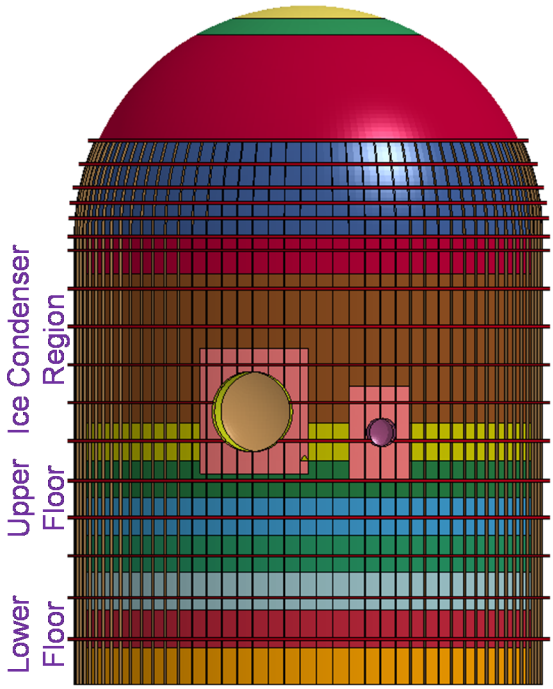

Figure 3-10 Three-dimensional finite element model of the Sequoyah containment

Containment Rupture Pressure and Location

Past NRC-sponsored research ([24][25][26][27][28]) extensively studied the capacity of the Sequoyah containment under internal pressurization associated with severe accident conditions. These studies used a variety of methods of analysis ranging from closed-form analytical approaches that relate the internal pressure capacity to the global membrane hoop strain in the containment shell to studies involving detailed three dimensional models of the containment shell including models that account for strain concentrations near abrupt increases in the thickness of the containment shell to accommodate large containment openings and other penetrations. Table 3-4 below shows best estimates (shown in parentheses) and ranges of internal pressure capacities calculated for the Sequoyah containment in studies completed since the later 1980s and the estimated location of containment rupture. The studies indicate that containment rupture would start where the containment shell thickness abruptly increases around the larger containment opening in the ice condenser region of the containment.

Table 3-4 Best estimate of rupture pressures for the Sequoyah containment from various NRC-sponsored studies.

Reference	Date	Rupture Pressure (psig)	Method of Analysis and Rupture Locations
NUREG/CR-5405 ([25])	1990	(63)	Finite element analysis Rupture location: where the containment shell thickness abruptly increases around the larger containment openings in the ice condenser region of the containment.
NUREG/CR-6706 ([27])	2001	(68) 62 ------- 74	Finite element analysis Rupture location: as above.
NUREG/CR-6920 ([28])	2006	(67) 54 ------- 82	Finite element analysis Containment fragility provided lower and upper bounds corresponding to 0.05 and 0.95 probabilities of failure Rupture location: as above.

The rupture pressure capacities shown in Table 3-4 are for:

- Normal ambient temperatures [25] show that the ultimate pressure capacity is relatively insensitive to temperature with a reduction in pressure in capacity of about 7 to 8 percent at about 300 °F)
- Material properties based on certified material property test reports (CMTRs) for the Sequoyah containment
- Strain-based rupture criteria associated with membrane strains in the containment shell that account for strain concentrations near abrupt increases in the thickness of the containment shell
- Containment strains calculated using three dimensional finite element analysis of the containment building that model either a 90 degree segment of the containment [25] or a chosen segment subtending an angle of, approximately, 53 degrees.
- Large penetrations are not included in the finite element models but increased plate thickness in the areas surrounding large openings is included in the models to account for strain concentrations near abrupt changes in plate thickness.

The values shown in Table 3-4 compare well to each and also to the 65 psig mean of the aggregate distribution of failure pressures from an expert elicitation panel reported in NUREG/CR-4551 [26] and used for the NUREG-1150 study [29].

A single, confirmatory, three-dimensional finite element analysis of the Sequoyah containment was made using the three-dimensional finite element model shown in Figure 3-10. This model includes the major containment penetrations and the increase in the containment shell plate thickness around these penetrations. This is an approximate model because not all information, for example the full extent of the thicker plates around the major penetrations, was available. However, the model permits a point estimate confirmation of the internal pressure ranges shown in Table 3-4 and of the likely rupture location. This confirmatory assessment used a yield

strength for the steel in the containment shell equal to the average value of the available CMTR data which is approximately equal to 47,800 psi. Analysis with this model shows that strains of the order of 3% are reached at an internal pressure of approximately 66 psig in the thinner containment shell plates where they join the upper part of the thicker steel plates that surround the equipment hatch. This is in the ice condenser region of the containment. Principal membrane strains in this region increase rapidly as the internal pressure increases above 66 psig and strains of the order of 2% to 3% become widespread in the thinner steel plates in the ice condenser region. These results are consistent with the best estimate and range of rupture pressures shown in Table 3-4.

The best estimates and ranges of containment rupture pressure shown in Table 3-4, together with the results of the three-dimensional finite element analysis permit recommending a best estimate and range for the rupture pressure for use in the Sequoyah accident progression analysis as follows:

- Best estimate rupture pressure equal to 67 psig

- Range of internal rupture pressure from 52 psig to 78 psig. This range is primarily based on the results reported in [28] and shown in the last line of Table 3-4.

On the basis of these values, the probability density function chosen for uncertainty analysis is a simple triangular probability density function with a lower bound of 52 psig, an upper bound of 78 psig and a most likely value of 67 psig.

Results and observations of 1:8 scale and 1:32 scale tests of steel containments under internal pressurization have shown that containment leakage can be considered insignificant (nominal leakage) until the rupture pressure is reached at which time the leakage area increases rapidly [27]. Therefore, for this study, the leakage area is taken as negligible for internal pressures below the rupture pressure with an abrupt transition to a rupture leakage area (assumed 3 ft^2 in this study) for pressures greater than the pressure capacity.

In summary, the Sequoyah units have freestanding steel vessels serving as primary containments. The vessels have been determined as nominally capable of resisting an internal pressure of 67 psig (before rupturing). Upon overpressure rupture, a 3 square foot hole is envisioned to open at the spring line of the dome. The MELCOR modeling reflects those attributes and the UA varied the pressure required to rupture the containment between 52 and 78 psig.

Containment Nominal Leakage Estimates

Nominal leakage from a Sequoyah primary containment is expected to be near or through penetrations into the annular space between the outside of the steel containment vessel and the inside of the surrounding concrete shield building. A flow path is included in the MELCOR model between lower containment and the annular space to facilitate this leakage. The path is defined as having a flow area of 2.518×10^{-6} m^2 and a length of 0.029 m based on the Sequoyah Modular Accident Analysis Program input file. Leakage from the annular space through the shield building boundary to the environment is assumed to be via a flow area 100 times larger.

Additional Containment Attributes for the MELCOR Modeling

An additional attribute of containment reflected in the MELCOR modeling is the possible failure

of the fabric seals that form part of the barrier between upper and lower containment. The seals are located along the bottom of the concrete floor under the ice condenser, between the ends of the ice condenser and the refueling canal concrete structure, and along the vertical sides of the refueling canal structure. The seals extend across the 4 inch gap between the inside surface of the steel containment vessel and the concrete structure within the vessel. The seals are modeled to fail variably in the UA given a differential pressure between upper and lower containment of between 12 and 57 psid.

Surrounding the Sequoyah steel containment vessel is a concrete shield building. There is a 5 foot distance between the outside of the steel vessel and the inside of the concrete building. The annular space is represented in the MELCOR model. There are two openings in the wall of the concrete shield building that are likely to become release pathways given an overpressure rupture of the steel containment vessel within – a 2’ x 7’-6” exhaust vent in the dome [FSAR, Amendment 20, p. 11.3-7 & "Concrete Dome Outline", Drawing 41N718-1, R5] and a 4'-0.5" x 7'-4.75" doorway between the annular space and the auxiliary building [Watertight Doors Arrangement & Details Sheet 2, CCD No: 1,2-44N286, R1]. The exhaust vent is 130 feet above grade and a release through it would lead directly to the environment. The doorway is below grade. Both the vent and door opening are represented in the MELCOR model. Both openings are configured to open fully coincident with an overpressure rupture of the steel containment vessel (see flow paths 801 and 804 in Figure 3-8). The auxiliary building is not used in the present MELCOR model and all releases are directly to the environment.

3.1.8 Hydrogen Combustion

In a station blackout that proceeds to severe core damage at an ice condenser plant, ample hydrogen will have been generated to threaten the integrity of containment should much of it burn at one time. Hydrogen threat mitigation at Sequoyah is based on the use of thermal igniters to induce periodic burns that have moderate energy addition rates. The igniters, however, require AC electrical power to function and AC power would not be immediately available in an STSBO. One primary mitigative measure in a station blackout is to restore power to igniters.

Hydrogen combustion has uncertainties in the ignition location, ignition timing, flammability limits, and combustion intensity. The previous SOARCA calculations included combustion at the default limit for spontaneous ignition (10%) [5]. There was no explicit recognition of an active ignition source (e.g., the hot jet at hot leg creep rupture, ex-vessel debris, or electrical sources). In the Surry SOARCA calculations [5], hydrogen burns occurred in the containment at the default spontaneous limit following hot leg failure and vessel failure. However, there were no late hydrogen burns after the burn at vessel failure. In contrast, the Surry UA [17] conservatively assumed an ignition source was always available. Combustion was assumed to occur at the lean limit for hydrogen as identified by Kumar [30]. The Sequoyah UA desired to expand the modeling of uncertainty to include an ignition source when there is a well-defined ignition source (e.g., hot gases above the hydrogen auto-ignition temperature exiting the RCS or hot debris in the reactor cavity) as well as provisions for a random ignition component (e.g., static electricity).

Combustion requires an ignition source and a combustible concentration of gases. Similar to the Surry UA study [17], the determination of combustion gas concentrations is based on the work by Kumar [30] illustrated in Figure 3-11 and Figure 3-12. Kumar describes the experimental determination of the flammability limits of hydrogen/oxygen mixtures with various diluents with an active ignition source. The burn propagation direction has different thresholds

for the lean limit on combustion [30]. The upward propagation limit for hydrogen is 4% (by volume %). The lean-downward limit is considerably higher because of the opposing effect of buoyancy on flame propagation. Downward propagation does not occur until the hydrogen concentration is 8.5%. Furthermore, the combustion efficiency is low at the lean thresholds for combustion. For example, the combustion efficiency is found near the lean limits of hydrogen, spanning from almost zero burn completeness at a 4% hydrogen concentration to 95% burn completeness at a 10% hydrogen concentration [30]. At the hydrogen rich condition, combustion is limited by the deficient reactant, which is oxygen. The experimental evidence shows at least 5% oxygen is required. Alternately, it can be expressed as,

H_2 (%) + Diluent (%) = 95%

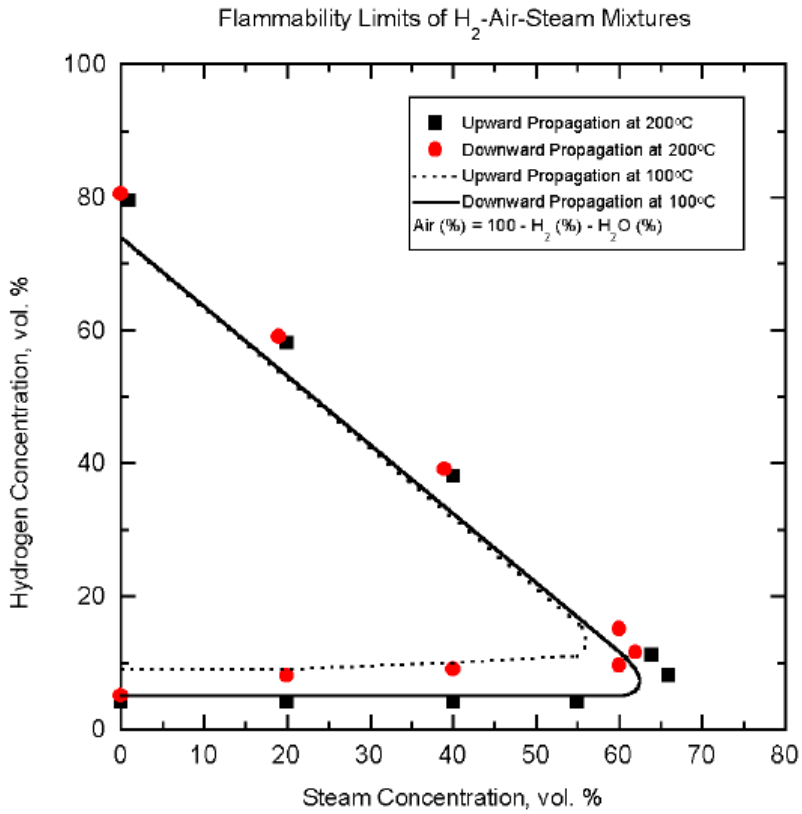

Figure 3-11 Flammability limits for hydrogen for Air-H_2-H_2O systems [30]

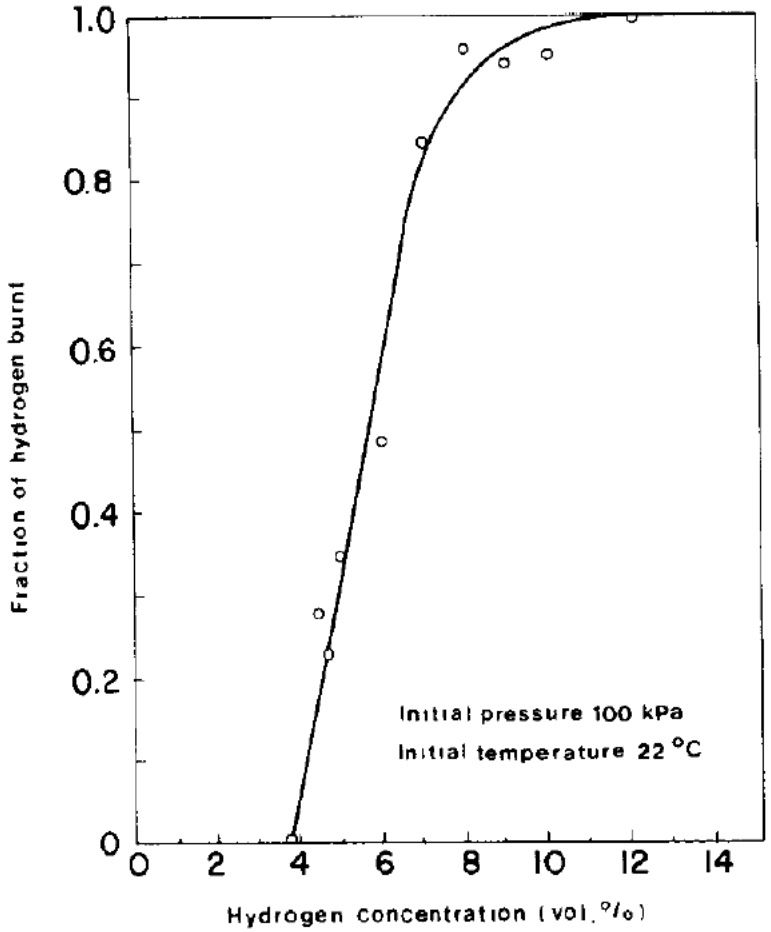

Figure 3-12 Combustion of hydrogen and air mixtures near lean limits for upward propagation of the flame [30]

However, the maximum hydrogen combustion with 5% oxygen is only 10% hydrogen due to the stoichiometric balance to create steam.

$$2H_2 + O_2 \rightarrow 2H_2O$$

The ice condenser is very effective at condensing steam and cooling the non-condensable gases. While the impact of steam as a diluent is noted above, the influence of the temperature is also incorporated using Kumar's experimental findings and deduced theoretical observations. Over the temperature range of the data, the lower limits of hydrogen flammability decreases by 0.5% hydrogen/100°C for upward propagation and 1% hydrogen/100°C for downward propagation. For rich limits, the oxygen concentration decreases by 0.5% oxygen/100°C. Hence, cooler temperatures require higher concentrations for combustion while higher temperatures can ignite at lower concentrations.

In research experiments at the lower flammability limit, a strong ignition source (1 Joule) was used to ensure ignition [30]. There is uncertainty in the availability of an ignition source during a station blackout sequence without igniters or energized electrical equipment. Sources of ignition in severe accidents may include ex-vessel core debris, high temperature jets of

combustible gases (e.g., above the auto-ignition temperature of hydrogen), static electrical discharges and, in the case of earthquake aftershocks, sparks from the falling debris. The minimum energy necessary for ignition in dry air has been characterized as << 1 Joule (see [31]). At the lower limit of flammability, the strength of the ignition source must be stronger. In previous research, [30], it is also noted the addition of a diluent, such as steam, will increase the required ignition energy, the amount is not quantified.

NUREG/CR-2486 reports the final results of the hydrogen igniter experimental program [32]. The hydrogen igniters were typical of those deployed in the Sequoyah ice condenser containment. The experiment results show complete combustion between 8% and 9% with dry mixtures and H_2 and no combustion for concentrations below 5%. Steam tests were done with hydrogen volume fractions of 8%, 10%, and 12%. Steam concentrations of up to 30% consistently resulted in ignition. Most of the 40% steam fraction tests resulted in combustion [32].

Identifiable Sources of Ignition

A severe accident in a PWR leading to a breach in the RCS would present obvious sources of ignition for a hydrogen deflagration, such as hot gas flowing from a rupture in a hot leg nozzle, or core debris relocated from the RPV to the containment floor is another. Given either of these developments in a MELCOR calculation, all of lower containment was taken to have an active ignition source, and if a combustible mixture of gasses existed, a burn initiated. A temperature greater than the auto-ignition temperature of hydrogen (> 847 K) and a flow velocity exceeding 0.1 m/s were conditions required of the gas flowing from a hot leg rupture. RPV lower head failure was taken to be an indication of core debris having relocated to the containment floor.

Random Sources of Ignition

Ignition of hydrogen by an unidentifiable source is a reasonable possibility. Static electrical discharges or sparks from falling debris during an earthquake aftershock are conceivable ignition sources. These sources could occur randomly in time and location. In one set of the MELCOR UA calculations, a source of ignition was momentarily introduced somewhere in containment every half hour. The location of the introduction, i.e., the control volume where the source was introduced, was randomly chosen. Actual combustion of hydrogen given an ignition source was still subject to flammability restrictions.

Detonation and Burn Propagation

As a practical consideration, MELCOR does not model detonation. However, a large deflagration has more than sufficient energy to over-pressurize the containment (e.g., a deflagration from a 14% hydrogen concentration provides up to a 4X increase in pressure [32]).

Burn propagation to adjacent cells in the MELCOR UA calculations was governed by the standard MELCOR burn package model with default concentration limits. The default limits are nominally consistent with research findings [30].

3.1.9 Operator Actions

The planned operator action at Sequoyah in the case of a LTSBO where the RCS will be rapidly cooled and depressurized at the rate of 100 °F/hr by venting two of the four SGs (Steam Generators 1 and 4) through the atmospheric relief valves (ARVs) to 160 psig, is represented in

the MELCOR model although not identically. The lumped representation of Loops 1, 3, and 4 in the model does not accommodate specifically venting Steam Generators 1 and 4. Consequently, the operator action of rapidly depressurizing the RCS was accomplished in the MELCOR calculations by venting just the single Steam Generator 2. Note that a loss of essential control air resulting from a loss of all AC power will require that the ARVs be opened by hand with reach rod operators. Steam Generators 1 and 4 have ARVs that are readily accessible (via the 480 V Shutdown Board Room near the Main Control Room), while Steam Generators 2 and 3 have ARVs that can only be accessed by entry into a high heat stress area.

The venting of the single SG in the MELCOR calculations to represent operators carrying out a maximum-rate depressurization is limited such that available full TDAFW delivery can maintain water level in the generator. This is consistent with what would be accomplished procedurally by the operators. The model was reviewed and it was confirmed that the TDAFW increases to maximum flow (i.e., limited by available SG pressure) upon DC power failure and that TDAFW fails when the SG overfills and flows water through the turbine.

Maximum-rate depressurization begins in the MELCOR LTSBO calculations 1 hour after the onset of the blackout.

In addition to the above, the following were accomplished to support the LTSBO scenario:

- Imposed MSIV leak areas of 0.1 in^2/MSIV.
- Enabled TDAFW injection. Following DC battery failure, the TD-ADW runs at full flow until the SG over-fills and damages the TDAFW steam turbine.
- Enabled DC batteries for 8 hours per Sequoyah post-Fukushima regulatory submittal crediting successful load shedding during the first 90 minutes after the onset of an LTSBO.
- Enabled an operator action to control TDAFW at 15 minutes. Timing from Surry SOARCA LTSBO.
- Enabled an operator action to perform controlled depressurization using one SG while maintaining TDAFW to one generator (based on ECA-0.0).
- Confirmed a technical specification minimum of 230,000 gal water resource from CSTs being used for TDAFW injection.

3.1.10 Mitigative Actions

Consistent with SOARCA NUREG-1935 [3] limited mitigated scenarios are also evaluated. The only mitigative action modeled for the containment response is the activation of the igniters before significant hydrogen is generated and transported to the containment. Upon any recovery of electrical power, igniters will be enabled throughout the MELCOR model. For the LTSBO, sensitivity analyses were conducted to investigate specific actions and operations. In the mitigated scenarios, auxiliary feed water is available at the start of the accident.

The Hydrogen Mitigation System (HMS), comprised of 68 individual igniters, is seismically supported and designed to mitigate sudden high pressure loads in the event of a hydrogen explosion [Ref. FSAR 6.2.5]. The thermal igniters induce periodic small burns and thus prevent

large hydrogen accumulations causing large burns. Power is provided by Class 1E 480 V AC-auxiliary and in the case of loss of offsite power, backed by emergency diesel generators. The HMS is energized manually from the main control room in accordance with emergency procedures following any accident which indicates inadequate core cooling. They remain inoperable during SBO without additional backup AC power supply. The 68 igniters are arranged with consideration for hydrogen release and transport throughout the containment. When local hydrogen ignition criteria at the active igniters exceed the lower flammability limit, the igniter may initiate a combustion event, typically a deflagration. By reducing the available hydrogen contributing to the explosion, the impulse pressure load challenging the containment barrier may be mitigated if the HMS is available before significant amount of hydrogen is released into the containment.

The HMS system is modeled within the Sequoyah MELCOR input file by designating which control volumes contain igniters, the availability of support power, and the atmospheric conditions which can support an HMS initiated deflagration. In the Sequoyah MELCOR model igniters are designated within all containment control volumes with the exception of the ice condenser lower plenum and ice chest. Each designated igniter in the modeled volumes represents multiple igniter pairs physically installed in the containment compartments. Power availability and mitigation application of diesel generators are defined by the sequence. Finally, the following MELCOR default atmospheric conditions support igniter-initiated deflagrations: H_2 > 7%, O_2 > 5%, and diluents < 55%.

The hydrogen igniters are powered by the 480 volt AC bus that is inoperable during a SBO. However, the igniters can be placed in operation by manual operator action if AC power is recovered. If the igniters are operable before significant hydrogen is released to the containment, then the likelihood of a large deflagration challenging the containment integrity can be minimized. According the FLEX instructions discussed in Section 2, the operator is expected to power 480 volt AC bus using a 225 kV generator, which is pre-staged on the roof of auxiliary building.

3.1.11 Modeling Practices

MELCOR includes capabilities to model the two-phase thermal-hydraulics, core degradation, fission product release, transport, and deposition, and the containment response. The SOARCA analyses include operator actions and equipment performance issues as prescribed by the sequence definition and mitigative actions. The MELCOR models are constructed using plant data and the operator actions were developed based on discussions with operators during site visits.

3.1.11.1 Pressure safety valves

Pressurizer safety valves and power operated relief valves

Each of the 3 SVs on a Sequoyah pressurizer is represented separately in the MELCOR model. Their opening pressures are staggered. The SV with the lowest opening pressure is configured to fail open according to an over-cycle criteria (for the valve type). The criteria is sampled as an uncertain parameter. It is judged that the valve will most likely fail in a partially open position, thus the valve open fraction at failure is also sampled.

Each of the 2 power operated relief valves (PORVs) on a Sequoyah pressurizer is also represented separately, and their opening pressures are staggered. The PORV with the lowest

opening pressure is configured to fail open according to standardized over-cycle criteria. The pressurizer PORVs were updated to fail at the best-estimate value of 45 cycles from the Surry UA study [17]. Additionally the valve is configured to fail open if a limited number of cycles at high temperature are exceeded.

The SVs and PORVs vent to a separate control volume in the MELCOR model representing the Pressurizer Relief Tank (PRT). A flow path representing the PRT rupture disks is included between the PRT control volume and one of the lower containment control volumes. The flow path is and configured to open at a differential pressure of 100 psi.

The PORVs are unavailable during a station blackout, and it is unlikely that the failure temperature of the SVs will be reached during these scenarios. However, due to the sampled number of cycles for over-cycle failure, it is expected that the lowest setpoint SV will fail open in the majority of uncertain realizations.

Secondary system atmosphere relief valves and safety relief valves

Each of the 4 steam lines serving a Sequoyah unit has 1 ARV and 5 SVs. The set points on the SVs are staggered. The representation of the Loop 2 main steam line in the MELCOR model has:

- 1 flow path representing the ARV with over-cycle and over-temperature failure included;
- 1 flow path representing the lowest-setpoint SV with over-cycle and over-temperature failure included; and
- 1 flow path jointly representing the remaining 4 SVs.

The lumped representation of the Loops 1, 3, and 4 main steam lines in the model has:

- 1 flow path jointly representing 3 ARVs with over-cycle and over-temperature failure included;
- 1 flow path jointly representing the 3 lowest-setpoint SVs with over-cycle and over-temperature failure included; and
- 1 flow path jointly representing the remaining 12 SVs.

The Sequoyah ARVs require control air (and hence AC power) to operate automatically or to be operated remotely. The ARVs serving Steam Generators 1 and 4 are readily accessible and can be manually opened (locally) with reach rod operators. This is not the case with the ARVs serving Steam Generators 2 and 3. Access to these ARVs requires entry into a high heat stress area. These attributes of the ARVs are reflected in the control logic included in the MELCOR model to manage the operation of the valves.

3.1.11.2 Pump seal leakage

Under normal operating conditions, cooling water is supplied to the RCP seals at a higher pressure than the primary. As a result, the water keeps the RCP seals cool while preventing any primary coolant from flowing up the RCP shaft and contaminating areas outside the primary boundary. When a loss of AC power occurs, the RCP seal cooling system no longer supplies

cooling water and as a result, primary coolant begins leaking along the RCP shaft through the mechanical seals at a rate of 21 gpm for pressures near operating pressure. RCP seal leakage was set at initially 21 gpm per pump for all scenarios.

3.1.11.3 Loop seal clearing and effects on the accident progression

No SGTRs were included in this analysis because SGTRs were studied in detail with the Surry UA [17]. Thus, no variation of loop seal clearing is included.

3.1.11.4 Fuel degradation and relocation treatment

MELCOR includes a model to characterize the structural integrity of the fuel rods under highly degraded conditions. The model acknowledges a thermal-mechanical weakening of the oxide shell as a function of time and temperature. As the local cladding oxide temperature increased from the Zircaloy melting temperature (i.e., represented as 2098 K in MELCOR) towards a default of 2500 K, a thermal lifetime function accrues increasing damage from 10 hours to 1 hour until a local thermo-mechanical failure.

3.1.11.5 Lower plenum debris/coolant heat transfer

Following the fuel-debris slump into the lower plenum, there may be fuel-coolant interactions. The lower plenum heat transfer settings were updated to reflect the approach adopted in Surry UA.

3.1.11.6 Core plate failure

The timing of core plate failure affects the relocation of the degraded core materials from the core region into the lower plenum. The local thermal-mechanical failure of the lower core plate, the flow mixer plate, and the lower support forging are calculated within MELCOR using the Roark engineering stress formulae. The yield stress is calculated based on the loading and local temperature.

3.1.11.7 Fission product release, speciation, and volatility

The release model is consistent with the Surry UA [17]. Since MELCOR does not calculate chemical changes of fission products in the RCS, the speciation needs to be specified in the initial fuel inventory. Thus the base case for cesium (after combination with iodine) is 80% cesium molybdate and 20% cesium hydroxide using the best estimate for cesium partitioning in Surry UA [17]. The released iodine combines with the cesium, although a small amount remains gaseous, taken as 0.182% which is the best estimate value at middle of cycle from the Surry uncertainty analysis.

Iodine is a volatile fission product and can be released as an elemental gas or bound together with cesium as CsI, an aerosol. Because of its volatility, a portion of iodine transports to the fuel-cladding gap, leading to early releases when gap failure occurs. Iodine has a relatively short half-life, particularly I-131 with a half-life of 8 days, compared to other fission products, and can dominate early health effects if releases occur before or during evacuation. Cesium is volatile but readily binds with other elements to form an aerosol. Specifically, it is known to bind with iodine as CsI, molybdenum as Cs_2MoO_4, and water as CsOH. Because of its volatility, a portion of cesium transports to the fuel-cladding gap, leading to early releases upon the occurrence of gap failure. Cesium has a relatively long half-life (i.e., ~30 years from the

dominant isotope of Cs-137) compared to other high yield fission products and dominates late health effects. The in-vessel cesium and iodine release from fuel is near 100 percent of its total inventory following a severe fuel damage.

The behavior of aerosol transport after release from fuel is very uncertain and is addressed by variation of the dynamic shape factor as described in Section 3.9.

3.1.11.8 Vessel lower head failure and debris ejection

The base case approach of modeling the vessel lower head failure and debris ejection includes some special non-default modeling options in MELCOR. First, all the solid debris in the lower plenum is in contact with water, if present. Previously, a restrictive one-dimensional counter-current flooding limitation criterion prevented penetration of water into the debris bed. Second, the vessel lower head fails using a creep rupture model. A Larson-Miller failure criterion is calculated based on the one-dimensional conduction and stress profile through the lower head. The failure of a lower head penetration prior to gross head failure was judged unlikely based on observations from experimental studies at Sandia National Laboratories lower head failure (LHF) tests [33].

3.1.11.9 Ex-vessel phenomena

The ex-vessel debris surface heat flux to an overlying pool of water was enhanced to replicate the magnitude observed in the melt attack and coolability experiments (i.e., MACE tests) [34]. The default model did not include multi-dimensional effects of fissures, other surface non-uniformities, and side heat fluxes. The modeling approach is consistent with Surry UA.

3.2 Selection of Uncertain MELCOR Parameters

MELCOR uses thousands of parameters in the evaluation of the equations and algorithms embedded in its constituent models. Many parameters are basic well-known input, such as core inventory, material properties, sizes and lengths of piping, etc. There are many parameters for which the base values were established through comparison to experiments. Some parameters were established long ago by subject matter experts (SMEs) and are assumed reasonable for the present application. In development of the Peach Bottom and Surry UAs, a common set of phenomenological areas were investigated. The approach for Sequoyah began with the same set of areas and reduced the investigation to limit the scope of the analysis as directed in SECY-12-0092 [10]. Information from the Surry UA review of the MELCOR Reference Manual [21] and preliminary results influenced the final list of parameters ultimately selected for Sequoyah. The MELCOR uncertain parameters were selected to cover the following issues of severe accident phenomenological areas:

- Sequence,
- In-vessel accident progression,
- Ex-vessel accident progression,
- Containment behavior, and
- Aerosol transport and deposition.

The extensive investigation into parameters for the Peach Bottom and Surry UAs [9][17] was leveraged for the Sequoyah analysis. The Sequoyah MELCOR team included the same members that were involved in the Surry UA. The Surry UA parameter list was used as a

starting point because it is also a PWR. The Sequoyah scope includes a limited UA together with the base case analyses. Thus, as a first step, those parameters that were not identified as having key importance in Surry were removed from consideration, after SMEs considered whether plant differences might raise their importance for Sequoyah. The main purpose of investigating Sequoyah was because it is an ice condenser design with a small containment. Therefore, parameters were added to research these aspects, notably the barrier seal and ice doors to represent the ice condenser design. Lastly, some parameters found to be important in Surry, such as the time at cycle, were not included in Sequoyah because the knowledge gained in Surry is judged to be sufficient to inform the analysis; therefore, these parameters were also removed to maintain the limited scope.

Table 3-5 lists the distributions and bounds related to each MELCOR parameter sampled in this analysis. The sampling approach for many of the parameters is quite complex and is described in the following sections along with the rationale for each distribution, and justification for the upper and lower bounds. The basis for defining many distributions is strong where known physical or chemical phenomena are well understood. Correlation of the MELCOR parameters was considered, but ultimately no correlations were implemented.

Table 3-5 MELCOR sampled parameters

Uncertain Parameter	Distribution type	Distribution Parameters		Lower Bound	Upper Bound	Comment
Sequence Related Parameters						
Primary SV stochastic FTC (priSVcycles)	Beta[1]	α: 17.5 β: 756.5		0	1	Distribution is used to sample on cycles to failure, full sampling is more complicated and described in reference [17]
SV open area fraction (SV_frac)	Uniform	-		0.01	1	Sampled independently for each primary SV
In-Vessel Accident Progression						
Effective temperature of the eutectic reaction for zircaloy oxide and uranium oxide (EU_melt_T)	Normal	Mean: 2479 K σ: 83		-	-	
Ex-Vessel Accident Progression						
Lower Flammability Limit (LFL) hydrogen ignition criteria with an obvious ignition source in the lower containment (H_2 LFL). Set up for downward, upward, and horizontal. (burn_dir)	Discrete	Bin	Prob.	-	-	Included in all uncertain realizations.
		4% (down)	0.33			
		6% (Horiz-ontal)	0.33			
		9% (Up)	0.33			

Uncertain Parameter	Distribution type	Distribution Parameters		Lower Bound	Upper Bound	Comment
Random CV sampling for ignition without an obvious ignition source	Discrete	30 minutes		-	-	This parameter described how often CVs will be checked for ignition conditions. Included in about half of uncertain realizations.
Containment Behavior						
Containment fragility curve (CFC) (rupture)	Triangle	Mode: 67 psi		52 psi	78 psi	Pressure at which the containment ruptures, which results in a 3 ft^2 hole
Barrier Seal Open Area (Seal_Open_A)	Discrete	Bin	Prob.	-	-	Unit of m^2
		0.054	0.034			
		0.068	0.005			
		0.192	0.015			
		0.304	0.024			
		0.321	0.026			
		0.325	0.026			
		0.622	0.149			
		0.676	0.054			
		0.894	0.071			
		1.012	0.081			
		1.117	0.089			
		1.732	0.276			
		1.893	0.151			
Barrier Seal Failure Pressure (Seal_Fail_Dp)	Bounded Beta	α: 5.0 β: 1.8		0.0	57.14	Units are psid (differential pressure)
Ice Condenser Doors Open Fraction Unitless (ajar)	Uniform	–		0.0	1.0	This parameter describes the fraction of the lower plenum doors that will remain open due to hinge deformation after they fully open
Aerosol Transport and Deposition						
Dynamic Shape Factor Unitless (shape_factor)	Scaled Beta[2]	α: 1 β: 5		1.0	5.0	

[1] The sampling scheme is more complicated than a simple Beta. The probability of failure conditional on demand is described by the given beta, and then the stochastic aspect is also modeled to arrive at a sampled number of cycles to failure.

[2] A Beta distribution by definition has bounds of 0 and 1. Any Beta with other bounds can be referred to as a Scaled Beta.

There are many alternative parameters that could represent the phenomenology of interest, and the process facilitated selection of a practical subset of parameters to capture important aspects of modeling without introducing unnecessary complications, such as the need to extensively specify correlations.

An objective established for each sampled parameter was to clearly identify the point of departure from a known technical basis, at which use of professional judgment begins. Such judgment was sometimes required in the development of parameters and has been identified, where applicable. To facilitate development of parameter justification and rationale, a

storyboard process, consistent with the one used in the Surry UA [17] was implemented. **Error! eference source not found.** illustrates the form that was used to identify the parameter, responsible owner, technical justification for uncertainty, type of distribution, and rationale for the distribution. The intent was to capture, in a concise format, specific information regarding each parameter from which the detailed technical bases could ultimately be developed.

Parameter Name:	Type of Distribution:
Technical justification for the uncertainties:	
Rationale for type of distribution:	
Were similar or related parameters considered and rejected.	
Graphic: (plot of the distribution)	

Figure 3-13 Parameter storyboard used to capture key information for each parameter investigated

The storyboards were reviewed internally where analysts explained and defended each parameter. The team challenged the technical leads to explain the basis and defend the appropriateness of supporting data. This approach often resulted in the need for additional research to support the rationale.

The timing of SV failure was found to be the most influential uncertain parameter of all the uncertain parameters considered in the Peach Bottom UA [9]. With this insight from the Peach Bottom analysis, failure probabilities of SVs on the pressurizer and MSLs were included as uncertain in the Surry UA and are also included in this Sequoyah analysis. Failure to open (FTO) due to over-cycling and failure to close (FTC) due to over-cycling, passing water or overheating, were modeled and sampled probabilistically for the SVs on the pressurizer. FTC due to over-cycling was modeled deterministically for the lowest set-point SV serving the steam generator. FTC due to overheating of the MSL SVs was not considered because the valves are only exposed to design temperatures. FTO due to over-cycling of these valves was not considered because of the multiple SVs on each line and the small probability associated with FTO. If one of these valves were to fail to open, the function of pressure relief would simply move on to the next valve. As the integrated UAs are for the STSBO scenario, PORVs are not available on either the pressurizer or MSLs.

3.3 Primary SV Stochastic Failure to Close (priSVcyles)

The Sequoyah modeling was based on the Surry UA approach which used information from the Surry SOARCA analysis [5]. In the Surry SOARCA analysis [5], SV stochastic failure was modeled for the lowest-set-point SV and only for an FTC failure mode. The mean probability of failure per demand was taken and used as the number of SV demands at which failure occurred. See the probability distribution and cumulative distribution functions for the negative binomial distribution below:

$$f(n|p) = P(N = n|p) = p(1-p)^{n-1}, 0 \leq p \leq 1, n \sim [1,2,3 \ldots]$$

Eq. 3-1

$$F(n|p) = P(N \leq n|p) = 1 - (1-p)^{n+1}, 0 \leq p \leq 1, n \sim [1,2,3 \ldots]$$

Eq. 3-2

Where *p* is the probability of a failed state for the SV per demand, and *n* is the number of valve cycles the SV experiences.

Once the distributions were defined, the Surry SOARCA analysis [5] used the mean of the number of SV demands at which failure occurred to define the number of cycles at which FTC occurs [5]. This approach did not include the FTO failure mode. The approach was justified by assuming that redundancy in the SVs would ensure an FTC state would be reached before an all valves FTO end state occurred. The Peach Bottom UA also assumed only FTC [9]. The sampling conducted to support the Peach Bottom UA was on the beta distribution for the FTC probability per demand and then taking the mean of the number of SV demands at which failure occurred instead of sampling directly from the distribution in Eq. 3-1 and Eq. 3-2. The Surry UA expanded upon the Peach Bottom UA approach by sampling from both the FTC and FTO uncertainty distributions. This application was used in the Sequoyah modeling.

The Sequoyah pressurizer has three SVs (see Figure 1-4) with differing set-points. The set-points serve automatic valve operation such that when pressure rises in the primary system to a set-point, the associated valve opens and steam is released to the PRT. Once the system reduces to 96 percent of the set-point, the valve reseats. This is considered one "cycle" of the SV. Every opening and closing of the SV has a failure probability associated with the state transition.

Only valve responses to actual scram events were considered, i.e., data from valve testing reported in NUREG/CR-7037 was not considered. The testing data was not considered because the failure rates in the testing differed largely from the failure rates associated with actual scram events suggesting that something was not prototypic in the testing. The data is typically only for failures in a single SV cycle, so there may be some limitation in extrapolating to repeated cycles during a severe accident, but this is the best data available. Bayesian updating was conducted on the failure and testing counts for the SV FTO and FTC failure modes with a Jefferys uninformed beta distribution ($\alpha = 0.5$, $\beta = 0.5$) as the 'prior,' which roughly corresponds to half a failure observed in a full trial. The Jefferys uninformed beta distribution is commonly used in Bayesian analysis with limited data because of invariance to transformation in the Fisher Information matrix, which describes the amount of information entropy within a distribution [35]. The failure information and the sampling distributions are presented in Table 3-6.

The FTO and FTC distributions were obtained from data in Table 20, "Failure probabilities for PWR code safety valves (behavior after scrams)," of NUREG/CR-7037 [36]. In the Failure probabilities obtained from Table 20, "Failure probabilities for PWR code safety valves (behavior after scrams)," in NUREG/CR-7037 [36] informed the uncertainty characterizations of stochastic SV failure. Table 20 reports on SV operation subsequent to actual scram events. Information is included for both main steam system (MSS) and RCS valves. The assumption was made in the UA that MSS and RCS SVs are alike enough in construct and servicing that their failure data can be jointly considered. Subsequent demands were assumed to have the same failure probabilities as initial demands. Recovered valve function, e.g., a previously stuck-open valve closing when pressure reduces, was not taken to be successful valve operation.

The "Main Steam System Code Safety Valves" section of Table 20, the value for all reports 0 failures to open and 15 failures to close, including in 769 demands considering all failures (recovered and non-recovered is 15). The "Reactor Coolant System Code Safety Valves" section of the table, the value for all reports 0 failures to open and 2 failures to close, including

recovered in 4 demands considering all failures. Combining the MSS and non-recovered is 2. RCS valve failures identify 0 failures to open and 17 failures to close in 773 demands. These failure rates served as the bases for uncertainty characterization of stochastic SV failure in the UA. Noteworthy with respect to these failure rates is that they are derived from actual events at US plants. NUREG/CR-7037 (Table 22) reports on failure rates in SV testing but the rates differ markedly from the rates evidenced by actual plant events suggesting (to the UA analysts) that aspects of the testing were inconsistent with actual conditions experienced by an installed valve. As such, the testing data was not considered applicable. The total FTC is therefore 17 as identified in Table 3-3 below. Table 20 identified no failures to open.

Table 3-6 SV failure data and associated epistemic uncertainty distributions for probability of occurrence on demand for FTO and FTC.

Mode	# Failures	# Tests	Distribution*
FTO	0	773	β(α = 0.5, β = 773.5)
FTC	17	773	β(α = 17.5, β = 756.5)

*Development of indicated distributions is described below.

The possible states of a 3-valve RCS primary pressure relief system are presented in **Error! eference source not found.** and the probability of being in a given state as a function of cycles can be seen in Figure 3-15. As FTOs occur, the system transitions from cycling on the lowest set-point valve (State 1), to cycling on the middle set-point valve (State 2), to cycling on the highest set-point valve (State 3). If an FTC does not occur at some point in the transition process such that a failed open state of the system develops (State 4), a failed closed state develops where pressure relief is no longer available (State 5).

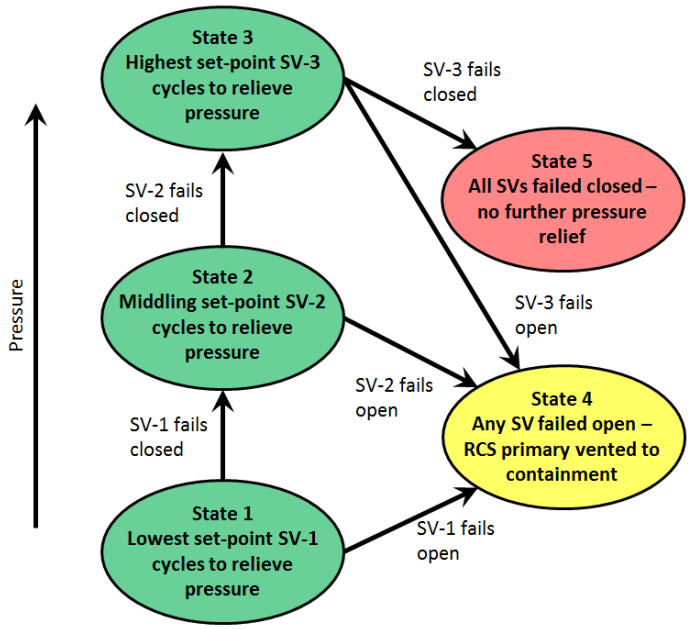

Figure 3-14 Possible transitions in the 3 SV pressurizer pressure relief system considering FTO and FTC valve conditions

Figure 3-15 shows the mean SV FTC and FTO distributions associated with the transitions outlined in **Error! Reference source not found.**. The probability of one valve failing open ersus the probability of all 3 valves failing closed is illustrated in the curves. The plot is truncated at 1,000 cycles based on professional judgment that an SV would likely not cycle more than a few hundred times prior to failure. It is noted that a very low possibility all 3 valves would fail to open was identified, but was never sampled in the 1,200 created uncertain realizations. However, failure to open was observed for the lowest set-point SV.

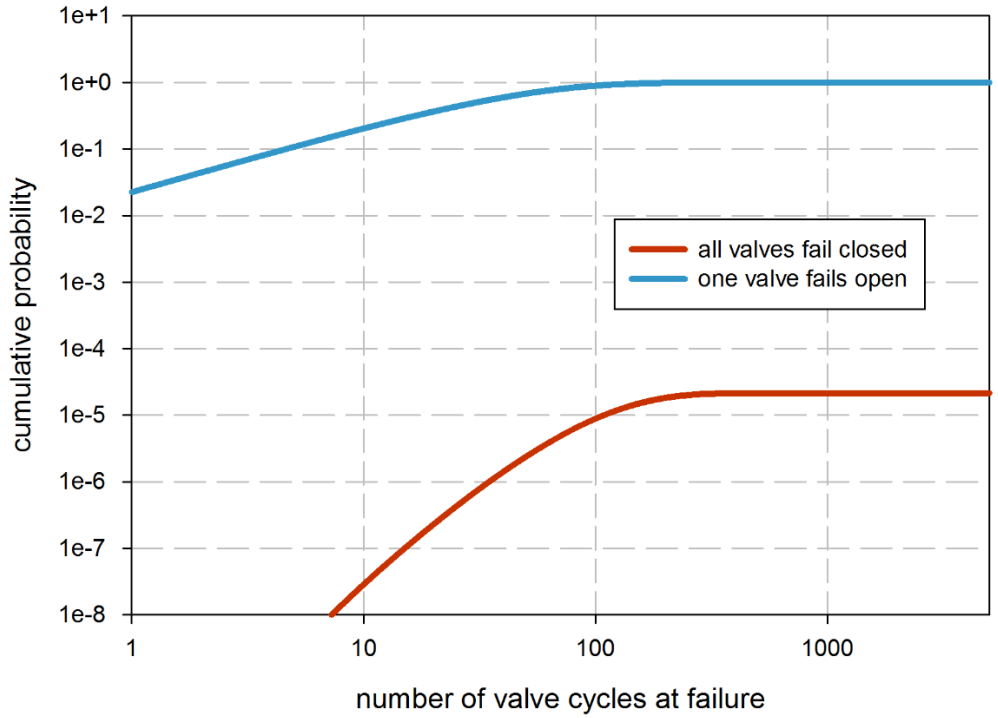

Figure 3-15 Mean CDF for number of cycles at which any SV of a 3-SV system fails open compared to the mean CDF for number of cycles at which all 3 valves fail

3.4 Primary SV Open Area Fraction (SV_frac)

The pressurizer SV thermal FTC open area fraction is represented by the MELCOR variable SVfrac. A uniform distribution is used to represent uncertainty with a lower bound of 0.01 and an upper bound of 1.

The Sequoyah approach again followed that used in the Surry UA which was based on information from the Surry SOARCA analysis [5]. There were no SV thermal failures observed for the unmitigated STSBO scenario in the Surry SOARCA analysis where an open area fraction of 1.0 (fully open) was used [5]. The Peach Bottom UA [9] explained there is no data available to predict the uncertainty of the SV valve position at the time when the SV sticks open from thermal seizure. The Peach Bottom UA applied a triangular distribution with a lower limit of 0.0 and mode and upper limit of 1.0 [9]. This was at least partially because Peach Bottom has a

different type of SV which cycles more rapidly, and would indicate a bias towards larger open fractions at the time of failure.

Rationale for Distribution

For this Sequoyah analysis, all three damage modes (steel softening, thermal expansion, and spring degradation) are considered, meaning that all open fractions will be physically possible. Since it is not known which damage mode is most probable, a uniform distribution between 0. and 1.0 was selected to measure the potential effects of this event on accident progression. This distribution is shown in Figure 3-16. The black dot shown at 1:1 is provided for information only and shows the Surry SOARCA value [5].

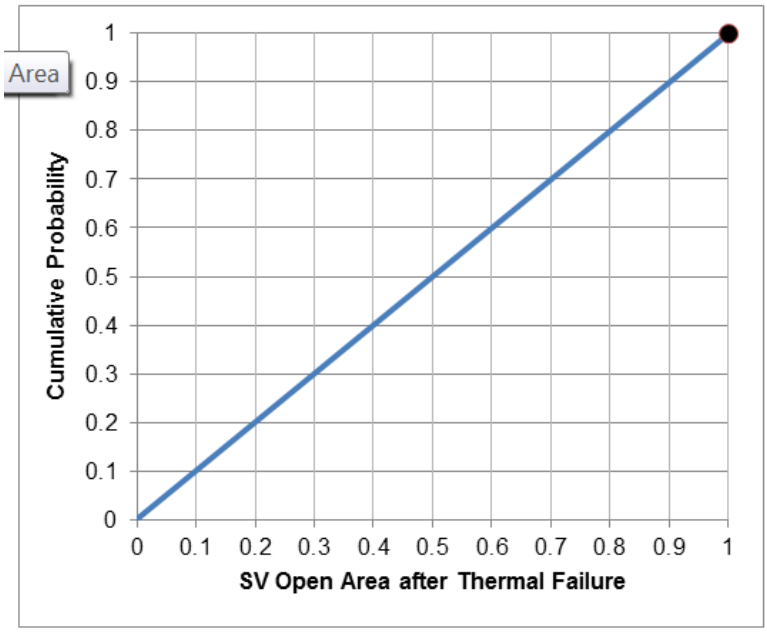

Figure 3-16 CDF for the SV thermal FTC open area fraction (SVfrac)

3.5 Effective Temperature of the Eutectic Reaction for Zircaloy Oxide and Uranium Oxide (EU_melt_T)

This parameter represents the effective temperature at which a eutectic reaction[13] between ZrO_2 in the cladding and UO_2 (and fission products) in the fuel causes the liquefaction and relocation of fuel rods. Within MELCOR, this is input as a eutectic sensitivity coefficient (SC1132) and a melting temperature. By including the temperature of the eutectic reaction between ZrO_2 and UO_2 as a sampled parameter, general fuel failure behavior of a complex non-equilibrium multi-component system is represented by simplifying the process to one reaction which can cause failure. This parameter affects the overall in-vessel melt progression and the amount of

[13] It is noted that the pure UO_2/ZrO_2 system has only a melting point, not a eutectic point. High burnup pins have complex intermetallic effects which are referred to as eutectic reactions in the VERCORS [42] experiments and the MELCOR users guide. This nomenclature is maintained for this analysis.

hydrogen generated that is released to the containment. The Sequoyah approach again followed that used in the Surry UA [17].

The binary phase diagram for ZrO_2/UO_2 suggests the melting point for equilibrium conditions is approximately 2800 K for a 50/50 molar mixture; hence this was the historical MELCOR default value. Any liquefaction below this temperature accounts for the effect of molten Zircaloy metal or alpha-Zr(O) 'wetting' the oxide surfaces. Observations of the Phebus ([37][38][39][40][41]) and VERCORS experiments [42] suggest that irradiated fuel and oxidized cladding exhibit eutectic liquefaction at significantly lower temperatures; thus the MELCOR default was subsequently modified to 2500 K. Following significant local cladding oxidation, the effective liquefaction of ZrO_2 and UO_2 mixtures results in local rod collapse as molten material rather than as rubble or debris. The parameter treatment for this work attempts to approximate the combined uncertainties associated with burnup, eutectic composition, material properties, and non-equilibrium effects on ZrO_2/UO_2 eutectic reactions.

The fuel melt associated with this parameter is a localized effect. This means that MELCOR evaluates the temperature independently for each core cell and allows the fuel in that specific cell to melt when it reaches a failure temperature, such as the eutectic temperature (i.e., melting temperature of the eutectic formed between ZrO_2 and UO_2). Thus, the entire core will not fail at once when the hottest region reaches the sampled temperature. It is possible that melting of a core cell can cause the subsequent failure of fuel above in the same radial ring that was previously supported by the failed cell. However, this is a physical effect and still only affects a section of a single ring, and keeping it localized.

In MELCOR, eutectic reactions are approximated by user-modification of melting and failure temperatures in model input. Thus, to represent the effective temperature of the eutectic reaction, the user must modify:

1. The sensitivity coefficient SC1132(1), which defines the cladding temperature resulting in rod collapse without Zr-metal cladding remaining, and

2. The melting temperatures of both UO_2 and ZrO_2 in the input deck (MP_PRC records).

Rationale for Distribution

Six experimental data points for eutectic induced core collapse are readily available from the VERCORS experiments to help inform the uncertainty distribution [42]. Table 3-7 shows the VERCORS test results along with the mean and standard deviation.

Table 3-7 VERCORS test results for collapse temperature.

Test	Collapse Temperature (K)
T1	2525
HT1	2550
HT2	2400
HT3	2525
V_6	2525
RT6	2350

Mean	2479
Standard Deviation	83

In selecting this experimental data, observed core slump is projected to a eutectic reaction. This was strongly indicated by the test results but cannot be definitively confirmed due to a lack of instrumentation.

The selection of a specific distribution is complicated by the lack of detailed experimental data over ranges of severe accident conditions and reactor operation (e.g. high burnup). While the VERCOR testing matrix does not provide randomly distributed evidence of eutectic formation temperatures, these tests do provide a range of temperatures over which eutectics were significant enough to cause core collapse. A normal distribution fitted to the data in was used to assess uncertainty in the average core collapse temperature for higher burnup fuel. The simple parameter treatment is not intended to rigorously quantify eutectic effects on severe accidents and core degradation; such treatment is impossible when the MELCOR eutectic model is not activated. Rather, the proposed treatment roughly evaluates the influences that the physical state of the core debris has on core degradation kinetics and subsequent severe accident progression. A lower temperature for this parameter results in an increased generation of molten pools in the RPV during core disassembly. Alternatively, a higher temperature for this parameter results in a decreased generation of molten pool formation for ZrO_2 and UO_2 debris. The relocation and cooling of molten pools after formation are treated by several other models and parametric inputs in MELCOR; hence the eutectic parameter only affects the initial creation of molten pools for ZrO_2 and UO_2 immediately upon rod collapse.

Even though the testing data was derived from independent, identical tests, a normal distribution was fitted to the VERCORS data in order to describe the general range of potential collapse temperatures from VERCORS given varying environmental conditions, and is seen in Figure 3-17. This normal distribution has a mean of 2479 K and a standard deviation of 83. The red star in Figure 3-17 is provided for information only and represents the 2800 K value used in SOARCA [5]. Even left unbounded, the probability of sampling beyond these bounds is effectively *de minimis*, thus the bounds should not affect the results of this work.

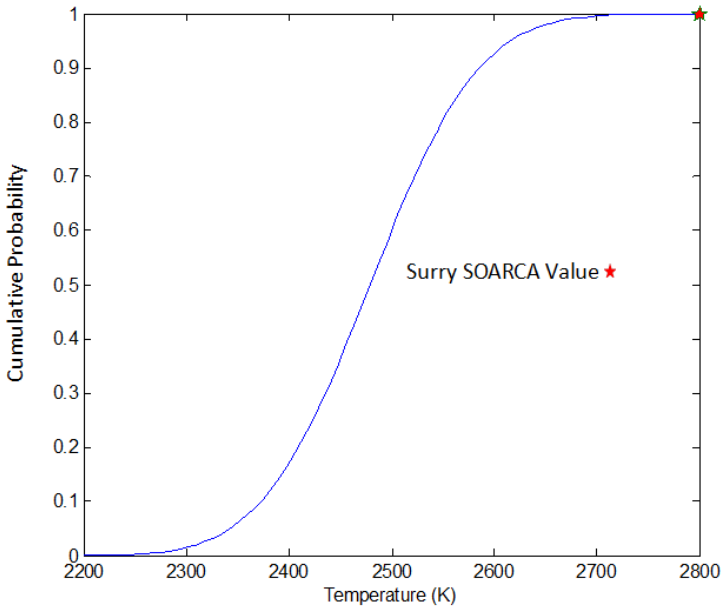

Figure 3-17 CDF of effective temperature of the eutectic reaction temperature

3.6 Hydrogen Ignition Criteria

The hydrogen ignition criteria has two components, (a) ignition with a well-defined source and (b) random ignition. Ignition from a well-defined source is modeled based on hot gases exiting the RCS hot leg failure location above the hydrogen auto-ignition temperature or ex-vessel debris with vigorous concrete ablation. These two conditions are assumed to provide well-defined ignition sources throughout the lower containment. The random ignition, when activated, randomly provides one 1 second ignition source every 30 minutes at a specific location inside the containment. For combustion to occur when an ignition source is present, the local gas concentration must satisfy the combustibility limits determined by the experimental research [30]; however, the combustibility limits from this research were varied to represent uncertainty in the direction of propagation from the ignition source for upward, horizontal, and downward propagation. In particular, the flammability, or propagation, limits are greatly influenced by the initial direction of propagation from the ignition source. For example, the limits for hydrogen-air mixtures for upward, horizontal, and downward initial propagation of the flame are 4, 6, and 9 percent hydrogen, respectively, demonstrating the effect of buoyancy [30]. Sampling is performed on upward, horizontal, and downward propagation direction from the ignition source. Hence, combustion will occur in the lower containment when a well-defined source is present and the combustible gas concentration is above the criteria for the sampled direction.

When random ignition sampling is activated, an ignition source is specified within a compartment. Each uniform time period (i.e., 30 min), a random ignition source will be present in a single control volume anywhere in the primary containment. A burn will be initiated in the specified control volume if the combustible gas concentration is above the hydrogen gas concentration criterion for the spontaneous ignition (i.e., using the MELCOR default value of 10% [20]).

Once a burn ignites from a well-defined or random source, the burn may propagate to adjacent control volumes based on well-established propagation limits (i.e., from research for upward, horizontal, and downward [30]).

Rationale for Distribution

Sources of ignition could be present throughout the compartmentalized containment such that the location(s) where hydrogen would ignite and the direction(s) the flame(s) would need to propagate would be uncertain and random. The experimental information [30] relied upon in defining the sampling distribution for hydrogen lower flammability limits is limited to flame propagation in the primary directions of upward, horizontal, or downward. This suggests a discrete distribution is applicable. No information is available to suggest that any one direction is more likely than another, thus a uniform weighting of the three discrete initial propagation directions (and corresponding lower flammability limits for hydrogen of 4%, 6%, and 9%) is appropriate. Figure 3-18 shows the discrete distribution, each equally likely, for each ignition source location and initial propagation direction.

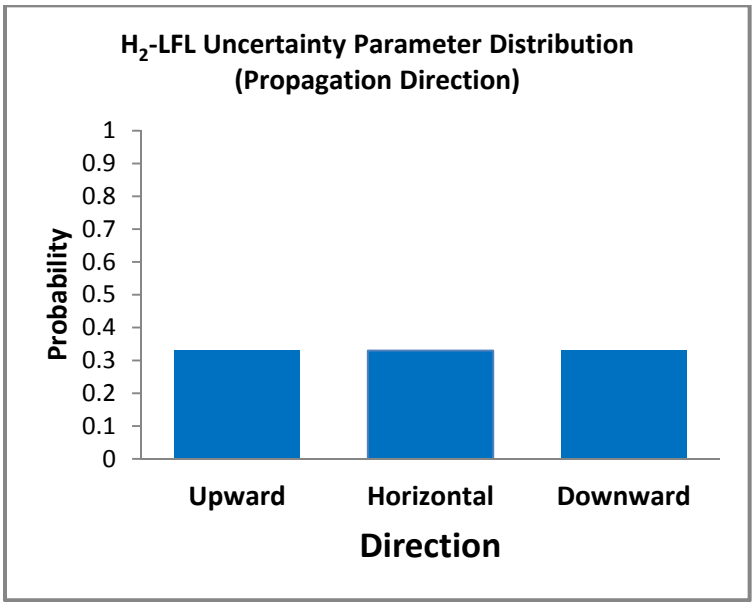

Figure 3-18 Uncertainty distribution for ignition propagation direction

Ignition by an unspecified random source (IGN_RANDOM) is also considered in the MELCOR calculations recognizing, for example, that a static electrical discharge could start a burn. (Note that a spark on the order of only a millijoule can ignite hydrogen.) Static electrical discharges, if they occurred in an accident, would likely be occasional and momentary as well as variable in location. Other conceivable sources are sparks from ice condenser door openings/closings and hot RCS piping. (A temperature greater than 847 K exceeds the autoignition temperature of hydrogen.) Ignition by an unspecified source was modeled with consideration of the potential for static electrical discharges.

3.7 Barrier Seal

The upper and lower compartments of Sequoyah's containment structure are separated by a divider barrier (see Figure 3-19). Under accident conditions, the divider barrier acts to limit the

amount of hot gases, steam and vapor that can bypass the ice condenser. The divider barrier is constructed of flexible, rubber coated fabric seals that extend across the gap between the inside surface of the outermost steel containment vessel and the concrete structure within each vessel. The seals consist of 12 vertical and 11 horizontal segments of flexible coated fabric that are bolted to the vessel and the concrete structure by clamps and seal bars. Each segment sealing surface is a minimum of 3.5 inches wide with lengths varying from 2.0 to 63.9 feet. In total, the barrier seal length is 463.7 feet with a total sealing area of 135.25 ft^2 (12.56 m^2).

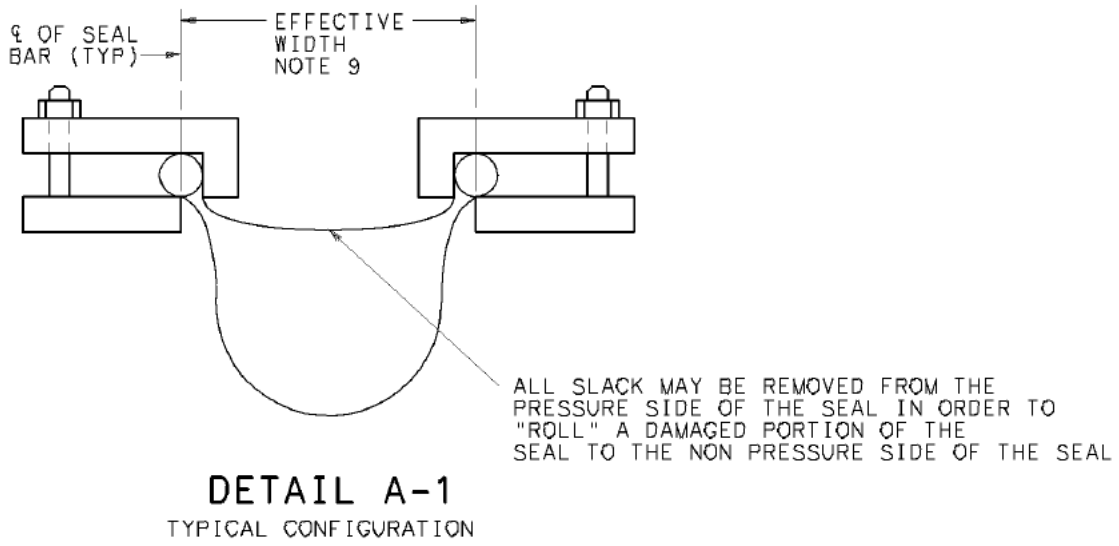

Figure 3-19 Barrier seal section

The seals are intended to maintain their integrity during operating or design basis accident conditions for a minimum of 12 hours with total leakage of less than 0.4 percent (0.5 ft^2). For comparison, it should be noted that the smallest segment (2.0 feet in length) seals have an area of 0.6 ft^2. As such, failure of the fabric coated seal in one or more segments during an accident could significantly increase the effective bypass area of the divider.

Postulated failure of the fabric seal under pressurized conditions would likely begin with a localized failure of the seal. This could occur due to a weakness in the fabric or could occur from shear stress during the seismic event. Possible weaknesses could be induced by clamping forces, clamping surface irregularities, localized fabric defects or strength reduction due to field splices. Once compromised, the failure could propagate along the length of the affected seal segment, thereby partially opening the associated segment seal area to bypass flow. The assumption that the entire seal area is opened for bypass upon seal segment failure is conservative because some fabric is likely to remain in place; however, no basis was identified to establish the amount of remaining fabric.

The sealing areas (ft^2) of the 23 segments are: 0.58 (8), 0.73, 2.07, 3.27, 3.45, 3.50, 6.70 (3), 7.28, 9.62, 10.89, 12.02, 18.64 (2), and 20.38. Since larger seal areas have a greater chance of local weakness than smaller seal areas, one can consider that the probability of each segment failure is proportional to its segment area. For example, given that a local failure occurs, the probability that the failure will occur within the segment having a sealing surface of 2.07 ft^2 is:

$$P_{failure,\ 2.07} = 2.07\ ft^2/135.25\ ft^2, \text{ or } 1.5\%.$$

This assumes that the probability of local failure is uniform along the entire length of the barrier seal. This creates the first distribution, (Figure 3-20) which samples on break area.

The coated fabric seal material is intended to maintain a tensile strength of 100 lb/in and exhibit no leakage up to 30 psid (psi differential). Given the linear seal geometry, the tensile strength of 100 lb/in corresponds to a pressure differential of 2 * 100 lb/in / 3.5 in = 57.14 psid.

To determine the pressure conditions upon which seal failure will occur (Figure 3-21), a beta function spanning the range of 0 psid to 57.14 psid is used, assuming failure will never be above the specified tensile strength. The values of α and β are chosen to force two boundary conditions, based on engineering judgement to sample the physical range. The first condition specifies that the total probability of failure at pressures up to 30 psid is 0.1, or 1 in 10. The second condition specifies that the median of the CDF occurs at about the midpoint of testing criteria and the ultimate tensile strength, 43.57 (30 + (57.14-30)/2). The result is a beta function with α = 5.0 and β = 1.8.

Rationale for type of distribution

A discrete distribution for the local failure is appropriate since although the likelihood of localized seal failure is uniform over the length of the seal, with bolting and direction changes in the seal, it is less likely multiple segments would fail. The failure of even the smallest segment would be large enough to dissipate pressure differences, limiting the potential for another segment to fail due to over-pressurization. The probability for each segment is based on the area ratio, since larger seal areas have more material and more clamping, contributing to an increase in the occurrence of seal weaknesses. The distribution also takes into account that there are multiple segments with the same area, which is why 0.58 ft^2 is more likely than 0.73 ft^2, for example. There is some possibility that a large fire could destroy multiple sections of the seal simultaneous, but due to the location of the seal and wetted conditions, it is considered very unlikely the entire seal area would be opened. The barrier seal failure is represented by flow path 805 connecting the lower annular region (CV11) to the containment dome (CV24) in Figure 3-8.

The beta distribution constraints were chosen so that the majority of failures occur between the design test pressure differential (30 psid) and the pressure difference corresponding to the ultimate tensile strength (57.14 psid). This tensile strength is also set as the upper bound of the distribution. Ten percent of samples are below design, to account for the possibility that even with testing, accident conditions could lead to failures at lower pressure differentials. The lower bound of the distribution is theoretically 0, but due to the Beta parameters chosen, it is effectively 15 psid.

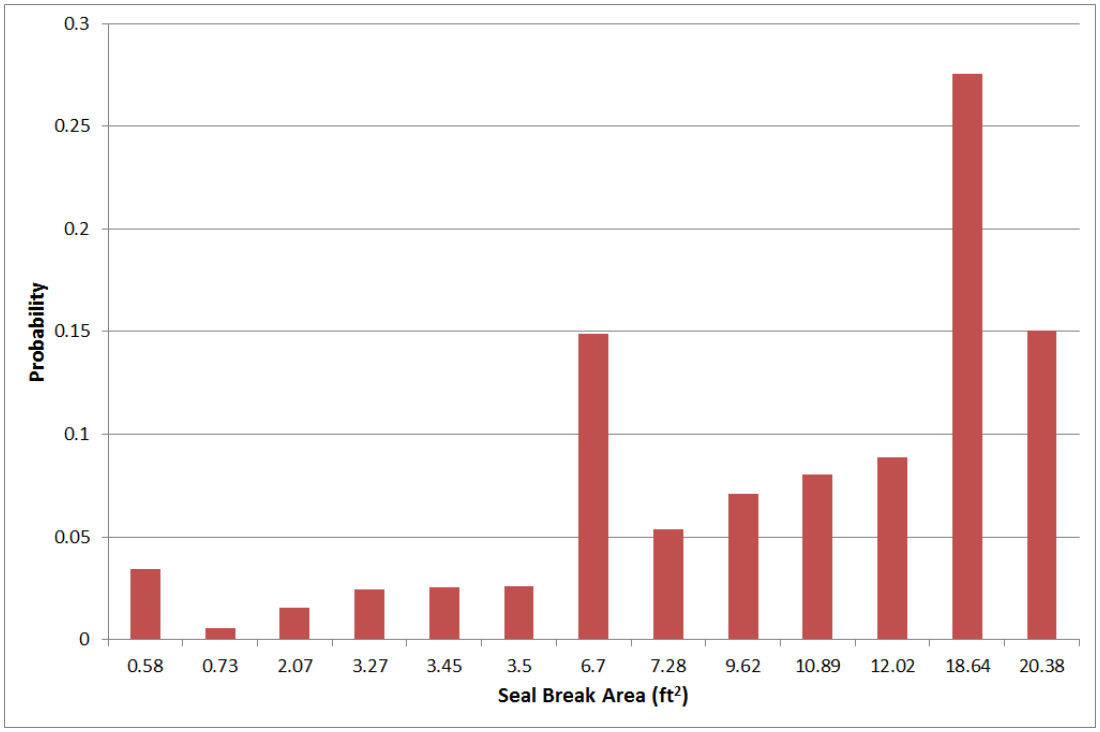

Figure 3-20 Seal break area probability

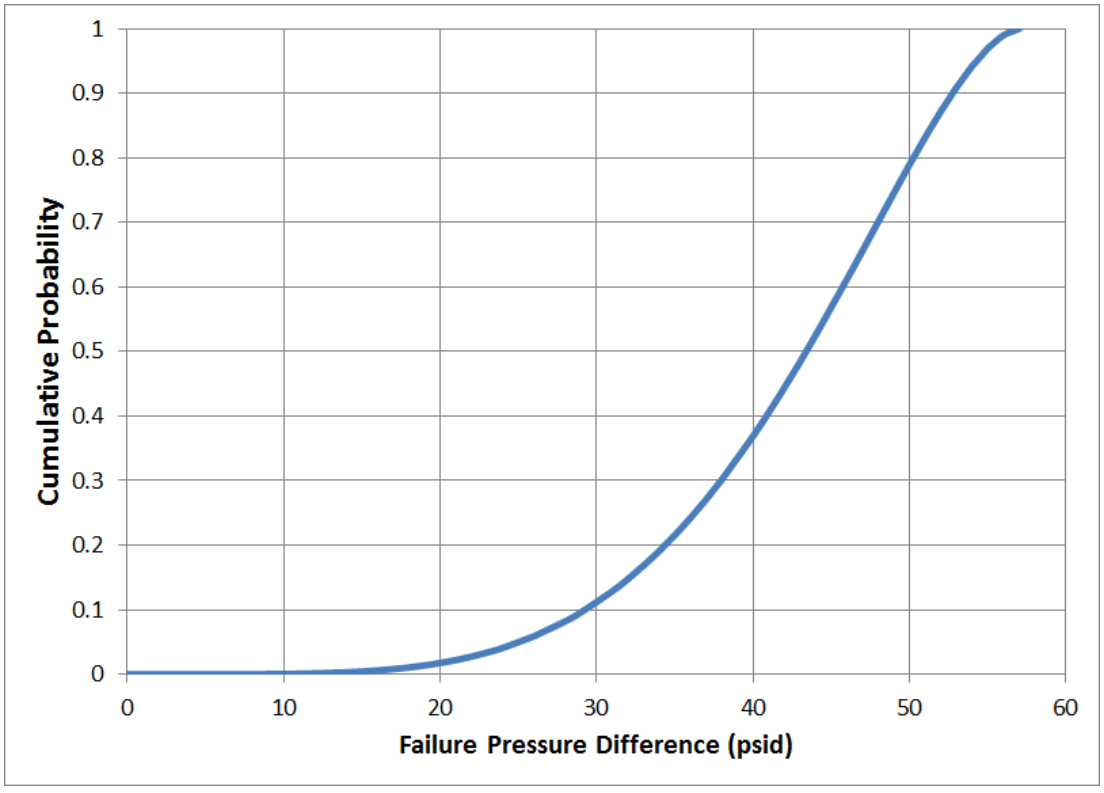

Figure 3-21 CDF of failure pressure difference

3.8 Ice Bed Lower Plenum Doors (AJAR)

The ice bed lower plenum doors, if forced open to the point where they do not reclose, allow recirculation flows between the ice condenser and the lower containment and can effect conditions in the lower containment [18]. A uniform distribution with a range from 0 to 1 was used for the fraction of the lower plenum doors stuck open after they are fully opened (see also Section 3.1.6 and Figure 3-9).

A discussion of various sensitivity calculations and uncertainty on the ice chest doors is provided NUREG/CR-5586 [18]. The base case calculations in NUREG/CR-5586 were based on the irreversible operation of the lower plenum doors, i.e., the doors were assumed to open and close until the maximum opening. The lower plenum doors characteristics are illustrated in Figure 3-22.

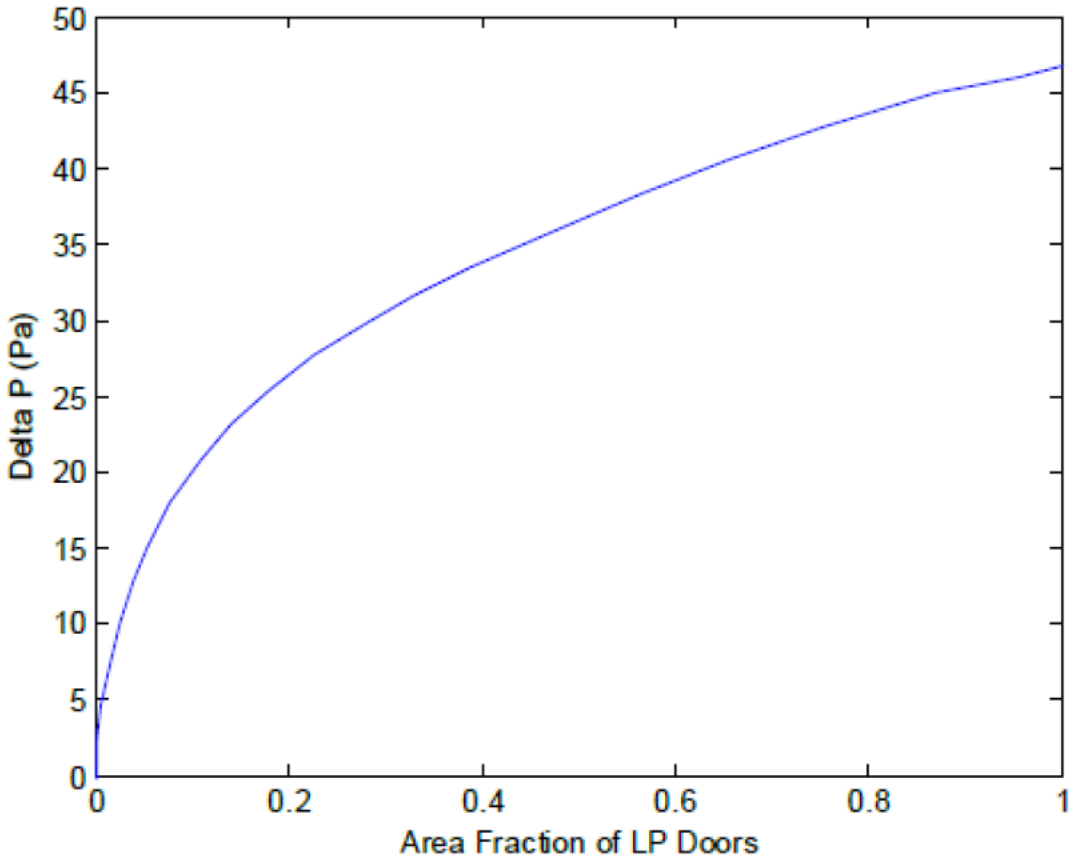

Figure 3-22 Lower plenum doors characteristics (developed from NUREG/CR-5586)

As explained in Table 2.4 of NUREG/CR-5586, once the pressure exceeds the value required for maximum opening, the lower plenum doors remained open [18]. This was considered to be more realistic (see Page 138 of NUREG/CR-5586 [18]). NUREG/CR-5586 acknowledges uncertainties in the behavior of the doors and two sensitivities were done (1) lower plenum doors are reversible, and (2) lower plenum doors are 50 percent reversible and 50 percent irreversible (as modeled in Table 2.2 of NUREG/CR-5586 [18]).

For the present MELCOR calculations, it was decided to combine the above sensitivities by assuming a certain fraction of the doors remain open after they are fully opened. This fraction is sampled from a uniform distribution (see Figure 3-23) and applied to all the flow paths connecting the lower compartments (CV8, 9) to the lower plenum volumes (CV14, 15, 16, and 17). The flow paths shown in Figure 3-9 are 49, 50, 54, 55, and 57. This is captured only in the initial full opening of the doors and for the remainder of the time, the doors are assumed reversible if they open again. For example, for a single realization, if 0.2 is sampled from the cumulative distribution in Figure 3-23, when FL49 (A=19.51 m^2) is opened fully, it is assumed that a minimum flow area of 19.51 x 0.2 would remain for the remainder of the transient while 80% of the doors continue to behave reversibly based on their differential pressure characteristics.

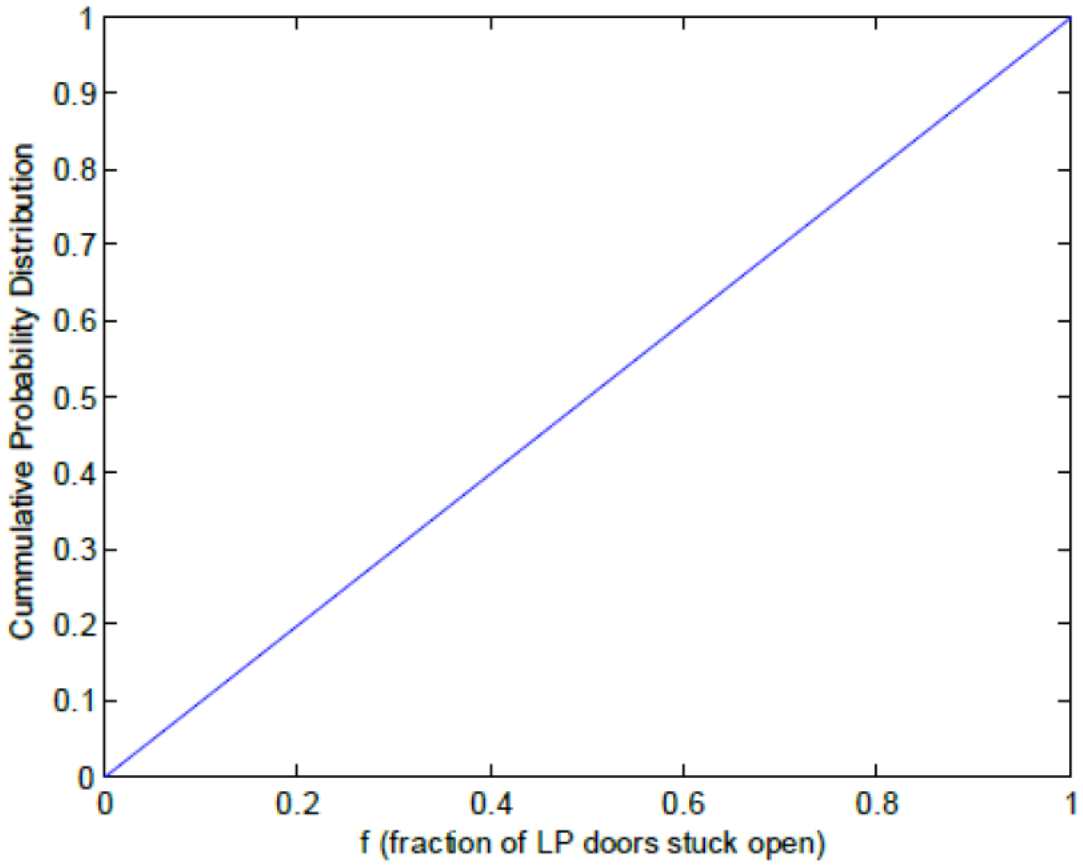

Figure 3-23 Fraction of LP doors stuck open

3.9 Dynamic Shape Factor (shape_factor)

The dynamic shape factor is defined as “the ratio of the actual resistance force of the non-spherical particle to the resistance force of a sphere having the same volume and velocity” [46]. This unitless dynamic shape factor is used to account for the stringing out of aerosol agglomerates in a linear or complex manner as opposed to growing as a perfect sphere. The dynamic shape factor is sampled directly, and the uncertainty of it is represented with a scaled beta distribution with the parameters of α=1 and β=5 and bounds of 1.0 and 5.0 (consistent with the Surry UA [17]). A value of 1.0 is a perfect sphere and it is the lower limit for the dynamic shape factor. This value is the default value in MELCOR.

Rationale for Distribution

The MAEROS model in MELCOR is used to determine the mass concentration evolution of aerosols in a spatially homogenous volume, as well as deposition on surfaces and injection/removal from volumes. One of the critical assumptions of this model is that non-spherical particle effects are adequately parameterized with the dynamic shape factor, the collision shape factor, and the effective material density. The importance of these parameters is demonstrated in several uncertainty analyses of the MAEROS aerosol model performed in support of the development of the MELCOR program [43][44]. To determine the uncertainty of this model, the uncertainty of the dynamic shape factor is addressed.

Kasper et al. [45] (Tables 9 and 10), experimentally measured values for the dynamic shape factor for linear chains with their long axis either parallel or perpendicular to the settling direction, as shown in Figure 3-24. As seen in the figure, the shape factor is reasonably linear with respect to the number of spheres. This data supports an upper bound of 2.8, with a weighting toward values less than 2.0. Compiled data from Hinds [46] (pg. 48) also supports a range of 1.0 to 2.04. However, Brockmann, J. E., et al [47], compiled data and models that yield a range of 1 to 10 for the dynamic shape factor. The same report includes a correlation for loosely-packed spheres which calculates dynamic shape factors to be in the range of 1 to 5 for void volumes ranging from 26 to 99 percent. Based on these sources, a range of 1 to 5 is reasonable and is the range used for this project.

Although the bounds of the distribution were informed by the experiments described, these works cannot inform the shape of the distribution since they do not contain information on the normal shape of aerosols during a severe accident. Kissane [48] compiled information on aerosols from a number of nuclear accident experiments, including the Phebus fission product tests. The report concluded, “Concerning particle shape, relatively compact particles without branching chain-like structures appear to be typical in the RCS;” although a visual inspection of post-test deposition images did show slight evidence of aerosol chains. Since a compact, spherical particle has a shape factor of 1.0, the distribution is weighted more heavily toward the lower end of the range (1.0). Additionally, most references support weighting more heavily in the 1.0 to 2.0 range. Because of this weighting, a beta distribution is used ($\alpha=1$; $\beta=5$), and the CDF of the distribution is shown in Figure 3-25. The α parameter yields a function that has a peak as close as possible to the lower bound of 1.0, while the β parameter gives the desired shape to the PDF and yields about 75 percent of samples between 1.0 and 2.0 while still allowing some samples at physically possible values up to 5.0.

Additionally, there is a fundamental MELCOR limitation for aerosols in that the dynamic and collision shape factors and density are set globally at the beginning of the run and cannot be updated as the accident progresses. This means that the dynamic shape factor chosen from the uncertainty distribution cannot be changed during the accident progression.

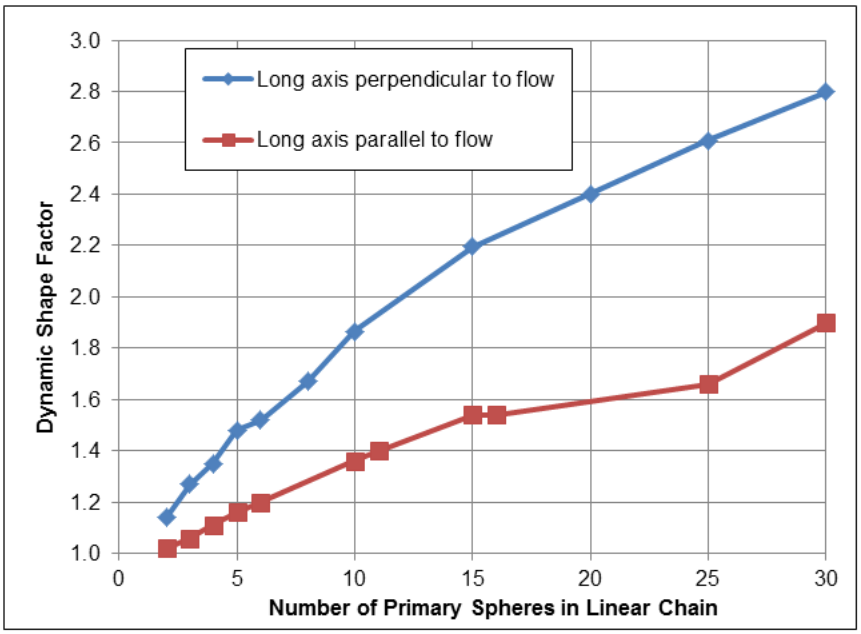

Figure 3-24 Dynamic shape factor compared to number of spheres within a chain

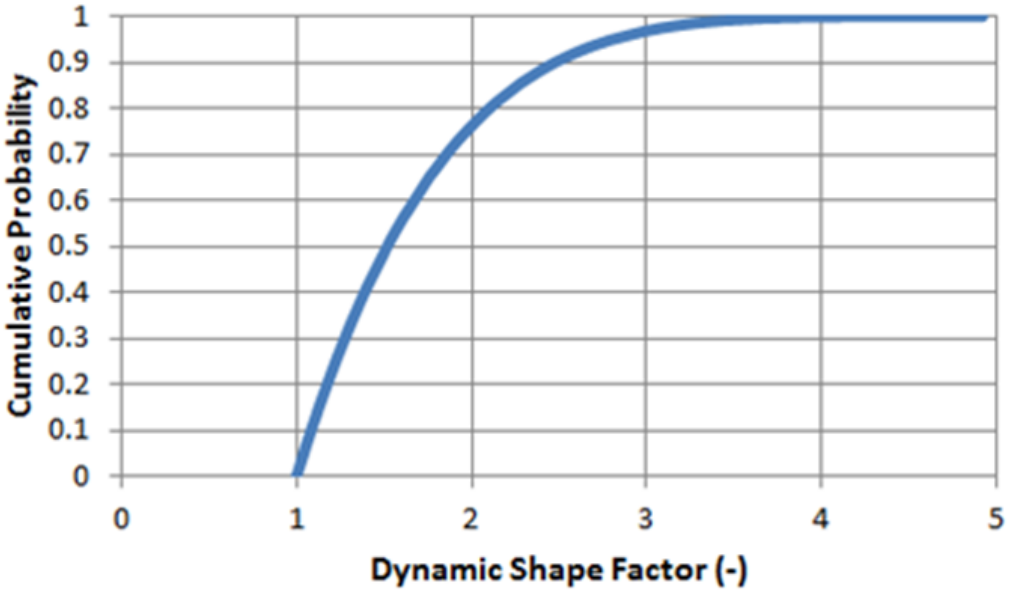

Figure 3-25 CDF of the dynamic shape factor

3.10 Containment Rupture Pressure (rupture)

Section 3.1.7 provides details on the containment design and the rationale for the uncertainty distribution for the containment failure pressure. The uncertainty in the internal pressure that a Sequoyah free-standing steel containment vessel can withstand before rupturing is addressed through the parameter "*rupture*". NRC SMEs suggested that 67 psig be considered in the UA as

the best-estimate magnitude of the pressure a Sequoyah containment vessel can withstand and that a range between 52 psig and 78 psig be considered possible. Accordingly, a triangular distribution with a mode of 67 psig and lower and upper bounds of 52 psig and 78 psig, respectively, was prescribed in the random sampling of *rupture.*

4. ACCIDENT PROGRESSION ANALYSIS

This section describes the results of the severe accident progression. The MELCOR 2.1 code was used for the analysis of the scenarios specified in Chapter **Error! Reference source not found.** (i.e., the STSBO and LTSBO) using the MELCOR model described in Chapter 3. The objective of this study is to extend the analysis performed for the Surry SOARCA (a large dry containment plant) to consider the accident progression in an ice condenser plant. The severe accident progression in an ice condenser plant has some different characteristics from a large dry containment due to the relatively small freestanding steel containment with ice chests. The Sequoyah in-vessel accident progression was expected to be similar to Surry, since both are Westinghouse PWRs. The thermal power of the Westinghouse PWRs are approximately scaled based on the number of recirculation loops. The Sequoyah plant has four recirculation loops and steam generators versus only three for Surry. Consistent with the RCS loop ratio, the Sequoyah thermal power rating is ~35% larger. However, the number of assemblies, the mass of the fuel, and the size of the vessel are also larger in Sequoyah by about ~23% (i.e., 193 assemblies in Sequoyah compared to 157 in Surry). Consequently, the in-vessel response is expected to scale somewhat similarly.

Unlike the in-vessel accident response, the containment response of an ice condenser plant is expected to be substantially different than a large dry containment following the breach of the RCS. The ice condenser containment is expected to be more susceptible to failure from hydrogen burns following the RCS hot leg failure or RPV lower head failure.[14] The analyses confirmed these expectations, which suggested two potential containment failure timings. An early containment failure was possible following the RCS breach due to a hydrogen deflagration that over-pressurizes the containment Alternatively, if hydrogen burns do not fail the containment early (in the initial 12 to 24 hours), ongoing steam production and noncondensable gas generation associated with core-concrete interaction eventually decrease oxygen concentration below combustible limits. However, the containment will fail later due to over-pressurization from ongoing steam production, unabated fission product decay heating and noncondensable gas generation associated with core-concrete interaction. The details of the analysis and final results, along with UA, are presented in the following sections.

4.1 Short Term Station Blackout (STSBO) Base Case

This section presents the results of a base case unmitigated STSBO scenario in the Sequoyah plant. Although mitigative actions would be recommended and attempted throughout the accident, the unmitigated STSBO assumes no mitigative actions are successful. As described in Chapter 2, the STSBO is initiated by a seismic event that fails power supply to operate most of the safety systems, but does not fail the structural integrity of the RCS or containment. In particular, the TDAFW is unavailable to inject cooling water into the SGs. No other water injection system is available to maintain the water level in the SGs or RPV due to loss of AC power which renders the ECCS inoperable.

Table 4-1 summarizes the timing of the key events in the base case unmitigated STSBO. There are two known sources of ignition included in the scenarios without random ignition as

[14] The RCS breach is used as a surrogate for an obvious hydrogen ignition source due to auto ignition from the hot jet from at the hot leg breach or the hot debris in the containment following RPV lower head failure. The scope of the results presented in this section also includes calculations with random ignition sources prior to RCS breach.

discussed in Section 3.1.8. The two ignition sources are the creep rupture failure of hot leg and the failure of vessel bottom head. The ignition sources are imposed in the MELCOR model when conditions of the accident progression create an identifiable source for auto-ignition of hydrogen (i.e., a hot jet above the auto-ignition temperature from the hot leg or hot core debris in the containment).

Table 4-1 Timing of key events for base case unmitigated STSBO.

Event Description	Time (hh:mm)
Initiating event Station blackout – loss of all onsite and offsite AC power	00:00
MSIVs close Reactor trip TDAFW start but fails to inject RCP seals initially leak at 21 gpm/pump	00:00
First SG SV opening	00:00+
First SG SV fails stuck open (after 45 cycles)	00:30
Steam generators dry out	00:42
Pressurizer SV opens	01:39
PRT rupture disk opens	01:56
1% of the ice melted	01:57
Water level below top of active fuel	02:13
Pressurizer SV stuck open (45 cycles)	02:43
First fission product gap releases	02:57
Accumulators begin injecting	03:48
25% of ice melted	03:50
Creep rupture failure of the hot leg nozzle in combined loop	03:50
1st hydrogen deflagration	03:50
Half of ice condenser lower plenum doors stuck open	03:51
Accumulator empty	03:52
50% of the ice melted	04:24
Vessel lower head failure by creep rupture	07:07
Debris discharge to reactor cavity	07:07
100% of the ice melted	10:22
Containment fabric seal torn	52:23
Containment failure due to slow over pressurization	52:23
Selected MELCOR Results	
Debris mass ejected (1000 kg)	161
In-vessel hydrogen generated (kg)	448
Iodine release fraction at 72 hr	6.93E-2
Cesium release fraction at 72 hr	6.31E-2

The response of the primary and secondary systems is shown in Figure 4-1. At the start of the accident sequence, the reactor protection system actuates to terminate the fission reaction in response to events from the loss of grid. The MSL, the main feedwater, and the containment

isolation valves also automatically close. The RCPs coast down due to the loss of power. The primary system PORVs and the secondary system atmospheric relief valves are not available to control pressure and remain closed. Consequently, the secondary system pressurizes to the SV opening pressure. The SG safety valves open to prevent an over-pressurization and subsequently close when their closing pressure criterion is achieved. Steam flow out the SG SVs is the principle primary system heat removal mechanism in the first hour as shown in Figure 4-1, while the secondary pressure is kept a little above 1000 psia. There is also energy removal through the RCP seals leakage, but the leakage flow is small relative to the SG SV flow.

After 0.57 hr, the SG SVs have cycled 45 times and are assumed to stick open at 50% of the nominal flow area. The SG SV failure starts a rapid depressurization of the SGs as shown in Figure 4-1. The SG depressurization greatly increases the cooldown and depressurization of the primary but also increases the loss of water inventory from the SGs. The water inventory in the steam generators decreases very rapidly and is completely gone in less than an hour as shown in Figure 4-2.

The pressure in the primary system starts to increase due to the loss of cooling from SGs. A safety valve on the pressurizer begins cycling to remove excess energy and maintain the primary pressure below 2500 psia. The steam from the pressurizer SV is directed to sparger located below the water level in the PRT. The steam flow heats the PRT water to boiling, which pressurizes the tank. The PRT rupture disk opens at 1.93 hr. The pressurizer SV cycling also causes a decrease in the primary system coolant inventory. The fuel starts to uncover slightly after 2 hours as shown in Figure 4-3. As the RPV level decreases, the fuel at the top of the core starts to heat up as shown in Figure 4-4. The steam in the core starts to oxidize the fuel cladding at high temperature, which is an exothermic reaction that further accelerates the fuel heat up. The cladding pressure barrier fails at 900°C, which starts the fission product release from the fuel. The reactant gas from the Zircaloy-steam oxidation is hydrogen. The in-vessel hydrogen generation is shown in Figure 4-5. The hydrogen and high temperature steam exiting the core develop natural circulation patterns in the vessel, the hot leg, and in the SGs. The hot gases heat the structures in the natural circulation pathways.

Similar to the SG SV response, the pressurizer SV is also assumed to stick open after 45 cycles. The pressurizer SV sticks open at 50% of the nominal flow area at 2.7 hr, which depressurizes the primary system (Figure 4-1). The stuck open pressurizer SV draws hot gases from the core and out the SV. The new hot leg flow pattern heats the hot leg nozzle, which is calculated to fail the hot leg piping near RPV nozzle at 3.84 hours. Upon creep failure of the hot leg piping, the primary system rapidly blows down into the containment since the PRT had already failed. The RCS accumulators completely discharge their water inventory into the RCS, which floods the hot and degrading fuel in the core (i.e., see rapid water level recovery at 3.84 hr in Figure 4-3).

The decay heat in the fuel subsequently boils away the accumulator water which starts a second heat up of fuel. The fuel collapses and forms a hot debris bed that fails the supporting core plate structures. The hot debris relocates to lower head region of RPV, boils away the remaining water, and heats the vessel lower head. The lower head fails at 7.12 hr. Nearly all the fuel debris from the vessel relocates into the reactor cavity in the containment under the reactor vessel by 10 hr. The hot debris boils away the residual water in the reactor cavity and starts ablating the concrete. The ex-vessel core concrete interaction (CCI) continues for the remainder of the calculation, which generates non-condensable gases. The concentration of gases in the containment dome is shown in Figure 4-6.

Initially the containment is heated and slightly pressurized by the loss of containment heat removal and the hot water leakage from the RCP seals. However, these small heat sources are inconsequential at melting any ice in the ice chests (see Figure 4-7). Following the PRT rupture disk opening at 1.93 hr, the ice begins melting. The rapid blowdown of the primary system following the hot leg failure at 3.84 hr swings the lower ice chest doors open and is assumed to deform the door hinges (see Section 3.8). The lower doors remain open at an assumed position of 50% for remainder of the accident. There is an increase in ice melting rate as hot gases from the degrading core flow out of the hot leg failure location and into the ice chests. The steam entering the ice compartments condenses and melts the ices. The ice melting rate slightly slows after the vessel dryout but increases following the start of CCI at 7.12 hr. All ice is melted before 10 hours.

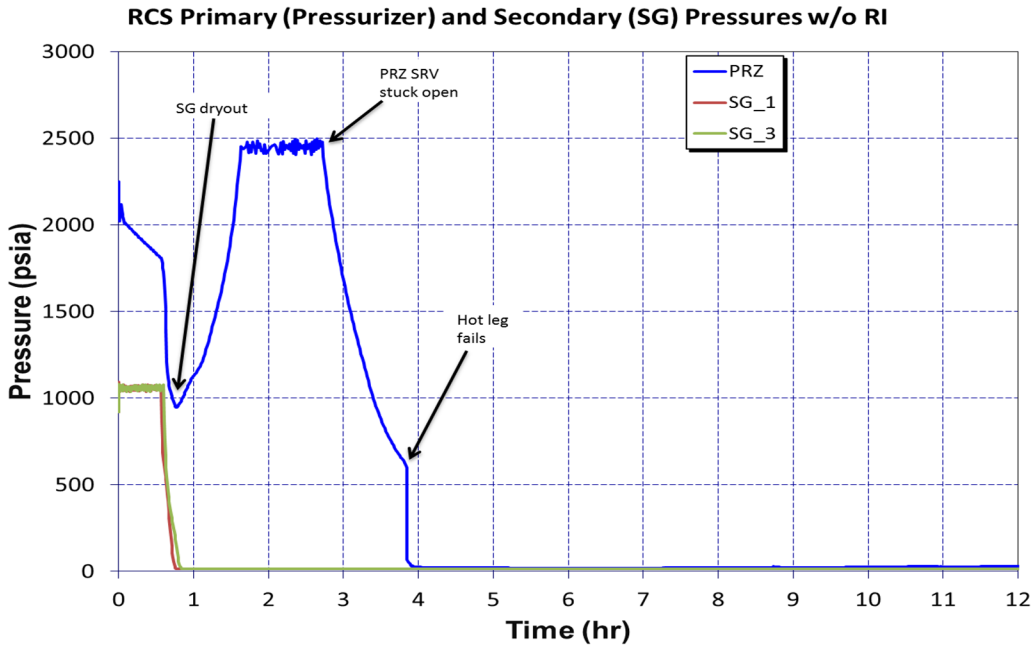

Figure 4-1 STSBO base case primary and secondary pressure history

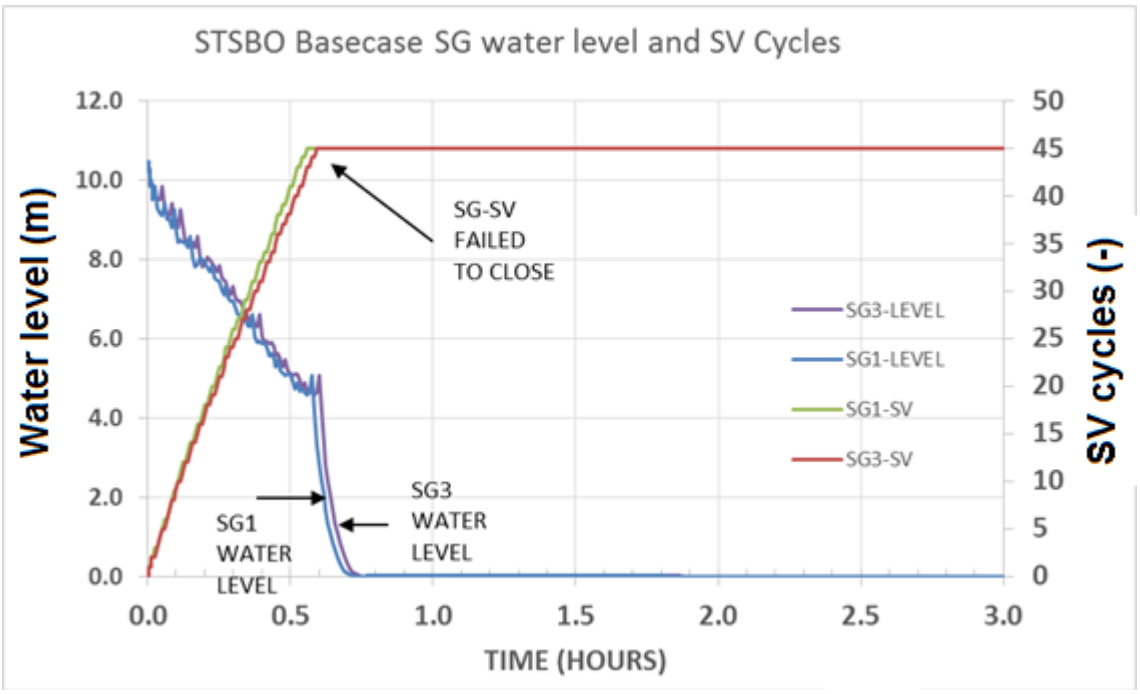

Figure 4-2 STSBO base case SG water level and SV cycling

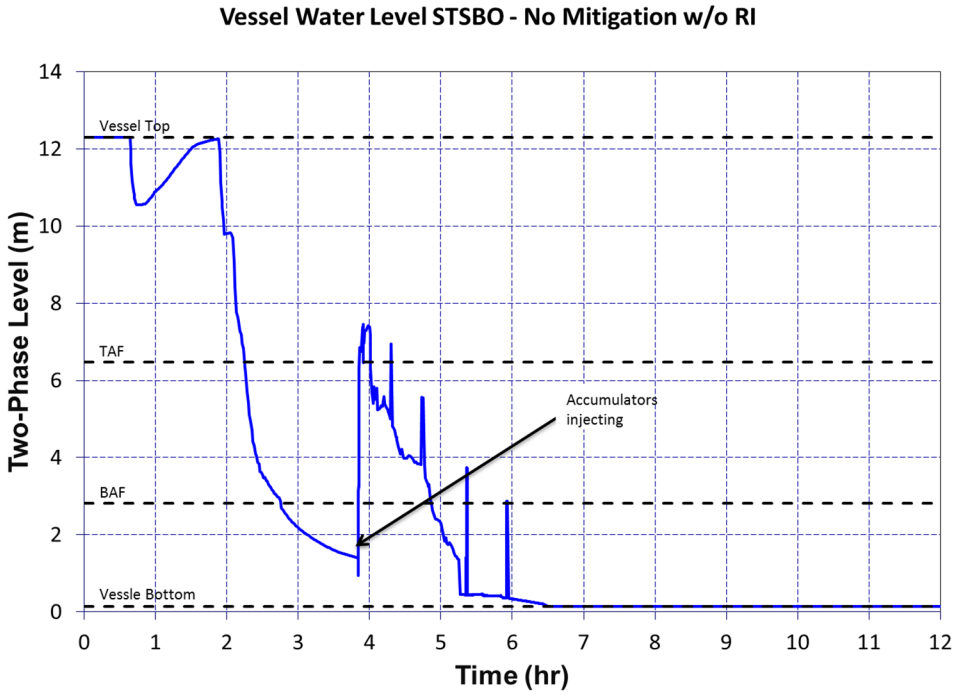

Figure 4-3 STSBO base case primary system water level

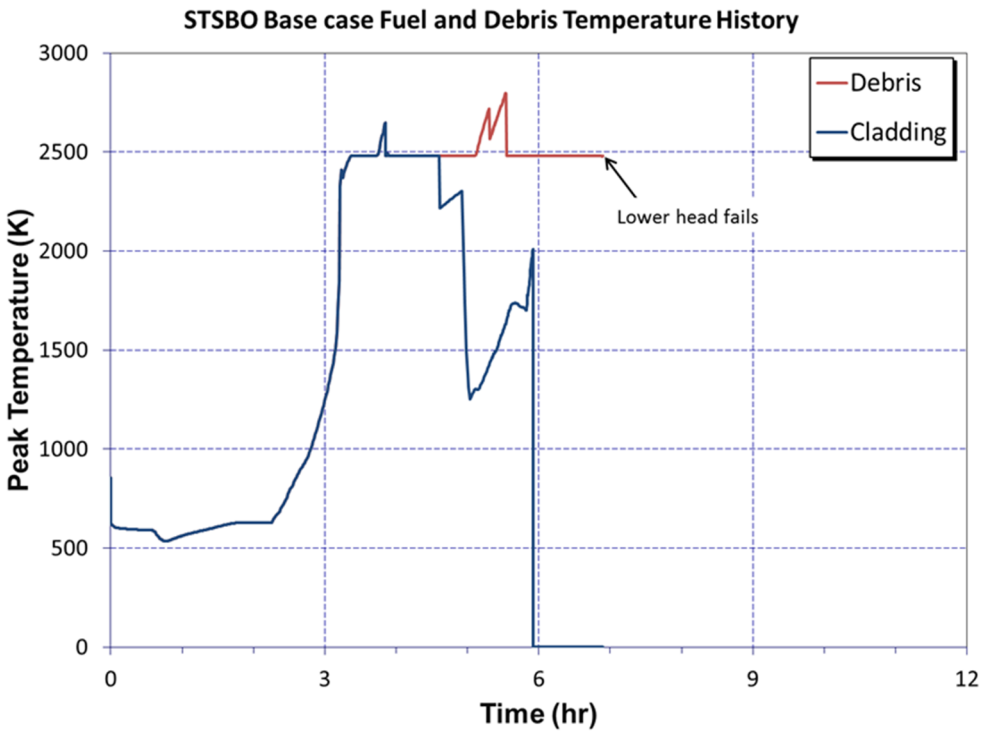

Figure 4-4 STSBO base case fuel and debris temperature history

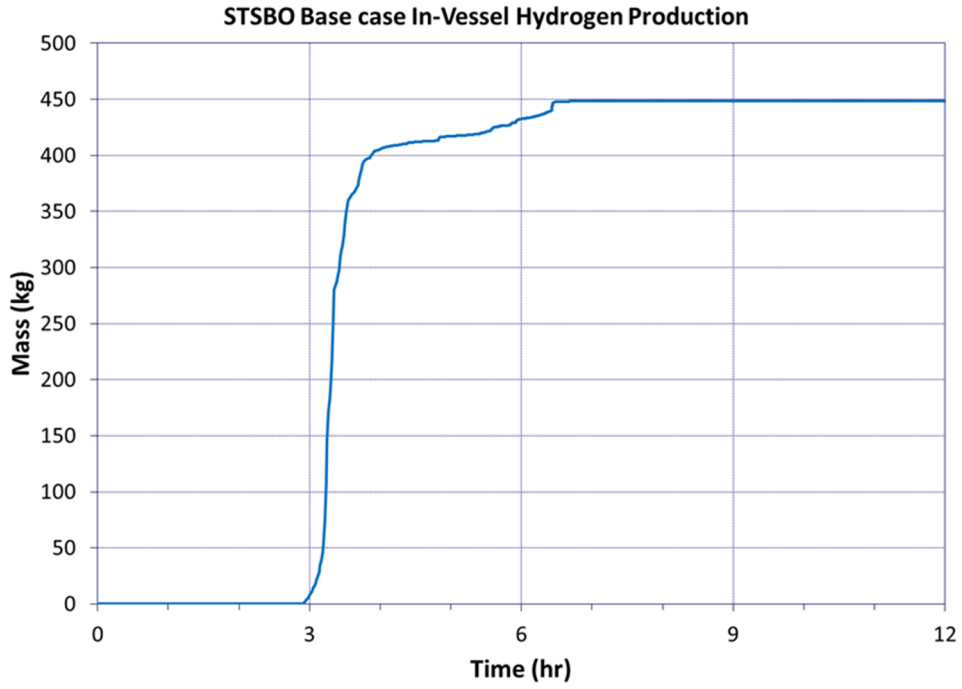

Figure 4-5 STSBO base case in-vessel hydrogen production

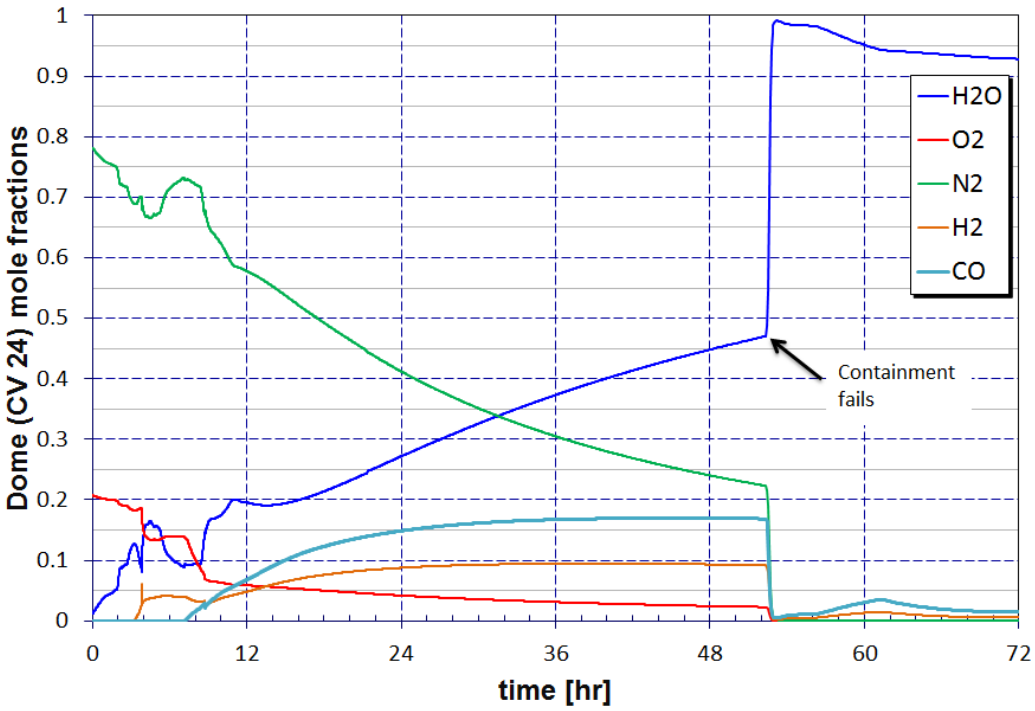

Figure 4-6 STSBO base case containment dome hydrogen, oxygen, and steam mole fractions

The containment pressure response is shown in Figure 4-8. As shown in Figure 4-7, the pressure suppression capacity of the ice is gone by 10 hours. In addition to the steam released to the containment, there was a release of hydrogen to the containment after 1.93 hr and gases from CCI after 7.12 hr. Although larger hydrogen burns are evident at the hot leg failure (3.82 hr) and shortly after the start of CCI (~8 hr), the magnitude of the initial burn is limited to the amount of hydrogen discharged through the open PRT rupture disk.[15] Immediately following hot leg failure, the lower containment is steam-inerted from the rapid steam generation in the core following the discharge of the accumulator water. However, the steam enters the ice chests and condenses. There are small burns thereafter as hydrogen exits the hot leg, which burns locally near the hot leg. Meanwhile, the gas generation from the CCI steadily pressurizes the containment. During the first 15 hours there is enough oxygen in the containment to allow deflagration of hydrogen. After 15 hours, the oxygen concentration in the lower containment decreases below the amount needed to support combustion (i.e., 5% molar concentration). The relative decrease in the oxygen concentration is due steam generation from evaporating water and CCI gas generation but also due to the oxygen consumed in the early burns.

The response of the reactor cavity and the lower containment is shown in Figure 4-9. The figure shows the erosion of the concrete due to ablation was well as the ex-vessel debris temperature and the water levels. Melting of the ice led to accumulation of water in the lower compartments

[15] The accumulator discharge not only creates a large steam source that fills and inerts the lower containment from hydrogen combustion, the water and steam decreases the temperature of the hot jet exiting the failed hot leg below the hydrogen auto-ignition temperature. Consequently, no combustion is possible until the steam concentration decreases and an ignition reappears.

and the failure of the containment resulted in the flashing of some of the water and water flowing into the cavity. The total concrete erosion in the reactor cavity is >1 m by 68 hr. The aggressive CCI erosion of the concrete generates a large amount of the gases (i.e., steam, carbon-dioxide, carbon-monoxide, and hydrogen). The CCI gas generation pressurizes the containment, which fails at 67 psig. The free-standing steel containment ruptures with a relatively large tear (i.e., ~3 ft^2) near the equipment hatch area. Previous analysis [49], as well as the current uncertainty realizations indicate an early containment failure due to a large hydrogen burn pressure spike is also possible near the initial RCS breach. Consequently, the base case is only representative of one possible containment failure timing.

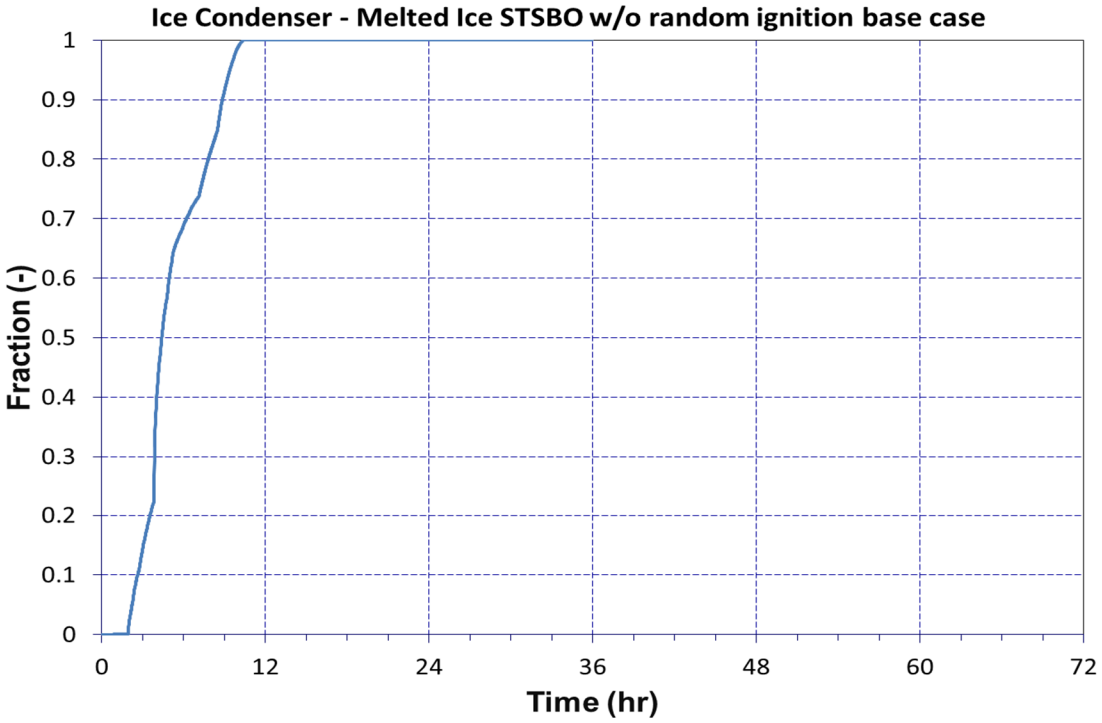

Figure 4-7 STSBO base case fraction of ice melted

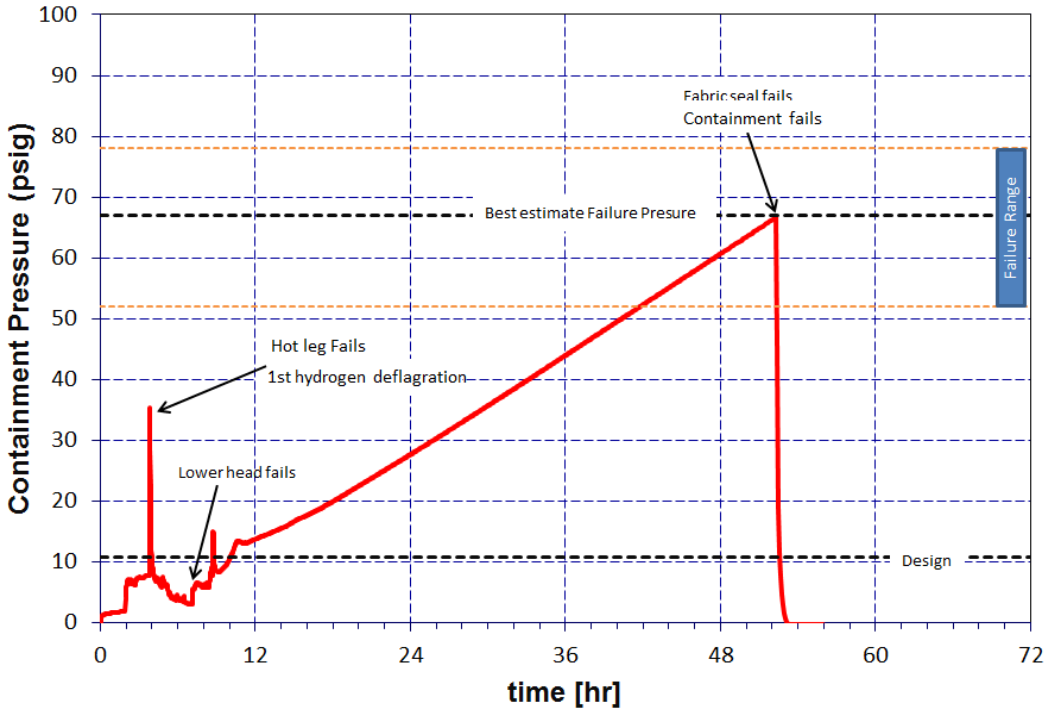

Figure 4-8 STSBO base case containment dome pressure

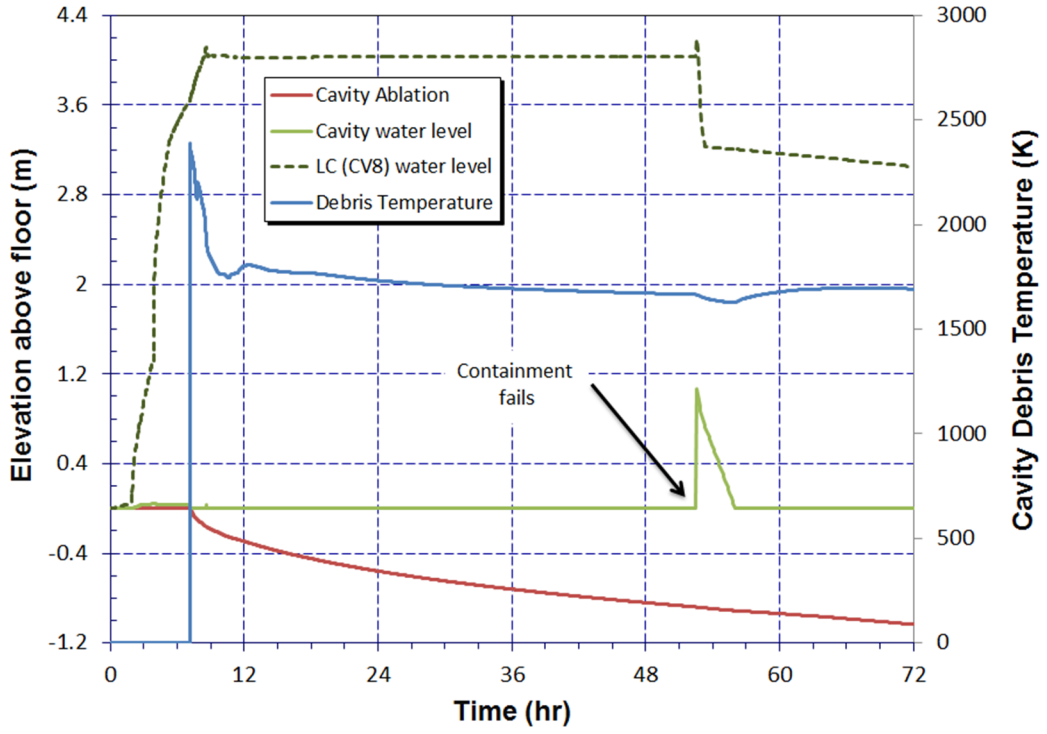

Figure 4-9 Base case containment ablation during STSBO with random ignition

Figure 4-10 and Figure 4-11 show the fission product distribution of the Iodine and Cesium radionuclides that were released from the fuel, respectively. The fission products are released from the fuel starting at about 3 hours. A substantial portion of the released fission products flow through the stuck open pressurizer SV to the sparger located at the bottom of the pool of water in the PRT. The hot gas entering the PRT water and the decay heat from the captured fission products heats the PRT water to boiling, which pressurizes the PRT until the rupture disk fails at 1.93 hr. The sparger is initially very effective at retaining most of the released fission products in the water. However, the sparger becomes less effective when the pool becomes saturated. After the hot leg failure at 3.84 hr, the flow from the RPV to the PRT stops and the hot leg failure is the primary fission product pathway to the containment.

Following the accumulator discharge at hot leg failure, the fuel continues heating and releases most of the remaining volatile fission products. The fission products that are released following hot leg failure are discharged into the containment. As shown in Figure 4-10 and Figure 4-11, the fission products are initially airborne but begin settling. Between 14 to 16 hours, the cesium-iodine and cesium hydroxide in the PRT revaporizes and flows into the containment.[16] Since most of the iodine is in the cesium-iodine compound, the impact of the cesium iodine revaporization from the PRT is more significant in the iodine distribution history (Figure 4-10). The aerosols slowly settle in the containment until the containment failure at 52.4 hours, which starts the radionuclide release to the environment. The subsequent containment depressurization also promotes revaporization of the cesium molybdate from the PRT, which greatly increases the cesium release to the environment after containment failure.

Figure 4-12 shows the release fractions of radionuclide to the environment. At 72 hours 99.8% of the noble gases, 20% of Molybdenum, 19% Cadmium, 6.9% of Iodine, and 6.3% of Cesium is released to the environment. The large increase in the Molybdenum release to the environment after 62 hours corresponds to the complete oxidation of the common metals in the CCI (i.e., the steel and Zr), which leads to oxidation of the Molybdenum and the release of gaseous MgO. Sections 4.2.1 and 4.2.2 further describes the results of accident progression uncertainty analysis including the attributes that lead to early versus late containment failure and the magnitude of the radionuclide release to the environment.

[16] The PRT is tracked as part of the in-vessel total. Once fission products exit the PRT into the containment, they are tracked in the containment airborne and deposited in Figure 4-10 and Figure 4-11.

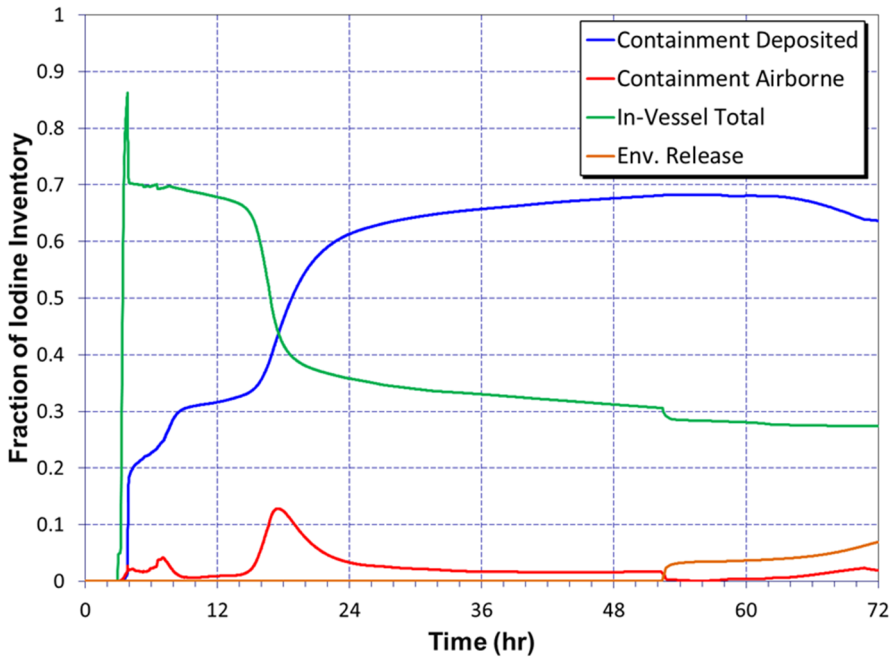

Figure 4-10 STSBO base case iodine fission product distribution history

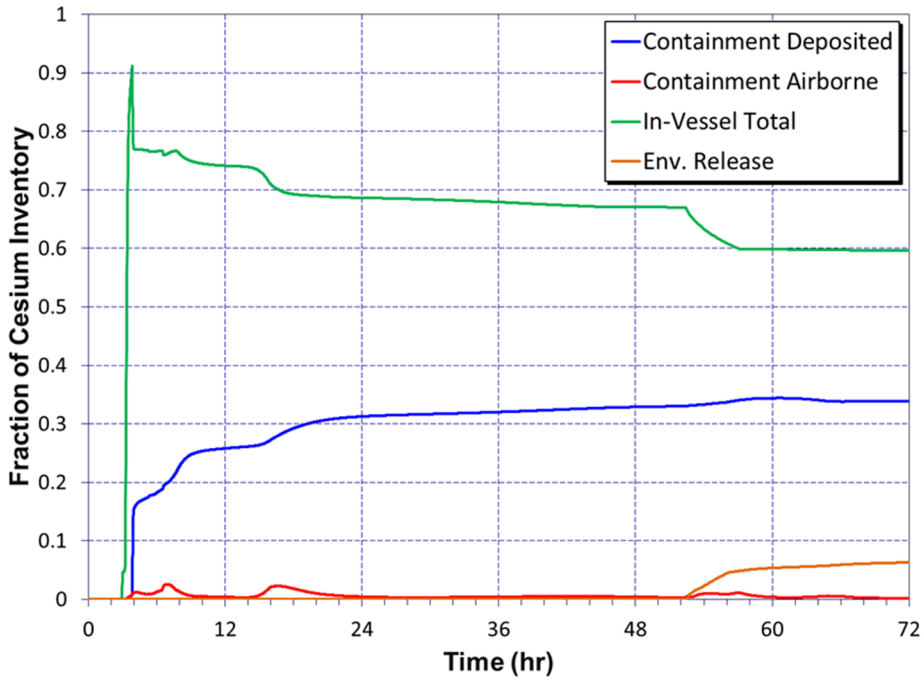

Figure 4-11 STSBO base case cesium fission product distribution history

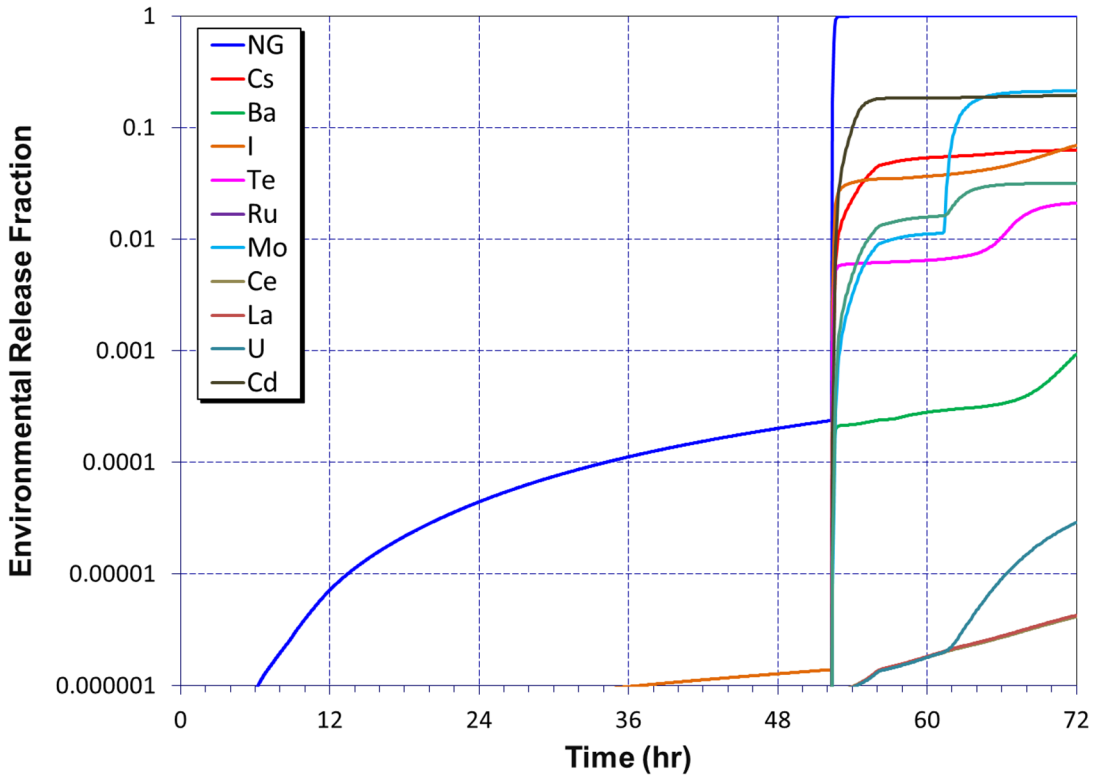

Figure 4-12 STSBO base case environmental release fraction history

4.1.1 Short-Term Station Blackout with Igniters

An STSBO analysis was performed to demonstrate the benefits of the igniters. The MELCOR results confirm that an early containment failure can be avoided using the igniters, which allows the implementation of emergency plan including completing evacuations prior to a late containment failure. In this sensitivity calculation, it is assumed that the power for igniters is established prior to a significant accumulation of hydrogen in the containment. Figure 4-13 shows containment pressure response for Realization 338, which resulted in earliest containment failure from the uncertainty assessment without random ignition. Realization 338 is discussed in more detail in Section 4.3. Realization 338 represents a sequence with earliest containment failure without power to the hydrogen igniters. The results of Realization 338 with and without operating igniters are shown in Figure 4-13. The igniters mitigate the large pressure spike at 3.79 hours and all subsequent other hydrogen burns. Without further mitigation, the accident progression proceeds to a late failure containment failure at 43 hr due the slow rise in pressure from to CCI. Nevertheless, the recovery of the igniters delays the large release of radionuclides for ~40 hours, which allows time to an evacuation.

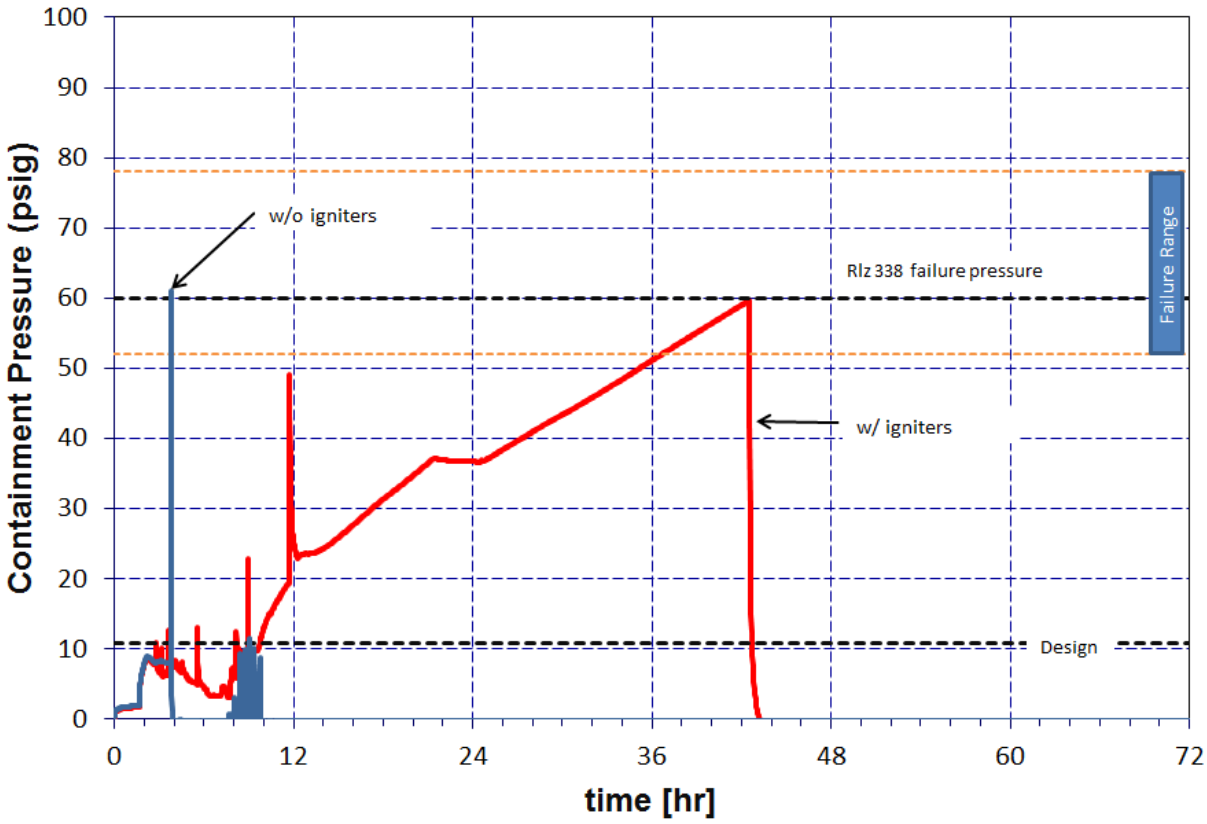

Figure 4-13 Containment Pressure for the STSBO with and without hydrogen igniters

4.2 STSBO Source Term Parameter Uncertainty Analysis

There were two sets of analyses conducted for the STSBO scenario, each of which included running 600 realizations. The two STSBO sets were identical except that the random ignition source was turned on in one set and random ignition was turned off in the other scenario. Section 4.2.1 describes results with non-random ignition and Section 4.2.2 discusses the results with random ignition. The non-random ignition cases included two active ignition sources; (1) auto-ignition from hot gases exiting the hot leg failure location and (2) the ex-vessel debris following the reactor pressure vessel melt-through. These active ignition sources would initiate a burn in the lower containment whenever the gas concentrations met combustible criteria. The random ignition cases included the active ignition sources and also a random ignition source at a specific location inside the containment every 30 min (see 3.6).

A few general insights related to containment rupture with and without random ignition scenarios can be observed in Figure 4-14. First, the likelihood of an early containment rupture is greater in cases without random ignition. Second, the probability of containment rupture by 72 hours was essentially identical by the two methods. Finally, both sets of realizations showed a gap in the results around 24 hours between early containment failures and the later containment ruptures. Due to the potential for random ignition throughout the containment, the gap is less pronounced using a random ignition model. There are also fewer early containment ruptures with random ignition. If you ignore the 3 early random ignition realization outliers, then the random ignition CDF does not start increasing until 11 hours whereas the non-random realizations start accumulating at 4 hours. Although the random ignition scenario specified

random ignition sources throughout the containment (i.e., including the potentially high hydrogen concentration ice chest region), the net effect was incremental combustion of hydrogen discharged from the pressurizer relief tank (PRT) in smaller quantities. Without random ignition, the hydrogen exiting the PRT following the rupture disk failure transported throughout the containment until hot leg failure (i.e., the earliest active ignition). The latter often provided conditions for a large burn that failed the containment at hot leg failure.

For these uncertainty analyses, the ranking of the variables is conducted using the four regression techniques. A consequence of the use of multiple regressions is that the ranking of the inputs amongst themselves is not obvious when the different regressions disagree. A quantitative approach was implemented for the current analysis due to a strong belief that such a quantitative ranking is only an indicator and should be supported by expert opinion based on the physics of the problem. Two effects of the uncertainty in the input onto the output of consideration are estimated in the present study. The 'Main Contribution' represents the influence of the uncertain input by itself and is estimated with R^2_{cont} in the stepwise regression and S_i for the other three regression techniques. Then the 'Conjoint Contribution' effect of the uncertain input from its interaction with other variables, which is ignored by the stepwise regression as it is an additive regression, is estimated with $T_i - S_i$ for the other three regressions. Section 2.2 of Appendix A provides a detailed discussion of the ranking method employed.

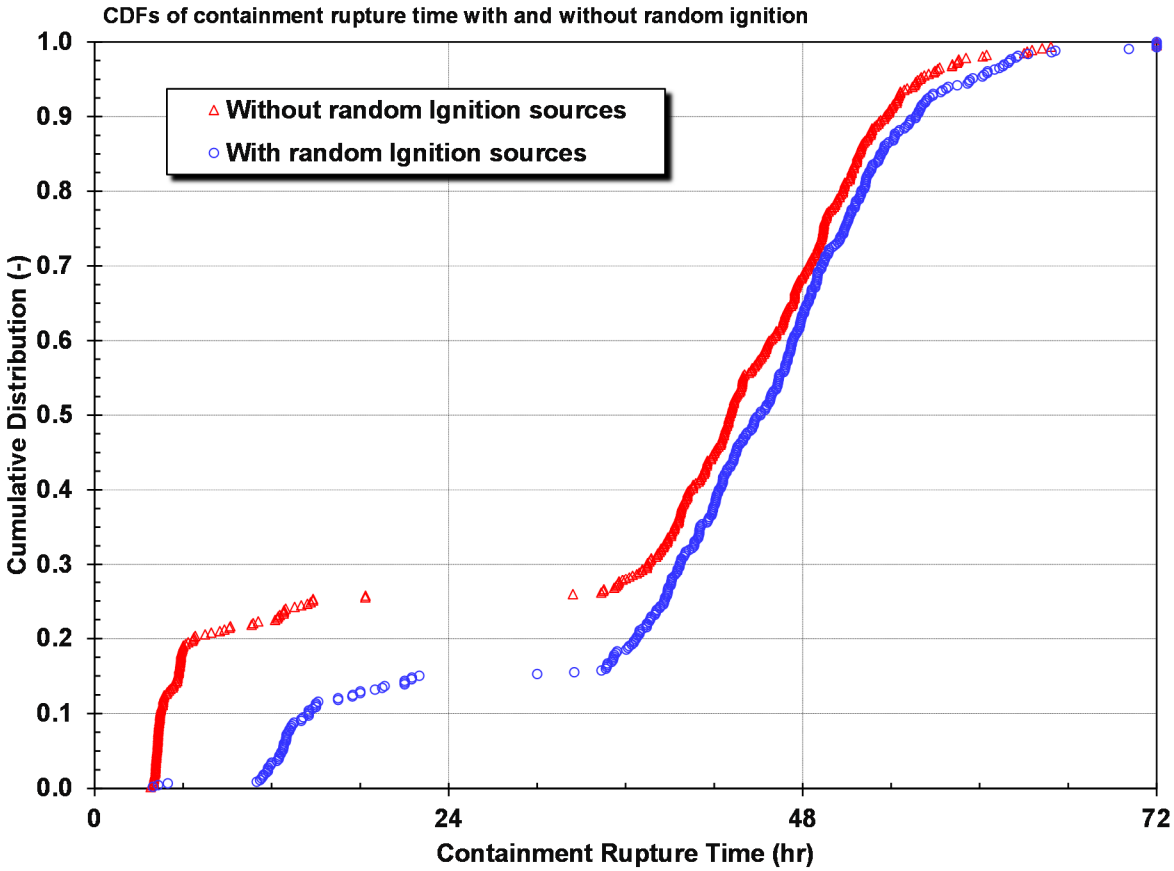

Figure 4-14 CDFs of containment rupture time with and without random ignition

4.2.1 Uncertainty Evaluations with No Random Ignition

Regression analyses were performed on the results of the Sequoyah MELCOR STSBO analyses. Regression tables in the following sections provide summaries of the analysis. In these tables, the parameters are listed first, followed by the four regression techniques used to create the results. The last two columns contain values of the main contribution of the parameter on the result metric and the conjoint influence[17] of the parameter on the result metric. These are calculated as arithmetic averages of the overall contributions from the four regression techniques. Values of main contribution greater than 0.02 and conjoint contributions greater than 0.1 are considered significant and are highlighted. The parameters in the first column of the tables are ordered by the values in the column labeled Main Contribution, thus the parameters appear in rank order.

It was not possible to include two parameters directly in the regression calculations because their sampled input value was due to the actual physical behavior of the reactor system. Because of this, these two parameters were post-calculated (see Table 4-2) for use in regressions, based on both the sampled input and actual behavior, and also to attempt complete coverage of the uncertainty space.

Table 4-2 Post-calculated regression parameters.

#	Parameter Name	Description	Notes
1	SV_Frac	Open area fraction for the safety relief valve system	Calculated as the sum of the open area fractions of the individual valves
2	priSVcycles	Cycles before failure experienced by the safety relief valve system	Calculated as the sum of the cycles to failure experienced by each of the valves

A high performance computing cluster was used to execute a Monte Carlo simulation with 600 MELCOR runs, of which 467 were successful for the STSBO scenario with no random ignition. The reasons for the failed runs are listed in Table 4-3. MELCOR code failures occur when executing large analyses such as this. Throughout the project, these errors are investigated and fixed, which further advances the state of the code. However, some random code failures also occur in MELCOR often because uncertainty parameter permutations create computationally difficult conditions that have not been previously addressed. These failures are investigated, and those that are random are not subject to correction. For the Sequoyah analysis, there were two calculation sets that required further action (but are not related to code run time errors). First, the Sandia High Performance Cluster had an unexpected failure that affected 24 realizations. Second, the uncertainty algorithm that generated the pressurizer safety valve cycle failure unexpectedly included 31 realizations that were initialized with an immediate safety valve failure. The effected realizations were identified and removed from the sample set. The error was not identified until all calculations were completed.

An analysis was also completed to determine whether there is a correlation between failed runs and having the realization set in a particular area of the input space. Such a situation would indicate that a particular value for one input (or combination of values for several inputs) would

[17] Conjoint influence is the influence of two or more input parameters acting together, which may have synergistic effects that would not be uncovered by studying the influence of each parameter separately and individually.

lead to failure, biasing the conclusion that could be drawn by only analyzing the successful runs. This analysis provided reasonable assurance that the failed runs should be randomly distributed in the input space, with one small exception. There was a small, but not significant, relationship between priSVcycles and realization completion. See Appendix A for further discussion.

Table 4-3 Summary of the number of realizations that were unsuccessful in the without random ignition set.

# Failed	Reason
	Code run time
3	Ex-vessel cavity surface heat loss error
28	Volume error in the COR Package
7	Bad debris temperature in the core lower head subroutine calculations
17	Executive detected abort signal (i.e., typically a failure to converge in the control volume hydrodynamics package)
20	Convergence error in an ex-vessel cavity routine (CCMLTR)
3	Convergence error in an ex-vessel cavity routine (CCSVLR)
	Other (hardware/input)
24	Sandia High Performance Cluster Failure
31	Failed pressurizer SV at time = 0 sec

4.2.1.1 General MELCOR results for the with no random ignition scenario

The MELCOR results for the cases with no random ignition were configured to show the containment rupture timing as a function of the timing to the first RPV breach (i.e., see Figure 4-15 through Figure 4-19). If the realization had containment failure immediately following a RPV breach, then the result would appear on “coincident” line. The RPV breach line identifies the earliest possible timing for an active ignition source (i.e., either hot leg failure or RPV lower head failure). Since the containment rupture is the start of the release of radionuclides to the environment, the figures identify important characteristics for the source term timing. The following bullets summarize the general observations and insights from the realizations with no random ignition. Sections 4.2.1.2 through 4.2.1.5 present the statistical evaluation for the specific figures of merit.

- The earliest containment failure occurs at 3.9 hours (Rlz 338). A pressurizer safety valve stuck almost fully open on the 2nd cycle. Almost all the hydrogen from the RPV was vented to the lower containment after the PRT rupture disk failed. The containment ruptured at hot leg failure (i.e., the first ignition source) at a relatively low sampled rupture pressure (i.e., the containment failure pressure). Rlz 338 is described in more detail in Section 4.3.

- The latest containment failure occurred after 72 hr (i.e., Rlz 171). There were three realizations with containment failure expected to occur after 72 hours due to ex-vessel core-concrete interactions. In contrast to Rlz 338, the pressurizer SV did not fail in Rlz 171. In addition, the sampled value for the containment failure pressure was

relatively high and not challenged by the hydrogen burns following the RPV breach. Rlz 171 is described in more detail in Section 4.3.

- There is a distinct set of realizations showing early containment failure at approximately 4 to 6 hours. These realizations lie on or near the RPV breach line (i.e., see the realizations in the lower left-hand side of Figure 4-15). The early containment failure in these realizations occurs following a hydrogen burn at RPV failure that fails the containment.

- There is a second distinct grouping of realizations exhibiting later containment failure ranging approximately between 32 and 65 hr. The later failures occur following a continual pressurization resulting from ongoing steam production, unabated fission product decay heating and noncondensable gas generation associated with CCI (i.e., see the realizations in the upper-right of Figure 4-15).

- The gap in containment failures between 20 and 32 hours differentiates between sudden containment over-pressurizations caused by deflagrations and gradual over-pressurizations resulting from steady steam production, continuous fission product decay heating and ongoing CCI generation of noncondensable gasses (see Figure 4-15).

- After RPV lower head failure, noncondensable gas produced by CCI combined with continued steam production and intermittent oxygen consumption by small deflagrations, lowers the relative concentration of oxygen in the containment atmosphere. The resultant oxygen concentration became insufficient to support hydrogen/carbon monoxide burns after about 15 hours.[18]

- As shown by the dense cluster of markers in the upper left of Figure 4-15, most late containment ruptures are associated with an RPV breach occurring early, sometime between 3.5 and 4.5 hours. While an early hot leg failure sometimes resulted in an immediate hydrogen burn large enough to fail containment, more often such a burn did not occur and the containment atmosphere progressed to an inert condition as described in the previous bullet.

- In contrast to late containment ruptures, early containment ruptures exhibit a slightly wider timing spread between 4 to 6 hours (see the grouping of realizations in the lower left of Figure 4-15). Noteworthy is that nearly all early containment ruptures are coincident with hot leg failure.

- There are a few interesting cases with intermediate containment rupture times (i.e., the grouping of red markers off the coincident line on the left side of Figure 4-15). For example, an energetic deflagration failed containment at 14.8 hr in Rlz 133 but this was 10.9 hr after hot leg rupture. This outcome resulted from a unique combination of an early pressurizer SV failure (3 cycles) and relatively high containment failure pressure

[18] The Sequoyah combustion model, which was developed from experimental data [30], shows a 5% oxygen concentration is required to support combustion. The number of moles of oxygen in the containment is reduced through the early hydrogen burns. The relative concentration is also reduced by the addition of gases from ex-vessel CCI. The combined effects caused the oxygen concentration to drop below 5% after about 15 hours.

(72.8 psia). When a pressurizer SV failed early in the MELCOR calculations, the hydrogen produced by fuel cladding oxidation vented to containment prior to the hot leg rupture through the stuck open valve and the (broken) rupture disk on the PRT. Then when a hot leg ruptured, the vented hydrogen often ignited in a large burn that failed containment. A large burn at hot leg rupture was not always the case however, as in Rlz 133 where the burn wasn't large enough to fail the containment. A later burn did fail containment in this realization as described in Section 4.3.

- Figure 4-16 shows a correlation to the number of pressurizer SV cycles to the containment rupture timing. If the pressurizer SVs operate without any failures (i.e., the black circles), then the containment only fails late.[19] The progression of events in these sequences includes a hot leg failure from high reactor coolant system (RCS) pressure followed by a rapid discharge of the accumulators into the degraded core. The high RCS pressure retains much of the hydrogen in the vessel until the rapid discharge of RCS gases into the containment at hot leg failure. Consequently, there is less hydrogen in the lower containment at the moment of the RPV breach. The discharge of gas through the hot leg failure includes a concentration of steam, which is immediately followed by a large steam source from the accumulator water quenching the degraded core. The large and rapid accumulator water source into the core also eliminated the ignition source at the hot leg (i.e., the gases exiting the hot leg no longer satisfied the auto-ignition temperature criterion). The lower containment remained steam inerted and/or without an active ignition source and always progressed to an oxygen deficient state.

- As described in the previous bullet, the realizations with 46 to 60 cycles (i.e., yellow triangles in Figure 4-16) and 61 to 74 combined cycles (i.e., red triangles on Figure 4-16) also primarily resulted in late containment failure. The SVs in these two groups functioned properly for second and third longest times. The other realizations with fewer SV cycles prior to a failure (i.e., 1 to 45 cycles) resulted in both early and late containment failures. There were more complicated factors that contributed to whether there was an early or late containment failure. However, the flow area of failed SV or SVs was an important factor (e.g., a small SV failure could stop further SV cycling but otherwise remain at relatively high RCS pressure, which is somewhat like a functioning SV realization).

- Figure 4-17 shows the correlation between the number of pressurizer SV cycles (i.e., the priSVcycle parameter) versus the SV failure area (i.e., the SV_Frac parameter). As noted above, most of the realizations with >46 cycles progressed to late containment failure. An analogous correlation was observed with the resultant SV failure area. If the SV failure area was <0.3 (i.e., the non-dimensional SV failure flow area), then the realizations progressed to a late containment failure. Whereas the priSVcycles parameter accounted to the delayed in timing to the RCS blowdown, the SV_Frac parameter accounted for the resultant depressurization rate. Consequently, if the SV failed too late to depressurize the RCS or did not have adequate flow area to depressurize the RCS, then the amount of hydrogen discharged to the containment prior

[19] The timing of the initial RPV breach is also very consistent between the cases. With any variability in the timing of the RPV depressurization due to a failed SV, the hot leg failed roughly at the same timing (i.e., 3.7 h). The impact of the other uncertain parameters had almost no impact on the accident progression through hot leg failure.

to the initial RCS breach was inadequate in its distribution and concentration to fail the containment by a hydrogen burn.

- Figure 4-18 shows a surprising lack of correlation between overall in-vessel hydrogen production and either early or late containment failure. In-vessel hydrogen production ranges from a minimum of 303 kg in Rlz 469 to a maximum of 667 kg in Rlz 225. Inspections of these realizations, which is discussed in Section 4.3 show the contrasting substantial importance of the amount of hydrogen produced prior to hot leg rupture and vented to containment - especially to upper containment. Larger hydrogen production prior to hot leg rupture with efficient venting of the hydrogen to containment allows even the realizations with lowest overall in-vessel hydrogen production to experience a burn sufficient to rupture containment (see the red triangles grouped in Figure 4-18).

- As identified above, containment rupture time exhibits substantial dependence on the amount of hydrogen produced prior to hot leg failure. Figure 4-19 further illustrates this dependence in that the majority of early containment failures had more than 400 kg of hydrogen production prior to hot leg failure.

- An early failed pressurizer SV accelerates inventory loss, core uncovery, and hydrogen production. It also reduces the mechanical stress on the hot legs by reducing pressure. The consequence of these influences was more extensive core damage prior to hot leg failure.

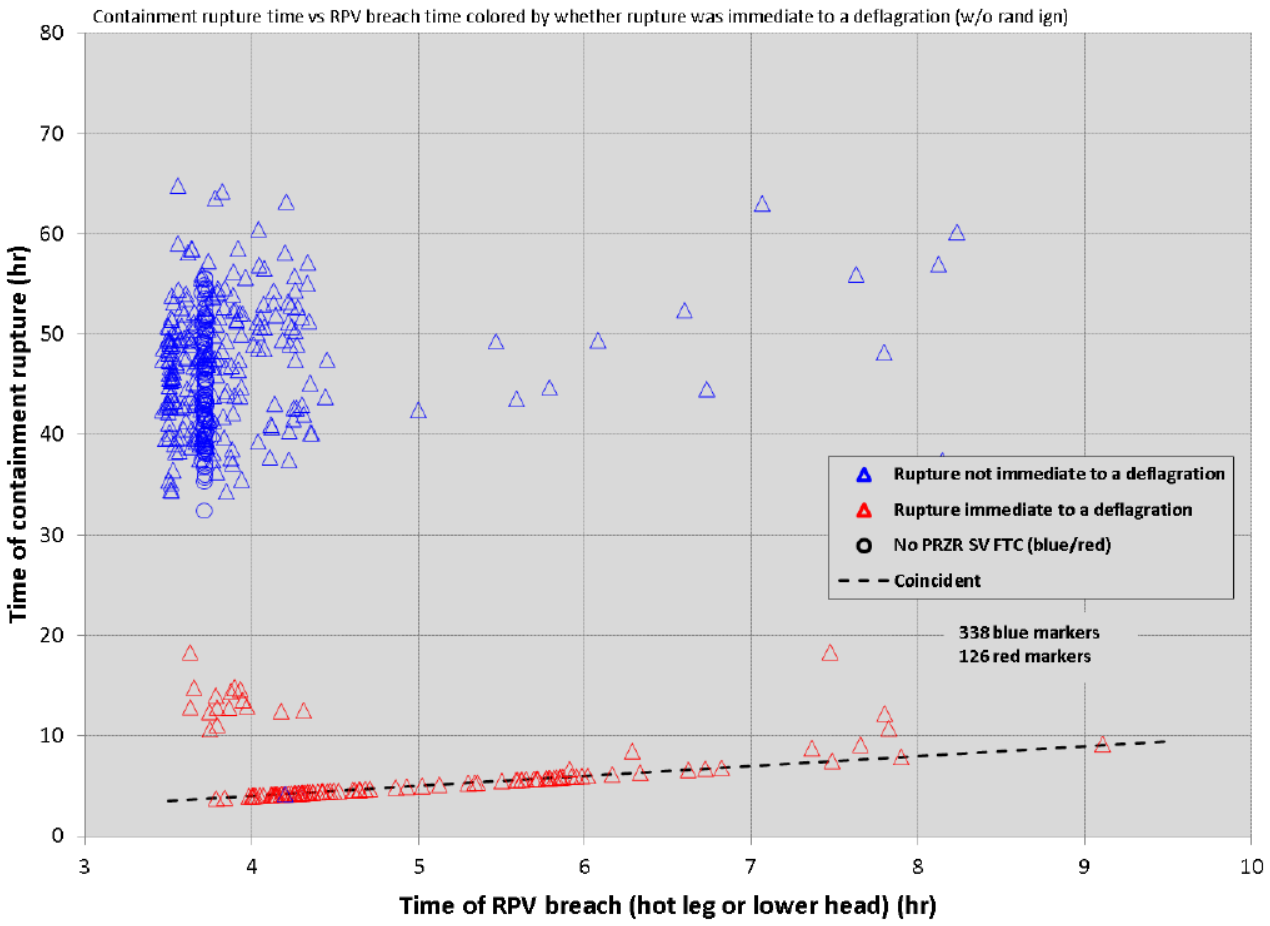

Figure 4-15 Containment rupture time versus RPV breach time colored by whether rupture was immediate to a deflagration – without random ignition

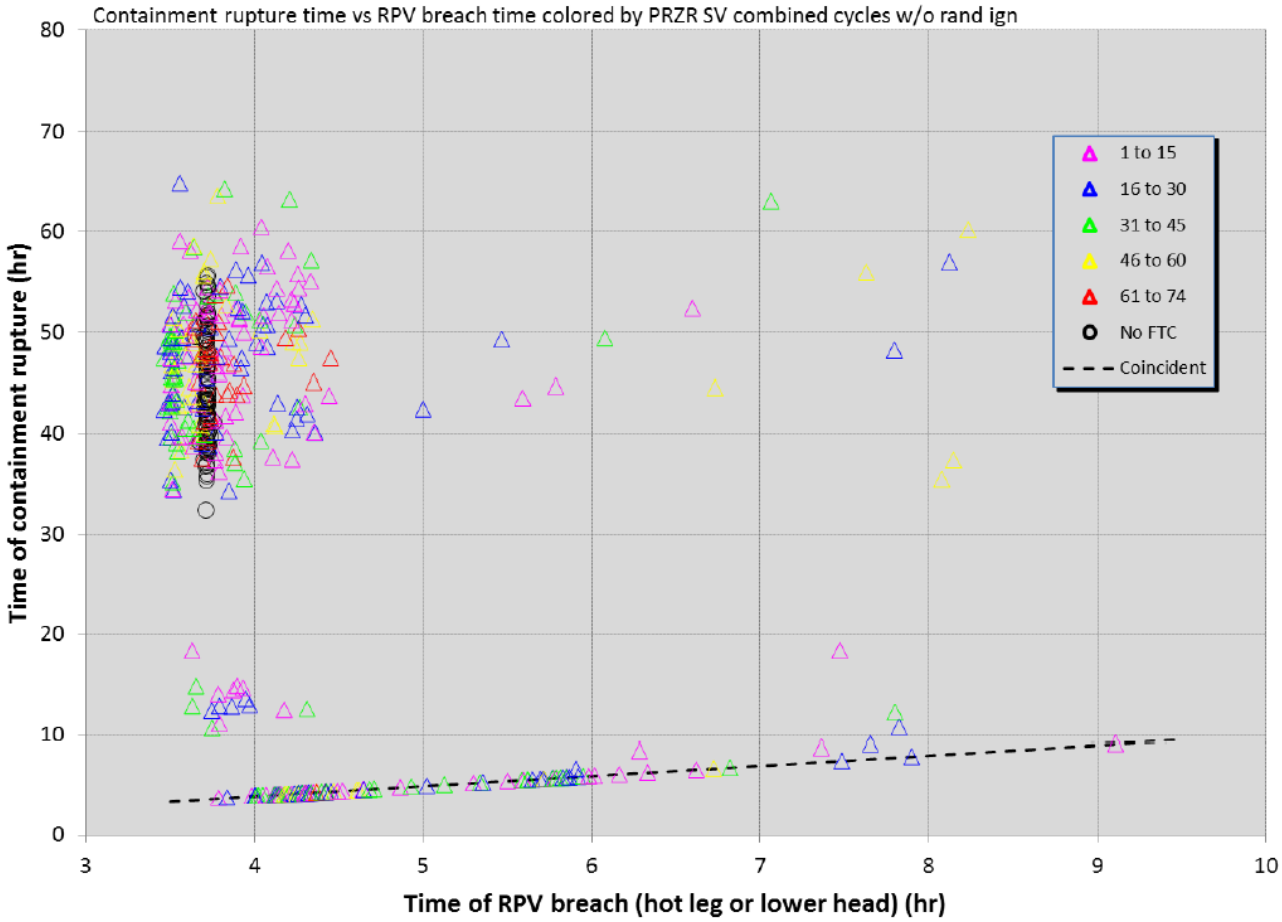

Figure 4-16 Containment rupture time versus RPV breach time colored by number of pressurizer SV cycles – without random ignition

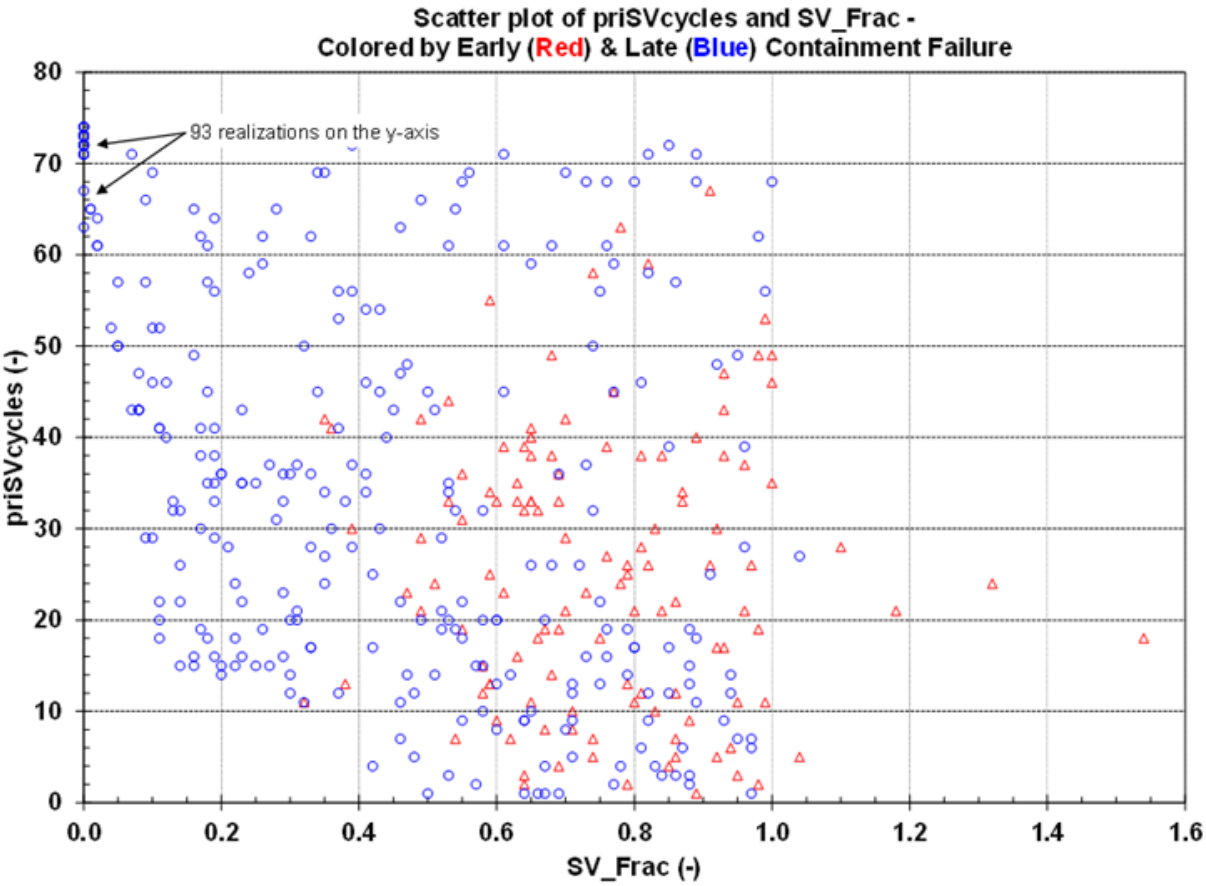

Figure 4-17 Relationship of priSVcycles to SV_Frac colored by containment failure timing – without random ignition

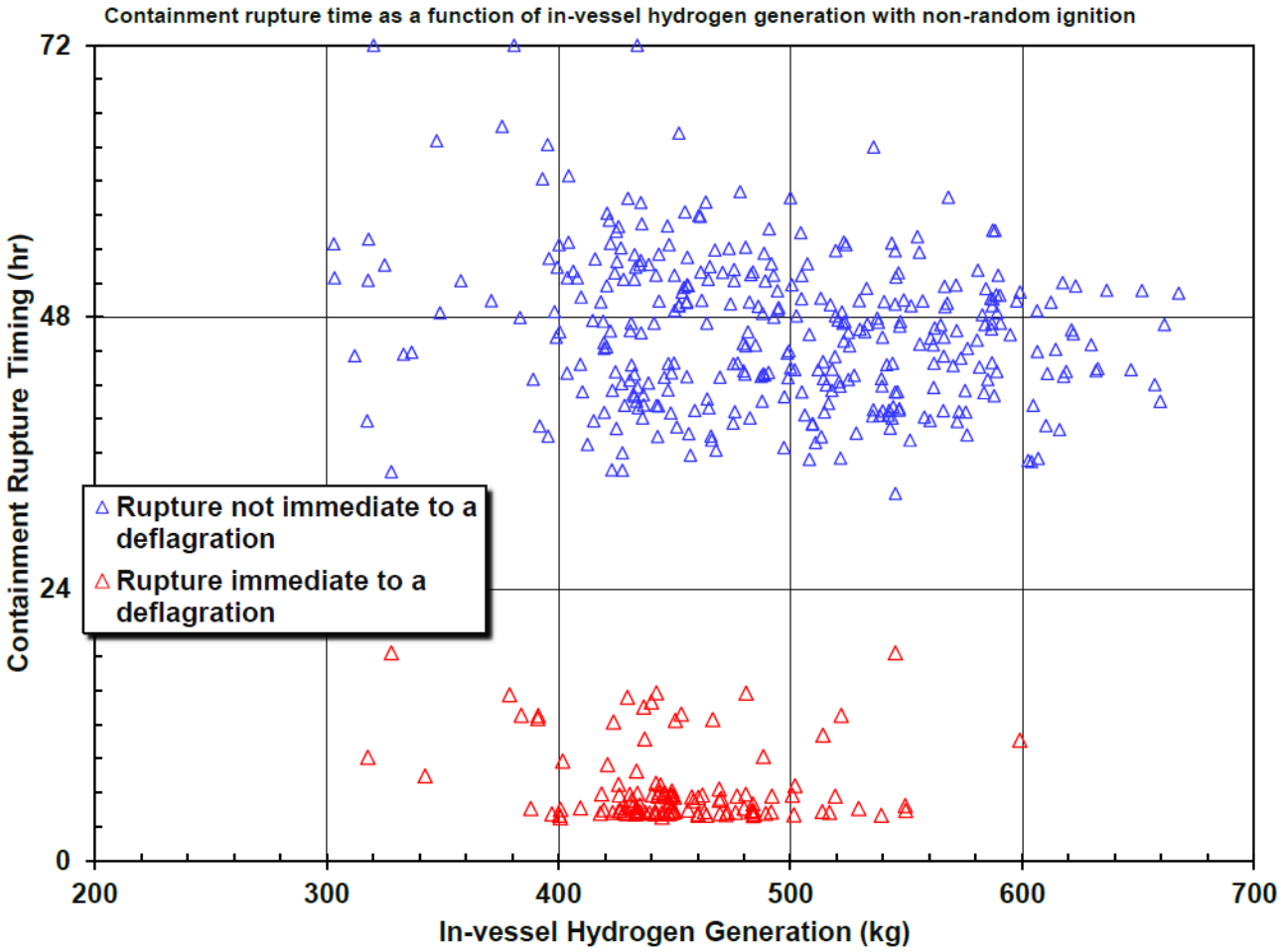

Figure 4-18 Containment rupture time versus in-vessel hydrogen production – without random ignition

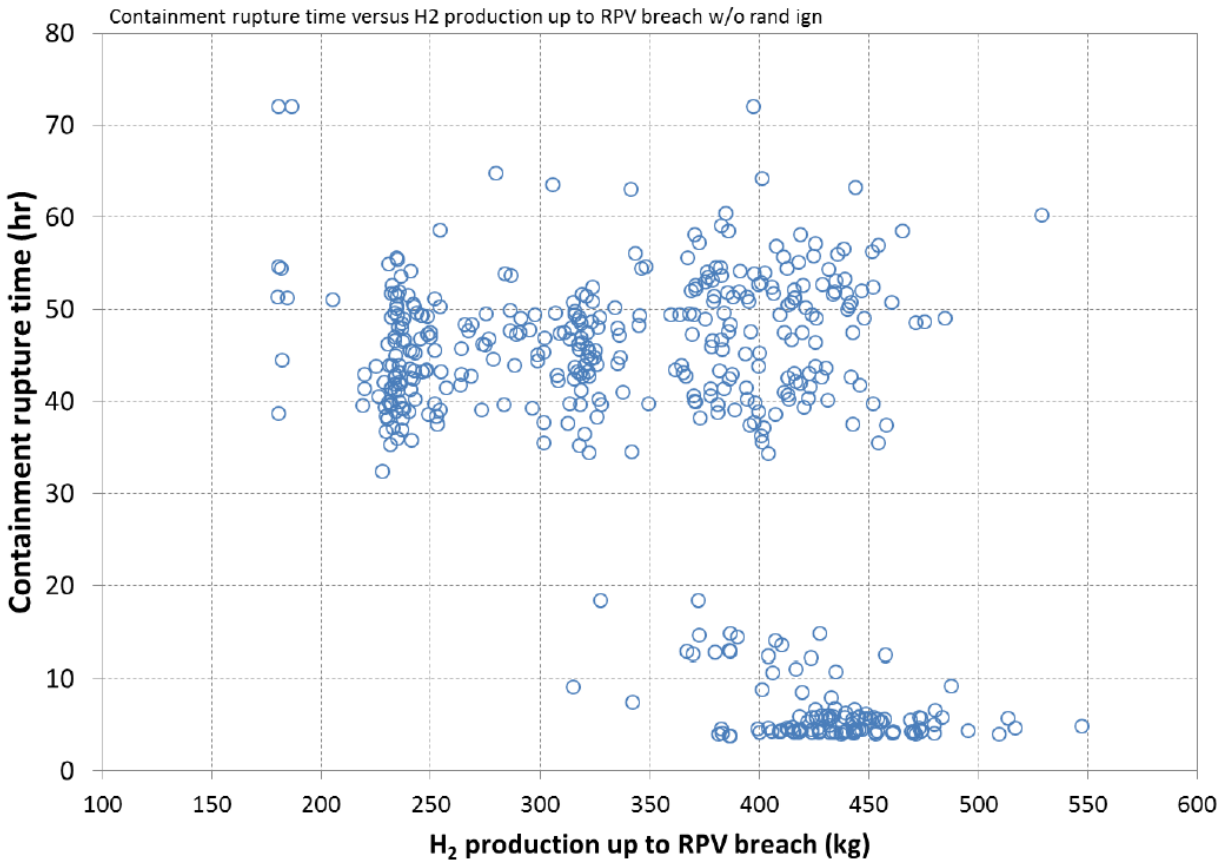

Figure 4-19 Containment rupture time versus in-vessel hydrogen production up to the RPV breach time – without random ignition

4.2.1.2 Iodine Release Fraction to Environment (with no random ignition)

The magnitude and timing of the iodine release is an important radionuclide to characterize the potential severity of the early health effects. The timing of the iodine release can be very important if it occurs during the evacuation phase. Consequently, the following regression evaluations paid particular attention to factors that influenced large and early releases of iodine.

4.2.1.2.1 Iodine Release History

The fractional release of iodine to the environment by 72 hours is a primary figure of merit in the UA. Figure 4-20 shows the time dependence of the fractional iodine release in all the realizations, as well as the mean, median, 5th and 95th percentiles of the releases. There is a distinct set of realizations showing early initial release of iodine between roughly 4 and 6 hours followed by a second distinct set of realizations showing an initial release of iodine between roughly 35 and 55 hours. Some releases plateaued before 72 hours but most continue to increase through to the end of the calculation. Mean, median, 5th and 95th releases are all on an increasing trend at 72 hours.

The split in the start of the iodine releases coincides with the containment rupture timing (e.g., Figure 4-15). The early iodine releases result from the early containment rupture following a hydrogen burn whereas the second grouping occurs from a late over-pressurization failure

resulting from ongoing steam production, fission product decay heating, exothermic core-concrete interactions and non-condensable gas generation from core-concrete interactions. As discussed previously in Section 4.2.1.1, there is a time gap following the containment becoming oxygen deficient (i.e., the end of combustion due to insufficient oxygen to support combustion) to the time required for ex-vessel steam production and non-condensable gas generation to over-pressurize the containment. The variation in the late over-pressure timings is influenced by the containment rupture pressure and the amount of hydrogen gas that was burned. The variation in the containment failure timing directly affects the start of the iodine release. However, the variation in the magnitude of the iodine release is a more complex function of other parameters that will be discussed in the following subsections.

The bifurcation in containment failure timings led to a wide spread between the calculated median and the 95th percentile curves. The median realization is characteristic of a late containment failure while the mean curve has contributions from both the early and late containment failure results. Most realizations resulted in a late containment rupture. The median and 5th percentile curves show larger increasing trends following the late containment failure. Late increasing iodine releases were driven by a “chimney effect” where there developed a sustained buoyant flow of hot gases emanating from CCI that rose up into the RPV through the failed lower head exited the RPV through the rupture in the hot leg. The hot gases drove a revaporization of CsI previously deposited in the RPV. The late revaporization releases were also driven by revaporization of CsI from the PRT.

The median curve approaches the mean curve by the end of the calculation, which shows the previous differences between the early and late containment failures have diminished. The mean, median, 5th and 95th traces all show continued releases at 72 hours. However, the slopes of the 5th percentile, median, and mean curves are higher than the 95th percentile. In contrast to the slower rise of the median result, the 95th percentile showed a large early release of iodine that exceeded 10% by 20 hr. The 95th percentile is characteristic of the trend of the iodine releases from the early containment failure results but not the magnitude (i.e., the magnitude is the 95th percentile of all cases). Since the airborne aerosol concentration in the containment is higher at the time of an early containment failure, the initial release upon the containment rupture is also higher. The trends of the horsetail curves show a broader range of results (i.e., 5th and 95th percentiles) for the late containment failure realizations but a lower median.

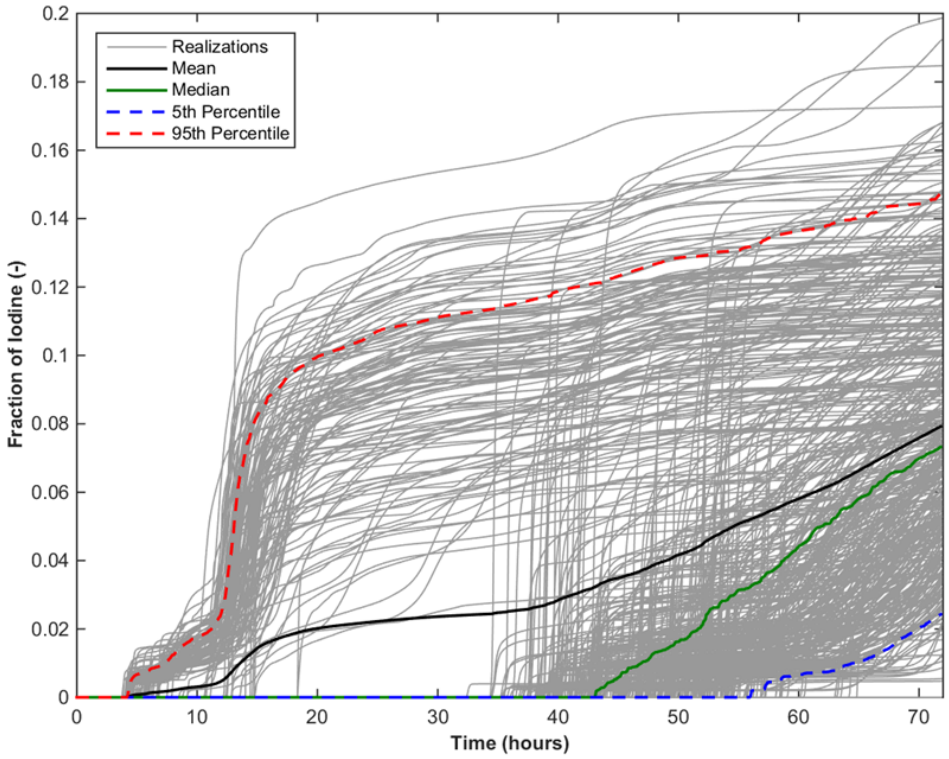

Figure 4-20 Iodine release fractions over 72 hours with mean, median, 5th and 95th percentiles

4.2.1.2.2 Regression Tables and Scatterplots

Table 4-4 shows the results for regression analysis of the iodine release fraction. A technical rationale explaining the contribution to uncertainty is provided for the top parameters. The SV open area (SV_Frac) fraction is the top parameter for iodine and is also the top parameter for cesium, in-vessel hydrogen production, and rupture regression analyses.

In review of the regression results for all successful realizations, SV open fraction was identified as the most important parameter by all regression techniques, except MARS, which identified it as second most important behind priSVcycles. SV stochastic FTC (priSVcycles) was identified as the second most important parameter by all regression techniques, except MARS, which identified it as the most important. Rupture and eutectic melt (EU_melt_T) were identified as the third and fourth most important, respectively, for all regression techniques, except MARS which reversed the order for these two parameters. No other parameters had a significant contribution to the iodine release fraction uncertainty.

Table 4-4 Regression analysis of iodine release fraction at 72 hours (with no random ignition).

	Rank Regression		Quadratic		Recursive Partitioning		MARS		Main Contribution	Conjoint Contribution
Final R^2	0.31		0.44		0.82		0.47			
Input	R^2 contr.	SRRC	S_i	T_i	S_i	T_i	S_i	T_i		
SV_frac	0.20	0.29	0.34	0.58	0.27	0.57	0.33	0.32	0.182	0.117
priSVcycles	0.04	-0.27	0.14	0.34	0.13	0.42	0.49	0.49	0.110	0.110
rupture	0.03	-0.17	0.06	0.08	0.06	0.25	0.05	0.05	0.031	0.055
EU_melt_T	0.02	0.13	0.08	0.09	0.02	0.10	0.10	0.10	0.028	0.025
burn_dir	---	---	0.01	0.05	0.01	0.09	0.03	0.02	0.009	0.026
shape_fact	0.01	0.11	0.01	0.03	0.01	0.10	0.02	0.02	0.007	0.027
ajar	0.01	-0.08	0.02	0.05	0.02	0.15	0.00	0.00	0.007	0.039
Seal_Open_A	---	---	0.01	0.05	0.01	0.05	0.00	0.01	0.003	0.018
Seal_Fail_Dp	---	---	0.00	0.09	0.00	0.07	0.00	0.00	0.002	0.030

* highlighted if main contribution larger than 0.02 or conjoint contribution larger than 0.1

Scatterplots were produced for the parameters that were ranked most important by the weighted average of the regression techniques (see Appendix A for a description of the calculation). Such plots are useful for verifying relationships between the parameter input values and iodine release fractions indicated by the regressions. The scatterplots of most interest are displayed in the respective parameter sections.

SV_Frac

The SV_Frac parameter indicates the open fraction of the primary SV system at 72 hours. All pressurizer SV cycling ceases following the RPV breach (i.e., <10 hours). Consequently, the final SV position represents the actual failure conditions, based on the post-calculated results. If there are no SV failures at 72 hours, then the open fraction is 0 (i.e., in the limit as the SV open fraction approaches zero, it approaches a normally operating SV). Finally, if one SV experienced cycling failure, then the sampled open fraction is used. If multiple SV experience cycling failure, then their open fractions are summed. Figure 4-21 shows the scatterplot of iodine release fraction versus SV_Frac. This scatter plot suggests a relationship between low fractional open areas and low fraction of iodine release (i.e., SV_Frac<0.28). Almost all of these realizations had an iodine release less than 0.1. In contrast, the fractional open area above 0.28 corresponds with the entire range of iodine release.

The response to the SV_Frac parameter has interdependence on the number of cycles. As discussed in Section 4.2.1.1, all the realizations where the pressurizer safety valves operated as designed without failures resulted in late containment failures. The progression of events in these sequences includes a hot leg failure from high RCS pressure followed by a rapid discharge of the accumulators into the degraded core. The early RPV failure occurred when ice was available to condense steam. Consequently, the hydrogen could burn in smaller amounts as it discharged from the hot leg. The hydrogen (and oxygen) was consumed without building to large concentrations that could threaten the containment. All these realizations progressed to a late containment failure (i.e., >32 hours, see Figure 4-16), which results in a delayed start of the iodine release. The late containment iodine releases were generally lower than the realizations with an early containment failure (see discussion in Section 4.2.1.2.1). Consequently, all the realizations with SV_Frac=0 include a late containment failure and correlate with smaller releases.

The SV_Frac realizations with a failure area less than 0.28 also had small source terms. The smaller leakage area behaved more closely to a normally operating pressurizer SV. Furthermore, if the leakage area on the first failed valve was too small to prevent further pressurizer SV cycling, then the behavior was also similar normally operating SVs and also resulted in late containment failure.

The SV_Frac realizations with valve failure areas between ~0.28 to 1 resulted in both early and late containment failures. These cases spanned the full spectrum of iodine releases. As discussed in Section 4.2.1.1, Realizations 133 and 225 are representative of early and late containment failure, which generally correlates with larger and smaller source terms, respectively. The two realizations had very similar sampled parameters except the number of cycles until the pressurizer SV failed. In particular, both realizations had similar SV failure areas (i.e., ~0.6). However, the pressurizer SV stuck failed after 3 cycles in Rlz 133 versus 69 cycles in Rlz 225. An early and large pressurizer SV failure will depressurize the RCS and transfer more hydrogen into the lower containment prior to the RPV breach. This often resulted in more energetic burns that failed the containment at the RPV breach (i.e., the timing of the first active ignition source). The realizations within this SV failure area range filled the spectrum of the results but were also dependent on the number of SV cycles before failure.

There is another factor influencing the iodine release for these cases. Prior to RPV breach, the iodine release pathway to the containment is through the pressurizer SV. The PRT can filter the releases from the SV sparger. The PRT rupture disk opens after ~25 SV cycles or shortly after a non-trivial SV failure (i.e., fails to close with SV_Frac > 0.28). An early SV failure with a large failure area can contribute to more iodine transport and capture in the PRT. Following hot leg failure, the hot leg becomes the dominant release pathway. While the PRT pool can be effective in the early retention of iodine, the decay heat from the captured radionuclides can evaporate the water. Following pool dryout, the radionuclides plate out on the PRT floor. The subsequent heating and release of radionuclides including iodine from the PRT dryout impacts the lower containment airborne concentration. With normally operating pressurizer safety valves, less iodine is transported to the PRT and the dryout timing is later. The SV_Frac realizations with valve failure areas between ~0.25 to 1 had variable effects from the PRT dryout due to timing of the valve failure. For example, Rlz 133 with an early SV failure (i.e., 3 cycles) and 0.64 fractional failure area captured 183 kg of volatile radionuclide aerosols in the PRT pool (see Figure 4-22) whereas Rlz 255 with a late SV failure (i.e., 69 cycles) and 0.56 fractional failure area only captured 31 kg of volatile radionuclide aerosols (see Figure 4-23). However, 83 kg and 7 kg revaporized by 72 hours, respectively, which included iodine revaporization releases.

The SV_Frac realizations with total combined valve failure areas greater than 1 resulted in moderate iodine releases that were slightly above the median and the mean. There were six realizations with a SV_Frac greater than 1 that ranged in a total failure flow area from 1.05 to 1.54. Since the SV_Frac is larger than 1, two or more pressurizer safety valves failed prior to a RPV breach. These realizations progressed to multiple valve failures because the initial valve failure did not depressurize the RCS. Closer examination of Rlz 139 (SV_Frac=1.54) shows the first valve failure occurred early with a flow area of 0.62 when the RCS pressurization rate was very high. The stuck-open SV contributed to a level swell in the pressurizer that limited the energy removal from through the open SV. The reduced energy flow from the RCS resulted in a second SV failure (flow area of 0.92), which coincidently had a failure after 1 cycle. Consequently, the total SV flow was equal to 1.54 (i.e., 0.62 + 0.92). The subsequent RCS depressurization promoted conditions that would lead to an early containment failure (i.e., an early complete release of the hydrogen from the RCS prior to the first ignition source). As

expected, Rlz 139 had an early containment failure after the hot leg rupture. The source terms for 5 of these 6 realizations were above the mean and median release, which is consistent with an early containment failure.[20] The remaining realization is consistent with a late containment failure magnitude iodine release where the second SV failure occurred late.

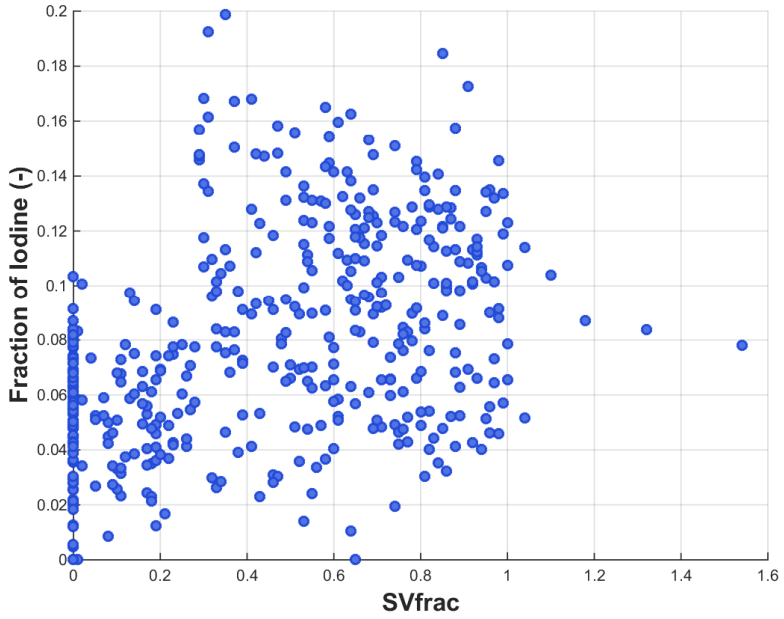

Figure 4-21 Scatterplot of iodine release fraction versus SV_Frac

[20] The large SV failure flow area and dual pathways in Rlz 139 resulted in an unexpected reverse flow pattern from the PRT to the pressurizer. Consequently, the revaporized iodine was retained in the pressurizer. This limited the magnitude of the revaporization source term from the PRT the environment as previously described with Figure 4-22. Two of the three of the SV_Frac between 1.05 and 1.1 had larger iodine source terms >0.1, which is consistent with a large revaporization release from the PRT.

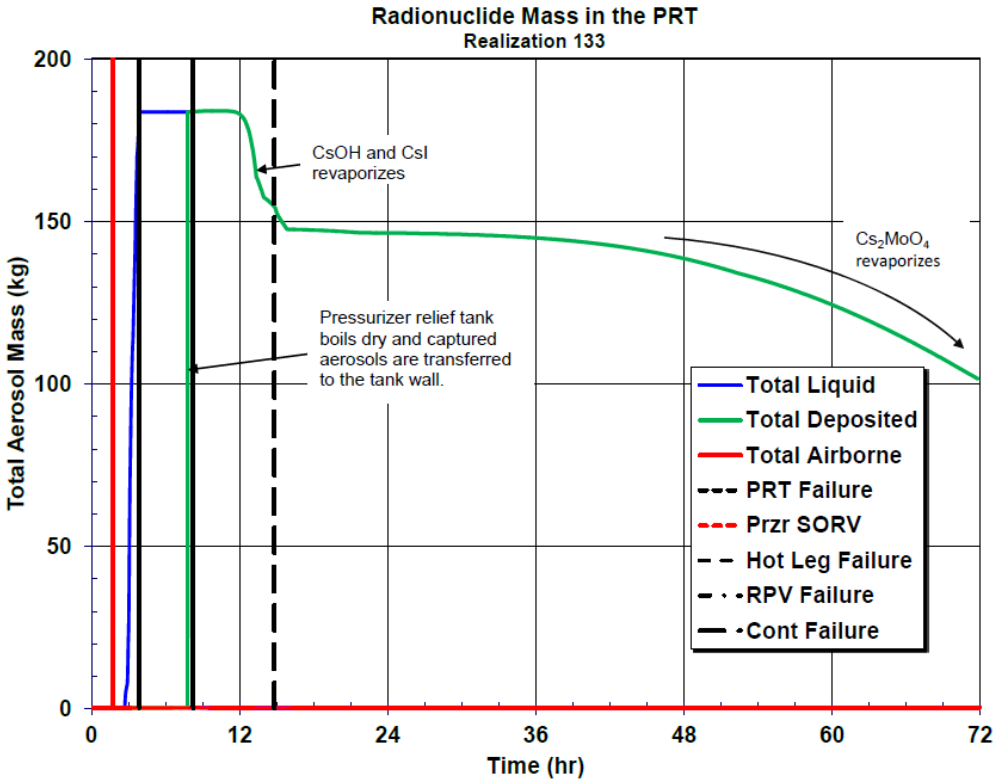

Figure 4-22 Radionuclide mass in the pressurizer relief tank for Rlz 133

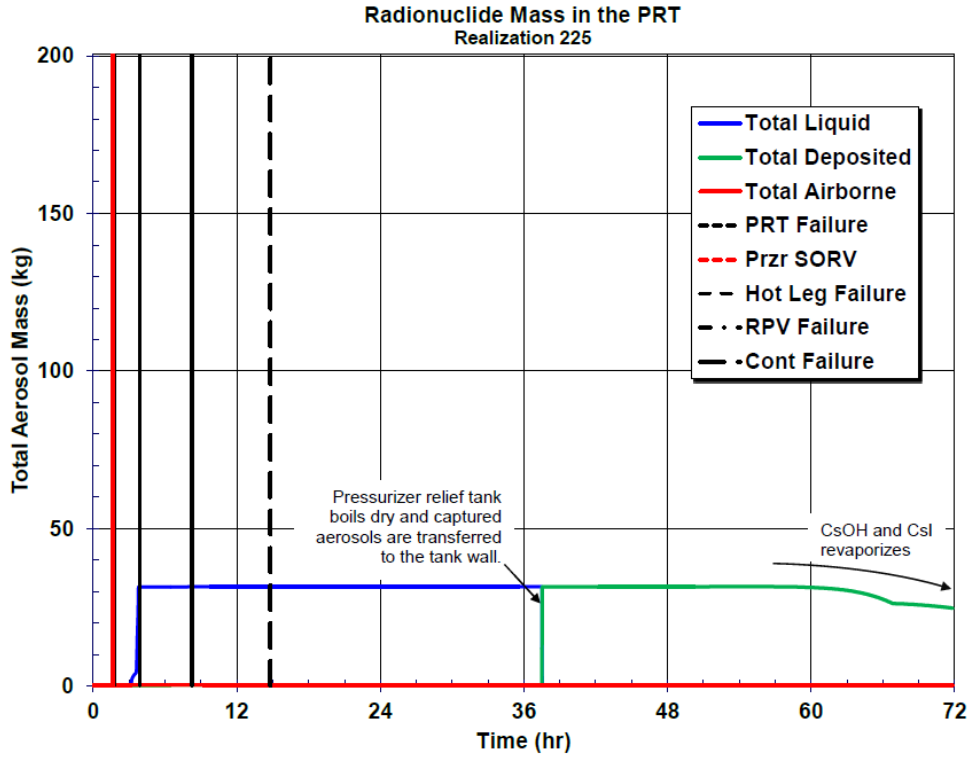

Figure 4-23 Radionuclide mass in the pressurizer relief tank for Rlz 225

priSVcycles

The probability that a pressurizer SV fails to close is based on a per demand failure probability variable named priSVcycles, which was implemented in the MELCOR model as the number of cycles the SVs experienced. Figure 4-24 is the scatterplot of the iodine release fraction versus priSVcycles. The maximum number of SV cycles is 74 cycles before there was a RPV breach. The dense clustering of realizations between 71 to 74 cycles indicates normally operating SVs until RPV breach (i.e., hot leg failure). If the pressurizer SVs operate without any failures (e.g., the black circles in Figure 4-16), then the containment only fails late. A late containment failure generally correspond to lower releases, as shown in Figure 4-24. Most of the realizations with 61 to 74 SV cycles resulted in a late containment failure (i.e., the red triangles in Figure 4-16). These realizations have lower iodine releases (i.e., <0.12, see Figure 4-24). Most of the realizations with 46 to 60 SV cycles also resulted in a late containment failure (i.e., the yellow triangles in Figure 4-16). All but two of the realizations from the 46 to 60 cycle group had iodine releases less than 0.13.

As discussed in Section 4.2.1.1, the realizations with 1 to 45 SV cycles included both early and late containment failures. The results from Figure 4-24 show the highest iodine release occurs between 10 to 42 SV cycles. However, there were also many very low releases within this grouping. Consequently, the correlation of the priSVcycles is less definitive within this range. Other factors such as the SV failure area (SV_Frac variable) and containment failure pressure (Rupture variable) combine with the number of SV cycles to impact containment failure timing and the magnitude of the iodine release.

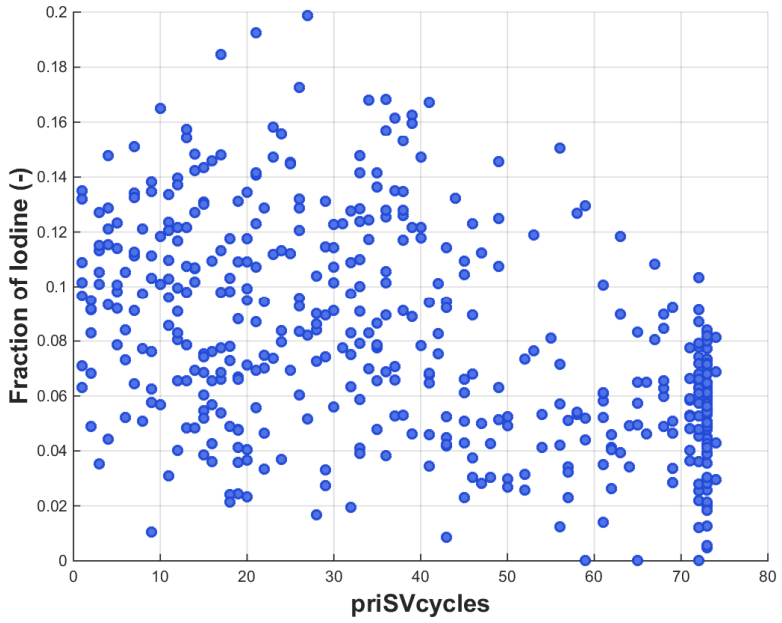

Figure 4-24 Scatterplot of iodine release fraction versus priSVcycles

Rupture

The Rupture parameter represents the failure pressure of the containment. The containment failure is simulated as an abrupt opening of a 3 ft^2 hole in the dome. Figure 4-25 is the scatterplot of the iodine release fraction versus rupture pressure. This plot shows a very slight

downward sloping trend, which is supportive of the -0.17 regression coefficient on rupture in the rank regression. A higher containment failure pressure has the potential to withstand the pressurization from early hydrogen burns. A higher containment failure pressure will also delay a late over-pressurization from ex-vessel steam and CCI gas generation versus a lower containment pressure. A delay to the containment rupture allows more time for aerosol settling and less cumulative effect from the long-term iodine revaporization within 72 hours. Consequently, the trend of higher containment failure pressure lowering iodine release is evident on Figure 4-25.

In contrast to the overall trend, some of the low containment failure pressure realizations include a small iodine release and some of the high containment failure pressure realizations include a large iodine release. Examples of a higher iodine release from a high containment failure pressure often results from a high airborne iodine concentration at containment failure (see Figure 4-20). A near vertical trend is most prevalent with an early containment failure but also occurs with late containment failures. As discussed in Section 4.2.1.1 (i.e., see Figure 4-15), all the early containment failures occurred following a hydrogen burn. In contrast, all the late containment failures occurred due to a gradual over-pressurization. Due to the variable nature of the hydrogen burn propagation, duration, and frequency, the influence of the containment failure pressure on the early containment failure and usually higher iodine releases was more uncertain. In contrast, the late containment failures always benefitted from a higher containment pressure. Since there were more late containment failures, the slight downward trend in iodine release as a function of containment failure pressure (and later containment failure) is reasonable. (The presentation in Figure 4-25 does not separate the early versus late containment failures.)

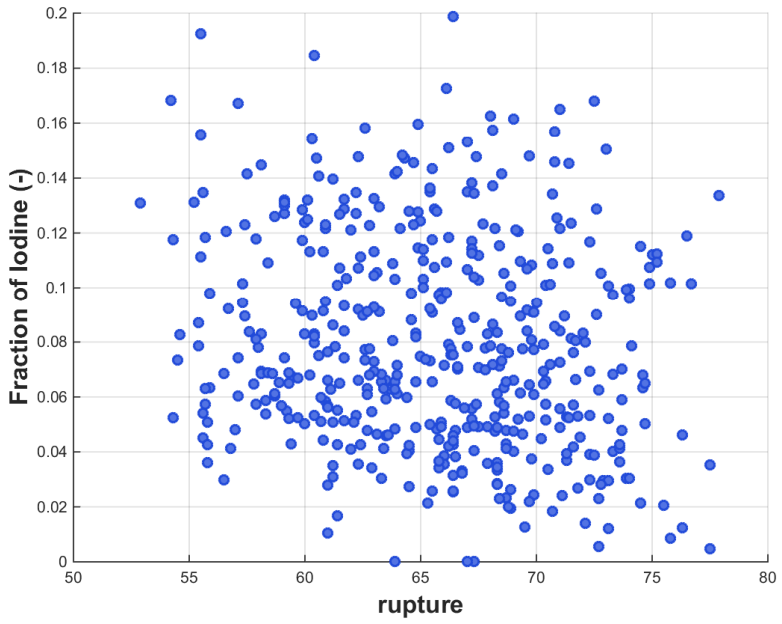

Figure 4-25 Scatterplot of iodine release fraction versus rupture

EU_melt_T

This parameter represents the temperature at which the eutectic formed from UO_2 and ZrO_2 melts. This parameter is input into MELCOR as a eutectic sensitivity coefficient (SC1132) and a melting temperature. By including the temperature of the eutectic reaction between ZrO_2 and UO_2 as a sampled parameter, the fuel failure characteristics and debris behavior are affected. Figure 4-26 is the scatterplot of the iodine release fraction versus the eutectic melt temperature. The points are distributed with an upward sloping trend. This is also reflected in the regression table with the 0.13 regression coefficient on EU_melt_T in the rank regression.

As discussed previously with the high ranked parameters affecting the iodine release, the timing of containment failure is an important factor. However, the amount of hydrogen production does not have a significant correlation on the timing of containment failure (see Section 4.2.1.1 and Figure 4-18). Figure 4-26 shows a weakly correlated upward slope in iodine release versus the eutectic melting temperature. However, all the high sampled eutectic temperatures (>2575 K) had iodine releases below 0.14. Consequently, the results do not suggest a meaningful correlation.

A few of the lowest sampled eutectic melting temperatures fell below the Zircaloy breakout temperature (2350 K), which may impact the in-vessel hydrogen production and the in-vessel iodine release from fuel. All these cases had a fractional iodine release to the environment that was less than 0.1. Closer examination of the radionuclide release from selected realization results show that nearly all the iodine within the fuel matrix is released during the in-vessel accident progression (i.e., including before and after hot leg failure). Any iodine remaining in the fuel matrix will be released during the ex-vessel core-concrete interactions. Since the total hydrogen production did not impact early versus late containment failure (i.e., see Section 4.2.1.1 and Figure 4-18), the impact of a low eutectic melting temperature to promote late containment failure and a lower iodine release to the environment was ruled out. The other remaining possible impacts from a low eutectic melting temperature could be the timing of the iodine release relative to the containment failure and the magnitude of the revaporization, which is dependent on other factors (i.e., SV failure timing and flow area). Therefore, the magnitude of the iodine release to the environment was not judged to be significantly impacted by the eutectic temperature.

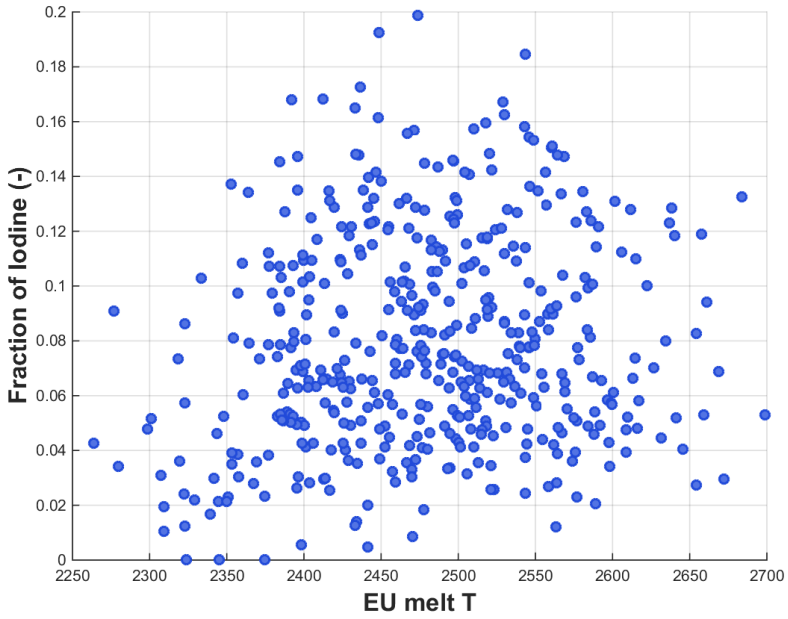

Figure 4-26 Scatterplot of iodine release fraction versus eutectic melt temperature

4.2.1.3 Cesium Release Fraction to Environment (with no random ignition)

The magnitude and timing of the cesium release is an important radionuclide to characterize the potential severity of the long-term health effects. The magnitude of the cesium release can be very important for latent effects. Consequently, the following regression evaluations paid particular attention to factors that influenced large releases of cesium.

4.2.1.3.1 Cesium Release History

The environmental release fraction of all chemical forms of cesium (percentage of initial cesium inventory) at 72 hours is a primary figure of merit for the analysis. Figure 4-27 shows the time dependent release fractions for the successful realizations, as well as the calculated mean, median, and 5th and 95th percentiles. Although the mean and median are reasonably well fit between the 5th and 95th percentiles, there is a significant difference in the release times for all curves.

The split in the start of the cesium release to the environment coincides with the containment rupture timing (see Figure 4-15). The early iodine releases result from the early containment rupture following a hydrogen burn whereas the second grouping occurs from a late over-pressurization failure due to ex-vessel steam production and CCI gas generation. As discussed previously in Section 4.2.1.1, there is a time gap following the containment becoming oxygen deficient (i.e., the end of combustion due to a lack of oxygen) to the time required for steam generation from evaporating water and non-condensable gas generation to over-pressurize the containment. The variation in the late over-pressure timings is influenced by the containment rupture pressure and the amount of hydrogen gas that was burned. The variation in the containment failure timing directly affected the start of the cesium release.

However, the variation in the magnitude of the cesium release is a more complex function of other parameters that will be discussed in the following subsections.

The bifurcation in containment failure timings led to a wide spread between the calculated median and the 95th percentile curves. Most realizations resulted in a late containment rupture; however, the median realization is characteristic of a late containment failure while the mean curve has contributions from both the early and late containment failure results. All statistical measure curves show increasing trends from the following containment failure. The median trend has the flattest slope, which is characteristic of a late containment failure release.

The median release of cesium is relatively low at 72 hours and reflective of the late containment failure response. The majority of the late containment failure realizations result in a relatively low cesium release (i.e., 0.025 or less). The mean release includes both early and late containment failure results. The mean result lies above the median and is rising slightly faster than the median result at 72 hours. This trend will be discussed further in the Section 4.2.1.3.2 and has to do with late revaporization of cesium from the PRT.

The overall magnitude of the cesium release to the environment (Figure 4-27) is smaller than the iodine release (Figure 4-20). The median cesium release at 72 hours is 0.025 (Figure 4-27) whereas the comparable iodine release is 0.075 (Figure 4-20). Similarly, the mean cesium release is 0.05 while the comparable iodine release is 0.08. The range of the releases is similar (i.e., 0 to 0.2 for both radionuclides except one cesium realization). The cesium release was expected to be lower than the iodine release due to the lower volatility of the characteristic compounds. The majority of the cesium is in the cesium molybdate compound (i.e., ~80% is Cs_2MoO_4), which has a lower vapor pressure than cesium iodide (i.e., the dominate iodine compound, see Figure 4-28). Consequently, the cesium released from the fuel forms aerosols more quickly than the iodine compounds, which promotes in-vessel deposition and is more difficult to revaporize. These attributes lead to a lower cesium release to the environment than iodine.

Figure 4-29 shows an expanded view of the cesium release fractions over the first 20 hours of the simulation. The early containment failure releases start occurring at about 3.9 hours. Most early containment failures occur at the initial vessel breach (i.e., almost always hot leg failure) and end by approximately 9 hours (see Figure 4-15). However, some of the early containment failures following a hydrogen burn occur as late as 18.5 hours. The early releases tend to increase to a 1 percent release by 10 hours with a subsequent increase to about 2 to 3 percent thereafter. The initial release often includes the cesium in the gap and the initial thermally-driven releases until the RPV breach. The subsequent increase in the cesium release occurs after the second fuel heatup after the accumulator discharge following the RPV breach.

A late phase release occurs in many realizations due to revaporization of cesium that was initially retained in the PRT (e.g., see Figure 4-22 and Figure 4-23). The magnitude of the revaporization from the PRT is a strong function timing of the failed pressurizer SV and the open area. If the pressurizer SV sticks open early, then more of the released radionuclides are transported to the PRT, which contributes to larger revaporization releases. A second source of revaporization releases is from hot gases from the ex-vessel debris flowing through the failed lower head and out the failed hot leg failure. The impact of the late-phase revaporization release is greatest when it occurs after the containment failure, which allows direct leakage to the environment without time to re-deposit.

Finally, Figure 4-30 summarizes the cumulative probability of a cesium release to the environment as a function of time. Initially, there is a small variation in the release to the environment. However, there is a large variability of the release at 72 hours, which reflects the impact of early and late containment failure as well as late revaporization sources.

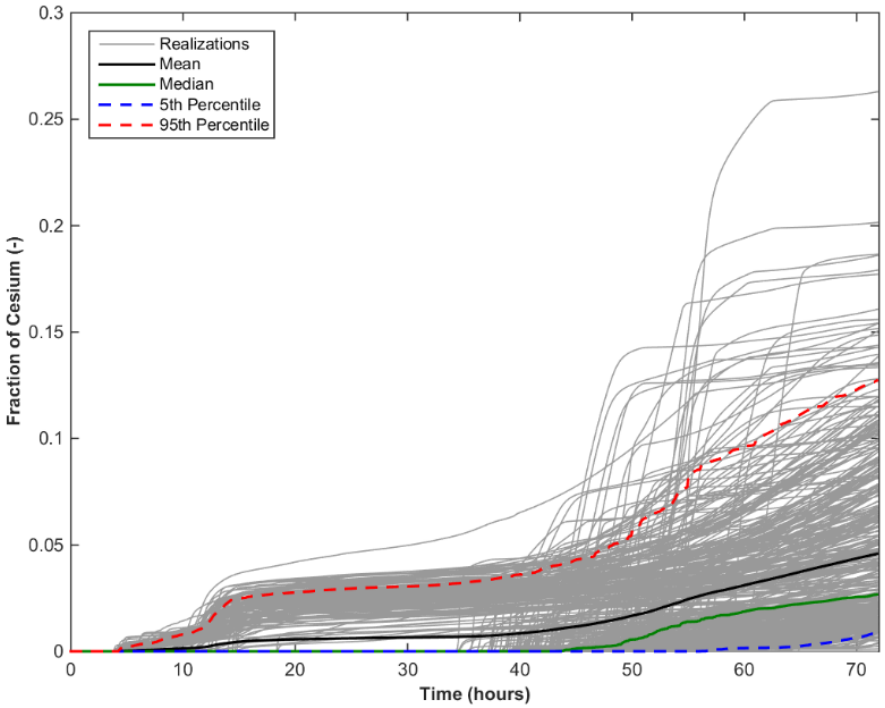

Figure 4-27 Cesium release fractions over 72 hours with mean, median, 5th and 95th percentiles

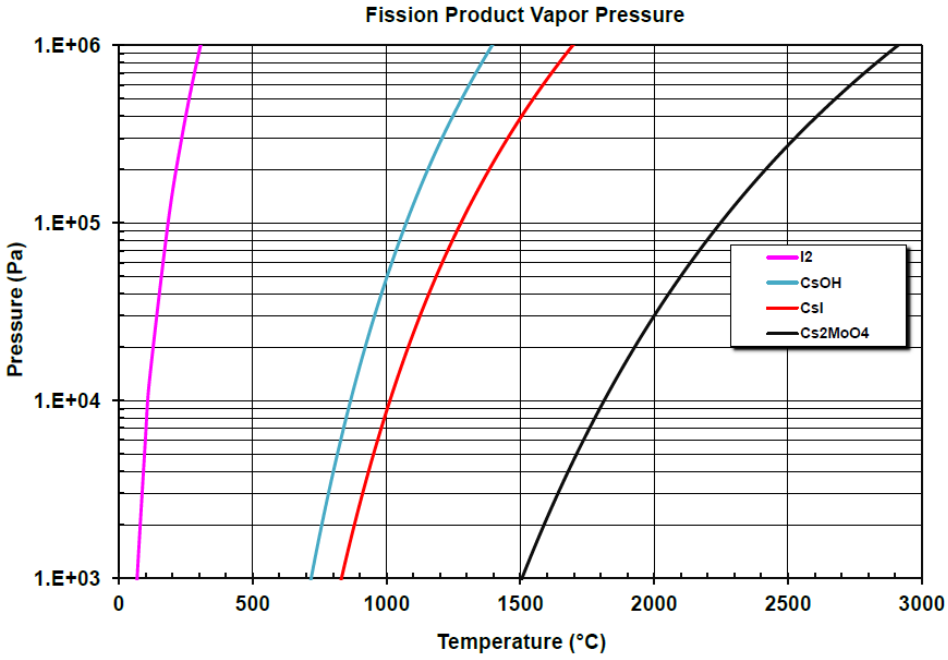

Figure 4-28 Comparison of Iodine and Cesium Compound Vapor Pressures

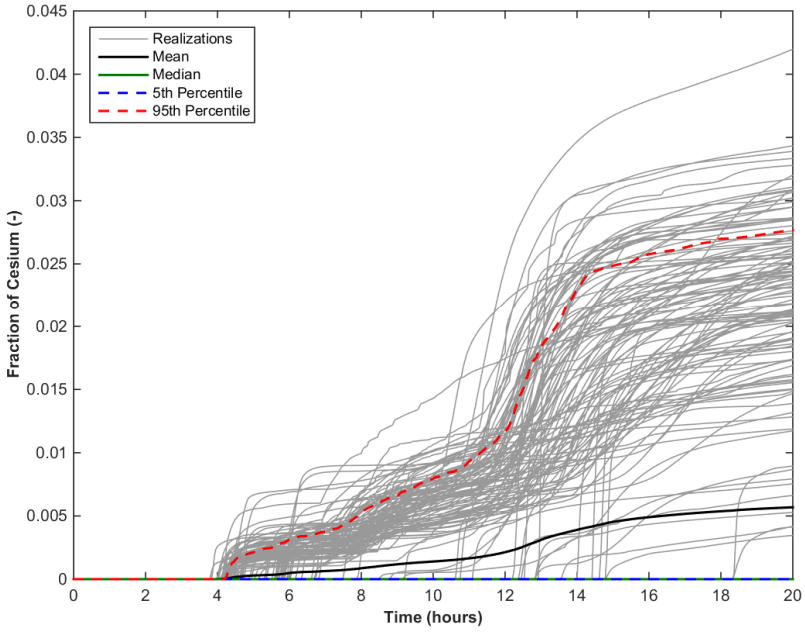

Figure 4-29 Expanded view of the cesium release fractions over the first 20 hours of the simulation

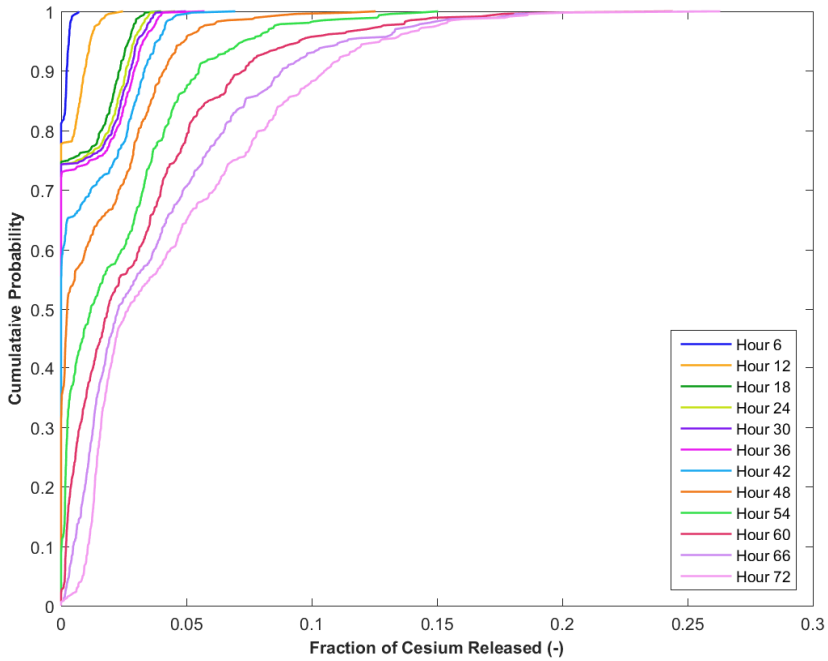

Figure 4-30 Cumulative probabilities for the fraction of cesium release for selected time intervals

4.2.1.3.2 Regression Tables and Scatterplots

Table 4-5 shows the results for regression analysis of the cesium release fraction. In review of the regression results for all successful realizations, the SV open fraction was identified as the most important parameter by all regression techniques. SV stochastic FTC (priSVcycles) was identified as the second most important parameter by all regression techniques, except Quadratic, which marginally identified it lower than shape_fact (shape factor). The parameters shape_fact and Ajar were identified as the third and fourth most important, respectively, for all regression techniques. No other parameters had a significant contribution to cesium release fraction uncertainty.

Table 4-5 Regression analysis of cesium release fraction (with no random ignition).

	Rank Regression		Quadratic		Recursive Partitioning		MARS		Main Contribution	Conjoint Contribution
Final R^2	0.71		0.68		0.88		0.75			
Input	R^2 contr.	SRRC	S_i	T_i	S_i	T_i	S_i	T_i		
SV_frac	0.66	0.72	0.82	0.93	0.57	0.84	0.62	0.74	0.546	0.135
priSVcycles	0.02	-0.16	0.02	0.09	0.12	0.32	0.21	0.33	0.073	0.105
shape_fact	0.01	0.10	0.03	0.05	0.02	0.11	0.03	0.04	0.017	0.033
ajar	0.01	-0.10	0.01	0.03	0.00	0.06	0.01	0.02	0.006	0.022
EU_melt_T	0.01	0.09	---	---	0.00	0.02	0.00	0.00	0.003	0.006
rupture	0.00	-0.04	0.00	0.03	0.00	0.01	0.00	0.00	0.001	0.010
Seal_Open_A	---	---	0.01	0.01	0.00	0.00	0.00	0.01	0.001	0.004
Seal_Fail_Dp	---	---	---	---	0.00	0.01	0.00	0.01	0.001	0.005
burn_dir	---	---	---	---	---	---	0.00	0.00	0.001	0.000

* highlighted if main contribution larger than 0.02 or conjoint contribution larger than 0.1

SV_Frac

Figure 4-31 is the scatterplot of the cesium release fraction versus SV_Frac. There is a clearly strong positive relationship between SV_Frac and the fraction of cesium released. In particular, the limited spread of the points with both low combined fraction of open area and fraction of cesium release is indicated by the high SV_Frac contribution measures in each of separate regression techniques. The SV_Frac consistently accounts for more than 50 percent of the variance in each model.

In comparison to the iodine release fraction to the environment (see Figure 4-21), the cesium release scatter plot shows a stronger correlation between the SV open areas and the total cesium release. The cesium release fraction generally increased as the SV_Frac increased. Similar to the low fraction of iodine release with SV_Frac<0.28, all of the realizations had a cesium release less than 0.03. With an SV_Frac>0.6, the scatter in the results increased. However, the overall trend was upward to a cesium release of ~0.12 as the SV_Frac approaches 1. As discussed in Section 4.2.1.2.2, the realizations with a SV_Frac>1 generally have different behavior because they include multiple SV failures.

The response of the SV_Frac parameter has interdependence on the number of SV cycles. As discussed in Section 4.2.1.1, all the realizations where the pressurizer safety valves operated as designed without failures resulted in late containment failures. The progression of events in these sequences includes a hot leg failure from high RCS pressure followed by a rapid discharge of the accumulators into the degraded core. The early RPV failure occurred when ice was available to condense steam. Consequently, the hydrogen could burn in smaller amounts as it discharged from the hot leg. The hydrogen (and oxygen) was consumed without building to large concentrations that could threaten the containment. All these realizations progressed to a late containment failure (i.e., >32 hours, see Figure 4-16), which results in a delayed start of the cesium release. The late containment cesium releases were generally lower than the realizations with an early containment failure (see discussion in Section 4.2.1.2.1). Consequently, all the realization with SV_Frac=0 include a late containment failure and correlate with smaller releases.

The SV_Frac realizations with a failure area less than 0.25 also had small source terms. The smaller leakage area behaved more closely to a normally operating pressurizer SV. Consequently, the SV_Frac<0.25 generally resulted in late containment failure and a smaller cesium release at 72 hours.

The SV_Frac realizations with valve failure areas between ~0.25 to 1 resulted in both early and late containment failure. These cases spanned the full spectrum of cesium releases. As discussed in Sections 4.2.1.1 and 4.2.1.2.2, Realizations 133 and 225 are representative of early and late containment failure, which generally correlates with larger and smaller source terms, respectively. The two realizations had very similar sampled parameters except the number of cycles until the pressurizer SV failed. In particular, both realizations had similar SV failure areas (i.e., ~0.6). However, the pressurizer SV stuck failed after 3 cycles in Rlz 133 versus 69 cycles in Rlz 225. An early and large pressurizer SV failure will depressurize the RCS and transfer more hydrogen into the lower containment prior to the RPV breach. This often resulted in more energetic burns that failed the containment at the RPV breach (i.e., the timing of the first active ignition source). The realizations within this SV failure area range filled the spectrum of the results but were also dependent on the number of SV cycles before failure.

Perhaps the most significant factor influencing the cesium release for the realizations with a SV_Frac between ~0.25 to 1 is the impact of the revaporization from the PRT. Prior to a RPV breach, the cesium release pathway from the fuel to the containment is through the pressurizer SV. The PRT initially retains cesium radionuclide releases in the PRT water. However, the PRT rupture disk opens after ~25 SV cycles shortly after a non-trivial SV failure (i.e. fails to close with SV_Frac>0.25). An early SV failure with a large failure area can contribute to more cesium transport and capture in the PRT. While the PRT pool can be effective in the early retention of cesium, the decay heat from the captured radionuclides can evaporate the water. Following pool dryout, the radionuclides plate out on the PRT walls. The subsequent heat-up and revaporization of radionuclides including cesium from the PRT dryout impacts the environmental release if the containment is failed. The SV_Frac realizations with valve failure areas between ~0.25 to 1 had variable effects from the PRT dryout due timing of the valve failure. For example, Rlz 133 with an early SV failure (i.e., 3 cycles) and 0.64 fractional failure area captured 183 kg of volatile radionuclide aerosols in the PRT pool. The revaporization of radionuclides in the PRT started at ~12 hours (i.e., just prior to containment failure, see Figure 4-22).[21] In contrast, Rlz 255 with a late SV failure (i.e., 69 cycles) and 0.56 fractional failure area only captured 31 kg of volatile radionuclide aerosols and did not start to revaporize cesium until ~60 hours (Figure 4-23). Consequently, both the timing of SV failure and the failure area are important.

The realizations with a combined total SV_Frac greater than 1 resulted in moderate cesium releases that were above the median release. There were six realizations with a SV_Frac greater than 1 that ranged in total failure flow area from 1.05 to 1.54. Since the SV_Frac is larger than 1, two or more pressurizer safety valves failed prior to a RPV breach. These realizations progressed to multiple valve failures because the initial valve failure did not

[21] Note the various compounds of cesium are revaporized according to their vapor pressure as the PRT heats (see vapor pressures on cesium compounds in Figure 4-28). The cesium hydroxide (CsOH) and cesium iodide (CsI) compounds release first, which is followed by cesium molybdate (Cs_2MoO_4). Most of the cesium is in the cesium molybdate compound. Consequently, this is the last compound to revaporize and requires extremely high decay heat (i.e., a result of an early SV failure like Rlz 133).

depressurize the RCS. Closer examination of Rlz 139 (SV_Frac=1.54) shows the first valve failure occurred early with a flow area of 0.62 when the RCS pressurization rate was very high. The stuck-open SV contributed to a level swell in the pressurizer that limited the energy removal through the open SV. The reduced energy flow from the RCS resulted in a second SV failure (flow area of 0.92), which coincidently had a failure after 1 cycle. Consequently, the total SV flow was equal to 1.54 (i.e., 0.62 + 0.92). The subsequent RCS depressurization promoted conditions that would lead to an early containment failure (i.e., a nearly complete release of the hydrogen from the RCS prior to the first ignition source). Rlz 139 had an early containment failure after the hot leg rupture. Three of the source terms for realizations were well above the median release, which is consistent with an early containment failure.[22]

Finally, the impact of SV_Frac on the revaporization from the PRT for the cesium release is more important than for iodine. This is evident on the cesium SV_Frac scatterplot (Figure 4-31) versus the iodine SV_Frac scatterplot (Figure 4-21). The simulated chemical forms of iodine are cesium iodide and elemental iodine. Elemental iodine is always a gas. The predominant form of cesium is cesium molybdate. As shown in Figure 4-28, cesium molybdate has a much lower vapor pressure than cesium iodide. If SV_Frac was 0 or small, then there was (a) an early hot leg failure with a larger amount of the fission products released through the hot leg failure location and (b) late containment failure. There was inadequate decay heat from the fission products captured in the PRT to reach the relatively high cesium molybdate vaporization temperature. Consequently, any released cesium generally settled in the containment at low values of SV_Frac. As the magnitude of the SV_Frac increased, the potential for early containment failure and revaporization of cesium molybdate increased. This is evident by the increase in cesium release in Figure 4-31. Due to the higher volatility of cesium iodine, it can revaporize more easily at lower temperatures. This could happen from the cesium iodine captured in the vessel or PRT. Consequently, the revaporization of iodine compounds is less sensitive to having a very large amount of captured fission products in the PRT and occurred at a wide range of SV_Frac values (i.e., compare Figure 4-21 and Figure 4-31). Nevertheless, both cesium and iodine have considerable scatter for SV_Frac >0.3 due to the inability of SV_Frac to adequately characterize both the timing and flow area to the PRT (i.e., see the discussion of Rlz 133 and 255 above).

[22] The large SV failure flow area in Rlz 139 resulted in an unexpected reverse flow pattern from the PRT to pressurizer. This limited the magnitude of the revaporization source term from the PRT as previously described with Figure 4-22. Two of the three of the SV_Frac between 1.05 and 1.1 had larger iodine source terms >0.1, which is consistent with a large revaporization release from the PRT.

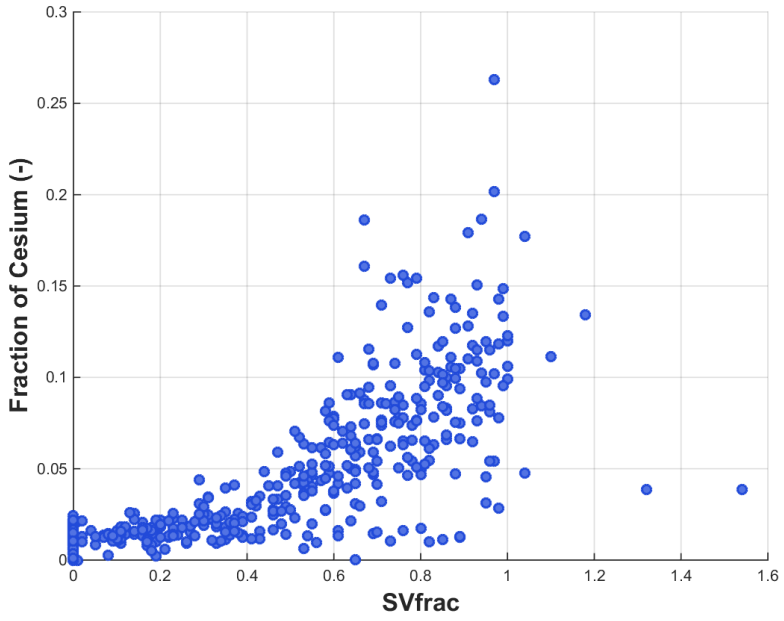

Figure 4-31 Scatterplot of cesium release fraction versus SV_Frac

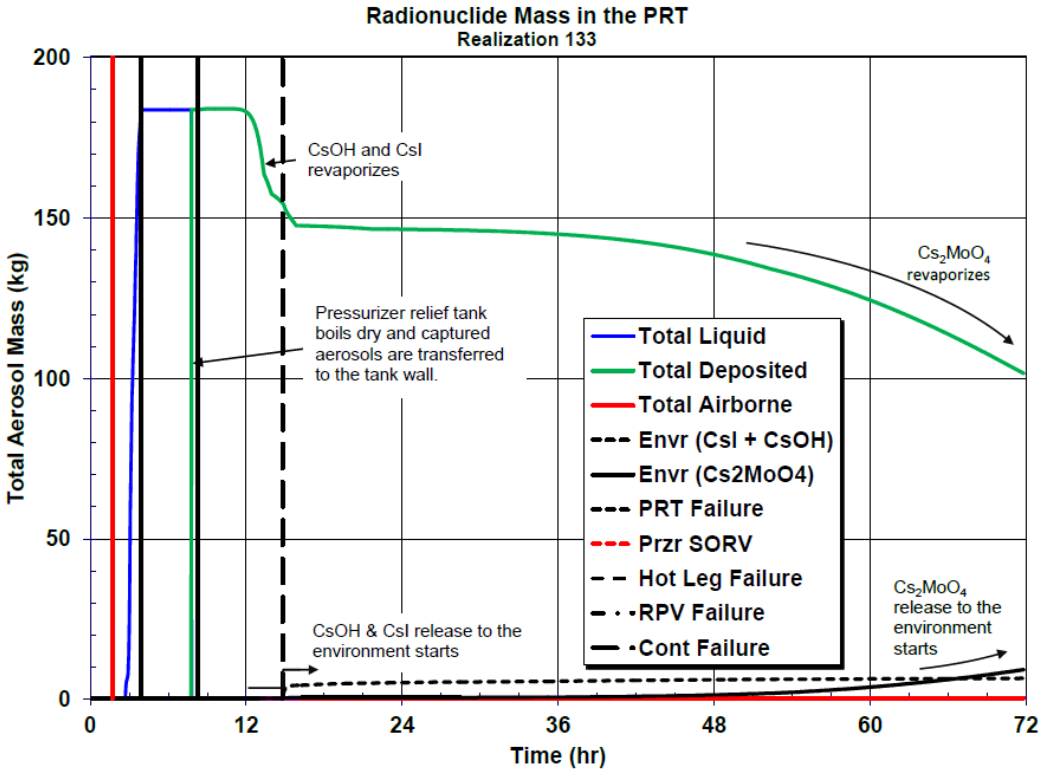

Figure 4-32 Radionuclide mass in the pressurizer relief tank for Rlz 133

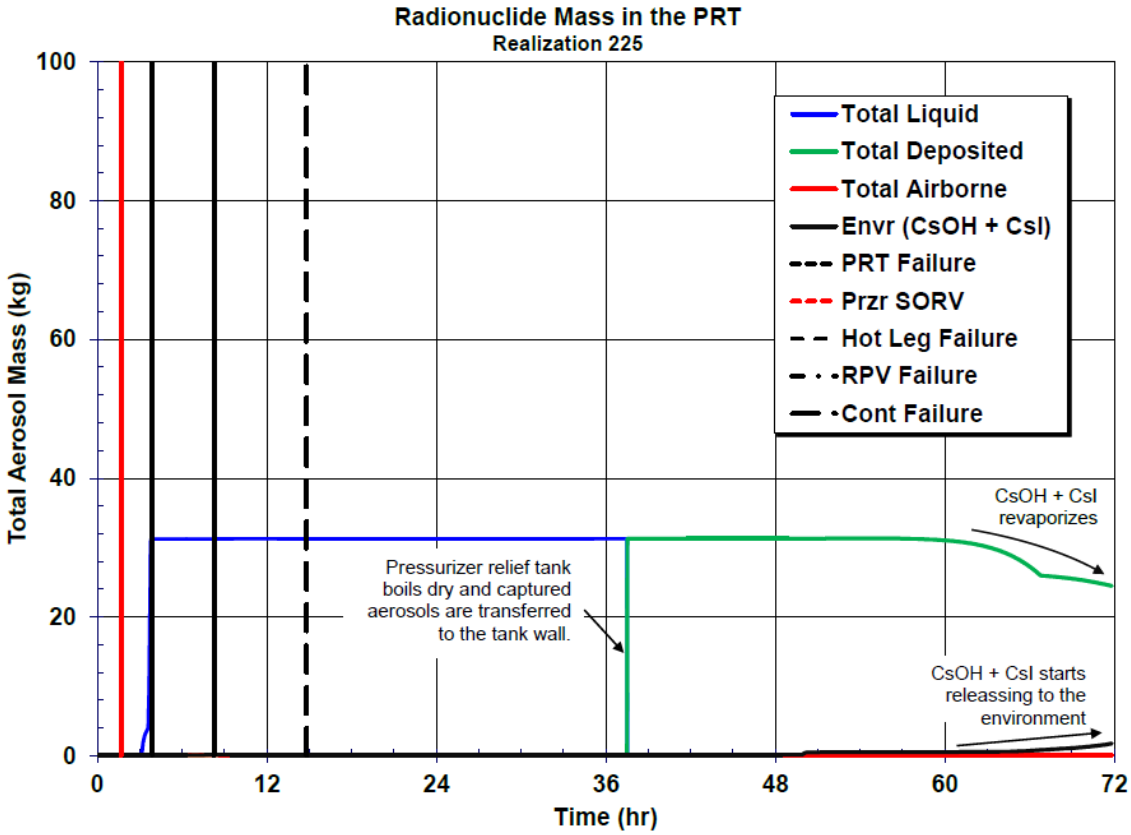

Figure 4-33 Radionuclide mass in the pressurizer relief tank for Rlz 225

priSVcycles

Figure 4-34 is the scatterplot of the cesium release fraction versus priSVcycles. The plot has a mild negative slope with a high density of points with a low fraction of cesium released and high combined cycles to failure. This supports the negative regression coefficient for priSVcycles in the rank regression results.

The maximum number of SV cycles is 74 cycles before there was a RPV breach. The dense clustering of realizations between 71 to 74 cycles indicates normally operating SVs until RPV breach (i.e., hot leg failure). If the pressurizer SVs operate without any failures (e.g., the black circles in Figure 4-16), then the containment only fails late. All the normally operating SV realizations had low cesium releases, as shown in Figure 4-34. The low environmental release with late containment failure is consistent with more time for aerosol settling and no significant revaporization releases prior to 72 hours.

Similarly, all of the realizations with 61 to 74 SV cycles also resulted in early containment failure (i.e., the red triangles in Figure 4-16). Most of these realizations have lower cesium releases (i.e., all but 3 are <0.1, see Figure 4-34).

As previously shown in Figure 4-16, most of the realizations with 46 to 60 SV cycles also resulted in a late containment failure (i.e., the yellow triangles). Most of the cesium releases

were low but there was more scatter. All but three of the realizations from the 46 to 60 cycle group had cesium releases less than 0.13.

As discussed in Section 4.2.1.1, the realizations with 1 to 45 SV cycles included both early and late containment failures. The results from Figure 4-34 show the many low cesium releases within this group (i.e., a trend of many cases with a cesium release <0.05). However, there were also many very high releases within this grouping (e.g., a group of >0.1 between 30 to 40 cycles). Consequently, the correlation of the SV_Frac is less definitive within this range. Other factors such as the SV failure area and containment failure pressure combine with the number of SV cycles to impact containment failure timing and the magnitude of the cesium release.

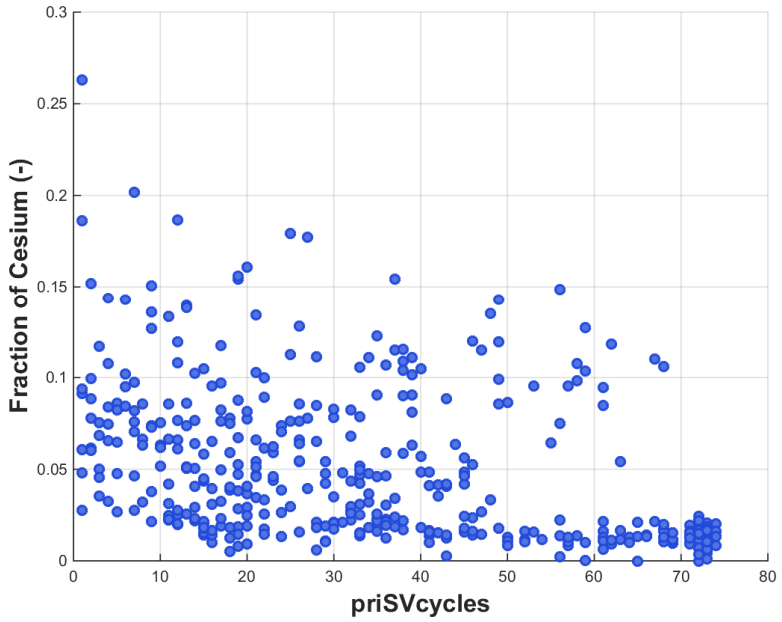

Figure 4-34 Scatterplot of cesium release fraction versus priSVcycles

Dynamic Shape Factor

The dynamic shape factor (shape_fac) parameter accounts for increased drag force for non-spherical aerosol particles. A perfect sphere has a dynamic shape factor of 1. The shape factor is identified by all regression techniques as the third most important parameter in explaining uncertainty in the cesium release, with minimal conjoint influence. Within MELCOR, the dynamic shape factor influences the three deposition processes: gravitational settling, Brownian diffusion, and thermophoresis. A higher sampling of the dynamic shape factor yields an increased aerodynamic drag, which allows aerosols to remain airborne longer and available for release. The various cesium compounds transport as aerosols in the containment (i.e., with the possible exception of initially revaporized cesium near high temperature regions by the ex-vessel debris and inside the PRT). Therefore, an increase in the shape factor was expected to increase the magnitude of the environmental releases.

Figure 4-35 shows the scatterplot of the cesium release fraction versus the shape factor. A slightly positive regression coefficient was calculated. The correlation was judged relatively weak as evidenced by a significant number of large cesium releases (i.e., >0.1) for

shape_fac<1.5 and small cesium releases (i.e., <0.03) for shape_fac>2.5. While the shape_fac affected the deposition rate within the containment, it had no effect on the timing of the containment failure. In particular, most early containment failures occurred at the time of the RPV breach. The containment fully depressurized following the rupture failure with low aerosol retention (i.e., little impact from variable settling time).

Any increase in the shape factor also appears to have a minimal impact on the late containment failure releases. Small cesium releases (i.e., <0.05), which are consistent with late containment failure, occurred at all values of the shape factor. A portion of the late cesium release comes revaporization of cesium in the PRT. The revaporization of the cesium usually occurs after containment failure and has low retention before release through the rupture failure location.

In summary, the aerodynamic shape factor had a small effect on the magnitude of the cesium release. Any cesium released through the RPV breach with an early containment failure did not benefit from long settling times before release to the environment. Similarly, late revaporization releases after a late containment failure also did not benefit from long settling times before release to the environment. In contrast to the large containment failure leakage response in Sequoyah following the containment rupture, the large concrete reinforced Surry containment had a relatively small leakage rate. The Surry containment slowly depressurized over many hours, which showed an important impact of the environmental release versus variations in the settling rates. Consequently, the Surry UA results [17] showed a greater impact by variations in aerosol shape factor whereas this Sequoyah analysis did not.

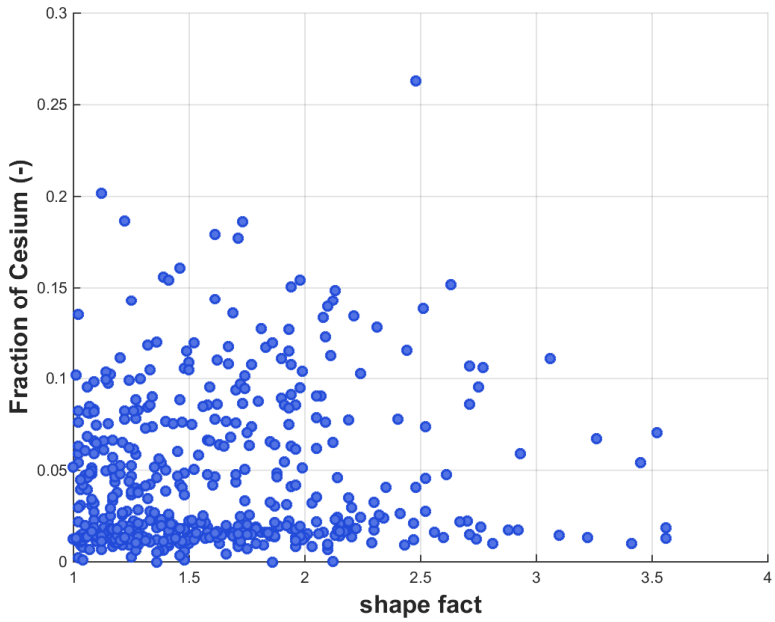

Figure 4-35 Scatterplot of cesium release fraction versus shape factor

Ajar

The Ajar parameter represents the non-dimensional opening area of the lower ice condenser doors after they fully opened (i.e., exceeded the maximum differential pressure for opening). The ice condenser doors will stick at the AJAR fraction thereafter. The AJAR parameter

addresses the uncertainty in the damage of the lower door hinges once they have opened the maximum range.

Figure 4-36 is the scatterplot of the cesium release fraction versus Ajar. This plot does not indicate any particular relationship between the Ajar parameter and the cesium parameter. The density of points is uniform with respect to the horizontal axis, so no particular values of Ajar account for higher or lower fractions of the cesium release. It was hypothesized that the Ajar parameter would impact the lower compartment steam concentration by forming a natural circulation pattern between the lower compartment and the ice compartment.

The typical results show the lower ice compartment doors operated normally until hot leg failure (e.g., see Figure 4-37). Events such as the PRT rupture disk opening did not fully open the lower doors. Consequently, there was no impact of the Ajar parameter prior to hot leg failure. The hot leg failure was the first RPV breach in nearly all of the calculations. If there was an early containment failure, it usually occurred immediately following the hot leg failure. Consequently, the value of Ajar would not affect the conditions of an early containment failure at hot leg failure. If there was no early containment failure, then the containment became oxygen deficient due to the steam generation from evaporating water and the non-condensable gas generation from the CCI as described in Section 4.2.1.1. There was adequate flow area for the slow pressurization via the ice compartment bypass routes even if Ajar was close to the minimum area. Consequently, the value of Ajar was not important. The low correlation of Ajar is evident by the uniform scatter at low cesium releases in Figure 4-36.

The most important impact of the Ajar area would be the conditions following hot leg breach but prior to an oxygen deficient condition. There were only a few realizations that failed due to a hydrogen combustion that was not coincident with hot leg failure (see Figure 4-15). However, the majority of the realizations went through this time period to a late containment failure. Figure 4-36 does not show any correlation of Ajar with the low cesium releases associated with late containment failure. Consequently, it was concluded that Ajar did not impact the cesium release.

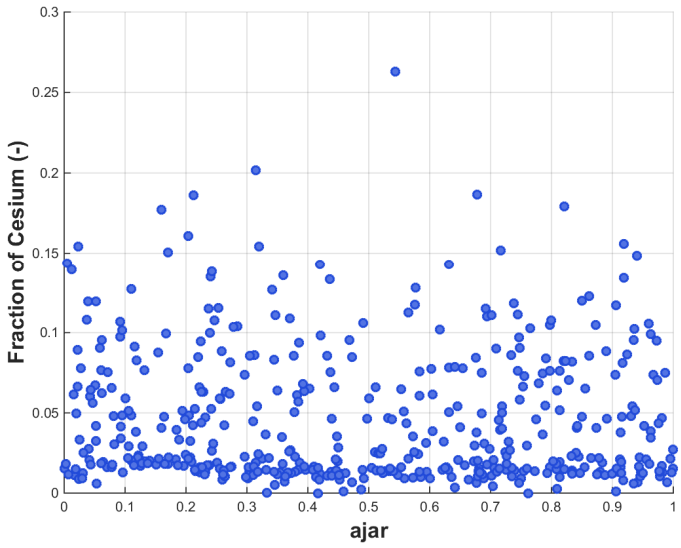

Figure 4-36 Scatterplot of cesium release fraction versus Ajar

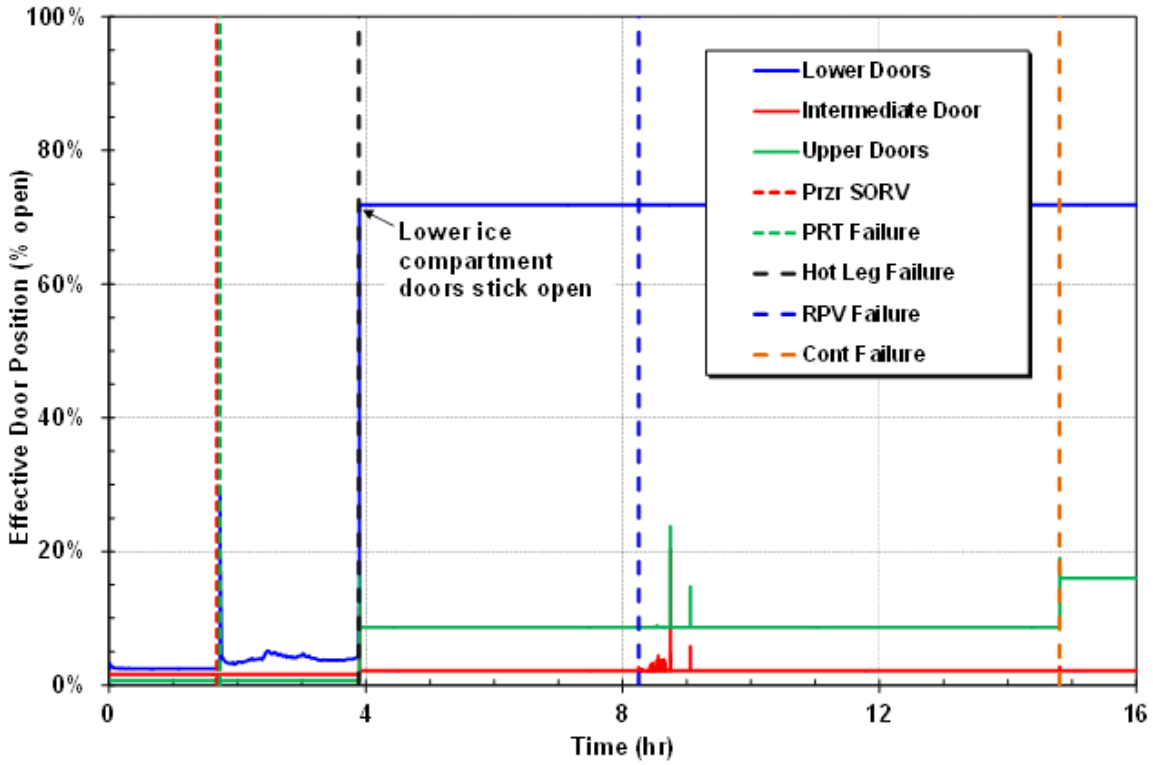

Figure 4-37 Lower door percentage open for Rlz 133

4.2.1.4 Hydrogen Production (with no random ignition)

The in-vessel hydrogen production in the Sequoyah model is primarily due to oxidation reactions of the Zircaloy fuel cladding, although there is also hydrogen produced by oxidation of stainless steel structures. The cladding oxidation will continue until unoxidized Zircaloy interior to the oxide shell melts, weakens the oxide layer, and relocates. The oxidation can further continue where the Zircaloy freezes after draining until the fuel itself reaches the melting temperature and collapses into a debris bed. The release of hydrogen is also an indicator for radionuclide releases as these occur during the fuel damage progression. The amount of hydrogen produced in-vessel along with the ex-vessel production of hydrogen and carbon monoxide during ex-vessel CCI are also the primary influences on whether deflagration and detonation conditions are reached in containment. A large burn can rupture the containment which starts the fission product release to environment.

The 100% oxidation of the Zircaloy cladding around the fuel in the Sequoyah core generates 1022 kg of hydrogen. In a rapidly progressing STSBO, the total hydrogen generation from Zircaloy and stainless steel oxidation is only 40% to 60% of this maximum value. In the STSBO realizations, approximately 85% of the total in-vessel hydrogen was from the Zircaloy oxidation while approximately 15% was from stainless steel oxidation. In addition to the in-vessel hydrogen generation, the ex-vessel CCI also generates hydrogen as well as other non-condensable gases (see Figure 4-38). The predominate gas generated from the ablation of the Sequoyah limestone concrete in the reactor cavity is carbon monoxide. The total carbon monoxide gas generation through 72 hours is ~30,000 kg. The CCI gas generation, along with evaporation of water from the hot CCI gases and radionuclide decay heat, will cause late

containment failure (i.e., if not already failed). While not as reactive as hydrogen, carbon monoxide is also combustible.

In addition to the large carbon monoxide gas production, other gases are also produced. For example, the ex-vessel hydrogen generation is about twice the magnitude of the in-vessel hydrogen production (e.g., 1173 kg in Figure 4-38). The carbon dioxide and steam gas generation are also comparable to the ex-vessel hydrogen generation over this time frame. Consequently, there is an ample source of hydrogen from in-vessel and ex-vessel processes.

As discussed in Section 4.2.1.1, the most important factors for hydrogen combustion are (a) an adequate oxygen concentration (i.e., >5%), (b) limited steam (i.e., <55%), and (c) an ignition source (i.e., hot jet from the hot leg or ex-vessel debris). Once the ex-vessel gas generation is established, the partial pressure of the oxygen drops below the necessary value for combustion (i.e., ~18 hr). Between the timing of the hydrogen addition to the containment (i.e., the PRT rupture disk opening or hot leg failure) and oxygen-inerting, most realizations had significant time periods where combustion is not possible (i.e., no ignition source, inadequate hydrogen, or steam-inerted). See Section 4.3 for detailed description of the inert conditions following hot leg failure.

In summary, the gas generation has three impacts on the accident progression. First, in-vessel and ex-vessel oxidation of Zircaloy and steel creates combustible gases that may lead to a burn that fails the containment. Second, the ex-vessel gas generation will eventually cause an over-pressurization failure if a combustion event does not fail the containment. The large ex-vessel gas production also helps vent airborne radionuclides following containment failure. Finally, the large ex-vessel gas production and steam generation from evaporating water will render the containment oxygen deficient as the oxygen partial pressure becomes small (i.e., <5%) compared to the total containment pressure. The uncertainty analysis only investigated the dependency of the uncertainty parameters on the total in-vessel hydrogen production. This is appropriate because nearly all the early containment failures occurred at hot leg failure, which was a direct result of only the in-vessel hydrogen production. The subsequent ex-vessel hydrogen gas sources were extremely large across all realizations. Since a focus of the Sequoyah UA is to investigate factors that lead to an early containment failure, the study did not investigate other uncertain parameters in the ex-vessel non-condensable gas production.

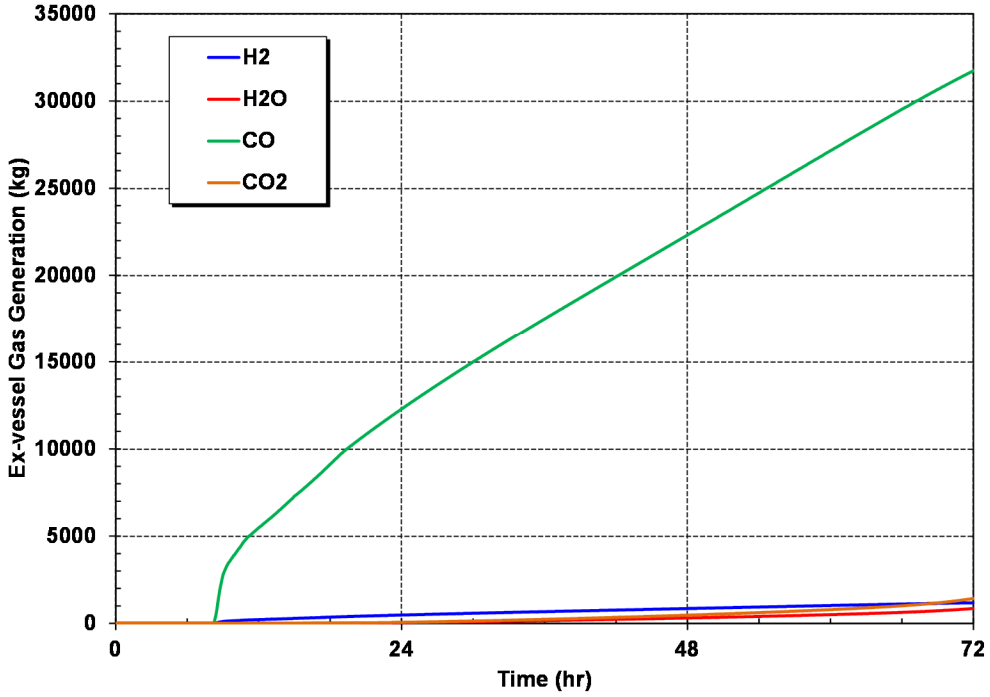

Figure 4-38 Typical ex-vessel gas production (Rlz 133)

4.2.1.4.1 Hydrogen Production History

The total amount of hydrogen produced in the vessel through 72 hours is a figure of merit for the analysis. Figure 4-39 shows the time-dependent, in-vessel hydrogen production for the successful realizations, as well as the calculated mean, median, and 5th and 95th percentiles. As shown by the 5th and 95th percentiles, which exclude rare outliers, the total in-vessel hydrogen production is between about 400 and 600 kg. A few high and low outliers are analyzed in the single realizations section (i.e., see Section 4.3). The timing of the onset of hydrogen production is essentially the same for the mean, median, 95th, and 5th percentile curves. The hydrogen production begins around 2.5 hours and almost every realization has stopped hydrogen production by about 7 hours. Figure 4-40 illustrates the cumulative probabilities for the quantity of hydrogen produced for selected time intervals through 72 hours. Figure 4-41 shows hydrogen CDFs by the hour for the first 20 hours of simulation and shows a more pronounced difference over time (converging to the CDFs in Figure 4-40).

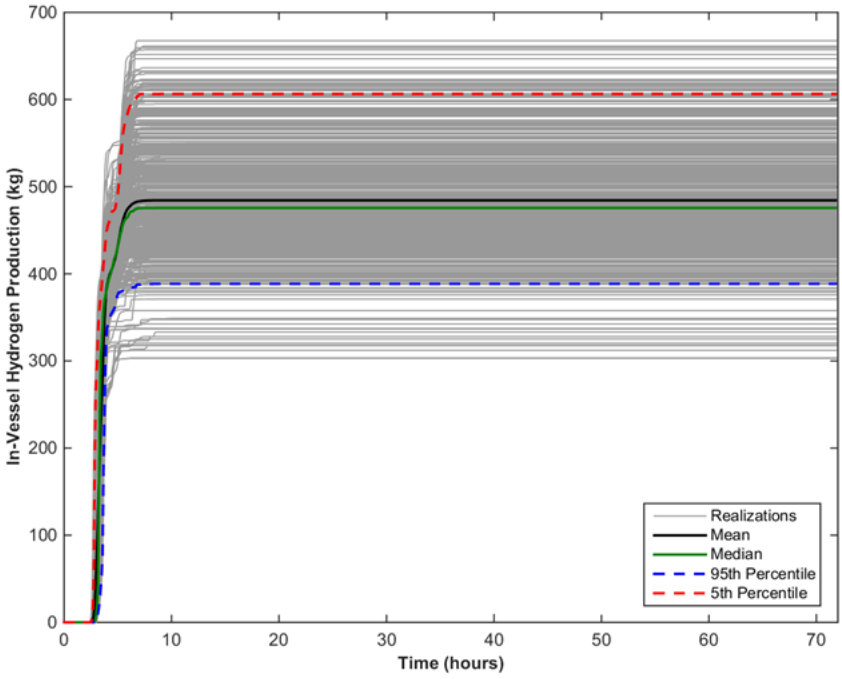

Figure 4-39 Total hydrogen production over 72 hours with mean, median, 5th and 95th percentiles

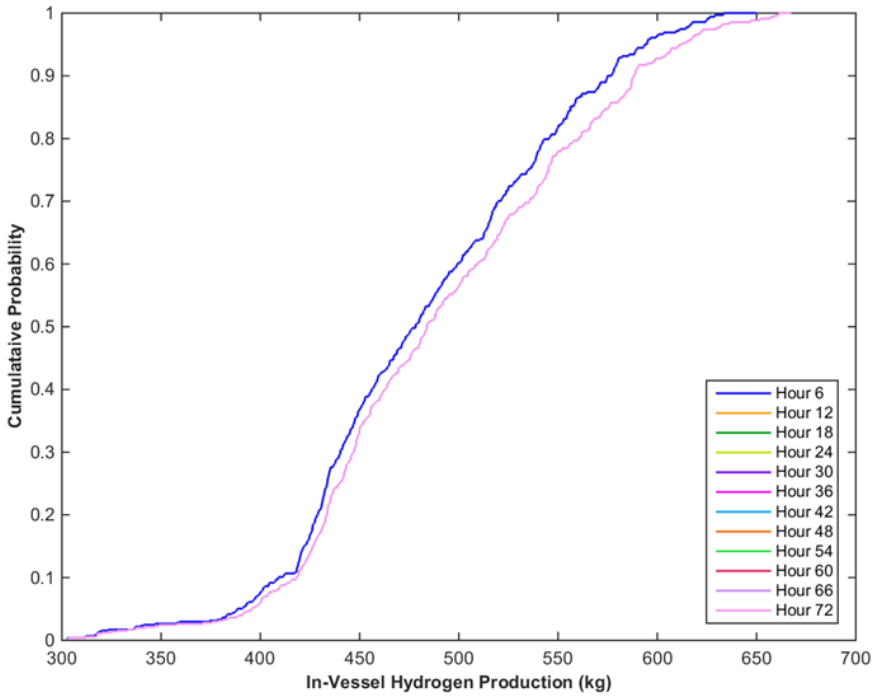

Figure 4-40 Cumulative probabilities for the quantity of hydrogen produced for selected time intervals to 72 hours

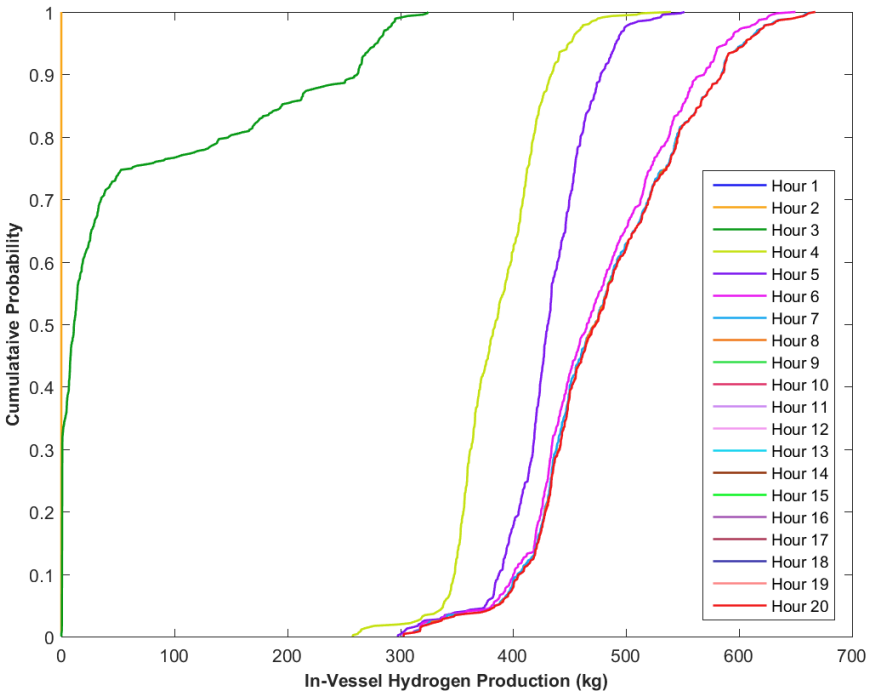

Figure 4-41 Cumulative probabilities for the quantity of hydrogen produced for selected time intervals to 20 hours

4.2.1.4.2 Regression Tables and Scatterplots

The regression results are presented in Table 4-6. The SV open fraction (SV_Frac) is the most important parameter by all regression techniques, except Recursive Partitioning, which identified it as second most important behind eutectic melt temperature (EU_melt_T). The eutectic melt temperature was the second most important parameter with a main contribution slightly lower than SV_Frac. SV stochastic FTC (priSVcycles) was identified as the third most important parameter by all regression techniques. No other parameters had a significant contribution to the results.

Table 4-6 Regression analysis of hydrogen production at 72 hours (with no random ignition).

	Rank Regression		Quadratic		Recursive Partitioning		MARS		Main Contribution	Conjoint Contribution
Final R^2	0.41		0.51		0.86		0.60			
Input	R^2 contr.	SRRC	S_i	T_i	S_i	T_i	S_i	T_i		
SV_frac	0.27	-0.45	0.46	0.68	0.15	0.50	0.33	0.54	0.208	0.181
EU_melt_T	0.13	0.36	0.30	0.30	0.28	0.47	0.31	0.30	0.177	0.055
priSVcycles	0.01	0.12	0.01	0.24	0.14	0.38	0.15	0.37	0.056	0.151
Seal_Fail_Dp	---	---	0.01	0.01	0.01	0.07	0.00	0.00	0.006	0.018
Seal_Open_A	---	---	---	---	0.01	0.03	0.00	0.00	0.002	0.008
burn_dir	---	---	---	---	0.00	0.01	0.00	0.01	0.001	0.004
rupture	---	---	---	---	0.00	0.02	0.00	0.00	0.001	0.006
shape_fact	---	---	---	---	0.00	0.04	0.00	0.00	0.001	0.012
ajar	---	---	---	---	0.00	0.01	0.00	0.01	0.000	0.003

* highlighted if main contribution larger than 0.02 or conjoint contribution larger than 0.1

SV_Frac

Figure 4-42 is the scatterplot of the in-vessel hydrogen production versus SV_Frac. The high density of points on either end of the scatter plot suggests a negative relationship between combined fraction of open area and hydrogen production, as reflected in the regression coefficient for the rank regression results.

As discussed in Section 4.2.1.1, a SV_Frac value of zero corresponds to no pressurizer SV failures. Consequently, the RCS remained at high pressure in all the realizations where the pressurizer safety valves operated normally until hot leg failure. In fact, almost all the realizations with SV_Frac <0.284 resulted in late containment failure. These cases remained at a higher RCS pressure prior to hot leg failure. Initially, oxidation is more efficient at high pressure because more steam is available (i.e., high density at high pressure). However, the high RCS pressure also leads to an early hot leg failure and complete accumulator discharge which interrupts the in-vessel hydrogen production as shown in Figure 4-19.[23] Since hot leg failure happens earlier prior to substantial core degradation, the intact core reheats and fills with steam at low pressure. The second hydrogen generation phase following hot leg failure increased the total hydrogen generation from the late containment failure values shown in Figure 4-19 (i.e., 225 to 450 kg) to the total hydrogen generation values in Figure 4-18 (i.e., 450 kg to 625 kg).

In contrast, the hydrogen production largely ceased following the RPV breach in realizations with an early containment failure (i.e., generally attributed to realizations with SV_Frac>0.4[24]). If a large SV_Frac occurred early, then the initial RPV breach was delayed due to low RCS pressure, which resulted in more inventory loss, more core degradation, and possibly some accumulator discharge prior to the RPV breach. Following RPV breach, the core fully degraded with little additional hydrogen generation.

In summary, the in-vessel hydrogen generation rate is generally higher at SV_Frac<0.4 and lower at SV>0.4. Almost all the realizations with a failure area less than 0.4 had hydrogen generation rates above the median. The larger valves of SV_Frac (i.e., >0.4) generally had hydrogen production rates below the median value. As SV_Frac increases from 0.4 to 1, there is a downward trend in hydrogen production. However, there is considerable scatter in the results in Figure 4-42. The variation in these realizations is due to timing of the pressurizer SV failure and eutectic melting temperature, which is discussed in the next section. In particular, the grouping of realizations with low hydrogen production at SV_Frac=0 had very low eutectic melting temperatures that limited in-vessel hydrogen production.

Finally the realizations with a combined SV_Frac value greater than 1 had four realizations below the median and two above. There did not seem to be a strong pattern attributable to just the SV_Frac for these realizations. All these realizations had multiple valve failures that would depressurize the RCS prior to start of core damage. Consequently, the RCS was at low pressure, which is consistent with the low hydrogen production in 4 of the realizations.

---

[23] Almost all the cases with SV_Frac<0.4 resulted in a late containment (see Figure 4-45). Consequently, the realizations in Figure 4-19 with late containment failure and lower hydrogen generation prior to the RPV breach are being used as a surrogate for SV_Frac<0.4, which results in lower hydrogen generation prior to the RPV breach.

[24] All the cases with an early containment failure had a SV_Frac>0.4 (see Figure 4-45). Consequently, the realizations in Figure 4-18 with early containment failure and a lower total in-vessel hydrogen generation are being used as a surrogate SV_Frac>0.4.

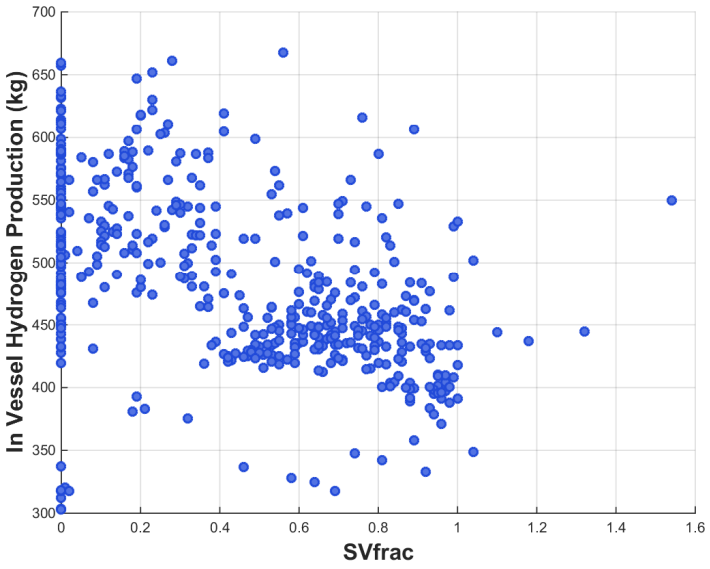

Figure 4-42 Scatterplot of in-vessel hydrogen production versus SV 72 hour post-calculated open fraction

Effective Eutectic Melt Temperature

Figure 4-43 shows the scatterplot of in-vessel hydrogen production versus the eutectic melt temperature. The positive sloping behavior in the scatter plot confirms the positive rank regression coefficient for EU_melt_T in the regression table. The variation in the EU_melt_T uncertainty parameter was expected to impact the in-vessel hydrogen. The fuel collapse criteria can occur by various mechanisms including the failure of the supporting structure, thinning or time-dependent thermal weakening of the oxide shell, and reaching the fuel melting temperature. A higher eutectic melting temperature failure generally results in higher peak fuel temperatures prior to collapse. The hydrogen generation rate is much higher from intact fuel rods due to the high surface areas and open hydraulic configuration. Consequently, if the fuel rods remain in an intact configuration longer due to a higher melting temperature, then there is potential for more hydrogen production. A higher eutectic melting temperature also increases the porosity of the debris, which enhances late phase oxidation. The scatter is attributed to the variation in the timing of the pressurizer SV failure and the SV failure area fraction.

A few of the lowest sampled eutectic melting temperatures fell below the Zircaloy breakout temperature (2350 K), which impacted the in-vessel hydrogen production. In these realizations, the fuel collapsed before the molten Zircaloy behind the oxide shell is released. Consequently, the fuel slumps without oxidizing molten Zircaloy portion of the cladding. The resultant debris geometry blocks steam flow for oxidation. These cases had the lowest hydrogen generation rates and explain the low outlying realizations previously discussed with SV_Frac.

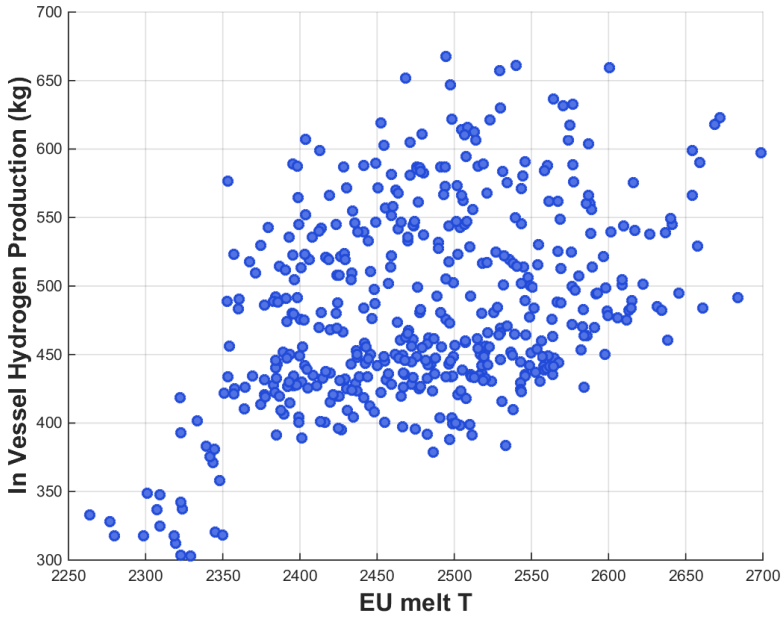

Figure 4-43 Scatterplot of in-vessel hydrogen production versus eutectic melt temperature input values

priSVcycles

Figure 4-44 shows the scatterplot of in-vessel hydrogen production versus the priSVcycles. The high density of points with hydrogen production above 400 kg with more than 70 combined cycles to failure explains the small but positive regression coefficient for priSVcycles in the rank regression results.

The maximum number of SV cycles is 74 cycles before there was a RPV breach. The dense clustering of realizations between 71 to 74 cycles indicates normally operating SVs until RPV breach (i.e., hot leg failure). The priSVcycles parameter complements the SV_Frac parameter, which showed normally operating valves when SV_Frac=0. The values of these parameters indicate the RCS is at high pressure during the initial core degradation, which enhances hydrogen production. Consequently, the in-vessel hydrogen generation rate is generally higher with more priSVcycles. Similar to the comments on the SV_Frac parameter, the variation in these realizations is due to eutectic melting temperature. In particular, the grouping of realizations with low hydrogen production at priSVcycles>71 had very low eutectic melting temperatures that limited in-vessel hydrogen production.

As the priSVcycles decreases from 71 to 1, the in-vessel hydrogen production decreases from primarily above the median to primarily below the median. Below 50 cycles, there is clustering of realizations below the median. The variations are caused by the variations in the pressurizer SV failure area (i.e., SV_Frac) and the eutectic melting temperature. Although the priSVcycles had a lower correlation than the SV_Frac, the two parameters are highly interrelated.

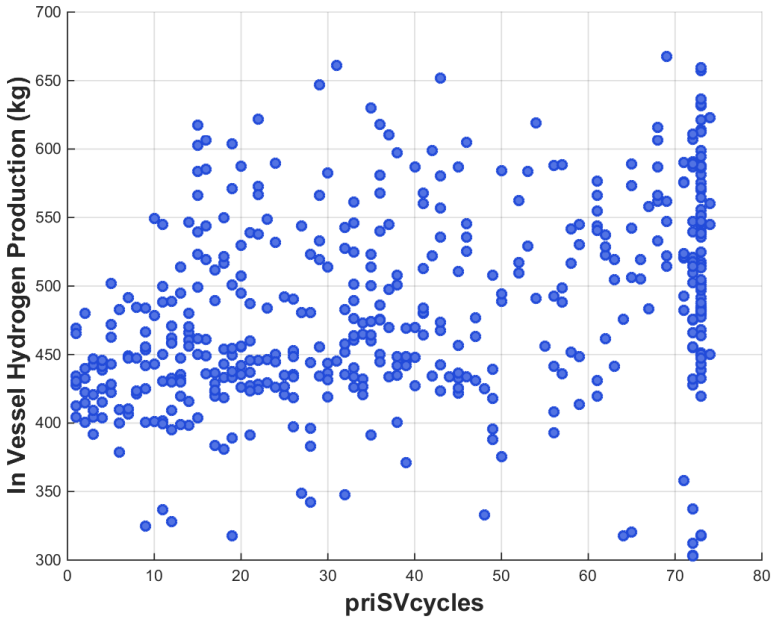

Figure 4-44 Scatterplot of in-vessel hydrogen production versus SV cycles to failure values

In summary, the magnitude of the in-vessel hydrogen production is influenced by conditions that keep the RCS pressure high during fuel degradation and increase the fuel temperature before slumping. These attributes coincide with small values of pressurizer SV failure area, high values of eutectic melting temperature, and a large number of the SV cycles. The density of the steam is higher at high RCS pressure, which enhances hydrogen production. Furthermore, the rate of hydrogen production is greatest at high fuel temperatures, which is more likely with a high eutectic melting temperature. The scatter plots show trends of each of these factors. However, the impact of the in-vessel hydrogen production on timing of containment failure is not correlated (i.e., see discussion in Section 4.2.1.1 and Figure 4-18). In particular, there is ample hydrogen to fail the containment across the full range of hydrogen production results. Consequently, the total in-vessel hydrogen production had a surprisingly small impact on the containment failure timing and the source term.

4.2.1.5 Containment Rupture Timing (with no random ignition)

Rupture timing is another figure of merit investigated. Rupture is defined as the point at which the specified containment pressure is exceeded and a 3 ft^2 hole opens. To determine parameters important to rupture, a regression analysis was performed using the rupture time as a metric.

4.2.1.5.1 Regression Tables and Scatterplots

Regression analyses presented in Table 4-7 show the SV open area fraction (SV_Frac) is the top parameter for three of the four regression techniques. The SV_Frac parameter was identified as the largest main contributor to timing uncertainty for three of the four regression techniques. With the Rank Regression technique, SV_Frac was identified second to rupture. Rupture was the second most important parameter with three of the four techniques, with Rank

Regression showing rupture as most important. The priSVcycles parameter was the third top parameter, with a considerably lower main contribution than the top two parameters. No other parameters had a significant contribution to rupture timing uncertainty, nor are there any other parameters that were expected to have a significant contribution.

Table 4-7 Regression analysis of rupture time for all realizations (with no random ignition).

	Rank Regression		Quadratic		Recursive Partitioning		MARS		Main Contribution	Conjoint Contribution
Final R^2	0.40		0.44		0.79		0.45			
Input	R^2 contr.	SRRC	S_i	T_i	S_i	T_i	S_i	T_i		
SV_frac	0.09	-0.35	0.40	0.63	0.30	0.67	0.40	0.63	0.170	0.164
rupture	0.26	0.51	0.20	0.23	0.09	0.43	0.23	0.22	0.131	0.093
priSVcycles	0.00	-0.08	0.07	0.25	0.04	0.23	0.10	0.28	0.027	0.104
ajar	0.04	0.20	0.01	0.01	0.01	0.09	0.02	0.07	0.013	0.028
EU_melt_T	0.01	-0.12	0.02	0.04	0.02	0.21	0.02	0.02	0.011	0.054
Seal_Fail_Dp	0.01	-0.08	0.01	0.08	0.01	0.14	0.00	0.01	0.005	0.045
shape_fact	---	---	---	---	0.01	0.06	0.00	0.00	0.002	0.013
burn_dir	---	---	0.00	0.04	---	---	0.00	0.00	0.000	0.005
Seal_Open_A	---	---	---	---	0.00	0.02	0.00	0.01	0.000	0.006

**** highlighted if main contribution larger than 0.02 or conjoint contribution larger than 0.1***

SV_Frac

Figure 4-45 is the scatterplot of rupture time (in seconds) versus SV_Frac. The two clusters of high density points account for the strong negative sloping relationship between the fraction of open area and the combined fraction of open area. The early and late timing of the containment rupture is described in Section 4.2.1.1. However, this presentation clearly shows an early containment failure (i.e., the lower group of points) only occurs when the SV_Frac>0.32. Furthermore, a containment rupture following the hot leg failure (i.e., the lowest line of points) only occurs when the SV_Frac>0.44. In the early containment failures with larger SV failures areas, the RCS depressurized and vented hydrogen to the containment prior to the hot leg rupture. When the hot leg ruptured and created an ignition source, the hydrogen from the RCS was already distributed throughout the containment. The resulting burn propagated throughout the containment and into the dome, which caused a containment failure.

In contrast to the early containment timings, the late containment failures generally occurred when more hydrogen was retained in the RCS prior to the hot leg failure. When the pressurizer SVs operated normally (i.e., SV_Frac=0), the burn at RPV breach was moderate and the containment ultimately failed by over-pressurization from ex-vessel gas generation (i.e., steam and CCI gases). Similarly, the containment always failed late if SV_Frac<0.3. A smaller SV failure area is less effective at depressurizing the RCS and transferring hydrogen throughout the containment. Between a SV_Frac of 0.3 and 1, there were both early and late containment failures. As discussed in Section 4.2.1.1 and with the priSVcycles parameter, the timing of the valve failure contributed to both results. An early valve failure would allow more hydrogen to be vented into the containment whereas a late valve failure vented less hydrogen.

With respect to the strong dependence of containment rupture timing on the combined fractionally open position of the 3 pressurizer SVs (SV_Frac), it is important to note that an SV is modeled as fractionally open position only when it has failed to close in the model. Whether or not an SV fails to close is dictated by the number of successful cycles it must complete before failing to close which is a sampled number specified in each realization. If the sampled number

for a valve is large, the valve will not fail. The time at which an SV fractionally open position occurs is also dictated by the sampled number of successful cycles it must complete before failing to close. Therefore, the importance of SV_Frac to containment rupture timing is not separable from the combined number of cycles experienced by the pressurizer SVs (priSVcycles), i.e., with respect to containment rupture timing, the influence of SV_Frac cannot be considered independently of the influence of priSVcycles.

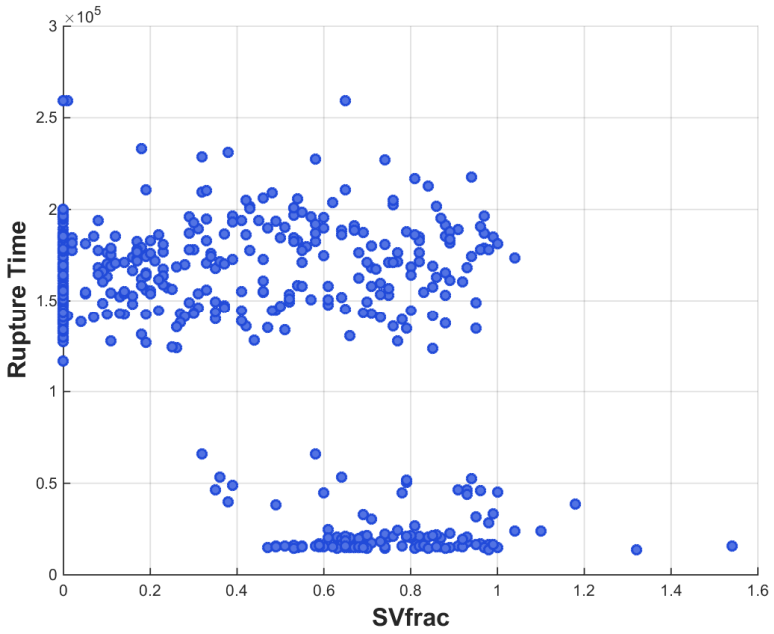

Figure 4-45 Scatterplot of rupture time versus the combined open fraction of the pressurizer SV system

Rupture

Figure 4-46 is the scatterplot of rupture time (in seconds) versus rupture (i.e., the containment failure pressure). Although neither high rupture time nor low rupture time can be attributed to specific values of the rupture parameter, there is a distinct positive trend among the high rupture time cluster of points. There are two interesting results from the scatter plot. First, the early containment failure timing shows no significant dependency on the rupture pressure. The early containment results spanned the entire range of rupture pressures. In addition, there did not seem to be any dependency on the rupture pressure for the containment failures that occurred a few hours after the initial RPV breach. If the hydrogen was adequately distributed, then there was enough pressurization from the burn to fail the containment at any rupture pressure.

The second key point evident on Figure 4-46 is the dependency of the rupture pressure on the late containment failure. Unlike the fast pressurizations from the combustion events that lead to an early containment failure, the late containment failure occurred due to a slow pressurization. The scatter plot shows an upward trend as the containment rupture occurs later with a higher rupture pressure. The parameters that led to the separation of the two groups of late failures (i.e., the lower trend line versus the main trend line) were not identified from this parameter or the other two high ranking parameters.

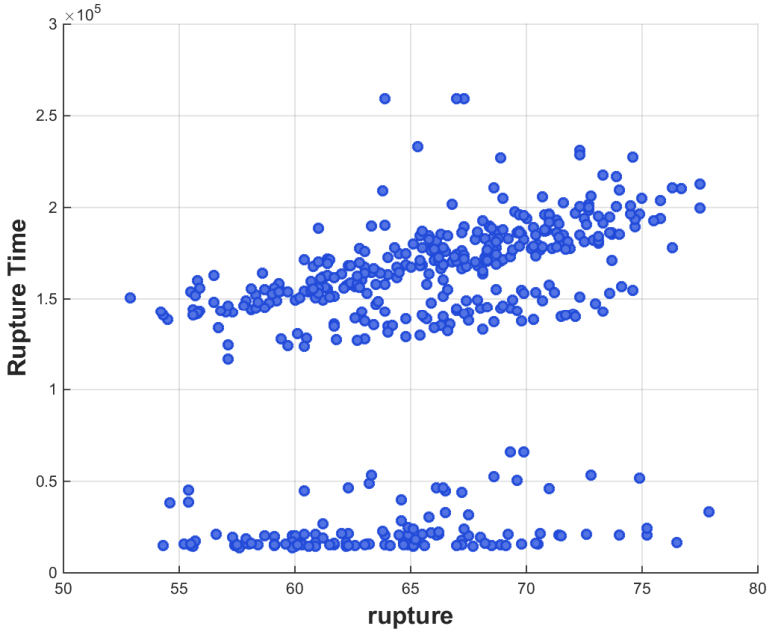

Figure 4-46 Scatterplot of rupture time versus rupture

priSVcycles

Figure 4-47 is the scatterplot of rupture time (in seconds) versus priSVcycles. The vertical cluster of points around 70 combined cycles to failure and the horizontal cluster of points with rupture time below 0.5-E5 seconds accounts for the negative regression coefficient for priSVcycles in the rank regression results. The correlation of this parameter is better described in conjunction with containment rupture time versus RPV breach time as a function of the number of SV cycles, which was done in Section 4.2.1.1 (i.e., also see Table 4-4).

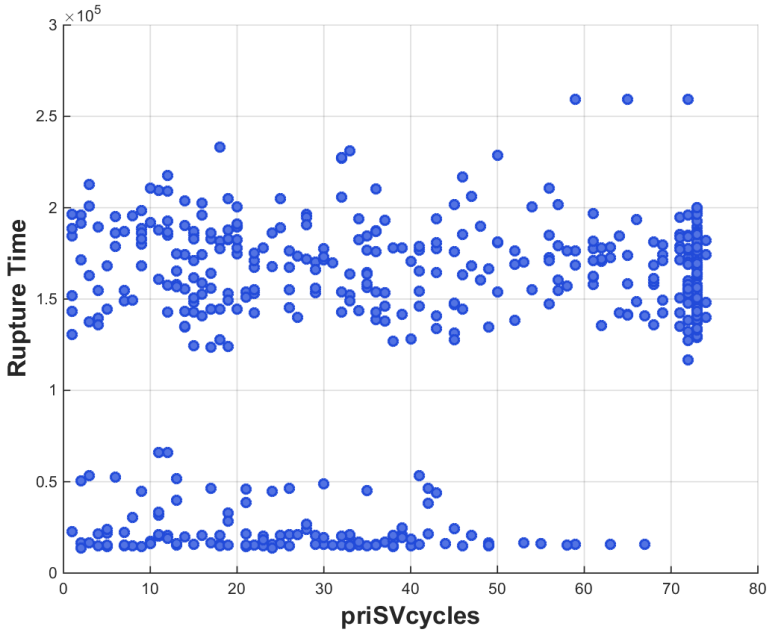

Figure 4-47 Scatterplot of rupture time versus priSVcycles

In summary, the rupture timing resulted in two groups (i.e., early and late containment failure). A large number of SV cycles primarily resulted in late containment failures. Similarly, a late containment failure could be correlated to a small or zero SV failure area. The SVs in these two groups functioned properly for second and third longest times. The other realizations with fewer SV cycles (1 to 45) or larger SV failure areas (>0.3) resulted in both early and late containment failures. There were more complicated factors that contributed to whether there was an early or late containment failure. However, an early containment failure only occurred if the SV failure area was >0.3.

4.2.2 Uncertainty Evaluations with Random Ignition

A second batch of MELCOR runs were completed for the 'with random ignition' feature turned on. The random ignition realizations introduce a "spark" of one second duration somewhere in containment every half hour. This modeling assumption recognizes the potential for random ignition sources. Sandia used a high performance computing cluster to execute a Monte Carlo simulation with 600 MELCOR runs, of which 432 were successful for the STSBO scenario with random ignition. The reasons for the failed runs are listed in Table 4-8. Some code failures are expected as the uncertainty parameter permutations create computationally difficult conditions that have not been previously addressed. Unfortunately, two conditions occurred that were not expected. First, the Sandia High Performance Cluster had an unexpected failure that affected 56 realizations. Second, the uncertainty algorithm that generated the pressurizer safety valve cycle failure unexpectedly included 32 realizations that were initialized with an immediate safety valve failure. The effected realizations were identified and removed from the sample set. The error was not identified until all the calculations were completed.

Table 4-8 Realizations that were unsuccessful with random ignition assumed to occur.

# Failed	Reason
	Code run time
1	Ex-vessel cavity surface heat loss error
30	Volume error in the COR Package
6	Bad debris temperature in the core lower head subroutine calculations
1	An error in the EDF file that specifies the uncertain parameters.
18	Executive detected abort signal (i.e., typically a failure to converge in the control volume hydrodynamics package)
23	Convergence error in an ex-vessel cavity routine (CCMLTR)
1	Convergence error in an ex-vessel cavity routine (CCSVLR)
	Other (hardware/input)
56	Sandia High Performance Cluster Failure
32	Failed pressurizer SV at time = 0 sec

4.2.2.1 General MELCOR results for the with random ignition scenario

Similar to the non-random ignition results presented in Section 4.2.1.1, the MELCOR results for the cases with random ignition were configured to show the containment rupture timing as a function of the timing to the first RPV breach (i.e., see Figure 4-48 through Figure 4-50). If the realization had containment failure immediately following a RPV breach, then the result would appear on "coincident" line. In the non-random realizations, the RPV breach line identifies the earliest possible timing for an active ignition source (i.e., either hot leg failure or RPV lower head failure). In contrast to the non-random realizations, the random cases include ignition sources prior to the initial RPV breach.[25] Consequently, the initial RPV breach does not represent a threshold event for the start of ex-vessel combustions. Nevertheless, the timing of the containment rupture and the relative timing from the initial RPV breach identify important characteristics for the source term progression. It should be noted that no containment failures occurred prior to the initial RPV breach.

The following bullets summarize the general observations and insights from the realizations with random ignition. Sections 4.2.2.2 through 4.2.2.5 will present the statistical evaluation for the specific figures of merit.

[25] The initial RPV breach was defined as either hot leg failure or vessel failure, whichever came first. In the realizations with random ignition, only 21 cases did not have a hot leg failure prior to the vessel breach. A hot leg failure usually occurs prior to vessel breach unless there were untypical conditions that include an early collapse of the core due to a low eutectic melting temperature of the fuel and an early failure of the pressurizer SV that greatly reduced the mechanical stress across the hot leg.

- The earliest containment failure occurs at about 3.9 hours, which is approximately the same earliest containment failure timing as the non-random ignition scenario. Both the random and the non-random ignition containment failures occurred coincidental to the initial RPV breach. An early SV failure with a large failure flow area that depressurizes the RCS were previously identified as attributes that lead to an early containment failure (see Section 4.2.1.1). The earliest containment failure in the random ignition realizations occurred with a SV stuck open in the grouping of 16 to 30 SV cycles (see Figure 4-49) with a fractional failure area of 0.7. Both of these parameters (i.e., number of cycles to failure and the failure flow area) are somewhat different than the earliest non-random ignition containment failure (i.e., the SV failed on the 2nd cycle with a 0.98 open area in Rlz 338). However, Figure 4-16 and Figure 4-45 show a relatively broad range of cycles and flow areas that led to early containment failure in the non-random realizations, respectively. Consequently, this realization has consistent attributes for an early containment failure as the early containment failures in the non-random realizations.

- Perhaps the most significant finding was that only 3 random ignition realizations resulted in an early containment failure at the time of the initial RPV breach (i.e., see only 3 realizations on the initial RPV breach line in Figure 4-48). This was significantly different from the non-random ignition realizations (see Figure 4-15). The key attributes that contributed to early containment failure at the time of the initial RPV breach in the non-random ignition were an early pressurizer SV failure that substantially depressurized the RCS prior to the initial RPV breach. These attributes allowed hydrogen to be distributed throughout the containment prior to the first ignition source (i.e., typically hot leg failure). However, almost all random ignition realizations (i.e., all but 3) did not allow a significant build-up of hydrogen prior to the initial RPV breach. Consequently, the random ignitions prior to the first active ignition source diminished the amount of hydrogen available to burn at the initial RPV failure.

- Unlike the non-random ignition realizations with an early containment failure, most realizations that failed the containment due to a hydrogen burn occurred hours after the initial RPV breach (see Figure 4-48). There is a less distinct separation between the set of realizations with direct failure due to combustion versus an over-pressurization. Similar to non-random conclusions, none of early containment failure cases had more than 60 SV cycles. The median SV cycle count and failure area for this grouping are 21 and 0.73, respectively. These attributes are consistent with an early containment failure in the non-random set of realizations. The random ignition burns mitigated the build-up of a large hydrogen burn at the initial RPV breach. However, the subsequent combustion events resulted in some early containment failures but far fewer than the random ignition realizations (i.e., 15% versus 25%, see Figure 4-15 versus Figure 4-48).

- There was one realization that resulted in a late containment failure by a hydrogen burn. Rlz 12 had a burn in the dome at 49 hr near the minimum oxygen concentration for combustion (i.e., just above 5%).[26] This realization was an in-vessel production outlier where the eutectic melting temperature was less than the molten Zircaloy temperature (see discussion in Section 4.2.2.4.2, Figure 4-68). It had very low in-vessel hydrogen

[26] A hand calculation shows the maximum possible oxygen mole fraction at the time of the late combustion is only 5.3% if no oxygen was consumed due to combustion. Most realizations were inert (i.e., oxygen mole fraction below 5%) at >30 hours.

generation, which resulted in very little oxygen consumption from early combustions. A random ignition in the dome at 49 hours caused a late containment failure by combustion. As evidenced by the graph, this was very unlikely.

- Similar to the non-random ignition results, there is second distinct set of realizations showing later containment failure from 32 to 55 hours. The late containment failures occur following the containment over-pressurization due to ex-vessel water evaporation and gas generation from ex-vessel core-concrete interaction (CCI) (i.e., see the realizations in Figure 4-48 in the upper right-hand side).

- The gap in containment failures between 22 and 33 hours is the transition from containment ruptures due to combustion to containment over-pressurization due to gas generation. This gap is smaller than non-random ignition realizations and contains two outliers[27] whereas there were no outliers in the non-random realizations. The inclusion of random ignition burns diminished the importance of the ignition source at the initial RPV breach while providing more variability. Similar to the non-random ignition realizations, the steam evaporation and non-condensable gas production from the ex-vessel debris pressurized the containment. The resultant gas concentration from the early combustions and the gas production left the containment oxygen deficient after about 22 hours. This is slightly later than non-random ignition realizations (i.e., generally oxygen deficient after ~15 hr).[28]

- Four realizations progressed to 72 hours without containment failure versus only three in the non-random ignition results. Relative to the total number of completed realizations, the results showed that nearly all cases resulted in containment failure within the simulation duration (i.e., 72 hours). The attributes of these four realizations were not easily identifiable as late containment failure cases. In particular, the number of pressurizer SV cycles ranged from 12 to 38 and the SV failure area fractions ranged from 0.25 to 0.83. However, all four cases had high containment failure pressures (i.e., 66 to 73 psia). In these cases, the random burns occurred without failing the containment.

- As discussed previously, most of the early containment failures in the random ignition realizations occurred several hours after the initial RPV breach versus at the timing of the initial RPV breach in the non-random ignition realizations. However, both scenarios had a tight timeframe of the initial RPV breach timing (~3.5 to 4.5 hours) for the early containment failure realizations that did not occur on the coincident line.

- Figure 4-49 shows a similar correlation of the number pressurizer SV cycles to the containment rupture timing as the equivalent figure for the non-random ignition realizations (i.e., see discussion of Figure 4-16 in Section 4.2.1.1). If the pressurizer SVs operate without any failures (i.e., the black circles), then the containment only fails late. Similarly, all the realizations with 61 to 74 combined cycles (i.e., red triangles on Figure 4-49) resulted in a late containment failure. Most of the realizations with 46 to 60

---

[27] There are two outliers to this grouping with containment failure due to a burn at 30 hr and 49 hr.

[28] This is an observation from the containment failure results, which showed an end of the containment failures due to combustion at 22 hours except for the two outliers noted in Footnote 25. The early containment failure due to combustion in the non-random ignition realizations ended at 15 hours.

cycles (i.e., yellow triangles on Figure 4-49) resulted in late containment failure. The SVs in these two groups functioned properly for second and third longest times. The other realizations with fewer SV cycles (1 to 45) prior to a failure resulted in both early and late containment failures. There were more complicated factors that contributed to whether there was an early or late containment failure. However, the flow area of the failed SV or SVs was an important factor (e.g., a small SV failure area could stop further SV cycling but otherwise remain at relatively high RCS pressure, which is somewhat like a functioning SV realization).

- Similar to the non-random ignition realizations, Figure 4-50 shows little correlation of the in-vessel hydrogen production to either early or late containment failure. The results may suggest slightly more in-vessel hydrogen production contributes to a late containment failure. This is similar to the findings in the non-random ignition realizations.

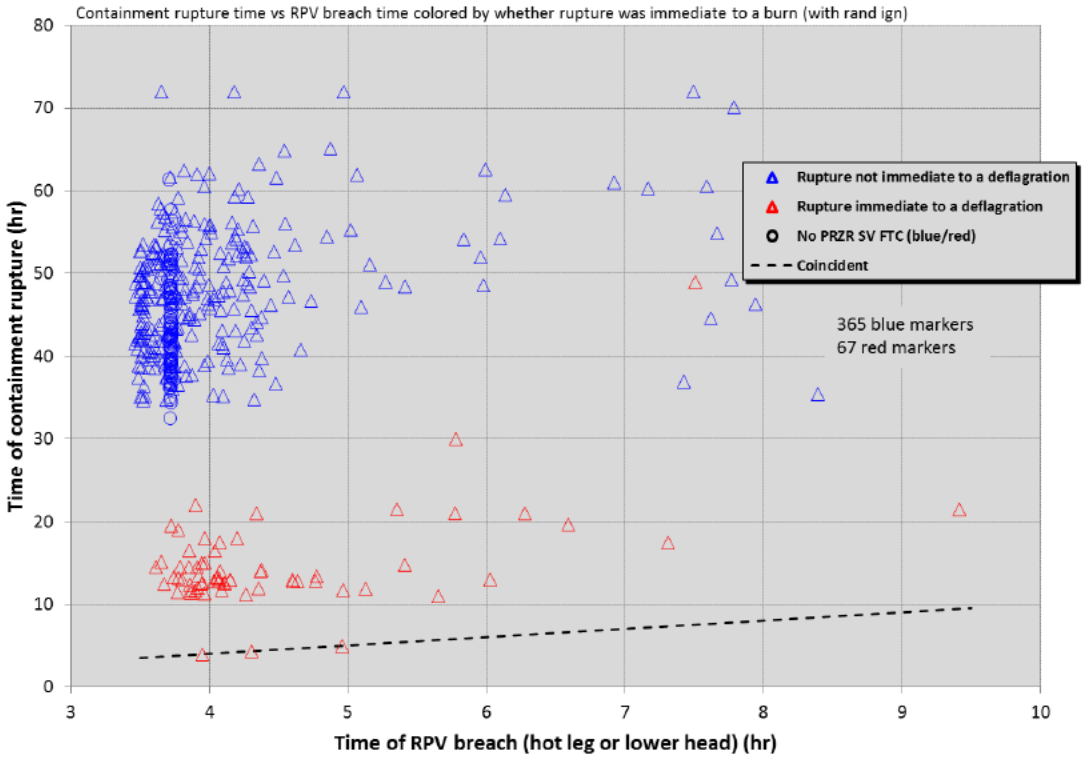

Figure 4-48 Containment rupture time versus RPV breach time colored by whether the rupture was immediate to a deflagration – with random ignition

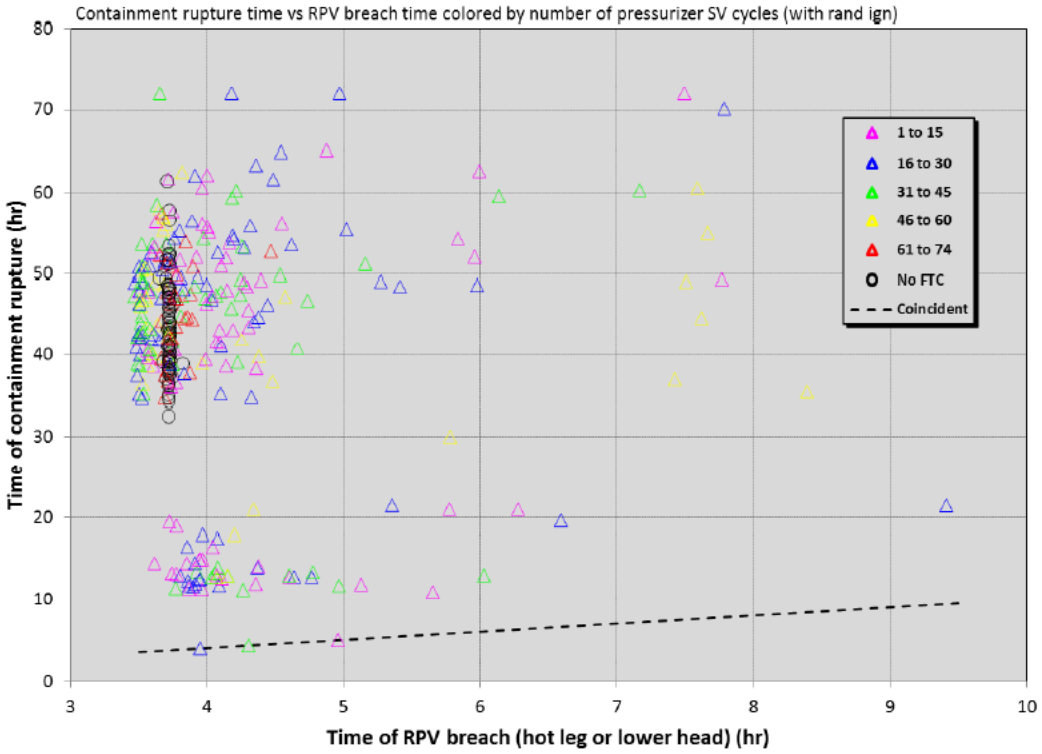

Figure 4-49 Containment rupture time versus RPV breach time colored by number of pressurizer SV cycles – with random ignition

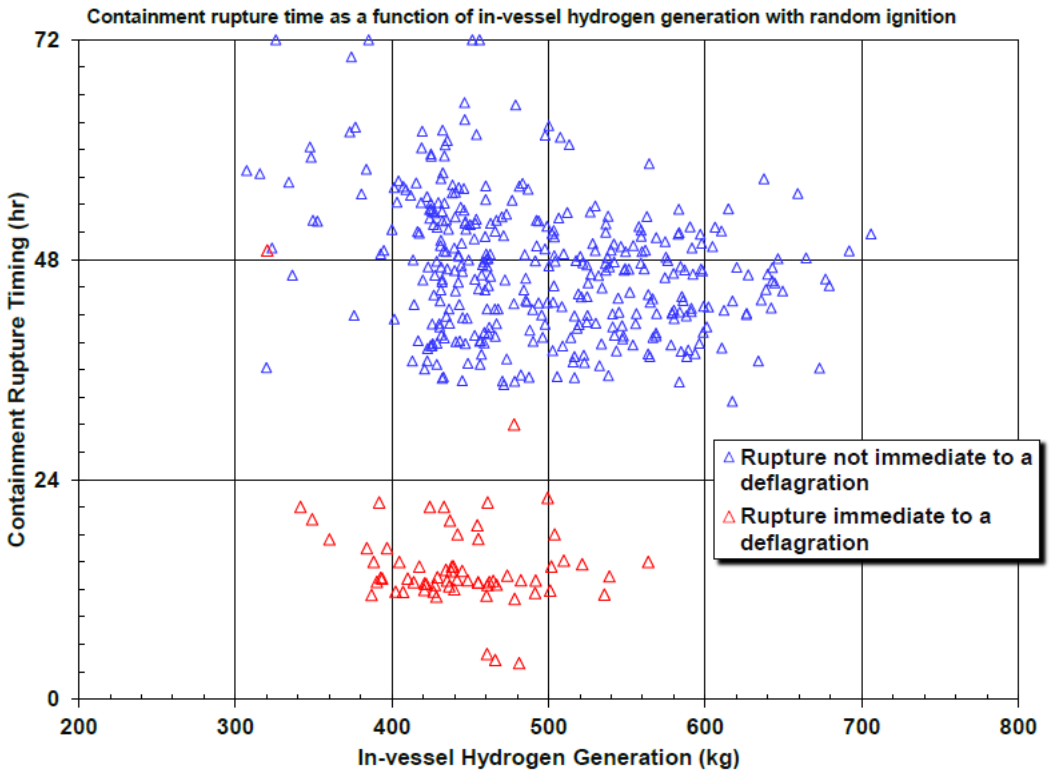

Figure 4-50 Time of containment rupture versus in-vessel hydrogen production – with random ignition

4.2.2.2 Iodine Release Fraction to Environment (with random ignition)

The magnitude and timing of the iodine release is an important radionuclide to characterize the potential severity of the early health effects. The timing of the iodine release can be very important if it occurs during the evacuation phase. Consequently, the following regression evaluations paid particular attention to factors that influenced large and early releases of iodine.

4.2.2.2.1 Iodine Release History

Figure 4-51 shows the time dependent release fractions for the successful realizations, together with the calculated mean, median, 95th and 5th percentiles of all realizations. The iodine release fraction is again separated into two distinct release patterns, very similar as those for the non-random ignition realizations. The first grouping contains the early containment failure realizations while the larger second grouping has the late containment failures. As discussed in Section 4.2.2.1, there were fewer early containment failures in the random ignition realizations and most early containment failure releases started later than the comparable non-random ignition realizations.

The split in the start of the iodine releases between 15 and 30 hours coincides with the containment rupture timing (e.g., Figure 4-48). The early iodine releases result from the early containment rupture following a hydrogen burn whereas the second grouping occurs from a late over-pressurization failure due to ex-vessel steam and CCI gas generation. As discussed

previously in Section 4.2.2.1, there is a time gap following the containment becoming oxygen deficient (i.e., the end of combustion due to a lack of oxygen) to the time required for ex-vessel gas generation to over-pressurize the containment. The variation in the late over-pressure timings is influenced by the containment rupture pressure and the amount of hydrogen gas that was burned. The variation in the containment failure timing directly affected the start of the iodine release. However, the variation in the magnitude of the iodine release is a more complex function of other parameters that will be discussed in the following subsections.

The bifurcation in containment failure timings led to a wide spread between the calculated median and the 95th percentile curves. The median realization is characteristic of a late containment failure while the mean curve has contributions from both the early and late containment failure results. Most realizations resulted in a late containment rupture. The median and 5th percentile curves show larger increasing trends from the late containment failure. The increasing iodine release is often characteristic of a chimney effect from the long term flow of hot gases from the ex-vessel CCI through the failed RPV lower head and out failed hot leg location. The hot gases cause a revaporization of the previously deposited cesium iodine in the RPV. It is also characteristic of a revaporization release from the PRT, which is discussed in Section 4.2.1.2.2.

In contrast to the non-random realization iodine horsetail results in Figure 4-20, there are fewer early containment failure realizations and a less coherent early iodine release to 0.10 by 20 hours. As discussed in Section 4.2.2.1, most of the random ignition early containment failures occurred hours after the initial RPV breach. This is in contrast to the non-random ignition results where most early containment failure realizations occurred at the initial RPV beach. The initial iodine releases that occurred at the initial RPV breach in Figure 4-20 were less than 0.02 but rapidly increased after 10 hours as more iodine was released from the fuel and flowed out the containment rupture. The early containment failure occurred after 11 hours in most of the random ignition realizations. Consequently, the early containment release trends more closely followed the non-random ignition rapid iodine release trends after 10 hours (i.e., a sharp increase in iodine release from the initial release of 0.02).

In general, the late containment releases were similar between the random (Figure 4-48) and the non-random (Figure 4-20) realization. The median curve on these graphs is characteristic of the late containment failure response and are in close agreement. The random and the non-random ignition medians were ~0.06 and ~0.07 at 72 hours, respectively. The 5th and 95th percentile and the mean values at 72 hours were also relatively similar.

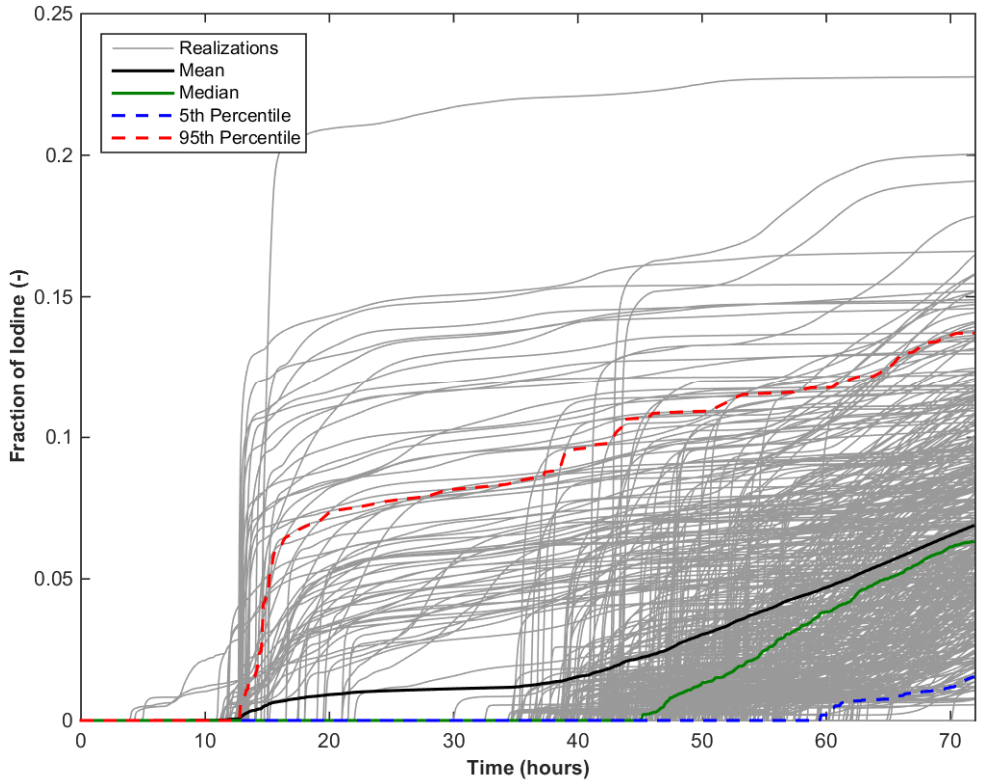

Figure 4-51 Iodine release fractions over 72 hours with mean, median, 5th and 95th percentiles

4.2.2.2.2 Regression Tables and Scatterplots

Table 4-9 shows the results for regression analysis of the iodine release fraction. The regression results show the main contribution from rupture and priSVcycles is almost equal. However, the regressions presented in the table are pretty weak. The recursive partitioning will always be high. Thus, while the scatter plots support some of these results, care should be taken in drawing any conclusions. Rupture was identified as the most important parameter for iodine release fraction by all regression techniques, except MARS, which identified it as second most important behind priSVcycles. The priSVcycles parameter was identified as the second most important by two regression techniques, with MARS identifying it as the most important, and Rank Regression showing it equal to rupture. SV_Frac and Ajar were identified as the third and fourth most important, respectively, with Rank Regression and MARS reversing the order for these two parameters. The eutectic melt temperature also showed a significant main contribution and was the fifth most important parameter. No other parameters had a significant contribution to iodine release fraction.

Table 4-9 Regression analysis of iodine release fraction at 72 hours (with random ignition).

	Rank Regression		Quadratic		Recursive Partitioning		MARS		Main Contribution	Conjoint Contribution
Final R^2	0.19		0.28		0.78		0.32			
Input	R^2 contr.	SRRC	S_i	T_i	S_i	T_i	S_i	T_i		
rupture	0.07	-0.25	0.21	0.22	0.13	0.45	0.22	0.22	0.075	0.082
priSVcycles	0.07	-0.29	0.13	0.25	0.08	0.43	0.38	0.38	0.072	0.103
SV_frac	---	---	0.25	0.46	0.14	0.57	0.00	0.00	0.060	0.132
ajar	0.03	-0.18	0.05	0.11	0.02	0.31	0.22	0.21	0.031	0.081
EU_melt_T	0.01	0.07	0.06	0.08	0.01	0.09	0.18	0.19	0.021	0.025
shape_fact	0.01	0.11	0.03	0.03	0.02	0.11	0.00	0.00	0.009	0.023
Seal_Open_A	0.01	0.09	0.03	0.06	0.00	0.01	0.00	0.00	0.005	0.006
Seal_Fail_Dp	---	---	0.02	0.05	0.00	0.05	0.00	0.00	0.002	0.014
burn_dir	---	---	---	---	0.00	0.02	0.00	0.01	0.000	0.005

* highlighted if main contribution larger than 0.02 or conjoint contribution larger than 0.1

Rupture

Figure 4-52 shows the scatterplot of the iodine release fraction versus rupture (i.e., the containment failure pressure). The densest region of points has a negative sloping trend, which supports the negative regression coefficient on rupture for rank regression. The rank regression overall, however, is not strong. In contrast, the random ignition realizations had two parameters with significantly higher correlations (i.e., SV_Frac=0.182 and priSVcycles=0.110). The non-random ignition Rupture parameter had the third highest correlation of 0.031 versus being the highest for random ignition.

The containment rupture pressure had an increased importance in the random ignition realizations due to fewer early containment failures. The likelihood of containment failure was not extremely sensitive to the magnitude of the Rupture failure pressure during the initial burn at the initial RPV breach. If a large burn occurred, then it often exceeded most Rupture failure pressure values. In contrast to an early sharp pressurization from a large hydrogen burn, the late is containment failure is due to a slow pressurization from ex-vessel gas generation. Consequently, the Rupture value has more importance. A higher Rupture value corresponds to a later containment failure with more time for aerosol settling and retention, which is generally reflected as a lower iodine release in the scatterplot. However, as discussed in Section 4.2.1.2 (i.e., and also occurred in the non-random ignition realizations), late revaporization of iodine from the PRT can greatly impact the benefits of more settling time. The importance of the late iodine revaporization is greater in realizations with an early SV failure that captures more iodine in the PRT.

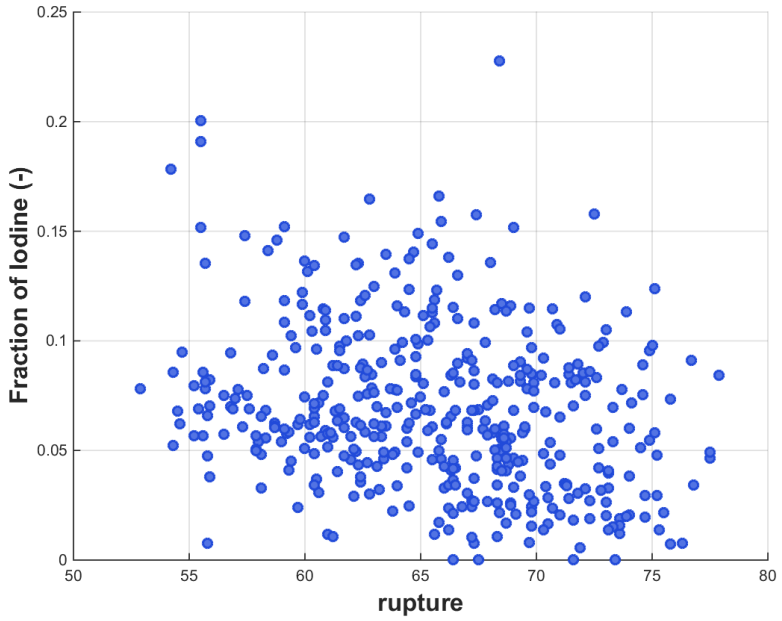

Figure 4-52 Scatterplot of iodine release fraction versus rupture

priSVcycles

Figure 4-53 shows the scatterplot of the iodine release fraction versus priSVcycles. The maximum number of SV cycles is 74 cycles before there was a RPV breach. The dense clustering of realizations between 71 to 74 cycles indicates normally operating SVs until RPV breach (i.e., hot leg failure). If the pressurizer SVs operate without any failures (e.g., the black circles in Figure 4-49), then the containment only fails late. A late containment failure generally corresponded to lower releases, as shown in Figure 4-53. All of the realizations with 61 to 74 SV cycles resulted in a late containment failure (see Figure 4-54). The realizations also have lower iodine releases (i.e., all but three realizations are <0.10, see Figure 4-53). Most of the realizations with 46 to 60 SV cycles also resulted in a late containment failure (i.e., the yellow triangles in Figure 4-49). This led to lower iodine releases for most realizations from this group of SV cycles (i.e., most realizations are <0.08).

The realizations with 1 to 45 SV cycles included both early and late containment failures (see Figure 4-47). However, as shown in Figure 4-14, the majority of the random ignition realizations progressed to a late containment failure. The results from Figure 4-53 show a wide range of iodine releases throughout this SV grouping. However, there were also many very low releases within this grouping. Consequently, the correlation of the SV_Frac is less definitive within this range. Other factors such as the SV failure area and containment failure pressure combine with the number of SV cycles to impact containment failure timing and the magnitude of the iodine release.

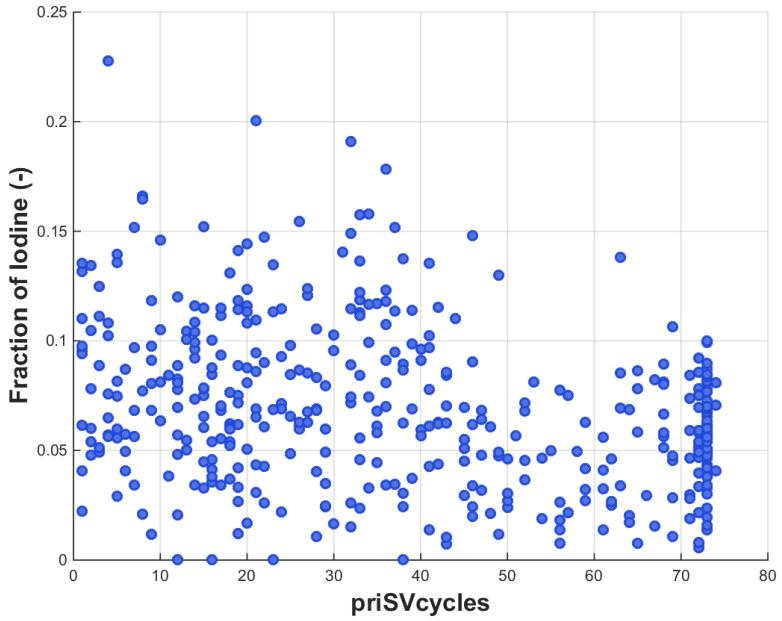

Figure 4-53 Scatterplot of iodine release fraction versus priSVcycles

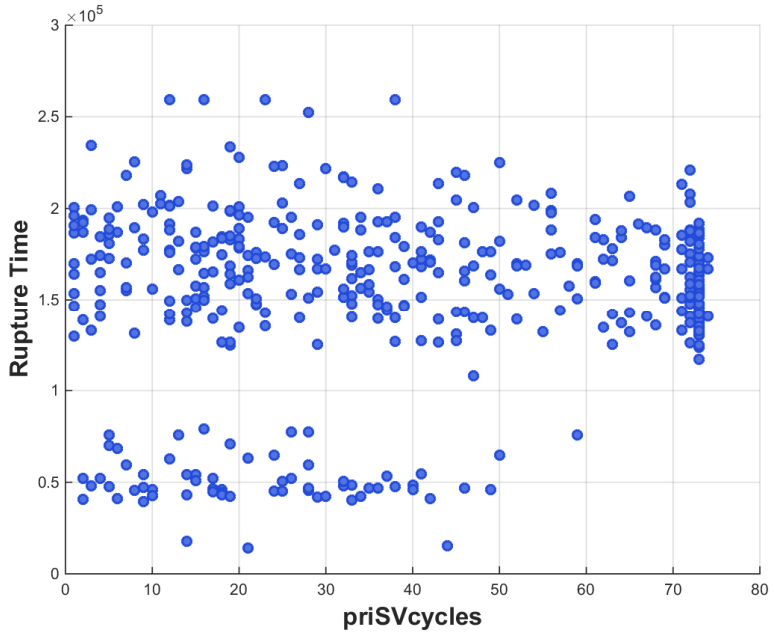

Figure 4-54 Scatterplot of rupture time versus priSVcycles

SV_Frac

Figure 4-55 shows the scatterplot of the iodine release fraction versus SV_Frac. Similar to the non-random ignition discussion in Section 4.2.1.2.2, the SV_Frac and priSVcycles parameters have interdependent relationships on the fraction of iodine released.

The SV_Frac parameter indicates the open fraction of the primary SV system at 72 hours. All pressurizer SV cycling ceases following the RPV breach (i.e., <10 hours). Consequently, the final SV position represents the actual failure conditions, based on the post-calculated results. If there are no SV failures at 72 hours, then the open fraction is 0 (i.e., in the limit as the SV open fraction approaches zero, it approaches a normally operating SV), which is also reflected with priSVcycles >70. Finally, if one SV experienced cycling failure, then the sampled open fraction is used. If multiple SV experience cycling failure, then their open fractions are summed. Figure 4-55 shows a relationship between low fractional open areas and low fraction of iodine release (i.e., SV_Frac<0.28). All but one of these realizations had an iodine release less than 0.1. In contrast, the fractional open area above 0.28 corresponds with the entire range of iodine release.

The response of the SV_Frac parameter has interdependence on the number of SV cycles. As discussed in Sections 4.2.1.1 and 4.2.2.1, all the realizations where the pressurizer safety valves operated as designed without failures resulted in late containment failures. The progression of events in these sequences includes a hot leg failure from high RCS pressure followed by a rapid discharge of the accumulators into the degraded core. The lower containment had long periods where it was steam-inerted or without an active ignition source and always progressed to an oxygen deficient condition without early containment failure. All these realizations progressed to a late containment failure (i.e., >32 hours, see Figure 4-49), which delayed the start of the iodine release. The late containment iodine releases were generally lower than the realizations with an early containment failure (see discussion in Section 4.2.1.2.1). Consequently, all the realizations with SV_Frac=0 include a late containment failure and correlate with smaller releases.

The SV_Frac realizations with a failure area less than 0.25 also had small source terms. The smaller leakage area behaved more closely to a normally operating pressurizer SV. Consequently, the small SV_Frac behavior resulted. Furthermore, if the leakage area on the first failed valve was too small to prevent further pressurizer SV cycling, then the behavior was also similar normally operating SVs and also resulted in late containment failure.

Similar to the results with priSVcycles between 1 and 45, the SV_Frac results >0.25 spanned the full spectrum of large and small releases. These realizations also included both early and late containment failures. As discussed in the non-random ignition realization results (see Section 4.2.1.2), the variability in iodine revaporization from the PRT increased the magnitude of the released iodine.

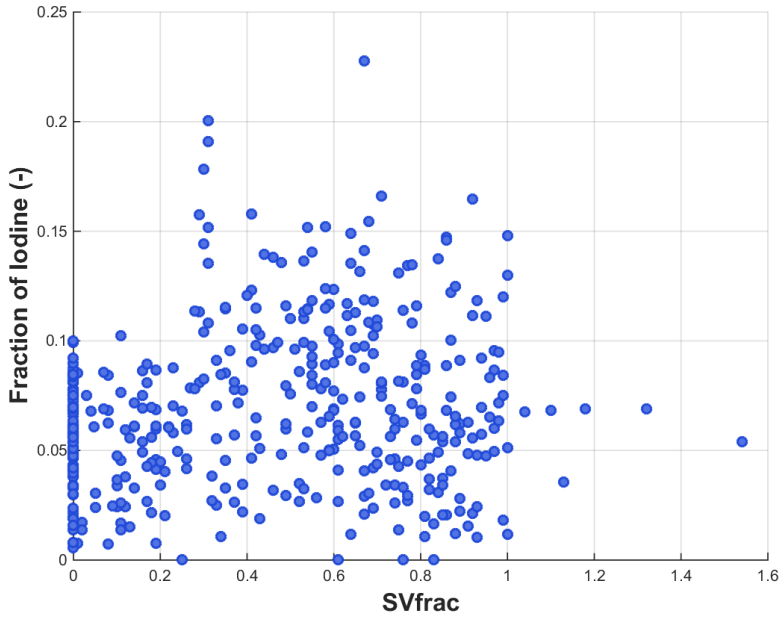

Figure 4-55 Scatterplot of iodine release fraction versus SV_Frac

Ajar

The Ajar parameter represents the non-dimensional opening area of the lower ice condenser doors after they fully opened (i.e., exceeded the maximum differential pressure for opening). The ice condenser doors will stick at the AJAR fraction thereafter. The AJAR parameter addresses the uncertainty in the damage of the lower door hinges once they have opened the maximum range. It was hypothesized that the Ajar parameter would impact the lower compartment steam concentration by forming a natural circulation pattern between the lower compartment and the ice chests. It was not a significant parameter in the iodine release for the non-random ignition realizations.

Figure 4-56 shows the scatterplot of the iodine release fraction versus Ajar. This plot does not indicate any particular relationship between the Ajar parameter and the iodine release fraction to the environment. The density of points is relatively uniform with respect to the horizontal axis, so no particular values of Ajar account for higher or lower fractions of iodine.

The most important impact of the Ajar area would be the conditions following hot leg breach but prior to an oxygen deficient condition. If there was an early containment failure in the random ignition realizations, then it usually occurred during this time frame. However, the majority of the realizations went through this time period to a late containment failure. Figure 4-57 shows a slightly higher density of early containment failures with larger values of Ajar and a slightly higher density of late containment failures with smaller values of Ajar. Higher releases are expected with an early containment failure versus a late containment failure. However, the weak impact shown in Figure 4-57 was relatively insignificant on the iodine release in Figure 4-56. Consequently, it was concluded that Ajar did not significantly impact the iodine release.

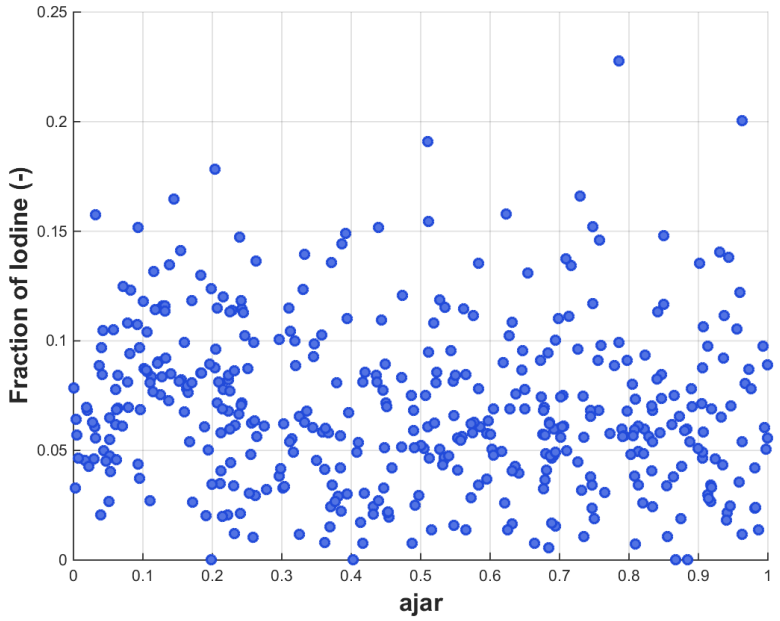

Figure 4-56 Scatterplot of iodine release fraction versus Ajar

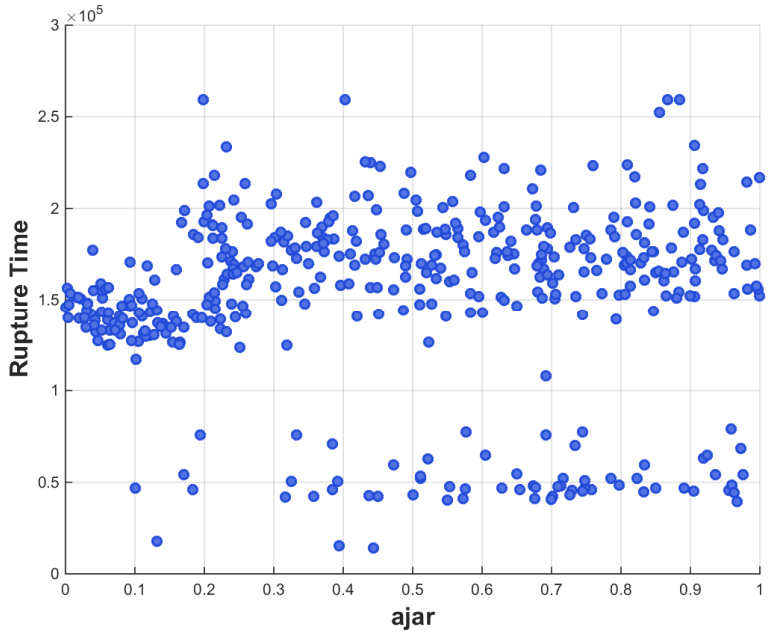

Figure 4-57 Scatterplot of rupture time versus Ajar

EU_melt_T

This parameter represents the temperature at which the eutectic formed from UO_2 and ZrO_2 melts. By including the temperature of the eutectic reaction between ZrO_2 and UO_2 as a sampled parameter, the fuel failure characteristics and debris behavior are affected.

Figure 4-58 is the scatterplot of the iodine release fraction versus the eutectic melt temperature. The points are distributed with an upward sloping trend. This is also reflected in the regression table with the 0.07 regression coefficient on EU_melt_T in the rank regression.

As discussed previously with the high ranked parameters affecting the iodine release, the timing of containment failure is an important factor. As will be discussed later, the amount of hydrogen production does not have a significant correlation on the timing of containment failure (see Section 4.2.2.1 and Figure 4-50). Figure 4-58 shows a weakly correlated upward slope in iodine release versus the eutectic melting temperature. However, all the high sampled eutectic temperatures (>2575 K) had iodine releases below 0.14. Consequently, the results do not suggest a meaningful correlation.

A few of the lowest sampled eutectic melting temperatures fell below the Zircaloy breakout temperature (2350 K), which may impact the in-vessel hydrogen production and the in-vessel iodine release from fuel. All but one of these realizations had a fractional iodine release to the environment that was less than 0.1. Closer examination of the radionuclide release from selected realization results show nearly all the iodine within the fuel matrix is released during the in-vessel accident progression (i.e., including before and after hot leg failure). Any iodine remaining in the fuel matrix will be released during the ex-vessel core-concrete interactions. Since the total hydrogen production did not impact early versus late containment failure (i.e., see Section 4.2.1.1 and Figure 4-18), the impact of a low eutectic melting temperature to promote late containment failure and a lower iodine release to the environment was ruled out. The other remaining possible impacts from a low eutectic melting temperature could be the timing of the iodine release relative to the containment failure and the magnitude of the revaporization, which is dependent on other factors (i.e., SV failure timing and flow area). Therefore, the magnitude of the iodine release to the environment was not judged to be significantly impacted by the eutectic temperature.

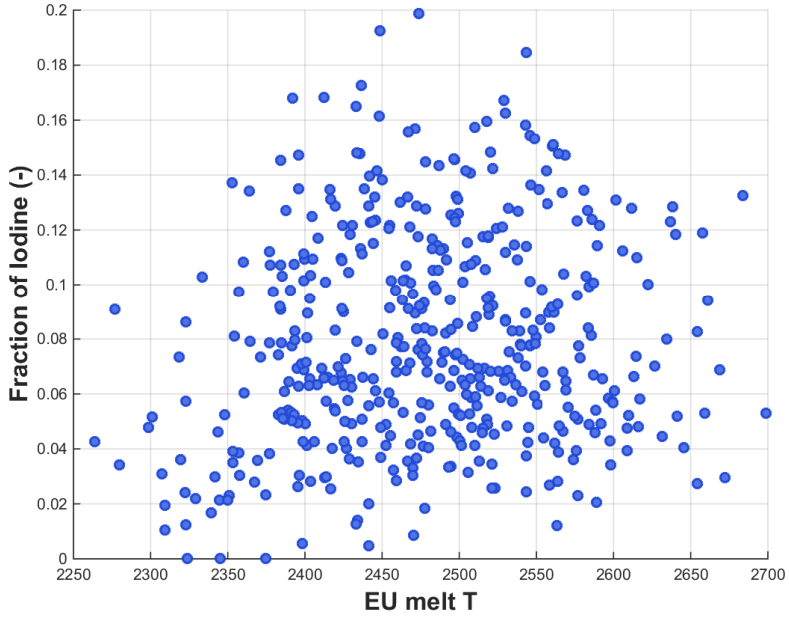

Figure 4-58 Scatterplot of iodine release fraction versus EU_melt_T

4.2.2.3 Cesium Release Fraction to Environment (with random ignition)

The magnitude and timing of the cesium release is an important radionuclide to characterize the potential severity of the long-term health effects. The magnitude of the cesium release can be very important for latent effects. Consequently, the following regression evaluations paid particular attention to factors that influenced large releases of cesium.

4.2.2.3.1 Cesium Release History

Figure 4-59 shows the time dependent release fractions for the successful realizations, as well as the calculated mean, median, and 5th and 95th percentiles. The cesium release fraction is again separated into two distinct release patterns, very similar as those for the non-random ignition realizations. The early cesium releases result from the early containment rupture following a hydrogen burn whereas the second grouping occurs from a late over-pressurization failure due to ex-vessel gas generation. As shown in Figure 4-48, there were fewer early containment failures in the random ignition realizations and fewer early containment failures that were coincident with the initial RPV breach (i.e., compare to Figure 4-15).

The bifurcation in containment failure timings led to a wide spread between the calculated median and the 95th percentile curves. The 95th percentile curve is characteristic of an early containment failure. The median realization is characteristic of a late containment failure while the mean curve has contributions from both the early and late containment failure results. Most realizations resulted in a late containment rupture. The median and 5th percentile curves show larger increasing trends from the late containment failure. The increasing cesium release is at 72 hours is often characteristic of a chimney effect from the long term flow of hot gases from the ex-vessel core-concrete interactions through the failed RPV lower head and out failed hot leg location. The hot gases cause a revaporization of the previously deposited cesium iodine in the RPV. It is also characteristic of a revaporization release from the PRT, which is discussed in Section 4.2.1.2.2.

In comparison to the non-random ignition iodine horsetail results in Figure 4-27, there are fewer early containment failure realizations and a less coherent start of early cesium release. As discussed in Section 4.2.2.1, most of the early containment failures occurred hours after the initial RPV breach. This is in contrast to the non-random ignition results where most early containment failure realizations occurred at the initial RPV beach. The initial cesium releases are shown on an expanded scale in Figure 4-60. The initial cesium releases rise to ~0.025 shortly after containment failure (i.e., all but one realization). The cesium releases remain near this level until ~40 hours. Thereafter, some realizations begin to rise due to revaporization of cesium from the vessel or the PRT (i.e., see discussion in Section 4.2.2.3.2).

Overall, the lower mobility of the cesium molybdate, which is the majority of the cesium, resulted in early releases were smaller than the iodine releases (see Section 4.2.2.2). Cesium molybdate generally transports as an aerosol and requires very high temperatures to revaporize. The long term cesium release to the environment spanned approximately the same range as the iodine (i.e., some realizations to >0.20). However, the mean cesium release is only 0.02 (Figure 4-59) versus 0.06 for iodine (Figure 4-51).

In general, the late containment releases were similar between the random (Figure 4-59) and the non-random ignition realizations (Figure 4-27). The median curve on these graphs is characteristic of the late containment failure response and are in close agreement. Both the random and the non-random ignition medians were ~0.03 at 72 hours, respectively. The 5th

percentile and the mean values at 72 hours were also relatively similar. The random ignition 95th percentile (0.17) was slightly larger than the non-random value at 72 hours (i.e., 0.14). However these results were impacted by a small sample of higher release realizations. Consequently, although there were differences in the combustion assumptions, the overall impact on the cesium releases were minor.

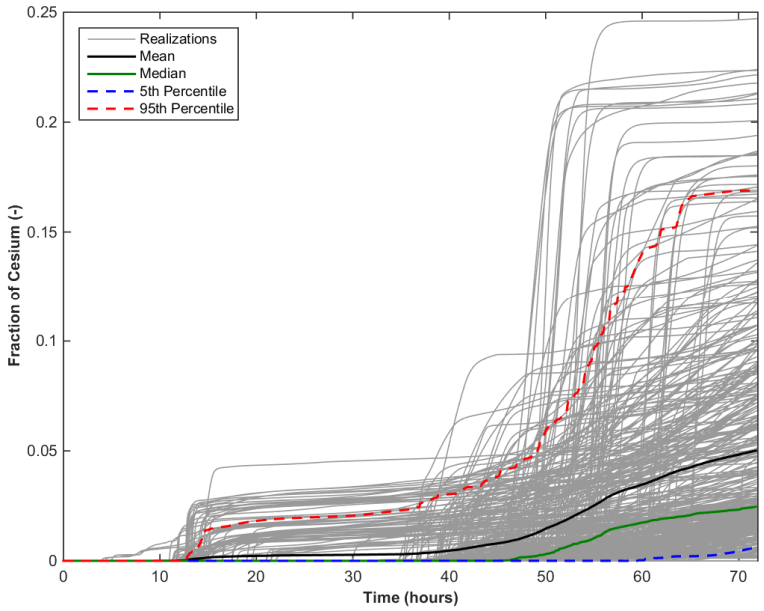

Figure 4-59 Cesium release fractions over 72 hours with mean, median, 5th and 95th percentiles

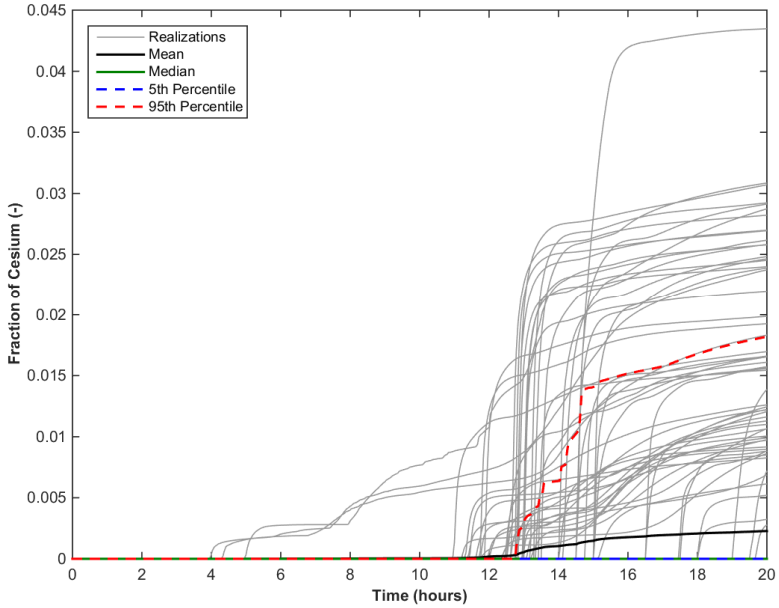

Figure 4-60 Expanded view of the cesium release fractions over the first 20 hours of the simulation

4.2.2.3.2 Regression Tables and Scatterplots

SV_Frac is the top parameter identified in Table 4-10, well above the second listed parameter, priSVcycles. No other parameters had a significant contribution to the results.

Table 4-10 Regression analysis of cesium release fraction (with random ignition).

	Rank Regression		Quadratic		Recursive Partitioning		MARS		Main Contribution	Conjoint Contribution
Final R^2	0.63		0.61		0.89		0.63			
Input	R^2 contr.	SRRC	S_i	T_i	S_i	T_i	S_i	T_i		
SV_frac	0.56	0.64	0.70	0.88	0.53	0.87	0.85	0.90	0.499	0.146
priSVcycles	0.02	-0.20	0.02	0.11	0.08	0.25	0.07	0.06	0.035	0.071
shape_fact	0.02	0.15	0.03	0.07	0.02	0.23	0.03	0.08	0.018	0.082
rupture	0.01	-0.06	0.00	0.06	0.01	0.03	0.00	0.01	0.004	0.018
EU_melt_T	0.00	0.05	0.02	0.02	0.00	0.04	0.00	0.00	0.004	0.013
ajar	0.01	-0.10	---	---	0.00	0.05	0.00	0.00	0.003	0.015
burn_dir	0.00	0.07	0.01	0.05	---	---	0.00	0.00	0.003	0.008
Seal_Fail_Dp	---	---	0.00	0.01	0.00	0.04	0.00	0.00	0.001	0.012
Seal_Open_A	---	---	0.00	0.02	0.00	0.02	0.00	0.00	0.001	0.010

* highlighted if main contribution larger than 0.02 or conjoint contribution larger than 0.1

SV_Frac

Figure 4-61 shows the scatterplot for cesium release fraction versus SV_Frac. This plot is very similar to that of SV_Frac versus the fraction of cesium released without random ignition. It suggests a strong trend that is reflected in the highly positive regression coefficient on SV_Frac in the rank regression results and in the S_i values in the regression results from the other methods. Similar to the non-random ignition discussion in Section 4.2.1.3, the SV_Frac and priSVcycles parameters have interdependent relationships on the fraction of cesium released.

The discussion in Section 4.2.1.3.2 concerning the dependency of the cesium release is also applicable for the random ignition results. In particular, a SV_Frac value between 0 and 0.25 develops conditions for a late containment failure, which generally has low releases. Although most of the random ignition realizations had late containment failure, only the realizations with SV_Frac >0.25 had early containment failures (see Figure 4-62). A late containment failure generally had lower releases whereas an early containment failure generally had larger releases. Consequently, the scatter in the cesium release with SV_Frac >0.5 increases substantially. As also noted in Section 4.2.1.3.2, a larger SV_Frac can lead to more fission product transport to the PRT and therefore more susceptible to revaporization. However, cesium is less susceptible to revaporization versus iodine and only occurs at larger values of SV_Frac. Consequently, the cesium release resulted in a better correlation with SV_Frac than the iodine releases. As discussed in Sections 4.2.1.2 and 4.2.2.2, iodine is more volatile than cesium, which led to higher iodine median releases and revaporization under more situations (e.g., a wider range of SV_Frac).

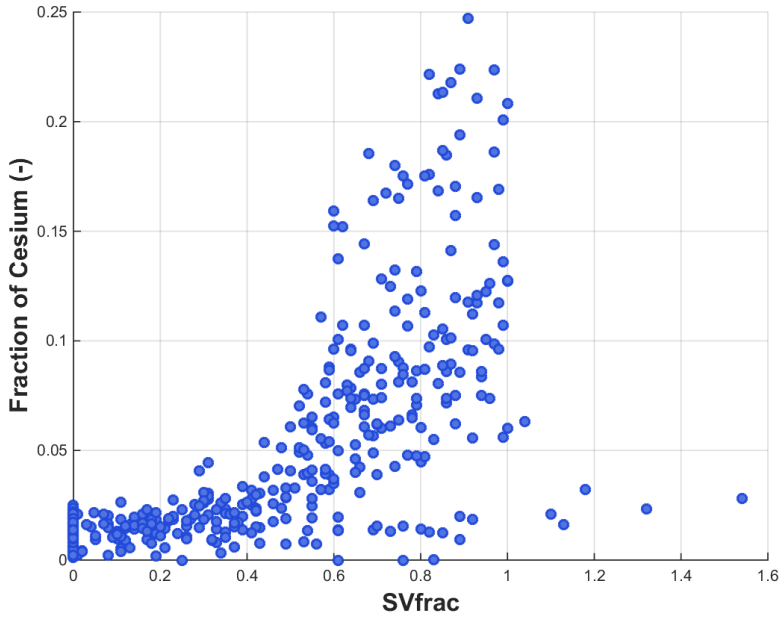

Figure 4-61 Scatterplot of cesium release fraction versus SV_Frac

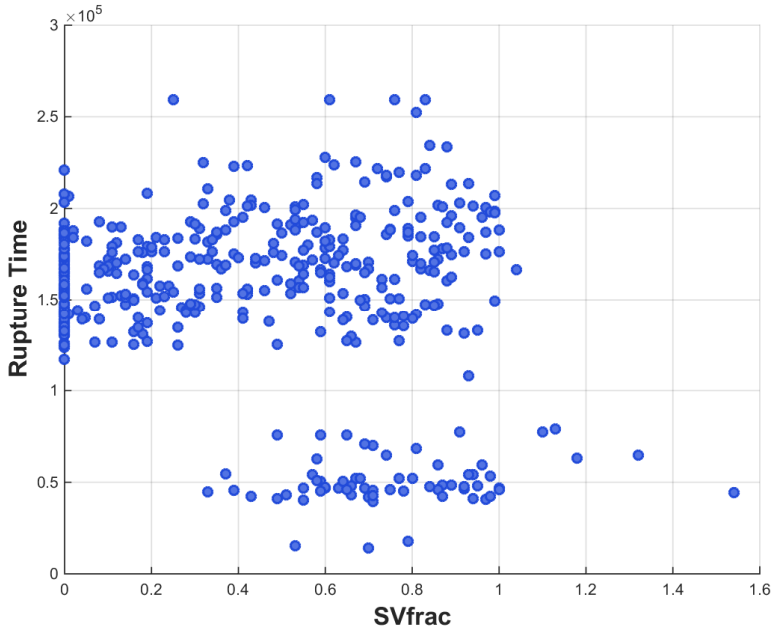

Figure 4-62 Scatterplot of rupture time versus SV_Frac

priSVcycles

Figure 4-63 shows the scatterplot for cesium release fraction versus priSVcycles. The maximum number of SV cycles is 74 cycles before there was a RPV breach. The dense clustering of realizations around 71 to 74 cycles indicates normally operating SVs until RPV breach (i.e., hot

leg failure). If the pressurizer SVs operate without any failures (e.g., the black circles in Figure 4-49), then the containment only fails late. A late containment failure generally corresponded to lower releases, as shown in Figure 4-63. All of the realizations with 61 to 74 SV cycles resulted in late containment failure (see Figure 4-54). The 61 to 74 SV cycle realizations also have lower cesium releases (i.e., all but two realizations are <0.03, see Figure 4-53). Surprisingly, the largest cesium release also occurred in the priSVcycles 61 to 74 grouping.[29]

Most of the realizations with 46 to 60 SV cycles also resulted in a late containment failure (i.e., the yellow triangles in Figure 4-49). There is a significant number of realizations with lower cesium releases in this group of SV cycles (i.e., cesium release <0.04). However, there is an almost comparable number of realizations with higher cesium releases (i.e., >0.04 to >0.20).

Similarly, there is a trend of gradually increasing cesium releases as priSVcycles decreases below 45 SV cycles. The realizations with 1 to 45 SV cycles included both early and late containment failures (see Figure 4-47). However, as shown in Figure 4-80, the majority of the random ignition realizations progressed to a late containment failure. The scatter of the cesium releases in this grouping is similar to the iodine results (Figure 4-53) but less defined than the cesium releases in the random ignition realizations (Figure 4-34). In general, the random ignition realizations showed a weaker correlation to priSVcycles versus the non-random realizations.

[29] No random realizations were analyzed in the individual realizations section (Section 4.3). However, the high cesium release outlier was particularly confusing because it did not have the key attributes of the Rlz 142, which was the maximum non-random ignition cesium release. Rlz 142 had the earliest SV failure (i.e., failed on the first opening), a large SV failure area (i.e., 0.97), and a high containment rupture pressure that delayed containment failure until the peak of the cesium revaporization from the PRT (74.9 psi). In contrast, the maximum random ignition cesium release realization had 68 SV cycles, which is not characteristic of a realization with large cesium revaporization potential from the PRT.

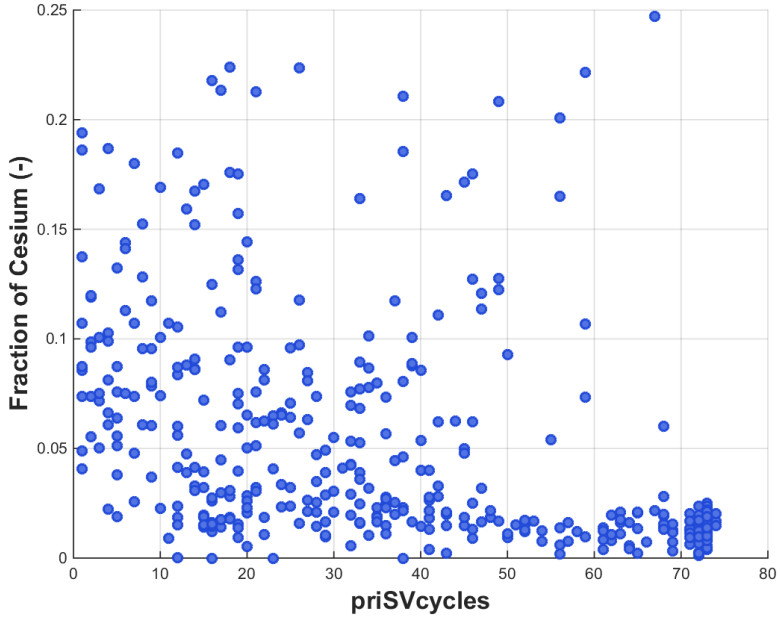

Figure 4-63 Scatterplot of cesium release fraction versus priSVcycles

4.2.2.4 Hydrogen Production (with random ignition)

As described in Section 4.2.1.4, the in-vessel hydrogen production in the Sequoyah model is primarily due to oxidation reactions of the Zircaloy fuel cladding, although there is also hydrogen produced by oxidation of stainless steel structures. The 100% oxidation of the Zircaloy in the fuel in the Sequoyah core generates 1022 kg of hydrogen. In both the random and non-random ignition realizations, the total hydrogen generation from Zircaloy and stainless steel oxidation is only 40% to 60% of this maximum value. The total in-vessel hydrogen generation was approximately 85% from the Zircaloy oxidation, while approximately 15% was from stainless steel oxidation. In addition to the in-vessel hydrogen generation, the ex-vessel debris and concrete interactions also generate hydrogen as well as other non-condensable gases. The predominate gas generated from the ablation of the Sequoyah limestone concrete in the reactor cavity is carbon monoxide. The total carbon monoxide gas generation through 72 hours is ~30,000 kg along with evaporation of water from the hot CCI gases will eventually cause late containment failure (i.e., if not already failed). While not as reactive as hydrogen, carbon monoxide is also combustible.

The amount of hydrogen produced in-vessel along with the ex-vessel production of hydrogen and other gases during CCI are also the primary influences on whether deflagration and detonation conditions are reached in containment, which cause sharp pressure increases leading to containment rupture and fission product release to environment. Finally, the large ex-vessel gas production (i.e., steam production and CCI gases) will render the containment oxygen deficient as the oxygen partial pressure becomes small (i.e., <5%) compared to the total containment pressure.

The uncertainty analysis only investigated the dependency of the uncertainty parameters on the total in-vessel hydrogen production. Very few random ignition realizations progressed to an early containment failure and most did not occur until after RPV failure (i.e., RPV lower head

failure occurred ~7 to 9 hours). Consequently, the random ignition realizations had early containment failure contributions from both in-vessel and ex-vessel combustible gas production.[30] In contrast, most of the early containment failures from a hydrogen burn in the non-random ignition realizations occurred immediately after hot leg failure and were only dependent on the in-vessel hydrogen production. However, for consistency with the non-random realizations, the in-vessel hydrogen production was selected as the primary hydrogen generation figure of merit.

4.2.2.4.1 Hydrogen Production History

Figure 4-64 shows the time dependent hydrogen production for the successful realizations. As shown by the 5th and 95th percentile curves, the total production of hydrogen is between 400 kg and 600 kg. The in-vessel hydrogen production begins around 2.5 hours and most realizations have stopped producing hydrogen by about 7 hours. The hydrogen production for the sequence is very similar as the sequence where random ignition is not implemented (i.e., see Section 4.2.1.4.1). The mean and median results in Figure 4-64 are relatively close at about 490 kg and 470 kg, respectively. Figure 4-65 illustrates the cumulative probabilities for the quantity of hydrogen produced for selected time intervals through 72 hours. Figure 4-66 shows hydrogen CDFs by the hour for the first 20 hours of simulation and shows a more pronounced difference over time (converging to the CDFs in Figure 4-65).

[30] For example, non-random ignition Rlz 133 reached 200 kg of ex-vessel hydrogen production in the first 3 hours after RPV lower head failure and exceeded the in-vessel hydrogen production by 14 hours after RPV failure (i.e., 442 kg of ex-vessel hydrogen at 22 hours). The total ex-vessel hydrogen generation was 1180 kg at 72 hours.

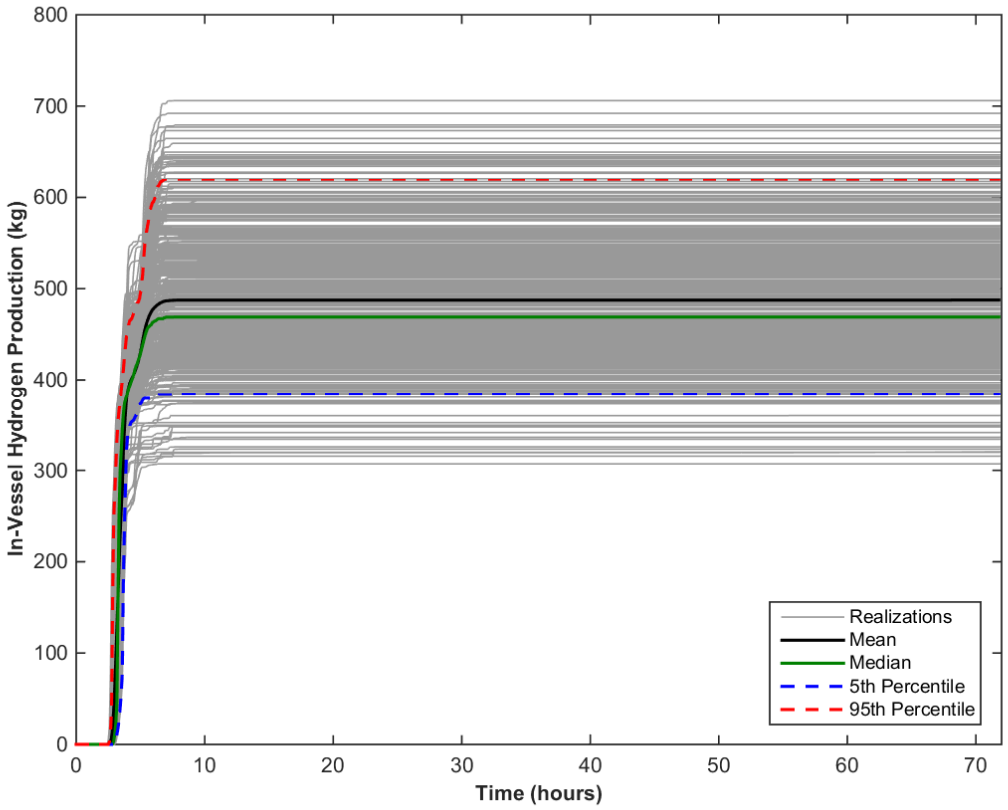

Figure 4-64 Total hydrogen production over 72 hours with mean, median, 5th and 95th percentiles

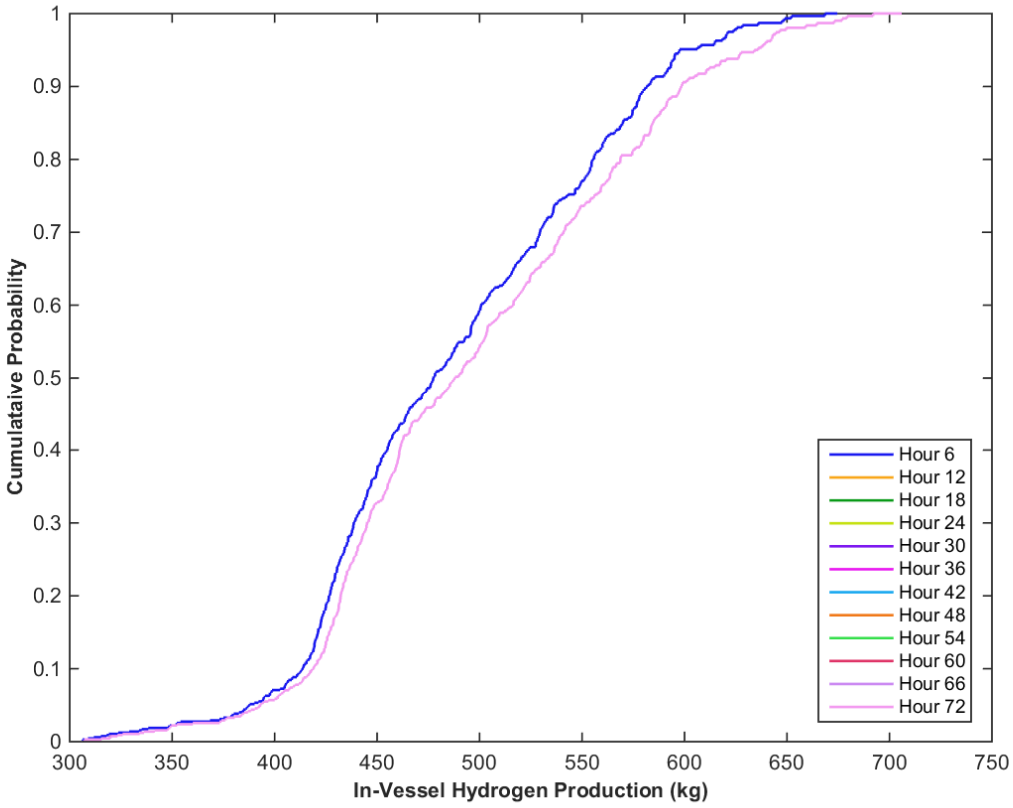

Figure 4-65 Cumulative probabilities for the quantity of hydrogen produced for selected time intervals through 72 hours

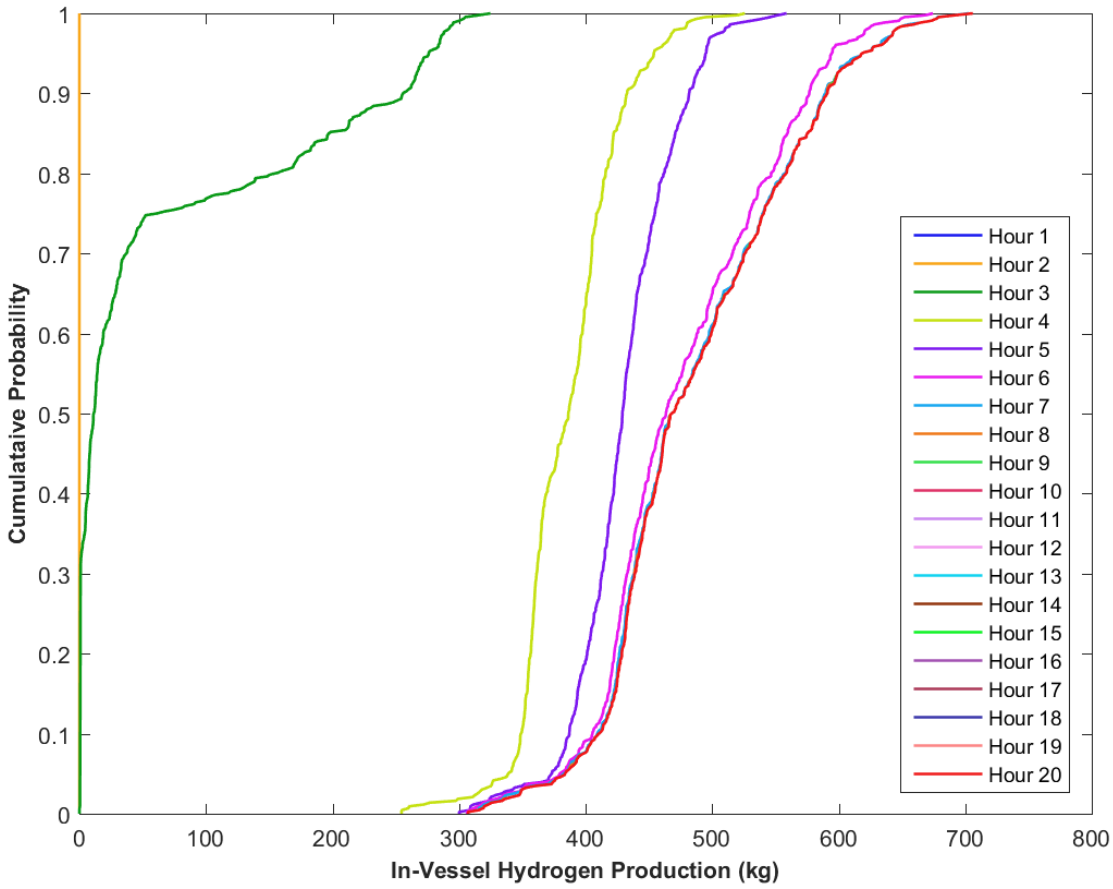

Figure 4-66 Cumulative probabilities for the quantity of hydrogen produced for selected time intervals to 20 hours

4.2.2.4.2 Regression Tables and Scatterplots

The review of the regression results for all successful realizations presented in Table 4-11 shows SV_Frac and eutectic melt as the most important parameters. The SV open area fraction was the top parameter with the Rank Regression technique, while eutectic melt temperature was the top parameter for all other techniques. The method for calculating the main contribution results in these two parameters having an equal main contribution. The third most important parameter is priSVcycles. The rank order of the top three parameters is identical to the regression rank order in the without random ignition scenario, and the main contributions are reasonably similar. No other parameters had a significant contribution to the results.

Table 4-11 Regression analysis of hydrogen production at 72 hours (with random ignition).

	Rank Regression		Quadratic		Recursive Partitioning		MARS		Main Contribution	Conjoint Contribution
Final R^2	0.42		0.54		0.86		0.61			
Input	R^2 contr.	SRRC	S_i	T_i	S_i	T_i	S_i	T_i		
SV_frac	0.24	-0.37	0.32	0.56	0.17	0.53	0.27	0.55	0.180	0.201
EU_melt_T	0.15	0.37	0.34	0.35	0.25	0.44	0.28	0.31	0.180	0.061
priSVcycles	0.02	0.19	0.06	0.31	0.11	0.39	0.15	0.46	0.059	0.186
rupture	0.00	-0.06	0.01	0.04	0.01	0.05	0.00	0.00	0.005	0.017
Seal_Fail_Dp	---	---	0.00	0.01	0.01	0.03	0.01	0.00	0.004	0.008
Seal_Open_A	---	---	---	---	0.01	0.03	0.00	0.00	0.002	0.006
burn_dir	0.01	0.09	---	---	0.00	0.01	0.00	0.00	0.002	0.001
ajar	---	---	0.00	0.02	0.00	0.07	0.00	0.00	0.000	0.024
shape_fact	---	---	---	---	0.00	0.06	0.00	0.00	0.000	0.016

* highlighted if main contribution larger than 0.02 or conjoint contribution larger than 0.1

SV_Frac

The SV_Frac parameter indicates the open fraction of the primary SV system at 72 hours. Figure 4-67 shows the scatterplot for in-vessel hydrogen production versus SV_Frac. As reflected in the rank regression coefficient on SV_Frac, there is a moderate negative trend between the clusters of points in the plot. The hydrogen production trends with SV_Frac discussed below are very similar to the non-random ignition realizations, which were discussed in Section 4.2.1.4.2.

As discussed in Section 4.2.1.4.2, the in-vessel hydrogen generation rate is generally higher at SV_Frac<0.4 and lower at SV>0.4. Almost all the realizations with a failure area less than 0.4 had hydrogen generation rates above the median. The larger valves of SV_Frac (i.e., >0.4) generally had hydrogen production rates below the median value. As SV_Frac increases from 0.4 to 1, there is a downward trend in hydrogen production. However, there is considerable scatter in the results in Figure 4-67. The variation in these realizations is due to timing of the pressurizer SV failure and eutectic melting temperature, which are discussed in the next sections. In particular, the grouping of realizations with low hydrogen production at SV_Frac=0 had very low eutectic melting temperatures that limited in-vessel hydrogen production.

The larger valves of SV_Frac (i.e., >0.4) generally had hydrogen production rates below the median value. As SV_Frac increases from 0.4 to 1, there is a downward trend in hydrogen production. The depressurization of the RCS occurs faster as the SV failure area gets larger. Similar to the previous grouping of cases, the timing of the SV failure will also impact the system pressure during the accelerated oxidation phase.

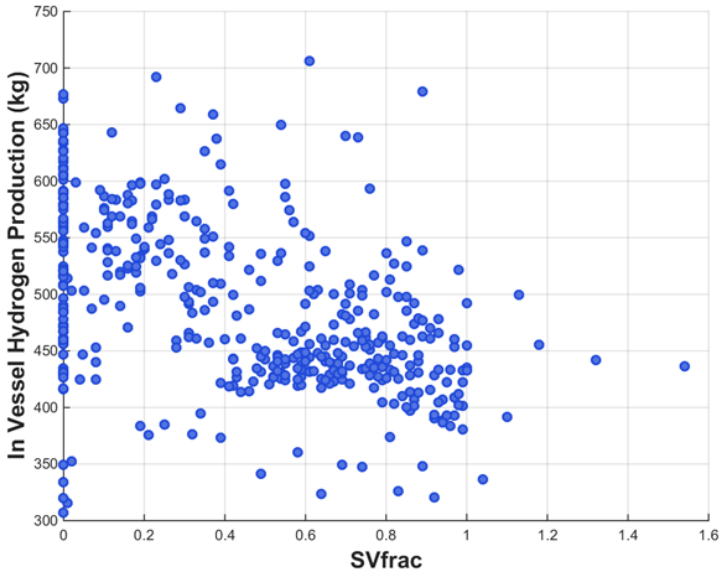

Figure 4-67 Scatterplot of in-vessel hydrogen production versus SV 72 hour post-calculated open fraction

Eutectic Melt Temperature

Figure 4-68 shows the scatterplot for in-vessel hydrogen production versus eutectic melt temperature. The positive sloping trend in this plot, and particularly the positive sloping trend of the densest cluster of points, supports the highly positive regression coefficient for EU_melt_T in the rank regression results. The variation in the EU_melt_T uncertainty parameter was expected to impact the in-vessel hydrogen. The fuel collapse criteria has many components including the failure of the supporting structure, thinning or time-dependent thermal weakening of the oxide shell, and reaching the fuel melting temperature, which is a surrogate for the eutectic formation. However, a higher eutectic melting temperature failure generally results in higher peak fuel temperatures prior to collapse. The hydrogen generation rate is much higher from intact fuel rods due to the high surface areas and an open hydraulic configuration. Consequently, if the fuel rods remain in an intact configuration longer, then there is potential for more hydrogen production. A higher eutectic melting temperature also increases the porosity of the debris, which enhances late phase oxidation. The scatter is attributed to the variation in the timing of the pressurizer SV failure and the SV failure area fraction.

A few of the lowest sampled eutectic melting temperatures fell below the Zircaloy breakout temperature (2350 K), which impacted the in-vessel hydrogen production. In these realizations, the fuel collapsed before the molten Zircaloy behind the oxide shell is released. Consequently, the fuel slumps without oxidizing molten Zircaloy portion of the cladding. The resultant debris geometry blocks steam flow for late phase oxidation. These cases had the lowest hydrogen generation rates and explain the low outlying realizations previously discussed with SV_Frac.

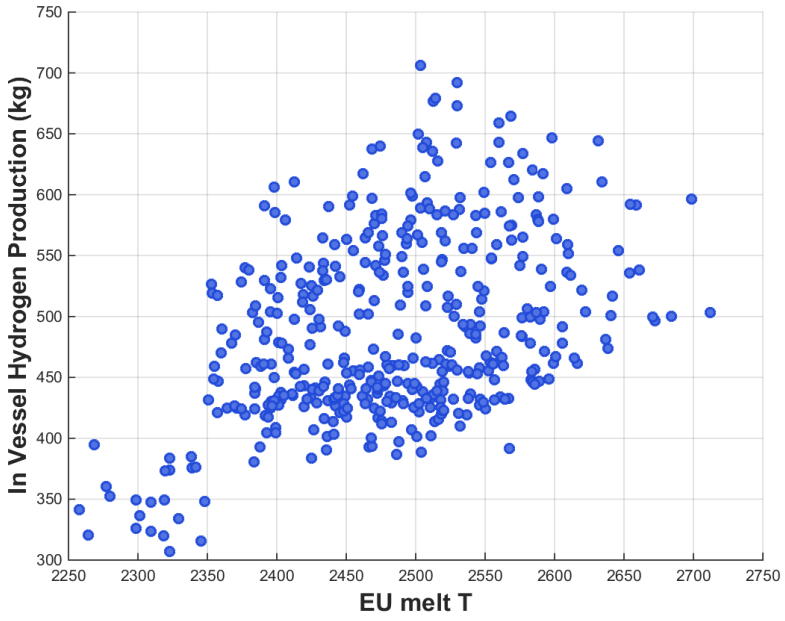

Figure 4-68 Scatterplot of in-vessel hydrogen production versus eutectic melt temperature input values

priSVcycles

Figure 4-69 shows the scatterplot for in-vessel hydrogen production versus priSVcycles. The maximum number of SV cycles is 74 cycles before there was a RPV breach. The dense clustering of realizations between 71 to 74 cycles indicates normally operating SVs until RPV breach (i.e., hot leg failure). The priSVcycles parameter complements the SV_Frac parameter, which showed normally operating valves when SV_Frac=0. The values of these parameters indicate the RCS is at high pressure during the initial core degradation, which enhances hydrogen production. Consequently, the in-vessel hydrogen generation rates are generally higher with more priSVcycles. In particular, the grouping of realizations with low hydrogen production at priSVcycles>71 had very low eutectic melting temperatures that limited in-vessel hydrogen production.

As the priSVcycles decreases from 71 to 1, the in-vessel hydrogen production decreases from primarily above the median to primarily below the median. Below 20 cycles, there are clustering of realizations below the median. The variations are caused by the failure area and the eutectic temperature. Although the priSVcycles had a lower correlation than the SV_Frac, the two parameters are highly interrelated.

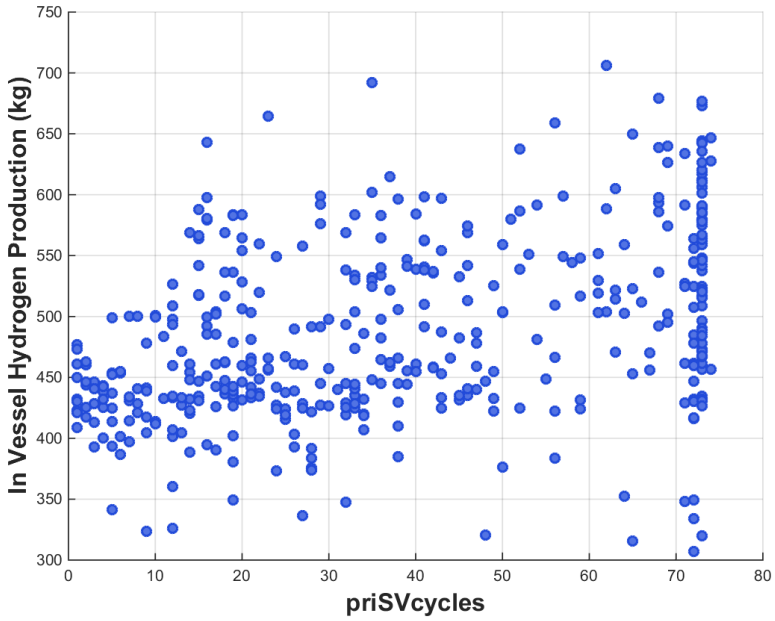

Figure 4-69 Scatterplot of in-vessel hydrogen production versus priSVcycles

4.2.2.5 Rupture Timing (with random ignition)

Rupture timing, defined as the point at which the specified pressure is exceeded and a 3 ft^2 hole opens is another figure of merit investigated. The rupture timing is important to the source term timing and often the source term magnitude.

4.2.2.5.1 Regression Tables and Scatterplots

The regression analysis in Table 4-12 shows rupture (i.e., the containment failure pressure) as the top parameter for all regression techniques. The main contribution from rupture was considerably higher than SV_Frac, which was the second most important parameter. Burn direction and Ajar were the third and fourth parameters, respectively, but had an equal main contribution. No other parameters had a significant contribution to rupture time uncertainty, nor were there any other parameters that were expected to have a significant contribution that didn't.

Table 4-12 Regression analysis of rupture time for all realizations (with random ignition).

	Rank Regression		Quadratic		Recursive Partitioning		MARS		Main Contribution	Conjoint Contribution
Final R^2	0.36		0.38		0.74		0.29			
Input	R^2 contr.	SRRC	S_i	T_i	S_i	T_i	S_i	T_i		
rupture	0.29	0.54	0.44	0.47	0.24	0.64	0.67	0.76	0.207	0.112
SV_frac	---	---	0.11	0.34	0.12	0.55	0.16	0.25	0.058	0.145
burn_dir	0.02	0.14	0.05	0.10	0.02	0.12	0.06	0.07	0.016	0.034
ajar	0.04	0.22	0.01	0.08	0.02	0.19	0.00	0.00	0.016	0.050
EU_melt_T	0.01	-0.10	0.02	0.12	0.02	0.22	0.00	0.00	0.007	0.063
priSVcycles	---	---	0.01	0.19	0.01	0.02	0.00	0.00	0.002	0.027
Seal_Fail_Dp	---	---	---	---	0.01	0.13	0.00	0.00	0.002	0.029
Seal_Open_A	---	---	0.01	0.07	0.00	0.01	0.00	0.00	0.002	0.011
shape_fact	---	---	---	---	0.00	0.10	0.00	0.00	0.000	0.026

**** highlighted if main contribution larger than 0.02 or conjoint contribution larger than 0.1***

Rupture

Figure 4-70 shows the scatterplot of rupture time (in seconds) versus rupture. Although neither a late rupture time nor an early rupture time can be attributed to specific values of the rupture parameter, there is a distinct positive trend among the high rupture time cluster of points. There are two interesting results from the scatter plot. First, the early containment failure timing shows no significant dependency on the rupture pressure. The early containment results spanned the entire range of rupture pressures. In addition, there did not seem to be any dependency on the rupture pressure for the failures that occurred a few hours after the initial RPV breach. If the hydrogen was adequately distributed, there was enough pressurization from the burn to fail the containment at any rupture pressure. As noted previously in the hydrogen production section (i.e., see Footnote 30), many of the random ignition realizations included a significant ex-vessel hydrogen source for the early containment failures that occurred after the RPV failure.

The second key point evident on Figure 4-70 is the dependency of the rupture pressure on the late containment failure. Unlike the fast pressurizations from the combustion events that lead to an early containment failure, the late containment failure occurred due to a slow pressurization. The scatter plot shows an upward trend as the containment rupture occurs later with a higher rupture pressure. The parameters that led to the separation of the two groups of late failures (i.e., the lower trend line versus the main trend line) were not identified from this parameter or the other two high ranking parameters.

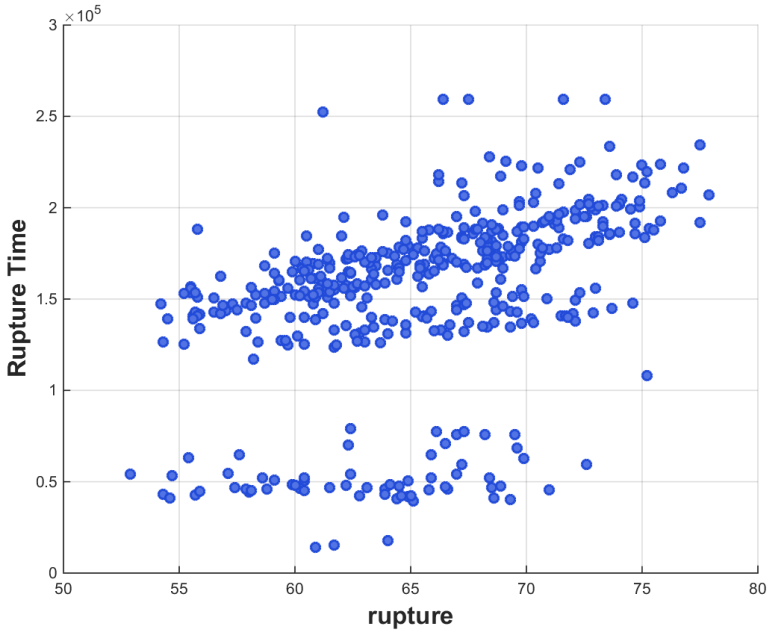

Figure 4-70 Scatterplot of rupture time versus rupture

SV_Frac

Figure 4-71 shows the scatterplot of rupture time versus SV_Frac. The two clusters of high density points account for the strong negative sloping relationship between the containment rupture timing and the SV_Frac. The early and late timing of the containment rupture is described in Section 4.2.2.1, However, this presentation clearly shows an early containment failure (i.e., the lower group of points) only occurs when the SV_Frac>0.32. In the early containment failures with larger SV failures areas, the RCS depressurized and vented hydrogen to the containment prior to the hot leg rupture. When the hot leg ruptured and created an ignition source, the hydrogen from the RCS was already distributed throughout the containment. The resulting burn propagated throughout the containment and into the dome, which caused a rupture. However, these characteristics did not lead to as many early containment failures in the random ignition realizations due to random burns that limited the hydrogen build-up throughout the containment (i.e., see Section 4.2.1.5 for the impact on the non-random realization rupture timing).

In contrast to the early containment rupture timings, the late containment failures generally occurred when more hydrogen was retained in the RCS prior to the hot leg failure. When the pressurizer SVs operated normally (i.e., SV_Frac=0), the burn at RPV breach was moderate and the containment ultimately failed by over-pressurization from ex-vessel gas generation. Similarly, the containment always failed late if SV_Frac<0.3. A smaller SV failure area is less effective at depressurizing the RCS and transferring hydrogen throughout the containment. Between a SV_Frac of 0.3 to 1, there were both early and late containment failures. As discussed in Section 4.2.2.1 and with the priSVcycles parameter, the timing of the valve failure contributed to both results. An early valve failure would allow more hydrogen to be vented into the containment whereas a late valve failure vented less.

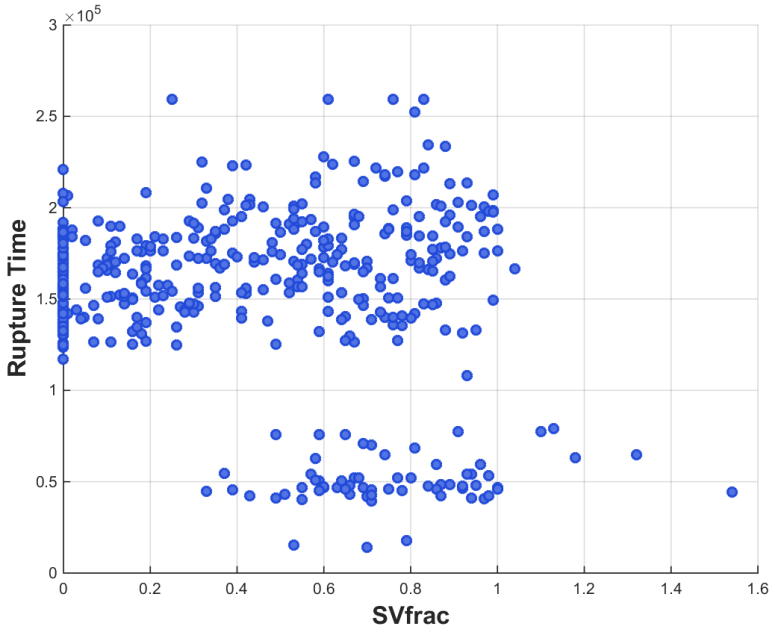

Figure 4-71 Scatterplot of rupture time versus SV_Frac

Burn Direction

Figure 4-72 shows the scatterplot of rupture time versus burn direction. The burn direction uncertainty parameter is interpreted as an integer. The parameter prescribes the values of 1, 2, and 3 to upward, horizontal, and downward ignition. The nominal hydrogen thresholds for those directions are 4%, 6.5%, and 9%, respectively. However, the precise hydrogen concentration for the parameters is also affected by the local temperature and the local steam concentration. The realizations with an upward burn direction allow ignition to occur at lower hydrogen concentrations. This can result in less energetic burns. However, it can also result in more burns that increases the potential for a burn propagation to other regions. The propagation criteria after a burn has started is identical for all values of burn direction. The results are relatively uniform and not suggestive of a significant correlation to rupture timing. [31]

[31] The random ignition criteria of 10% hydrogen concentration was used, which is the MELCOR default concentration for spontaneous ignition. In addition, all active ignition values used this value. Consequently, this parameter had no impact in the uncertainty sampling.

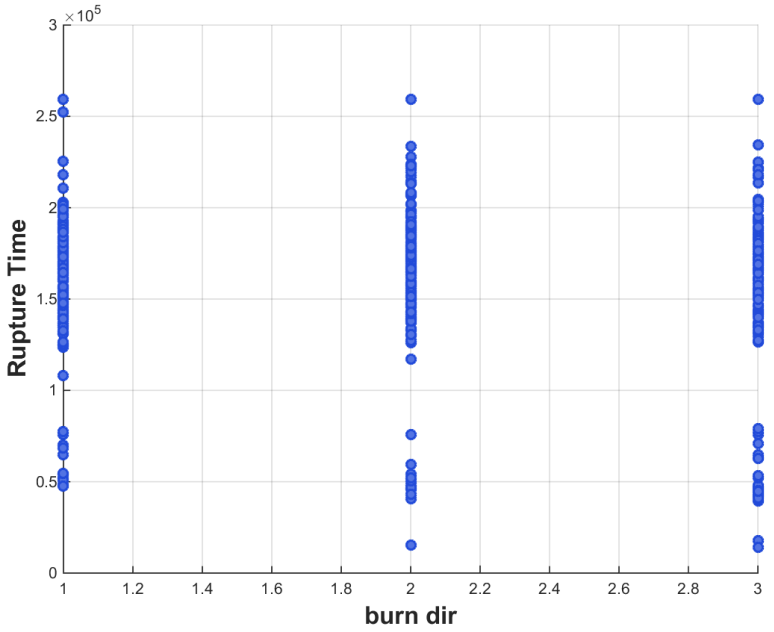

Figure 4-72 Scatterplot of rupture time versus burn direction

Ajar

The Ajar parameter represents the non-dimensional opening area of the lower ice condenser doors after they fully opened (i.e., exceeded the maximum differential pressure for opening). The ice condenser doors will stick at the AJAR fraction thereafter. The AJAR parameter addresses the uncertainty in the damage of the lower door hinges once they have opened the maximum range.

Figure 4-73 shows the scatterplot of rupture time versus Ajar. The dense cluster of points with low values of Ajar and high rupture time supports the positive regression coefficient on Ajar in the rank regression results. Additionally, the same region of the input space has the least dense collection of low rupture time data points. Thus, for low values of Ajar, the rank regression model can attribute variance in rupture time to variation in Ajar, whereas this relationship is not apparent for higher values of Ajar.

It was hypothesized the Ajar parameter would impact the lower compartment steam concentration by forming a natural circulation pattern between the lower compartment and the ice chests. The results show some trends for the impact of Ajar on the containment failure timing. Figure 4-73 shows a trend between a large number of late containment realizations at low values of Ajar versus more early containment failures with larger values of Ajar. In addition, the timing of the late containment failure is relatively uniform at small values of Ajar while values >0.2 show more scatter. These trends are consistent with the expected impact of Ajar.

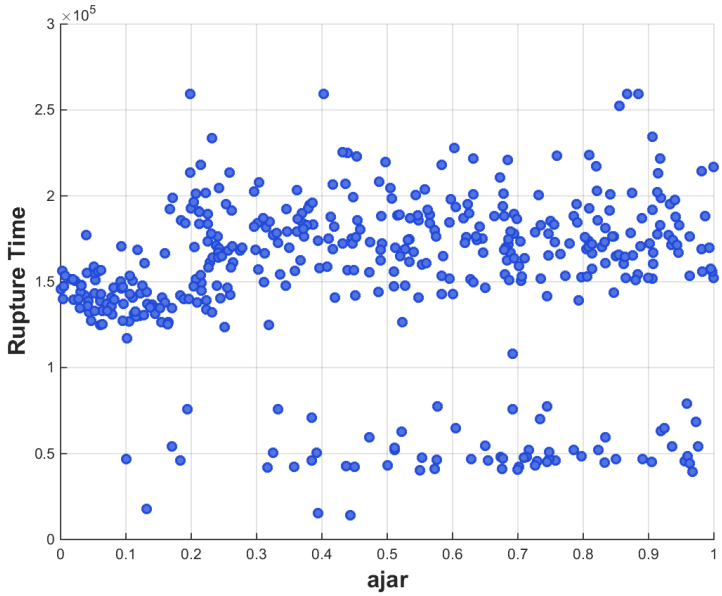

Figure 4-73 Scatterplot of rupture time versus Ajar

4.3 Analysis of Select MELCOR Individual Realizations

Additional insights related to accident progression can be obtained through investigation of single realizations. A set of single realizations listed in Table 4-13 was chosen for investigation in greater detail to identify phenomena driving the Cs and I releases to the environment and in-vessel hydrogen production. The set was selected from those realizations where early or late release was observed or low or high release magnitudes were observed. Note that numbers 2 and 6, 4 and 10, and 5 and 7 represent the same realization; thus, a total of 10 single realizations were investigated.

Table 4-13 Single realizations for detailed analysis.

I.D.	Selection criterion	Rlz number (Rlz)*
1	The base STSBO UA case	Base calculation
2	The case with earliest containment rupture	338
3	A case with containment remaining intact at 72 hr	171
4	The case with the earliest FTC of a pressurizer SV	142
5	A case without a FTC of a pressurizer SV	469
6	A case with coincident RPV breach and containment rupture	338
7	The case with the least in-vessel hydrogen production	469
8	The case with the most in-vessel hydrogen production	225
9	The case with the smallest Cs release to the environment	174
10	The case with the largest Cs release to the environment	142
11	The case with the earliest RPV breach	551
12	The case with the latest RPV breach	148
13	A case without hot leg rupture	77
14	A case with early RPV breach and early containment rupture not coincident	133

*Note, all realizations are without random sources of ignition

Figure 4-74 illustrates a comparison of the select realizations with respect to when the reactor vessel is first breached and when the steel containment vessel ruptures. The reactor vessel could breach first from a hot leg rupture or from lower head failure. The containment rupture could be sudden in response to a large deflagration or eventual as the containment continually pressurized from heat produced by fission product decay and from gasses produced through core-concrete interactions. Containment failure coincident with hot leg rupture and a large deflagration occurred in realizations 338, 77 and 148. In realization 171, containment rupture did not occur within the 72 hours modeled in the MELCOR calculation.

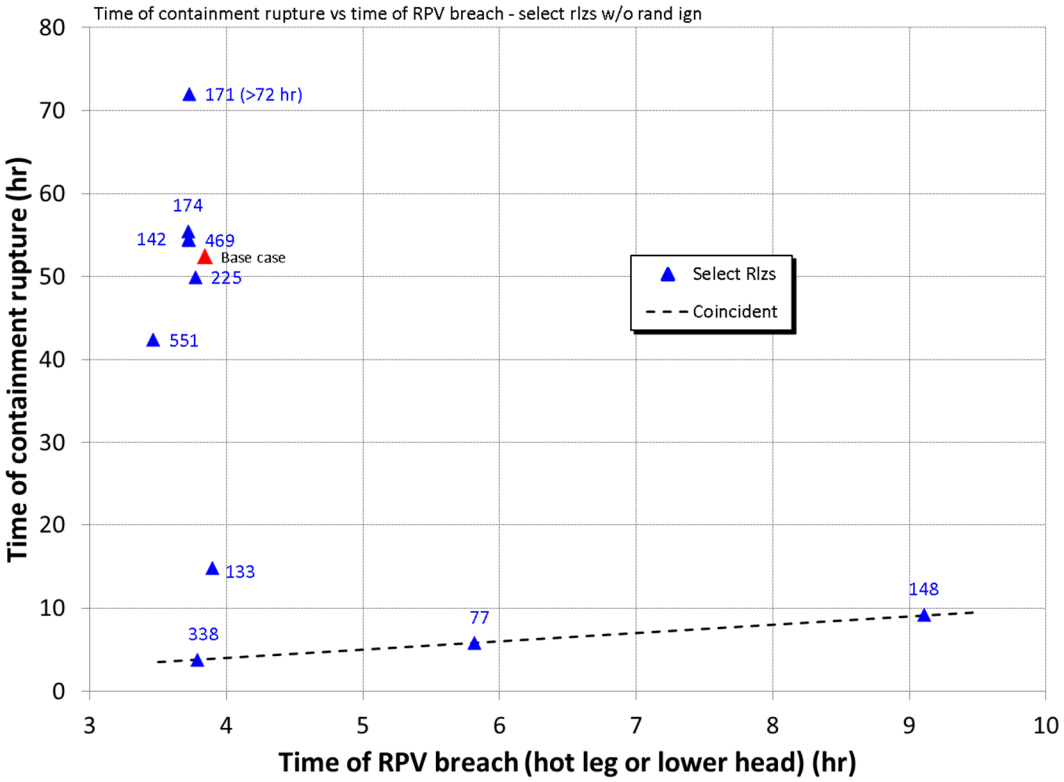

Figure 4-74 Time of containment rupture versus time of RPV breach for selected realizations without random ignition

The sampled values of the uncertain parameters in the select realizations are presented in Table 4-14. Table 4-15 lists the timing of key events, important occurrences and attributes, the magnitudes of Cs and I releases, and the amounts of hydrogen produced in-vessel in the realizations.

Table 4-14 Select realizations sampled parameters.

	Pressurizer SV cycles to FTC			Pressurizer SV open area fraction given FTC									
Rlz	SV-1	SV-2	SV-3	SV-1	SV-2	SV-3	Melting temperature of UO2-ZrO2 eutectic	Containment rupture pressure (psig)	Burn direction*	Aerosol shape factor	Differential pressure that tears the fabric seal (psid)	Fabric seal open area fraction given tearing	Ice condenser door open area fraction given FTC
77	33	10	6	0.65	0.55	0.51	2384.5	65.5	1	1.03	41.25	1.12	0.25
133	3	145	25	0.64	0.87	0.95	2483.2	72.8	2	1.40	49.54	1.73	0.72
142	1	7	139	0.97	0.93	0.63	2399.4	74.9	1	2.48	44.51	0.05	0.54
148	11	42	41	0.99	0.04	0.80	2566.8	77.9	2	2.08	35.68	1.73	0.44
171	148	65	32	0.75	0.59	0.53	2324.0	63.9	2	1.86	38.40	1.01	0.76
174	246	20	3	0.67	0.61	0.38	2441.2	77.5	3	1.48	39.61	1.89	0.91
225	69	27	23	0.56	0.14	0.60	2494.5	70.5	2	2.10	43.70	1.73	0.57
338	2	19	106	0.98	0.11	0.19	2454.8	59.9	2	1.22	48.06	0.05	0.20
469	159	145	229	0.34	0.20	0.74	2329.1	69.7	3	1.75	53.54	0.30	0.36
551	2	137	5	0.16	0.44	0.31	2475.5	59.0	3	1.08	26.59	0.05	0.31
Base	45	45	45	0.50	0.50	0.50	2479.0	67.0	1	1.5	43.00	1.73	0.50

* Direction of propagation from the ignition location: 1 = upward, 2 = lateral, 3 = downward

Table 4-15 Selected realization results.

Rlz	Przr SV combined number of cycles	Przr SV combined open area fraction given FTC	Time of RPV breach (hr)	Progression of containment pressure to rupture*	Time of containment rupture (hr)	In-vessel H_2 production (kg)	Fractional I release by 72 hr	Fractional Cs release by 72 hr
77	33	0.65	5.82	Sudden	5.82	440.4	0.091	0.031
133	3	0.64	3.90	Sudden	14.81	442.2	0.105	0.050
142	1	0.97	3.72	Continual	54.50	404.3	0.102	0.263
148	11	0.99	9.11	Sudden	9.20	488.3	0.134	0.133
171	72	No FTC	3.73	Continual	>72.00	337.4	0.000	0.000
174	73	No FTC	3.72	Continual	55.44	588.2	0.005	0.001
225	69	0.56	3.77	Continual	49.91	667.4	0.034	0.009
338	2	0.98	3.79	Sudden	3.79	400.7	0.091	0.078
469	72	No FTC	3.73	Continual	54.40	303.1	0.022	0.007
551	16	0.16	3.46	Continual	42.42	585.1	0.057	0.017
Base	45	0.50	3.85	Continual	52.39	448.5	0.069	0.063

* A sudden rise to rupture immediate to a deflagration or a continual increase without rupture immediate to a deflagration

To support an understanding of the differences between selected realizations, comparisons of pairs of realizations were made.

Comparisons between the realization with earliest containment rupture (Rlz 338) and a realization with containment remaining intact at 72 hr (Rlz 171)

Rlz 338 experienced the earliest rupture of the steel containment vessel while Rlz 171 did not experience a rupture of the vessel within the 72-hr duration of the calculation. Figure 4-75 and Figure 4-76 show the pressure responses of containment in Rlz 338 and Rlz 171, respectively. Also shown in these figures is the integral energy produced by deflagrations in the whole of containment and in the containment dome. Evidenced is that containment ruptured in Rlz 338 on an energetic deflagration where over half of the energy in the burn was produced in the containment dome. The deflagration was coincident with the rupture of an RCS hot leg. There were no deflagrations in Rlz 171 energetic enough to rupture containment and there was no involvement of the containment dome in the deflagration that occurred coincident with the hot leg rupture in Rlz 171.

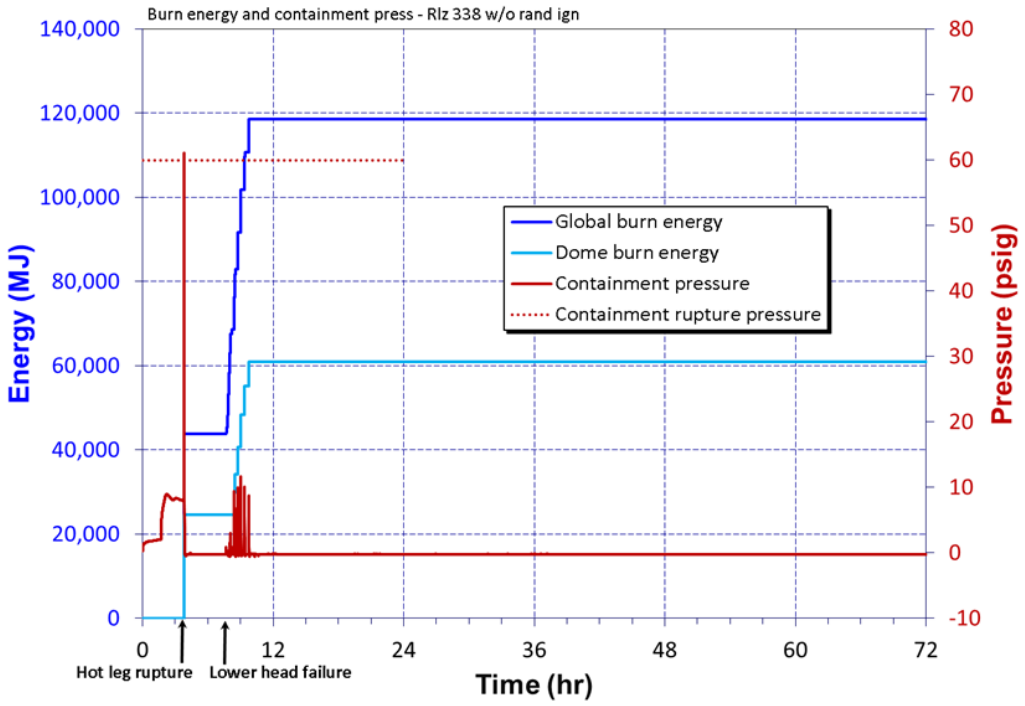

Figure 4-75 Burn energy and containment pressure for Rlz 338 w/o random ignition

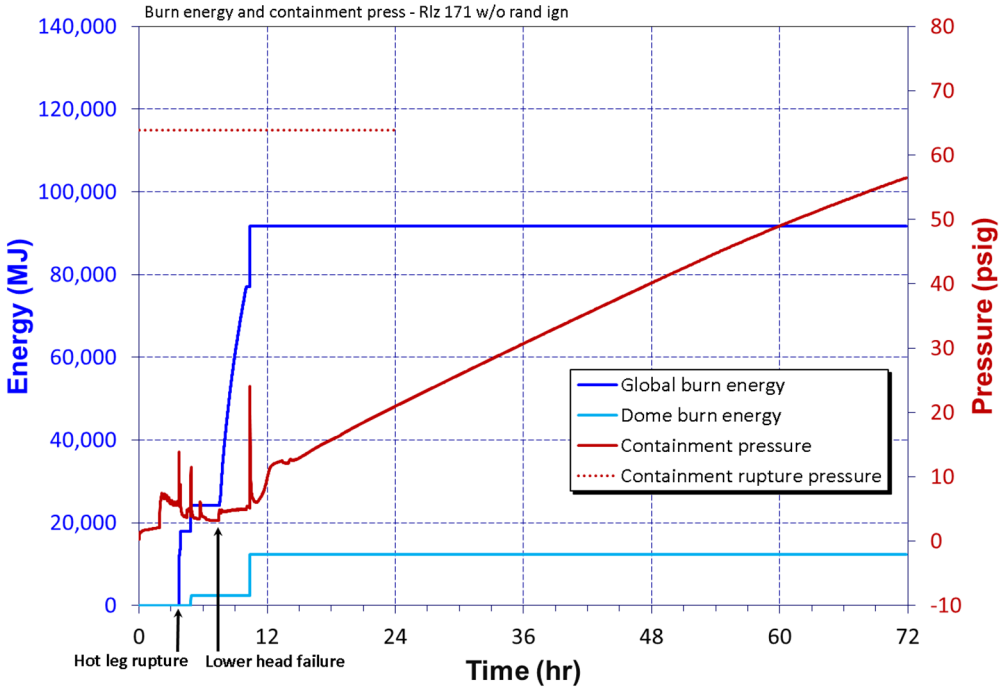

Figure 4-76 Burn energy and containment pressure for Rlz 171 w/o random ignition

In the calculation set performed without random ignition, it is important to note that ignition was disallowed until a hot leg ruptured, the pressurizer surge line ruptured, or core debris relocated to the containment floor. In the MELCOR calculations, typically a hot leg rupture occurred first. Consequently, the first opportunity for hydrogen to burn was at hot leg rupture. Substantial hydrogen may have vented to containment through the pressurizer SVs and a broken PRT burst disk before hot leg rupture, but it would not have been allowed to burn until a hot leg ruptured. As shown in Figure 4-77, roughly twice the hydrogen was produced by the time of hot leg failure in Rlz 338 than in Rlz 171 clearly providing potential for a substantially larger burn in Rlz 338 at hot leg rupture.

The difference in the amount of hydrogen produced up to the time of hot leg failure in Rlzs 338 and 171 is attributable to a difference in pressurizer SV function. In Rlz 338, the lowest set-point valve failed to close in a fully open position (as opposed to failing to close in a partially open position) after only 2 successful cycles of operation. In Rlz 171, the lowest set-point valve did not experience a failure to close. The venting of the RCS by the stuck-open SV in Rlz 338 was conducive of greater hydrogen production leading up to hot leg rupture. Virtually all hydrogen produced up to the time of hot leg rupture in Rlz 338 was vented through the stuck-open SV and a broken PRT burst disk to the containment as can be seen by comparing Figure 4-77 and Figure 4-78. Much of this hydrogen passed through the ice chests to the containment dome. Comparatively little hydrogen was vented through the functioning SV in Rlz 171.

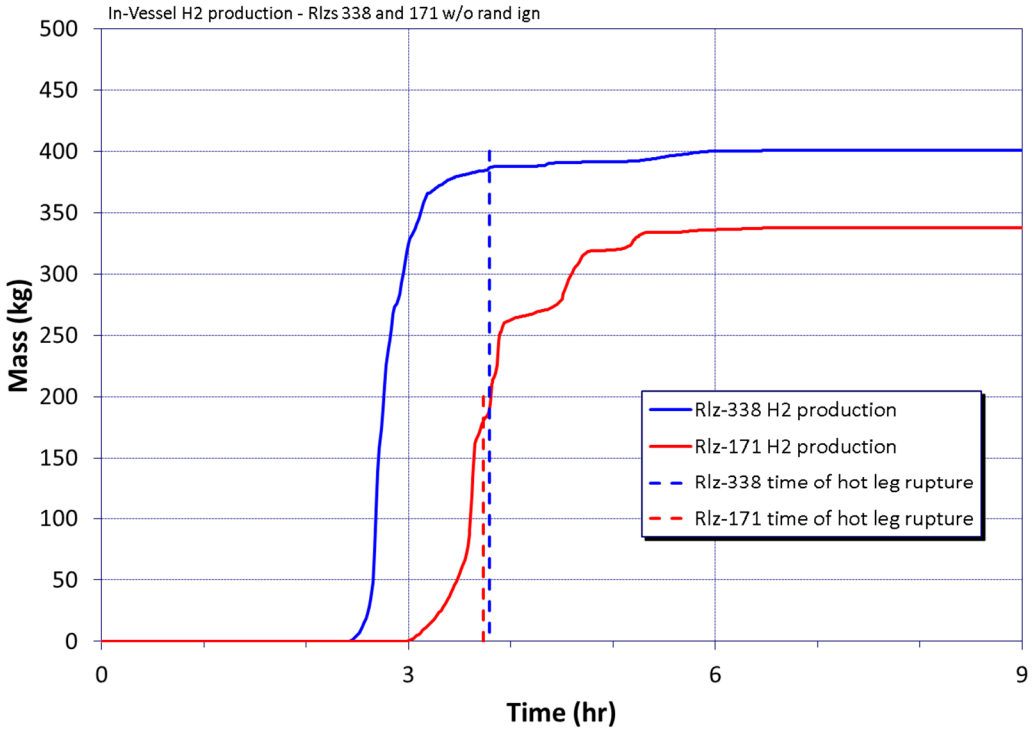

Figure 4-77 In-vessel hydrogen production for Rlzs 338 and 171 w/o random ignition

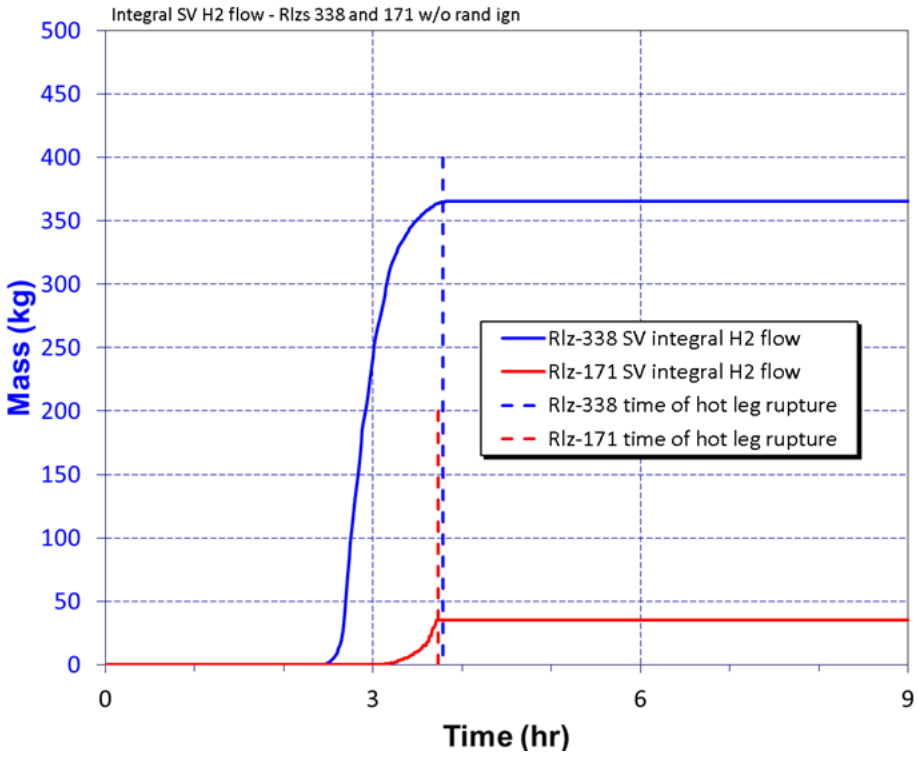

Figure 4-78 Integral safety valve hydrogen flow for Rlzs 338 and 171 w/o random ignition

For Rlz 338 leading up to hot leg rupture, Figure 4-79, Figure 4-80 and Figure 4-81 show a containment primed with hydrogen ready to burn given an ignition source. Figure 4-79 shows hydrogen concentration throughout containment being supportive of a burn while Figure 4-80 shows containment not overly laden with steam so as to prohibit a burn. Figure 4-81 shows the conditions in the containment dome in detail relative to supporting a burn. The information in Figure 4-81 is relative to a burn being propagated to the dome as opposed to originating in the dome, because burns were only allowed in lower containment in the calculations without random ignition. The only way a burn could occur in the dome was if a burn propagated there from lower containment. The conditions in Figure 4-81 are supportive of a burn when lines are solid and not supportive of a burn where the lines are dashed. Inerting gas and fuel lines in the figure are reflective of each other, e.g., too much inerting gas for the amount of fuel present is indicative in the same way as too little fuel for the amount of inerting gas.

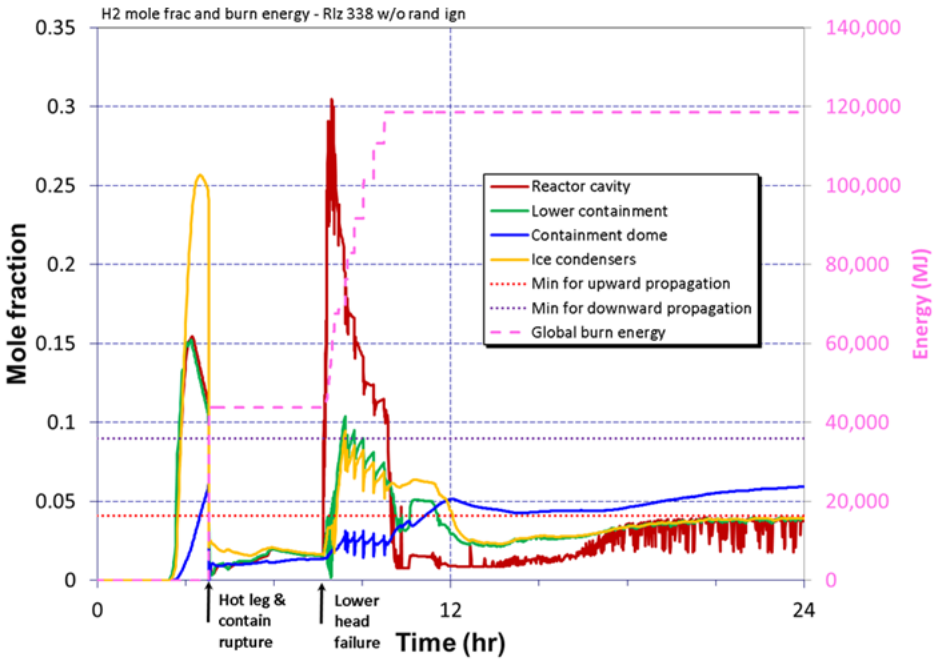

Figure 4-79 Hydrogen mole fraction and burn energy for Rlz 338 w/o random ignition

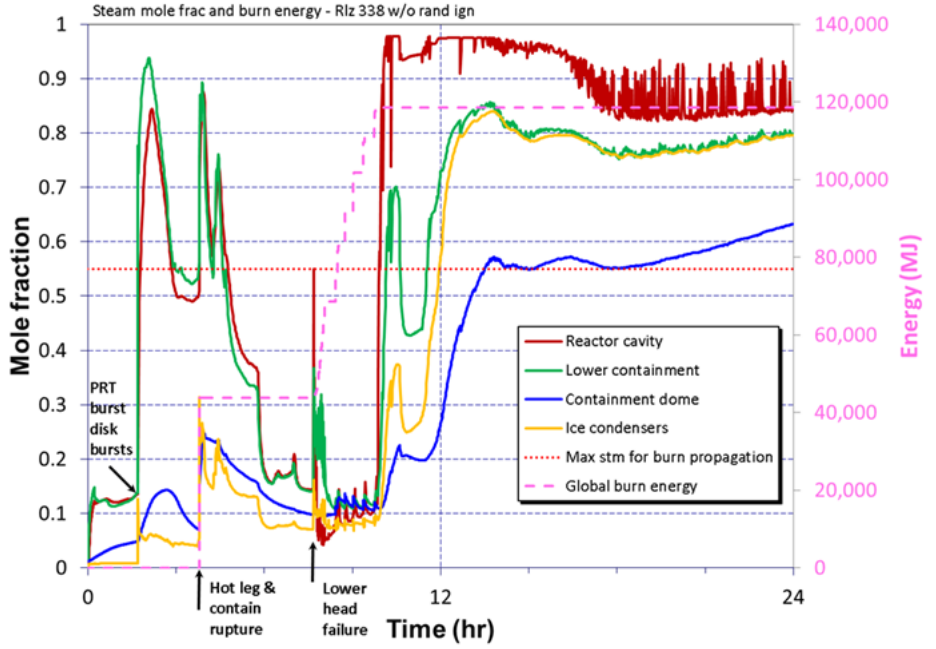

Figure 4-80 Steam mole fraction and burn energy for Rlz 338 w/o random ignition

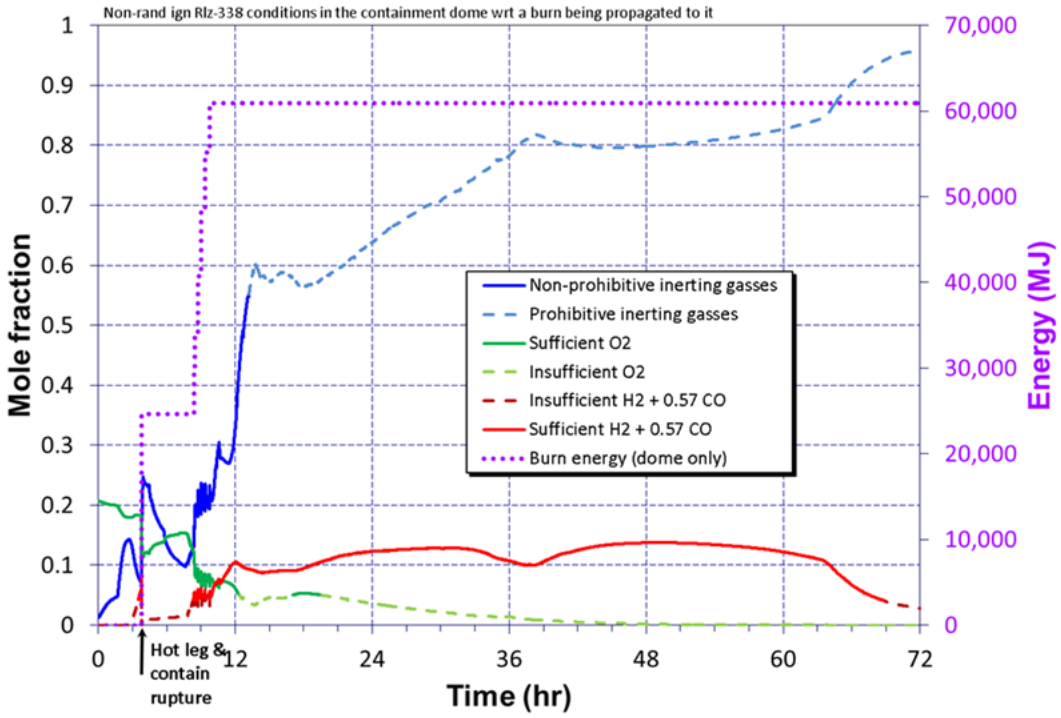

Figure 4-81 Conditions in containment dome with respect to burn propagation for Rlz 338 w/o random ignition

For Rlz 171 Figure 4-82 shows, leading up to hot leg rupture, a containment with considerably less hydrogen than in Rlz 338. Similar to Figure 4-80 for Rlz 338, Figure 4-83 shows containment not overly laden with steam so as to prohibit a burn. Figure 4-84 shows the conditions in the containment dome in detail relative to supporting a burn being propagated to the dome. A burn occurred in Rlz 171 at hot leg rupture but of considerably less magnitude than in Rlz 338 and the burn was insufficient to rupture the steel containment vessel.

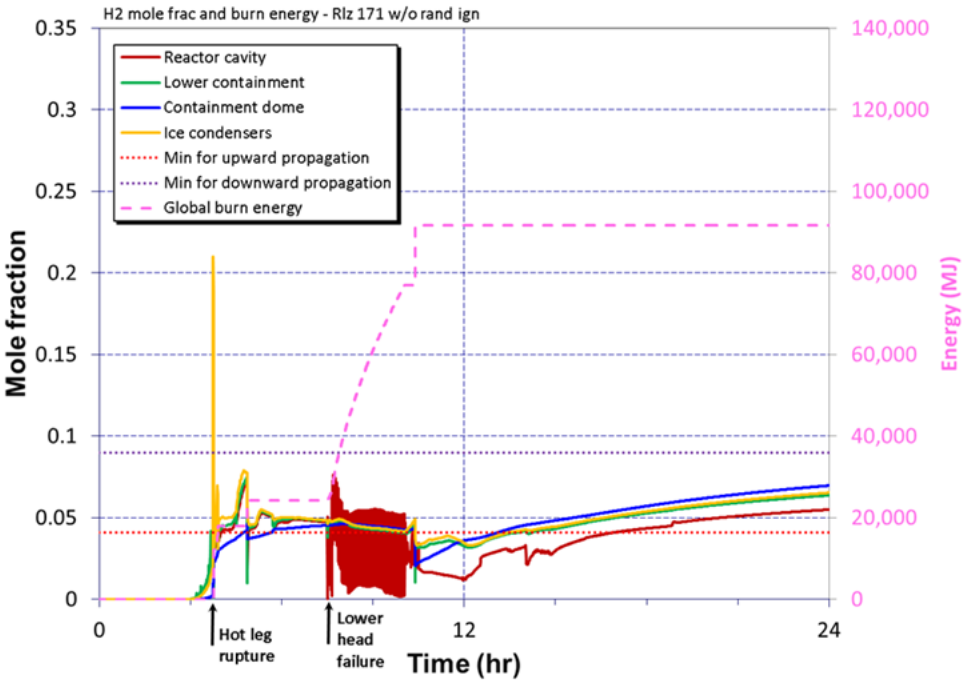

Figure 4-82 Hydrogen mole fraction and burn energy for Rlz 171 w/o random ignition

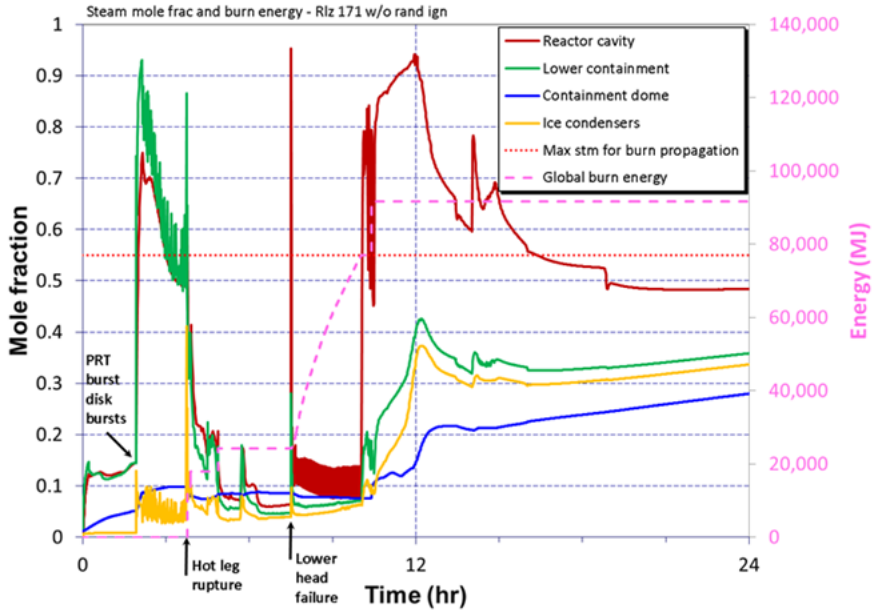

Figure 4-83 Steam mole fraction and burn energy for Rlz 171 w/o random ignition

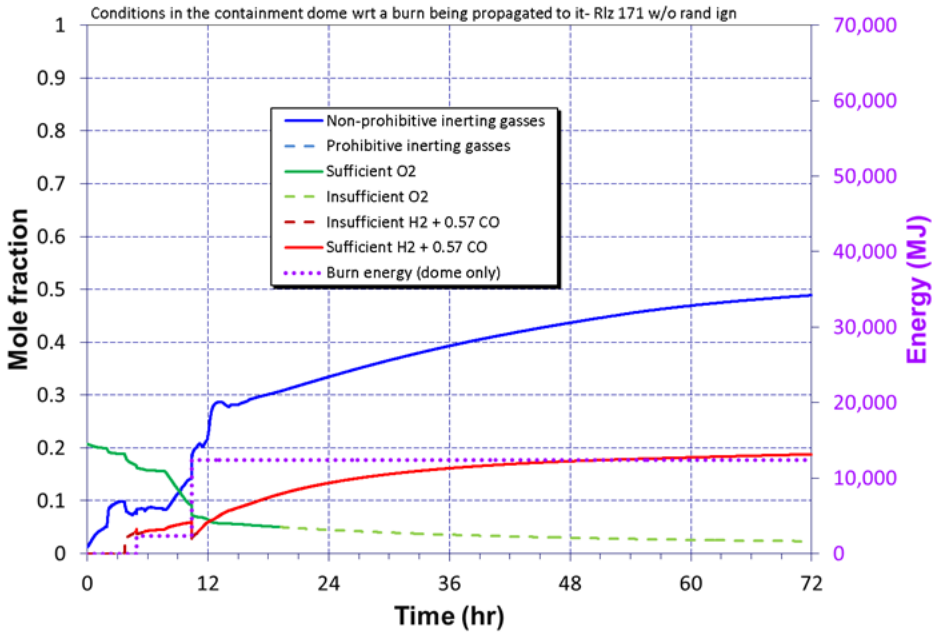

Figure 4-84 Conditions in containment dome with respect to burn propagation for Rlz 171 w/o random ignition

Following hot leg rupture in Rlz 171 through to the end of the calculation, there is little opportunity for large deflagrations to occur. This is because of either a lack of sufficient hydrogen or an excess of inerting gasses. A couple of energetic burns occur, as evidenced in Figure 4-76, but the burns don't threaten containment. Figure 4-85 shows how conditions in lower containment are almost continually unsupportive of a burn originating in lower containment. The existence of an ignition source, i.e., hot gas emanating from a hot leg breach or core debris relocated to the containment floor, is included in this Figure 4-85. A large number of inconsequential burns occur in the reactor cavity as combustible gasses generated by core-concrete interactions are burned off locally. These burns don't propagate elsewhere because of conditions in lower containment being unsupportive.

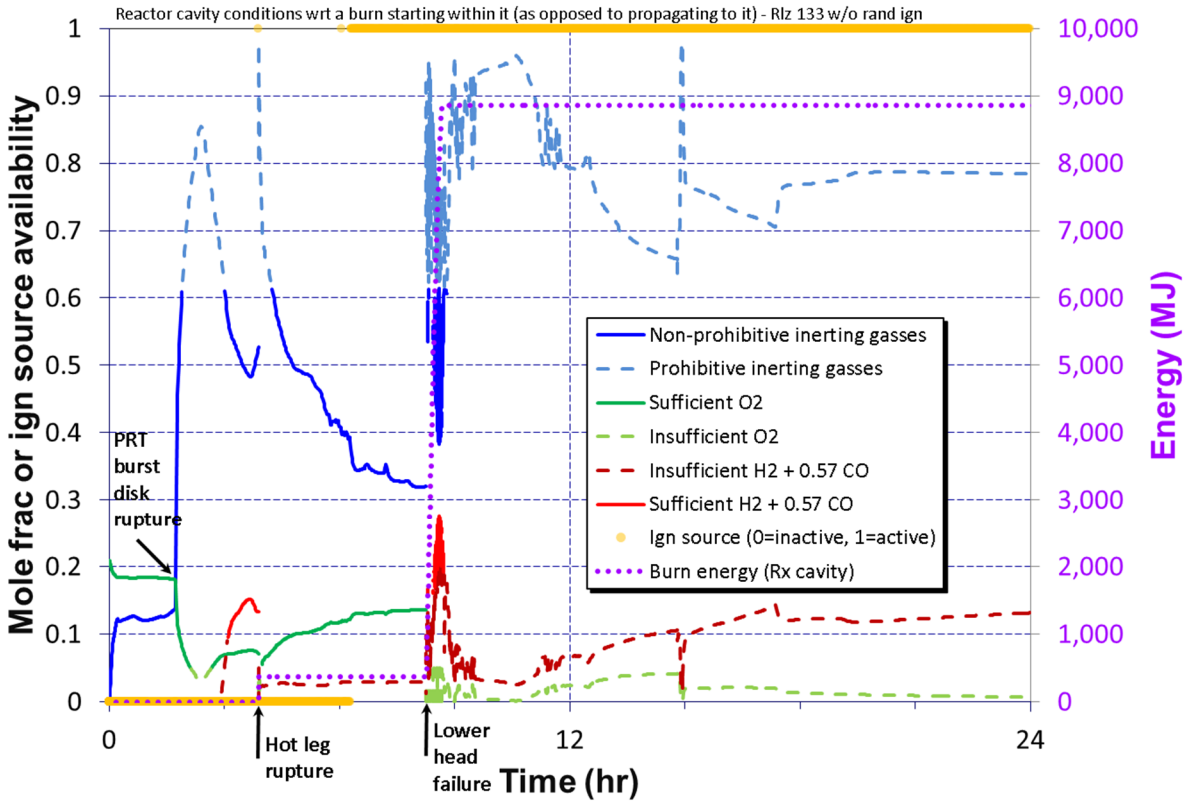

Figure 4-85 Lower containment conditions for Rlz 171

Comparisons between the case with the earliest FTC of a pressurizer SV (Rlz 142) and a case without a FTC of a pressurizer SV (Rlz 469)

The results of Rlzs 338 and 142 differ markedly in that Rlz 338 ruptured containment at 3.79 hr coincident with hot leg rupture and a large deflagration; whereas, Rlz 142 didn't fail containment until 54.5 hr after a continual pressurization. The sampled parameter of the pressure necessary to rupture the steel containment vessel was responsible for this difference. The two realizations show nearly identical trends through hot leg rupture but the higher containment rupture pressure defined in Rlz 142 isn't reached. This can be seen by comparing Figure 4-86 associated with Rlz 142 to Figure 4-75 associated with Rlz 338.

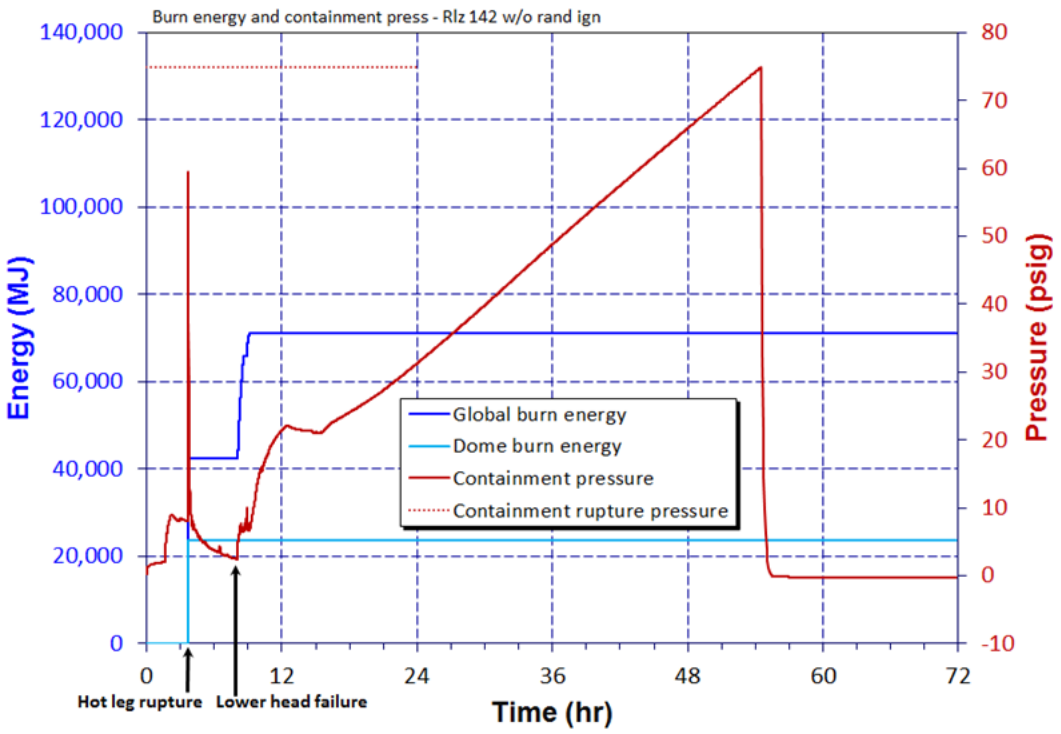

Figure 4-86 Burn energy and containment pressure for Rlz 142 w/o random ignition

Comparisons between a case with coincident RPV breach and containment rupture (Rlz 338) and a case with early RPV breach and early containment rupture not coincident (Rlz 133)

Rlz 338, characterized above, suffered a very energetic burn at the time of hot leg rupture that ruptured the steel containment vessel. Rlz 133 suffered a very similar burn but, as evidenced in Figure 4-87, a higher sampled value of the pressure necessary to rupture the containment vessel allowed the vessel to survive the sharp pressure rise resulting from the burn. The strong burn at the hot leg breach in Rlz 133 is attributable to a pressurizer SV failing to close after very few cycles, the same as described above for Rlz 338. While containment survived the strong burn in Rlz 133 at hot leg rupture, a later burn drove the containment pressure over sampled rupture pressure and the containment vessel ruptured. Review of Figure 4-88 through Figure 4-91 identifies that the later burn originated in the lower annulus (CV 11) and propagated to most of lower containment inside the crane wall (CV 9) and then to the containment dome. The energy released from burning in the dome contributed most to the overall energy released in the burn. Not all of containment participated in the burn, e.g., CV 8 and the reactor cavity, did not participate.

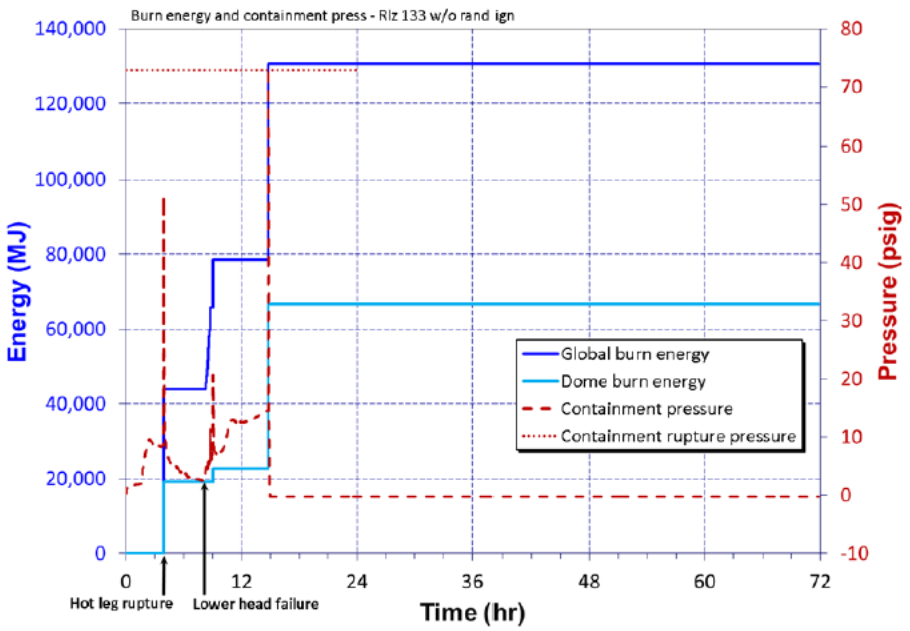

Figure 4-87 Burn energy and containment pressure for Rlz 133 w/o random ignition

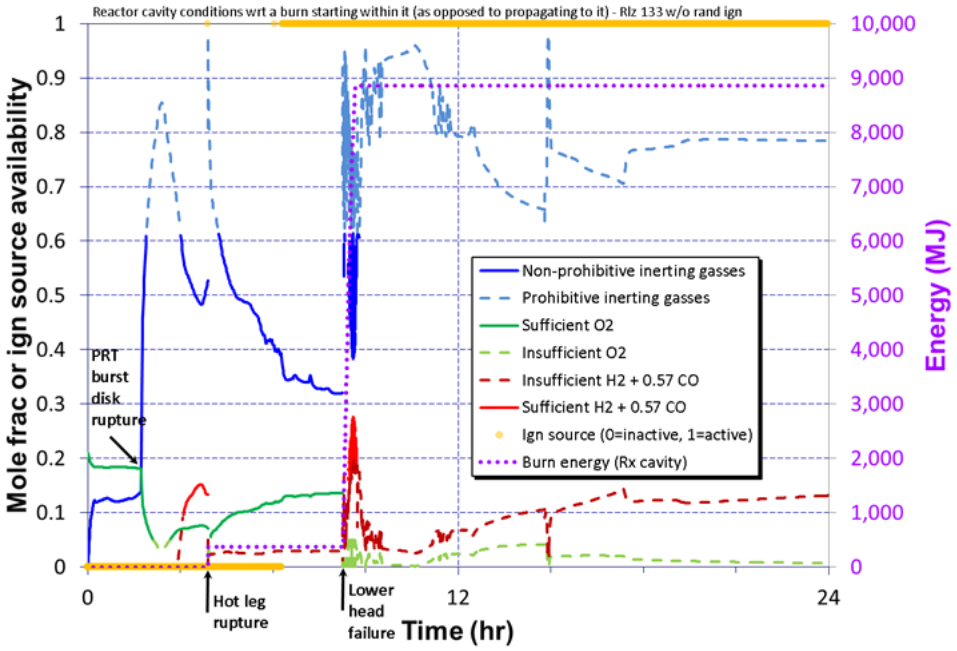

Figure 4-88 Reactor cavity conditions for Rlz 133 w/o random ignition

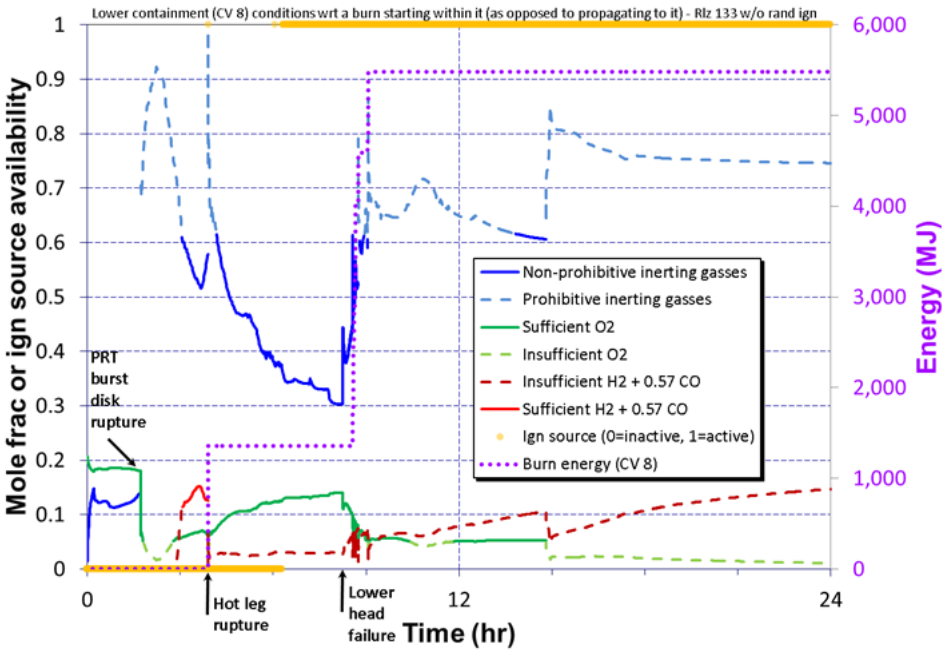

Figure 4-89 Lower containment conditions (CV 8) for Rlz 133 w/o random ignition

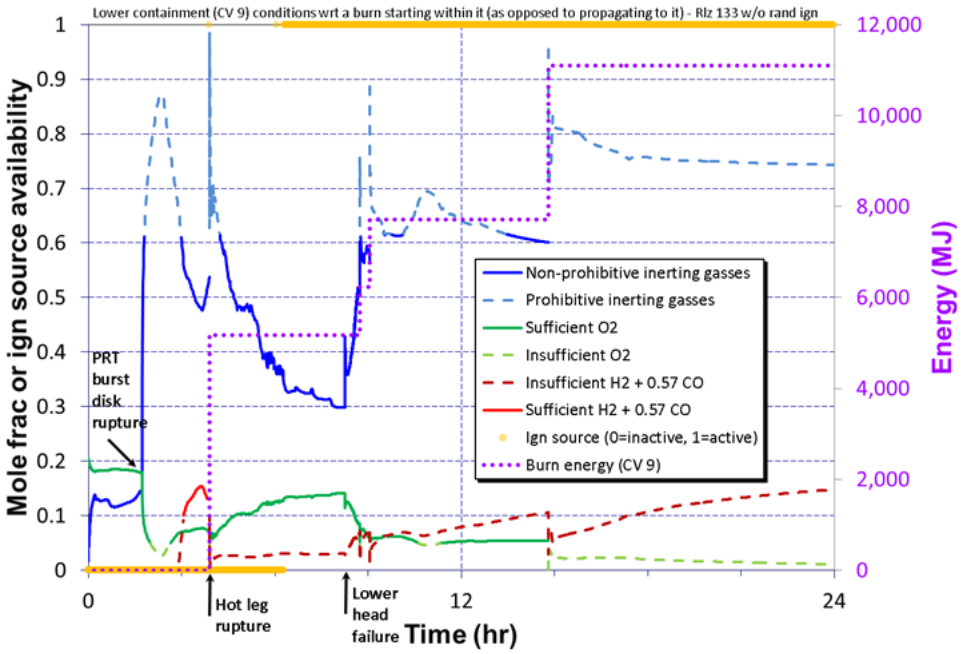

Figure 4-90 Lower containment (CV 9) for Rlz 133 w/o random ignition

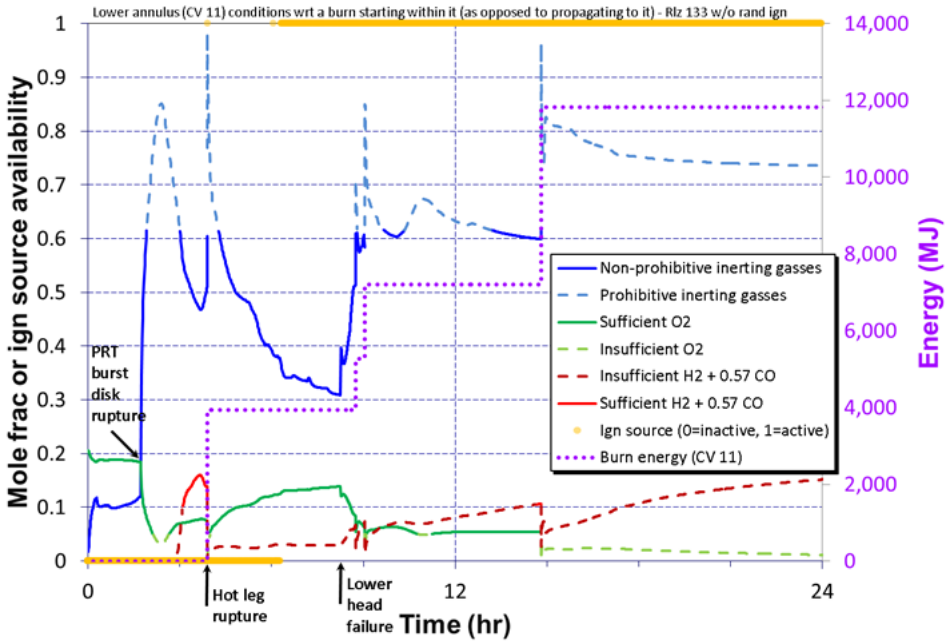

Figure 4-91 Lower annulus (CV 11) for Rlz 133 w/o random ignition

Comparisons between the case with the least in-vessel hydrogen production (Rlz 469) and the case with the most in-vessel hydrogen production (Rlz 225)

Table 4-14 and Table 4-15 identify general dependencies in the MELCOR calculations of in-vessel hydrogen production on the sampled values of the melting temperature of the eutectic formed between UO_2 and ZrO_2 and the combined number of cycles completed by the system of 3 parallel SVs atop the pressurizer. Higher melting temperatures and larger numbers of cycles generally led to greater hydrogen production with melting temperature being the dominant influence. Fuel rod collapse was configured to occur in the MELCOR calculations when oxidized cladding reached the sampled value of the melting temperature UO_2-ZrO_2 eutectic. Robust oxidation of a fuel rod ends when the rod collapses and lower melting temperatures of the eutectic lead to earlier rod collapse. Rlz 469 had a considerably lower eutectic melting temperature than Rlz 225. Consequently, fuel collapsed earlier, less oxidation took place, and less hydrogen was produced in Rlz 469 relative to Rlz 225. Figure 4-92 illustrates these differences. The vertical violet color in the reactor core insets in Figure 4-92 indicate intact fuel rods. At 5 hours little fuel remains intact in Rlz 469 and hydrogen production has abated. In Rlz 225, contrarily, substantial fuel remains intact at 5 hr and hydrogen production remains strong. The Rlz 469 sampled eutectic melting temperatures fell below the Zircaloy breakout temperature (2350 K). As shown in Figure 4-43, all the realizations with a sampled eutectic melting temperatures below the Zircaloy breakout temperature resulted in the very low in-vessel hydrogen generation. Since the fuel collapsed before the molten Zircaloy behind the oxide shell is released, molten Zircaloy does not oxidize. The resultant debris geometry is not supportive of steam flow for oxidation as shown Figure 4-92.

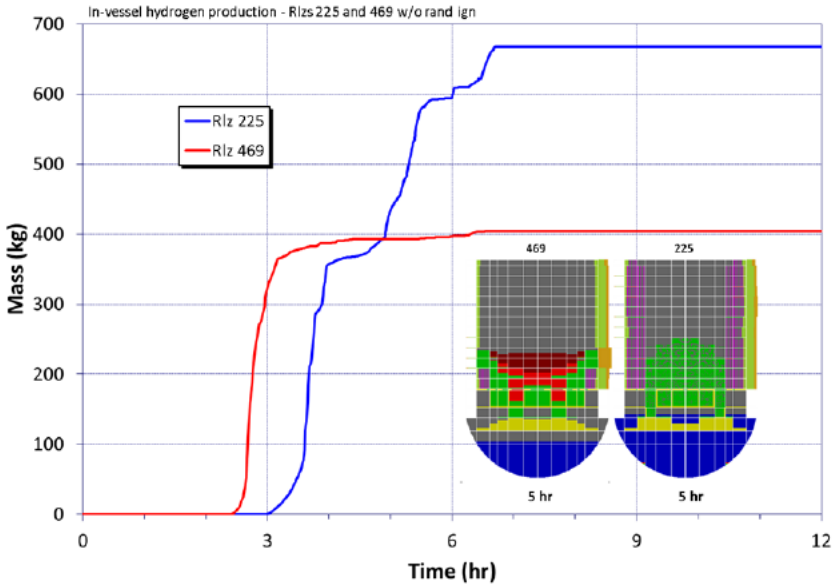

Figure 4-92 In-vessel hydrogen production for RLZs 225 and 469 w/o random ignition

Comparisons between the case with the smallest Cs release to the environment (Rlz 174) and the case with the largest Cs release to the environment (Rlz 142)

Figure 4-93 and Figure 4-94 show the distribution of cesium between the RCS, containment, and environment for Rlz 174 and Rlz 142, respectively. These figures differ dramatically for reasons associated with successful functioning of the lowest set-point pressurizer SV in Rlz 174 and the very early failure (first cycle) of the valve to close in Rlz 142. The early stuck-open condition of the valve in Rlz 142 resulted in it being open at the onset of core damage. Consequently, much of the core inventory of fission products, including Cs as CsOH, CsI, and Cs_2MoO_4, carried to the PRT as the RCS vented through the stuck-open valve. The fission products deposited in the water volume of the tank and on the wall of the tank once the water boiled away. The heat generation from decay of the deposited fission products was considerable, and the PRT heated as a consequence. The heating is evidenced in Figure 4-95. The cesium compounds in the PRT vaporized continually in response to the heating, migrated from the tank, and aerosolized in the containment atmosphere. When the containment ruptured at 54.5 hr, as can be seen in Figure 4-96, the resulting drop in containment pressure aggravated the vaporization and the cesium released from the PRT escaped to the environment carried by flows seeking the breach in the dome of the containment vessel. The cesium escaping containment was considerable (26.3% of the initial core inventory). The fact that PRT wall temperature in Figure 4-95 exceeds the melting temperature of steel is a complication not accounted for in the MELCOR modeling. The excessive temperature suggests that the integrity of the tank would be lost. This temperature would probably reduce somewhat if the outside of the PRT were not modeled as adiabatic, i.e., facilitating heat rejection via convection and radiation might realistically lower the temperature to a value tolerable by steel. If the tank were to lose its integrity, some aerosolization of the fission products that had deposited in it seems likely as does the relocation of some fission products to the floor of containment. Neither of these redistributions of material are addressed in MELCOR. It is likely, however, that both would

reduce the concentration of fission products that caused the failure of the PRT, leading to less revaporization and less release to the environment than suggested by Rlz 142.

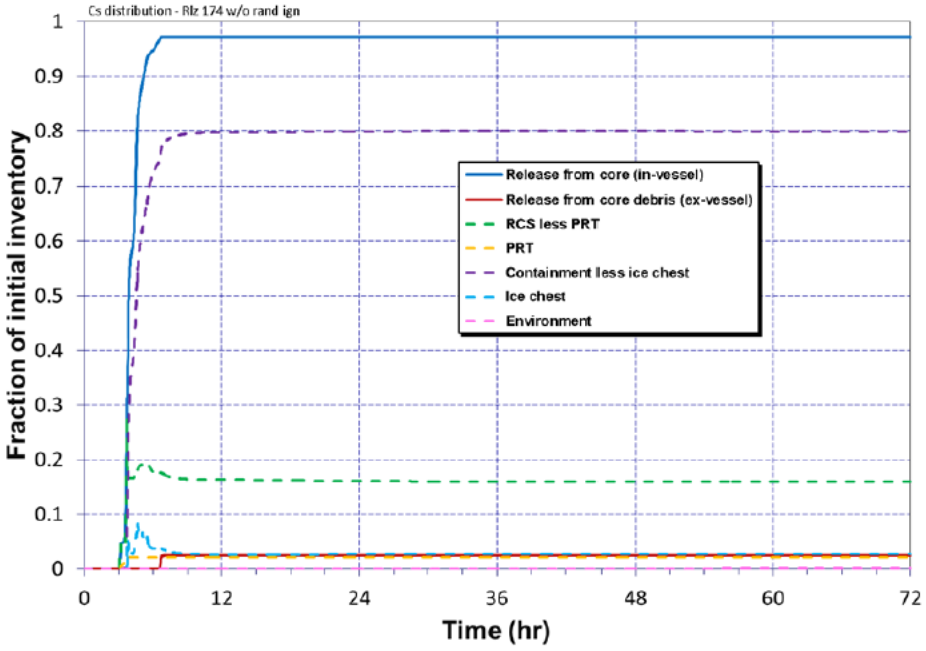

Figure 4-93 Cesium distribution for Rlz 174 w/o random ignition

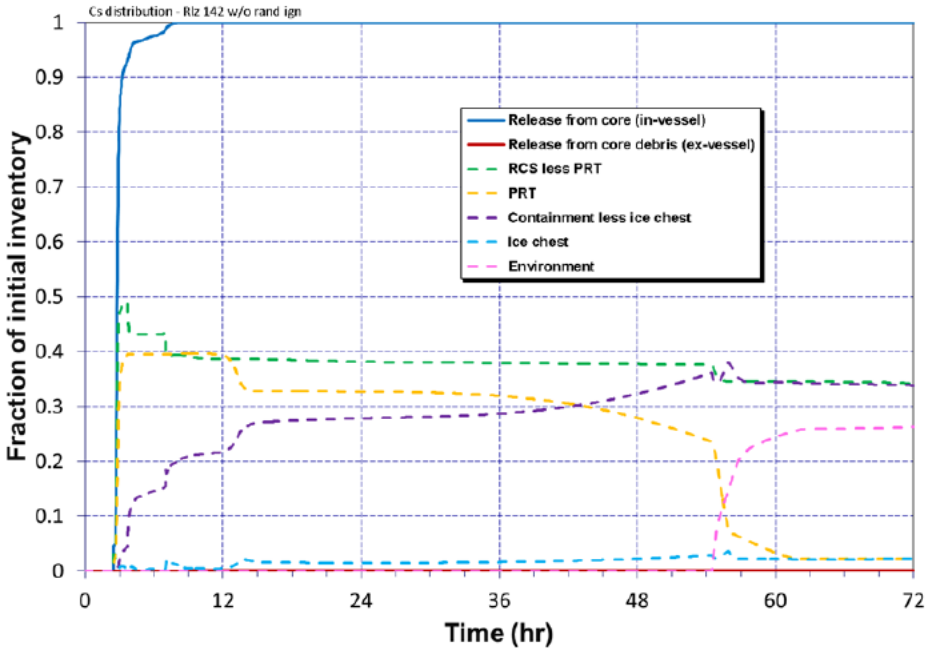

Figure 4-94 Cesium distribution for Rlz 142 w/o random ignition

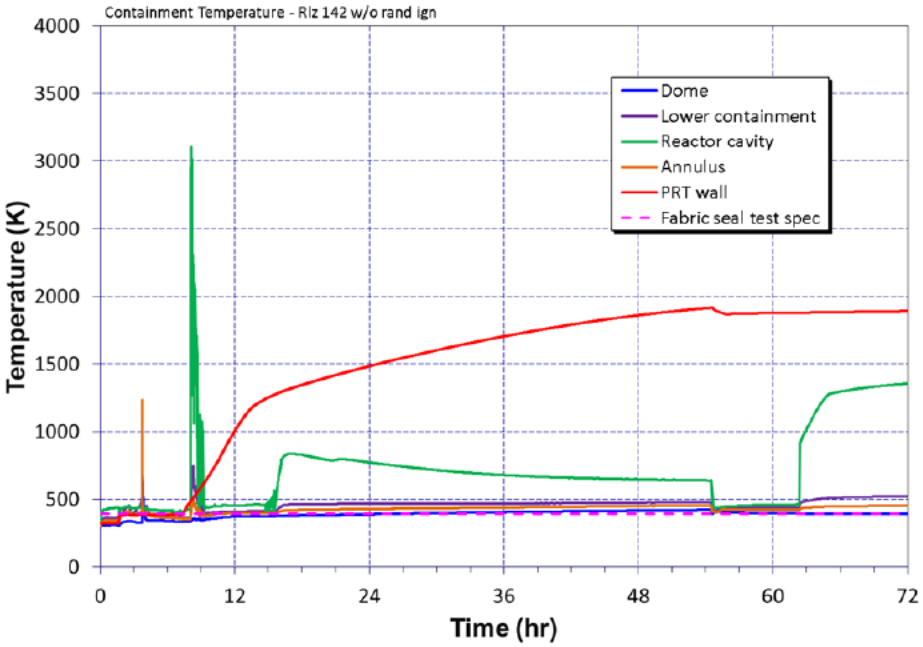

Figure 4-95 Containment temperature for Rlz 142 w/o random ignition

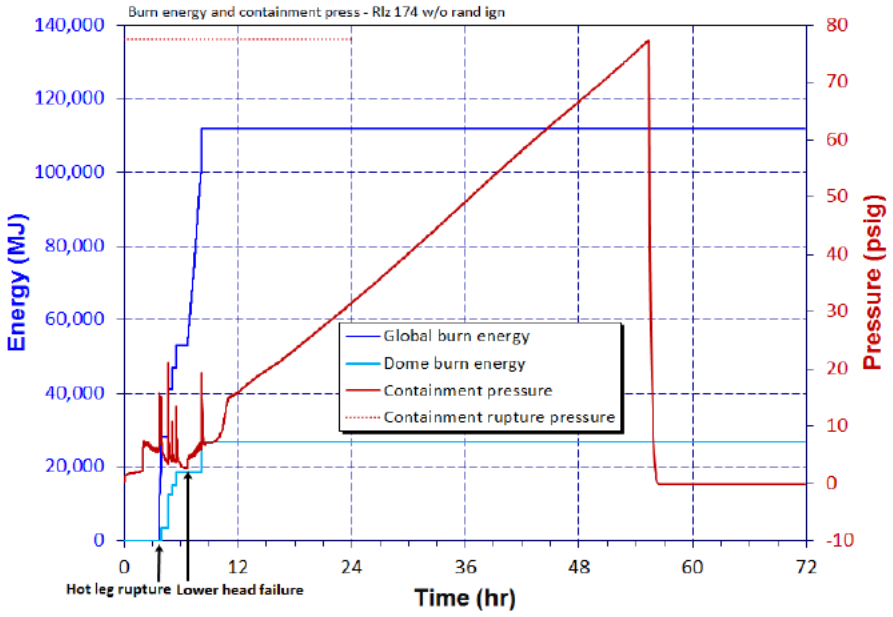

Figure 4-96 Burn energy and containment pressure for Rlz 174 w/o random ignition

Figure 4-96 and Figure 4-97 show for Rlz 174, information analogous to the information shown in Figure 4-86 and Figure 4-95 and for Rlz 142. Without a stuck-open SV, Rlz 174 exhibits little fission product deposition in the PRT, little heating of the PRT, and no release of cesium from the PRT at containment rupture. Cesium released from the fuel in-vessel and ex-vessel simply deposits and resides in a stable condition in the RCS and containment.

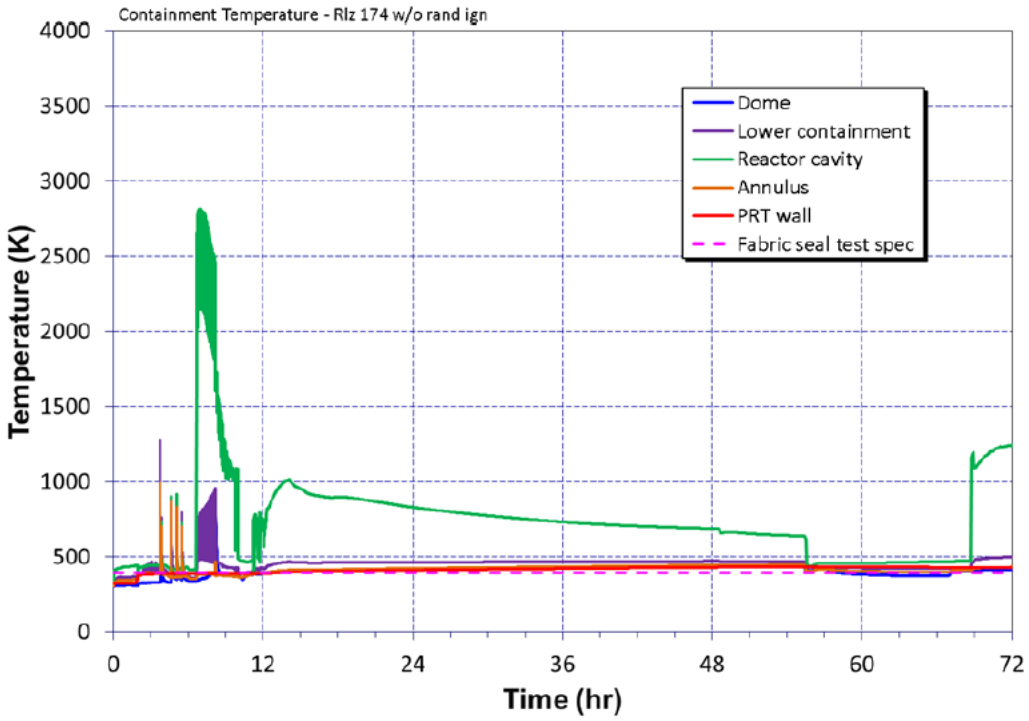

Figure 4-97 Containment temperature for Rlz 174 w/o random ignition

Comparisons between the case with the earliest RPV breach, Rlz 551 and the case with the latest RPV breach, Rlz 148

Realizations 551 and 148 were selected to compare the earliest versus the latest initial RPV breach. The specified uncertainty parameters in the two realizations uniquely accelerated and delayed the timing to the initial RPV breach, respectively. The key in-vessel uncertainty parameter differences and results included the following;

- Realization 551
  - SV #1 fails after 2 cycles with a fraction area of 0.1579
  - SV #2 cycled normally for 14 times, which was much less than the maximum number of cycles until failure (i.e., failure at 137 cycles)
  - The total number of SV cycles for the two SVs was 16
  - The eutectic melting temperature was 2475.5 K
  - The accumulator did not discharge prior to the initial RPV breach
  - The hot leg failed at 3.464 hr
- Realization 148
  - SV #1 fails after 11 cycles with a fraction area of 0.9867
  - SV #2 did not open
  - The total number of SV cycles was 11

- The eutectic melting temperature was 2566.8 K
- There was no hot leg failure
- The accumulator fully discharged prior to the initial RPV breach
- The RPV lower head failed at 9.109 hr

As noted above, SV #1 in Rlz 551 failed after two cycles with a small flow area. The SV #1 failure area was not sufficient to immediately depressurize the RPV as noted in Figure 4-98. Consequently, SV #2 cycled 14 times before the RPV began to depressurize due to the leakage through SV #1. The inventory loss out SV #1 led to the core uncovery but with a minimal RCS depressurization (see Figure 4-98 and Figure 4-99). The small SV #1 leakage area created optimum conditions for an early hot leg creep rupture. In particular, the small SV leakage area promoted high temperature gas flow from the degrading core towards the pressurizer while maintaining a relatively high RCS pressure. The hot leg creep index rose rapidly to 1 at 3.464 hr (see Figure 4-101), which indicates a hot leg failure. Following the rapid depressurization from the initial RPV breach of the hot leg, the full inventory of the accumulators discharged into the RCS (see Figure 4-100).

In contrast to the progression of events in Rlz 551, SV #1 cycled 11 times in Rlz 148 and then stuck almost fully open (i.e., 0.9867). The RCS depressurized below the accumulator set pressure (4.4 MPa) during the initial core uncovery, which started the accumulator water injection. The accumulator water flooded the core and cooled the hot leg nozzles (i.e., see the level response in Figure 4-99 and the first plateau in the hot leg creep rupture index in Figure 4-101). There was a rapid increase in steam production as the hot fuel boiled the accumulator water. The resultant steam production increased the RCS pressure, which stopped the accumulator injection (see the sharp pressurization at 3.5 hr in Figure 4-98). The RCS subsequently depressurized through the failed SV. The subsequent loss of inventory through the open SV uncovered the fuel (Figure 4-99) and heated the hot leg nozzle (i.e., see the second increase in the hot leg creep index at 4.8 hr in Figure 4-101). The RCS pressure fell below the accumulator pressure, which allowed a second accumulator injection. The cycle of an accumulator injection, an increase in core cooling, and an increase steam generation repeated three more times until the accumulator was empty. The accumulator water injection was very effective at interrupting the increase in the creep rupture index, which reached a maximum of 0.67 at 6.3 hr. The accumulator water was also effective at slowing the fuel core degradation. However, an uncoolable debris plenum formed in the lower bed following the final accumulator injection at 7.2 hours. The debris on the RPV lower head slowly heated the RPV lower head inner surface after 7.9 hours to above 1500 K (see the black line for the maximum lower head temperature in Figure 4-101). The RPV lower head yielded at 9.109 hours with the hot leg creep index below the failure threshold.

In summary, Rlz 551 included conditions that maximized an inventory loss while preventing a significant RCS depressurization. The early core uncovery at high pressure led to the earliest hot leg creep rupture of all the realizations. Rlz 148 included conditions that allowed a full RCS depressurization below the accumulator injection pressure. The resultant intermittent accumulator injections cooled the fuel and the hot leg, which prevented a hot leg failure and delayed the RPV lower head failure. The differences in the initial RPV breach timing from these two realization was the SV failure area as both had a relative small number of SV cycles.

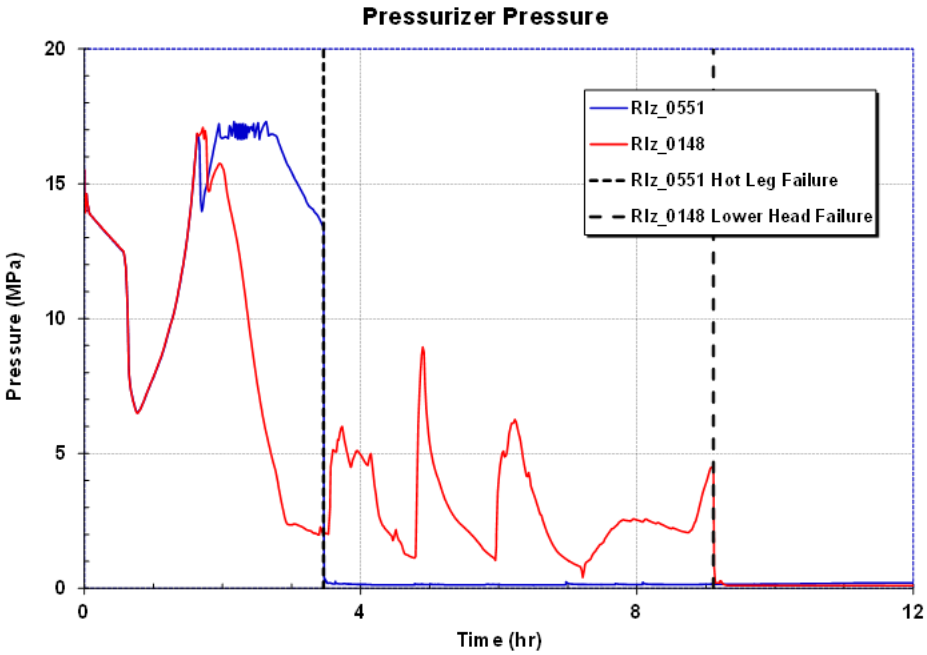

Figure 4-98 Pressurizer pressure responses for RIz 551 and 148

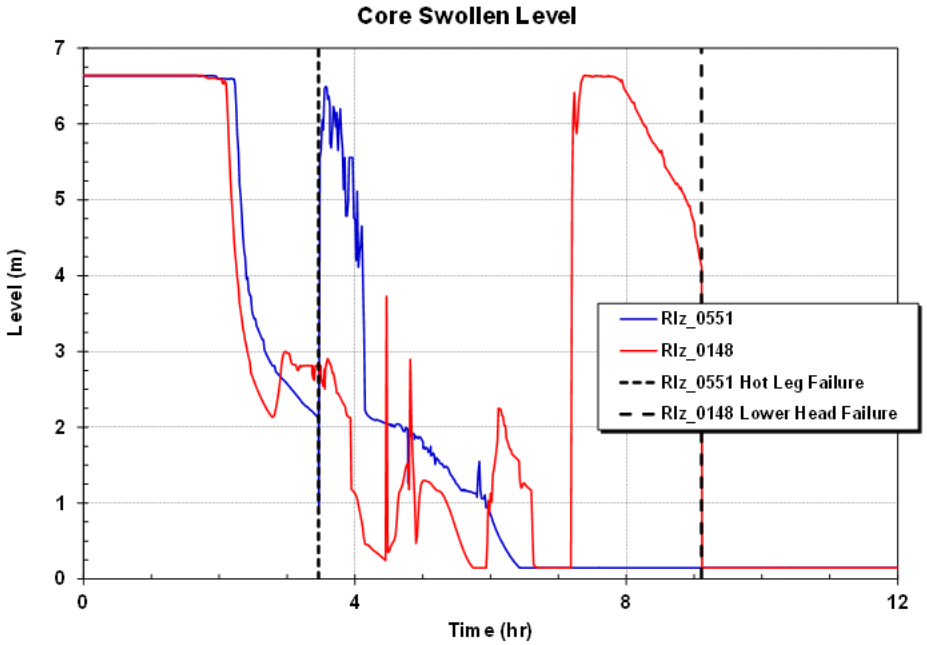

Figure 4-99 Core swollen water level responses for RIz 551 and 148

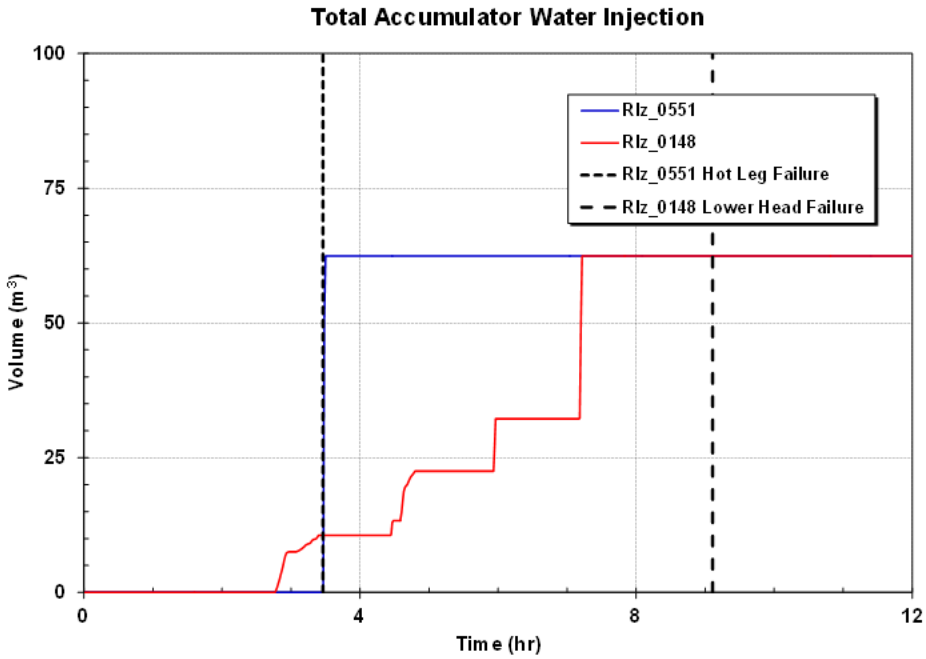

Figure 4-100 Total accumulator water injection responses for Rlz 551 and 148

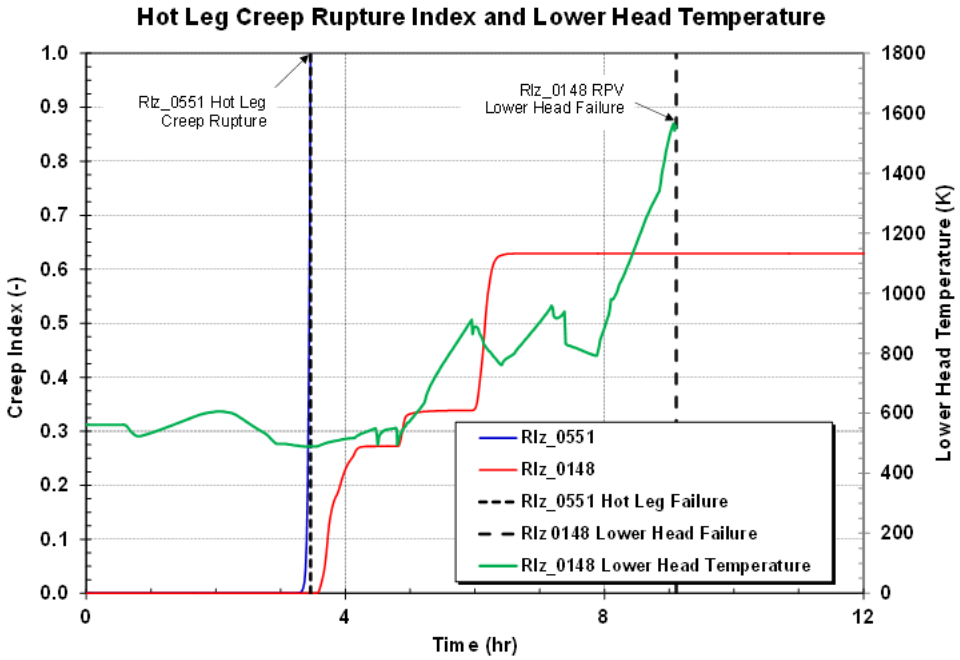

Figure 4-101 Creep rupture index and lower head temperature responses for Rlz 551 and 148

Rlz 469

Analysis of Rlz 469 is presented in Figure 4-102 and Figure 4-103 and illustrates what is often happening in the calculations to keep deflagrations from occurring. Any time all the lines in these figures are solid, conditions are ripe for a burn, i.e., enough fuel and oxidizer (e.g.,

hydrogen and oxygen) are present to facilitate a burn and insufficient inerting gasses (e.g., steam) reside to suppress a burn. Figure 4-102 pertains to the ignition of a burn within a control volume (burning downwards in this instance) while Figure 4-103 pertains to the propagation of a burn to a control volume upwards from another volume. In Figure 4-102, excessive inerting gas and insufficient combustible gas are reflective, i.e., there could be too little combustible gas for a burn given the amount of inerting gas or likewise too much inerting gas for a burn given the amount of combustible gas. In this realization, containment ruptures at about 50 hours, as observed in the figure.

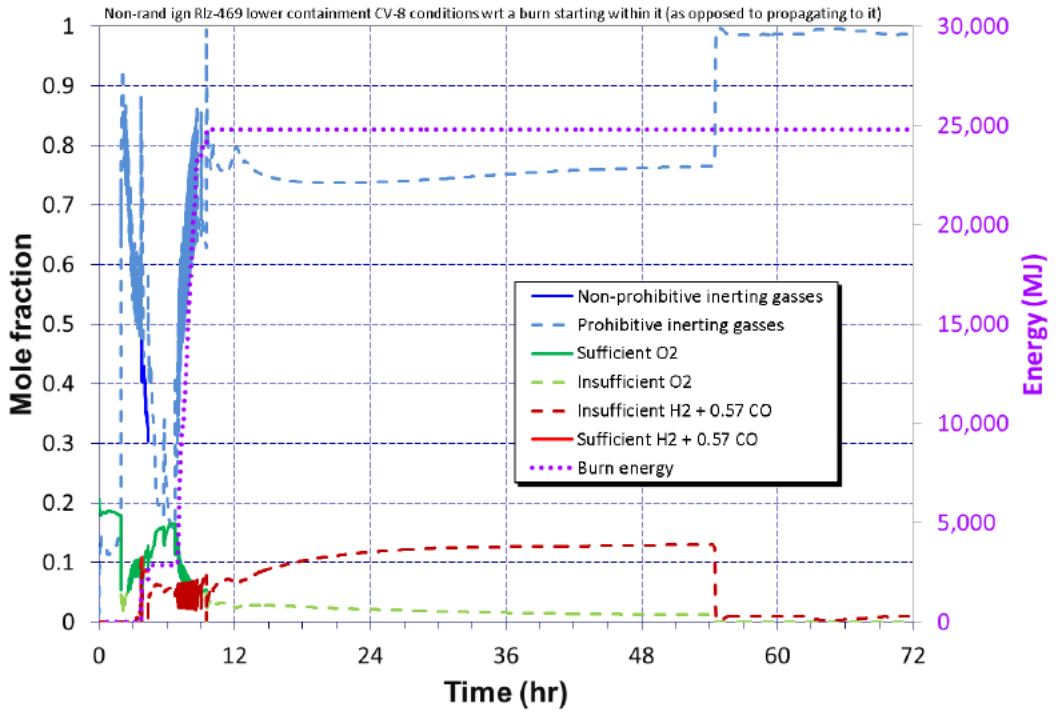

Figure 4-102 Rlz 469 no random ignition, lower containment CV-8 conditions with respect to a burn starting within the CV, as opposed to propagating to the CV

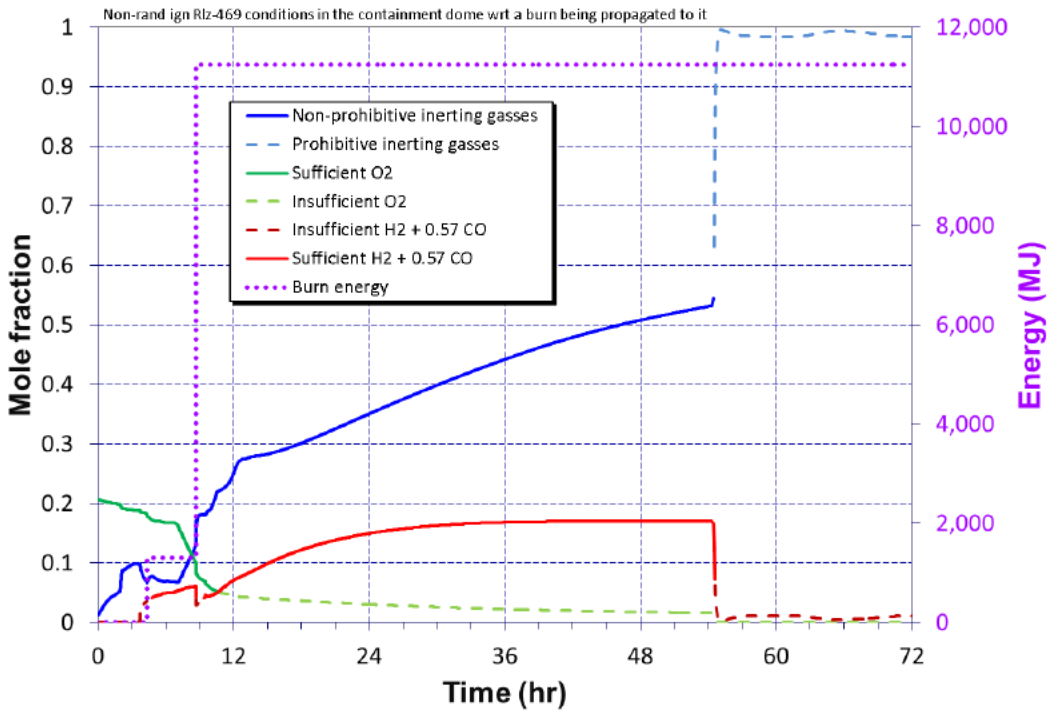

Figure 4-103 Rlz 469, no random ignition, conditions in the containment dome with respect to a burn being propagated to the dome

4.4 LTSBO Accident Progression Analysis

The LTSBO is assumed to be initiated by a seismic event. Section 4.4.1 presents the results of an unmitigated scenario with initially successful operator actions to depressurize the RCS and maintain TDAFW flow. However, once the DC station batteries fail at 8 hours, no more operator actions are successful. The analysis in Section 4.4.3 assumes that power to the igniters is restored prior to core damage and onset of hydrogen generation. Section 4.4.2 presents the results of a series of sensitivity calculations.

4.4.1 Unmitigated Long-Term Station Blackout Base Case

The accident scenario initiates with a complete loss of all onsite and offsite AC power but the DC station batteries are available. The reactor successfully scrams and the containment isolates but all powered safety systems are unavailable except the TDAFW. The MELCOR parameters for the base case are the mean values sampled for the short-term uncertainty distributions. Table 4-16 summarizes the timing of the key events in the unmitigated LTSBO base case.

Table 4-16 Timing of key events for unmitigated LTSBO base case.

Event Description	Time (hh:mm)
Initiating event Station blackout – loss of all onsite and offsite AC power	00:00
MSIVs close Reactor trip RCP seals initially leak at 21 gpm/pump	00:00
TDAFW auto initiates at full flow	00:00+
First SG SRV opening	00:00+
Operators control TDAFW to maintain level	00:15
Operators initiate controlled RCS cooldown of secondary at ~100°F/hr	01:00
Accumulators begin injecting	03:08
SG cooldown stopped at 300 psig to maintain TDAFW flow	03:42
DC Batteries Exhausted	08:00
SG ARVs reclose	08:00
1% of the ice melted	08:16
SG1 fills up and floods the AFW steam turbine (AFW shuts down)	10:14
SG3 SV stuck open (after 45 cycles)	14:36
SG1 SV stuck open (after 5 cycles with water flow)	17:06
Pressurizer SV opens	20:06
PRT failure (4% ice melted)	20:30
Water level below top of active fuel	20:48
Pressurizer SV stuck open (45 cycles)	22:20
First fission product gap releases	22:48
25% of ice melted	24:42
Creep rupture failure of the hot leg nozzle in combined loop	24:42
1st hydrogen deflagration	24:42
Half of ice condenser lower plenum doors stuck open	24:42
Containment fabric seal torn	24:42
Accumulator empty	24:44
50% of the ice melted	24:14
Containment failure due to hydrogen combustion	24:42
Vessel lower head failure by creep rupture	28:36
Debris discharge to reactor cavity	28:36
100% of the ice melted	34:38
Selected MELCOR Results	
Debris mass ejected (1000 kg)	169
In-vessel hydrogen generated (kg)	510
Iodine release fraction at 72 hr	9.23E-2
Cesium release fraction at 72 hr	2.27E-2

The heat removal through the steam generator depressurizes the primary system to 11.2 MPa by 60 min. At 60 min, the operator starts a controlled (100oF/hr) cooldown of the primary

system by opening an atmospheric relief valve (ARV) in a single steam generator32. As the secondary pressure in the single steam generator (SG1) decreases, the saturation temperature of the water in the boiler section of the steam generator also decreases, which cools the primary system fluid and also the fluid in the other steam generators (SG3). At about 3.7 hr, steam generator SG1 reached 2.17 MPa (300 psig), where the secondary system pressure was stabilized. Figure 4-105 shows that the TDAFW adequately maintained the steam generator level until 8 hr when DC power fails, and by 10.2 hr, the SG1 overfills and fails the AFW steam turbine. By this time, the CST water has decreased to 37% of the original inventory.

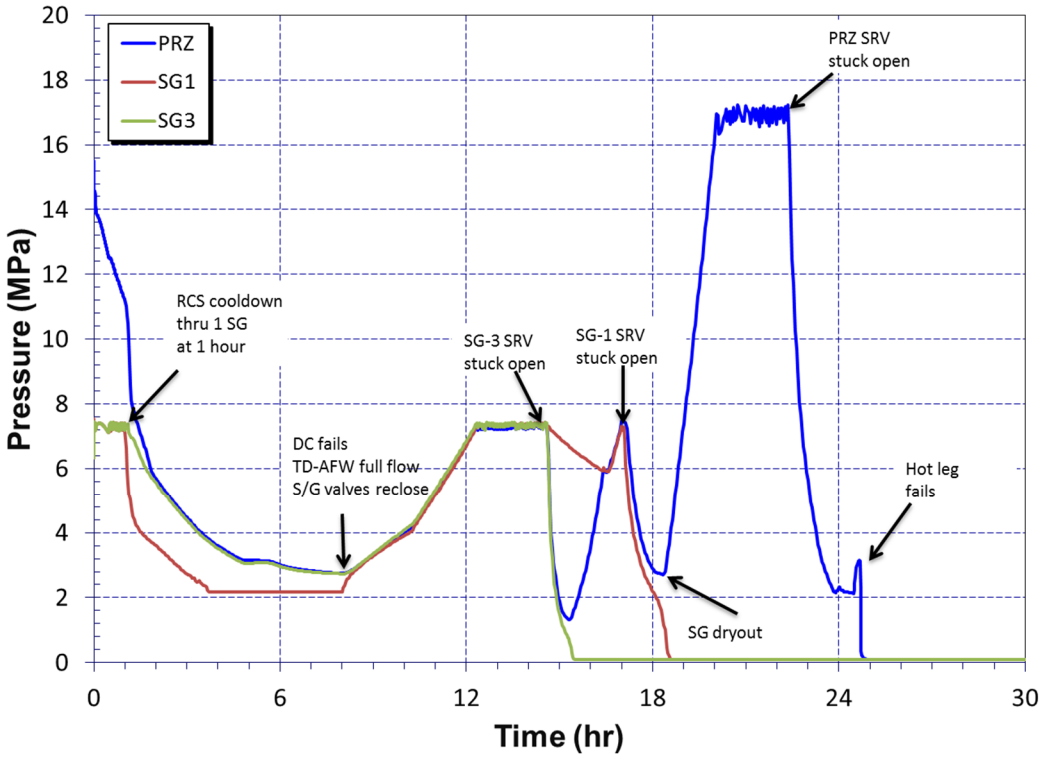

Figure 4-104 Unmitigated LTSBO base case primary and secondary pressure history

The primary system depressurization via the secondary system cooldown has some short-term benefits, i.e., a reduction in the leakage through the RCP seals, and the actuation of the accumulators. In the base case calculation, it is assumed that the RCP seals do not fail (leakage corresponds to 21 gpm at full system pressure). Even if the RCP seals fail the resulting leakage flow would be much lower than if the primary system pressure was not actively controlled to low pressure. The accumulators begin injecting at 4.4 MPa at about 3 hours until 7.3 hours discharging about 9% of their water inventory. The accumulators are a source of cold water to replace the losses due to RCP seal leakage and the volume shrinkage during the cooldown. The accumulators discharge again at 14.6 hours in response to the second primary system depressurization for a total of 31% of their initial inventory.

[32] The single SG is identified as SG1, and the combined other three SGs are identified as SG3.

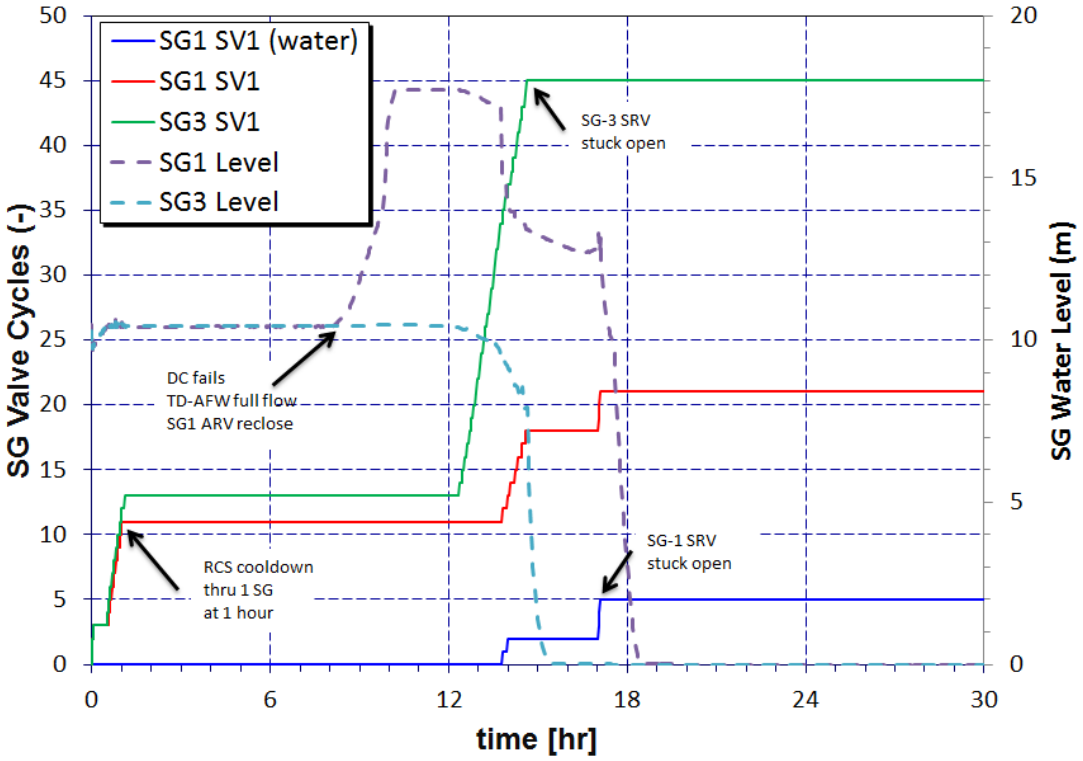

Figure 4-105 Unmitigated LTSBO base case secondary system water level and valve history

The station batteries were estimated to fail at 8 hours. At the same time, the steam generator atmospheric relief valve closed in the single steam generator (SG1) and was no longer actively controlled. In response to the steam generator valve closure, both the primary and secondary systems rapidly pressurized to the secondary safety valve opening pressure at 12.3 hours and remained around this pressure until 14.6 hours when the lowest opening pressure safety valves in the lumped steam generators (SG3) were stuck open at 45 cycles (Figure 4-105). This led to a rapid depressurization of SG3 and the primary system until the water loss resulted in the dryout of SG3 at 15.5 hours as shown in Figure 4-105. The primary system and the single steam generator (SG1) pressures were then equilibrated and once again reached the secondary safety valve opening pressure at about 17 hours. Note that the leakage through the main steam isolation valves was not sufficient to avoid secondary side safety valve cycling. Because of relatively high water level in the single steam generator, there were only a few cycles before water began passing through SG1 safety valves. The valves were assumed to be stuck open after 5 cycles with water flow. Shortly after SG1 depressurization through the stuck open safety valve and the associated water loss, SG1 dried out at 18.2 hours. With no more cooling available, the primary system pressurized to the pressurizer safety valve opening set point at 20.1 hours and began to relieve steam and water. The pressurizer safety relief valves began cycling until they were stuck open after 45 cycles at 22.4 hours. The loss of coolant during the valve cycling resulted in a rapid drop in the vessel water (see Figure 4-106) and the top of the fuel was uncovered by 20.8 hr and the core heatup began (see Figure 4-107).

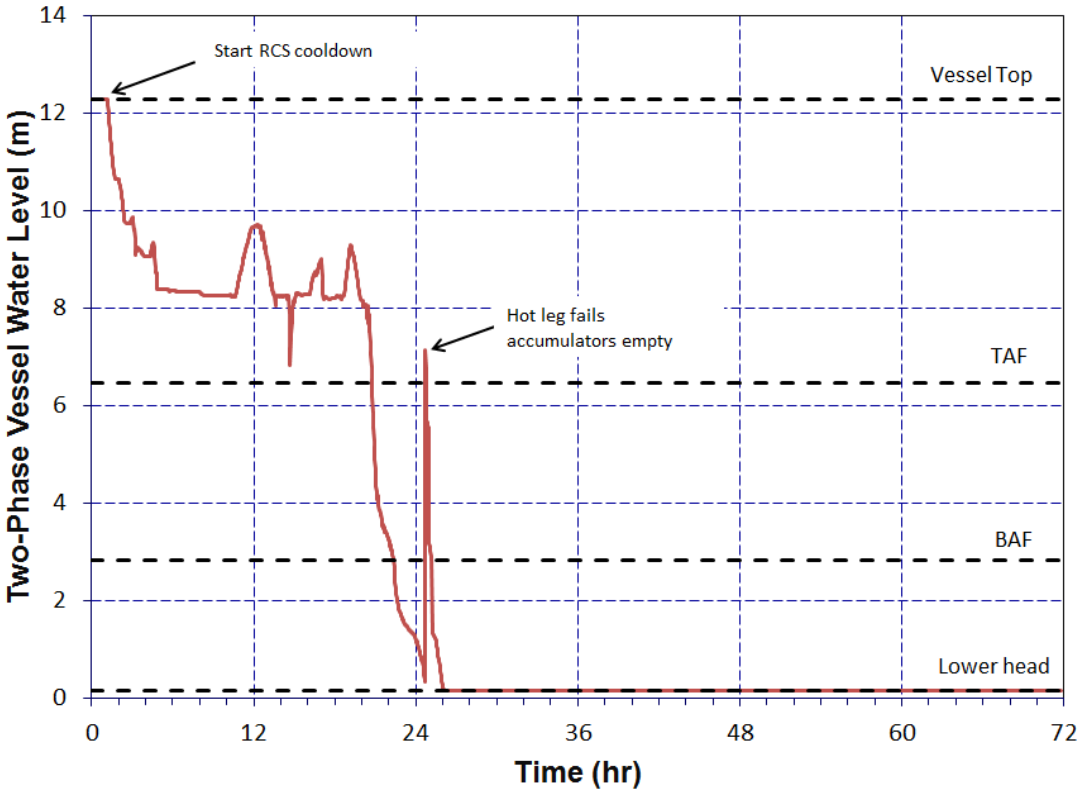

Figure 4-106 Unmitigated LTSBO base case primary system water level history

Following the core heatup, an in-vessel natural circulation flow develops between the hot fuel in the core and the cooler structures in the upper plenum. Hot gases rise out of the center of the core to the upper plenum and return down the cooler peripheral sections of the core. Simultaneously, a natural circulation circuit develops between the vessel and the steam generator[33]. The flow of the hot gases through the hot leg causes the hot leg nozzle to fail by creep rupture at 24.7 hours. The failure of the hot leg results in rapid depressurization of the vessel and injection of the remaining 69% of the accumulator water inventory. Figure 4-106 shows the temporary surge in the vessel water level all the way up to the top of active fuel and the cooldown of the debris (see Figure 4-107).

[33] Failure of the steam generator tube is not modeled in the present calculations.

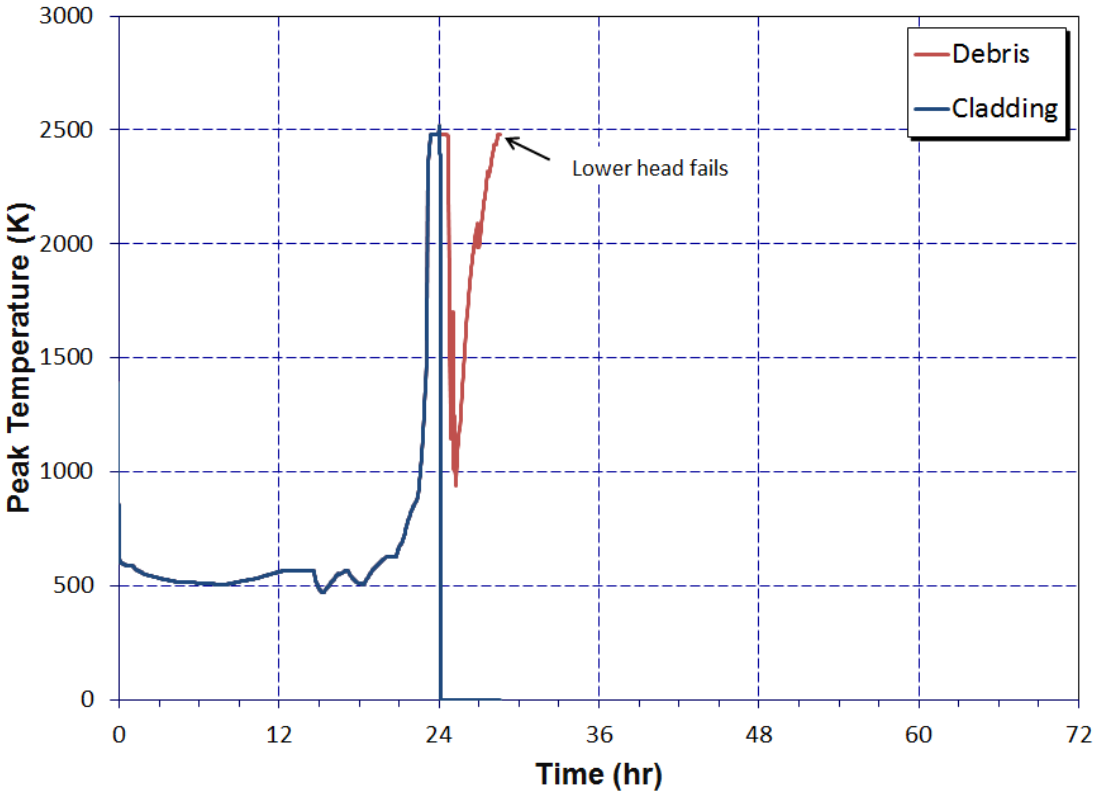

Figure 4-107 Unmitigated LTSBO base case peak fuel and debris history

During the heatup and degradation of the fuel, the outer surface Zircaloy cladding reacts with the steam to form an oxide shell. The oxidation reaction is an exothermic process that greatly increases the fuel heatup rate and releases hydrogen. During the rapid fuel heatup, the oxide shell thickness increases and the unoxidized Zircaloy clad material in the interior of rod melts. The molten Zircaloy cladding weakens the oxide shell and drains to lower regions of the core, leaving a fragile ZrO_2 shell around over-heated fuel. This mechanically weak material subsequently fragments into particulate debris, which relocates toward the lower regions as rubble. The changes in core geometry during this time frame, which are caused by the formation and downward relocation of molten and particulate debris, are illustrated in Figure 4-108.

A large debris bed formed in the center of the core resting on the core plate at 23.9 hour. By 24.1 hr, most of the core fuel assemblies (i.e., the central three of five radial rings in the MELCOR model) have collapsed. Highly oxidized, but vertically intact assemblies remain standing in the outer rings of the core. The outer core assemblies also fail a short time later (24.2 hr) and accumulate on top of the lower support plate. The hot debris fails the lower support plate at 24.4 hr. Following the lower support plate failure, the debris relocated onto the lower head. The hot debris starts to boil away the lower head water, but the failure of the hot leg and accumulator injection recover the water level in the core at 24.7 hr. The decay heat from the debris takes an additional 1.2 hours to boil away the remaining water (see Figure 4-106).

Following the lower plenum dryout, the hot debris started heating the lower head, which eventually failed at 28.6 hr due to the creep rupture failure criterion. Because reactor vessel

pressure is relatively low during the heat up of debris in the lower plenum, the failure of the lower head is more strongly influenced by thermal rather than mechanical stresses. The failure of the lower head results in the ejection of core debris onto the floor of the reactor cavity.

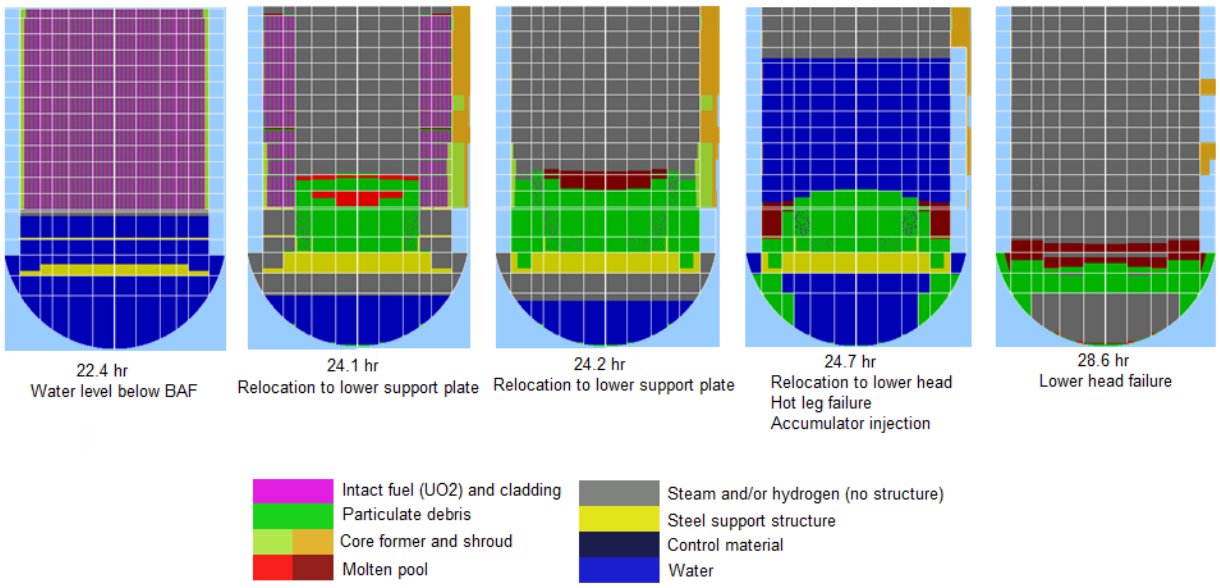

Figure 4-108 Unmitigated LTSBO base case core degradation and relocation history

The containment pressure remains relatively low until the failure of the PRT at 20.5 hours (see Figure 4-109). The containment pressure gradually increases as the coolant (and later hydrogen) is discharged from the vessel. The containment pressurization following PRT failure leads to the flow of the steam through the ice bed. Significant in-vessel hydrogen generation began at 22.8 hours and the hydrogen was released to the containment. By the time the hot leg failed, there was a substantial amount of hydrogen in the lower containment and with the steam mole fraction below the threshold of 55%, a hydrogen deflagration started in the lower compartments that propagates to the upper dome. The source of ignition is the hot gases exiting the vessel. The containment was still below the design pressure at the time of hot leg failure. The hydrogen burn resulted in the failure of the fabric seal dividing the lower and upper parts of the containment, and more importantly, the gross failure of the containment. It is important to note that containment failed before lower head failure.

The response of the ice is shown in Figure 4-110. In the absence of containment cooling, the flow of gases through the lower plenum doors results in some melting of the ice (~4%) by the time the PRT rupture disk fails. The discharge of the coolant during the cycling of the pressurizer safety valve and the flow of steam through the ice bed results in substantial melting of the ice until the hot leg fails. The melting of the ice continues after containment failure as the gases circulate through the ice chest and by the time of lower head failure more than 60% of the ice has melted. The flow of hot gases from the cavity and the lower compartments melted the remaining ice by 34.6 hr. The hot debris in the reactor cavity started to ablate the concrete soon after lower head failure as shown in Figure 4-111, and the ex-vessel core-concrete interactions (CCI) continued for the remainder of the calculation, which generated non-condensable gases. The CCI gases promote flow from the containment to the environment.

Consequently, there is low retention of fission products that are released or revaporized after containment failure.

Even though the cavity is dry at the time of the lower head failure, continued melting of the ice and accumulation in the lower compartments eventually led to flow of water to the cavity at about 33 hr. Soon after lower head failure and discharge of the debris to the cavity, the debris temperature started to gradually decrease as a result of heat transfer to the concrete basemat and from the top of the debris bed. The flow of water to the top of debris at 33 hr resulted in increased heat transfer from the top debris crust and lowered the average debris temperature significantly. However, as long the interface temperature between the core debris and the concrete basemat remained above the ablation temperature, concrete ablation continued. By the end of the calculation about 80 cm of concrete was eroded.

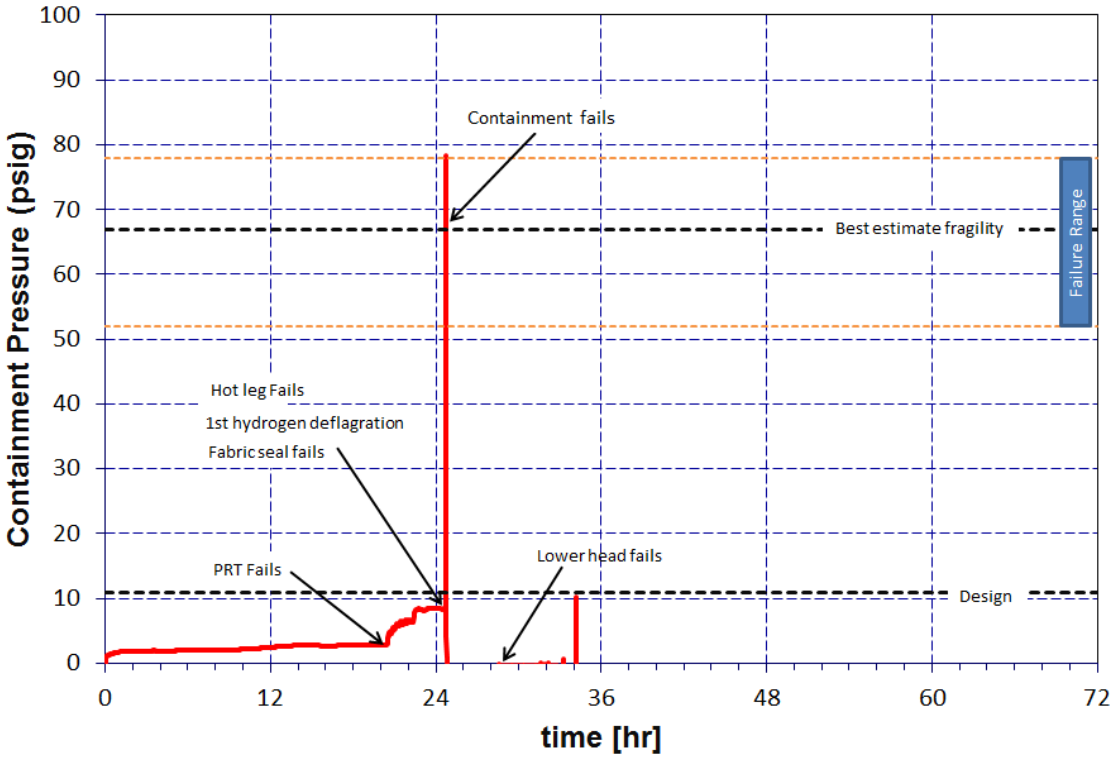

Figure 4-109 Unmitigated LTSBO base case containment pressure history

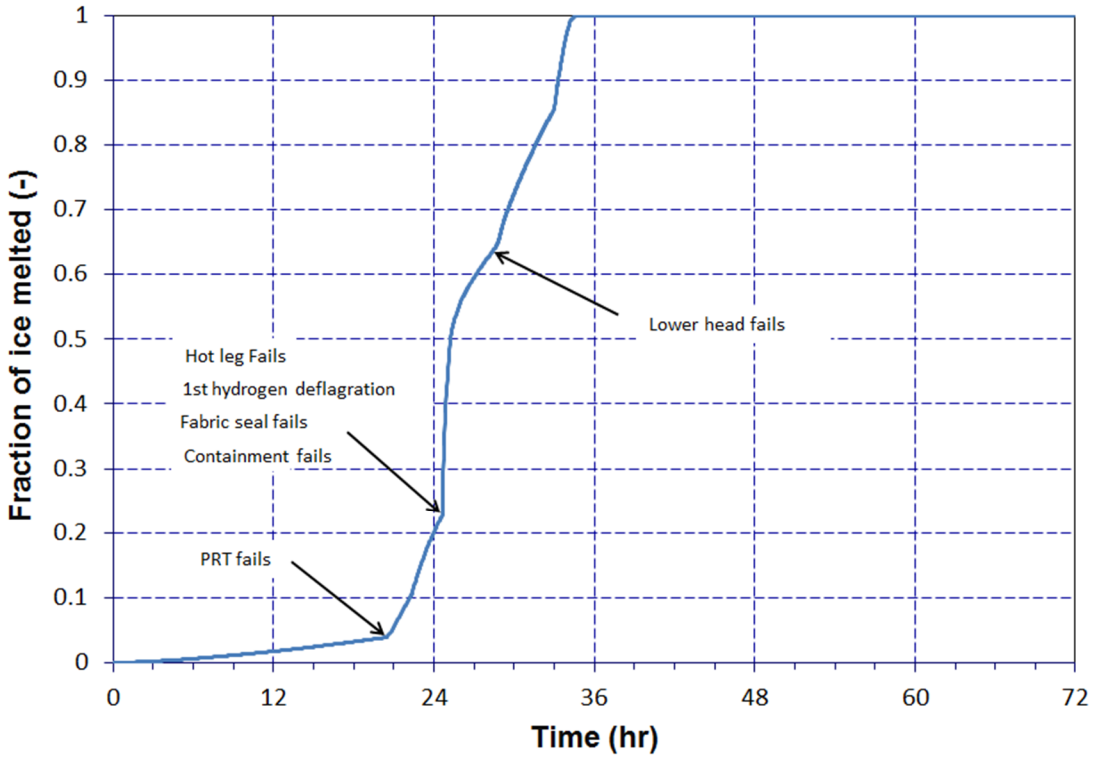

Figure 4-110 Unmitigated LTSBO base case ice melting history

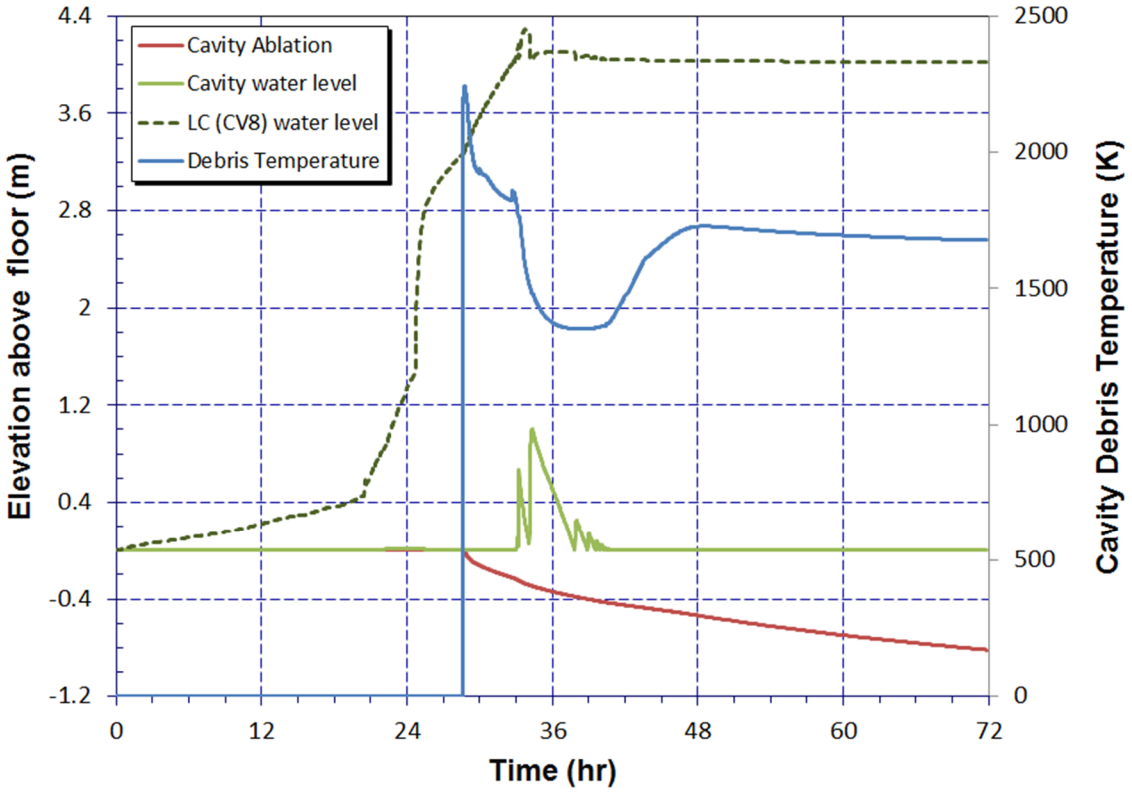

Figure 4-111 Unmitigated LTSBO base case concrete ablation history

4.4.1.1 Radionuclide Release

Figure 4-112 and Figure 4-113 show the fission product distributions of the iodine and cesium radionuclides that were released from the fuel, respectively. Approximately 98% of the iodine and 99% of cesium were released from the fuel in-vessel while the remaining amount was released ex-vessel.

The fission product releases from the fuel started following the first failures of the fuel cladding at 22.8 hr, or about 2 hours after the uncovery of the top of the fuel rods. The in-vessel fission product release phase continued until 32.7 hr or about 4 hours after lower head failure when the remaining debris from the vessel was discharged to the cavity[34]. Initially, the fission product releases from the fuel circulated through the primary system as well as being released to the PRT and the containment through the pressurizer safety valves. The start of the fission product release occurred more than 2 hours after failure of the RPT rupture disk and 28 minutes after the pressurizer safety valve was stuck open. The water inside the PRT remained slightly subcooled after fission product release and nearly 30% of the iodine and cesium initial inventories were retained in the tank. Between the start of the fission product release and the failure of hot leg (nearly 2 hours), a significant amount of volatile radionuclides released from the fuel remained in-vessel (PRT is considered part of the RCS in the MELCOR model). The resultant blowdown of the vessel after hot leg failure immediately discharged some of radionuclides to the containment. The radionuclides settled on the containment surfaces after being released from the RCS (about 10% of the cesium and 15% of the iodine). The retention of the radionuclides inside the RCS, the PRT, and the containment was significant since containment failure occurs shortly after the hot leg failure, but there was little airborne mass released to the environment.

The chemical form of the released iodine was cesium iodide, which was more volatile than the predominant form of the released cesium, which was cesium-molybdate (Cs_2MoO_4) and CsOH. As shown in the iodine distribution figure (see Figure 4-112), the in-vessel iodine mass was slightly decreasing until the PRT dried out and started to heatup. The decrease of mass represents a revaporization process of previously deposited radionuclides. The large increase in iodine resident in the containment was coincident with a decrease in the RCS due to the release of much of inventory of iodine in the PRT to the containment atmosphere. The late in-vessel revaporization continued after this time and had a contribution to the environmental release. In contrast to the iodine behavior, the deposited cesium-molybdate was less volatile and mostly remained deposited in the RCS and the PRT. Only about 6% of the cesium was released from the PRT (compared to nearly complete release of iodine).

Figure 4-114 summaries the releases of the radionuclides to the environment. At 3 days, 99.7% of the noble gases, 8.7% of the tellurium, 9.23% of the iodine, 2.27% of the cesium, and 0.88% of the barium had been released to the environment. The release of the less volatile fission products does not start until after the lower head failure and start of the core concrete interaction.

[34] Only a very small amount was released during this time.

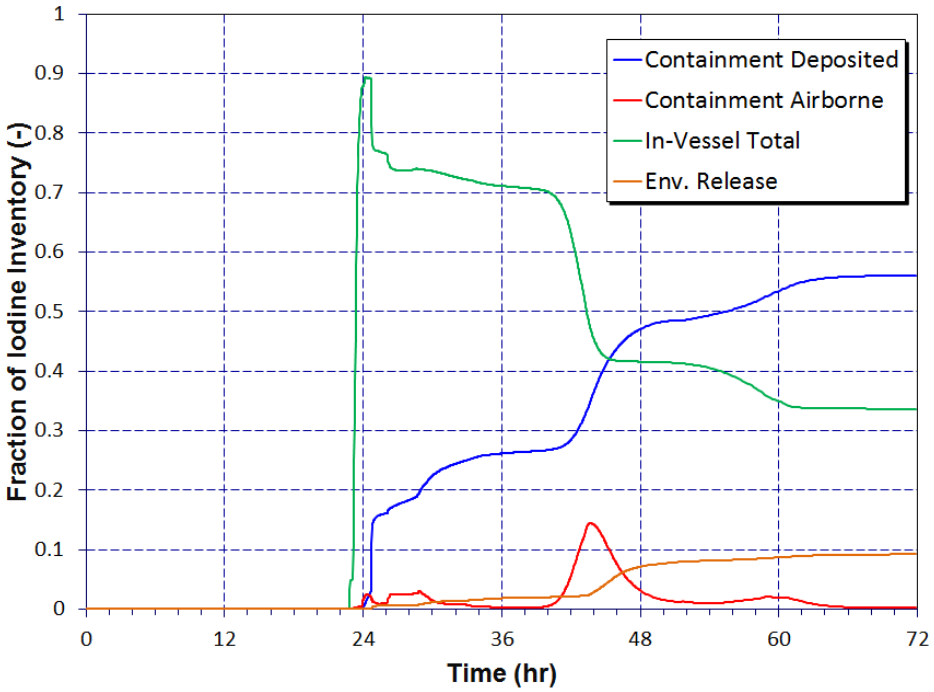

Figure 4-112 Unmitigated LTSBO base case Iodine fission product distribution history

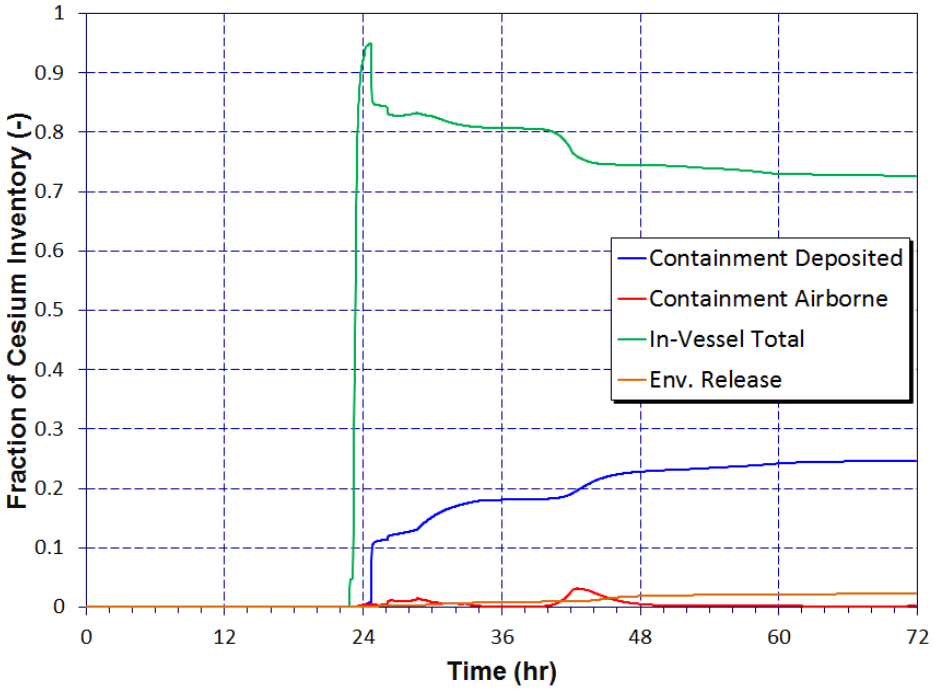

Figure 4-113 Unmitigated LTSBO base case Cesium fission product distribution history

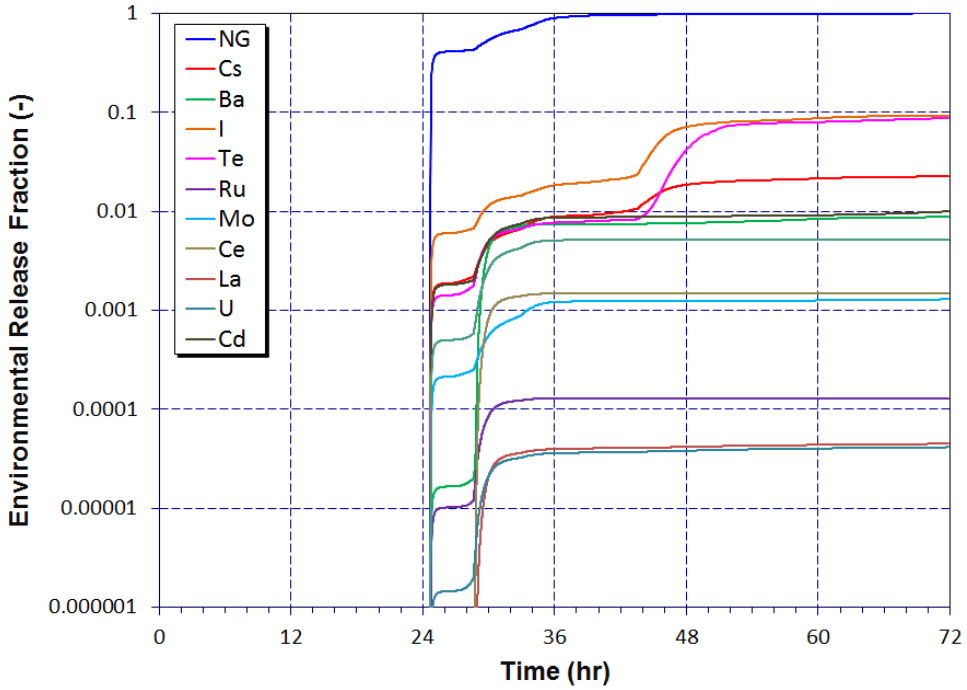

Figure 4-114 Unmitigated LTSBO base case environmental release fraction history

4.4.2 Unmitigated Long-Term Station Blackout Sensitivity Calculations

This section presents the results of a series of sensitivity calculations to better understand the response of the reactor and the containment for the LTSBO scenario. These limited sensitivity calculations are informed by the uncertainty analysis for the STSBO scenario and focus on the assumptions regarding valve cycling and the availability of station batteries. A description of the cases is given in Table 4-17. The results of the calculations are presented in Figure 4-115 through Figure 4-119.

Table 4-17 Description of unmitigated LTSBO sensitivity cases.

Case	Description
S1	SG1 SRV is assumed to fail at 1st cycle with water flow (see Figure 4-105)
S2	Secondary side SRVs do not fail
S3	Same as S1 but the flow area for SG3 SRV is reduced to correspond to a single SG
S4	Station batteries run out at 4 hours
S5	Pressurizer SRV is assume to stick open on 1st cycle

In sensitivity case S1, it was assumed that the secondary side safety valve fails on the 1st opening with water flow (see Figure 4-105, which shows the base case SG SV sticks open after 5 cycles). However, the depressurization of the single steam generator (SG1) also resulted in the delay of stuck open safety valve on the lumped steam generators (SG3). The loss of secondary side cooling was a result of steam generator dryout, which occurred slightly sooner in

S1 as compared to the base case. However, the heatup of the primary system and the pressure increase was not significantly different between the two cases as shown in Figure 4-115. Therefore, the timing of hot leg failure and the containment failure were only different by about half an hour.

For sensitivity case S2, it was assumed that the safety valves on the steam generators did not stick open but both the single and lumped steam generators could gradually depressurize after dryout due to the leakage from the main steam isolation valves. The behavior is not very different from the base case but includes a delay in the hot leg and containment failure that is similar to case S1.

Since three steam generators were lumped together in the MELCOR model, sensitivity (S3) calculation was done to examine the effect of secondary side depressurization assuming that the area for the valve sticking open corresponds to a single steam generator. This caused a slower depressurization but only delayed the dryout by about half an hour.

Although the availability of the station batteries (4 hours in case S4) had a significant effect on the timing of the accident progression, the overall behavior and trends were very similar to the base case. A difference of only 4 hours of station batteries in the base case resulted in the delays of about 5.5, 6.0, and 6.5 hours in the timing of the steam generator dryout, pressurizer safety valve stuck open, and hot leg creep rupture, respectively.

In sensitivity case S5 with the pressurizer safety valve stuck open at the first cycle, the core damage started sooner due to higher coolant loss from the vessel compared to the base case. In-vessel hydrogen generation started about 1.5 hour earlier as compared to the base case with somewhat similar differences in the timing of the hot leg and containment failure.

The amount of in-vessel hydrogen generation between the various sensitivity cases and the base case was also similar. This parameter is most sensitive to the eutectic melt temperature (see the discussion on STSBO) but was not varied for the LTSBO sensitivity calculations. The mean settings on the uncertain parameters, including the eutectic melt temperature produced sufficient hydrogen to fail the containment at the time of hot leg failure.

Figure 4-118 and Figure 4-119 show the environmental release fractions for iodine and cesium, respectively. The horsetail plots from the STSBO uncertainty analysis (without random ignition) are also superimposed on the figures. The behavior of release for the LTSBO is similar to the STSBO scenarios with early containment failure since all the sensitivity cases discussed here resulted in containment failure following the hot leg failure. With 8 hours of station batteries, the release timing can be significantly different (by as much as 20 hours) between the short-term and LTSBO scenarios. The differences in the total releases shown in Figure 4-119 are attributed to variations in the late revaporization from the RCS and PRT (see Figure 4-112 and Figure 4-113 for the base case).

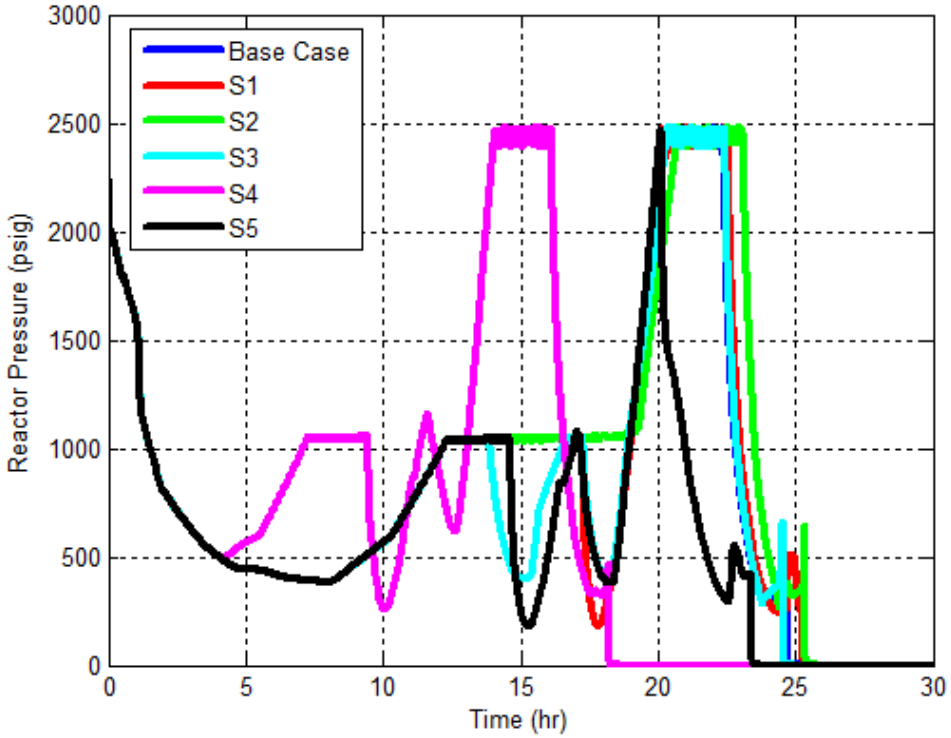

Figure 4-115 Unmitigated LTSBO reactor pressure sensitivity cases

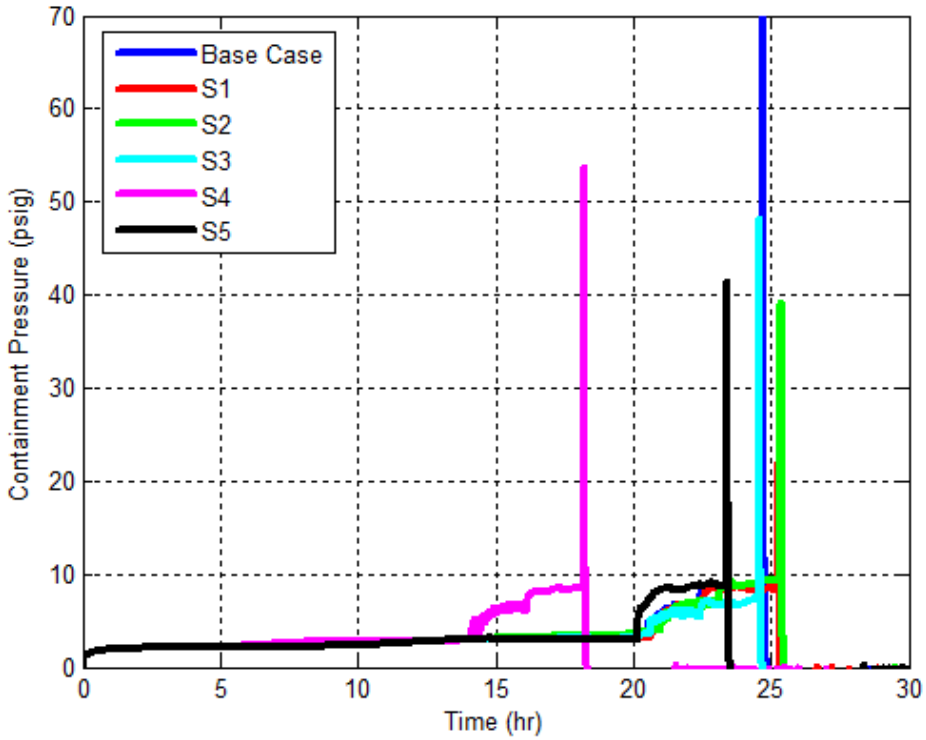

Figure 4-116 Unmitigated LTSBO containment pressure sensitivity cases

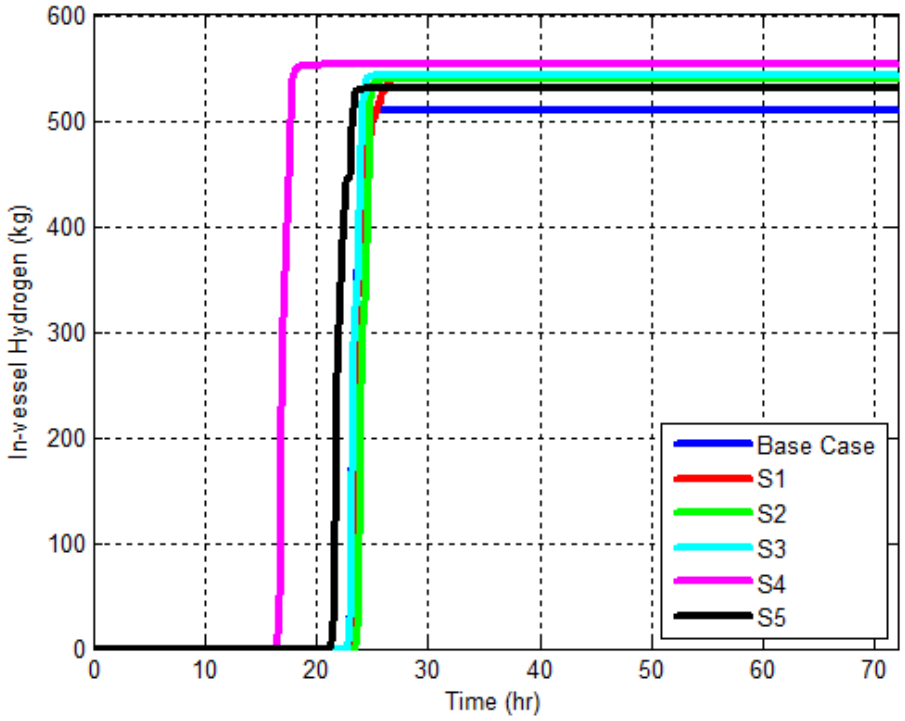

Figure 4-117 Unmitigated LTSBO in-vessel hydrogen sensitivity cases

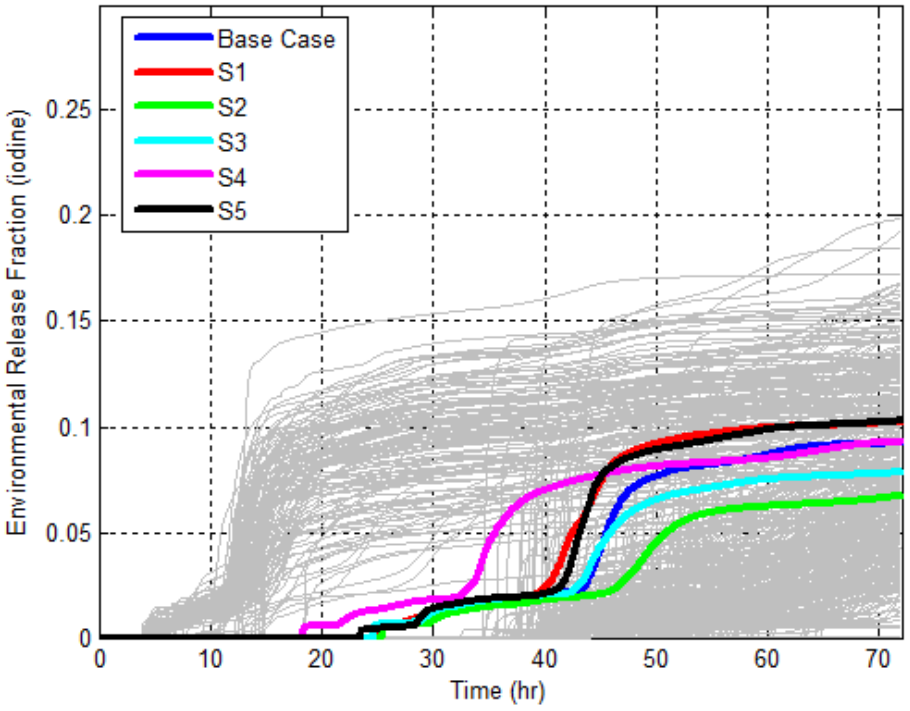

Figure 4-118 Unmitigated LTSBO iodine environmental release fraction sensitivity cases

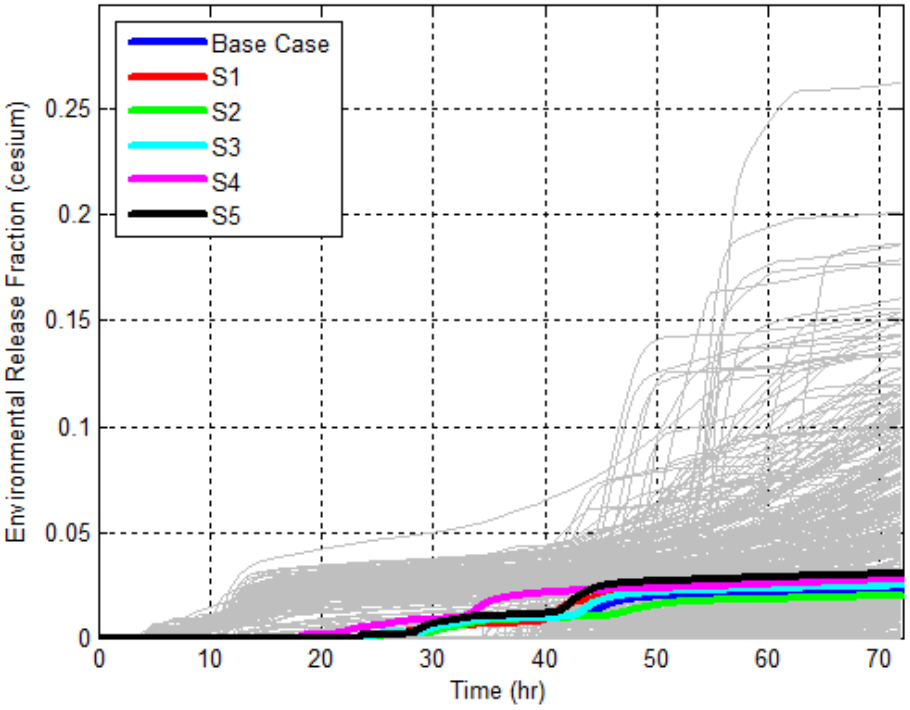

Figure 4-119 Unmitigated LTSBO cesium environmental release fraction sensitivity cases

4.4.3 Long-Term Station Blackout with Igniters

The effect of igniters on the containment performance is presented in this section. The igniters are assumed to be available in all control volumes inside the containment except the ice condenser lower plenum and the ice chest. However, a burn in any control volume is allowed to propagate to other regions including the ice chest when it satisfies the propagation criteria.

Table 4-18 Description of mitigated LTSBO sensitivity cases with igniters.

Case	Description
S6	Ignition occurs once hydrogen mole fraction reaches 7%
S7	Ignition occurs once hydrogen mole fraction reaches 4%
S8	Same as S6 with 4 hours of station batteries

Figure 4-120 compares the response of the containment pressure to the burning of the hydrogen with igniters versus the base case response without igniters. The most revealing impact of the igniters was that they prevented early containment failure. In the unmitigated base case, hydrogen accumulated to high levels so that at the time of hot leg failure when an ignition source became available, the first deflagration failed the containment. In case S6, ignition is not allowed until the hydrogen mole fraction reaches 7% (i.e., the MELCOR default for control volumes with igniters). In sensitivity case S7, the criterion for ignition was decreased to the lower flammability limit. The pressure spikes for the lower ignition criterion were smaller

because of more gradual burning of the hydrogen. The slow containment pressurization was a result of the non-condensable gas generation (including CO and H_2) from core concrete interaction. The containment pressure; however, remained below the lower bound of containment fragility at 3 days.

Figure 4-121 through Figure 4-123 show the time history of the hydrogen, oxygen, and steam in the upper containment (CV24). The steam mole fraction in the containment remains well below 55% threshold for inerting. In the base case without the active igniters, the hydrogen mole fractions exceeded 10% and with enough oxygen present (Figure 4-122) resulted in the combustion induced failure of the containment. Activation of the igniters controls the hydrogen concentration through multiple burns and prevents containment failure. In all cases, however, the igniters were not effective after about 35 hours once the oxygen concentration fell below 5% (see Figure 4-123).

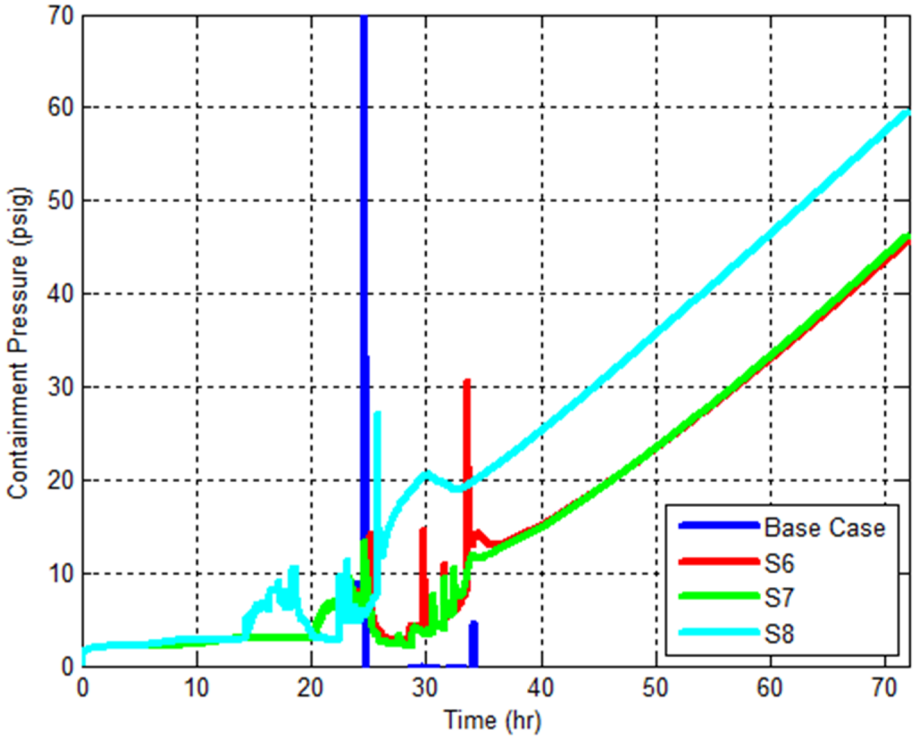

Figure 4-120 LTSBO containment pressure history with igniters

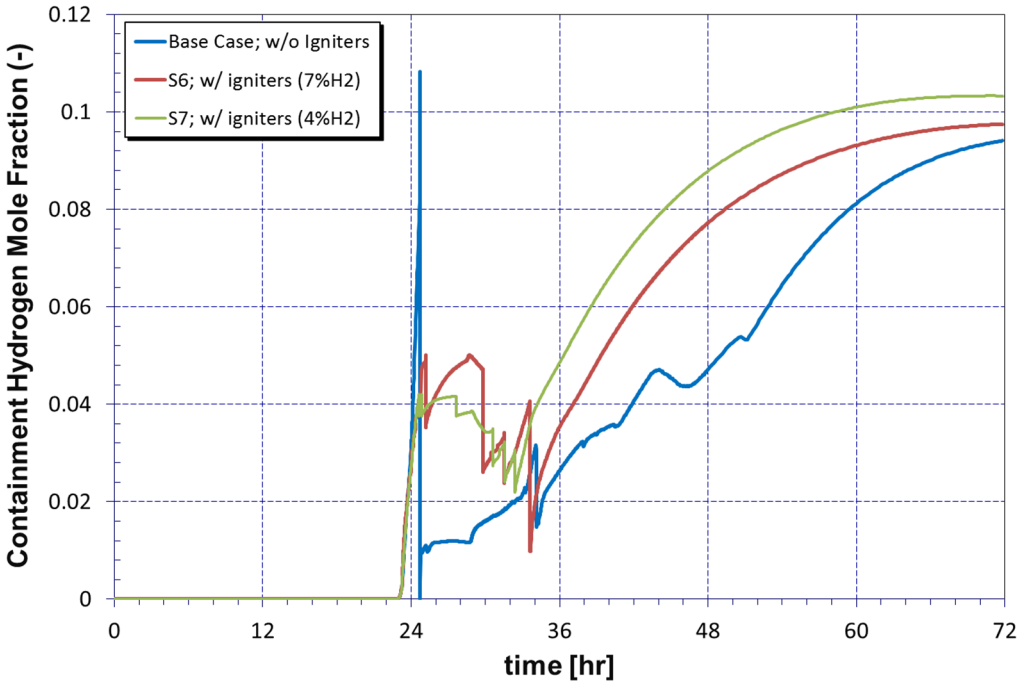

Figure 4-121 LTSBO containment hydrogen mole fraction history with igniters

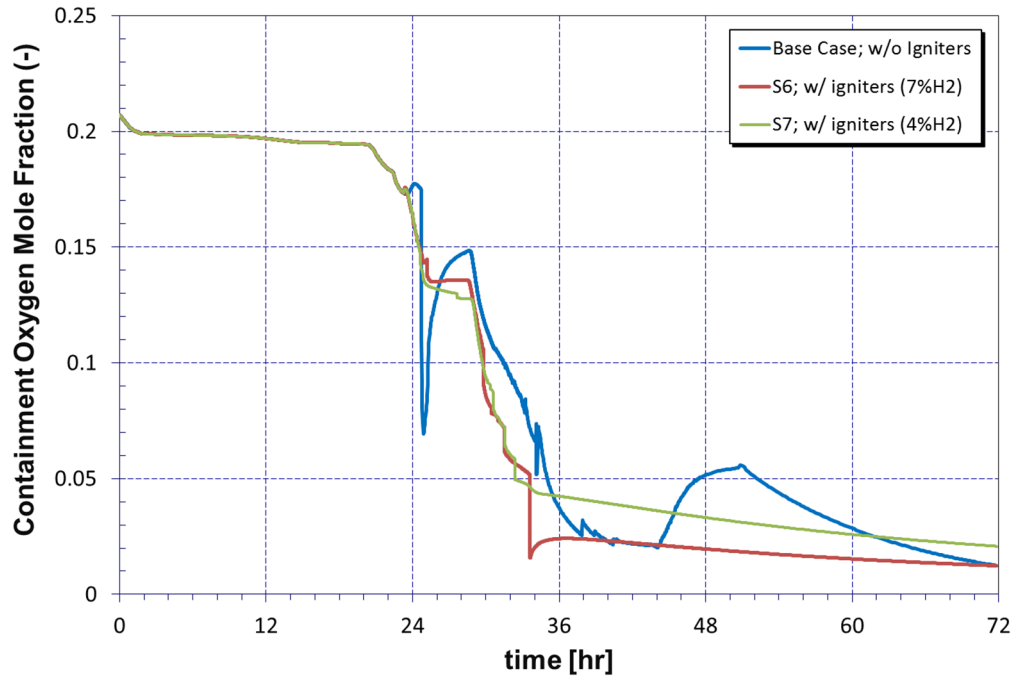

Figure 4-122 LTSBO containment oxygen mole fraction history with igniters

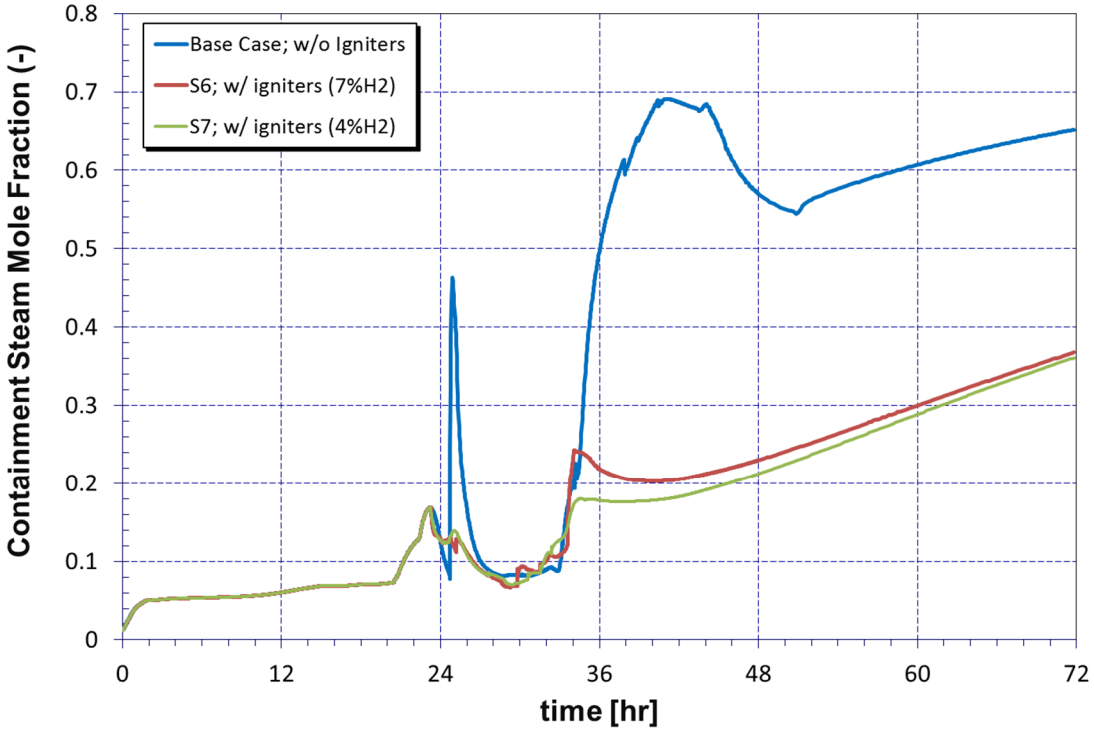

Figure 4-123 LTSBO containment steam mole fraction history with igniters

5. SEQUOYAH MACCS MODEL

5.1 Introduction

The Sequoyah Nuclear Plant, Unit 1 SOARCA offsite consequence analysis uses MACCS to calculate potential doses and risk metrics for the population in the vicinity of Sequoyah. The MACCS consequence model (Version 3.10), along with the graphical user interface (GUI) WinMACCS, was used in this analysis to calculate offsite doses and their effect on members of the public. MACCS and WinMACCS are developed at SNL under the direction of the NRC. The codes have been used extensively in commercial nuclear reactor PRAs and other regulatory applications to simulate the impacts of accidental atmospheric releases of radiological materials on humans and on the surrounding environment.

The principal phenomena considered in MACCS are atmospheric transport using a straight-line Gaussian plume segment model, short-term and long-term dose accumulation through several exposure pathways including cloudshine, groundshine, inhalation, deposition onto the skin, and food and water ingestion. The ingestion pathway was not treated in the analyses reported here because uncontaminated food and water supplies are abundant within the United States and it is unlikely that the public would consume radioactively contaminated food or water. This section discusses various site-specific MACCS model parameters. A complete list of the MACCS model inputs are found in Appendix B. In this report, calculations and results are reported based on 2015 data, except for weather data which is based on 2012.

Site-specific MACCS input parameters for Sequoyah and its surrounding area include:

- demographic information,
- weather or meteorological data,
- land cover information to inform atmospheric transport and dispersion, and
- protective actions and emergency response timelines.

As a brief overview of the major elements of a MACCS offsite consequence analysis, a source term describes the quantities and types of radionuclides released into the atmosphere from a nuclear power plant along with the timing and related characteristics of the release. The release information and onsite meteorology data are used to calculate the atmospheric transport, dispersion, and deposition of the radionuclides. The emergency response and protective actions are designed to minimize exposures or avoid them if possible. Doses can result from exposure to radionuclides via various exposure pathways.

The risk metrics reported for this analysis are individual latent cancer fatalities (LCFs) and individual early fatality (EF) risks to residents within selected radial distance intervals centered on the reactor site. The individual early fatalities are those expected to occur within a relatively short period from the time of exposure and the latent cancer fatalities are those expected to occur later in life of exposed individual as a result of early or chronic exposure to radioactive. As the risk metrics LCF and early fatality affect the entire population in each region, the individual risk metrics represent the average over each population modeled. That is, the risk values represent the predicted number of fatalities divided by the population.

Two types of results can be presented in a consequence assessment: scenario frequency-weighted risk or conditional risk. The scenario frequency-weighted risk is the product of the core damage frequency for the accident scenario and the conditional risk for that scenario. The

scenario frequency-weighted risk is the likelihood of a latent cancer fatality or early fatality for an individual living within specified radii of the plant per year of plant operation (i.e., LCF risk per reactor year (pry) or early fatality risk pry). Conditional risks, alternatively, are the risks predicated on the accident occurring. That is, the core damage frequency is assumed to be unity. To simplify presentation of results, all consequence results presented in Section 6 of this analysis are conditional risks.

The consequence analysis has three phases that are user-defined time periods:

- early phase of seven days,
- intermediate phase of one year, and
- chronic (long-term) phase of 50 years.

Throughout this section certain input parameters have a single deterministic value specified while other parameters (or parameter groups) are varied across a specified distribution of values. These varied parameter distributions enable investigation of the sensitivity of the result measures to uncertainty in input parameters. This process of incorporating uncertainty in input parameters is referred to as the UA and is applied to the STSBO analysis with and without random ignition sources. The remainder of this section describes the basis for selecting both the deterministic value parameters and the UA parameters.

5.2 Site Location and Surrounding Area

Sequoyah is near the center of Hamilton County, Tennessee, 18 miles northeast of the Chattanooga, Tennessee, and 14 miles west-northwest of Cleveland, Tennessee. Sequoyah is a two-unit nuclear power plant site where reactors Unit 1 and Unit 2 are located adjacent to each other sharing a common turbine building. This analysis considers results and release pathways from Sequoyah Unit 1. Therefore, the radial distance intervals considered in the MACCS analysis originate from the center of the Unit 1 reactor containment building with latitude and longitude coordinates of 35° 13' 35.65" N and 85° 05' 28.17" W (UTM Coordinates: Zone 16, N 3,899,640.62 and E 673,718.24). The spatial grid is divided into 64 radial sectors with sector one oriented North and the sector index increasing in a clockwise direction. Grid radii extend from the Unit 1 reactor building to various distances of interest.

Figure 5-1, Figure 5-2, and Figure 5-3 show the site in relation to the surrounding area in increasingly finer detail [50]. Figure 5-1 shows that Tennessee, Alabama, Georgia, and North Carolina are within a 50 mile radius of Sequoyah. To facilitate a preplanned strategy for protective actions during a nuclear power plant emergency, there are two emergency planning zones (EPZs) around each nuclear power plant. The first is the plume exposure pathway EPZ which has a radius of about 10 miles from the reactor site. The second is the ingestion exposure pathway EPZ which has a radius of about 50 miles from the reactor site. For this analysis, further references to the “EPZ” are referring to the 10 mile plume exposure pathway EPZ, although results out to 50 miles are presented. Figure 5-2 is a six mile radius map of the plant site with the town of Soddy-Daisy approximately five miles west of the plant. An aerial photograph with site boundary and location descriptions is presented in Figure 5-3. For the offsite consequence analysis, some of the key distances include the 0.345 mile exclusion area boundary (EAB), the 10 mile EPZ, and the 50 mile ingestion exposure pathway zone. As mentioned previously, the ingestion pathway was not included in analysis results at 50 miles.

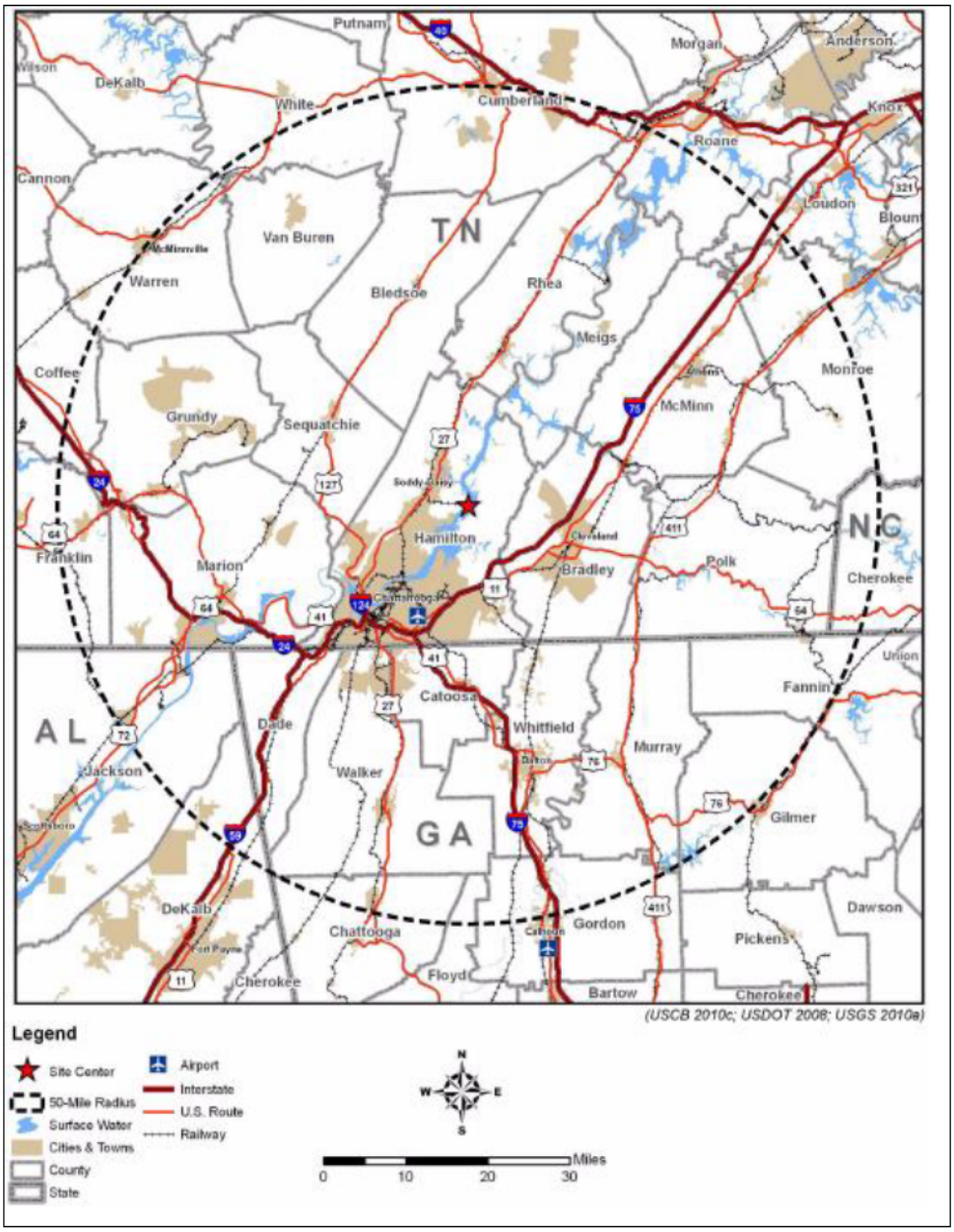

Figure 5-1 Sequoyah Nuclear Power Plant site with 50-mile radius [50]

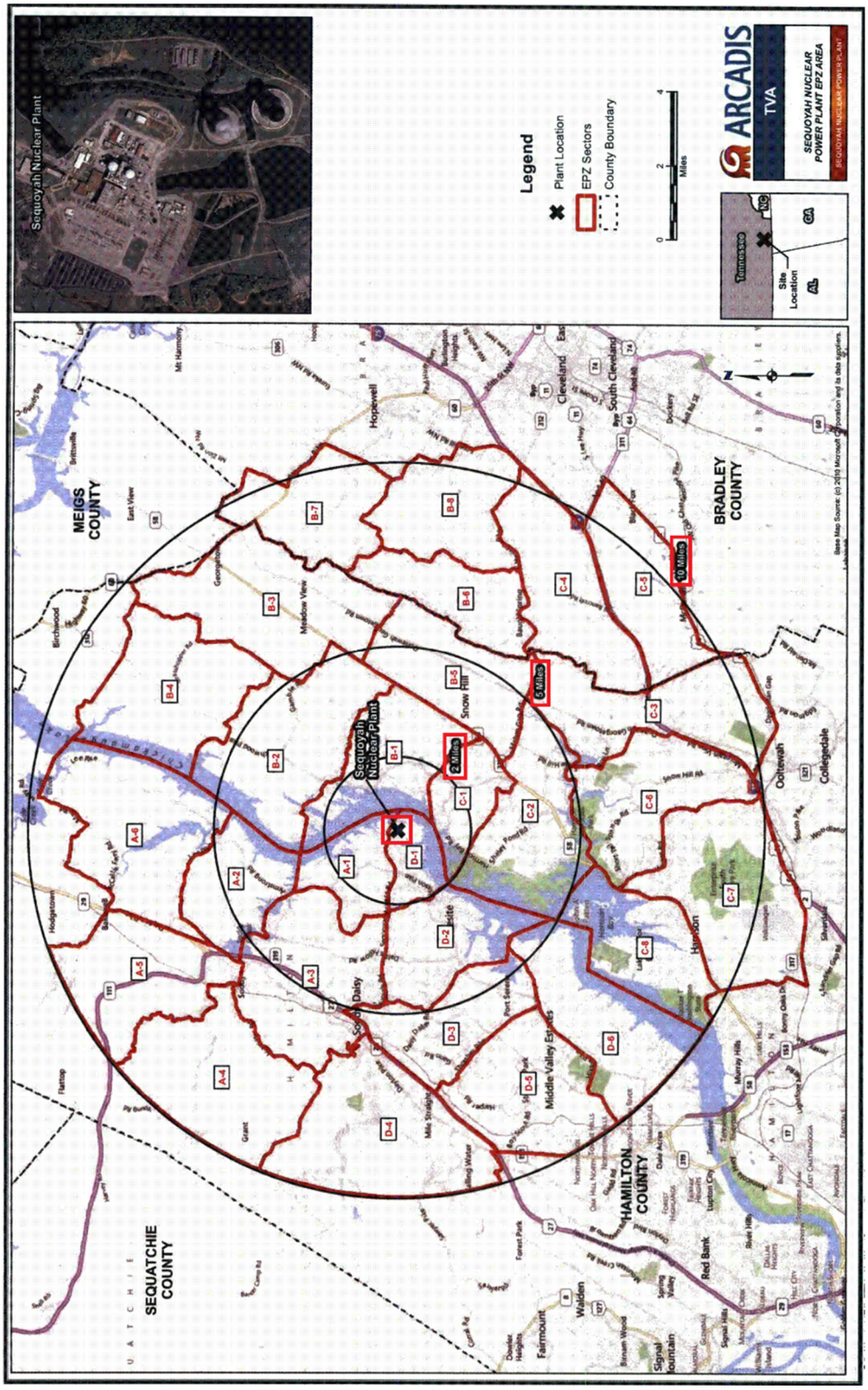

Figure 5-2 Sequoyah 2 mile, 5 mile and 10 mile radial distances and EPZ sectors [50]

Figure 5-3 Sequoyah site boundary and aerial layout [50]

5.3 Site Demographics and Economic Data

SecPop version 4.3 was used to calculate estimated population, economic, and land use data in the vicinity of Sequoyah. SecPop accesses population, land use, and economic value databases to map pertinent data to each grid element for any continental United States (U.S.) location [51].

SecPop uses population data from the 2010 Census and therefore needs to be adjusted to the project's target year, 2015. To calculate the adjustment factor, county level population data for all counties within 50 miles for 2010-2014 were used to calculate an average annual growth rate [52]. This growth rate (0.41 percent) was then applied from 2014 forward to 2015 which resulted in a 50 mile region population multiplier of 1.0208. By this method, the estimated 2015 population within 10 miles and 50 miles of the plant is 97,731 and 1,106,196, respectively.

SecPop uses economic data from a variety of databases for 2012 farmland wealth, farmland annual sales, and non-farmland wealth. In order to adjust the county level economic data available in SecPop for years beyond 2012, a SecPop MACCS economic multiplier parameter can be derived. Using the same methodology as in Surry and Peach Bottom SOARCA analyses [4][5], the economic multiplier is based on the U.S. Consumer Price Index (CPI). For this analysis, data was used from the U.S. Bureau of Labor Statistics Consumer Price Index for urban consumers (CPI-U-RS). The CPI-U-RS is a modified value of the CPI-U that excludes the more volatile pricing components such as food and energy [53]. To adjust the 2012 data to the project's target year, 2015, a ratio of the most recently available data of the CPI-U-RS for 2014 (342.4) to the 2012 value (330.7) was used to compute a resulting adjustment factor of 1.0535. This economic multiplier is then used to adjust 2012 farmland wealth, farmland annual sales, and non-farmland wealth values to 2015 values.

5.4 Site Topography and Land Cover

Sequoyah is located on two peninsulas totaling 630 acres on the western shore of the Chickamauga Lake at Tennessee River mile marker 484.5. The larger peninsula includes the power block and support facilities surrounded primarily by grass fields. The smaller peninsula includes the training center surrounded by evergreen and deciduous forests. The major structures onsite include two reactor buildings, turbine building, auxiliary building, control building, service and office building, diesel generator building, intake pumping station, ERCW pumping station, and two natural draft cooling towers. The largest structures onsite are the two cooling towers at approximately 459 feet (140 m) high. The Tennessee River bounds the site to the East and South. Private properties bound the northern and western portions of the site. Several housing developments are located adjacent to the site EAB.

The Sequoyah site lies in the Tennessee River valley which is oriented in a north-northeasterly to south-southwesterly direction. The Sequoyah river valley orientation exhibits significant influence on the wind direction near the plant, as discussed in the meteorology section below. Local topography is characterized by small ridges and valleys with a generally similar orientation. The local terrain varies from flat to rolling hills with the ground cover primarily consisting of forested land. Recent GPS land use data obtained from the U.S. Department of Agriculture (USDA) CropScape indicates a 30 mile radius around the plant is 60 percent forested, 20 percent grass/pasture, 14 percent developed, 4 percent cropland, and 2.5 percent is covered by water [53]. On a larger scale, the Tennessee River Valley is adjacent to the Cumberland Plateau to the west and the Appalachian Mountains to the east.

5.5 Meteorological Data

Weather bin sampling was chosen as the meteorological sampling option for this analysis; therefore, the MACCS model requires one year of complete weather data for Sequoyah. Data was obtained from three sources for analysis and selection of site-specific representative

weather data: the TVA meteorological tower located onsite, the Environmental Protection Agency (EPA) SCRAM website[35] database of seasonal mixing layer height data, and the National Weather Service (NWS). Sequoyah onsite meteorological tower hourly weather data was obtained from TVA for years 2008 through 2012. The onsite data were compared to the NWS data collected from a nearby weather station to better understand how a particular year compared to long-term regional trends. The MACCS Sequoyah meteorological data file contains one year of onsite weather data and the long-term EPA mixing height data.

TVA maintains a meteorological facility at Sequoyah consisting of a 91 meter (300 feet) tower instrumented at 10 meters, 46 meters, and 91 meters. Data collected at those heights include wind direction (degrees) and speed (miles per hour), averaged wind speed, and air temperature (degrees Fahrenheit). Dew point was collected at 10 meters and solar radiation (Langley/minute) and rainfall (inches) data were collected at 1 meter. These data are compiled in hourly increments that represent averaged values of hour-long intervals for each hour of a 365 day year (a total of 8760 observations). Wind direction and speed are measured every 5 seconds and averaged over the one-hour intervals.

The meteorological data required for the MACCS model include:

- the time as sequential day and hour,
- the direction the wind is moving toward,
- the average hourly wind speed (m/sec),
- the atmospheric stability class,
- the precipitation rate (1/100th inch/hr), and
- winter, spring, summer and autumn mixing heights for neutral (morning) and unstable (afternoon) conditions.

Table 5-1 presents the average diurnal mixing heights for each season. The seasonal mixing heights for neutral (morning) and unstable (afternoon) conditions are calculated by averaging 90-day blocks of data from the EPA SCRAM website. The Sequoyah mixing height data is based on EPA data from Memphis, Tennessee (the only station in Tennessee).

Table 5-1 Seasonal diurnal mixing heights for Tennessee (m).

Time of Day	Winter	Spring	Summer	Fall
Morning	580	520	420	490
Afternoon	1110	1790	1820	1000

Other than seasonal diurnal mixing height data, the weather sampling algorithm invoked for this analysis requires meteorology data for each hour of the year. EPA has published acceptable methods for synthesizing data to fill gaps. Missing data are calculated as follows:

1. To synthesize a single hour of missing data, averaging the hour prior with the hour subsequent to the missing datum was used.

[35] http:\\www.epa.gov/scram001/mixingheightdata.htm. For data analysis using EPA SCRAM data, winter is considered to start on January 1st, not December 21st.

2. For two hour periods of missing data, the average of the two hours of data prior to and subsequent to the missing data was used for each of the hours.

3. In relatively very few instances, data from a station located at an adjacent height is utilized.

4. During the few extended time periods (more than a few hours) in which data was unavailable, substitution of a similar day from the adjacent time period is performed to maintain similar daylight and seasonal weather variables.

In accordance with NRC Regulatory Guide 1.23 [54], the meteorological data recovery rate should be above 90 percent (i.e., all parameters were measured in a given hour for at least 90 percent of the hours of the year). Sequoyah 2008 to 2012 weather data completeness is well above the 90 percent threshold and is computed as two percentages shown in Table 5-2. Complete hours refers to the percentage of hourly meteorology data points that exist within a year's worth of data. For instance, in 2008, 187 hourly data points were not logged out of 8760 hours in a year, thus the complete hours are 8573 out of 8760, or 97.8 percent. Within that 8573 hours of recorded data, some of the hours may be missing one or more data points for wind speed, temperature, etc. In 2008, 111 hours of the 8573 recorded hours were missing at least one data type. Thus, the complete data percentage is 8462 out of 8573 recorded hours, or 98.7 percent.

Table 5-2 Meteorology data completion rates.

Year	Complete Hours	Complete Data
2008	97.8%	98.7%
2009	98.2%	98.9%
2010	97.4%	99.0%
2011	99.4%	99.7%
2012	98.9%	99.4%

5.5.1 Selection of Representative Weather Data

In general, the annual site meteorological data are remarkably consistent with respect to wind speed, wind direction, and stability class. Table 5-3 lists the total precipitation measured onsite for each year. Figure 5-4 presents the Sequoyah site precipitation data as monthly precipitation for each year. The year 2012 is representative of the site weather because the annual precipitation was consistent with the five year average precipitation, and it has the second highest data completion of years 2008 to 2012.

Table 5-3 Summary of precipitation by year (inches).

Year	Total
2008	39.7
2009	47.9
2010	25.5
2011	52.9
2012	39.3
Average	41.1
Std Dev	10.4

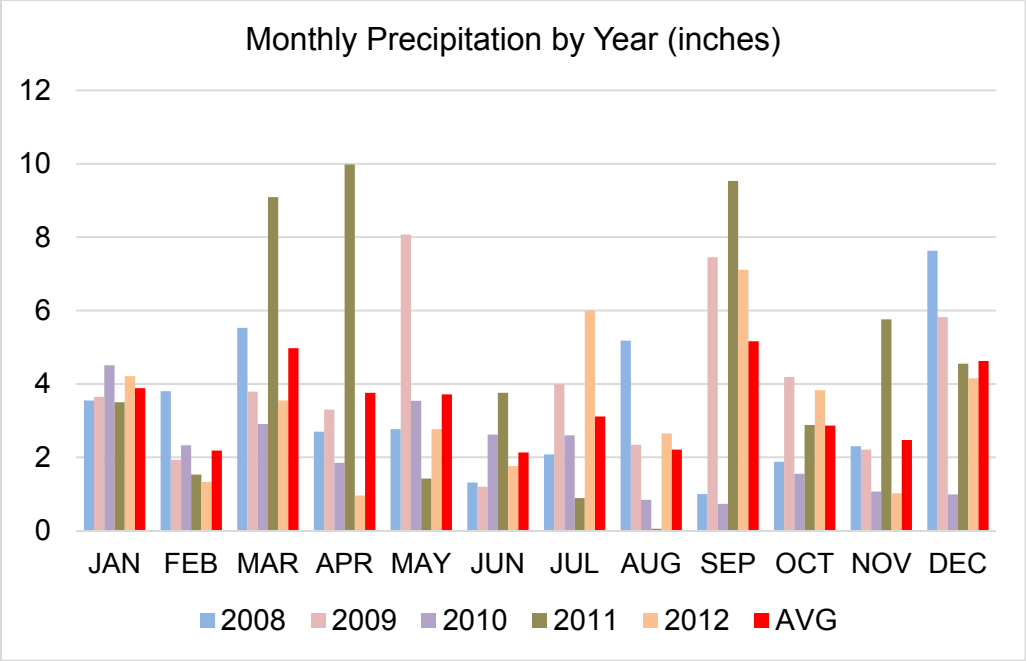

Figure 5-4 Monthly precipitation by year (inches)

5.5.2 Sequoyah Site Meteorological Features

Table 5-4 summarizes the 2012 stability class, precipitation, and wind speed average derived from the hourly data. The site has very stable weather conditions. Measurable precipitation was recorded for 528 hours out of 8760 hours per year which is 6 percent of the year. The Sequoyah site stability class, wind direction, and wind speed characteristics are described below.

Table 5-4 Summary of 2012 meteorological statistics.

Category	Metric	Frequency
Stability Class	Unstable (%)	6.0%
	Neutral (%)	42.0%
	Stable (%)	52.0%
Precipitation	Total (in)	39.3
	Frequency (hr)	528
	Frequency (%)	6.0%
Wind Speed	Average (m/s)	1.66

Atmospheric stability can be categorized using the Pasquill-Gifford scale where stability classes in MACCS are numbered 1 through 7 corresponding to classes A through G in the Pasquill-Gifford scale [55]. The hourly stability class occurrences are shown as unstable (classes 1, 2, 3)[36], neutral (class 4)[37], and stable (classes 5, 6, 7)[38] in Figure 5-5. Generally, nighttime hours are the most stable. The mornings and evenings transition from stable to neutral stability. Mid-day hours have the highest proportion of unstable classes, although neutral conditions occur two to three times more frequently than unstable conditions. Figure 5-5 presents the overall stability class frequency for 2012 and is recorded by the hour of the day. The dominant classes, 4 and 5, occurred more than 75% of the time.

[36] This corresponds to Pasquill-Gifford stability classes A, B, and C.
[37] This corresponds to Pasquill-Gifford stability classes D.
[38] This corresponds to Pasquill-Gifford stability classes E, F, and G.

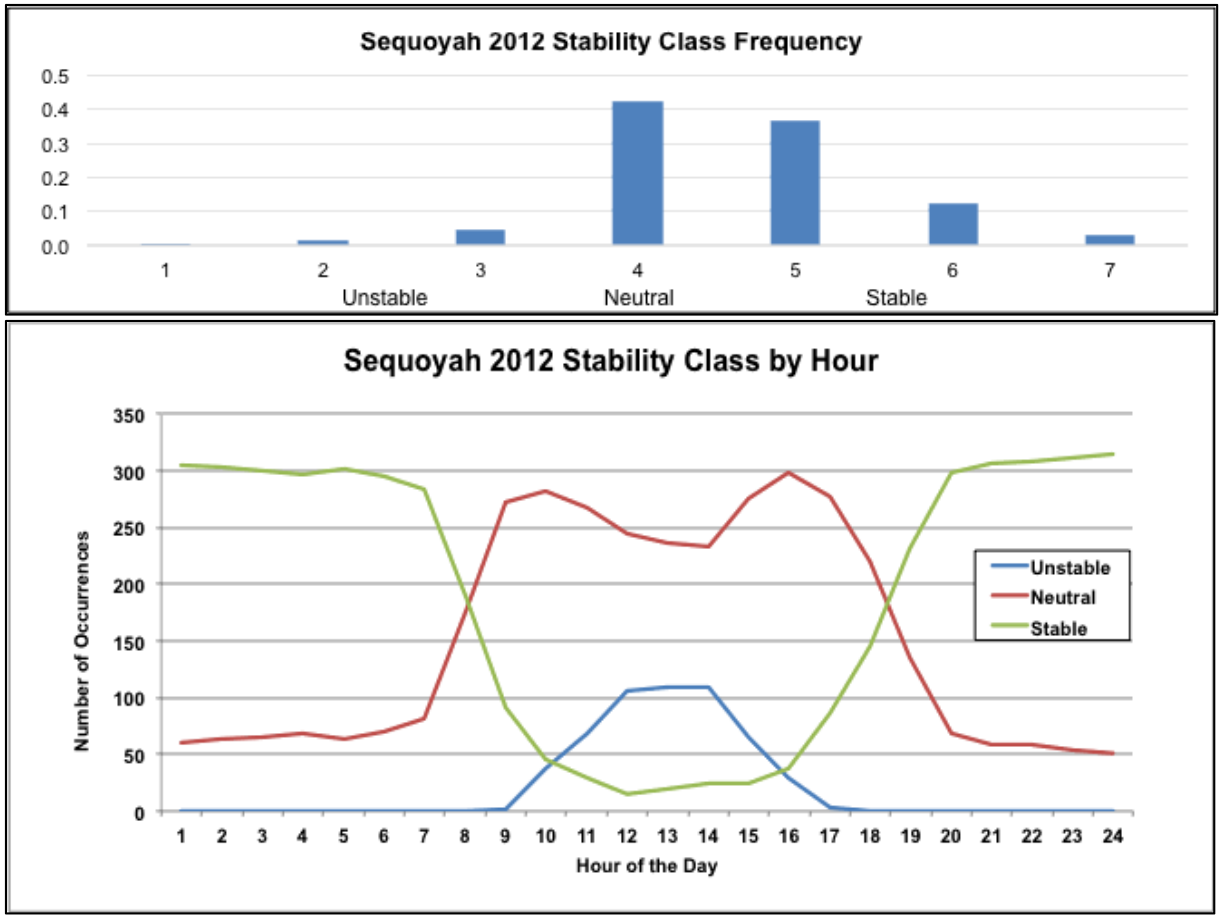

Figure 5-5 2012 stability class frequency annually and by time of day

Figure 5-6 presents 16 sector windrose data. The near-surface wind pattern is oriented North-Northeast and South-Southwest. At left, the representative weather year used in this analysis, 2012, is shown alone; at right, the windrose frequencies are shown for years 2008-2012. These consistent wind fields indicate a strong river valley wind pattern, which means the onsite wind is preferentially aligned with the Tennessee River valley at Lake Chickamauga. The wind direction data recorded at 46 meters and 91 meters exhibit the same pattern. Figure 5-7 shows the 2012 wind speed data arranged by various bins. Wind speeds between 1-5 meters per second were most frequently observed.

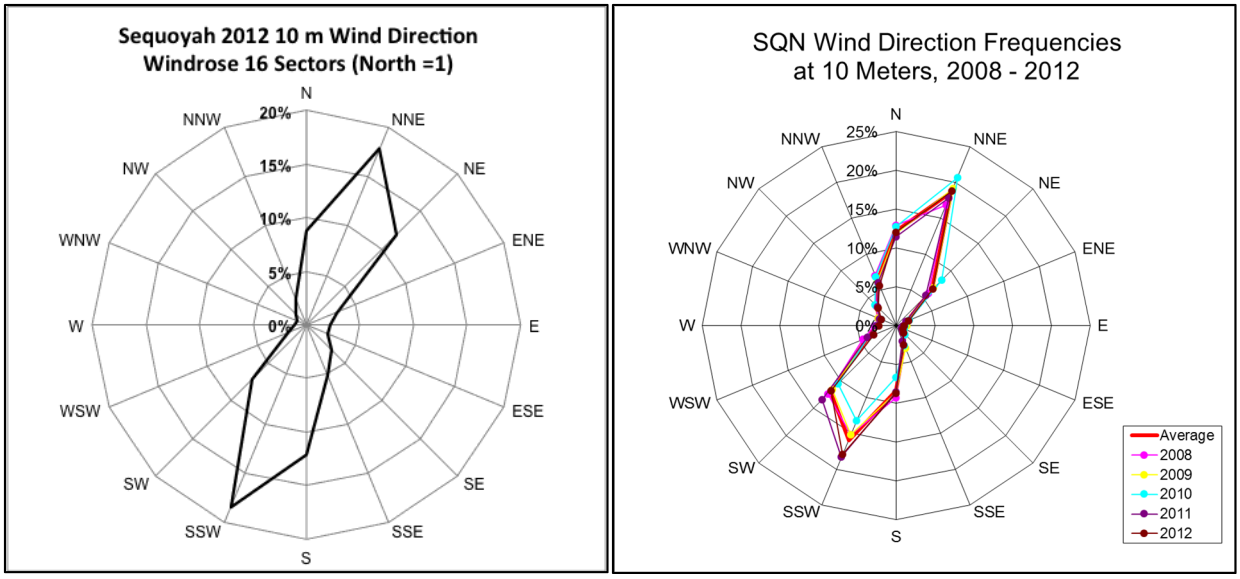

Figure 5-6 Sequoyah combined Windrose plots for 2012 and 2008 – 2012

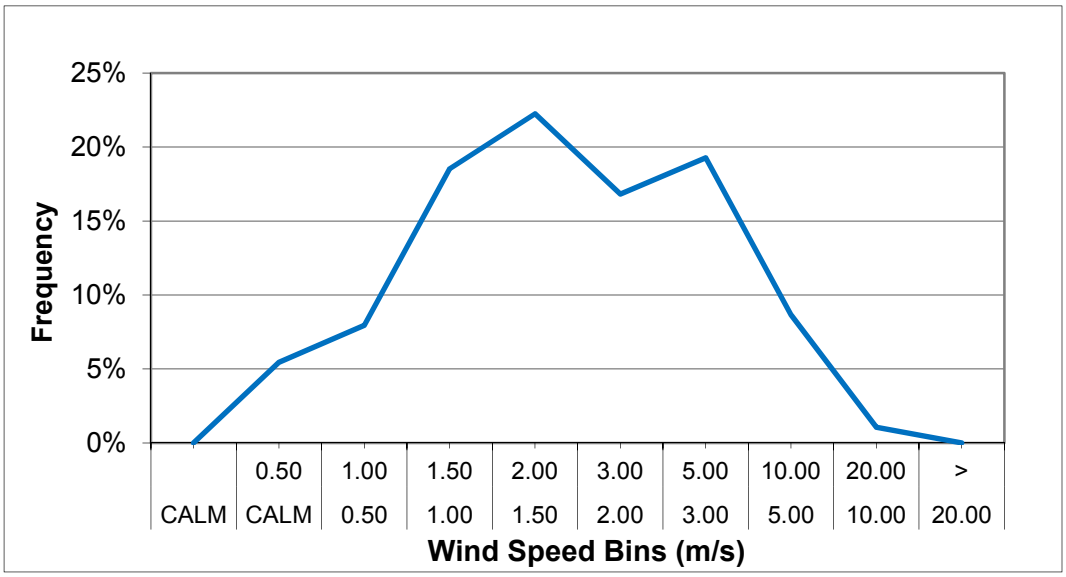

Figure 5-7 Wind speed bins for 2012

5.5.3 Weather Sampling

The timing of a future hypothetical release of radioactive materials from a severe nuclear accident is by nature impossible to predict. Future weather conditions cannot be known in advance, thus the use of historical data to quantify the consequences of a future event assumes future weather data will be statistically similar to historical data.

MACCS has several options for treatment of meteorological data, which include the ability to directly input weather data, or the ability to sample weather data from an external input file. Sampling options include a strategy that uses meteorological bins defined by the user (weather

binning), or one or more random samples from each day of the weather file. Weather binning is a type of importance sampling used to categorize similar weather data based on wind speed, stability class, and precipitation. With regard to wind direction, the assumption is that sampling within each weather bin is sufficient to represent the wind rose for that bin, i.e., the likelihood of the wind blowing in each compass direction. Because each plume segment travels in its own direction, as explained below, this assumption should be satisfied.

The weather sampling strategy adopted for Sequoyah SOARCA uses the nonuniform weather-binning approach in MACCS [8]. The weather binning structure is the same as in the Surry and Peach Bottom SOARCA analyses [4][5], which consists of 16 predefined bins for combinations of stability class and wind speed and 20 user-defined bins for rain occurring before the plume travels 32 kilometers (20 miles) [8]. The number of weather trials selected from each bin was the maximum of 12 trials and 10 percent of the number in the bin. Some bins contain fewer than 12 trials. In those cases, all trials in the bin are used. This strategy results in roughly 1,000 weather trials to represent the 8,760 hours of data in a 365-day year. A sensitivity study conducted for the Peach Bottom UA showed that this sampling strategy matched the mean results that would have been obtained by choosing every hour in the weather file (8,760 samples) within 3 percent for health risks evaluated with the linear, no-threshold (LNT) dose-response assumption and within 12 percent for health risks evaluated with the non-LNT dose-response assumptions [9]. This comparison of the current weather binning approach (1,000 weather trials) with the UA analysis (8,760 weather trials) shows that the weather binning approach, while reducing the required number of simulations, produces results that are acceptably close to the mean results of using all hours of weather data.

5.6 Atmospheric Transport and Dispersion

The transport and dispersion of radioactive materials is calculated in MACCS using a Gaussian plume segment model and the sampled site weather data. A plume segment is an integrated one hour source term characteristic of the release. MACCS allows for as many as 500 plume segments to be created through the MELMACCS pre-processor. MELMACCS transforms the environmental release output information generated from MELCOR into a MACCS source term input file.

As the release evolves in time, the wind direction, wind speed, and stability class change in hourly increments. However, once released, each individual plume segment is transported throughout the domain with their initial wind speed, direction, and dispersion conditions constant until the radioactive materials in the plume deposit on the ground and other surfaces or exit the domain.

The model calculations consider the release of plume segments, building wake effects, plume rise resulting from sensible heat content (i.e., buoyancy), dispersion, dry and wet deposition (precipitation), and the decay and ingrowths of up to 150 radionuclides for a maximum of six generations. Plume meander is calculated in accordance with NRC Regulatory Guide 1.145 [56]. More detailed descriptions are provided in the sections below. The model does not consider temporal variations in wind direction (within a single hour), spatial variations in the wind field, or terrain differences at increasing radial distances.

5.6.1 Radiological Release Information

The MELMACCS analysis process captures the characteristics of environmental releases (i.e., the accidental release from Sequoyah plant containment systems) generated from MELCOR. The release features include:

- timing, magnitude, and location(s) of releases,
- physical data such as mass flow rate, mass density, heat contents, as well as the building height and plume release height,
- plume segment radionuclide release fraction, and
- total number of plume segments and the plume segment estimated to be risk dominant.

MELMACCS calculates radionuclide specific information for use in MACCS. The Sequoyah Unit 1 middle-of-cycle core inventory was estimated using ORIGEN and is listed in Appendix B. MELCOR tracks all radionuclides as nine groups which each behave similarly within the reactor systems. It also accounts for the deposition and internal holdup of radionuclide groups within the reactor systems (i.e., the fractions of radionuclides which are released from fuel but not released into the environment). MELMACCS calculates release fractions and particle size information for each group, then sub-divides each group into constituent radionuclides based on the reactor inventory and individual radionuclide decay.

The plume segments are divided into approximately one hour increments to align with the hourly weather data. In the Sequoyah SOARCA study, quantitatively minor segments containing either flow path fractions or mass fractions of less than 0.001 of the total amount released were excluded.

5.6.2 Surface Roughness

Surface roughness affects the atmospheric transport and dispersion of radioactive material because increased surface roughness increases plume vertical mixing and increases disposition velocities for all aerosol sizes. The methodology to determine an appropriate site-averaged surface roughness measure accounting for site topography and land cover for Sequoyah is discussed in this section.

The USDA CropScape database provides data for EPA land use categories for any area in the continental U.S. Table 5-5 summarizes the surface roughness data for Sequoyah. The surface roughness calculated for use in MACCS characterizes the degree of interaction that a plume would have with ground cover, based on the height of the ground cover. Data for different ground covers, such as deciduous and coniferous forests or corn and soybeans, are combined and designated by major land use type. The surface roughness value is a weighted-averaged of aggregated land use data from within a 30 mile radius of Sequoyah. This distance is considered sufficient to characterize the area before the plume can be considered well-mixed between the ground and mixing layer height. The resulting weighted-average surface roughness is 39 centimeters. Eq. 5-1 describes the calculation of MACCS parameter ZSCALE using the surface roughness length value for Sequoyah.

Table 5-5 Surface roughness.

Type of Land Use	Acreage	Area Fraction	Surface Roughness (cm)
Open Water	44,553	2.5%	0.03
Barren	2,025	0.11%	1
Grass/Pasture	333,206	18%	3
Developed/Open Space and Developed/Low Intensity	148,153	12%	5
Shrubland	53,498	3%	5
Wetlands	5,478	0.31%	5
Crops, vegetables, fruit	11,088	4.1%	10
Forest	797,351	58%	60
Developed/Medium Intensity	22,222	1.2%	70
Developed/High Intensity	11,103	0.61%	350
Sum	1,806,113	100.00%	
Weighted-Average Surface Roughness			**39**

The effect of surface roughness of vertical dispersion is calculated as the MACCS parameter ZSCALE.

$$ZSCALE = \left(\frac{39\ cm}{3\ cm}\right)^{0.2} = 1.67$$

Eq. 5-1

5.6.3 Atmospheric Dispersion

Within MACCS, plume dispersion during downwind transport is modeled using a segmented Gaussian plume model. As the plume segment moves away from the source, dispersion generally increases the "spread" or volumetric distribution of the contamination which simultaneously decreases the concentration of the radionuclides in a particular volume of air. The plume is vertically bounded (Z-direction) between the ground surface and the mixing layer height.

The Gaussian plume model uses two spatially dependent dispersion parameters, sigma-y (σ_y) and sigma-z (σ_z), to estimate the atmospheric dispersion. These parameters can be specified in two ways in MACCS: as power-law functions or with lookup tables. The dispersion parameters are specified for each stability class. Sequoyah SOARCA used the power law function option as a function of time beyond 800 meters. The crosswind (horizontal perpendicular to the plume transport direction) and vertical dispersion coefficients, σ_y and σ_z, respectively are discussed in more detail in the UA section.

5.6.4 Dry and Wet Deposition

Deposition is the transfer of aerosol particles containing radionuclides from the atmospheric plume onto ground-level surfaces (e.g., crops, lakes, etc.). As described in Section 5.5, precipitation occurs during six percent of the hours at Sequoyah. Therefore, dry deposition is the predominant mechanism for plume depletion. However, wet deposition is also important because when precipitation occurs it is very effective in removing aerosols.

Dry deposition is calculated dependent on the particle size, atmospheric turbulence, and other factors. Wet deposition is primarily a function of the precipitation rate within a particular vertical region of the atmosphere. For example, rainout or removal of radionuclides during rain can create localized relatively high concentrations of contamination called hotspots. Both dry and wet deposition are strongly influential parameters which are discussed extensively in the UA section.

5.7 Protective Action Parameters

Protective actions can include evacuation, sheltering in place, relocation, and potassium iodide (KI) administration. For Sequoyah, the Tennessee Department of Health has a KI program, but does not pre-distribute KI to EPZ residents. KI is available for pickup by residents that live within 5 miles of the plant, and KI is planned to be available at mass-care shelters [50]. The population within 5 miles is approximately 10 percent of the total EPZ population, and it is assumed that many residents will not have KI on hand at the time of an accident. There is also a reduction in efficacy if KI is not ingested within the appropriate time. Furthermore, the impact from dose to the thyroid is a risk injury, which is not reported in the SOARCA results; therefore, no KI administration was modeled.

This Sequoyah SOARCA report differs from earlier Peach Bottom and Surry SOARCA documents [4][5] with regard to the state of infrastructure assumed in the analyses. In those prior analyses, the the impacts to the evacuation road networks and infrastructure were considered in sensitivity analyses. The Sequoyah MACCS model has been developed using the assumption that the large seismic initiating event not only disrupts Sequoyah plant systems, but also affects the evacuation conditions. Roadway access and capacity are affected due to the assumed loss of all bridges in the EPZ. In order to account for this scenario, a limited-scope roadway capacity analysis was conducted of the EPZ surrounding Sequoyah and is described in Appendix C. Evacuation routes are dispersed throughout the EPZ such that addressing the infrastructure issues by quadrant provides a reasonable approach for developing evacuation time estimates (ETEs) that account for damage to bridges. All bridges along these roadways were assumed to fail due to the earthquake. The roadway network was reviewed using aerial mapping to determine alternate routes to exit the EPZ. Accessible routes out of the EPZ were identified, and the capacities of these routes were calculated. Topography of the area was reviewed using United States Geological Service mapping to identify low lying areas where the potential for roadway flooding exists, should the upstream Watts Bar dam fail. From the ETE study, the number of vehicles exiting different areas of the EPZ was identified [57]. An estimate of the evacuation time was then developed using the number of vehicles, available evacatuion routes, and roadway capacity at the available exit points of the EPZ. A description of the capacity analysis methodology, bridge locations, alternate routes, vehicles and results is discussed in Appendix C. The earthquake-impacted roadways increase the times required for evacuees to exit the EPZ.

5.7.1 Cohort Definitions

Modeling of emergency response includes the timing of response actions related to protecting the public health and safety. MACCS treats protective action response activities at the cohort levels. A cohort is defined as a segment of the population with unique response characteristics. The cohort groupings used for Sequoyah are shown in Table 5-6.

Table 5-6 Sequoyah evacuation cohorts.

Cohort	Distance	Cohort Description
1	0 to 10 miles	Schools
2	0 to 10 miles	Special facilities (e.g., hospitals)
3	0 to 10 miles	Transit dependent evacuees
4	0 to 10 miles	Early public evacuees
5	0 to 10 miles	General public evacuees
6	0 to 10 miles	General public tail evacuees
7	10 to 15 miles	Shadow evacuees
8	0 to 10 miles	Non-evacuating public

Cohorts were established to represent members of the public who may evacuate early, evacuate late, those who refuse to evacuate, and those who evacuate from areas not under an evacuation order (e.g., shadow evacuees). SOARCA [3] was the first application of the newly increased number of allowable cohorts in MACCS. At the time, there was uncertainty regarding increased computer runtime with increasing cohorts, and it was decided that a maximum of 6 cohorts would be used for Surry and Peach Bottom SOARCA analyses [4][5]. The run time issues never materialized, and MACCS analyses have since included many cohorts with no computer run time issues. Thus, when structuring the populations in this Sequoyah analysis, the use of 8 cohorts was determined to best represent the response. Further description of each cohort group is provided below:

Cohort 1: 0 to 10 mile schools

This cohort included elementary, middle, and high school student populations within the EPZ. Schools within the Sequoyah EPZ receive notification upon declaration of a Site Area Emergency (SAE). Approximately 19 percent of residents within the EPZ are school-aged children, based on data provided in the site ETE.

Cohort 2: 0 to 10 mile special facilities

The special facilities population includes residents of medical facilities, such as hospitals and nursing homes. In an emergency, special facilities would be evacuated individually over a period of time based upon available specialized transportation (e.g., ambulances) and the number of return trips needed to evacuate a facility. In this regard, the special facilities cohort behaves similarly to the transit dependent cohort in that they shelter for an extended period of time prior to evacuating. Special facilities were modeled as a single cohort because the percentage of the total Sequoyah population is less than one percent.

Cohort 3: 0 to 10 mile transit dependent evacuees

This cohort includes EPZ permanent residents who do not have access to a vehicle or are dependent upon help from outside the home to evacuate. This group depends upon public transportation to evacuate, which can take additional time to implement. Approximately one percent of residents within the EPZ are identified in the ETE as transit-dependent [50].

Cohort 4: 0 to 10 mile early public evacuees

This cohort includes one of three general public categories. It represents a portion of the general public that begins to evacuate prior to other cohorts which allows their potential evacuation speed to be higher. Under the postulated earthquake and assumed damage

to infrastructure within the EPZ (e.g., bridge failures, power outage, etc.), it was assumed this cohort responds following the first sirens, which are sounded at SAE for this site. Sirens are expected to activate because they have backup batteries. The extensive infrastructure damage, assumed in this scenario, would be evident to EPZ residents, and there is the possibility that a power outage could limit ability of residents to receive instructions via the Emergency Alert System (EAS) messages. Thus, it was assumed this cohort evacuates in response to the first sirens heard. This cohort enters the roadway network prior to congestion. Evacuation speeds are estimated to be slow due to the extent of infrastructure damage. Approximately 40 percent of residents within the EPZ were modeled as early public evacuees. This is based on the ETE mobilization curves, but applied after the SAE sirens in this scenario.

Cohort 5: 0 to 10 mile general public evacuees
This cohort includes EPZ permanent residents who leave after the sirens are sounded for GE, and the evacuation order is broadcast via EAS messages. Even with a power outage, many residents and facilities have tone alert radios, battery powered radios, and car radios, where EAS messaging is transmitted. Thus, this group is assumed to receive the official evacuation order prior to departing. Approximately 30 percent of residents within the EPZ are considered general public.

Cohort 6: 0 to 10 mile general public tail evacuees
This cohort includes the last remaining members of the general public to evacuate from the 10 mile EPZ. The evacuation tail takes longer to evacuate for valid reasons, such as shutting down farming or manufacturing operations, performing other time consuming actions prior to evacuating, or they may have missed the initial notification. Approximately 10 percent of residents within the EPZ are tail evacuees (i.e., the last fraction of the general population to evacuate).

Cohort 7: 10 to 15 mile shadow evacuees
This cohort includes evacuees from beyond the EPZ who leave after the advisory to evacuate. The size of the shadow evacuation can be influenced by communication during the emergency and may be influenced due to external events such as the earthquake. Shadow evacuations typically begin shortly after a general evacuation begins. It is assumed 20 percent of the population from the 10 to 15 mile area beyond the EPZ shadow evacuate [58].

Cohort 8: 0 to 10 mile non-evacuating public
This cohort includes evacuees who may refuse to evacuate and are modeled as though they are performing normal activities. Approximately 0.5 percent of the population is considered to be non-evacuating. This percentage of the population that does not evacuate is consistent with research on large scale evacuations that has shown a small percentage of the public refuses to evacuate [88].

This Sequoyah SOARCA analysis differs from earlier Peach Bottom and Surry SOARCA analyses [4][5] because it implements a keyhole evacuation model representative of the expected protective action recommendation (PAR) and protective action decision (PAD). The PAR is a recommendation that is considered by offsite authorities when they make their PAD. This keyhole evacuation modeling feature was not available when the previous SOARCA analyses were performed. It is intended to reflect site-specific protective actions where the full EPZ is not evacuated, but instead a smaller region around the plant is evacuated together with downwind sectors. The keyhole model accounts for changing wind direction over the course of

the release and preferentially evacuates the population in the downwind sectors as wind shifts occur. If the wind shifts, based on hourly weather data, the evacuation is expanded to include additional sectors as illustrated in Figure 5-8. The model requires that an inner radial distance be defined, along with the number of compass sectors on either side of the wind direction.

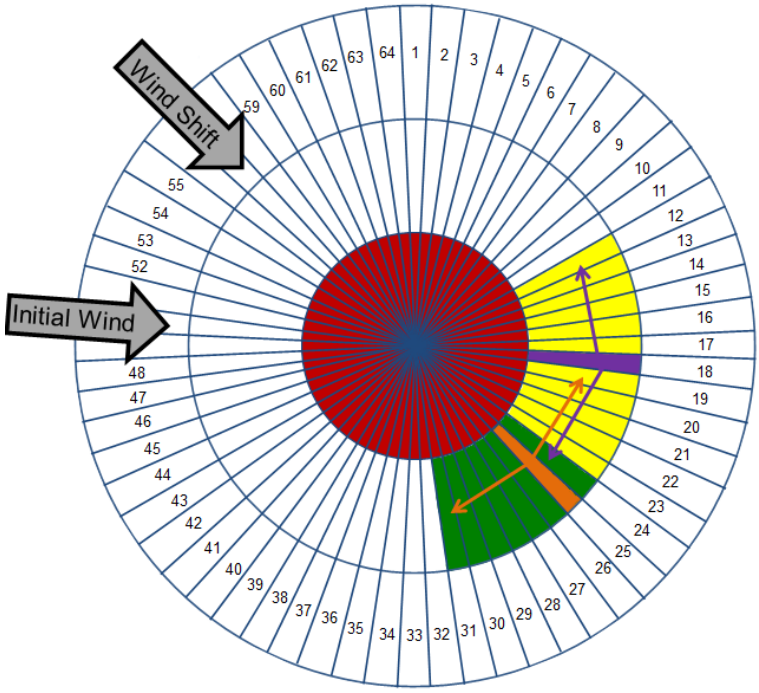

Figure 5-8 Keyhole evacuation area with a wind shift

MACCS implements the keyhole model using radial distances and sectors as discussed above; however, offsite protective actions are implemented using emergency response planning areas (called “Sectors” at Sequoyah). These Sectors are established by local authorities and align with geographical features or political boundaries. Thus, to accommodate the modeling, the expected response was reviewed and the most appropriate radial distances, available in the MACCS model, were used to define the keyhole dimensions.

To determine the keyhole distances to be modeled (radius and downwind distance) the licensee protective action recommendation (PAR) procedures and the 2013 FEMA After Action Report (AAR) for a full scale exercise were reviewed [58], [95]. The licensee PAR procedures include multiple keyhole descriptions, suggesting a keyhole is a likely PAR. The FEMA AAR provides information on a PAD that was determined in a 2013 full scale exercise [95]. The initial evacuation in the 2013 exercise included Sectors A-1, B-1, C-1 and D-1, three of which extend beyond the 2 mile radial distance. The initial evacuation in the PAD also included Sectors B and C, which extend to the 10 mile EPZ boundary as shown in Figure 5-2. Reviewing the potential keyhole options, all of which would include Sectors A-1, B-1, C-1 and D-1 plus downwind sectors, it was determined that modeling a 5 mile radius, together with downwind sectors to 10 miles was most appropriate. The shadow evacuation is modeled following the keyhole approach to a distance of 5 miles beyond the limit of the area for which an evacuation was ordered.

5.7.2 Emergency Response Timelines

Response timing, travel speeds, and durations of elements of the response are developed to represent emergency response actions directed by offsite response organizations (OROs) and implemented by the public. The modelling considers that notification of the public occurs first, followed by sheltering of the public, and then evacuation. MACCS employs three evacuation phases (early, middle, and late) where travel speeds and durations are defined for each evacuating cohort. In order to ensure all individuals complete their evacuation, the late phase of the evacuation is considered to last as long as necessary for all evacuating individuals to fully evacuate.

Figure 5-9 illustrates the modeling implemented for the Sequoyah emergency response timeline and travel speeds. The MACCS input parameters related to mobilization and evacuation route information were developed primarily from the ETE for Sequoyah [57]. The postulated initiating event for the accident is an earthquake of such magnitude that damage to offsite infrastructure would be expected. The figure shows the normal activity, sheltering, and the early and middle phases of the evacuation by cohort relative to the timing of the SAE, SAE siren, General Emergency (GE), and GE sirens (0.25, 0.50, 2.0 and 2.75 hours, respectively). In the evacuation phases, it also lists the estimated average EPZ travel speeds in miles per hour. The cohort travel speeds are consistent at a particular time of the evacuation with the exception of cohort 7 (shadow evacuees located outside of the EPZ and travelling on the roads outside of the EPZ). For the STSBO and LTSBO scenarios modeled in this analysis, it is assumed Sequoyah would declare a SAE and notify the OROs within 15 minutes. Comparing Sequoyah emergency action levels (EALs) with results from a full participation plume exposure pathway EPZ exercise reported in the FEMA AAR [95], it was determined that a GE would likely be declared two hours after accident initiation for both the STSBO and LTSBO. OROs then make a PAD, activate sirens, and broadcast EAS messages. From the FEMA AAR for Sequoyah [95], the time from ORO receipt of the GE declaration to sounding of the GE sirens was 36 minutes which was rounded to the next 15 minute increment (45 minutes). A 15 minute increment in modeling response actions is generally applied.

An assumption is that the earthquake is of such magnitude that the early general population cohort (#4 on Figure 5-9) responds to the SAE siren, rather than the GE siren. This cohort is assumed to prepare to evacuate based on having felt the earthquake, heard the SAE sirens, become aware of school evacuations, and other media broadcasts. Although this is an early response, the timing is such that their departure occurs 1.25 hours after the earthquake, and they exit the EPZ in 4.5 hours; whereas the tail, which is the latest population to mobilize, exits the EPZ in 11.75 hours.

There is some uncertainty surrounding the timing, delays, durations, and travel speeds; therefore, the input parameters for these are discussed extensively in the UA section. In addition, the specific behaviors of each cohort are also discussed in that section particularly as they apply to the UA and ranges of sampled parameters.

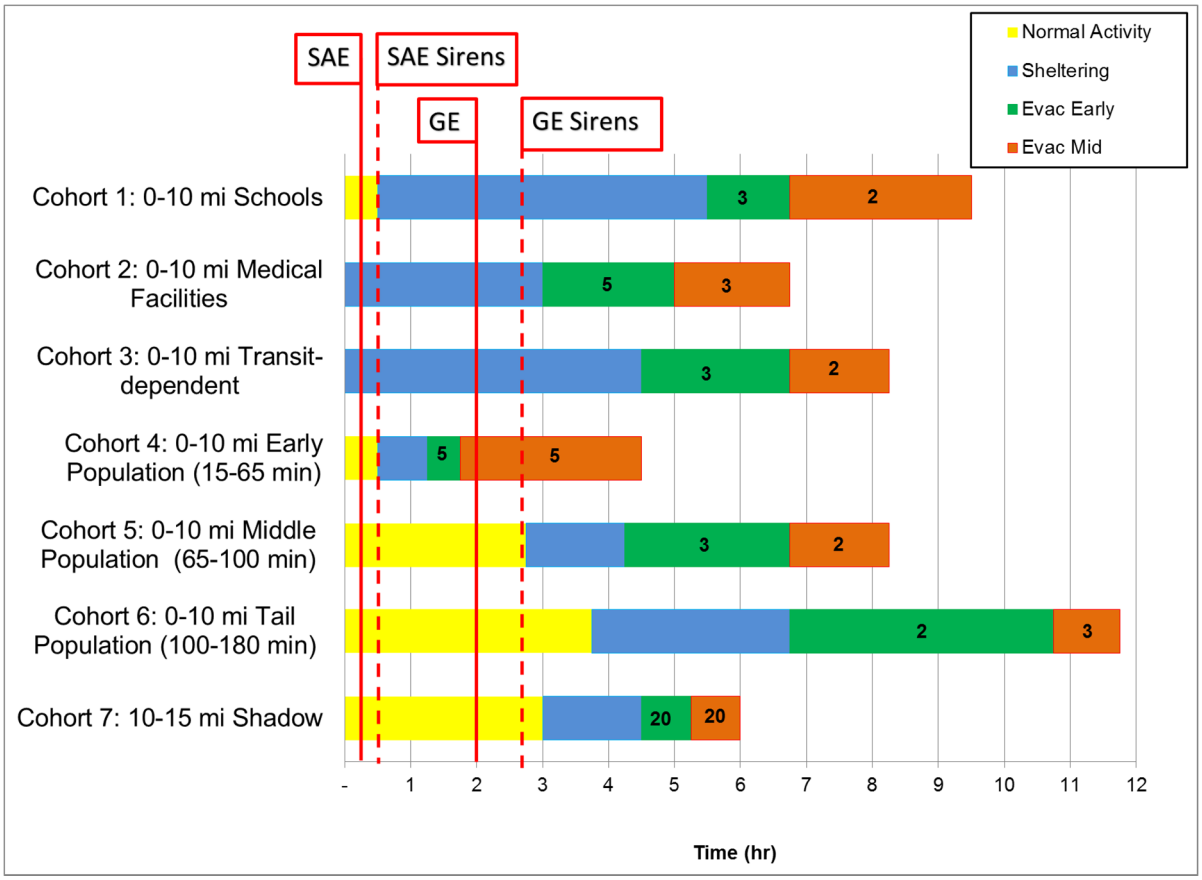

Figure 5-9 Sequoyah emergency response timeline and travel speeds (mph)

MACCS allows implementation of a delay to shelter (DLTSHL) in which shielding values are applied based on normal activity. This period is followed by delay to evacuation (DLTEVA) which represents the time residents are in their homes preparing to evacuate. One value is provided for each cohort, thus it is an average value applied to that entire cohort population.

- DLTSHL represents a delay from the time of the start of the accident until a cohort begins to shelter. Activities during this period typically include the licensee providing a PAR to the offsite authorities, OROs notification of the public to evacuate, and the time needed to begin sheltering. Sheltering is typically assumed to be a place of residence.

- DLTEVA defines the length of the sheltering period from the time a cohort enters the shelter until the cohort begins to evacuate. Delay to evacuate represents the shelter period. The duration may reflect a delay in response to the evacuation order, a need to wait for the return of commuters, a need to wait for public transportation, a need to shut down operations prior to leaving work, etc.

The phase durations are defined by DURBEG (duration of beginning phase), DURMID (duration of middle phase) and the late phase defining whatever additional time is needed for a cohort to complete the evacuation. Durations are assigned uniquely for each cohort and are adjusted based on the cohort specific attributes. The times are typically assigned such that DURBEG plus DURMID provides sufficient time for evacuees to exit the EPZ. The late phase begins at the end of DURMID and ends when the last cohort exits the analysis area. MACCS allows one

speed value for each cohort for each phase duration described as ESPEED1, ESPEED2, and ESPEED3.

The weather can affect emergency response by reducing the travel speeds. An evacuation speed multiplier (ESPMUL) reduces travel speed when precipitation is occurring, as indicated from the meteorological data file. The speed multiplier was set at 0.8, which reduces the ESPEED values to 80 percent of the fair weather travel speed whenever precipitation is identified in the weather data. The meteorology data does not distinguish the type of precipitation, however the climate data indicates historically snow and ice are rare (less than 10 percent of the precipitation) as compared to rain.

5.7.3 Shielding From Dose

The shielding or protection factor is a unitless quantity used to reduce the radiation dose to account for protection provided by a given protective action or mitigating environmental condition. Shielding is specified by the user for the cloudshine, inhalation, groundshine, and skin dose exposure pathways, and for three activity types (normal activity, sheltering, and evacuation). A shielding factor of unity represents the limiting case of a person receiving the full dose (i.e., standing outdoors and completely unprotected from exposure), and a shielding factor of zero represents the limiting case of complete shielding from the exposure.

Normal activity refers to a combination of activities that are averaged over a week and over the population, including being indoors at home or work, commuting, and being outdoors. The normal activity values assume that the average person spends 19 percent of the day outdoors and 81 percent of the day indoors [96]. MACCS shielding parameters (CSFACT, GSHFAC, PROTIN, and SKPFAC) were researched in the development of NUREG/CR-4551, Vol. 2, Part 7 [80]. For other SOARCA analyses, the normal activity shielding values for CSFACT and GSHFAC started with the site-specific NUREG/CR-4551 recommended values and adjusted these to represent the percent time indoors and outdoors. The values used for Sequoyah were similarly adjusted using site-specific shielding factor recommendations. For example, in NUREG/CR-4551, the recommended Sequoyah values for evacuation CSFACT and sheltering CSFACT were 1.0 and 0.65, respectively [80]. The normal activity, regular facilities CSFACT value presented in Table 5-7 is developed by multiplying 81% of the time indoors by the 0.65 sheltering value and adding this to the 1.0 evacuation value (because evacuation represents predominately unshielded time outdoors) multiplied by 0.19 for a time-weighted result of 0.72.

As show in Table 5-7, regular facilities are normal residences and special facilities are larger, more robust buildings with different shielding values, such as hospitals and schools. The breathing rate, skin protection, and inhalation protection are unchanged from Peach Bottom and Surry SOARCA [4][5]. Normal activity alone is assumed for nonevacuees. While some near the EPZ may shelter, most of the exposure to the plume is not in the near vicinity of the EPZ since results show the plume typically depletes slowly with distance.

Table 5-7 Shielding and Protection Factors for Evacuating Cohorts.

Population Facility Type	Cloudshine Shielding (CSFACT)			Inhalation and Skin Protection (PROTIN and SKPFAC)			Groundshine Shielding (GSHFAC)		
	Normal Activity	Sheltering	Evacuating	Normal Activity	Sheltering	Evacuating	Normal Activity	Sheltering	Evacuating

Regular Facilities	0.72	0.65	1.00	0.46	0.33	0.98	0.26	0.20	0.50
Special Facilities	0.31	0.31	1.00	0.33	0.33	0.98	0.05	0.05	0.50

Two specific shielding factors important for the UA, GSHFAC and PROTIN, are described in detail in Section 5.9.3.

5.7.4 Hotspot Relocation Time (TIMHOT)

The hotspot relocation time (TIMHOT) is the estimated time needed to relocate residents from areas that exceed the hotspot dose threshold (DOSHOT). This user specified time (36 hours) is implemented in MACCS after plume arrival. Hotspot and normal relocation are determined in MACCS based on the total effective dose commitment projected to be received by an individual who remained in place for the entire emergency phase period while engaging in normal activity. For Sequoyah base case analyses, this is 5 rem over a 36 hour exposure period. The pathways used for calculating the total effective dose commitment are cloudshine, groundshine, direct inhalation, and resuspension inhalation. The reference time for the relocation dose criteria is plume arrival. Relocated individuals are removed from the problem for the duration of the emergency phase and receive no additional dose during this phase.

The EPA PAGs for evacuation are typically used in MACCS as the dose thresholds at which the public would be relocated. In practice, when these thresholds are projected to be exceeded, OROs would be expected to relocate individuals from the affected areas. This application is typically considered for residents beyond the EPZ, but also applies to residents within the EPZ who may have refused to follow the initial evacuation orders. It is assumed these individuals will relocate when they understand a release has occurred, and they are informed they are located in elevated dose areas.

The hotspot and normal relocation time, TIMHOT and TIMNRM, should include all temporal elements that contribute to the relocation activities. This includes time for OROs to define the affected areas, develop messaging and initiate the EAS to notify the public. This also includes time for the public to prepare to leave and travel out of the affected area. Each of these elements can be influenced by factors such as size of the affected area, number of affected residents, location of residents when the warning is received, available resources to coordinate the relocation, clarity of data, weather, etc. Notification may be augmented by route alerting (which is identified in the offsite emergency plan), Reverse 911®, or other communication methods.

MACCS implements this parameter by removing the entire affected population from the dose equation a point in time, the time after plume arrival specified by TIMHOT. Because relocation takes time to implement, this user specified value was developed as an average time for relocation. In the UA section, a distribution has been developed to account for a range of source terms, population densities, seismic impact, and other characteristics that influence relocation.

5.7.5 Normal Relocation Time (TIMNRM)

TIMNRM is the time to relocate residents from areas that exceed the normal dose threshold (DOSNRM). This user specified time is relative to plume arrival. For Sequoyah base case analyses, this is 1 rem over a 24 hour exposure period. The time includes the elements

described for TIMHOT. In addition, time may be needed to allow clearance of residents relocated due to the hotspot criteria. MACCS implements this parameter by removing the entire affected population from the dose equation at a point in time after plume arrival specified by TIMNRM. As with TIMHOT, an average time is developed by considering the influencing factors. Both TIMHOT and TIMNRM time periods are varied linearly and discussed in the UA section.

5.7.6 Intermediate and Long-Term Phase

The previous sections have focused on protective actions that occur during the early phase. The early phase, also referred to as the emergency phase, focuses on the time scale of the release, emergency response, and prompt dose effects associated with exposure to radiation from the atmospheric plume via direct inhalation, cloudshine, groundshine, and skin deposition. Although the early phase lasts for days, the cumulative health effects that could result from early phase exposure are calculated over a period of one year [55]. Unlike previous Surry and Peach Bottom SOARCA analyses [4][5], Sequoyah SOARCA models an intermediate phase,

5.7.6.1 Intermediate Phase

The intermediate phase is modeled as one year, beginning at the end of the early phase. It spans the time period required for authorities to determine whether contaminated areas are suitable for habitation (MACCS habitability criterion) and prepare to decontaminate where needed. It is, therefore dependent on the magnitude of a release and the size of contaminated areas. The dose criteria for the intermediate phase was selected as 2 rem in the first year, which is consistent with the EPA protective action guide (PAG) [94]. The chronic phase spans 50 years to account for doses accumulated from groundshine (mainly longer lived gamma emitting radionuclides) and inhalation from re-suspension of contaminated soils. The dose criteria for the long-term phase was selected as 500 millirem per year after the intermediate phase, which is also consistent with the EPA PAGs [94].

5.7.6.2 Long-term Phase

This analysis also uses updated long-term protective action parameters to reflect changes in cost parameters. Decontamination and cost parameters were based on values from updated guidance on MACCS cost parameters related to protective measures and decontamination [97]. However, these parameters are not used to calculate economic consequences in this analysis, as was similarly done in Surry and Peach Bottom SOARCA analyses. Instead, cost decisions were only used to support the habitability decisions in the model to evaluate long-term doses. These parameters affect decisions on whether contaminated areas can be restored to habitability and therefore affect predicted doses and health effect risks. Unlike previous analyses, Sequoyah SOARCA evaluated three levels of decontamination represented by dose reduction factors (DRF) of 3, 5 and 15. Using three DRFs provides a level of conservatism because for any area where a DRF of 3 is insufficient, the model applies progressively higher DRFs, up to 15, which costs more to implement than a DRF of 3. For example, if the model calculates the need for a DRF of greater than 5 but less than 15, such as a DRF of 10, the full cost for a DRF of 15 is applied. All long-term protective action values for the dose projection period, dose limit, population relocation cost, along with all associated decontamination parameters can be found in Appendix B.

While SecPop enables grid-element-specific values of farmland wealth and non-farmland wealth, MACCS requires a single value of each for the entire region to determine whether

decontamination would be cost-effective if needed to restore habitability. The non-farmland wealth parameter, VALWNF, escalated to 2015 was calculated to be $342,714 per person based on a population-weighted average of all grid elements within 50 miles. This value includes public and private property, not associated with farming that would be unusable if a portion of the land was temporarily or permanently interdicted due to contamination. A similar process, using farmland-area-weighted averages was used to identify the single value of farmland wealth parameter, VALWF, for the region as $11,287 per hectare. VALWF represents farmland property such as publicly and privately owned grazing lands, farm buildings, and machinery.

5.8 Dosimetry

The doses computed by MACCS use dose conversion factors. The radiological dose to an individual in a spatial grid element is the sum product of (1) the integrated air concentration or total ground deposition of a radionuclide (in that element), (2) the exposure duration for an exposure pathway, (3) the shielding factor for an exposure pathway, (4) the dose conversion factor for a radionuclide and pathway, and (5) the usage factor for an exposure pathway. The total dose to an organ or the whole body used for modeling of health effects or protective action decision-making is then summed across all radionuclides and applicable exposure pathways. Several key dose and risk components are examined in the UA section of this report.

For the early phase, two kinds of doses are calculated: (1) acute doses used for calculating early fatalities and injuries and (2) lifetime dose commitment used for calculating cancers resulting from the early exposure. For the long-term phase, only lifetime dose commitments are calculated.

The quantities used in the dose equations depend on the source term from the accident and the exposure pathway and are either user inputs or are computed by MACCS. The radionuclide ground level concentrations are calculated by MACCS along the plume centerline. In order to calculate doses at different locations within a grid element, a correction factor (discussed in Section 3.1.1 and 3.2.1 of NUREG/CR-4691, Volume 2 [108]) is derived to reduce concentration moving away from the plume centerline. Shielding factors for the long-term phase use the early phase normal activity value for the entire population.

The dose conversion factors used in this analysis are identical to those used in the Surry UA [17]. They are based on a methodology which considers the updated dosimetry and health effects models from Federal Guidance Report No. 13 (FGR-13), as well as the instantaneous dose rate values provided in the supplemental files provided with FGR-13 [96]. This allows both a consideration of the acute effects due to short-term exposure, as well as the ability to consider annual doses as well as committed doses. The dose conversion factor file set used in this analysis, “FGR13GyEquivDCF.INP”, together with its annual dose files, contains dose conversion factors based on FGR-13 for 825 radionuclides, 26 tissues, organs, and the whole body effective dose, and four exposure pathways. MACCS contains a more limited set of organ dose quantities than are available in the DCF file based on FGR-13. MACCS considers nine organs (including whole body) for stochastic effects from chronic exposures and six organs for deterministic effects from acute exposures. Due to a current use of eight cancer sites (organs), MACCS calculates the dose to seven specific cancer sites and one residual cancer site. To estimate residual cancers, the dose coefficients for the pancreas are used as a surrogate for dose to soft tissue, following recommendations of the Oak Ridge National Laboratory letter report [82].

The dosimetry calculation considers a usage factor for the inhalation and ingestion exposure pathways. For cloudshine and groundshine, the value in the calculation is one. For inhalation, the usage factor is a volumetric breathing rate. Consistent with past studies, this parameter is 2.66E-4 m^3/s for all populations and time periods. This value was derived in NUREG/CR-4551, Vol. 2, Rev. 1, Part 7 for an adult man who sleeps 8 hours per day and engages in light activity when awake [80].

The effective dose (ICRP60ED) is used internally by MACCS for simulating protective action decisions based on dosimetric quantities computed under a system of radiation protection. The tissue weighting factors used in the computation of the dose conversion factor for the ICRP60ED effective dose are taken from ICRP-60 and are identical to those used in the Surry UA [17].

5.8.1 Exposure and Commitment Periods

The exposure period for internal pathways, inhalation and ingestion, is the period of time when the inhalation or ingestion occurs; however, doses can continue over a person's entire lifetime following the exposure. The period of time over which doses are received from an internal pathway is accounted for in the construction of dose coefficients by integrating the doses over a finite period, representing a person's lifetime, called a dose commitment period, which is usually taken to be 50 years when calculating internal pathway dose coefficients for adults. The assumption is that the average adult lives for an additional 50 years following the exposure.

Most of the exposures during the long-term phase are from groundshine; a smaller fraction is from ingestion inhalation of resuspended aerosols. Since groundshine is an external pathway, doses received are concurrent with the exposure, whereas, exposures from inhalation and ingestion during each year of the long-term phase contribute to doses received over the subsequent 50-year commitment period.

The total dose received in the first year thus corresponds to:

- all dose from external exposure during the emergency phase,
- most of the dose from internal exposure during the emergency phase,
- all of the dose from external exposure during the first year of the long-term phase, and
- most of the dose from internal exposure during the first year of the long-term phase.

The annual doses received in subsequent years correspond to:

- a fraction of the dose from internal exposure during all previous years
- most of the dose from internal exposure during that year, and
- all of the dose from external exposure during that year.

The maximum exposure time (EXPTIM) is 50 years. This was chosen to be the same as the commitment period.

5.8.2 Dose-Response Models

Analysis of different dose threshold levels, including those that limit health effects from exposure to doses above the threshold values stated, are investigated to understand how the risk of

cancer changes with radiation dose. Table 5-8 compares five dose threshold levels considered in this analysis. The types of models are LNT, annual threshold, and combined annual and lifetime thresholds. Three predominate dose-response models were considered in previous Surry and Peach Bottom SOARCA analyses [4][5]. The dose-response relationships can be described as follows:

1. The NRC accepts the LNT hypothesis as a model for estimating radiation risk and thus is reported here consistent with prior Surry and Peach Bottom SOARCA analyses.
2. Annual threshold models truncate dose-response below an average background radiation to a US citizen of 620 millirem including the averaged medical exposure or 310 millirem solely from US averaged natural background radiation. These thresholds are based on background radiation estimates from the National Council on Radiation Protection and Measurements (NCRP) [96].
3. The highest truncation level used in this analysis is consistent with the Health Physics Society (HPS) position statement which states that a quantified risk should not be assigned to doses below 5 rem annually with a lifetime limit of 10 rem [100].

The 10 millirem annual dose truncation level was investigated in this analysis, but as determined for the other SOARCA analyses produced results that were only slightly lower than the LNT assumption, and thus were not included in offsite consequence results [8].

Table 5-8 Dose responses modeled.

Model type	LNT	Annual	Annual	Annual	HPS
Annual threshold	n/a	10 mrem/year	310 mrem/year	620 mrem/year	5 rem/year
Lifetime threshold	n/a	n/a	n/a	n/a	10 rem

The probability of a LCF is calculated separately for each cancer syndrome related to each target organ and is based on the technical approach described in the National Academy of Sciences / National Research Council Biological Effects of Ionizing Radiation (BEIR) V report [101]. In 2009, the National Research Council released the BEIR VII report, which is the most up to date study of cancer induction from exposure to ionizing radiation [102]. However, because the dose coefficients used in the SOARCA studies are from FGR-13 which was developed using risk factors from BEIR V, it was decided to use risk factors from BEIR V rather than BEIR VII.

A dose and dose rate effectiveness factor (DDREF) was applied to all doses in the late phase of the offsite consequence calculation and to those doses in the early phase that were less than 20 rem (0.2 Sv) to the whole body. This factor, which reduces the health impact of dose, accounts for the fact that protracted low doses are believed to be less effective in causing cancers than acute doses. DDREF for all cancers, except the breast, was 2.0, and for the breast, it was 1.0, as recommended in the BEIR V report [101]. The cancer dose-response linear and quadratic factors originate from BEIR V, which recommends a linear dose-response model for all cancer types. A complete list of cancer risk factors is provided in Appendix B.

5.9 Uncertain MACCS Input Parameters and Distributions

There are potentially thousands of parameter values that could be varied in MACCS. The phenomenology of the submodels (meteorology, dose response, atmospheric transport, etc.) is well studied; therefore the UA focuses on a smaller set of parameters. The figures of merit for MACCS are individual LCF risk and individual early fatality risk at specified distances. The Surry UA [17] included a complete review of MACCS parameters identified in Appendix D, "Glossary of Input File Variables," of NUREG/CR-6613, "Code Manual for MACCS2," [55]. The results of that review influenced the selection of the Sequoyah parameters. A review of the MACCS parameters in the Peach Bottom and Surry UAs was conducted, and it was determined that all parameters previously considered would be considered in this analysis. The following parameter sets were included in the analysis.

- deposition,
- dispersion,
- shielding,
- early health effects,
- latent health effects, and
- emergency response.

Both epistemic and aleatory uncertainty exists for many MACCS parameters, and the combined effect adds complexity when developing the distributions. Furthermore, for some MACCS parameters, compromise values were necessary when a large number of different situations (e.g., weather trials and time of day) exist, but only one input value may be assigned. The specified values selected were deemed the most appropriate to use for these situations. As a result, the epistemic uncertainty distributions for these parameters attempt to characterize the uncertainty of the most appropriate values.

Aleatory uncertainty in weather is treated in MACCS. Weather conditions that would apply in the case of a potential accident at some time in the future cannot be known in advance. MACCS accounts for weather variability by analyzing a statistically significant set of weather trials, and the modeled results are ensemble averages of weather that represent the full spectrum of meteorological conditions. This sampling strategy was chosen to represent the statistical variations of the weather and is consistent with MACCS best practices [8]. Emergency response to a potential accident cannot be predicted in advance either, because it is dependent on source term magnitude, time of day, weather, and site specific characteristics. The MACCS parameters varied in the analysis are listed in Table 5-9.

Table 5-9 Sequoyah MACCS model uncertain parameters.

Epistemic Uncertainty
Deposition
Wet Deposition Coefficient (CWASH1)
Dry Deposition Velocities (VDEPOS)
Shielding Factors
Groundshine Shielding Factors (GSHFAC)
Inhalation Protection Factors (PROTIN)
Early Health Effects
Early Health Effects LD_{50} Parameter (EFFACA)

Epistemic Uncertainty
Early Health Effects Exponential Parameter (EFFACB)
Early Health Effects Threshold Dose (EFFTHR)
Latent Health Effects
Dose and Dose Rate Effectiveness Factor (DDREFA)
Lifetime Cancer Fatality Risk Factors (CFRISK)
Long-Term Inhalation Dose Coefficients
Dispersion
Crosswind Dispersion Linear Coefficient (CYSIGA)
Vertical Dispersion Linear Coefficient (CZSIGA)
Time-Based Crosswind Dispersion Coefficient (CYCOEF)
Emergency Response
Evacuation Delay (DLTEVA)
Evacuation Speed (ESPEED)
Hotspot Relocation Time (TIMHOT)
Normal Relocation Time (TIMNRM)
Hotspot Relocation Dose (DOSHOT)
Normal Relocation Dose (DOSNRM)
Aleatory Uncertainty
Weather Trials

The storyboard process described in Section 3.2 was also implemented for MACCS parameters. Many of the uncertain MACCS parameters have both epistemic and aleatory contributions, and the combined effect adds complexity when developing the distributions. The focus of this analysis is on epistemic uncertainty; however, some of the distributions developed for the uncertain inputs include aleatory uncertainty. For example, some of the evacuation parameters also include the effects of weather, which is considered aleatory uncertainty. While the effects of adverse weather on evacuation speed are partially accounted for through use of a single speed reduction factor, this may not address all weather conditions, and this leads to some uncertainty in the input parameters resulting from weather uncertainty. No effort was taken to separate aleatory and epistemic uncertainties when they both contribute to individual parameters; instead, a simple approach is taken where weather is considered to be aleatory in nature, and all other uncertainties are considered to be epistemic in nature. A total of 622 parameters were sampled for the MACCS portion of the UA. Table 5-10 lists the distributions and bounds related to each parameter. For many of these parameters, the sampling approach is quite complex and is described in detail in this section.

Several of the parameter distributions selected for this analysis are based on expert elicitation data captured in NUREG/CR-7161, “Synthesis of Distributions Representing Important Non-Site-Specific Parameters in Off Site Consequence Analysis” [79]. The United States and the Commission of European Communities conducted a series of expert elicitations to obtain distributions for uncertain variables used in health consequence analyses related to accidental release of nuclear material. The distributions reflect degrees of belief for non-site specific parameters that are uncertain and are likely to have significant or moderate influence on the results. The methodology in NUREG/CR-7161 [79] used a resampling of the expert values and was based on the assumption of equal weights of the expert opinions.

Table 5-10 Uncertain MACCS parameters applied in the analysis.

Uncertain Parameter		Distribution type		Mode α, β	Lower Bound	Upper Bound
Wet Deposition (CWASH1)		Log uniform			10^{-6}	10^{-4}
Dry Deposition Velocities (VDEPOS, m/s)		Triangular	1	5.04E-04	1.60E-04	1.60E-03
			2	4.63E-04	1.46E-04	1.46E-03
			3	6.06E-04	1.92E-04	1.92E-03
			4	1.02E-03	3.23E-04	3.23E-03
			5	2.00E-03	6.32E-04	6.32E-03
			6	4.09E-03	1.29E-03	1.29E-02
			7	7.89E-03	2.50E-03	2.50E-02
			8	1.29E-02	4.09E-03	4.09E-02
			9	1.60E-02	5.07E-03	5.07E-02
			10	5.15E-02	1.63E-02	1.63E-01
Groundshine Shielding Factors (GSHFAC)*		Continuous Linear				
Inhalation Protection Factors (PROTIN)*		Uniform				
Early Health Effects LD_{50} Parameter (EFFACA)*	Hematopoietic	Continuous Linear				
	Pulmonary					
	Gastrointestinal					
Early Health Effects* Exponential Parameter (EFFACB)	Hematopoietic	Continuous Linear				
	Pulmonary					
	Gastrointestinal					
Early Health Effects Threshold Dose (EFFTHR)*	Hematopoietic	Continuous Linear				
	Pulmonary					
	Gastrointestinal					
Dose and Dose Rate Effectiveness Factor (DDREFA)*		Continuous Linear				
Lifetime Cancer Fatality Risk Factors (CFRISK)	Multiple organs	Truncated Log normal		Varies by organ	Varies by organ	Varies by organ
Long-Term Inhalation Dose Coefficients	Multiple organs and radionuclides	Log normal		Varies	Varies	Varies
Crosswind Dispersion Linear Coefficient (CYSIGA, m)	A/B	Continuous Log triangular		0.7507	0.3002	1.8768
	C			0.4063	0.1625	1.0158
	D			0.2779	0.1112	0.6948
	E/F			0.2158	0.0863	0.5395
Vertical Dispersion Linear	A/B	Continuous Log triangular		0.0361	0.0144	0.0903
	C			0.2036	0.0814	0.509

Uncertain Parameter		Distribution type	Mode α, β	Lower Bound	Upper Bound
Coefficient (CZSIGA, m)	D		0.2636	0.1054	0.659
	E/F		0.2463	0.0985	0.6158
Evacuation Delay (DLTEVA, hr)	Cohort 1	Triangular	5	1	8
	Cohort 2		3	2	6
	Cohort 3		4.5	3	9
	Cohort 4		0.75	0.25	3
	Cohort 5		1.5	0.5	3
	Cohort 6		3	1	5
	Cohort 7		1.5	1	3
	Cohort 8		N/A	N/A	N/A
Evacuation Speed (ESPEED, mph)	Cohort 1	Triangular	2	0.5	5
	Cohort 2		3	0.5	10
	Cohort 3		2	0.5	5
	Cohort 4		3	0.5	10
	Cohort 5		2	0.5	5
	Cohort 6		3	0.5	10.0
	Cohort 7		20	10	30
	Cohort 8		N/A	N/A	N/A
Hotspot Relocation Time (TIMHOT, hr)		Uniform		24	48
Normal Relocation Time (TIMNRM, hr)		Uniform		36	72
Hotspot Relocation Dose (DOSHOT, rem)		Triangular	5	1	7.5
Normal Relocation Dose (DOSNRM, rem)		Triangular	1	0.5	2
Weather Trials - Aleatory Uncertainty					

*Multiple values, refer to specific parameter section for discussion

The MACCS parameters described below represent some of those that were considered but not included in the analysis.

Risk of Early Injury
The figures of merit for all of the SOARCA activities have not included risk of early injury. For consistency, this metric was also not included in the Sequoyah analysis.

Ingestion Pathway
The ingestion pathway was not treated in the SOARCA analyses because uncontaminated food and water supplies are abundant within the United States, and it is unlikely that the public would eat radioactively contaminated food.

Habitability
The habitability criteria is considered to be an important uncertain parameter, but was not included because a detailed sensitivity analysis was performed with the Peach Bottom UA. The Peach Bottom analysis showed, as would be expected, that when the dose truncation models

were used, the LCF risks within the EPZ were orders of magnitude lower when the habitability criteria was below the dose truncation level. Beyond the EPZ, the habitability criteria showed a smaller effect on the overall LCF risk when a dose truncation model was applied.

Non-Evacuees
Evacuation research has documented that some residents refuse to evacuate. As a contributor to the risk in previous analyses [4][5], investigating uncertainty in the number of non-evacuees would be of interest. However, MACCS does not have a capability to reapportion population fractions in an uncertain application.

Wet Deposition
The wet deposition model parameters include CWASH1 and CWASH2. CWASH1 was selected to vary because there is considerable research and data available to support development of the distribution. The same is not true for CWASH2. Although this would be a reasonable parameter to evaluate, it was not considered because there are insufficient data to support development of a defensible distribution. Furthermore, CWASH1 captures the effect of wet deposition sufficiently, such that it was not necessary to evaluate CWASH2 as an exploratory parameter.

Cloudshine Shielding Factor
The cloudshine shielding protection factor (CSFACT) was included in the Peach Bottom uncertainty analysis [9]. However, it was subsequently determined there was an error in the reference from which the cloudshine distribution was taken. There was no other source found to inform an accurate distribution for this parameter. This was not identified as an important parameter in the Peach Bottom UA and the team lacked a basis for specifying a distribution for this parameter; therefore, a single point estimate was used.

5.9.1 Wet Deposition Model (CWASH1)

CWASH1 is a linear factor in the expression for the wet deposition rate for aerosols. A log uniform distribution was used to represent uncertainty with a lower bound of 10^{-6} and an upper bound of 10^{-4}. Under rainy conditions, wet deposition is very effective and rapidly depletes the plume. This process can produce concentrated deposits on the ground and create what is often referred to as a hotspot (i.e., an area of higher radioactivity than the surrounding areas) [87]. The epistemic uncertainty associated with CWASH1 is potentially important in reactor accident consequence calculations because increasing values for CWASH1 result in increased local concentrations of radionuclides deposited by rainfall events. In turn, such increased local radionuclide concentrations can have two opposing effects on radiation exposure and resulting health effects. First, high local radionuclide concentrations can increase early individual exposure and resulting early health effects. Second, high local radionuclide concentrations can increase the total fraction of a radionuclide release that is interdicted, and thus decrease long-term population exposure and resulting latent health effects. This happens because the localized, high-concentration area created by the rain is likely to be interdicted, reducing the exposures to the residents in the long term. Populations at longer distances receive less exposure because most of the plume has been washed out by the rain.

Rationale for Distribution

The model used in MACCS for wet deposition of aerosols over a unit area for a time interval [t_i, t_{i+1}] is formally given by Eq. 5-2

$$dC(t)/dt = -\lambda C(t) = -c_1 R^{c_2} C(t),$$

Eq. 5-2

where t = time (units: seconds), $C(t)$ = vertically integrated aerosol concentration in the plume at time t (units: Bq/m^2), $\lambda = c_1 R^{c_2}$ = fractional removal rate for aerosols (units: 1/second), R = rainfall rate (units: mm/hr), and c_1 (units: $1/\mathrm{s(mm/hr)}^{c_2}$) and c_2 (units: dimensionless) are constants used in the definition of λ. In turn, Eq. 5-3

$$\begin{aligned} D(t_i, t_{i+1}) &= C(t_i) - C(t_{i+1}) \\ &= C(t_i) - C(t_i)\exp\left[-\lambda(t_{i+1} - t_i)\right] \\ &\cong \lambda(t_{i+1} - t_i) C(t_i) \end{aligned}$$

Eq. 5-3

is the estimated aerosol deposition (units: kg/m^2) that takes place over the time interval [t_i, t_{i+1}].

In the computational implementation of aerosol deposition in MACCS, the rainfall rate R changes hourly for each rainfall event; however, the same values for c_1 and c_2 are used for all rainfall events throughout a year. Although rainfall rate is taken into account in the definition of λ, it is well known that many additional properties of a rainfall event affect aerosol deposition, including (i) distribution of aerosol size, (ii) chemical and physical properties of aerosols, (iii) distribution of rain drop size, (iv) different aerosol removal rates within clouds (i.e., rainout) and below clouds (i.e., washout), and (v) short-term temporal variations in rainfall rate that are lost in reported hourly rainfall rates [70][71][72][73].

Given that MACCS uses fixed values for c_1 and c_2 for all rainfall events over the course of one year, the indicated range of properties that can affect aerosol deposition presents a major challenge in defining uncertainty distributions for c_1 and c_2. Specifically, the values used for c_1 and c_2 in MACCS compromise values that are used for a large number of different rainfall situations, while being the most appropriate values to use for only a few of these situations. As a result, the epistemic uncertainty distributions for c_1 and c_2 should characterize the uncertainty in the locations of the most appropriate values to use for c_1 and c_2, given that a single value for c_1 and a single value for c_2 are used for all rainfall events during a year. Given the manner in which c_1 and c_2 are used in MACCS, care should be taken to avoid using distributions for c_1 and c_2 that are intended to characterize the variability in c_1 and c_2 over the range of individual rainfall events, as the use of such distributions may produce unrealistic uncertainty analysis results. For example, the results of the expert elicitations for the wet deposition of aerosols in Appendix A of [74] appear to be for aleatory uncertainty over individual rainfall events.

The strategy adopted here to quantify the epistemic uncertainty associated with values for c_1 and c_2 chosen for universal use (i.e., for all rainfall conditions in a year of weather data) was

first to look at the results of a number of studies that obtained values for c_1 and c_2 from data for real rainfall events or from computational models that incorporate effects that are difficult to quantify for observational data (e.g., [70] Tables 10 and 11; [71] Tables 7-11; [72] Table 3; [73] Equations (16) and (21); [75] Table 1; [76] Equations (1) and (2); [77] Figures 2 and 3; [78] Table 9). Next, choose a range of possible values for c_1 and c_2 that is representative of these values, while avoiding extreme values. The outcome of this effort was a range of [10^{-6}, 10^{-4}] for c_1 and a fixed value of 0.7 for c_2. A fixed value for c_2 was selected because, given a potential range of perhaps [0.6, 0.8] for c_2, the effects of the much larger range for c_1 should dominate the effects of the uncertainty associated with c_2. Given the absence of a reason to assign a particular distribution to the possible values for c_1, a log-uniform distribution is specified for the indicated range of [10^{-6}, 10^{-4}] so that each order of magnitude is assigned the same probability (i.e., 0.5). The CDF is presented in Figure 5-10. c_1 and c_2 in the above discussion correspond to CWASH1 and CWASH2 in the MACCS framework, respectively.

Dr. Hanna, one of the experts involved in the expert elicitation documented in NUREG/CR-6244 [74], was asked to review the wet deposition parameter distribution. He offered a number of constructive comments and indicated that this distribution is appropriate for this application. Most of Dr. Hanna's comments have been addressed in the final version of this document.

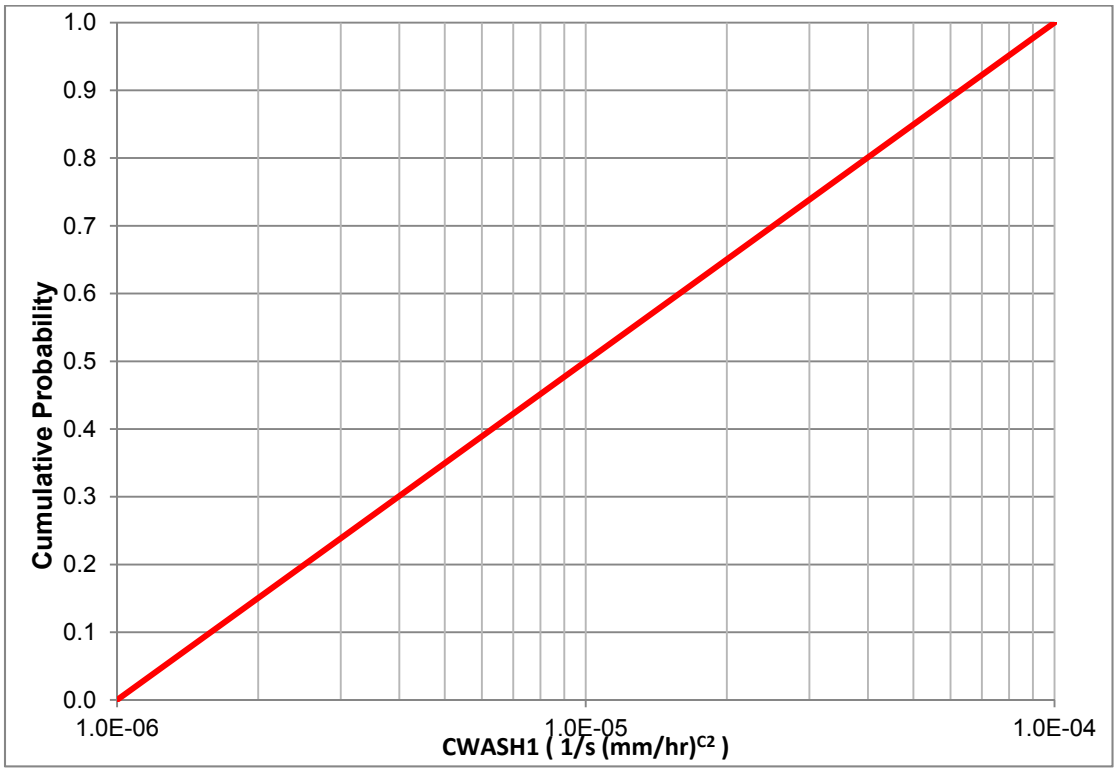

Figure 5-10 CDF of the linear coefficient in the MACCS wet deposition model, CWASH1

5.9.2 Dry Deposition Velocities (VDEPOS)

Dry deposition velocities are established for each aerosol bin to represent the dependence of deposition velocity on particle size. Because MELCOR predicts less than one percent of the iodine release group to be in vapor form and subject to deposition, vapors are not explicitly considered in this section.

A triangular distribution is used to represent uncertainty in each of nine aerosol particle sizes. Dry deposition is the only mechanism for deposition onto the ground for about 94 percent of the hours of the year at Sequoyah. Since long-term exposures usually contribute more than 50 percent of the overall exposure, deposition is important because deposited material is the only source of exposure during the long term. Furthermore, the Peach Bottom UA [9] indicated that dry deposition velocity is the most important parameter of all those considered for individual latent cancer risk.

Dry deposition involves a variety of mechanisms that cause aerosols to deposit, including gravitational settling, impaction onto surface irregularities, including buildings and other manmade structures, and Brownian diffusion. Dry deposition is a much slower process than wet deposition but occurs continuously; whereas, wet deposition occurs intermittently. Larger values of dry deposition velocity result in larger long-term doses at shorter distances and smaller doses at longer distances. The converse is also true that smaller values of dry deposition velocity result in smaller long-term doses at shorter distances and larger doses at longer distances.

Rationale for Distributions

As a starting point, the distributions for dry deposition velocity use the expert elicitation data in NUREG/CR-6244 [74]. These expert data are evaluated in Revision 1 of *Synthesis of Distributions Representing Important Non-Site-Specific Parameters in Off-Site Consequence Analysis* [13], Section 3. The expert data show uncertainty ranges of nearly five orders of magnitude for small particles (0.1 μm) and about three orders of magnitude for large particles (10 μm). These ranges seem larger than should be expected for representative values that are to be applied to an entire year of weather trials. In reviewing the expert elicitation documents, it is likely that the experts interpreted the uncertainty to represent instance by instance uncertainties rather than representative values for a large set of weather trials to represent one year of weather data.

In NUREG/CR-4551, Vol. 2, Rev. 1, Part 7, (pp. 2-18 to 2-20) [80], the authors describe the uncertainty in deposition velocity for NUREG-1150 [12]. In that study, a single deposition velocity was used to characterize the entire range of aerosol sizes that would be released into the atmosphere during a reactor accident. The best estimate, based on empirical equations and physical models, was that deposition velocity is 0.3 cm/s and that the reasonable range of uncertainty is 0.03 to 3 cm/s, a range of a factor of 100. This range accounts for uncertainties in aerosol size, wind speed, surface roughness, and aerosol density. Of these uncertainties, aerosol size is explicitly accounted for in the current study, but uncertainty in the other three parameters should have an effect on the overall uncertainty in deposition velocity. This reasoning should lead to an uncertainty range for a specific aerosol size that is less than two orders of magnitude, which is clearly narrower than the range provided in the expert elicitation study. Another parameter not discussed in the NUREG-1150 documentation is aerosol shape factor, but this should have a relatively minor contribution to uncertainty in deposition velocity.

Estimation of the importance of wind speed, surface roughness, and aerosol density can be made from Eq. 5-4, which is a modified version of Equation 3.1 in NUREG/CR-7161 [79]. The coefficients *a* through *f* are updated 50th percentile values based on Table 3-1 from NUREG/CR-7161 [79]. For establishing a range of deposition velocities considering uncertainties in surface roughness and wind speed, the important parameters in the equation are *e* and *f*, which are respectively 1.061 and 0.169 in the table. By examining the meteorological data file for Sequoyah, a representative range for wind speed is 1 to 10 m/s, with 1.66 m/s being the annual mean wind speed.

From Eq. 5-4, this range in wind speed leads to about a factor of 5 in deposition velocity. Aerosol density has a significant effect for larger particles and a negligible effect for small particles. For larger particles, a range of 4 in particle density corresponds to a range of about 2 in deposition velocity. For small aerosols, particle density has almost no effect on deposition velocity and for that reason it is not included here. If a reasonable range of surface roughness is 10 cm to 60 cm (0.1 m to 0.6 m), the deposition velocities vary by about a factor of 1.5. From this discussion, assuming that the influences of wind speed and surface roughness are independent, which is reasonable, then the uncertainty range in deposition velocity to account for these effects should be about a factor of 8, as explained below.

$$ln(v_d) = a + b\left(\ln d_p\right) + c\left(\ln d_p\right)^2 + d\left(\ln d_p\right)^3 + e \cdot z_0 + f \cdot V$$

Eq. 5-4

Where

$d_p = hydrodynamic\ particle\ diameter, (\mu m)$
$z_0 = surface\ roughness, m$
$v_d = deposition\ velocity, cm/s$
$V = wind\ speed, m/s$
$a, b, c, d, e, f =$ correlation coefficients

The above discussion corresponds to the following equation, which is simply the difference in Eq. 5-4 evaluated at an upper bound and a lower bound set of values:

$$ln(v_d)_{UB} - ln(v_d)_{LB} = \ln\left(\frac{(v_d)_{UB}}{(v_d)_{LB}}\right) = e \cdot [(z_0)_{UB} - (z_0)_{LB}] + f \cdot [(V)_{UB} - (V)_{LB}]$$
$$= 1.061 \cdot (0.6 - 0.1) + 0.169 \cdot (10 - 1)$$

Eq. 5-5

Where
UB indicates an upper bound value
LB indicates a lower bound value

Solving Eq. 5-5 for the ratio of the upper bound to the lower bound value of deposition velocity produces a factor of about 8. This value is rounded up to a factor of 10 to account for variations in particle size and density within a bin.

To construct distributions to be used in this study for each aerosol size, the 50th percentile values from the expert elicitation are used as the modes of a set of triangular distributions. These values were chosen because, although the distributions from the expert elicitation process are considered too wide, the median values from these distributions should represent best estimates from the group of experts. The lower and upper bounds of triangular distributions

are chosen to be the mode divided and multiplied by the square root of 10, respectively. The 50th percentile values from the expert elicitation (modes of the triangular distributions) are evaluated from Eq. 5-4 with choices for surface roughness to be 0.39 m and wind speed to be the mean wind speed, 1.66 m/s. The distribution parameters are tabulated in Table 5-11 and shown in Figure 5-11. Dr. Hanna, one of the experts involved in the expert elicitation documented in NUREG/CR-6244 [74], was asked to review the dry deposition distributions. He offered a number of constructive comments but did not indicate that the bounds should be modified or that the distribution is inappropriate for this application.

Table 5-11 Dry deposition velocities.

Triangular Distributions	Deposition Velocity (m/s)		
Representative Aerosol Diameter (μm)	Lower Bound	Mode	Upper Bound
0.15	1.60E-04	5.04E-04	1.60E-03
0.29	1.46E-04	4.63E-04	1.46E-03
0.53	1.92E-04	6.06E-04	1.92E-03
0.99	3.23E-04	1.02E-03	3.23E-03
1.8	6.32E-04	2.00E-03	6.32E-03
3.4	1.29E-03	4.09E-03	1.29E-02
6.4	2.50E-03	7.89E-03	2.50E-02
12	4.09E-03	1.29E-02	4.09E-02
22	5.07E-03	1.60E-02	5.07E-02
41	1.63E-02	5.15E-02	1.63E-01

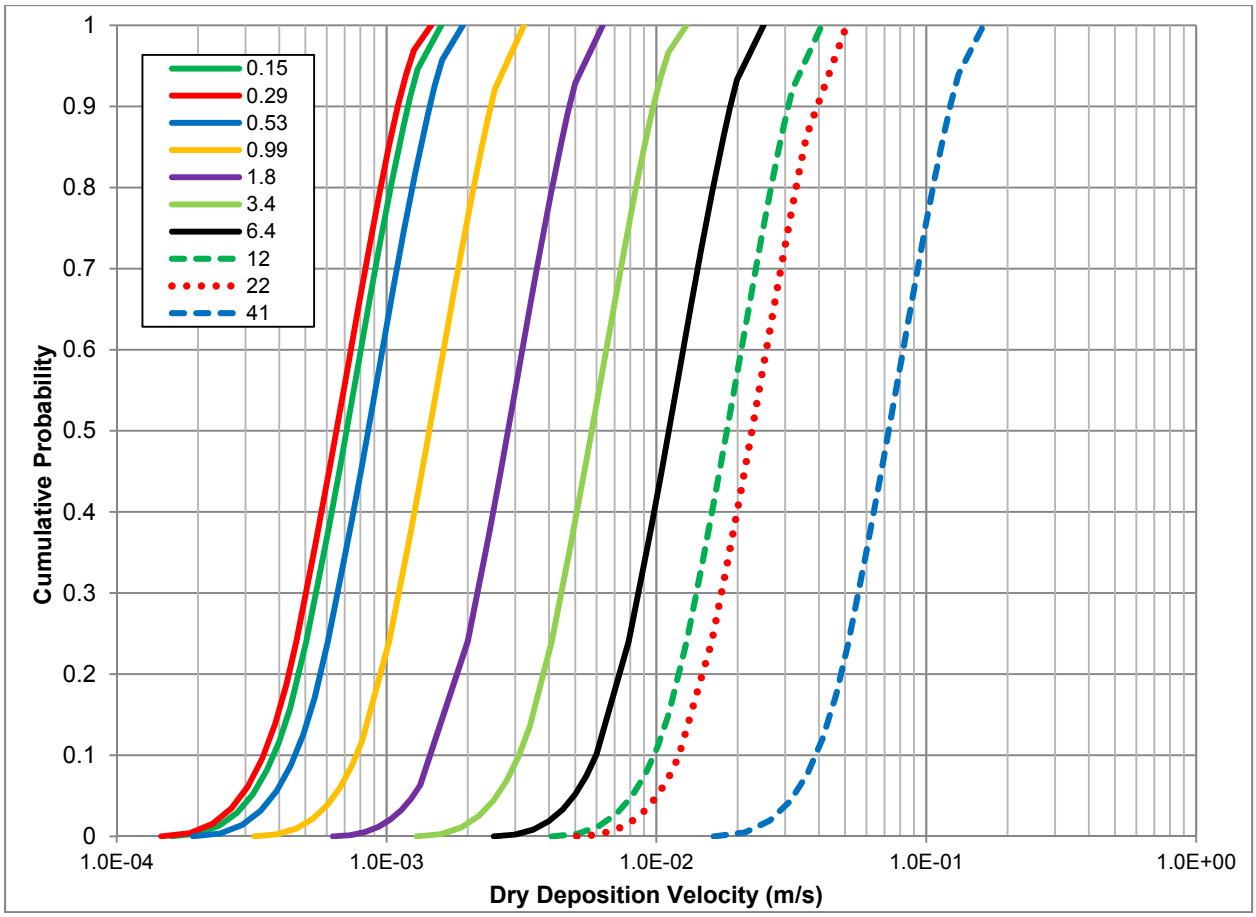

Figure 5-11 CDF of dry deposition velocities for mass median diameters representing MACCS aerosol bins

VDEPOS is assumed to be perfectly rank-order correlated across the aerosol sizes. This prevents small aerosols from depositing faster than large aerosols, which would contradict our understanding of aerosol physics. Rank-order correlation is the most commonly used method of computing a correlation coefficient using the rank order of the sampled values between two variables.

5.9.3 Shielding Factors (GSHFAC and PROTIN)

As part of the overall SOARCA project, an updated technical basis and methodology for radiation dose and health risk estimation was established [82]. This technical basis, updated shielding factors as described below and other risk factors discussed within this study.

During the investigation of the cloudshine shielding factor, CSFACT, issues were identified regarding the source data, which was an unpublished internal Sandia document "Recommendations for MACCS2 Parameter Uncertainty Distributions," prepared by Heames, et al. in 2003. The internal Sandia report was an attempt to use data from expert elicitation to create distributions for MACCS parameters, and was based on an earlier Sandia letter report written by Gregory [81]. However, while the distributions in Gregory for inhalation and groundshine are identical to Heames, there is no distribution in Gregory [81] for cloudshine and no supporting discussion. Physically, cloudshine shielding and inhalation protection are

completely different. Protection from cloudshine represents the fraction of radiation from a plume external to a structure that is able to penetrate the structure; inhalation protection is the fraction of the external concentration that leaks into a structure and is able to be inhaled. Because physically the two distributions should not be identical and because there is no discussion in either source regarding the basis for a distribution for cloudshine shielding factor, a point value was used in the analysis. Since the cloudshine pathway is typically a small contributor to overall dose in MACCS analyses, using a point value for the shielding factor should have a minor effect on the estimated uncertainties.

Groundshine Shielding Factors (GSHFAC)

The values of GSHFAC are important because the doses received from groundshine are directly proportional to these factors and groundshine is usually the most important of the long-term dose pathways. Uncertainty exists in factors that affect GSHFAC, such as indoor residence time, household shielding value, and departures from the infinite flat plane assumptions. There are additional contributions to uncertainty in the energy deposited within a human organ for a specified incident radiation, which is represented by the groundshine deposited energy (GSDE) scaling factor. GSDE is a dimensionless scaling factor used to account for the amount of ionizing radiation energy deposited within various human organs from external radiation emanating from the ground. These uncertainties of the deposition in individual organs stem from age, height, and weight variations of the exposed population and are incorporated into GSDE uncertainty; but GSDE is not a specific MACCS input. So the uncertainty in GSDE is incorporated into GSHFAC uncertainty distribution as explained below. The two mechanisms, shielding from structures and energy deposition into organs, are independent and so are treated as being uncorrelated.

Rationale for Distributions

Piecewise uniform distributions (normal activity, sheltering, and evacuation) for the combined GSHFAC and GSDE uncertainty were implemented in MACCS as an overall uncertainty for GSHFAC. Construction of this distribution function is described in the following paragraphs.

The piecewise uniform values used in GSHFAC represent a combination of uncertainty derived from NUREG/CR-6526 [83] and uncertainty in GSDE. Gregory et al. [81] evaluated the expert data to derive distributions for groundshine from NUREG/CR-6526. In Gregory et al. [81], three types of activity, normal, sheltering, and evacuation, are evaluated for the groundshine dose pathway, resulting in three sets of shielding factors, shown on Figure 5-12.

Regarding GSDE, to simplify the implementation of uncertainty in the energy deposited within a human organ for a specified incident radiation, Eckerman [82] recommends that a single triangular distribution be applied as a multiplicative factor for all radionuclides and for all organs. Eckerman [82] recommends a triangular distribution with a minimum of 0.5, a peak (mode) of 0.8, and a maximum of 1.5 that incorporates variations in ionizing radiation energy and human body variations from age, sex, height, and weight. The triangular distribution used to represent uncertainty in the dose coefficients for GSDE is shown in Figure 5-13.

Furthermore, Eckerman [82] suggests that the uncertainties in organ-specific groundshine dose conversion factors are highly correlated. As a result, this UA combines the uncertainty in GSHFAC and the uncertainty in the dose coefficients (i.e., through the GSDE uncertainty distribution) into a single uncertainty factor, which can be implemented as an overall uncertainty in the GSHFAC input for MACCS. The uncertainties in the GSHFAC and the groundshine dose

coefficients are treated as uncorrelated, since they have no relation (i.e., the shielding from a building (GSHFAC) does not bear upon variations in organ geometry or variations in ionizing radiation energy).

Figure 5-14 shows an example of the combination of uncertainty in GSHFAC and GSDE for evacuation. For long-term groundshine exposure, the distribution is assumed to be the same as for normal activity. GSHFAC is specified to be the same for each of the six cohorts in this UA, with one exception. Cohort 2, which is the population in special facilities, uses the same shielding factors for normal activity as for sheltering because this cohort is normally indoors and resides in fairly stout concrete structures that provide better shielding than typical housing.

The distributions for normal activity and evacuation are uncorrelated, i.e., a rank correlation coefficient of 0.0. The distributions for normal activity and sheltering are correlated with a rank correlation coefficient of 0.8 because both represent fractions of time spent indoors. The distributions for sheltering and evacuation are taken to be uncorrelated. The distributions for normal activity and long-term groundshine shielding factors are considered perfectly rank correlated. No correlation is assumed between GSHFAC and inhalation protection factors (PROTIN). Table 5-12 lists the groundshine shielding factor distribution parameters. A value of unity represents full groundshine for a person standing on an infinite flat plane with uniform concentration; a value of zero represents complete shielding.

Figure 5-12 shows the final piecewise uniform distributions used for GSHFAC, which represent both types of uncertainty described above. The long-term shielding factor is taken to be identical to the value for normal activity during the emergency phase.

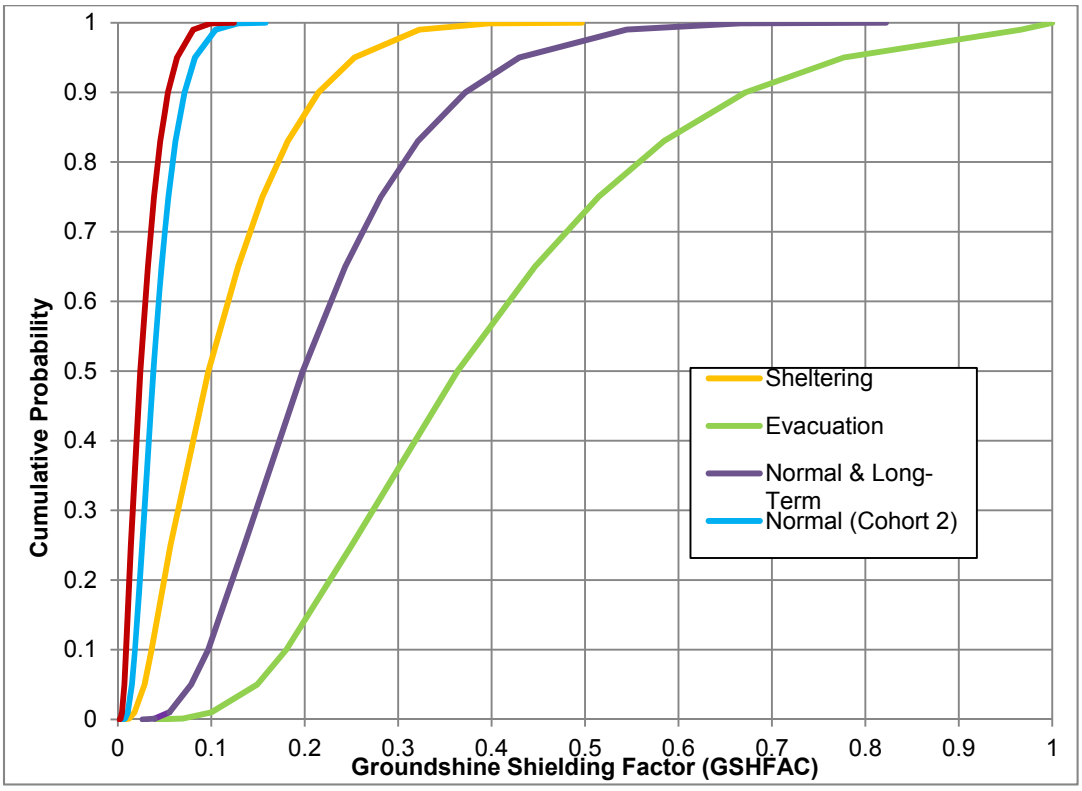

Figure 5-12 Cumulative distribution functions of GSHFAC for normal activity, sheltering, and evacuation based on expert elicitation data

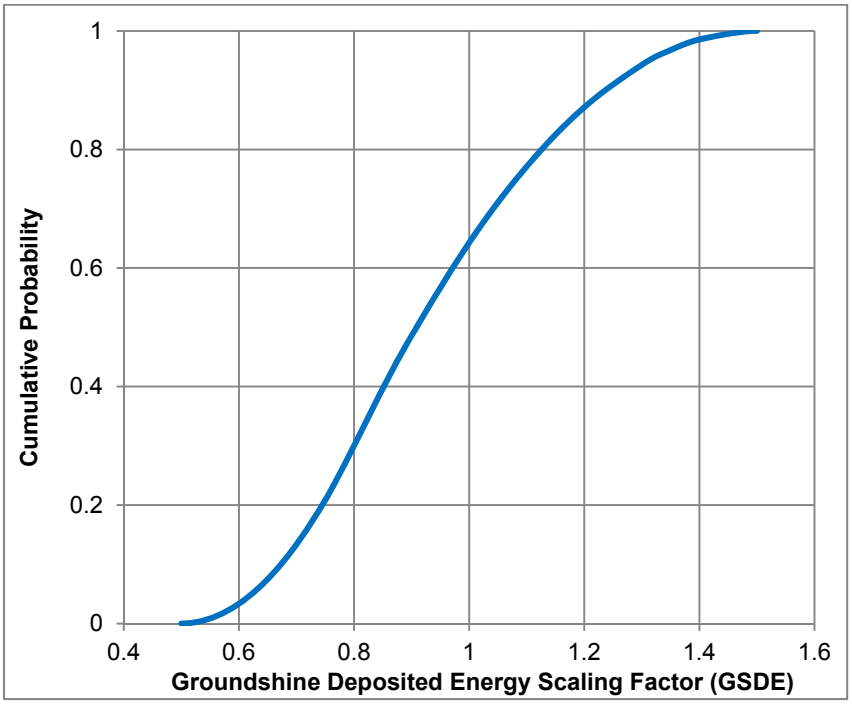

Figure 5-13 Cumulative distribution function of GSDE

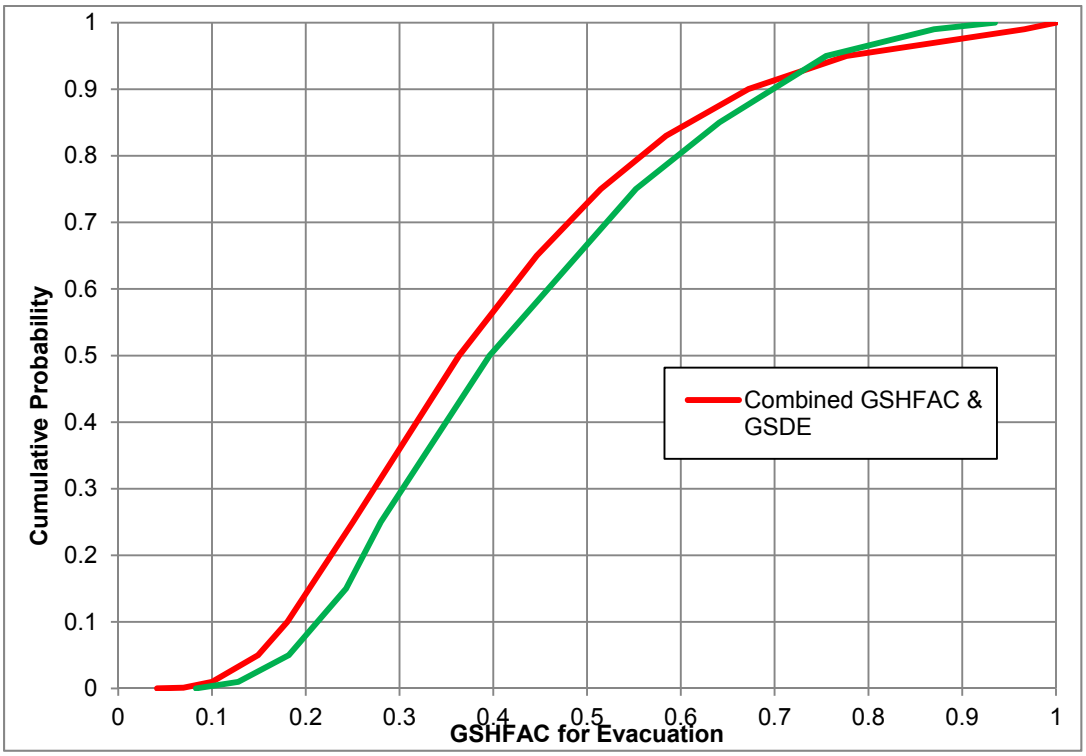

Figure 5-14 CDF of GSHFAC for evacuation accounting for uncertainty in GSDE

Table 5-12 Simplified groundshine shielding factor (GSHFAC) for Sequoyah.

Special Facilities Cohorts 1 and 2			
Quantile	**Evacuation**	**Normal Activity**	**Sheltering**
0	0.042	0.008	0.008
0.5	0.500	0.050	0.050
1	1.000	0.497	0.497
Point Values	0.500	0.050	0.050
General Population Cohorts 3-8			
Quantile	**Evacuation**	**Normal Activity**	**Sheltering**
0	0.042	0.027	0.008
0.5	0.500	0.260	0.200
1	1.00	0.822	0.497
Point Values	0.500	0.260	0.200

Inhalation Protection Factors (PROTIN)

The inhalation dose protection factor is represented by PROTIN. Population dose is reduced by the PROTIN inhalation protection factor based on the activity the population is engaged in, such as sheltering, evacuating, or performing normal activities. The inhalation protection factors used in the MACCS calculation are important because the doses received from inhalation are directly proportional to these factors and inhalation is the dominant dose pathway during the emergency phase. The distributions used in this analysis are derived from NUREG/CR-6526 [83] which collected data from an expert elicitation panel on deposited material and external doses. The expert data indicates that there is a large range of uncertainty in current expert best estimates on the inhalation protection factor.

Rationale for Distributions

Gregory et al. [81] evaluated the expert data in NUREG/CR-6526 [83] to derive distributions for the inhalation protection factor. Three distributions were derived, one each for normal activity, sheltering, and evacuation. Only data from the U.S. expert were used to determine the time spent in various structures (outdoors, vehicles, and low-, medium-, and high-shielded buildings). These data provided the needed information for normal activity. The times were shifted towards outdoors in vehicles for evacuation and shifted towards highly shielded buildings for sheltering. To determine the final distributions from all the experts, the air concentration ratios (indoors/outdoors) were considered for both normally ventilated buildings and buildings with all windows closed.

In reviewing these distributions, it appears that the ranges of the distributions are too large, especially for sheltering and evacuation, with the protection factor for sheltering skewed toward too little protection and evacuation skewed toward too much protection. The experts seemed to be answering the question of what are the maximum and minimum possible protection factors for any individual person in the zone, whereas for this work, a representative value for all people in the zone is needed.

To verify that these judgments are correct, the Gregory distributions were compared to distributions for inhalation protection factor given in NUREG/CR-4551 [80], which were prepared for NUREG-1150 [12]. This source recommended a uniform distribution from 0.15 to 1.0 for normal activity, a uniform distribution from 0.1 to 0.4 for sheltering, and a constant value of 1.0 (no protection) for evacuation.

The recommended distribution for normal activity is similar to the distribution in [81]; whereas, the distribution for sheltering has a significantly smaller range because it only allows for relatively high amounts of protection, indicating sheltering is in stouter building structures. In practice sheltering may be enforced wherever people currently are (shelter in place), so the higher values in [81] are plausible for some individuals but not for an entire cohort.

Thus, the decision was made to use the distributions for sheltering and normal activities from [81], except with a truncation at the 0.2 and 0.8 quantiles of each CDF to be representative of cohorts instead of a single member of a cohort. New CDFs were drawn, using the .02 and 0.8 quantile values as the upper and lower bound while maintaining the 0.5 quantile value and shape of the distributions. The distributions are defined to be piecewise-uniform to reflect information from the expert elicitation. Figure 5-15 also shows the SOARCA values as black triangles, which were obtained from the NUREG-1150 values used for Sequoyah.

The single inhalation protection factor of 1 for evacuation [80] is significantly different than the values from the distribution in [81], which includes low values for PROTIN that are difficult to defend. Additionally, the SOARCA default for evacuation of 0.98, which came from NUREG/CR-6953, Volume 1 [84], is still considered the best estimate. Therefore, the best judgment was to create a uniform distribution from 0.9 to 1.0, which allows for a limited uncertainty investigation in PROTIN for evacuation but doesn't include high amounts of protection as indicated in Gregory et al. that do not seem physically possible for an entire cohort.

The distribution for the long-term inhalation protection factor is assumed to be the same as the distribution for normal activity during the emergency phase. PROTIN must be specified for each cohort (population group) in a MACCS analysis. The protection factors for Cohorts 1 and 3 through 8 were chosen to be identical. Because normal activity for Cohort 2 would be approximately the same as sheltering due to the robust nature of the special facility buildings, the distribution for normal activity was chosen to be the same as for sheltering for Cohort 2. These distributions are shown in Figure 5-15 as dashed lines overlaying the base distributions.

The distributions for normal activity and sheltering are correlated with a rank correlation coefficient of 0.75, based on the assumption that the majority of normal activity is indoors. Therefore, if sheltering is sampled with a lower value, normal activity should also be a lower value. The distributions for normal activity and long-term inhalation are perfectly rank correlated. No correlations are assumed between PROTIN and GSHFAC for any of the three activity types, evacuation, normal activity, and sheltering. Table 5-13 lists the inhalation protection factors (PROTIN) for Sequoyah.

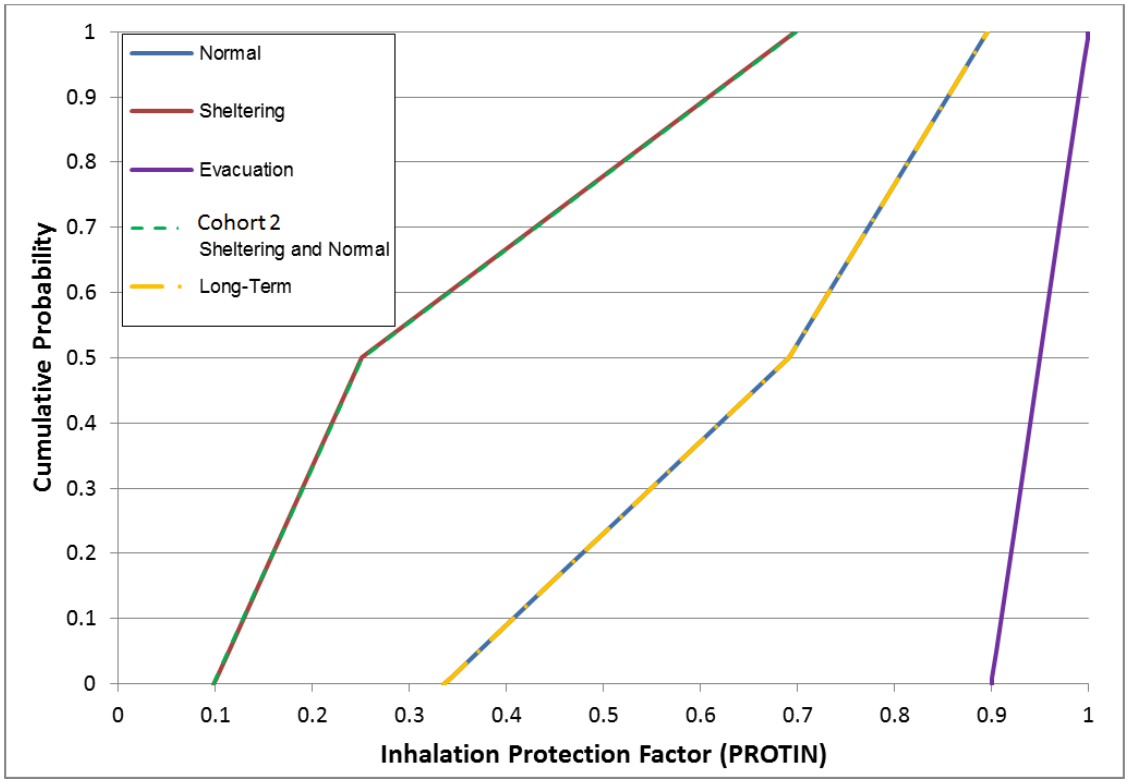

Figure 5-15 CDFs of PROTIN for normal activity, sheltering, and evacuation

Table 5-13 Inhalation protection factor (PROTIN) for Sequoyah.

Special Facilities Cohorts 1 and 2			
Quantile	**Evacuation**	**Normal Activity**	**Sheltering**
0	0.900	0.098	0.098
0.5		0.330	0.330
1	1.000	0.699	0.699
Point Values	0.98	0.330	0.330
General Population Cohorts 3-8			
Quantile	**Evacuation**	**Normal Activity**	**Sheltering**
0	0.900	0.336	0.098
0.5	0.950	0.460	0.330
1	1.000	0.896	0.699
Point Values	0.98	0.460	0.330

5.9.4 Early Health Effects (EFFACA, EFFACB, EFFTHR)

When radioactive material is inhaled and retained in the respiratory system, an individual may continue to receive a radiation dose for long periods of time after the material was inhaled. Depending on particle size and chemical form, clearance mechanisms may remove the material from the body or transport it from the respiratory system to other organs of the body. The MACCS early health effects model accounts for dose protraction from radioactive material inhaled and retained within the body and calculates an effective acute dose, i.e., a one-day dose that would induce the same effects as the protracted dose [55]. External radiation is only received during the exposure period, so dose protraction is not an issue.

The individual risk of an early fatality is modeled in MACCS using a three-parameter hazard function, expressed in Eq. 5-6 for specified target organs (i.e., red bone marrow, lungs, and stomach) with an acute dose threshold. The early health effects parameters represented in the equation include:

- LD_{50} parameter (EFFACA),
- Exponential parameter (EFFACB) also called shape factor, and
- Threshold dose (EFFTHR).

The Weibull function contains the EFFACA parameter for the lethal dose to 50 percent of the population (LD_{50}), EFFACB as an exponential parameter that defines the steepness of the dose-response function, and a threshold dose defined by EFFTHR, below which no health effects are estimated to occur.

$$H = 0.693 \left(\frac{DOSE}{EFFACA}\right)^{EFFACB} \qquad \text{Eq. 5-6}$$

Where:

H = hazard function for individual risk of an early fatality (unitless)
DOSE = effective acute dose (Gy) to a target organ. DOSE is set to zero when it is below the threshold, EFFTHR
EFFACA = LD_{50} (Gy) for a specific health effect
EFFACB = the exponential parameter in the hazard function (unitless)

All three of the variables used to determine the individual risk of early fatality in Eq. 5-6 are treated as uncertain. Furthermore, there are three values for each of the parameters for the three organs listed above. A dose to each of the organs is associated with a specific type of early fatality, as follows: (1) an acute dose to the red bone marrow is used to assess occurrences of the hematopoietic syndrome, (2) an acute dose to the lungs is used to assess occurrences of the pulmonary syndrome, and (3) an acute dose to the stomach is used to assess occurrences of the gastro-intestinal syndrome.

When estimating early health effects, it is appropriate to use gray (Gy) as the unit of measure for doses. Doses measured in gray and Sieverts (Sv) are the same for low linear energy transfer (LET) radiation (gamma and beta), but different for high LET radiation (alpha). Doses in Sieverts are based on a standard radiation weighting factor for high LET radiation of 20; doses from high LET radiation in units of gray are based on either a value of unity or a nonstandard value for radiation weighting factor. In the case of latent health effects, a Sievert captures the biological

effects of radiation in terms of the risk of cancer induction. In the case of early health effects, a nonstandard radiation weighting factor of 10 is used for acute doses. This difference is because high LET radiation has a different biological impact for early health effects than it does for latent health effects.

Early Health Effects LD_{50} Parameter (EFFACA)

As explained above, the EFFACA parameter represents LD_{50}, the lethal dose to 50 percent of the population, in the hazard function for a target organ [55]. The EFFACA distribution is based on expert elicitation data for four types of early health effects, hematopoietic syndrome, gastrointestinal syndrome, pulmonary syndrome, and pneumonitis [79]. The first three of these early health effects are potentially fatal and are included in the documented results in this report. Pneumonitis is nonfatal and is not reported.

Rationale for Distributions

The EFFACA distribution for the three target organs considered are piecewise uniform and are based on linear interpolation between data points taken from Table 6-1 of Bixler et al. [79]. The basis for the EFFACA distribution are uncertain characteristics associated with estimation of four types of early health effects, and are taken directly from Bixler et al. [79] and are derived expert elicitation values provided in NUREG/CR-6545. The parameter distributions and SOARCA values associated with the three fatal, early health effects are shown on Figure 5-16. The upper and lower bounds of each of the distributions incorporate the entire range of the expert elicitation data [79].

Bixler et al. [79] recommended that EFFACA be correlated with the threshold parameter (EFFTHR) for the same health effect using a 1.00 rank correlation coefficient.

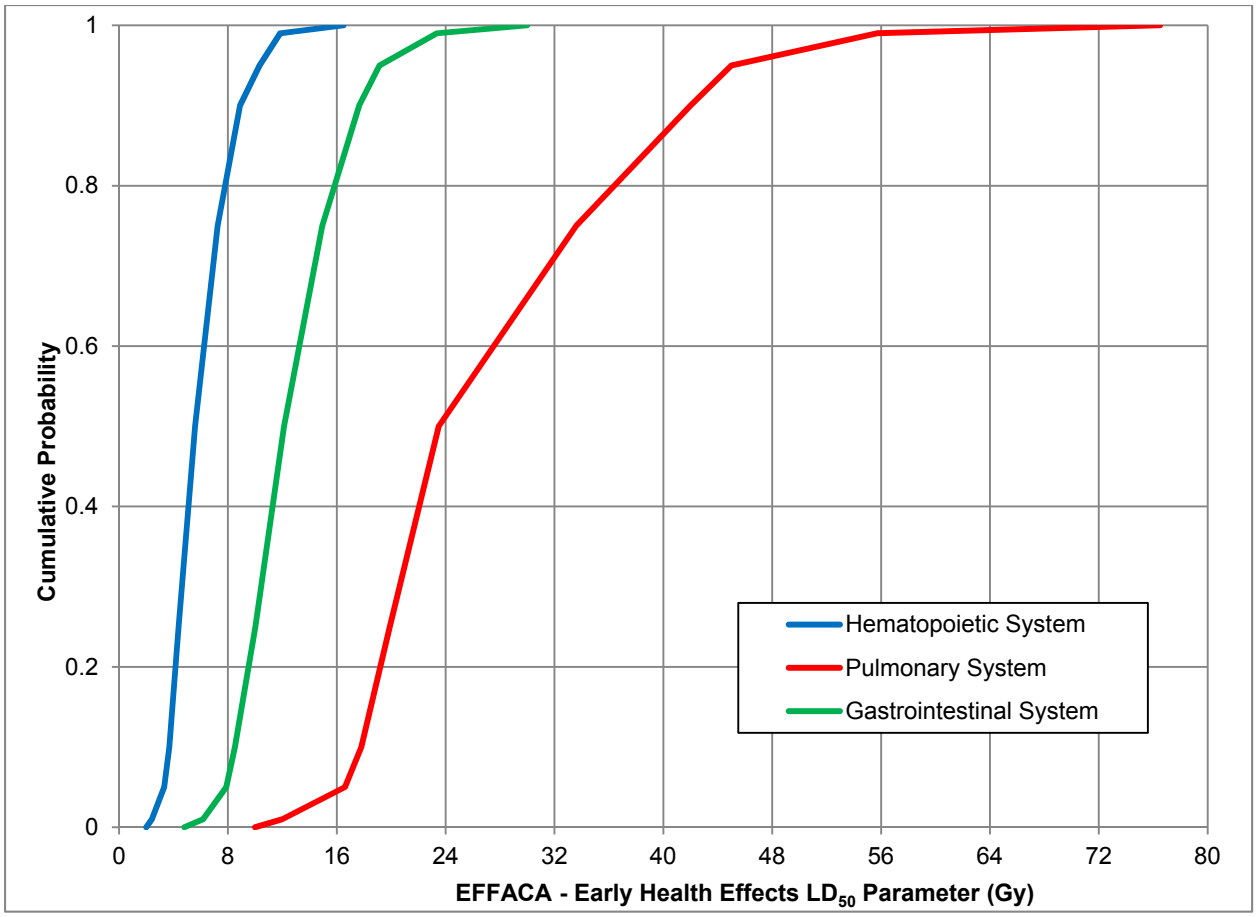

Figure 5-16 CDFs of EFFACA for specified health effects

Early Health Effects Exponential Parameter (EFFACB)

The EFFACB parameter represents the exponential or shape factor in the hazard function for the target organ [55]. The same target organs identified with EFFACA are considered here.

Rationale for Distributions

The EFFACB distribution for all three target organs considered are piecewise uniform, and are based on linear interpolation between data points taken from Table 6-1 of Bixler et al. [79]. The basis for the EFFACB distributions is derived from NUREG/CR-6545 and evaluated by Bixler et al. [79]. The parameter distributions and SOARCA values associated with these three potentially fatal early health effects for EFFACB are shown on Figure 5-17. The upper and lower bounds of each of the three distributions incorporate the entire range of the expert elicitation data [79].

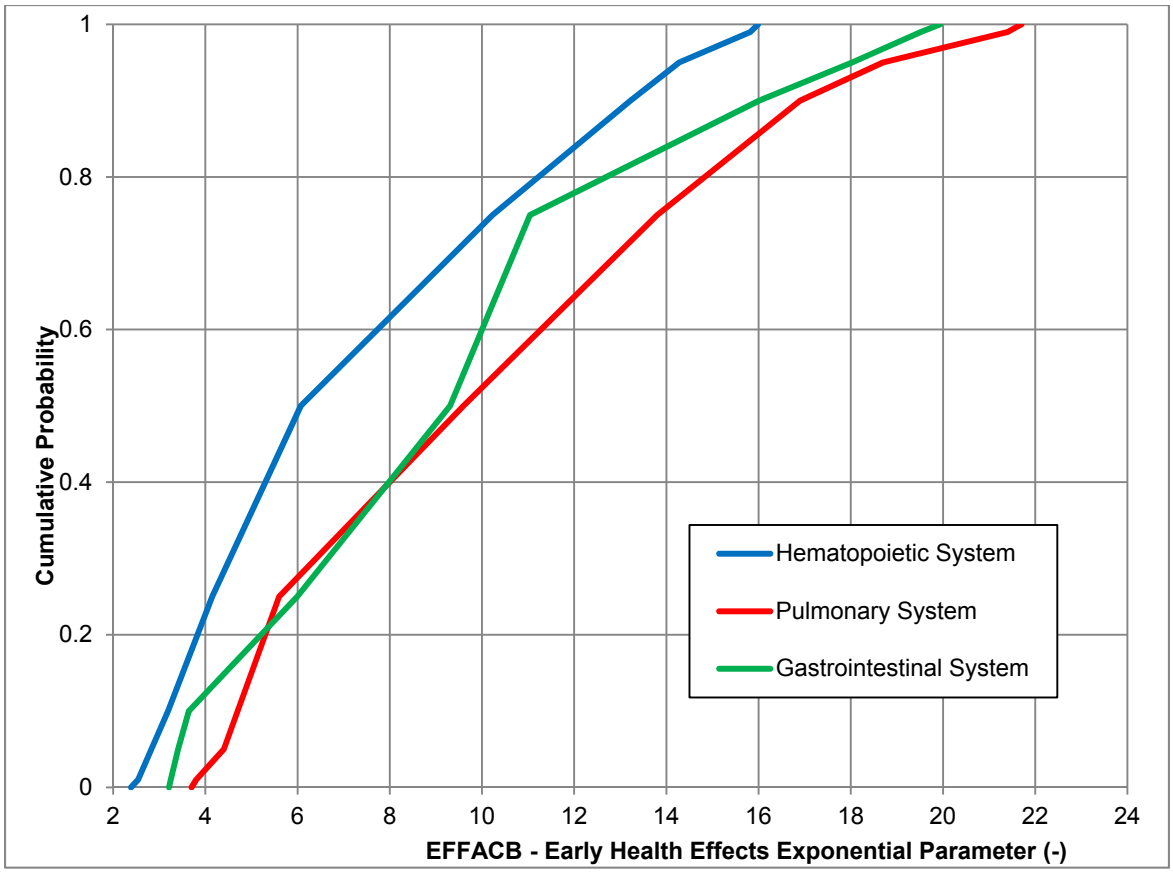

Figure 5-17 CDFs of EFFACB for specified health effects

Early Health Effects Threshold Dose (EFFTHR)

The EFFTHR parameter represents the threshold dose associated with the target organ [55]. The same target organs identified with EFFACA and EFFACB are considered here.

Rationale for Distributions

The EFFTHR distribution for all three target organs considered are piecewise uniform, and are based on linear interpolation between data points taken from Table 6-1 of Bixler et al. [79]. The EFFTHR distributions are derived from NUREG/CR-6545 and evaluated by Bixler et al. [79]. The parameter distributions and SOARCA values associated with these three potentially fatal early health effects for EFFTHR are shown on Figure 5-18. The upper and lower bounds of each of the three distributions incorporate the entire range of the expert elicitation data [79].

For each health effect, EFFTHR is correlated with the LD_{50} parameter (EFFACA) for the same health effect using a rank correlation coefficient of 1.00 [79].

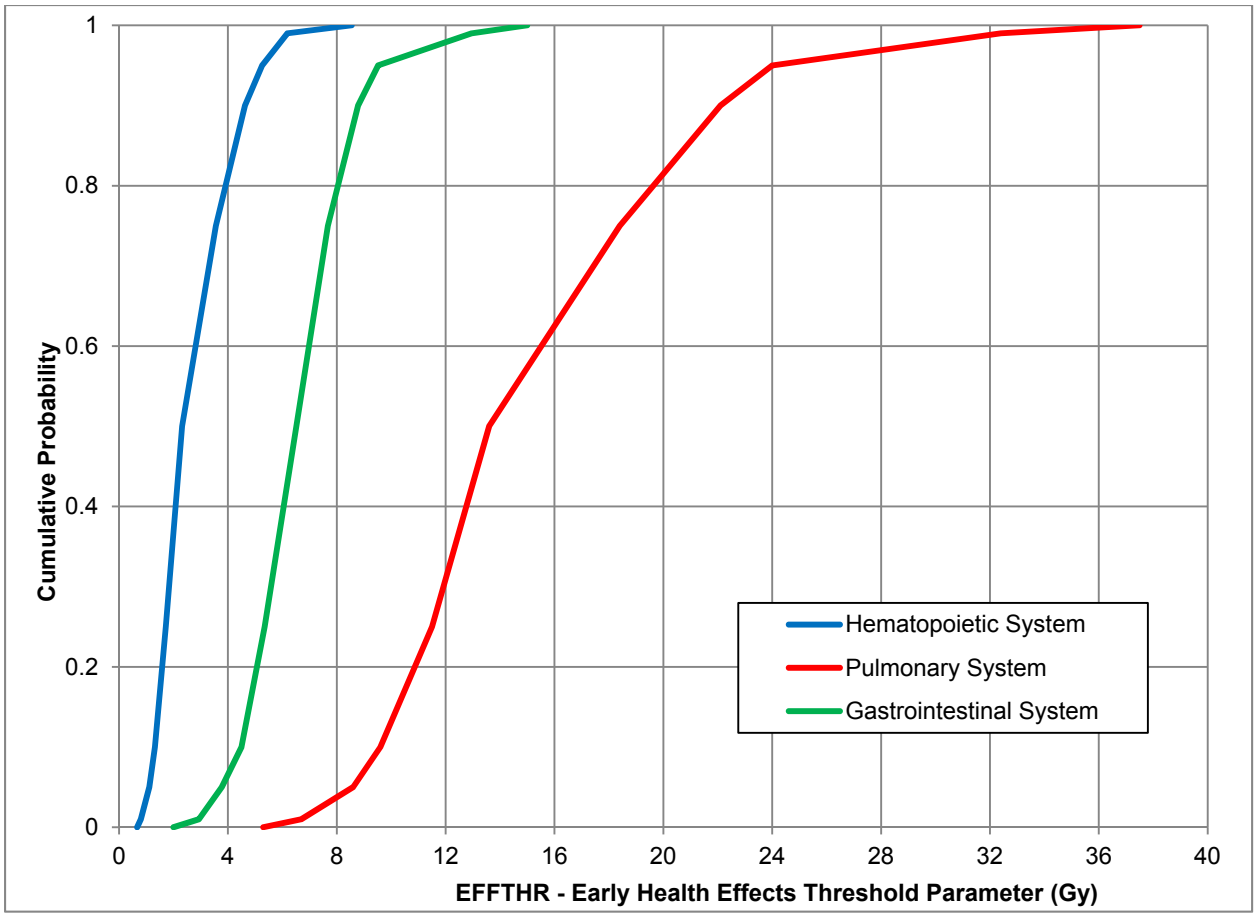

Figure 5-18 CDFs of EFFTHR for specified health effects

5.9.5 Latent Health Effects (DDREFA, CFRISK, Long-Term Inhalation Dose Coefficients)

Dose and Dose-Rate Effectiveness Factor (DDREFA)

The dose and dose-rate effectiveness factor (DDREFA) is a dimensionless dose- and organ-dependent reduction factor. Epidemiological studies used in the development of radiation-exposure risk models involved subjects who experienced high radiation doses delivered in a relatively short time period [82]. There is evidence that indicates that the biological response per unit dose at low doses may be overestimated if one extrapolates from observations made with high doses and dose rates [82]. The degree of overestimation is commonly expressed in terms of a dose and dose-rate effectiveness factor. DDREFA is used in MACCS to modify the organ-specific lifetime cancer fatality risk factors (CFRISKs) in order to distinguish between low and high dose exposures incurred during the early phase. There is significant uncertainty in DDREFA because there is a large amount of scatter in dose-response data at low doses.

Low dose is generally defined as 0.2 Gy (20 rad) or less and low dose rate is defined as 0.1 mGy/min (600 mrad/hr) or less 16]. MACCS only considers dose and not dose rate in the implementation of DDREFA. In MACCS, doses received during the emergency phase are divided by DDREFA when the committed dose is less than 0.2 Sv (MACCS does not estimate doses in units of Gy for the purpose of calculating latent health effects, so the dose threshold is

implemented as dose measured in Sv to the target organ). Doses received during the long-term phase are assumed to be controlled by the habitability criterion to be well below 0.2 Gy, so the risk factors are always divided by DDREFA in the calculation of latent health effects during this phase.

Rationale for Distributions

Age- and gender-averaged cancer mortality risk uncertainties were developed for SOARCA [82]. Additionally, a PDF specific for breast cancer and one for all other types of cancers was developed [82]. However, the PDFs provided in [82] did not integrate to unity; therefore, the PDF equations were normalized to the curves shown in Figure 5-19. An upper limit of DDREFA is 3.0 for breast and 8.0 for other cancers [82].

Eckerman recommended that high LET radiation be assigned a DDREFA of unity (1.0) with no uncertainty [82]; however, the distinction between low and high LET radiation to an organ cannot be distinguished within the MACCS framework; therefore, the PDFs suggested for low LET radiation are applied to all types of radiation. To implement the uncertainty in DDREFA, the CDF was segmented into equally spaced quantiles to construct a piecewise uniform distribution as shown in Figure 5-20.

The value of DDREFA for each organ is independent of the other organs and so they are not correlated [82]. The DDREFA for each organ has a corresponding CFRISK parameter, and these parameters are also uncorrelated.

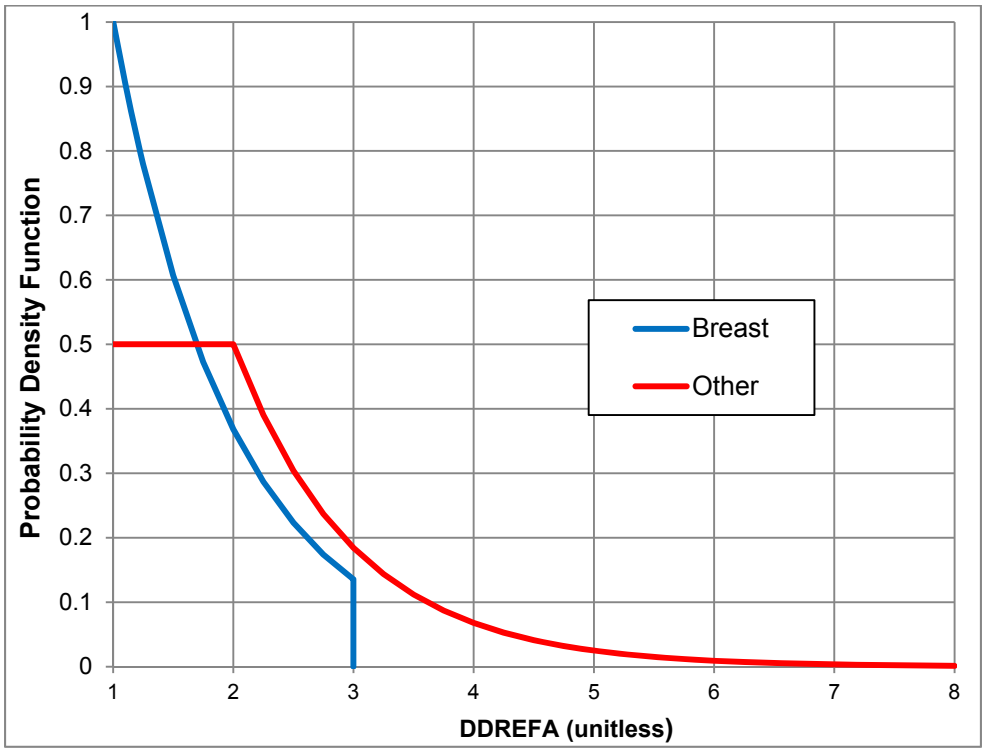

Figure 5-19 Normalized PDFs for DDREFA for breast and other cancers

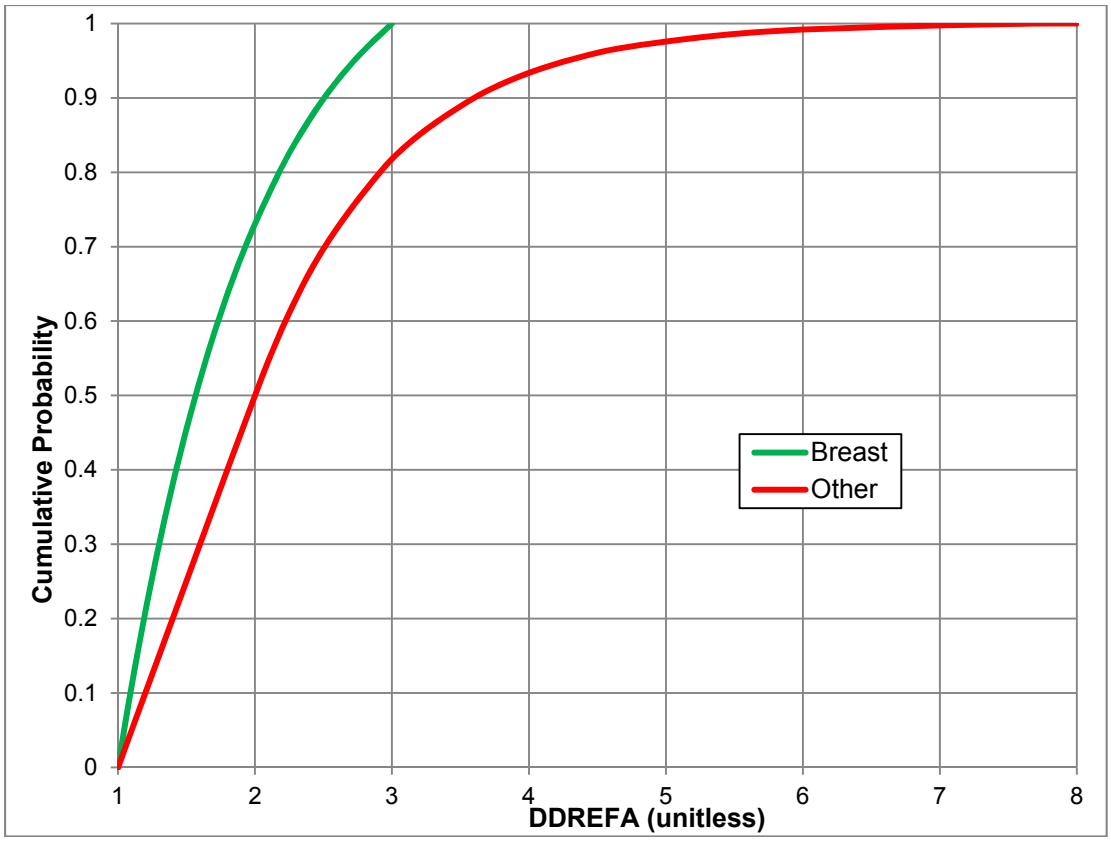

Figure 5-20 CDFs of DDREFA for breast and other cancer types

Lifetime Cancer Fatality Risk Factors (CFRISK)

The lifetime CFRISKs are based on a 50-year lifetime dose commitment to specified target organs (risk/Sv). The probability of a LCF is calculated separately for each cancer syndrome related to each target organ and is based on the technical approach described in the National Academy of Sciences / National Research Council Biological Effects of Ionizing Radiation (BEIR) V report [101]. The BEIR V risk models are used in FGR-13.

Lifetime doses can occur during all phases of an accident, early, intermediate, and long-term. Projected doses are the basis for decisions to relocate individuals during each of these phases. When allowed to return, doses are used to estimate potential health effects. Return of the population falls within the scope of radiation protection and uses the standard dosimetric quantities of radiation protection, i.e., effective doses. Estimating health effects is based on doses to specific organs and organ-specific risk factors to estimate the number of excess cancer fatalities in a population. Both the dose coefficients and risk factors are uncertain. This section evaluates uncertainties in the cancer fatality risk factors and a subsequent section evaluates uncertainties in the dose coefficients.

Rationale for Distributions

Truncated log-normal distributions were selected for the cancer fatality risk factors based on guidance from Keith Eckerman [82]. Estimates of the gender and age averaged uncertainty in CFRISK for each of the organs used for latent health effects were obtained from Eckerman [82].

The uncertainty distributions provided by Eckerman [82] indicate that cancer risk for leukemia has a very small uncertainty; lung, breast, colon, and residual (cancer sites not explicitly identified – esophagus, stomach, skin, ovaries, bladder, kidney, etc.) are moderately uncertain; and thyroid, liver, and bone have large uncertainties. Eckerman [82] concludes this based on the premise that inconsistency in expert judgment is a valid measure of uncertainty in CFRISK.

To implement the uncertainty in CFRISK, a CDF was developed for each of the organs as shown in Figure 5-21. Each log normal distribution is truncated at ±3 sigma for each distribution. This represents a truncation at quantile 0.001 and 0.999. CFRISK for each organ is considered independent of the other organs and therefore the risk factors are not correlated [82].

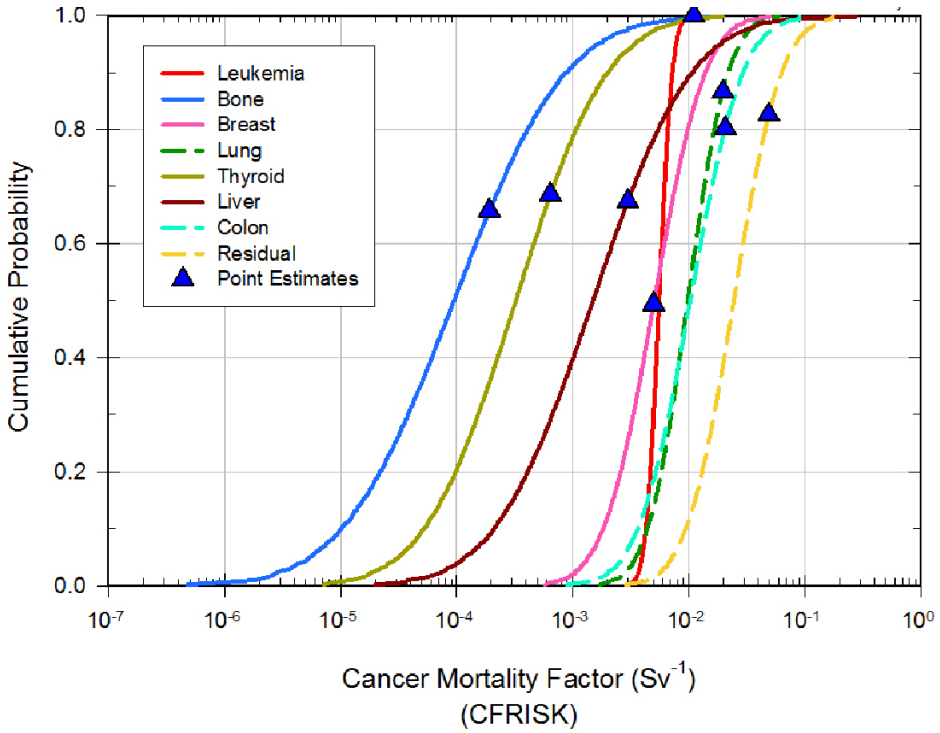

Figure 5-21 CDF for CFRISK for each of the included organs

Long-Term Inhalation Dose Coefficients

The long-term inhalation dose coefficients are used to calculate the committed organ-specific equivalent dose and the effective dose (all in Sv) from the inhalation of 1 Bq of a radionuclide integrated over a 50-year commitment period. Uncertainties in inhalation dose coefficients were examined by Pawel et al. [85] to evaluate the uncertainties in the cancer risk coefficients of FGR-13. Based on the Eckerman report for SOARCA [82], the assignment of uncertainty distributions to long-term inhalation dose coefficients for individual radionuclides is difficult because these values are the end products of complex calculations. These calculations involve a collection of uncertain biokinetic and dosimetric coefficients and assumptions, which Pawel et al. [85] determined to be the largest uncertainty for most risk coefficients.

The LCF risk factors in MACCS are based on the technical approach described in BEIR V in which long-term inhalation dose coefficients are part of that approach. The assessment of the uncertainty in dose is evaluated on the basis of sensitivity analyses in which various

combinations of plausible biokinetic and dosimetric models are used to generate alternative dose coefficients, such as those discussed in Pawel et al. [85], and Eckerman report [82].

Rationale for Distributions

For the long-term dose coefficients related to the inhalation pathway, Eckerman [82] recommends that the uncertainty distributions for the coefficients be treated as truncated log normal distributions with the geometric means and standard deviations for the 58 radionuclides listed in Table 3. The upper and lower values used to create the distributions are assumed to represent the 90 percent confidence interval for each dose coefficient.

For an individual radionuclide, the long-term inhalation dose coefficients are treated as correlated with a rank correlation coefficient of 1.0 for all of the organs except the lung. The lung is correlated with a rank correlation coefficient of -1.0 with the dose coefficients of all of the other organs (red bone marrow, bone, breast, thyroid, liver, colon, and 'residual'). This, in effect, means that only one input is sampled independently (e.g., long-term inhalation dose coefficient for the red bone marrow) to represent all organ-specific long-term inhalation dose coefficient uncertainty. The logic behind this is that the inhaled radionuclides may spend more or less time (residence time) in the lungs, depending on the chemical form of the radionuclide and its solubility, and subsequently after departing from the lung, the radionuclide is carried through the blood stream to other systemic tissues. Thus, the longer the time spent in the lungs, the greater the dose in the lungs and the less the dose to the other systemic tissues. The shorter the time spent in the lungs, the smaller the dose in the lungs and the greater the dose to the other systemic tissues.

There are 69 radionuclides considered in the analysis. Of those, only 58 radionuclides have nonzero dose coefficients for inhalation. In this UA, these 58 radionuclides, listed in Table 5-14, are assigned uncertain long-term inhalation dose coefficients for each of the eight organs used in this analysis, which are lung, red bone marrow, bone surface, breast, thyroid, liver, colon, and residual. The residual dose coefficient represents the collection of organs that are not specifically represented and that are important for cancer induction.

Figure 5-22 and Figure 5-23 provide examples of the truncated log normal distributions for two radionuclides, Cs-137 and Pu-241, for the eight different organs included in this analysis. Uncertainties in the acute inhalation dose coefficients (used to estimate the early health effects discussed earlier) were considered to be less important and were not included as uncertain parameters in this analysis.

Peach Bottom and Surry SOARCA [4][5] did not include the ingestion dose pathway because uncontaminated food and water supplies are abundant within the United States, and it is unlikely that the public would eat radioactively contaminated food. Therefore, Sequoyah SOARCA also does not consider the ingestion pathway in the analysis. Uncertainties in groundshine dose coefficients are treated through uncertainties in the groundshine shielding factors, as explained above. Cloudshine uncertainty is not treated because it is a relatively unimportant dose pathway compared with groundshine and inhalation.

Table 5-14 Radionuclides treated as having uncertain inhalation dose coefficients.

Radionuclides							
Co-58	Y-90	Nb-97	Te-127	I-132	Ba-140	Pr-144	Cm-242
Co-60	Y-91	Mo-99	Te-127m	I-133	La-140	Nd-147	Cm-244

Radionuclides						
Rb-86	Y-91m	Tc-99m	Te-129	I-134	La-141	Np-239
Rb-88	Y-92	Ru-103	Te-129m	I-135	La-142	Pu-238
Sr-89	Y-93	Ru-105	Te-131	Cs-134	Ce-141	Pu-239
Sr-90	Zr-95	Ru-106	Te-131m	Cs-136	Ce-143	Pu-240
Sr-91	Zr-97	Rh-103m	Te-132	Cs-137	Ce-144	Pu-241
Sr-92	Nb-95	Rh-105	I-131	Ba-139	Pr-143	Am-241

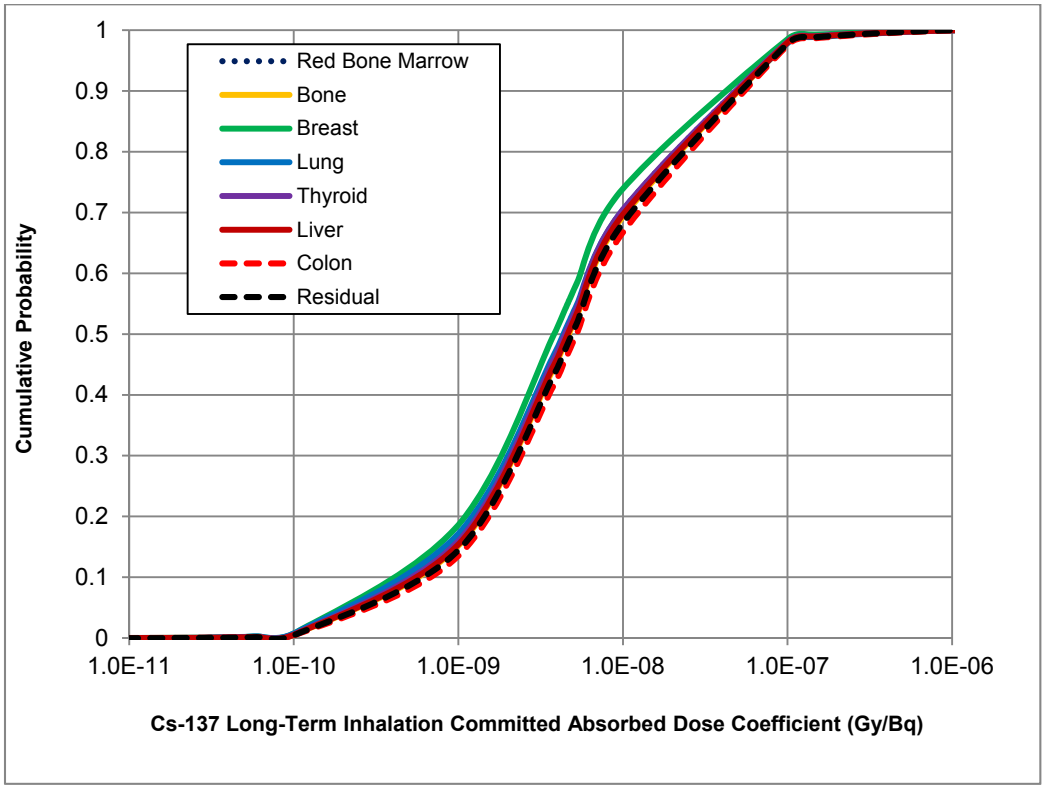

Figure 5-22 Cs-137 lifetime inhalation dose coefficient distributions for organs included in the consequence analysis

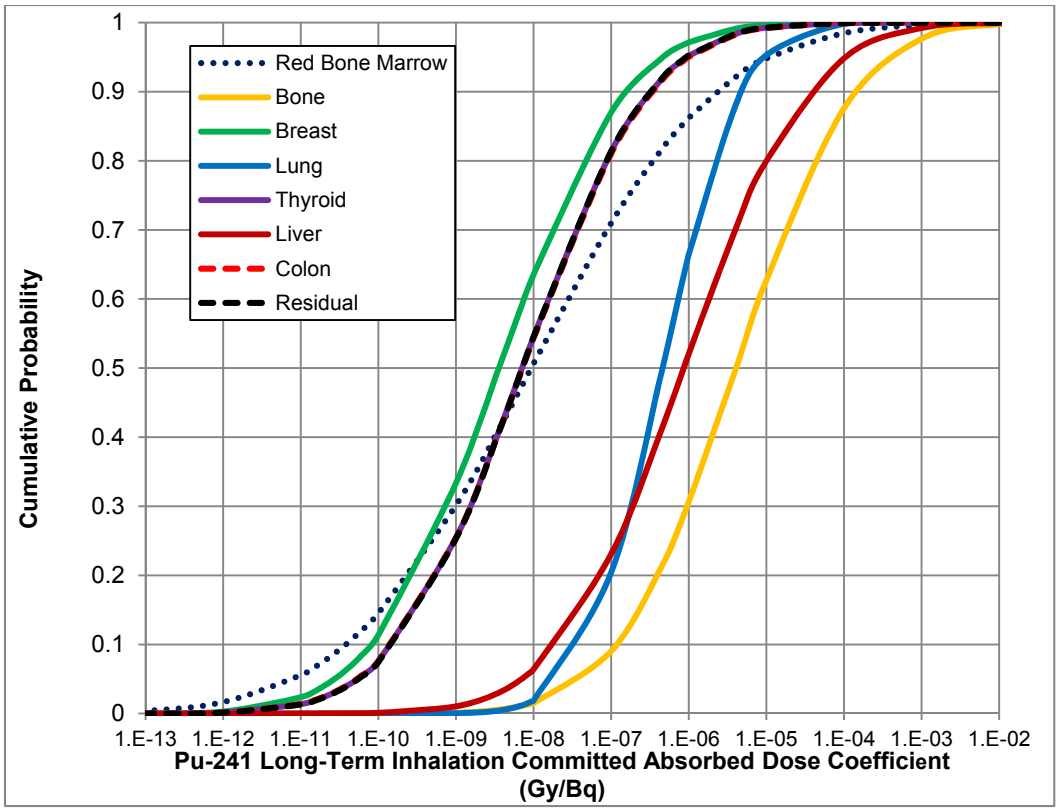

Figure 5-23 Pu-241 long-term inhalation dose coefficient distributions for organs included in the consequence analysis

5.9.6 Dispersion (CYSIGA, CZSIGA)

Dispersion of a radioactive plume following a severe accident directly affects doses to members of the population and resulting health effects. Thus, the dispersion parameters used to estimate atmospheric dispersion are important to the outcome of the calculation. The coefficients used to calculate dispersion were chosen to be the median values from an expert elicitation for SOARCA, but there is significant uncertainty in these values [79].

In terms of predicted health effects, these parameters tend to have a non-linear effect when using the LNT hypothesis for estimating latent health effects because dispersion influences the amount of land that is interdicted. Dispersion has an even greater influence on estimated health effects when truncation is used in the dose-response model because a smaller dose to an individual can reduce a nonzero risk to zero and, conversely, a larger dose can raise a zero risk to be nonzero.

Within MACCS, plume dispersion is calculated using the Gaussian plume model, shown in Eq. 5-7 for the simple case of an unbounded plume.

$$\chi(x,y,z) = \frac{Q}{2\pi\,\bar{u}\,\sigma_y\,\sigma_z} \exp\left[-\frac{1}{2}\left(\frac{y}{\sigma_y}\right)^2\right] \exp\left[-\frac{1}{2}\left(\frac{z-h}{\sigma_z}\right)^2\right]$$

Eq. 5-7

where χ(x,y,z) is the time-integrated air concentration at a downwind location (x,y,z), Q is the emitted activity, ū is the mean wind speed, h is the release height, and σ_y and σ_z are the standard deviations of the crosswind and vertical normal concentration distributions, respectively. Q and h are determined by the accident sequence, while ū, σ_y, and σ_z are functions of weather. Uncertainty in σ_y is used to capture the uncertainty in crosswind dispersion. The function used to define σ_y is given in Eq. 5-8.

$$\sigma_y = CYSIGA \cdot x^{CYSIGB}$$

Eq. 5-8

where *x* is the downwind distance and CYSIGA and CYSIGB are empirical constants chosen to fit observed results. A value for both of the constants must be entered for each of the six Pasquill-Gifford stability classes (A-F).

In this work, it was beneficial to only sample one of the two constants to simplify the specification of uncertainty. Bixler et al. [79] characterized the uncertainty as an uncertainty in *CYSIGA* and this characterization is used here.

Crosswind Dispersion Linear Coefficient (CYSIGA)

The crosswind dispersion linear coefficient is represented by *CYSIGA*. The SOARCA best estimate values for CYSIGA were chosen to be the median of the results of an expert elicitation [79]. Distributions were fit to the expert data and these were roughly lognormal. The median of the distributions is considered to be a reasonable best estimate value for this parameter; however, the distributions created from the elicitation are not used in this analysis. The expert data indicate about one order-of-magnitude uncertainty within the 90 percent confidence interval and about two orders of magnitude at the 100 percent confidence interval.

In retrospect, it appears that the experts considered the question: what is the uncertainty in the dispersion at a specific point in time, i.e., for a specific weather instance. The appropriate question for this UA is rather: what is the uncertainty in dispersion that is representative of a year of weather data? The second question leads to a narrower distribution because a single set of dispersion parameters is selected to represent a whole year of weather variability in MACCS. This distinction is important when the primary results are means over weather variability. If an extreme value of a parameter could exist at a point in time but is highly unlikely to persist over a large collection of randomly chosen weather variations, then it should not be used in this study to characterize the mean over a year of weather variations. Distributions that express the values that a parameter could take at a specific weather instance should be used in conjunction with a single weather trial or possibly just a single hour from a weather trial, not with a set of weather trials that characterize a whole year of weather data. The sampling method used in this study does not draw a set of epistemic parameters for each weather trial but rather for a whole year of weather trials, so this is an important consideration for a correct treatment of uncertainty.

There are a number of other sources for CYSIGA, three of which are given as examples in the MACCS User's Guide. These values were compared to the best estimate values from expert elicitation. It was found that 2/3rds of the values were within a factor of 3 of the best estimate value and were about evenly distributed between larger and smaller. These historic values (from 1977, 1979, and 1989) were used by multiple experts in constructing their distributions, showing they continue to be regarded as reasonable bases to estimate dispersion.

Additionally, NUREG/CR-6853 [86] compared results from MACCS (a Gaussian plume code) with 3 other codes for transport and dispersion and found that the results from the 4 codes were within a factor of 2 for compass averaged concentrations and a factor of 3 for sector specific concentrations. This factor can be considered to be an approximation of the uncertainty in transport and dispersion. As a first-order approximation at short distances, the uncertainty in plume concentration is inversely proportional to the uncertainty in σ_y multiplied by the uncertainty in σ_z. Accounting for an uncertainty in concentration of a factor of three above and below the median corresponds to a range of uncertainty in CYSIGA from 1/1.73 to 1.73 times the median assuming that both cross-wind and vertical dispersion have the same ranges of uncertainty. If this range is considered to be the uncertainty at the 90 percent confidence level, the entire range of uncertainty is reasonably chosen to be bounded by factors of 1/2.5 and 2.5 on the median value for CYSIGA.

Rationale for Distributions

The 50th percentile of the distribution from the expert elicitation [79] is a reasonable and defensible choice for the best estimate value to use for CYSIGA. Expert elicitation results are based on a combined category for stability classes A and B and a combined category for stability classes E and F, yielding 4 distributions for A/B, C, D, and E/F. Based on the previous discussion, the bounds of the distribution are set to be a factor of 2.5 higher and lower than the best estimate value for each weather class. All calculated values are found in Table 5-15.

In the Peach Bottom UA, a piecewise log-uniform distribution was used for CYSIGA because the expert elicitation data were approximately lognormal [17]. Since the range of uncertainty was chosen to be different for this analysis, a simpler log-triangular distribution was chosen. This choice is consistent with a most likely value at the center of the distribution and a likelihood that decreases as the bounds are approached. A log-triangular distribution was used instead of a triangular one because it gives equal sampling weight on either side of the mode when using a multiplicative factor for the lower and upper bounds.

Table 5-15 Log-triangular values for dispersion parameter CYSIGA for each stability class.

Class	Lower Bound	Mode	Upper Bound
A/B	.3002	.7507	1.8768
C	.1625	.4063	1.0158
D	.1112	.2779	0.6948
E/F	.0863	.2158	0.5395

Values of CYSIGA are perfectly rank correlated across the stability classes. These values are also perfectly rank correlated with the values of CZSIGA, the vertical dispersion parameters

discussed below. This indicates that uncertainty in CYSIGA is partially caused by changing weather conditions that would result in an increase or decrease in both the crosswind and vertical dispersion together. It also ensures that the order between the stability classes is preserved. The CDFs are presented in Figure 5-24.

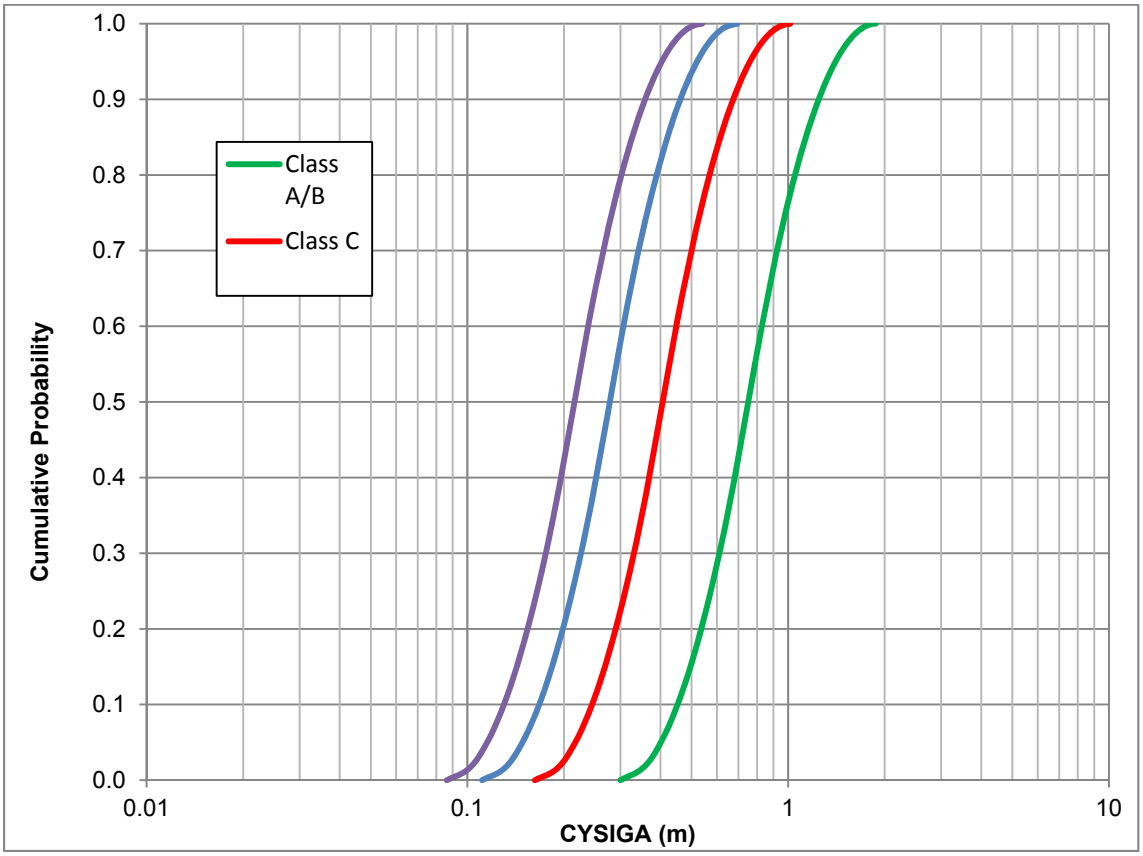

Figure 5-24 CDFs of CYSIGA for individual stability classes

Vertical Dispersion Linear Coefficient (CZSIGA)

The Surry and Peach Bottom SOARCA best estimate values for CZSIGA were also chosen to be the median results of an expert elicitation [79]. Distributions were fit to the expert data, which were again roughly lognormal. These median values are appropriate to be used as median value in the UA for Sequoyah. However, the distributions for CZSIGA have the same issues as the distributions for CYSIGA described above, so a narrower distribution is developed and used in this work. The same approach described in the previous subsection leads to distribution bounds on CZSIGA that are also factors of 2.5 above and below the median value for each stability class.

Rationale for Distributions

The 50th percentile of the distribution from the expert elicitation [79] is a reasonable and defensible choice for the best estimate value for CZSIGA. Based on the previous discussion, the bounds are set at a factor of 2.5 higher and lower than the best estimate value for each stability class. The distribution parameters are provided in Table 5-16.

CZSIGA distributions are perfectly rank correlated with each other and with values of CYSIGA. This indicates that uncertainty in CZSIGA is partially caused by weather conditions that would result in an increase or decrease in both the crosswind and vertical dispersion together. It also ensures that the order between the stability classes is preserved. Figure 5-25 shows the CDFs of a log-triangular distribution for each of the four SOARCA stability class groupings.

Table 5-16 Log-triangular values for dispersion parameter CZSIGA for each stability class.

Class	Lower Bound	Mode	Upper Bound
A/B	.0144	.0361	.0903
C	.0814	.2036	.509
D	.1054	.2636	.659
E/F	.0985	.2463	.6158

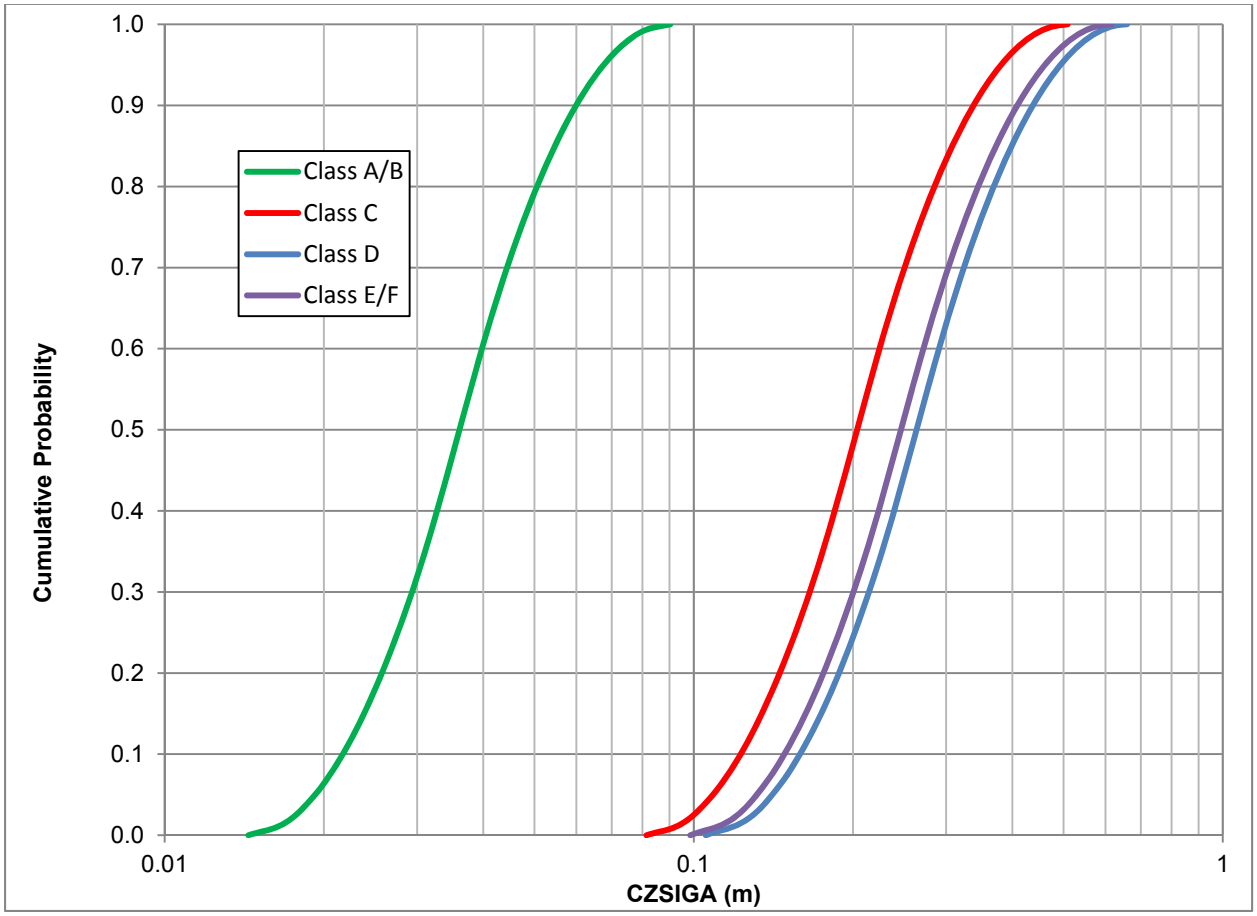

Figure 5-25 CDFs of CZSIGA for individual stability classes

5.9.7 Weather Forecast (KEYFORCST)

During an emergency response, protective action decisions for a keyhole evacuation require consideration of wind direction. Because wind tends to shift over time, MACCS allow the

keyhole to be expanded to account for such wind shifts. It also allows the expansion to occur in advance of an actual wind shift to account for weather forecasting. A parameter in MACCS, KEYFORCST, defines the number of hours of weather forecasting to use in the model. A uniform distribution was used with a lower bound of 1 hour and an upper bound of 6 hours as shown in Figure 5-26. MACCS assumes perfect foreknowledge of wind direction for the number of hours defined by KEYFORCST.

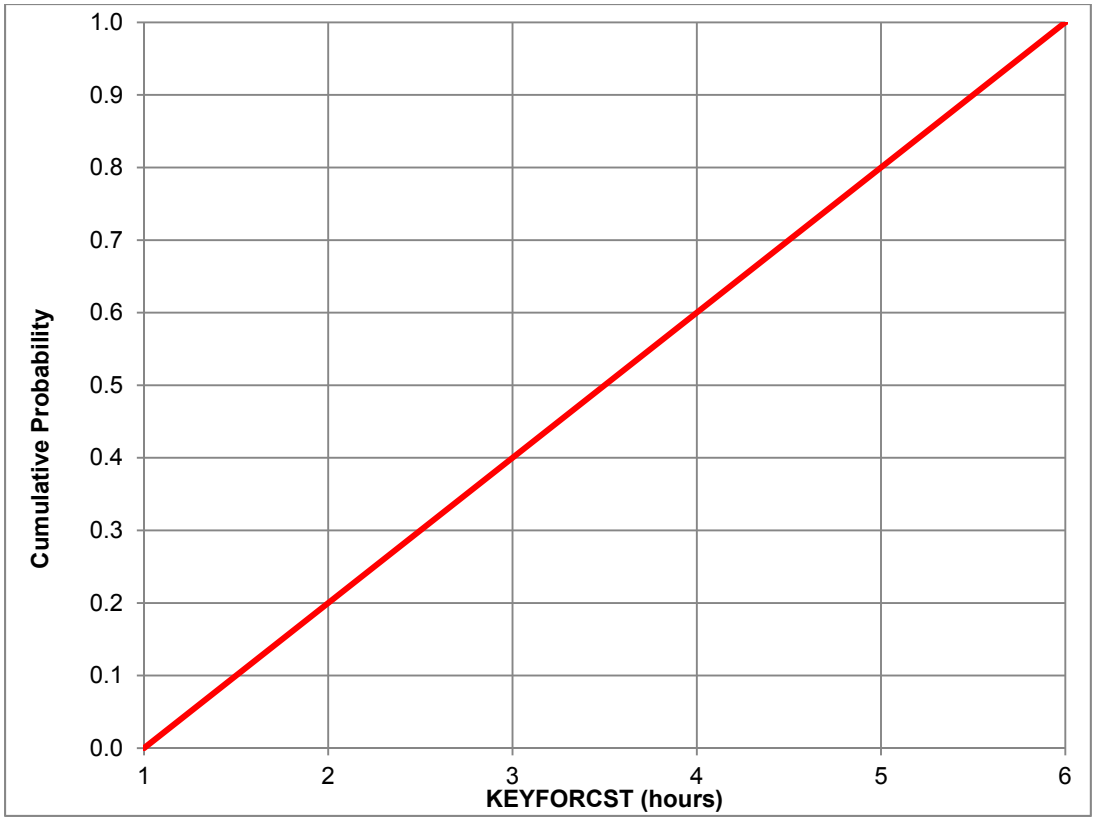

Figure 5-26 CDF of KEYFORCST

5.9.8 Time-Based Crosswind Dispersion Coefficient (CYCOEF)

CYCOEF is the linear coefficient for the time-based, crosswind dispersion model. Hanna [109] recommends that plume dispersion beyond 30 kilometers (19 miles) be based on time, not on distance. The basis for the recommendation of 30 kilometers is that most measurements upon which dispersion tables are based have a limit of about 30 kilometers. In the MACCS implementation of the time-based crosswind dispersion model, this downwind distance, along with the linear coefficient, are used to define the switching point from distance-based to time-based dispersion. The recommended default value for the linear coefficient is 0.5 m/s [109].

Sequoyah is the first in the SOARCA series of analyses to use this parameter, so no distribution had been developed for Peach Bottom or Surry [9][17]. Switching to a time-based dispersion model at longer downrange distances is a commonly-used practice in atmospheric transport modeling, and this MACCS model option was selected for the Sequoyah UA study. This approach homogenizes variations due to stability class, so it is expected to give somewhat different, less variable, results than in the previous SOARCA studies. However, any differences in results are not expected to change the relative importance of dispersion for the overall

results. As implemented in this study and discussed above for the switch from distance-based to time-based dispersion, CYCOEF only affects results beyond 30 kilometers (19 miles), so it affects 50 mile results but has no influence within 10 miles and little influence within 20 miles.

To be consistent with the short-range uncertainty modeling of atmospheric dispersion, the linear parameter in the long-range model was made uncertain and assigned a similar distribution to those used for the short-range parameters. All of the dispersion parameters were fully correlated to ensure smooth transitions with changes in stability class and a smooth transition between short-range and long-range dispersion modeling.

The approach used to develop a distribution for this parameter is the Sequoyah uncertainty analysis is the same as that used to develop distributions for CYSIGA and CZSIGA, as described above. Since 0.5 m/s is the recommended value, it is used as the median of a log-triangular distribution. The lower bound is chosen to be 0.5 / 2.5 = 0.2 and the upper bound of the distribution is chosen to be 0.5 · 2.5 = 1.25.

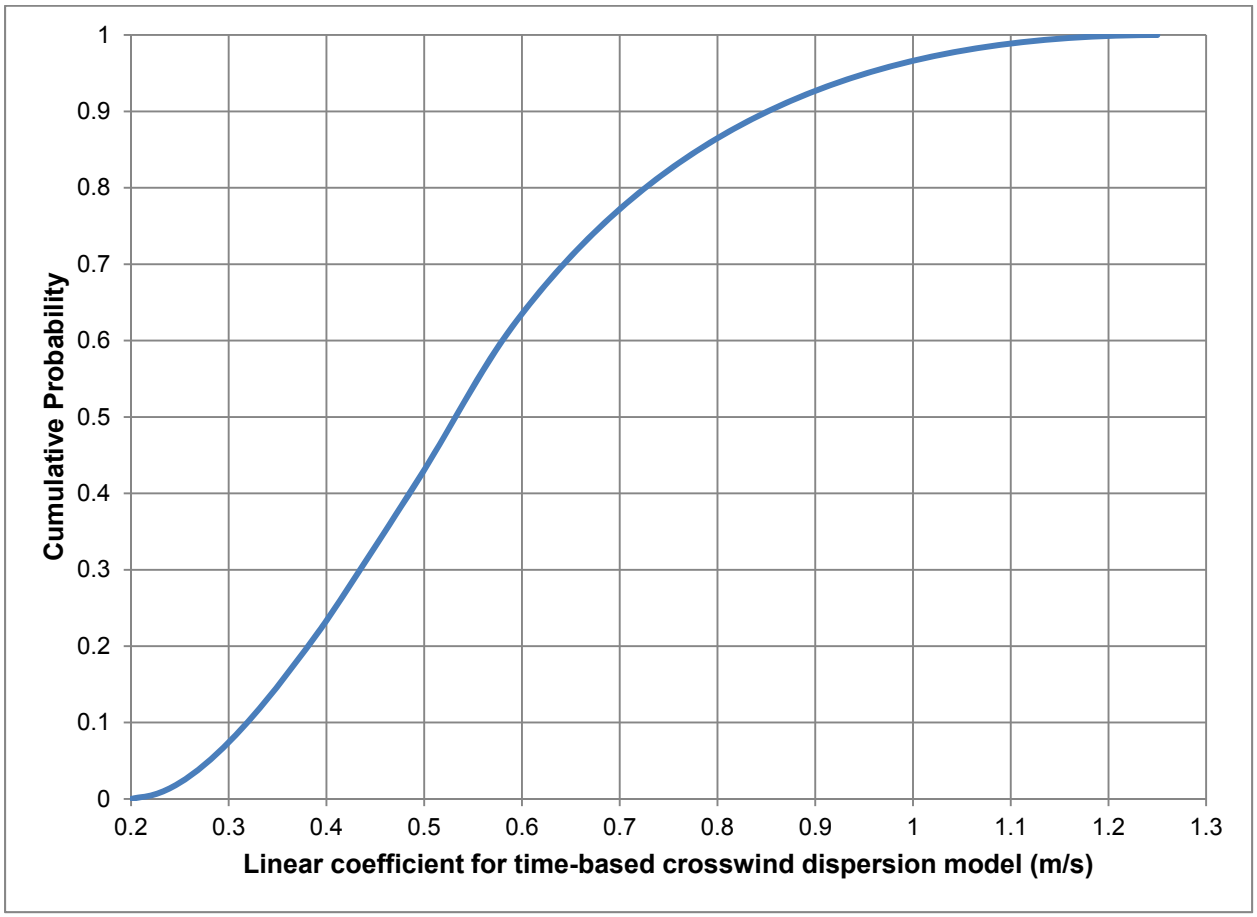

Figure 5-27 CDF of CYCOEF

5.9.9 Emergency Response (Evacuation and Relocation)

The phase durations DURBEG, DURMID, and the late phase and corresponding speed values ESPEED1, ESPEED2, and ESPEED3 were defined above. For the uncertainty analysis, it was not necessary to make each of these parameters uncertain. In determining which parameters to

select, it was decided that one delay parameter (DLTEVA) and one speed parameter would adequately represent the uncertainty of the set. ESPEED2 was selected to be uncertain because this occurs during the middle phase when congestion within the EPZ is at its greatest.

In addition to speed and delay, relocation parameters are sampled to reflect uncertainty in post evacuation activities. Following a release of radioactive material, levels of deposition can vary resulting in areas with elevated dose rates called hotspots [87] that may warrant the relocation of residents from affected areas. MACCS implements relocation using the hotspot and normal relocation parameters to represent these ORO actions, which would be determined based on dose projections using state, utility, and federal agency computer models and field measurements. In practice, this protective measure could be implemented as a post-accident relocation or as an expanded evacuation.

5.9.9.1 Evacuation Delay (DLTEVA)

The evacuation delay (DLTEVA) for each cohort is unique. Although there is high confidence in the alert and notification system used to warn the public, time varying evacuation response rates in relation to the issuance of evacuation orders have been observed. Wolshon et al. [91] found that delay is not uniform with most of the evacuees experiencing a smaller delay (e.g., 90 percent of the public evacuates in about 60 percent of the response time). However, there are reasons for expecting delays in response to nuclear power plant emergencies to be limited. Research has found that EPZ residents understand actions that may be expected during an emergency and are well prepared, with 20 percent of EPZ residents having go-bags and are ready to leave promptly [92]. The variation in public response makes this a good candidate for an uncertain parameter. Information used to develop the DLTEVA distributions was obtained from the ETE report.

Rationale for Distribution

A triangular distribution is used to represent DLTEVA uncertainty because there is data that supports a peak in the response, representing some people leaving early, some late, and most during the middle portion of the response. Delays can increase due to a slow response to the evacuation order, a need to wait for the return of commuters, a need to wait for public transportation, a need to shut down operations prior to leaving work, etc. Likewise, those members of the public with go-bags may respond promptly. MACCS moves cohorts as a group based on population fraction; therefore, compromise (average) values are used to represent the entire cohort response.

Cohort 1 represents the schools within the EPZ. The ETE report [50] identifies school bus mobilization time under normal conditions taking 150 minutes for most schools and identifies two waves of evacuation. This time begins after schools are notified directly by OROs, which is 0.5 hours after the initiating event (15 minutes for licensee to notify OROs of the SAE and 15 minutes for OROs to notify schools).

In this seismic scenario, conditions are not assumed to be normal; thus, some additional assumptions are added for schools including:

- One wave of evacuation would be conducted.
- High school students with vehicles would not wait for bus arrival and would also transport friends.

- The number of teachers necessary to support loading buses would stay and evacuate with children on the buses. Any remaining teachers would evacuate in their personal vehicles taking as many children as possible.

- The EPZ is close to Chattanooga, thus it is reasonable to assume additional buses could be acquired such that a second wave would not be necessary.

The earthquake is assumed to damage bridges and local communications may also be affected; thus, the time for bus drivers to be notified and travel to the bus depot to pick up their bus is assumed longer than under normal conditions. Driving from the depot to the schools may also be expected to take longer than normal conditions. An additional 2.5 hours was added to the school bus mobilization to account for these activities.

A mode of 5 hours was selected which includes the initial 2.5 hours mobilization time identified in the ETE study, and the additional 2.5 hours for mobilization described above. A lower bound of 1 hour was judged reasonable for this cohort for conditions where the evacuation occurs in the morning at the beginning of school or in the afternoon at the end of school when buses are already mobilized and are at or near the school when the event occurs. Furthermore, it is possible the earthquake would not significantly damage roadways. The Loma Prieta earthquake caused extensive building damage; however, except for the collapse of a single link span of the double deck section of the San Francisco-Oakland Bay Bridge, most bridges in the area of the San Francisco Bay survived the earthquake with relatively minor damage [93]. An upper bound of 8 hours was established to account for a broader range of delays in school notification, communication with drivers, driver mobilization time to pick up the buses, roadway impediments on the way to the schools, etc.

Cohort 2 represents the special facilities. There are 756 special facility residents identified in the 2013 ETE [50], and these facilities would evacuate as resources are available. It is not necessary to model each facility individually; therefore, special facilities are modeled as a group. The departure time represents an average of when the facilities may depart. The 2013 ETE report identifies about 1.5 hours to mobilize the first wave of vehicles under normal conditions. The 1.5 hours begins after OROs have notified the facilities, which is 0.5 hours after the initiating event. The ETE study identifies an insufficient number of vehicles to complete the evacuation in a single wave, and shows a second wave beginning 4 hours after notification. Unlike the schools, it is not assumed that nurses or other staff would load residents into personal vehicles. However, as close as the EPZ is to Chattanooga, it is assumed that vehicles could be acquired such that a second wave would not be necessary. A mode of 3 hours was selected for Cohort 2. This includes the 1.5 hours to mobilize as described in the ETE study and an additional 1.5 hours to acquire additional resources and account for additional travel time to the facilities due to damaged infrastructure. A lower bound of 2 hours was selected to represent that there are some facilities with onsite transportation resources and 3 of the 5 facilities (80% of the special facility population) are within 2 miles of the EPZ boundary. A factor of 2 was applied to the mode providing a value of 6 hours for the upper bound. The factor of 2 was based on analyst judgment which considered the proximity to Chattanooga provides access to additional resources; however, additional time may be needed to acquire these resources due to competing priorities.

Cohort 3 represents the 0-10 mile transit dependent population. The ETE study identifies 5.25 hours to evacuate the transit dependent public. This group is identified in the ETE study as evacuating in two waves due to the limited resources, which are first used for special facilities. Because this population is made up of individuals who require specialized transportation, there

are no assumptions on additional resources provided to expedite their evacuation. This cohort represents the homebound residents who are considered sheltered until they begin to evacuate. A mode of 4.5 hours was selected which includes 0.5 hours for the licensee to notify OROs and OROs to initiate contacts with response agencies to provide transportation and 4 hours to mobilize vehicles. Evacuating individual residents from random locations throughout the EPZ can be time consuming. A lower bound of 3 hours was selected to represent conditions where there are potentially fewer transit dependent evacuees due to support from family and friends who assist with evacuation. An upper bound of 9 hours (double the mode) was selected to represent the second wave of vehicles needing to travel through areas with damaged infrastructure.

Cohort 4 represents the first group of the 0-10 mile public to evacuate and includes about 50 percent of the EPZ population. It is expected that this group of public responds early and spontaneously, beginning to mobilize and evacuate prior to the official evacuation order. This assumption is based on the large seismic event which would be felt by everyone within the EPZ. Research has found that EPZ residents understand actions that may be expected during an emergency and are well prepared, with 20 percent of EPZ residents having go-bags and are ready to leave promptly. The focus groups conducted with this research identified a small number of EPZ residents had pre-planned their actions in case of an emergency and were ready to leave promptly [92]. Because this is a large earthquake, it is assumed this cohort leaves after the SAE sirens. A DLTEVA mode of 0.75 hours was selected for the average of the mobilization time of the early evacuees. This was selected considering sirens for SAE will be activiatedand residents take some time to prepare and pack prior to leaving. A DLTEVA mode of 0.75 hours, together with 0.5 hours for DLTSHL, equates to the early evacuees being modeled departing at 1.25 hours after the initiating event. A lower bound of 0 hours would indicate there is no delay after the public has been notified, which it is not realistic. A lower bound of 0.25 hours was selected because of an implied urgency from the earthquake and SAE sirens are sounded for this EPZ. An upper bound of 3 hours was used for this early evacuating cohort because impediments, such as inability to open garage doors, need to shut off gas and electricity, etc., could delay residents as they are preparing to leave.

Cohort 5 represents the 0-10 mile general public. The 2013 ETE report shows that 90 percent of the general public is mobilized in about 1.5 hours after the siren. This value was used as the mode. Although there may be greater urgency due to the earthquake, there may be impediments that slow the preparation activities. Therefore, a lower bound of 0.5 hours was selected to represent the urgency due to the earthquake, and potentially fewer impediments that might slow preparations. An upper bound of 3 hours was selected to represent additional potential impediments, such as inability to open garage doors, need to shut off gas and electricity, etc., could delay residents as they are preparing to leave.

Cohort 6 represents the evacuation tail for the 0 to 10 mile public. The 2013 ETE report [57] shows that 90 percent of the general public complete evacuation in about 5 hours under the roadway impact scenario, which is the time the tail would begin. A mode of 3 hours was selected representing the tail takes longer to mobilize than the general public [91]. A lower bound of 1 hour was selected to reflect a reduction in delay because residents sense of urgency having felt the earthquake. An upper bound of 5 hours was selected to reflect a range of potential delays that contribute to the tail, such as waiting for commuters, shutting down equipment, and the potential delays identified with cohort 4.

Cohort 7 represents the shadow evacuation in the 10 to 15 mile area. The size of the shadow evacuation can be influenced by communication during the emergency and may be influenced

due to the earthquake. The timing and content of messaging can cause the shadow to increase or decrease and can cause residents to leave earlier or later in the event depending on their perceived risk. Shadow evacuations typically begin shortly after a general evacuation begins. A mode of 1.5 hours was selected because early evacuees have begun evacuating and schools have begun to mobilize within the EPZ. A lower bound of 1 hour was selected to reflect a reduction in delay due to resident's sense of urgency having felt the earthquake. An upper bound of 3 hours was selected to reflect an effective communication strategy that delays shadow evacuees allowing EPZ evacuees to travel through the area first.

Cohort 8 does not have an associated uncertainty distribution. An uncertainty distribution is not applicable to Cohort 8 because they are deterministically considered to be non-evacuating during the accident. Therefore, there is no variability considered in their evacuation delay or speed.

Table 5-17 provides a listing of the cohorts and the values used in the triangular distribution. The cohort sampling approach is shown in Figure 5-28. Evacuation delays are sampled independently for each cohort. Cohorts 4, 5 and 6 were perfectly correlated to ensure for example, that the tail does not evacuate prior to the early public. For each cohort the timing of evacuation is specified independently at each radial distance in the grid (a ring). These values are rank correlated so that the entire cohort begins to evacuate at approximately the same time.

Table 5-17 MACCS uncertain parameters – evacuation delay.

Cohort	Mode (hours)	Bounds (hours)
Cohort 1: 0-10 mile schools	5.0	LB = 1.0 UB = 8.0
Cohort 2: 0-10 mile special facilities	3.0	LB = 2.0 UB = 6.0
Cohort 3: 0-10 mile transit dependent population	4.5	LB = 3 UB = 9
Cohort 4: 0-10 mile early public evacuation	0.75	LB = 0.25 UB = 3
Cohort 5: 0-10 mile general public evacuation	1.5	LB = 0.5 UB = 3.0
Cohort 6: 0-10 mile general public tail of the evacuation	3.0	LB = 1.0 UB = 5.0
Cohort 7: 10-15 mile shadow evacuation	1.5	LB = 1.0 UB = 3.0

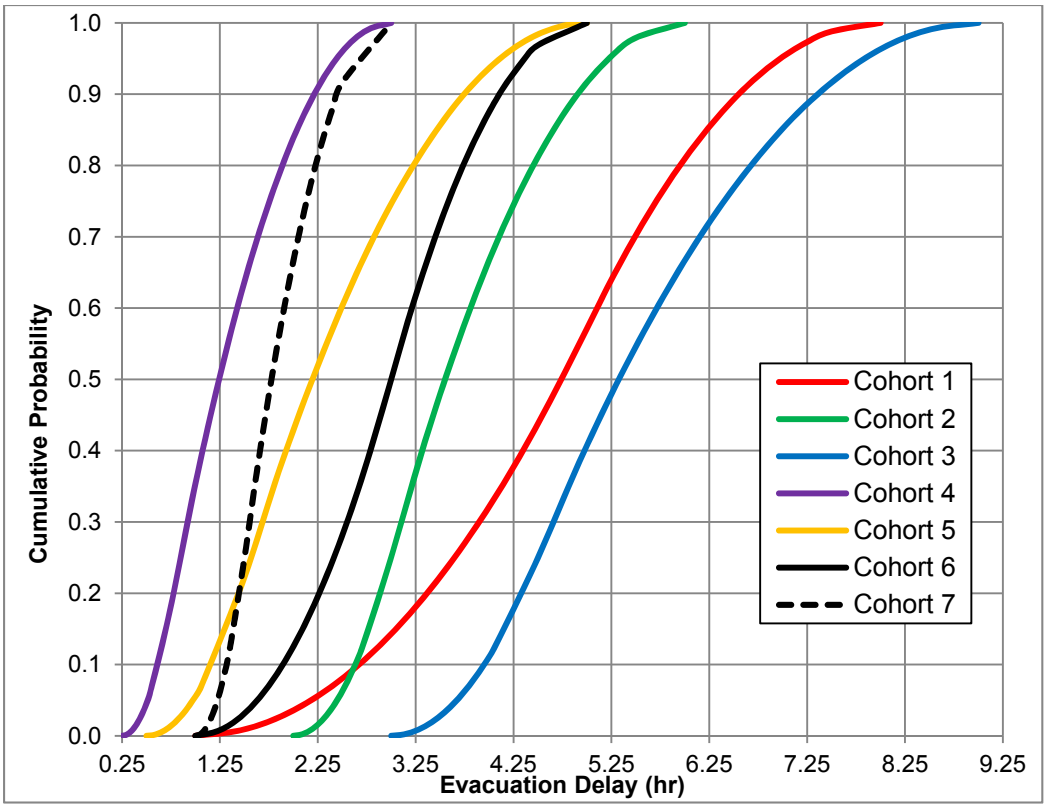

Figure 5-28 CDF of DLTEVA for each cohort

5.9.9.2 Evacuation Speed (ESPEED)

The ESPEED2 parameter represents the speed for each of the evacuating cohorts for the duration of the middle phase. Speeds are developed for the cohorts as a group. As cohorts enter the roadway network, congestion builds and speeds slow down. The approach to developing speeds begins with the ETE study which provides the time to evacuate 90% and 100% of the public and time to evacuate schools, special facilities, and the transit dependent public. Thus, the time to evacuate 90% and 100% of the public is known. The time to depart is also known from the ETE study. The difference in depart and exiting the EPZ is the travel time. With knowledge of the evacuation distances, the speeds are developed for each cohort. Similar to the delay times, the speeds are also adjusted to account for the earthquake.

Following the NRC guidance on developing ETE studies [58], the Sequoyah ETE report [50] includes a roadway impact scenario, in which SR 58 was removed from the evacuation network and evacuees were rerouted to exit points out of the EPZ. SR 58 is the primary evacuation route on the eastern side of the EPZ [50]. The ETE study provides an evacuation time of about 5 hours and 8 hours for the 90 and 100% ETEs respectively. Because the earthquake affects the entire EPZ, not just SR 58, a separate capacity analysis, provided as Attachment A, was completed to determine the evacuation speeds.

Rationale for Distribution

A triangular distribution was used to represent uncertainty because there is confidence that the mode developed from the capacity analysis is a most likely value. These speeds can vary by

cohort depending on the evacuation routes selected by each cohort, the location of the cohort within the EPZ (e.g., schools may be near the edge of the EPZ), and the time the cohort enters the roadway. After speeds were established for the roadways, adjustment factors were applied using the ESPGRD parameter to account for congestion.

For Cohort 1 (schools), a speed of 2 mph was used for the mode because the long mobilization time places the school buses on the roadway during the peak of the evacuation when congestion is greatest. A lower bound of 0.5 mph was judged reasonable to account for additional congestion and other impediments to the evacuation. An upper bound of 5 mph was judged reasonable based on the potential for less if the evacuation were to occur in the morning or afternoon while buses are already mobilized. This would place them on the roadway network before significant congestion occurs.

Cohort 2 represents the special facilities within the EPZ. A mode of 3 mph was developed and reflects facilities that evacuate independently, but on average, are likely to enter the roadway network while some congestion exists. A lower bound of 0.5 mph was selected to represent the potential for greater congestion and the need to travel further to find accessible exits from the EPZ. An upper bound of 10 mph was judged reasonable to represent evacuating later in the event when roadways are less congested or very early for those facilities with transportation resources onsite.

Cohort 3 represents the 0-10 mile transit dependent population. The mobilization to evacuate this group takes time putting the evacuees on the roadway while other cohorts are also on the roadway. The mode is 2 mph which reflects the transit dependent population evacuating under congested conditions while the schools, general public, and tail are evacuating. A lower bound of 0.5 mph was selected to reflect the potential for greater congestion and the need to travel further to find accessible exits from the EPZ. An upper bound of 5 mph was selected to reflect the possibility that the evacuation is less impeded.

Cohort 4 (the first group of the 0-10 mile public to evacuate) enters the roadway network prior to congestion. Infrastructure damage is quickly encountered, as reflected by the slow speeds. A mode of 3 mph was estimated based on the potential extent of infrastructure damage which will cause evacuees to alter their routes and find less obstructed pathways out of the EPZ. A lower bound of 0.5 mph was selected to reflect the potential for greater congestion and the need to travel further to find accessible exits from the EPZ. An upper bound of 10 mph was selected to reflect the possibility that evacuation is less impeded. This cohort is on the roadway prior to other cohorts which allows the potential for their speeds to be higher than other cohorts.

Cohort 5 represents the EPZ general public evacuees who begin to evacuate after OROs declare an evacuation is needed. At this time in the event, schools, medical facilities, and the early evacuees have mobilized and congestion is already assumed to have occurred. A mode of 2 mph was estimated based on the evacuation times calculated in the capacity analysis (Attachment A). A lower bound of 0.5 mph was selected to reflect severe congestion. An upper bound of 5 mph was selected to reflect the possibility that the evacuation is less impeded.

Cohort 6 represents the evacuation tail for the EPZ public, which follows the general public evacuation. The initial speed of the tail is the same as the general public because they enter the roadway immediately behind the general public. A mode of 3 mph was estimated because this cohort is on the last group on the roadway and speeds increase slightly as congestion diminishes. The lower bound was set at 0.5 mph (the same as the lower bound for Cohort 5) because the tail enters the roadway network at the end of the peak congestion. The upper

bound of 10 mph represents roadways have less congestion once the majority of vehicles have left the area. At this time in the event, it is likely local news would broadcast the locations of bridge failures, reducing the time needed for the tail to find their alternative routes.

Cohort 7 represents the 10 to 15 mile shadow evacuation which is travelling on different roadways than the EPZ population, thus the speeds are not directly related to the EPZ evacuees. Although shadow evacuations occur in response to emergencies, the effect of the shadow evacuation on the evacuees from the hazard area is seldom significant [88]. A mode of 20 mph was judged reasonable to reflect the shadow evacuees are beyond the congested EPZ when they begin their travel. An upper bound of 30 mph was judged reasonable to account for limited traffic congestion and increased roadway capacity beyond the EPZ. Furthermore, the infrastructure beyond the EPZ is not assumed damaged in this scenario, thus the roadways are assumed accessible. A lower bound of 10 mph was selected to reflect the potential that power outages exist in the Chattanooga area causing traffic delays. An upper bound of 30 mph was selected to represent an unimpeded evacuation of shadow evacuees due to the available roadway capacity.

Cohort 8 does not have an associated uncertainty distribution. An uncertainty distribution is not applicable to Cohort 8 because they are deterministically considered to be non-evacuating during the accident. Therefore, there is no variability considered in their evacuation delay or speed.

Table 5-18 provides a listing of the cohorts and the values used in the triangular distribution. Cohorts are sampled as shown on Figure 5-29. Evacuation speeds are perfectly rank correlated between cohorts.

Table 5-18 MACCS uncertain parameters – evacuation speeds.

Cohort	Speed Mode (mph)	Speed Bounds (mph)
Cohort 1 (0-10 Schools)	2.0	LB = 0.5 UB = 5.0
Cohort 2 (Special Facilities)	3.0	LB = 0.5 UB = 10.0
Cohort 3 (Transit Dependent)	2.0	LB = 0.5 UB = 5.0
Cohort 4 (0-10 Early)	3.0	LB = 0.5 UB = 10.0
Cohort 5 (General Public)	2.0	LB = 0.5 UB = 5.0
Cohort 6 (Evacuation Tail)	3.0	LB = 0.5 UB = 10.0
Cohort 7 (10-15 Shadow)	20.0	LB = 10 UB = 30

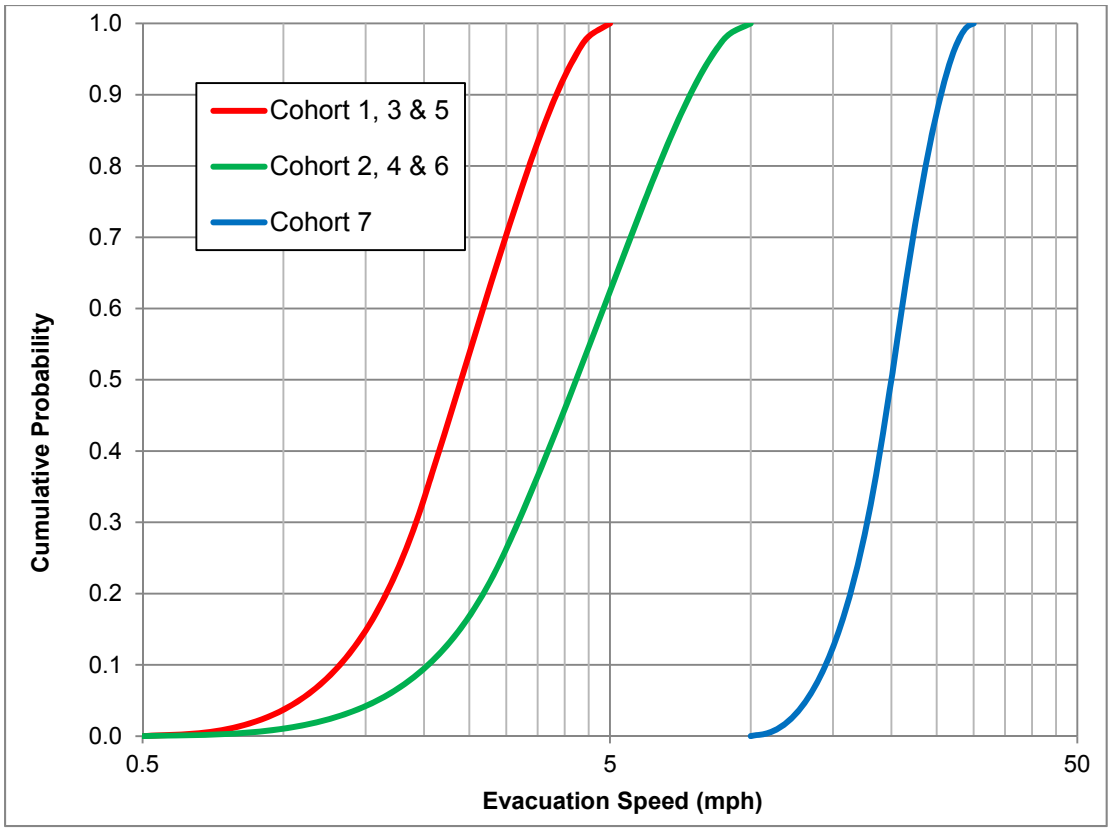

Figure 5-29 CDFs of ESPEED for each cohort

5.9.9.3 Hotspot Relocation Time (TIMHOT)

A hotspot relocation time distribution has been developed to account for a range of source terms, population densities, seismic impact, and other characteristics that influence relocation.

Rationale for Distribution

A uniform distribution was used to represent uncertainty, because the potential influences in activity duration during the emergency make any value within the range described below possible. Few of the time contributing activities can be estimated with confidence prior to an event, such as the affected area, affected population, available transportation infrastructure, need for traffic control, and plume travel speed. Furthermore, data related to prompt relocation of residents was identified in research, thus values were developed from large scale evacuations that have aspects that resemble relocation type activities.

It is assumed relocation is implemented after evacuation is complete to limit extra traffic in areas through which the evacuees are travelling. This approach allows emergency responders who were supporting the evacuation transition to relocating residents. The lower bound was developed based on an optimal relocation implemented promptly after plume arrival. Capabilities exist to project hotspot areas, and OROs could request the public make preparations to leave, prior to the release. Relocation could then begin promptly once it is determined the plume has passed. Assuming the public is prepared to leave, the final time element is travel out of the affected area. A review of the SOARCA results from NUREG/CR-

7110 Volume 2 was conducted to understand the extent to which contamination was projected beyond the EPZ for that sequence and plant. The review identified that the release fraction of cesium for the STSBO scenario might only exceed the hotspot dose threshold over a small portion of the 5 mile area beyond the EPZ. The review of a different plant with different source terms was only used to inform the process. Sequoyah has a much different containment, the seismic event is larger than previous analyses, and the source terms identified in early runs are large. The review would suggest that relocation would affect a larger population than the previous analysis. Therefore, for this analysis, it is assumed that hotspot relocation will be implemented for the entire population within the 5 mile ring beyond the EPZ as shown in Figure 5-30. This is about 390 square miles.

From SecPop, the 2010 population within the radial area 5 miles beyond the EPZ (i.e., 10 to 15 miles from the plant) is about 184,000. The emergency response scenario includes an assumption that 20 percent of the population in this area evacuates as a shadow evacuation, which reduces the number of people potentially affected by hotspots. It is assumed the remaining population of 147,000 residents (80% of 184,000) will be relocated under the hotspot criteria. It is also assumed that OROs have competing priorities due to the seismic event such as damaged infrastructure, injured residents, power outages, and inaccessible roadways and are unable to implement relocation promptly.

A time of 36 hours was used in the base case analysis. Considering the number of people potentially affected, the need for authorities to notify these people and support the relocation, a lower bound value of 24 hours after plume arrival was judged reasonable. The 24 hour value represents an average time for relocation of the affected area. This value was compared to evacuation information in NUREG/CR 6981, “Assessment of Emergency Response Planning and Implementation for Large Scale Evacuations,” [104] which includes case studies of 11 evacuations, seven of which involved populations between 100,000 and 3 million people. Very large evacuations almost always occur in a staged manner, and for hurricanes, where there is ample time to prepare, these resemble prompt relocation activities. The large evacuations that were reviewed were generally completed in 24 hours or less.

The upper bound represents conditions in which there is a delay in relocation, which could occur for many reasons. For example, OROs may decide to wait until the morning, rather than trying to mobilize families at night. Dow and Cutter [105] identified that the majority of hurricane evacuation trips begin during normal waking hours. Fu and Wilmot [106] profiled a hurricane evacuation time of day pattern which showed people are least likely to evacuate at night, with an increasing likelihood during the morning and even greater during the afternoon. Loss of communication, infrastructure damage, or OROs focused on activities within the EPZ or having other conflicting priorities that could contribute to such a delay. Because relocation is based on projected dose over the emergency phase, it may not have the same priority as other urgent requirements. It is also possible that response officials may choose to shelter in place for a period of time. An upper bound of 48 hours after plume arrival was judged reasonable for the affected area. This represents an average time for relocation of the affected area. The CDF is presented in Figure 5-31.

Figure 5-30 Assumed hotspot and normal relocation areas

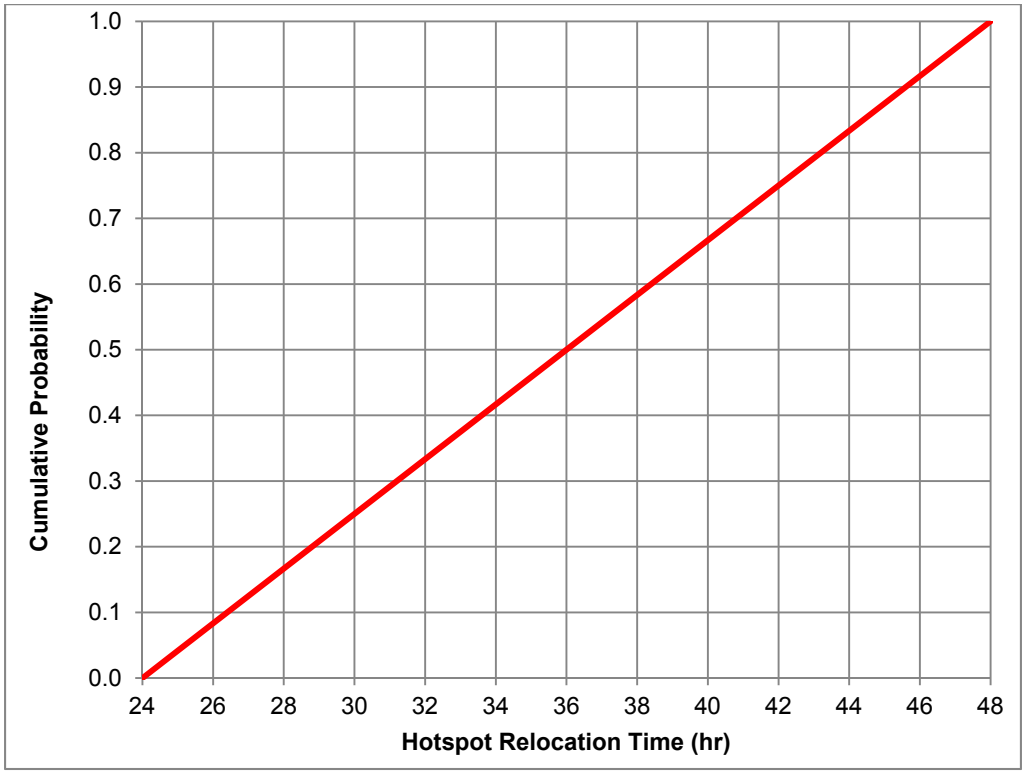

Figure 5-31 CDF of TIMHOT

5.9.9.4 Normal Relocation Time (TIMNRM)

The normal relocation time (TIMNRM) is the time to relocate residents from areas that exceed the normal dose threshold (DOSNRM). This user specified time is relative to plume arrival. The time includes the elements described for TIMHOT. In addition, time may be needed to allow clearance of residents relocated due to the hotspot criteria. MACCS implements this parameter by removing the entire affected population from the dose equation at a point in time after plume arrival, the specified TIMNRM. As with TIMHOT, an average time is developed by considering the influencing factors.

Rationale for Distribution

A uniform distribution is used to represent uncertainty in TIMNRM because the potential influences in activity duration during the emergency make any value within the range described below possible for the same reasons described with TIMHOT. However, normal relocation has a lower dose threshold and may not be implemented with the same urgency as hotspot relocation. As described above, in some aspects, relocation resembles hurricane evacuation. This lack of directly applicable data also supports use of a uniform distribution.

Similar to TIMHOT, the lower bound is developed based on an optimal response where OROs relocate residents promptly after plume arrival. As described above, it is assumed that the area from 10 to 15 miles, also shown on Figure 5-30, is relocated due to exceeding the hotspot criteria. For normal relocation, it is assumed that the entire area from 15 to 20 miles (about 550 square miles) would be relocated due to exceeding normal relocation criteria. From SecPop, the 2010 population of the 15 to 20 mile area is about 195,000. Notifications can be accomplished via EAS messaging, but route alerting would be necessary to notify the affected public and is estimated to take about 8 hours to complete. For this size of population, traffic control would likely be established to support a relocation effort. A time of 48 hours was used in the base case analysis. A lower bound of 36 hours after plume arrival was judged reasonable to represent an average time for relocation of the affected area.

The upper bound represents conditions where OROs may be focused on activities within the EPZ or have other conflicting priorities which delay relocation activities. Furthermore, OROs may delay relocation until daylight hours. Because normal relocation is due to a 1 rem dose projected over the emergency phase, it may not have the same priority as other urgent requirements. An upper bound of 72 hours after plume arrival was judged reasonable. The CDF is presented in Figure 5-32.

TIMNRM is perfectly rank correlated with TIMHOT because MACCS requires TIMNRM be less than TIMHOT.

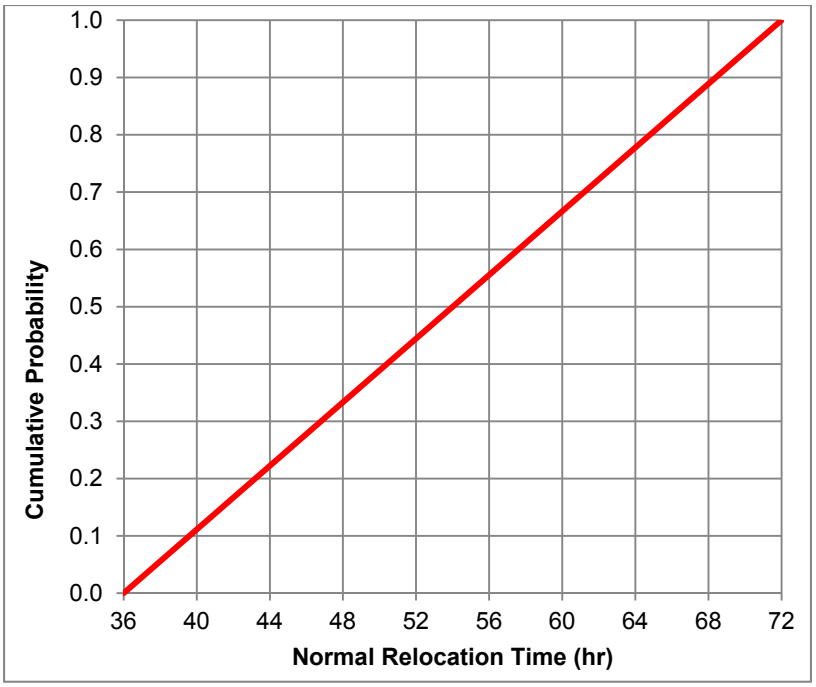

Figure 5-32 CDF of TIMNRM

5.9.9.5 Hotspot Relocation Dose (DOSHOT)

The hotspot relocation dose (DOSHOT) is a projected dose used to initiate hotspot relocation. If the total dose to individuals exceeds DOSHOT, those people are relocated (i.e., removed from the analysis) at a user specified hotspot relocation time (TIMHOT) in the early phase. DOSHOT is often represented as the upper bound of the projected dose range provided in the EPA PAG Manual (Table 1-1. Planning Guidance and Protective Action Guides for Radiological Incidents) [94]. This should not be confused with the EPA PAG Manual criteria for relocation, which is specified for the intermediate phase.

Rationale for Distribution

A triangular distribution is used to represent the uncertainty in DOSHOT because the mode is considered to be the most likely value (5 rem) based on the EPA PAGs. The range was developed recognizing that ORO decisions are influenced by many factors that could result in a higher or lower value.

The EPA PAG Manual provides a range of 1 to 5 rem for implementing protective actions and explains that under normal conditions, evacuation should be implemented if residents are expected to receive 1 rem over a 4 day emergency phase. The upper bound for this distribution was increased 50 percent above the EPA PAG to 7.5 rem, based on analyst judgment. The lower bound was set at 1 rem, which is the mode of the normal relocation criteria (DOSNRM). The CDF is presented in Figure 5-33.

DOSHOT is perfectly rank correlated (i.e., coefficient of 1.0) with the normal relocation dose (DOSNRM) because MACCS requires DOSNRM to be less than DOSHOT.

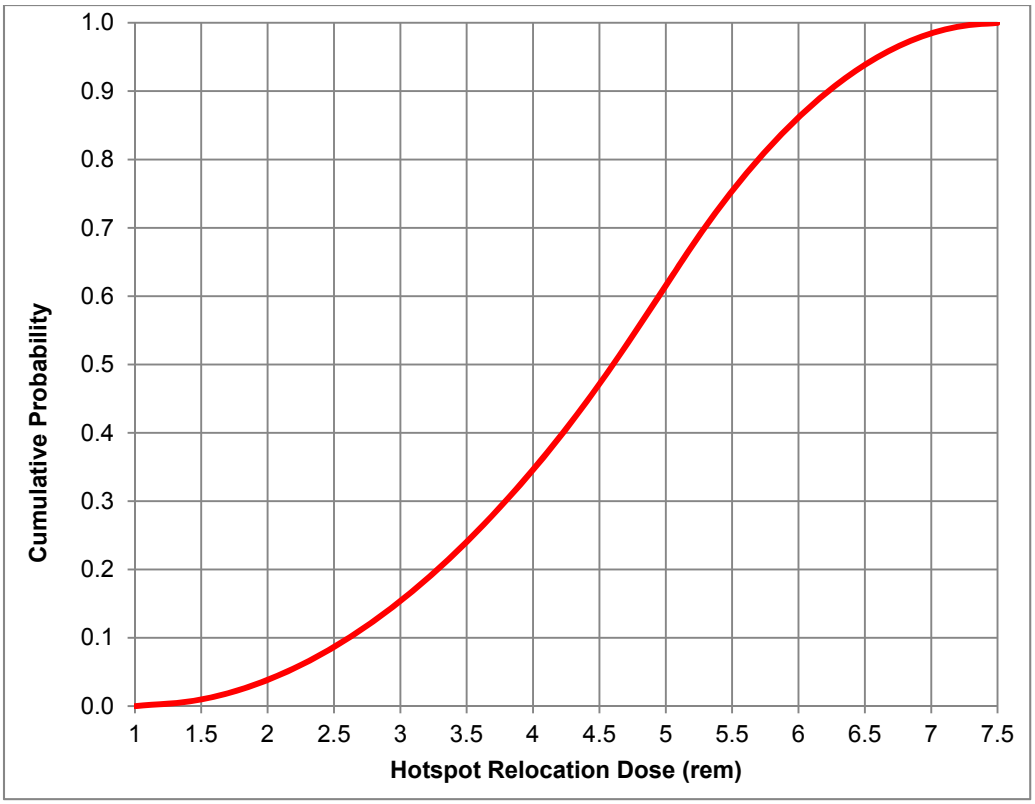

Figure 5-33 CDF of DOSHOT

5.9.9.6 Normal Relocation Dose (DOSNRM)

The normal relocation dose (DOSNRM) is a projected dose used to initiate normal relocation. If the total dose to individuals exceeds DOSNRM, those people are relocated (i.e., removed from the analysis) at a user specified normal relocation time (TIMNRM) in the early phase. DOSNRM is typically represented as the lower bound of the projected dose range provided in Table 1.1 of the EPA PAG Manual.

Rationale for Distribution

A triangular distribution is used because the mode (1 rem) is considered to be the most likely value based on EPA PAGs. It is assumed that OROs would attempt to meet the EPA PAG barring unforeseen circumstances. Using judgment, the upper bound for this distribution was increased by a factor of two over the mode to 2 rem. The lower bound of 0.5 rem was judged reasonable. A low threshold value causes the size of the affected area to increase, which would increase the number of people requiring relocation. The number of people affected would likely influence ORO decisions on the lower threshold value. The CDF is presented in Figure 5-34.

DOSNRM is perfectly rank correlated with the hotspot relocation dose (DOSHOT) because MACCS requires DOSNRM to be less than DOSHOT.

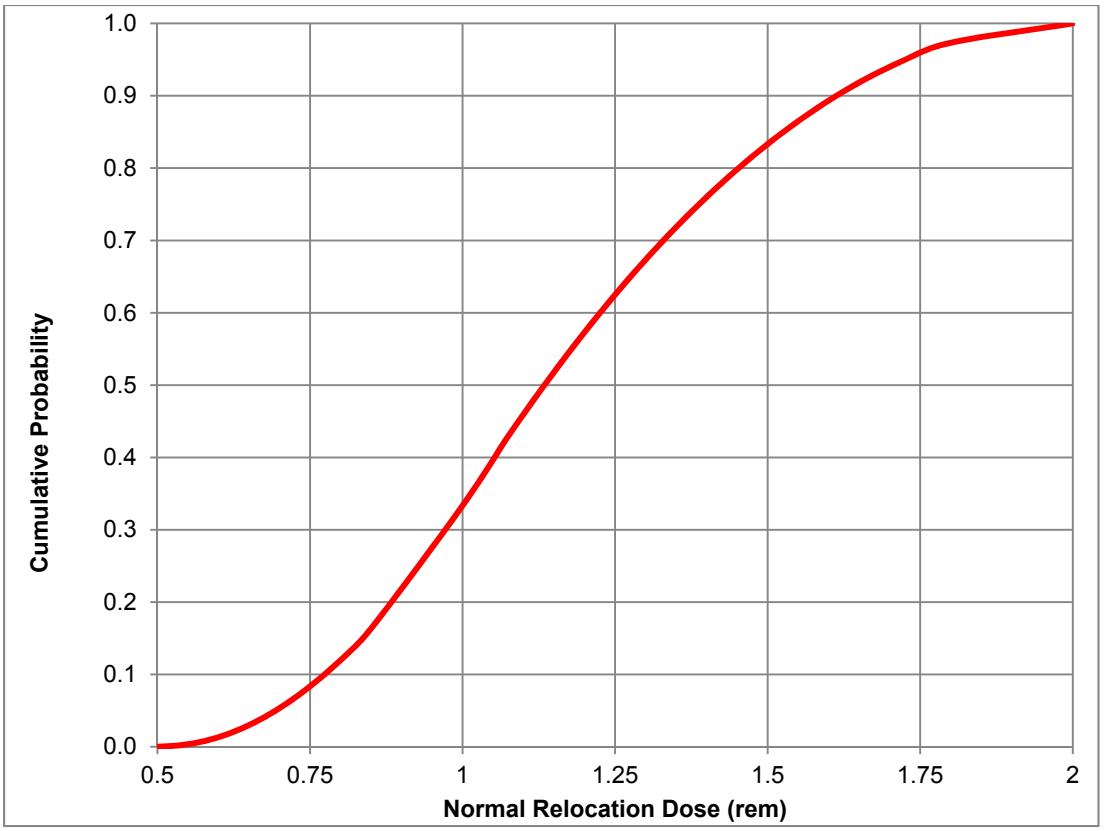

Figure 5-34 CDF of DOSNRM

5.9.9.7 Weather

The deterministic offsite consequence values are the expected (mean) value of the probability distribution obtained from a large number of weather trials. The UA uses the same weather-sampling strategy adopted for SOARCA, as reported in the MACCS Best Practices document, and also applied in the Peach Bottom UA.

5.9.9.8 MACCS Correlated Parameters

Many of the parameters in the analysis have correlations. Some of these are perfectly rank ordered and others have rank correlation coefficients between -1.0 and +1.0. Unless specified in Table 5-19 below, parameters are not correlated.

Table 5-19 MACCS correlated parameters.

Input Parameter	Perfectly Rank-Order Correlated with	Comments
PROTIN(2)	LPROTIN	Long-term is tied to normal activity
GSHFAC(2)	LGSHFAC	Long-term is tied to normal activity
TIMHOT	TIMNRM	TIMHOT is always less than TIMNRM
DOSHOT	DOSNRM	TIMHOT is always greater than TIMNRM

Input Parameter	Perfectly Rank-Order Correlated with	Comments
EFFTHR(1)	EFFACA(1)	Red bone marrow
EFFTHR (2)	EFFACA (2)	Lungs
EFFTHR (3)	EFFACA (3)	Stomach
CYSIGA(1)	CYSIGA(2-6)	All weather conditions
CYSIGA(1)	CZSIGA(1-6)	All weather conditions
ESPEED(2)-1	ESPEED(2)-(2-5)	Middle Phase of ESPEED for all Cohorts evacuating
VDEPOS(1)	VDEPOS(2-10)	All particle size bins
Co-58_ICH(1)	Co-58_ICH(2,4-9)	Lifetime inhalation dose coefficient
Co-60_ICH(1)	Co-58_ICH(2,4-9)	Lifetime inhalation dose coefficient
Rb-86_ICH(1)	Co-58_ICH(2,4-9)	Lifetime inhalation dose coefficient
Rb-88_ICH(1)	Co-58_ICH(2,4-9)	Lifetime inhalation dose coefficient
Sr-89_ICH(1)	Co-58_ICH(2,4-9)	Lifetime inhalation dose coefficient
Sr-90_ICH(1)	Co-58_ICH(2,4-9)	Lifetime inhalation dose coefficient
Sr-91_ICH(1)	Co-58_ICH(2,4-9)	Lifetime inhalation dose coefficient
Sr-92_ICH(1)	Co-58_ICH(2,4-9)	Lifetime inhalation dose coefficient
Y-90_ICH(1)	Co-58_ICH(2,4-9)	Lifetime inhalation dose coefficient
Y-91_ICH(1)	Co-58_ICH(2,4-9)	Lifetime inhalation dose coefficient
Y-91m_ICH(1)	Co-58_ICH(2,4-9)	Lifetime inhalation dose coefficient
Y-92_ICH(1)	Co-58_ICH(2,4-9)	Lifetime inhalation dose coefficient
Y-93_ICH(1)	Co-58_ICH(2,4-9)	Lifetime inhalation dose coefficient
Zr-95_ICH(1)	Co-58_ICH(2,4-9)	Lifetime inhalation dose coefficient
Zr-97_ICH(1)	Co-58_ICH(2,4-9)	Lifetime inhalation dose coefficient
Nb-95_ICH(1)	Co-58_ICH(2,4-9)	Lifetime inhalation dose coefficient
Nb-97_ICH(1)	Co-58_ICH(2,4-9)	Lifetime inhalation dose coefficient
Mo-99_ICH(1)	Co-58_ICH(2,4-9)	Lifetime inhalation dose coefficient
Tc-99m_ICH(1)	Co-58_ICH(2,4-9)	Lifetime inhalation dose coefficient
Ru-103_ICH(1)	Co-58_ICH(2,4-9)	Lifetime inhalation dose coefficient
Ru-105_ICH(1)	Co-58_ICH(2,4-9)	Lifetime inhalation dose coefficient
Ru-106_ICH(1)	Co-58_ICH(2,4-9)	Lifetime inhalation dose coefficient
Rh-103m_ICH(1)	Co-58_ICH(2,4-9)	Lifetime inhalation dose coefficient
Rg-105_ICH(1)	Co-58_ICH(2,4-9)	Lifetime inhalation dose coefficient
Te-127_ICH(1)	Co-58_ICH(2,4-9)	Lifetime inhalation dose coefficient
Te-127m_ICH(1)	Co-58_ICH(2,4-9)	Lifetime inhalation dose coefficient
Te-129_ICH(1)	Co-58_ICH(2,4-9)	Lifetime inhalation dose coefficient
Te-129m_ICH(1)	Co-58_ICH(2,4-9)	Lifetime inhalation dose coefficient
Te-131_ICH(1)	Co-58_ICH(2,4-9)	Lifetime inhalation dose coefficient
Te-131m_ICH(1)	Co-58_ICH(2,4-9)	Lifetime inhalation dose coefficient

Input Parameter	Perfectly Rank-Order Correlated with	Comments
Te-132_ICH(1)	Co-58_ICH(2,4-9)	Lifetime inhalation dose coefficient
I-131_ICH(1)	Co-58_ICH(2,4-9)	Lifetime inhalation dose coefficient
I-132_ICH(1)	Co-58_ICH(2,4-9)	Lifetime inhalation dose coefficient
I-133_ICH(1)	Co-58_ICH(2,4-9)	Lifetime inhalation dose coefficient
I-134_ICH(1)	Co-58_ICH(2,4-9)	Lifetime inhalation dose coefficient
I-135_ICH(1)	Co-58_ICH(2,4-9)	Lifetime inhalation dose coefficient
Cs-134_ICH(1)	Co-58_ICH(2,4-9)	Lifetime inhalation dose coefficient
Cs-136_ICH(1)	Co-58_ICH(2,4-9)	Lifetime inhalation dose coefficient
Cs-137_ICH(1)	Co-58_ICH(2,4-9)	Lifetime inhalation dose coefficient
Ba-139_ICH(1)	Co-58_ICH(2,4-9)	Lifetime inhalation dose coefficient
Ba-140_ICH(1)	Co-58_ICH(2,4-9)	Lifetime inhalation dose coefficient
La-140_ICH(1)	Co-58_ICH(2,4-9)	Lifetime inhalation dose coefficient
La-141_ICH(1)	Co-58_ICH(2,4-9)	Lifetime inhalation dose coefficient
La-142_ICH(1)	Co-58_ICH(2,4-9)	Lifetime inhalation dose coefficient
Ce-143_ICH(1)	Co-58_ICH(2,4-9)	Lifetime inhalation dose coefficient
Ce-144_ICH(1)	Co-58_ICH(2,4-9)	Lifetime inhalation dose coefficient
Pr-143_ICH(1)	Co-58_ICH(2,4-9)	Lifetime inhalation dose coefficient
Pr-144_ICH(1)	Co-58_ICH(2,4-9)	Lifetime inhalation dose coefficient
Nb-147_ICH(1)	Co-58_ICH(2,4-9)	Lifetime inhalation dose coefficient
Np-239_ICH(1)	Co-58_ICH(2,4-9)	Lifetime inhalation dose coefficient
Pu-238_ICH(1)	Co-58_ICH(2,4-9)	Lifetime inhalation dose coefficient
Pu-239_ICH(1)	Co-58_ICH(2,4-9)	Lifetime inhalation dose coefficient
Pu-240_ICH(1)	Co-58_ICH(2,4-9)	Lifetime inhalation dose coefficient
Pu-241_ICH(1)	Co-58_ICH(2,4-9)	Lifetime inhalation dose coefficient
Am-241_ICH(1)	Co-58_ICH(2,4-9)	Lifetime inhalation dose coefficient
Cm-242_ICH(1)	Co-58_ICH(2,4-9)	Lifetime inhalation dose coefficient
Cm-244_ICH(1)	Co-58_ICH(2,4-9)	Lifetime inhalation dose coefficient

Linear correlation coefficients

Input Parameter	Rank-Order Correlated With	Correlation Coefficient	Comments
PROTIN(2)	PROTIN(3)	0.75	Applies to all evacuation cohorts for normal activity and sheltering inhalation protection factors
GSHFAC(2)	GSHFAC(3)	0.8	Applies to all evacuation cohorts for normal activity and sheltering groundshine shielding factors

6. OFFSITE CONSEQUENCE ANALYSIS

6.1 Introduction

The Sequoyah SOARCA offsite consequence analysis includes the results of deterministic analyses and probabilistic uncertainty analyses. The deterministic cases have common MACCS input parameters as shown in Appendix B, but unique source terms. The deterministic cases are:

- STSBO base case[39] without random ignition,
- An STSBO case, also without random ignition, with an early release, approximately 3 hrs after the initiating event, (STSBO ER), and
- LTSBO base case.

The probabilistic uncertainty analysis results are based on sampled MELCOR and MACCS input values. An uncertainty analysis was conducted for the STSBO cases without and with random ignition (STSBO w/o random ignition and STSBO with random ignition). Each realization represents a sampled parameter set that is unique. The uncertainty analysis comprised 467 realizations for the STSBO w/o random ignition and 432 for STSBO with random ignition for a total of 899 realizations. The selected uncertainty analyses which resulted in the maximum cesium release, the maximum LCF risk, and the maximum EF risk are discussed. Finally, a sensitivity analysis was conducted for the STSBO-ER scenario, in which the effectiveness of sheltering in place versus evacuation was examined under varied shielding assumptions.

The results of the consequence analyses are presented in terms of individual LCF risk and individual EF risk for the population residing near the plant. The primary results are mean values of more than 1,000 weather trials. To examine the variation of risk with distance from the site, the reported risk measures are evaluated for residents within specified radial distance intervals (i.e., circular or annular areas with specified radii) centered on the reactor site. They are averaged over the entire residential population within each interval and over weather variability. These individual risk values are population weighted and are computed by dividing the predicted number of excess fatalities (early or latent) by the population living within the specified interval. These risk measures account for the distribution of the population within the distance interval and for the interplay between the population distribution and the wind rose probabilities.

The results are presented as conditional risks, which are the risks predicated on the accident occurring. The scenario frequency-weighted risk is the product of the core damage frequency for the accident scenario and the conditional EF or LCF risk for that scenario. The scenario frequency-weighted risk is the average likelihood of an individual dying of latent cancer or from acute radiation exposure per year of plant operation (i.e., LCF risk per reactor year (pry) or EF

[39] "Base case" describes the STSBO without random ignition and the LTSBO scenarios in which all uncertain MELCOR parameters are set to their most likely value (mode). The STSBO Early Release was selected from the STSBO w/o random ignition set of UA realizations as an example of an early release.

risk pry) as a result of the specific scenario under consideration. Selected results present both conditional and frequency-weighted risk values for comparison for each scenario.

For the deterministic cases, individual LCF risk results are presented for four approaches to quantify the risk from radiation exposure at low doses and dose rates. Cancer dose-response curves for low doses and dose rates are subject to considerable uncertainty, so it is instructive to examine how much of the computed risk arises from low doses or dose rates. The primary approach is the use of the LNT model to quantify individual latent cancer fatality risk, which considers all doses and dose rates for estimating cancer risk. The LNT dose-response relationship suggests that any increase in dose, no matter how small, results in an incremental increase in risk. The alternate dose quantification approaches examine the contribution to LCF risk arising only from doses above a specified dose or dose-rate threshold. The three alternate dose quantification approaches used in this study are:

- consideration of cancers arising only from dose rates above the US average natural background dose rate (310 mrem/yr) (NCRP),

- cancers from dose rates above the US average natural background dose rate combined with average annual manmade (primarily medical) exposure as a dose threshold level (620 mrem/yr) [96], and

- a dose and dose-rate threshold level based on the Health Physics Society's Position Statement that, due to uncertainties, a quantified risk should not be assigned to dose rates less than 5 rem/yr with a lifetime dose limit of 10 rem [100].

A 10 mrem/yr dose threshold level was also investigated. It produced results that were modestly lower than results calculated using the LNT assumption; therefore, these results are not included. Finally, the UA and the sensitivity analysis results are based solely on the LNT approach.

Like the SOARCA report NUREG-1935 [3], the individual LCF risks reported for Sequoyah do not include potential doses from food or water ingestion. MACCS does not include ingestion doses in the estimation of individual EF and LCF risks. Ingestion doses are considered to be societal, or population, doses and are difficult to apportion to individuals. This is because foods grown in a specific area are not necessarily consumed in that area. Instead, locally grown food is distributed to various parts of the country and, conversely, food consumed in a local area comes from other domestic and international sources. This complexity makes it very difficult to apportion ingestion doses to specific individuals. Therefore, individual doses only consider cloudshine, groundshine, and inhalation exposure pathways for which the exposure occurs locally.

6.2 Sequoyah Source Terms

Some of the key characteristics of a release of radiation to the environment are the magnitude and type of radioactive materials as well as the timing and duration of release. These influence the risk results of both the emergency and long-term phases of an accident. The long-term individual LCF risk is strongly correlated with the concentration of cesium deposited on the ground. A larger release provides more cesium source term, however the rate of release combined with local weather conditions influence where and when the cesium will deposit. As an example, a release of high magnitude and short duration is more likely to result in higher

ground concentrations at certain locations than a long gradual release. This is because the longer release is more likely to disperse over a larger area as the wind direction changes. An early release can be important because of its potential to challenge emergency response protective actions such as evacuation.

Table 6-1 lists source term environmental releases of the deterministic scenarios and summarizes the total release fraction by MELCOR chemical class. The environmental release fraction is that portion of the radionuclide inventory of each class that is released to the environment. The total release fraction is the result of integrating over the duration of the release. The start time is the beginning of the release to the environment, no matter how small. Some releases may begin with a small release, which subsequently increases significantly due to containment failure or some other release mechanism. The "increase" time describes the time when the release significantly increases in rate. For the Sequoyah project, all cases were truncated at 72 hours.

Table 6-1 Source term releases for Sequoyah accident scenarios.

Scenario	Environmental Release Fraction by MELCOR Chemical Class									Time (hr)	
	Xe	Cs	Ba	I	Te	Ru	Mo	Ce	La	Start*	Increase**
STSBO base case	0.998	0.063	0.001	0.069	0.021	0.000	0.212	0.000	0.000	4.0	52.0
STSBO ER	1.000	0.039	0.004	0.084	0.093	0.002	0.141	0.000	0.000	2.6	3.6
LTSBO base case	0.997	0.023	0.009	0.092	0.087	0.000	0.001	0.001	0.000	23.8	28.8

*The "start" time indicates the timing of the first environmental release, no matter how small (e.g., release fraction on the order of 1E-9).

**The "increase" time indicates the timing of the first significant increase in the rate of release.

Figure 6-1 illustrates the progression of releases of the cesium and iodine classes over time for the STSBO w/o random ignition. The release begins at 4 hours, however the initial magnitudes are miniscule (~10^{-9}). The cesium and iodine releases both increase rapidly at 52 hours. Ultimately, the cumulative cesium and iodine released to the environment equal 6.3% and 6.9% of the respective quantities contained in the Sequoyah Reactor unit 1, middle-of-cycle inventory.

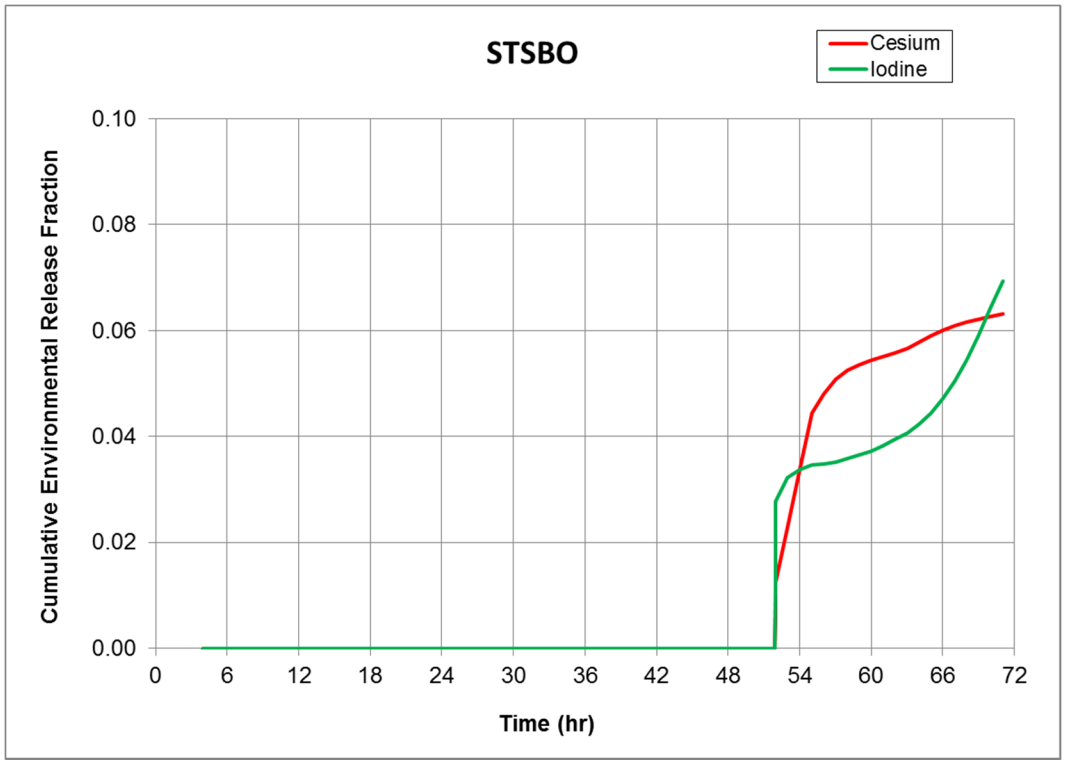

Figure 6-1 Cumulative environmental release fraction of cesium and iodine as a function of time for the STSBO base case scenario

Figure 6-2 shows the cumulative iodine and cesium class release profile of the STSBO-ER scenario. The release starts at 2.6 hours, increases in multiple steps, and then increases relatively slowly from about 24 through 72 hours. For the STSBO-ER case, the total cesium release of 3.9 percent is about half of the total iodine release of 8.4 percent.

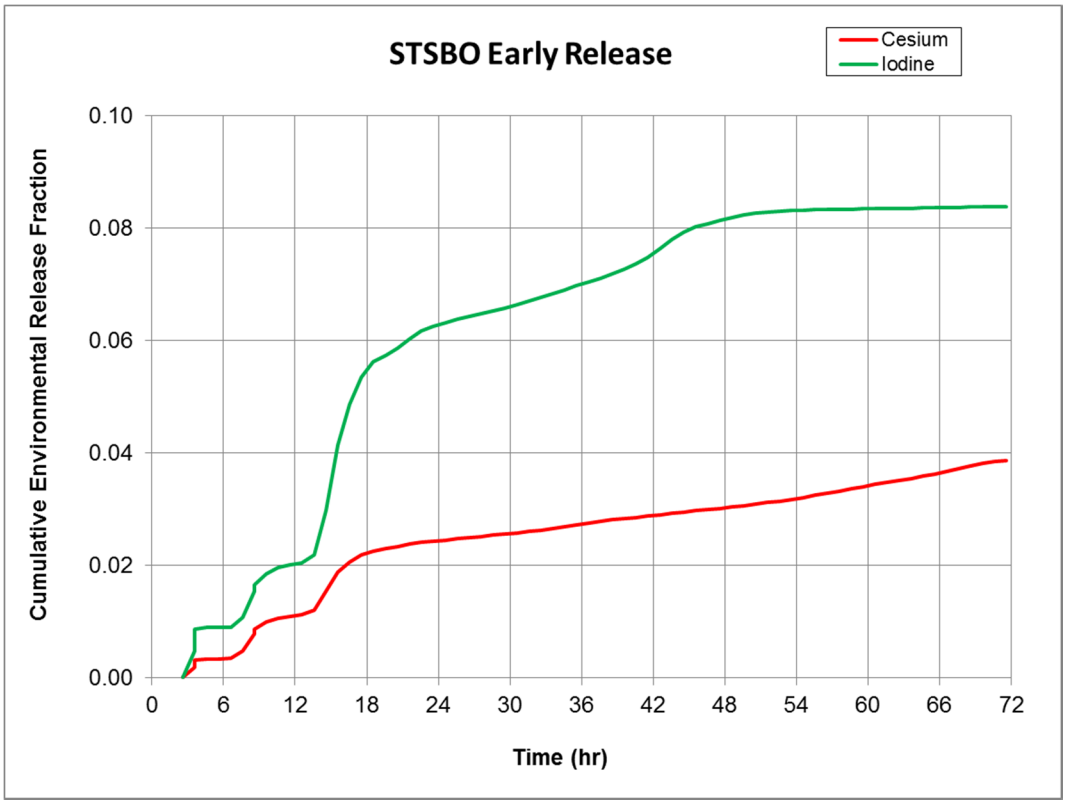

Figure 6-2 Cumulative environmental release fraction of cesium and iodine as a function of time for the STSBO early release scenario

Lastly, Figure 6-3 shows the LTSBO scenario release to the environment begins at 24 hours, increases in rate at 28 hours, and has another large increase at about 45 hours. The cesium and iodine class releases total 2.3 and 9.2 percent, respectively.

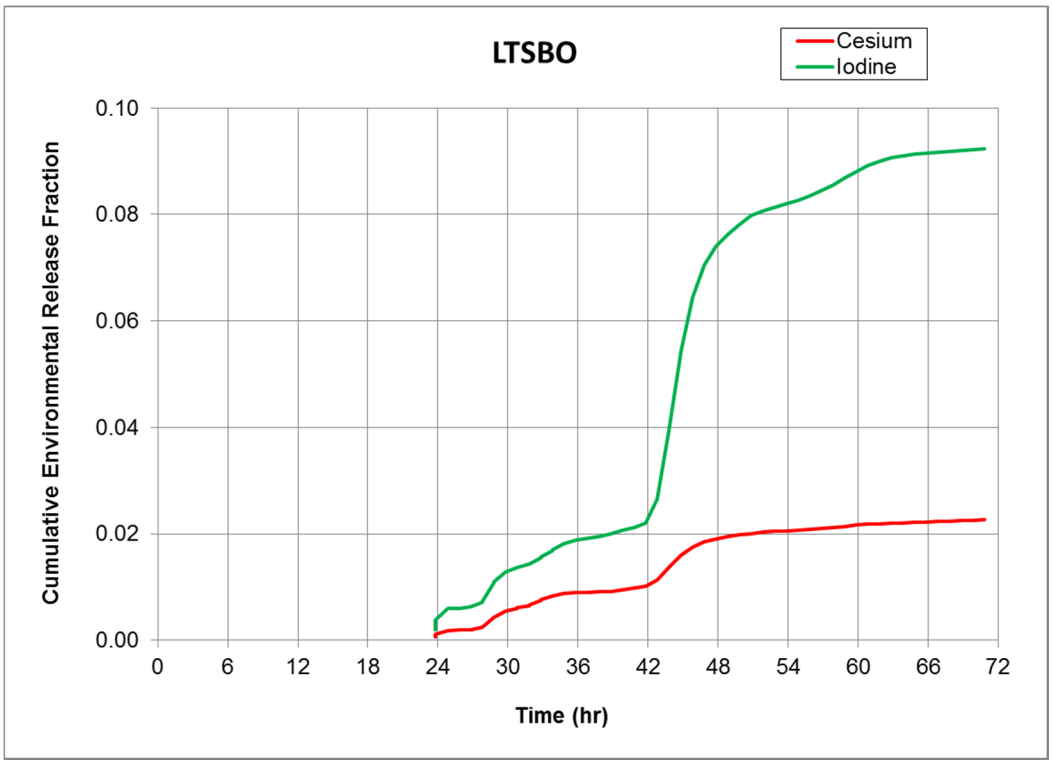

Figure 6-3 Cumulative environmental release fraction of cesium and iodine as a function of time for the LTSBO base case

6.3 Deterministic Analysis of Individual Latent Cancer Fatality Risk

6.3.1 Summary of Deterministic Results

For all deterministic cases analyzed, the individual early fatality risks were zero. The discussion below focuses on the individual latent cancer fatality risk.

Table 6-2 presents the core damage frequencies, and the 0–10 mile radial interval (i.e., a circular area with a 10 mile radius centered on the Sequoyah plant) conditional and scenario frequency-weighted individual LCF risk results for the deterministic base case scenarios. The core damage frequencies are expressed as the probability of an unmitigated accident occurring per reactor year of operation (pry). The core damage frequencies for STSBO and LTSBO are estimated to be 2E-06 and 9E-06 per reactor year, respectively. The conditional individual LCF risks range from 4.8E-04 to 8.5E-04. The scenario frequency-weighted risks are the products of the core damage frequency for the scenario and conditional risk given that scenario has occurred. Taking the STSBO base case conditional LCF risk as an example, the scenario frequency-weighted risk is ~ 1E-9 pry. To simplify the presentation of results, the remainder of this section discusses conditional risk results only. The frequency of the STSBO scenarios (without random ignition and early release) were not quantitatively assessed. These STSBO scenarios are all weighted by the base STSBO core damage frequency. Thus, the reader is cautioned not to sum the unconditional risks for the variations on the STSBO in the table because this would count the risk twice.

Table 6-2 The Sequoyah core damage frequency and conditional scenario-specific individual LCF risks for the 0 – 10 mile radial interval assuming LNT dose response.

Scenario	Core Damage Frequency (pry)	Conditional Risk of LCF for an individual located within 10 miles
STSBO base case without random ignition sources	2E-06*	4.8E-04
STSBO-ER		8.5E-04
LTSBO base case	9E-06	5.7E-04

* The core damage frequency is not equally likely for each scenario variation. This term reflects the overall frequency of an STSBO scenario. As discussed in Chapter 4, early releases were observed in roughly 20 percent of the STSBO w/o random ignition uncertainty analysis realizations.

Table 6-3 and Figure 6-4 present individual LCF risks for exposures occurring during the emergency phase and for exposures occurring during both the intermediate and long-term phases (the latter category is simply termed long-term phase risk in the subsequent discussion). The emergency phase is the first seven days following the beginning of release into the environment. The intermediate phase follows the emergency phase and lasts one year. The long-term phase follows and lasts an additional 50 years. The emergency phase risks are calculated from doses received during the first seven days. The long-term phase risks include dose contributions from the long-term and intermediate phases.

The LCF risks by phase are shown for 0-10 mile, 10-20 mile, and 0-50 mile radial distance intervals around the Sequoyah plant. The distance intervals presented are shown because the 10-mile radius corresponds to the NRC's Quantitative Health Objective (QHO) for latent cancer risk [107] and it also encompasses the Sequoyah plant EPZ. The second interval (10-20 miles) is adjacent to the EPZ and is presented to compare results to the EPZ, wherein nearly all of the population is evacuated, and the next most distant region, wherein a small fraction of the population (the shadow cohort) is assumed to evacuate. The 0-50 mile interval is used to identify regional impacts in regulatory analyses and is compatible with previous SOARCA reports.

Table 6-3 Summary of the mean emergency and long term phase individual LNT, LCF risks for residents within 0 - 10, 10 - 20, and 0 - 50 mile intervals of the plant.

Radius (miles)	Accident Phase	STSBO Base Case	Early Release	LTSBO Base Case
0-10	Emergency	1.0E-07	6.7E-05	2.8E-06
	Long Term	4.8E-04	7.8E-04	5.7E-04
10-20	Emergency	3.5E-05	2.3E-04	3.7E-05
	Long Term	4.0E-04	5.8E-04	4.0E-04
0-50	Emergency	4.8E-05	1.4E-04	1.8E-05
	Long Term	3.4E-04	4.5E-04	2.8E-04

Figure 6-4 shows key features of the data. In general, the emergency phase risks are small relative to the long term phase risks. Over all of the distance intervals, the total conditional LCF risks range between approximately 3E-04 to 9E-04, where the total is the sum of the long term phase and emergency phase risk values. The total risk magnitudes decrease as the distance intervals increase. Conversely, the 0-10 mile emergency phase risks are much lower than the corresponding risks for the 10-20 and 0-50 mile intervals. This is due to the effectiveness of emergency response actions. For the STSBO ER case, there is an increase in the emergency phase LCF risk relative to the STSBO and LTSBO base case emergency phase LCF risks. Each deterministic case is discussed in detail in the following subsections.

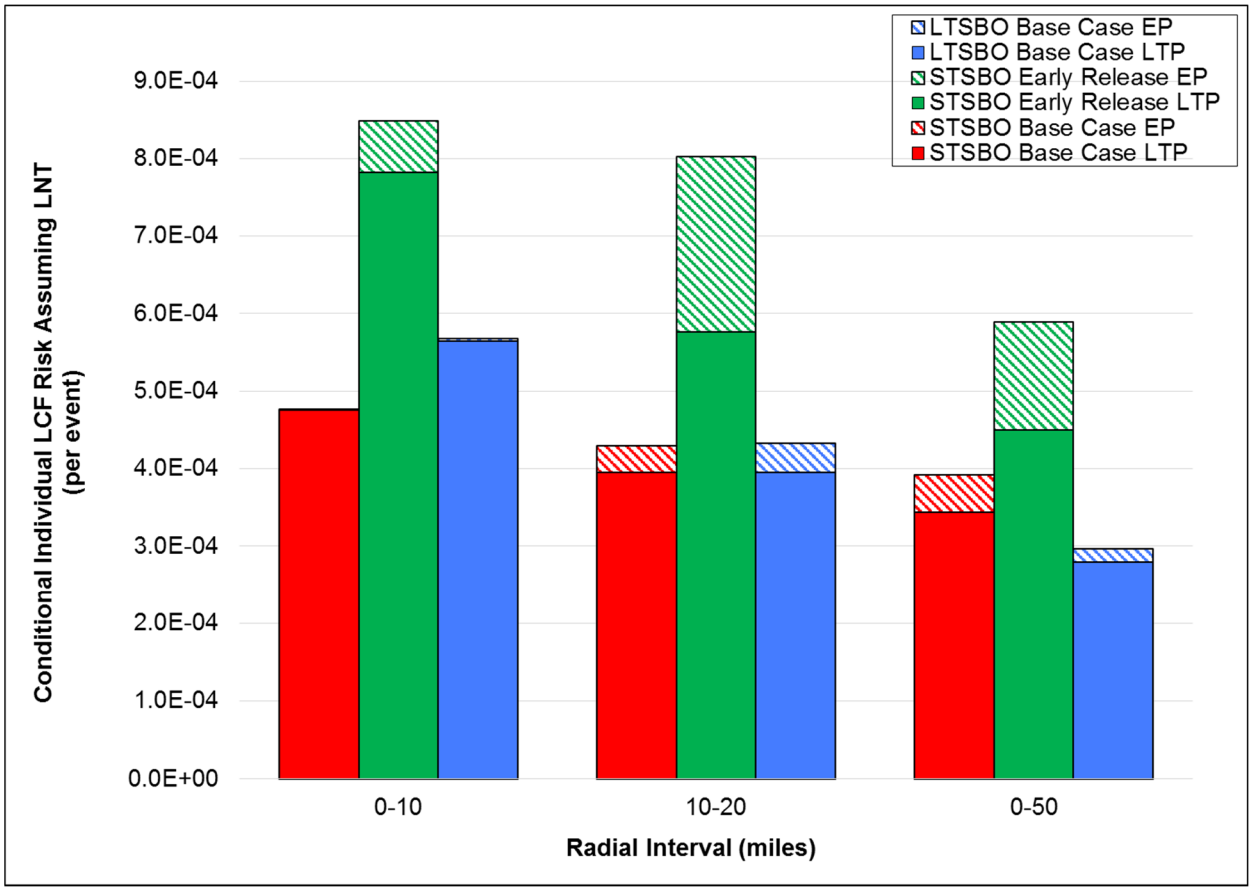

Figure 6-4 Mean long term and emergency phase individual LNT, LCF risks for residents within 0 - 10, 10 - 20, and 0 - 50 mile intervals of the plant

The solid bars in Figure 6-4 indicate risks from both the long term and intermediate phase (LTP in Figure 6-4 legend) exposures and the hatched bars indicate risk from emergency phase (EP) exposures.

6.3.2 STSBO Base Case Scenario

Figure 6-5 presents the mean individual LCF risk from the STSBO w/o random ignition scenario for specified intervals around the plant. In the 0-10 mile region, the emergency phase contribution to total individual LCF risk is 0.021%. For the 10-20 and 0-50 mile regions, the emergency phase contributes 8% and 12% of the total individual LCF risk, respectively. The emergency response is very effective within the EPZ, as demonstrated by the small contribution of the emergency phase to overall risk. Nearly all of the emergency phase risk is attributable to the 0.5 percent of the population that is modeled to not evacuate.

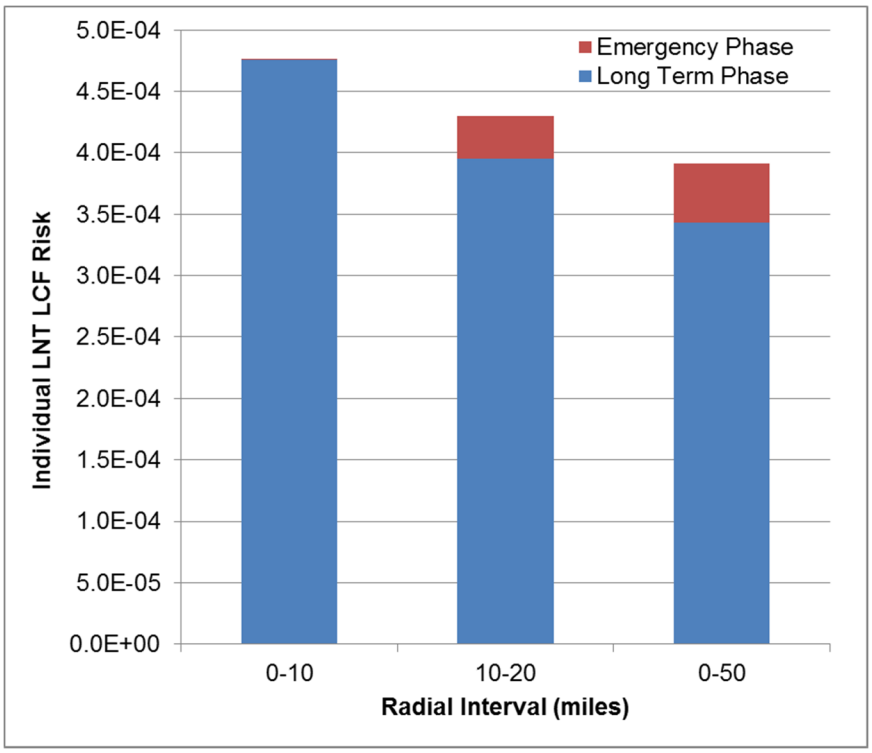

Figure 6-5 Mean individual LCF risk from the Sequoyah STSBO base case for residents within 0 - 10, 10 - 20, and 0 - 50 mile intervals of the plant showing contribution from different accident phases

Table 6-4 and Figure 6-6 show the total LCF risk as a function of alternate approaches to quantifying cancer risk from low doses and dose rates. As discussed in Section 6.1, these include the LNT (linear no threshold), a 310 mrem per year threshold (US natural background dose rate), a 620 mrem per year threshold (US background dose rates for natural and man-made radiation sources), and a threshold based on the HPS position statement. The 310 mrem and 620 mrem are annual thresholds. The HPS recommended approach has both annual (5 rem) and lifetime (10 rem) components.

Table 6-4 Individual LCF risk calculated using alternate low dose risk quantification approaches for the STSBO base case scenario.

Interval (miles)	LNT	310 mrem/yr	620 mrem/yr	HPS
0-10	4.8E-04	7.9E-05	4.0E-05	3.7E-09
10-20	4.3E-04	1.2E-04	9.0E-05	1.2E-06
0-50	3.9E-04	1.5E-04	1.1E-04	6.6E-07

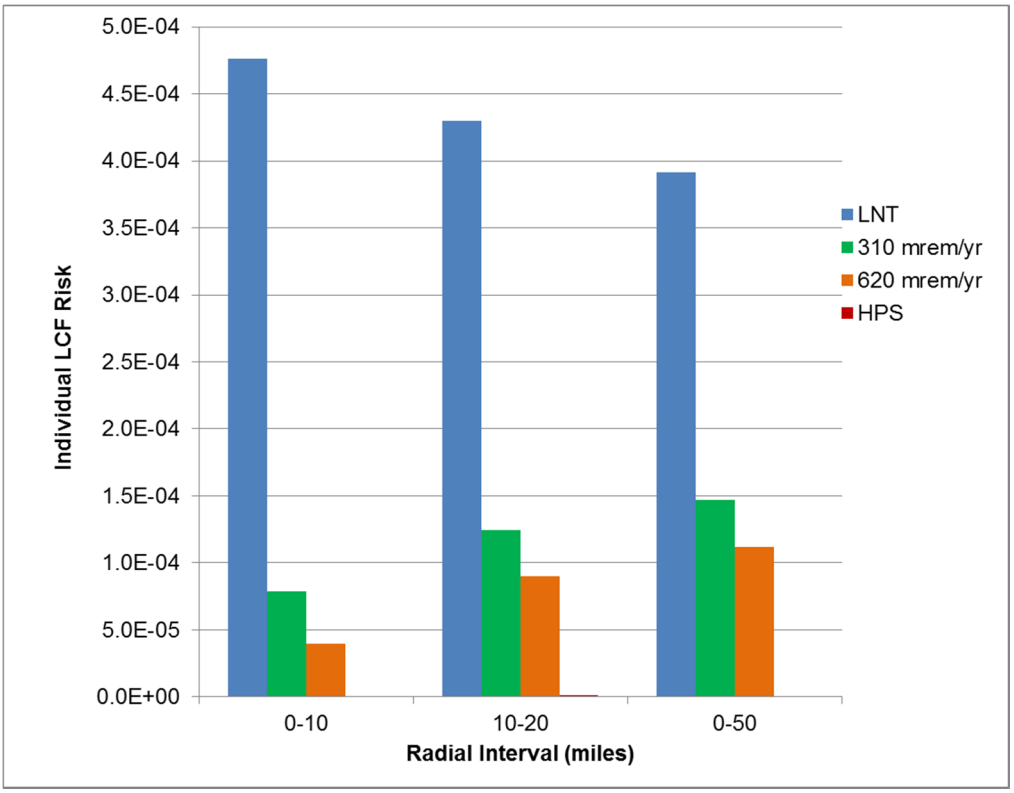

Figure 6-6 Mean individual LCF risk as a function of risk quantification threshold for the STSBO base case scenario

Examining Table 6-4 and Figure 6-5, as the dose threshold increases the corresponding risks decrease. With non-LNT dose response approaches, only annual doses above the thresholds contribute to the LCF risk.

As stated previously, the 0 – 10 mile interval emergency phase risk is a small fraction (0.021%) of the total LCF risk. The STSBO base case (Figure 6.1) produces a tiny release rate beginning at 4 hours that does not increase significantly until 52 hours, therefore the great majority (99.5%) of the EPZ residents evacuate prior to plume arrival. In effect, for this scenario and within the EPZ, virtually all of the LCF risk stems from the intermediate and long term phase risk.

Assuming the LNT dose-response, the LCF risks fall modestly with increasing distance from the plant. For the 310 and 620 mrem per year dose thresholds, the LCF risk results increase with increasing distance from the plant. The habitability criteria are 2 rem committed dose during the intermediate phase (from 7 days to one year after the start of the accident), and 500 mrem for each year thereafter. Considering the habitability criteria and the dose thresholds, most of the dose comes from the first one or two years of exposure (i.e., the intermediate phase and possibly a few years of the long term phase for the 310 mrem/yr threshold). The increasing risk with distance implies that a proportionately larger fraction of the population closer to the plant may be relocated during the intermediate phase, compared with the population farther from the plant, due primarily to groundshine dose rates exceeding the habitability criterion.

Referring to Figure 6-5, the population in the 10-20 and 0-50 mile intervals received larger emergency phase doses (implied by the higher risks) than the population in the 0-10 mile interval. The emergency phase doses also contribute to the total LCF risk. For the HPS dose response approach (the largest dose threshold), the total LCF risks are relatively very small in the 0-10 mile interval, increase in the 10-20 mile interval, and decrease again in the 0-50 mile interval. This implies that the dose thresholds are exceeded to a higher degree beyond the EPZ where most of the population is not evacuated and therefore receives an exposure during the emergency phase.

Within the EPZ, the risks decrease from LNT by a factor of six for 320 mrem, twelve for 630 mrem, and five orders of magnitude for the HPS dose threshold. Similarly, for the farther regions, the LCF risks decrease from by roughly three orders of magnitude with increasing dose threshold.

6.3.3 STSBO Early Release Scenario

The results from the STSBO early release (STSBO-ER) scenario differ from the previous results. Comparing Figure 6-5 with Figure 6-7 shows that the total LCF risks are somewhat higher for the STSBO-ER. Since the total release fractions of iodine and cesium (Figure 6-2) are roughly the same as the previous case and the main differences are the release timing and duration, the radioactivity released is dispersed over a larger area because of wind shifts during the more prolonged release. Thus, the ground surface concentrations are expected to be lower on average. This results in lower doses to more people. These lower doses are less likely to require remediation, and this increases the long term risk of health effects when evaluated with the LNT dose-response model.

Figure 6-7 indicates that, like the other cases, the long term phase dominates the emergency phase contribution to total risks, however emergency phase risks as a fraction of total risks increase are greater than those in the previous scenario. The fractions for this scenario are 8%, 28%, and 24% for the 0-10 mile, 10-20 mile, and 0-50 mile regions, respectively. Although the final magnitudes of the release fractions of cesium and iodine do not differ significantly from the other cases, the timing of release during the STSBO-ER scenario does. The major release begins much earlier, at 3.6 hours; whereas, the significant increases in the release rates for the STSBO and LTSBO base cases releases occur at 52 and 29 hours respectively.

For the 0-10 mile region, the increase in the early contribution to the total LCF risk shows there is an increased risk to the evacuating cohorts in the EPZ corresponding to an increased possibility of part of the population evacuating under the plume.

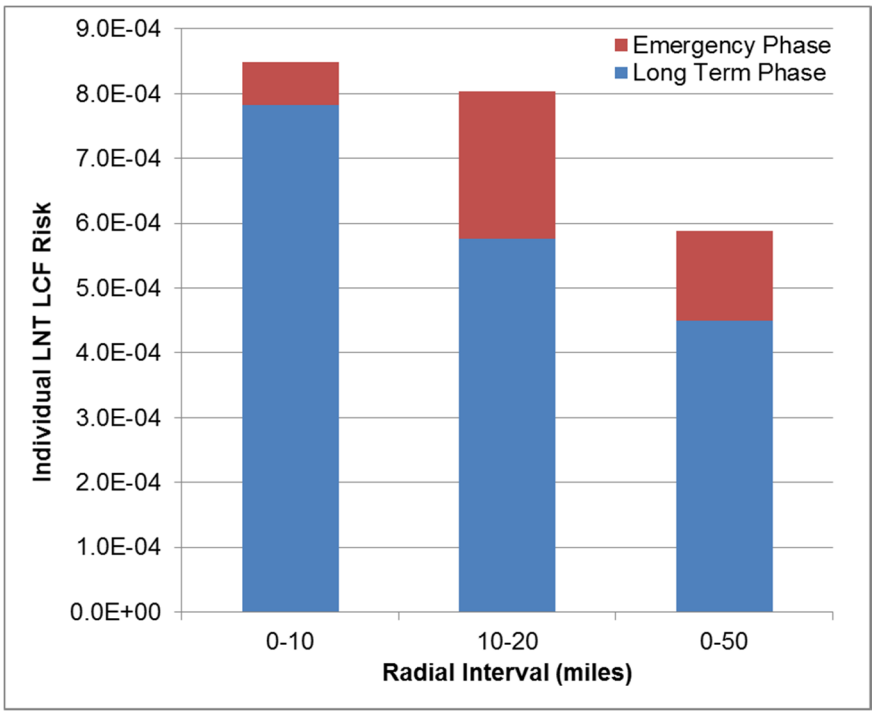

Figure 6-7 Mean individual LCF risk from the Sequoyah STSBO Early Release scenario for residents within 0 - 10, 10 - 20, and 0 - 50 mile intervals of the plant showing contribution from different accident phases

Table 6-5 and Figure 6-8 present the total LCF risk as a function of dose threshold for the STSBO ER scenario. In this case, there are significantly higher results for the 0 – 10 mile interval for the non-LNT approaches than the previous scenario, which reflects a larger contribution from of the emergency phase dose. This is in large part due to the timing and duration of the release. Over all distance intervals, both the emergency and long term phase doses are greater for the STSBO ER than for the STSBO or LTSBO base cases. Unlike the STSBO base case dose threshold results, the non-LNT results have a maximum in the risk values for the 10-20 mile interval. This is consistent with a larger contribution to total dose from the emergency phase for areas beyond the EPZ. All of the dose threshold LCF risks are larger than for the STSBO base case.

Table 6-5 Mean individual LCF risk calculated using low dose risk quantification approaches for the STSBO Early Release scenario.

Interval (miles)	LNT	310 mrem/yr	620 mrem/yr	HPS
0-10	8.5E-04	2.2E-04	1.6E-04	6.1E-05
10-20	8.0E-04	3.8E-04	3.3E-04	7.0E-05
0-50	5.9E-04	2.7E-04	2.3E-04	3.1E-05

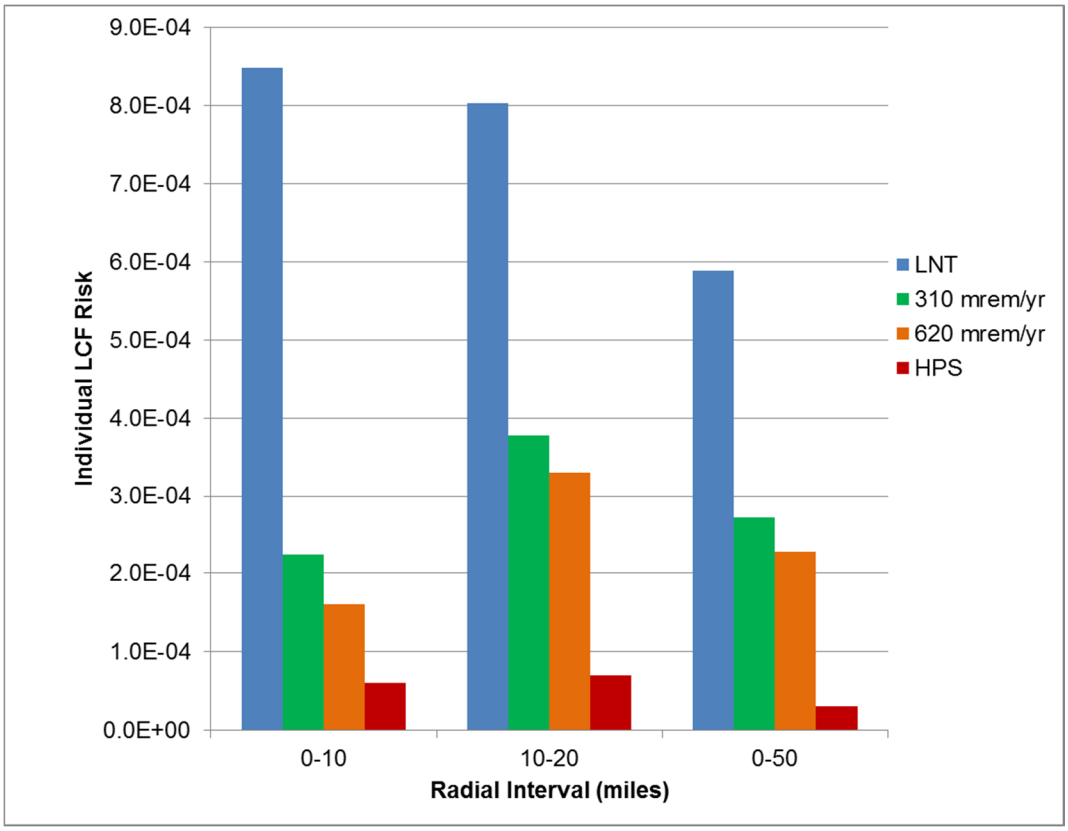

Figure 6-8 Mean individual LCF risk as a function of risk quantification threshold for the STSBO Early Release scenario

6.3.4 LTSBO Scenario

Figure 6-9 shows that for the LTSBO case, the long term phase again dominates the emergency phase contributions to total risks, with emergency phase risks as a fraction of total risks equal to 1%, 27%, and 22% for the 0-10, 10-20, and 0-50 mile intervals, respectively. In this case, the emergency response is effective in part because the release begins at 24 hours.

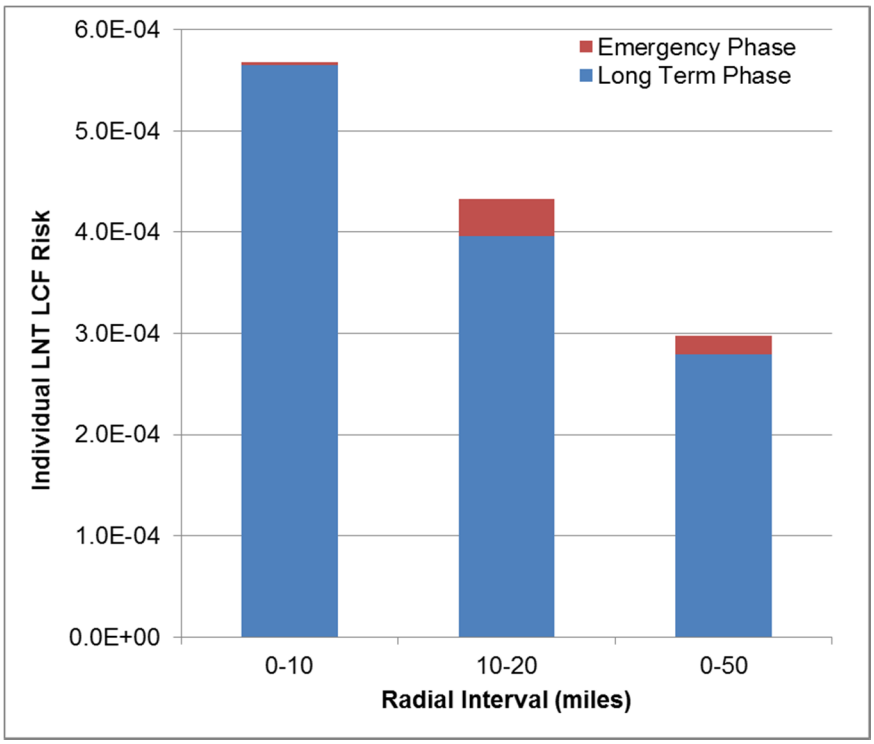

Figure 6-9 Mean individual LCF risk from the Sequoyah LTSBO base case for residents within 0 - 10, 10 - 20, and 0 - 50 mile intervals of the plant showing contribution from different accident phases

Table 6-6 and Figure 6-10 present the Total LCF risk as a function of dose threshold for the LTSBO scenario. The dose threshold comparison for the LTSBO is similar to the other cases. The risks for this scenario are between those for the STSBO-ER and the STSBO base case scenarios.

Table 6-6 Total LCF risk as a function of dose threshold for the LTSBO scenario.

Interval (miles)	LNT	310 mrem/yr	620 mrem/yr	HPS
0-10	5.7E-04	1.4E-04	9.3E-05	6.7E-06
10-20	6.0E-04	3.2E-04	2.9E-04	8.1E-05
0-50	3.8E-04	1.8E-04	1.5E-04	3.0E-05

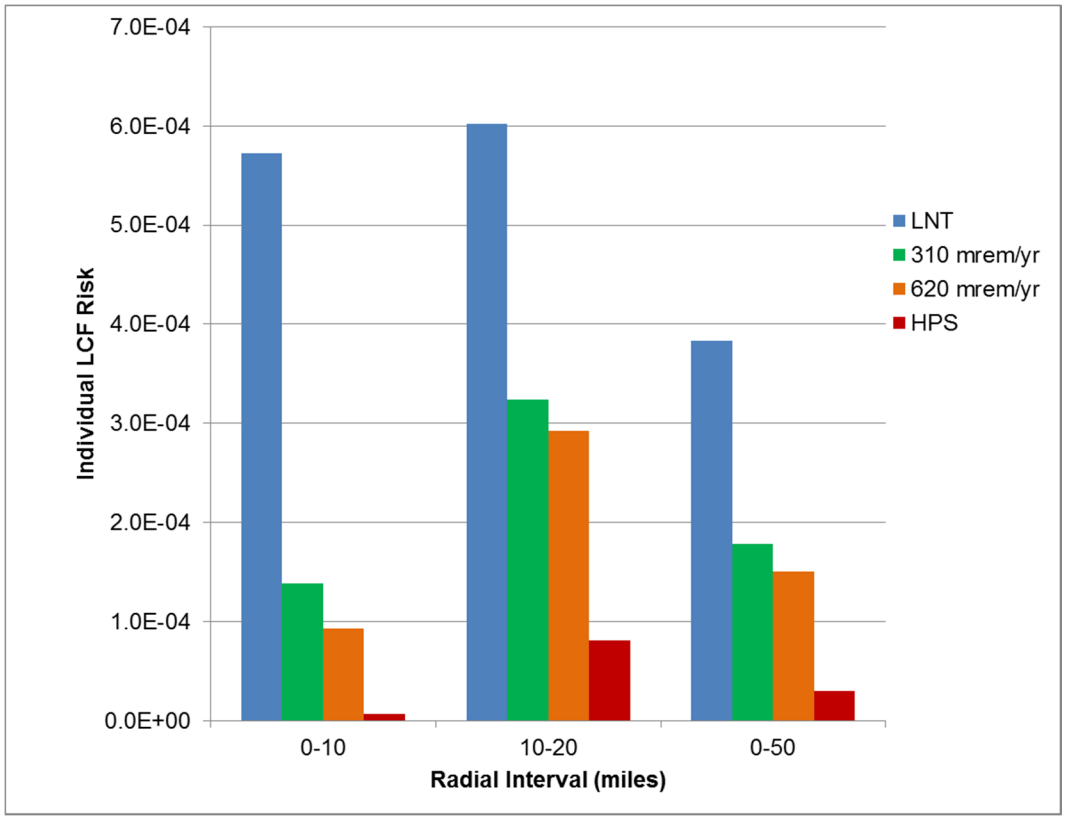

Figure 6-10 Mean individual LCF risk as a function of risk quantification threshold for the LTSBO scenario

6.4 Uncertainty Analysis – STSBO without Random Ignition

This subsection describes the primary results for the uncertainty analysis of LCF and EF risk. The Sequoyah UA focuses on the LNT dose response model. The results in this section were generated from the statistical analysis of a relatively large number of individual results (realizations); therefore, the data include complementary cumulative distribution functions (CCDFs).

6.4.1 LCF Risks for the Unmitigated STSBO Scenario without Random Ignition

Table 6-7 and Table 6-8 show four statistics (mean, median, 5th percentile, and 95th percentile) for the mean individual LCF risk conditional on an accident occurring (per event) from the 467 realizations from the MACCS uncertainty analysis. Results are provided at nine spatial intervals representing concentric circles and annular areas all centered on Sequoyah. The distance intervals are the radii of the corresponding inner and outer circles defining each area. The results in these tables are the mean value averaged over weather variability. Each of the statistics in the table represents the overall epistemic (state of knowledge) uncertainty on the mean for the groups of MELCOR (Level 2) and MACCS (Level 3) inputs that were treated as uncertain. The results show that mean conditional risks are on the order of 10^{-4} and diminish slightly with distance from the plant.

Table 6-7 Mean individual LCF risk conditional on the STSBO w/o random ignition

accident occurring (per event) for five intervals centered on Sequoyah.

	0-10 Miles	0-20 Miles	0-30 Miles	0-40 Miles	0-50 Miles
Mean	3.5E-04	3.9E-04	3.6E-04	3.3E-04	2.9E-04
Median	2.9E-04	2.9E-04	2.8E-04	2.5E-04	2.3E-04
5th Percentile	8.4E-05	7.8E-05	7.6E-05	7.1E-05	6.7E-05
95th Percentile	8.3E-04	9.9E-04	9.0E-04	7.8E-04	7.1E-04

Table 6-8 Mean individual LCF risk conditional on the STSBO w/o random ignition accident occurring (per event) for four intervals centered on Sequoyah.

	10-20 Miles	20-30 Miles	30-40 Miles	40-50 Miles
Mean	4.0E-04	3.1E-04	2.0E-04	1.5E-04
Median	2.9E-04	2.5E-04	1.7E-04	1.2E-04
5th Percentile	7.6E-05	6.8E-05	3.8E-05	2.5E-05
95th Percentile	1.0E-03	7.3E-04	4.7E-04	3.5E-04

For comparison between the deterministic analysis and the probabilistic uncertainty analysis, the mean value from Table 6-7 for the 0-10 mile ring (3.5E-04) is somewhat lower than the corresponding result of 4.8E-04 from the deterministic analysis shown in Table 6-2.

Figure 6-11 and Figure 6-12 show the CCDFs for the same radial intervals summarized in Table 6-7 and Table 6-8. The points on the curves represent the mean LCF risk over variable weather for each of the 467 realizations representing epistemic uncertainty in this UA and are conditional on the accident occurring. The curves show that the conditional risks span the range of about 10^{-6} to more than 10^{-3} per event.

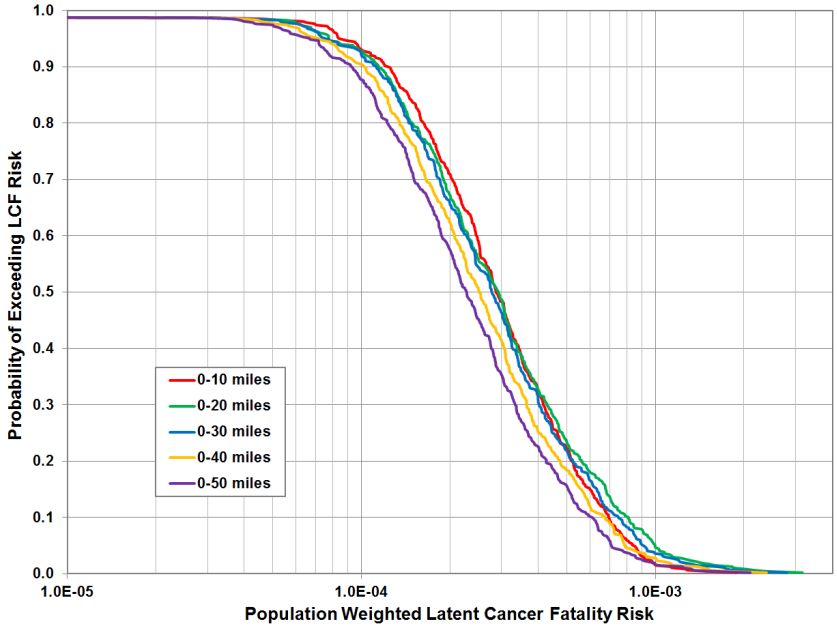

Figure 6-11 Complimentary cumulative distribution function of mean, population-weighted LCF risk (w/o random ignition) within five intervals centered on Sequoyah

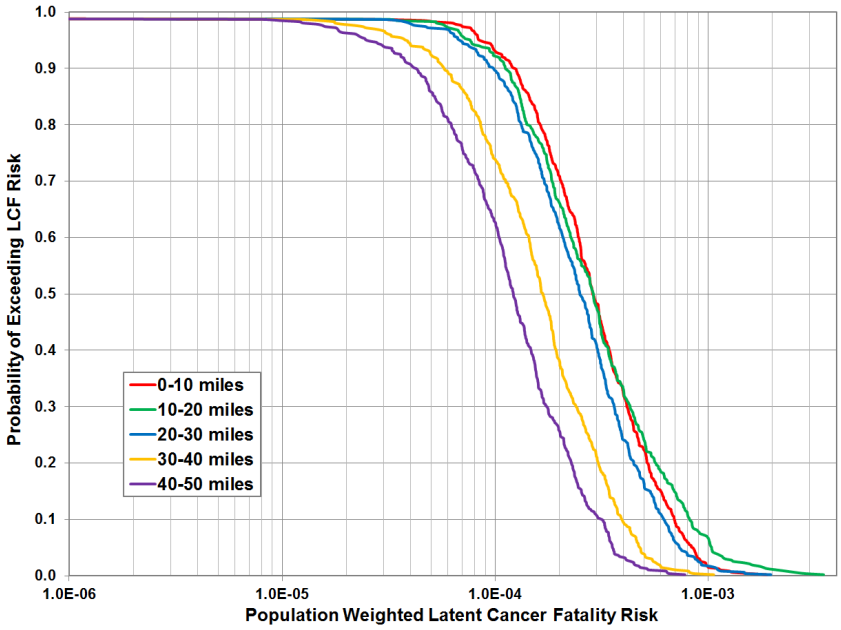

Figure 6-12 Complimentary cumulative distribution function of mean, population-weighted LCF risk (w/o random ignition) within five intervals centered on Sequoyah

Figure 6-13 shows the fraction of the total risk from the emergency phase for the set of LCF risk results shown in Figure 6-12.

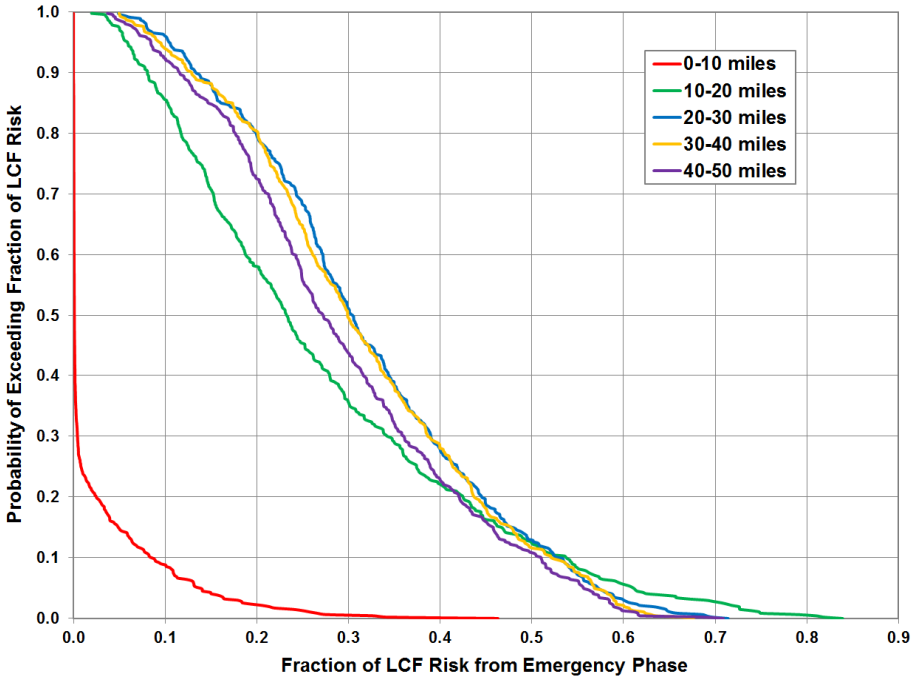

Figure 6-13 Complimentary cumulative distribution function of fraction of mean, population-weighted LCF risk (w/o random ignition) from the emergency phase for residents within five intervals centered on Sequoyah

These results show that the contributions from the emergency phase to the individual latent cancer fatality risk are small in comparison to the contributions from the long term phase to the individual latent cancer fatality risk. This is consistent with the results from the deterministic STSBO w/o random ignition analysis shown in Figure 6-4. Table 6-9 shows the mean contribution of the emergency phase to the overall risk for the STSBO w/o random ignition scenario, and Table 6-10 shows the fractions of STSBO w/o random ignition MACCS realizations in which the emergency phase contributions to dose exceeded those of the long term phase.

Table 6-9 Mean contribution of emergency phase to overall risk.

0-10 miles	10-20 miles	20-30 miles	30-40 miles	40-50 miles
2%	27%	32%	32%	30%

Table 6-10 Fraction of STSBO w/o random ignition MACCS realizations in which the emergency phase contributions to dose exceed those of the long term phase.

10-20 miles	20-30 miles	30-40 miles	40-50 miles
12%	13%	12%	11%

The curve for the distance range from 0 to 10 miles in Figure 6-13 has a different character than those for the other distance ranges because evacuation is very effective in reducing risk during the emergency phase for the population living within the EPZ. Most of the overall risk within 10 miles is to the 0.5 percent of the public that is assumed to not evacuate; however, some of the risk is to the slowly evacuating cohorts for the realizations with relatively early releases.

The core damage frequency for a STSBO at Sequoyah is 2×10^{-6} pry. Thus, the frequency-weighted risk of a STSBO, assuming that there are no random ignition sources within the containment is estimated to be about 6×10^{-10} to the population living within 10 miles of the reactor site.

6.4.2 Regression Analysis of STSBO w/o Random Ignition Latent Cancer Fatality Risk

Each of the four regression techniques was applied to the 467 successful realizations that were evaluated for the scenario where random ignition is assumed not to occur. Regression analyses for nine distance intervals were performed: five intervals with outer radii of 10, 20, 30, 40, and 50 miles; and four intervals from 10 to 20 miles, 20 to 30 miles, 30 to 40 miles, and 40 to 50 miles. However, only the results from 0 to 10, 10 to 20, and 0 to 50 miles are discussed in this report. The trends are similar at the distance intervals that are not discussed.

Table 6-11 through Table 6-13 show the regression results for mean LCF risks from the 467 realizations. The results are based on the LNT dose-response model at three distance intervals from the site: 0 to 10 miles, 10 to 20 miles, and 0 to 50 miles. The word 'mean' is used to indicate a statistical mean over variable weather.

The first four major columns in the tables are labeled with the regression technique used to create the results. The last two columns contain average values of the main contribution of the parameter on the result metric and the conjoint influence of the parameter on the result metric. These are calculated as weighted averages of the overall contributions from the four regression techniques (R^2 from rank regression and S_i from the others) and a weighted average of the values of (Final R^2) * (T_i – S_i) for the three nonlinear regression techniques (i.e., all but rank regression). Appendix A explains the calculation of these metrics.

Values of main contribution greater than 0.02 are considered significant, are highlighted, and are discussed in subsequent paragraphs. Conjoint contributions greater than 0.1 are considered significant and are highlighted. The parameters in the first column of the tables are ordered by the value in the column labeled Main Contribution, so the most important parameters appear in rank order at the top of the table.

The first two parameters in all three regression tables are SV_frac, which indicates the open area of the relief valves on the primary side of the reactor and CFRISK(8), which represents residual cancer risk and accounts for all cancers that are not explicitly modeled. Residual cancers are based on doses to the pancreas, which is a surrogate organ to represent generic soft tissues. Residual cancers are a larger contributor to cancer risk than any of the cancer types that are explicitly modeled. The SV_frac parameter is important to the extent that it influences the depressurization of the reactor primary and subsequent containment failure related to a hydrogen burn.

Table 6-11 Mean, individual, LCF risk regression results within a 0 – 10 mile interval for all realizations based on LNT.

	Rank Regression		Quadratic		Recursive Partitioning		MARS		Main Contribution	Conjoint Contribution
Final R^2	0.67		0.85		0.86		0.73			
Input	R^2 contr.	SRRC	S_i	T_i	S_i	T_i	S_i	T_i		
SV_frac	0.28	0.50	0.28	0.36	0.26	0.55	0.35	0.39	0.247	0.117
CFRISK(8)	0.14	0.32	0.17	0.23	0.18	0.50	0.27	0.31	0.158	0.120
CFRISK(7)	0.06	0.26	0.08	0.11	0.01	0.08	0.10	0.11	0.050	0.033
DDREFA(8)	0.04	-0.21	0.05	0.07	0.03	0.17	0.07	0.09	0.040	0.052
GSHFAC(2)	0.03	0.19	0.03	0.08	0.02	0.11	0.05	0.05	0.029	0.039
rupture	0.04	-0.21	0.02	0.03	0.01	0.12	0.06	0.06	0.028	0.034
CFRISK(4)	0.02	0.15	0.03	0.05	---	---	0.03	0.03	0.018	0.005
CFRISK(6)	0.02	0.15	0.03	0.09	---	---	0.02	0.03	0.015	0.020
VDEPOS(1)	0.01	0.12	0.01	0.02	---	---	---	---	0.006	0.003
EU_melt_T	0.01	0.08	0.01	0.02	---	---	0.01	0.01	0.006	0.004
priSVcycles	---	---	0.00	0.08	0.00	0.07	0.00	0.00	0.002	0.040
GSHFAC_2(2)	0.00	-0.07	---	---	0.01	0.03	---	---	0.002	0.007
DLTEVA(10)	0.00	0.05	0.00	0.02	0.00	0.02	0.00	0.01	0.002	0.012
DLTEVA(7)	---	---	0.00	0.02	0.00	0.02	---	---	0.002	0.008
PROTIN(1)	---	---	---	---	0.00	0.06	0.00	0.01	0.001	0.018
DLTEVA_3(4)	0.00	0.06	---	---	0.00	0.03	---	---	0.001	0.008
DLTEVA_2(6)	---	---	---	---	0.00	0.03	---	---	0.001	0.006
RB-86_ICH(9)	0.00	-0.05	0.00	0.03	---	---	---	---	0.001	0.007
CO-58_ICH(9)	0.00	-0.05	---	---	---	---	0.00	0.01	0.001	0.001
DDREFA(5)	---	---	0.00	0.02	---	---	---	---	0.000	0.005
DLTEVA(9)	---	---	---	---	0.00	0.03	---	---	0.000	0.010
GSHFAC_8(2)	---	---	---	---	0.00	0.02	---	---	0.000	0.005

** highlighted if main contribution larger than 0.02 or conjoint contribution larger than 0.1*

Table 6-12 Mean, individual, LCF risk regression results within a 10 - 20 mile interval for all realizations based on LNT.

	Rank Regression		Quadratic		Recursive Partitioning		MARS		Main Contribution	Conjoint Contribution
Final R^2	0.64		0.74		0.73		0.56			
Input	R^2 contr.	SRRC	S_i	T_i	S_i	T_i	S_i	T_i		
SV_frac	0.33	0.55	0.26	0.33	0.29	0.60	0.41	0.51	0.239	0.116
CFRISK(8)	0.08	0.25	0.09	0.15	0.08	0.20	0.13	0.24	0.069	0.065
CFRISK(7)	0.04	0.21	0.06	0.11	0.03	0.10	0.06	0.08	0.036	0.034
rupture	0.05	-0.21	0.04	0.07	0.03	0.27	0.07	0.12	0.034	0.076
DDREFA(8)	0.03	-0.16	0.06	0.11	0.00	0.01	0.07	0.10	0.027	0.021
CFRISK(4)	0.03	0.15	0.03	0.06	0.05	0.21	0.04	0.04	0.027	0.048
GSHFAC(2)	0.02	0.16	0.02	0.06	0.00	0.03	0.02	0.05	0.012	0.021
VDEPOS(1)	0.02	0.12	0.01	0.04	0.02	0.11	---	---	0.008	0.032
EU_melt_T	0.01	0.10	---	---	0.02	0.10	0.01	0.01	0.008	0.019
CFRISK(5)	0.00	0.05	0.01	0.05	---	---	0.02	0.02	0.006	0.010
CFRISK(6)	0.02	0.12	0.00	0.05	0.00	0.02	---	---	0.005	0.017
priSVcycles	---	---	0.01	0.07	0.00	0.05	---	---	0.003	0.025
GSHFAC_5(1)	---	---	0.01	0.03	---	---	---	---	0.003	0.005
PROTIN_4(2)	0.01	-0.09	---	---	---	---	0.00	0.01	0.002	0.001
DLTEVA(10)	0.01	0.08	---	---	---	---	---	---	0.002	0.000
PROTIN_3(1)	---	---	0.01	0.03	---	---	---	---	0.001	0.007
RB-86_ICH(9)	0.00	-0.05	0.00	0.06	---	---	---	---	0.001	0.014
DLTEVA_3(4)	0.00	0.06	---	---	---	---	---	---	0.001	0.000
GSHFAC_2(2)	---	---	---	---	0.00	0.02	---	---	0.001	0.003
DLTEVA_3(11)	---	---	---	---	0.00	0.06	---	---	0.000	0.015
DLTEVA(9)	---	---	---	---	---	---	0.00	0.01	0.000	0.001
DLTEVA_2(6)	---	---	0.00	0.04	0.00	0.02	---	---	0.000	0.013

** highlighted if main contribution larger than 0.02 or conjoint contribution larger than 0.1*

Table 6-13 Mean, individual, LCF risk regression results within a 0 – 50 mile interval for all realizations based on LNT.

	Rank Regression		Quadratic		Recursive Partitioning		MARS		Main Contribution	Conjoint Contribution
Final R^2	0.64		0.80		0.80		0.72			
Input	R^2 contr.	SRRC	S_i	T_i	S_i	T_i	S_i	T_i		
SV_frac	0.29	0.51	0.26	0.37	0.29	0.62	0.36	0.41	0.245	0.129
CFRISK(8)	0.09	0.25	0.12	0.19	0.06	0.15	0.10	0.16	0.076	0.055
CFRISK(7)	0.05	0.23	0.07	0.13	0.02	0.07	0.09	0.12	0.045	0.035
DDREFA(8)	0.03	-0.18	0.03	0.05	0.04	0.26	0.06	0.11	0.032	0.075
CFRISK(4)	0.04	0.17	0.04	0.06	0.01	0.07	0.05	0.05	0.028	0.021
rupture	0.04	-0.20	0.04	0.06	0.00	0.06	0.05	0.12	0.027	0.038
shape_fact	0.00	0.06	0.02	0.04	0.07	0.15	0.01	0.09	0.021	0.044
GSHFAC(2)	0.03	0.18	0.03	0.08	0.00	0.03	0.03	0.05	0.019	0.025
EU_melt_T	0.01	0.10	0.02	0.03	0.00	0.03	0.03	0.04	0.012	0.014
CFRISK(6)	0.02	0.13	0.01	0.03	---	---	0.01	0.03	0.008	0.011
VDEPOS(1)	0.02	0.12	---	---	0.00	0.03	0.02	0.02	0.008	0.008
CFRISK(5)	0.00	0.06	0.01	0.03	0.00	0.08	0.02	0.02	0.006	0.026
priSVcycles	---	---	0.02	0.09	---	---	0.00	0.00	0.004	0.021
GSHFAC_8(2)	0.01	0.10	---	---	---	---	---	---	0.003	0.000
DLTEVA(10)	0.00	0.07	0.01	0.03	---	---	---	---	0.002	0.006
RU-105_ICH(9)	---	---	---	---	0.01	0.09	---	---	0.002	0.021
DLTEVA_2(9)	0.00	-0.07	0.01	0.04	---	---	---	---	0.002	0.010
GSHFAC_5(1)	---	---	---	---	0.00	0.02	---	---	0.001	0.005
I-132_ICH(9)	---	---	---	---	0.00	0.02	---	---	0.001	0.005
ESPEED(2)	---	---	0.00	0.02	---	---	---	---	0.000	0.006
DLTEVA_7(13)	---	---	---	---	0.00	0.02	---	---	0.000	0.006
DDREFA(5)	---	---	---	---	---	---	0.00	0.01	0.000	0.003

** highlighted if main contribution larger than 0.02 or conjoint contribution larger than 0.1*

The third parameter in the above tables is CFRISK(7), which is the cancer fatality risk factor for colon cancer. At least for this scenario, colon cancer turns out to be the most important single cancer type.

The fourth parameter in Table 6-11 and Table 6-13 and the fifth parameter in Table 6-12 is DDREFA(8). It is the dose and dose rate effectiveness factor corresponding to residual cancers. This parameter has a minor conjoint influence with CFRISK(8) because the two parameters appear together in the relationship between organ dose and cancer risk for that organ. DDREFA appears in the denominator of the equation, so the risk diminishes as the parameter increases, which explains the negative value of the correlation coefficient (SRRC) in the tables for this parameter.

The fifth parameter in Table 6-11 and seventh parameter in Table 6-12 is GSHFAC(2), which is the groundshine shielding factor for normal activity during the emergency phase and is perfectly correlated with the groundshine shielding factor during the long term phase. Normal activity is an average for the population over a normal week of activity, including time spent indoors at home and at work, outdoors, and commuting. Groundshine is not a particularly important dose pathway during the emergency phase, but it is generally the dominant dose pathway during the long term phase. Since the groundshine dose received by any individual during the long term phase is directly proportional to the long term groundshine shielding factor, it is important for latent cancer risk. This is especially so when the long term-phase dominates the emergency-phase contribution to risk, which is demonstrated to be true in Figure 6-13.

The MELCOR rupture parameter is the sixth parameter in Table 6-11 and Table 6-13 and the fourth parameter in Table 6-12. This parameter controls the pressure at which the containment is modeled to rupture. Thus, it influences whether and when the containment fails.

One other important parameter in Table 6-12 and Table 6-13 is CFRISK(4), which is the cancer risk factor for lung cancer. Lung cancer risk is primarily driven by inhalation of alpha-emitting radionuclides, and this occurs predominately during the emergency phase.

The scatter plots provided in Figure 6-14 through Figure 6-17 show the trends between the five most important inputs for LCF risk within a 50-mile circular area, as discussed in the preceding paragraphs. The trends in these figures are very similar for the other circular and annular areas that were evaluated in this study. The plots qualitatively show the sign and strength of the correlation between the parameters and LCF risk, although the trend is sometimes hard to distinguish by eye because of the density of the dots.

Figure 6-14 shows a significant correlation between the area fraction of one or more stuck-open valves with LCF risk. Values greater than one indicate multiple stuck-open valves. Though none of the individual valves necessarily have an open area fraction of 1, the sum of the open area fractions of the individual valves (SV_frac) can be greater than 1 because multiple values can stick open. The regression coefficient on SV_frac is positive in the rank regression results in Figure 6-15. This is supported by the slight positive trend in Figure 6-16, indicating a tendency for cancer risk to increase with the combined open area fraction. The open area fraction directly influences the magnitude of the source term, and thus the consequences, because it allows for early release of hydrogen that provides an efficient burn source that can contribute to containment failure simultaneous with RCS failure.

Figure 6-15 shows a clear trend between CFRISK(8) and cancer fatality risk with a positive correlation coefficient, indicating that cancer fatality risk increases with CFRISK(8). This is the expected trend since cancer fatality risk is the sum of the product of the organ doses and risk coefficients. The number eight represents the risk coefficient for residual cancers, which represents all cancers not specifically treated, which turns out to be a larger contributor than any of the individual cancer risks.

Figure 6-16 shows a similar trend as Figure 6-15, but for CFRISK(7), which is the cancer fatality risk coefficient for colon cancer, the most important single cancer type for the Sequoyah STSBO accident scenario. Risk increases with the value of CFRISK(7), as expected, for the reason given in the previous paragraph.

Figure 6-17 shows a somewhat difficult-to-perceive negative trend between DDREFA(8), the dose and dose-rate effectiveness factor for residual cancers, with cancer fatality risk. The negative correlation indicates that cancer risk decreases with the value of DDREFA(8), which is expected since cancer risk has an inverse dependence on this parameter.

Figure 6-18 shows a clear but modest, positive correlation between GSHFAC(2), representing the value of the groundshine shielding factor for normal activity during the emergency phase and the value of the long term groundshine shielding factor. This indicates that risk increases with the value of the groundshine shielding factor. This is an expected trend since groundshine is the dominant pathway during the long term phase and the long term phase contribution to risk usually exceeds the emergency-phase contribution to risk, as shown in Figure 6-13. Groundshine dose is proportional to this parameter.

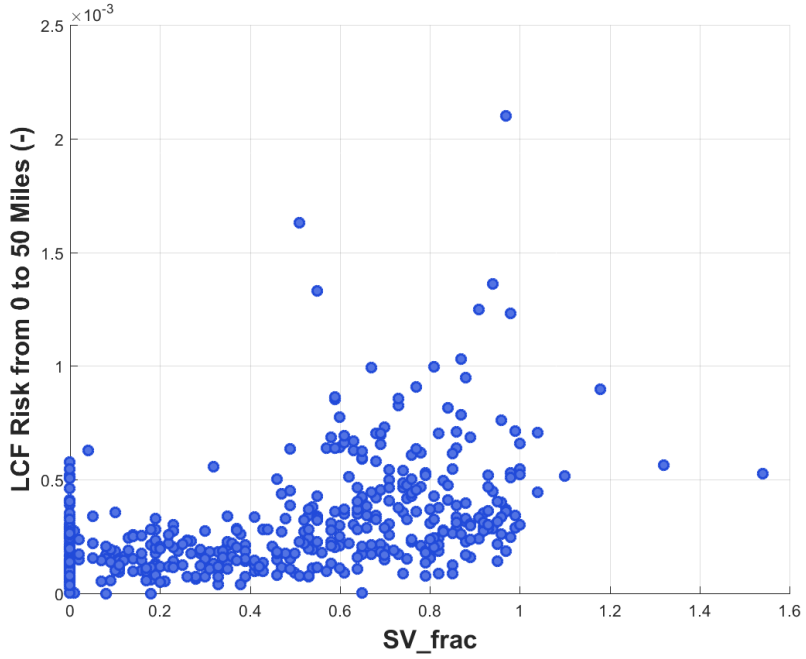

Figure 6-14 Scatter plot of mean, individual, LCF risk within a 0 - 50 mile interval for all realizations versus safety valve open area fraction, SV_frac, conditional on an STSBO accident occurring

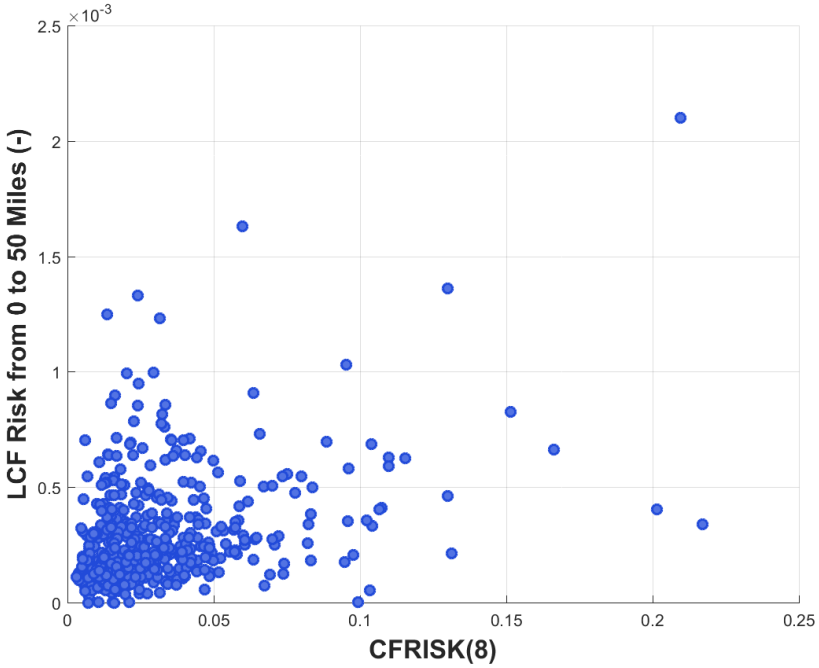

Figure 6-15 Scatter plot of mean, individual, LCF risk within a 0 – 50 mile interval for all realizations versus CFRISK(8), conditional on an STSBO accident occurring

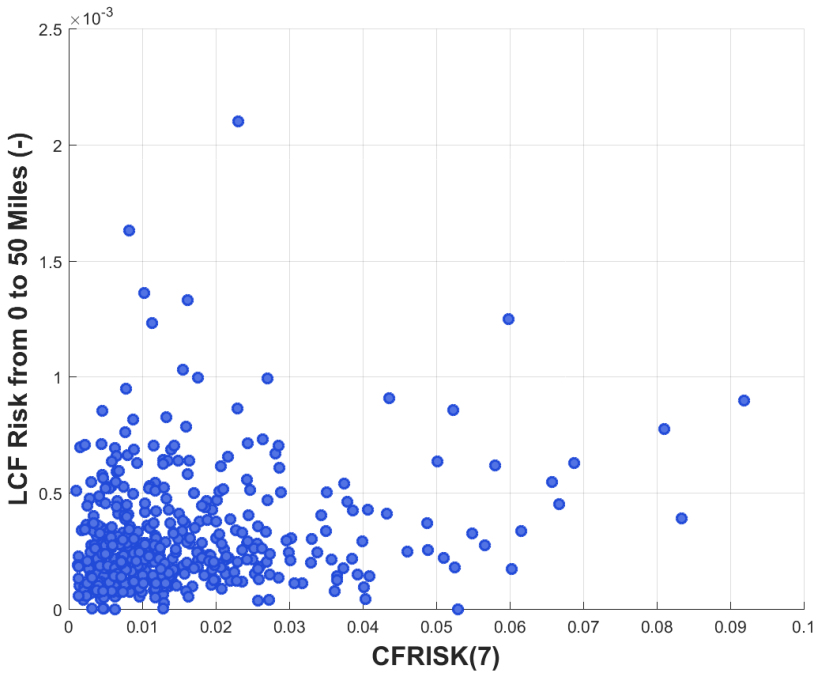

Figure 6-16 Scatter plot of mean, individual, LCF risk within a 0 – 50 mile interval for all realizations versus CFRISK(7), conditional on an STSBO accident occurring

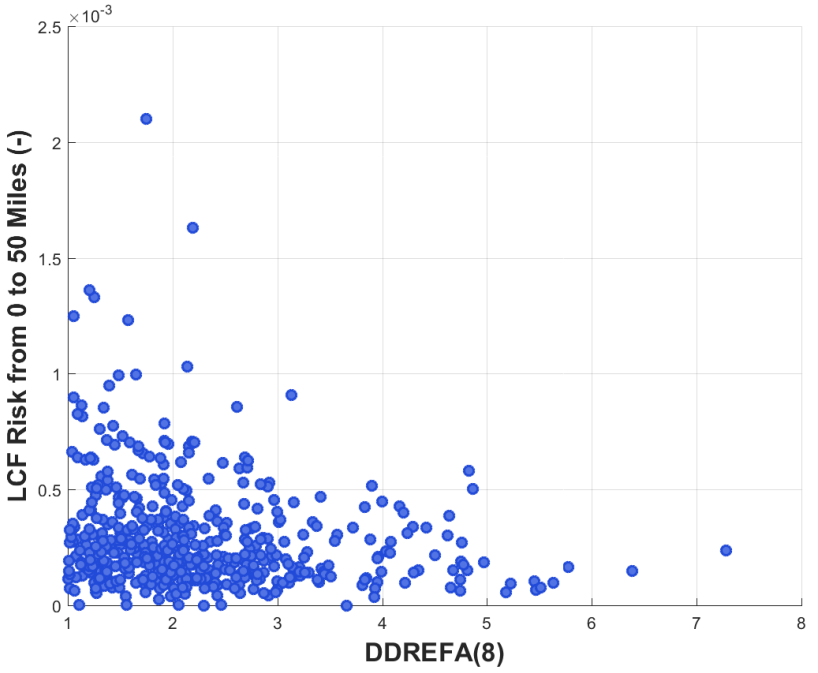

Figure 6-17 Scatter plot of mean, individual, LCF risk within a 0 – 50 mile interval for all realizations versus DDREFA(8), conditional on an STSBO accident occurring

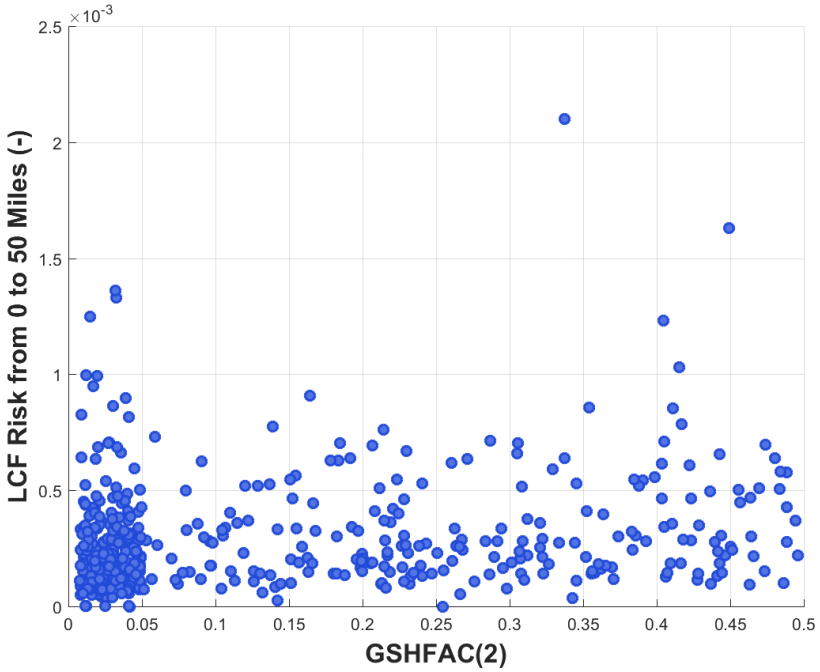

Figure 6-18 Scatter plot of mean, individual, LCF risk within a 0 – 50 mile interval for all realizations versus groundshine shielding factor, GSHFAC(2), conditional on an STSBO accident occurring

6.4.3 Results for Early Fatality Risks

Table 6-14 show four statistics (mean, median, 5th percentile, and 95th percentile) for mean (over weather variability) individual early fatality risk conditional on an accident occurring (per event) from the MACCS uncertainty analysis. Results are provided for seven spatial intervals centered on Sequoyah. The results in this table are the mean value averaged over weather variability. The statistics in the table represent the overall epistemic (state of knowledge) uncertainty for the groups of MELCOR and MACCS inputs that were treated as uncertain. The results show that mean conditional risks are approximately 10^{-6} within 1 mile and diminish rapidly with distance from the plant. There is no early fatality risk beyond 5 miles for any of the realizations.

Table 6-14 Mean individual early fatality risk without random ignition, conditional on accident (per event) for the MACCS uncertainty analysis for seven distance intervals centered on Sequoyah.

Figure 6-19 shows the complimentary cumulative distribution functions for the same circular areas summarized in Table 6-14. The points on the curves represent the mean early fatality risk over variable weather for each of the 467 realizations representing epistemic uncertainty in this

UA and are conditional on the accident occurring. The curves show that the conditional risks span the range from 0 to 10^{-4} per event. Realizations with zero risk are not shown on the plot because of the logarithmic scale.

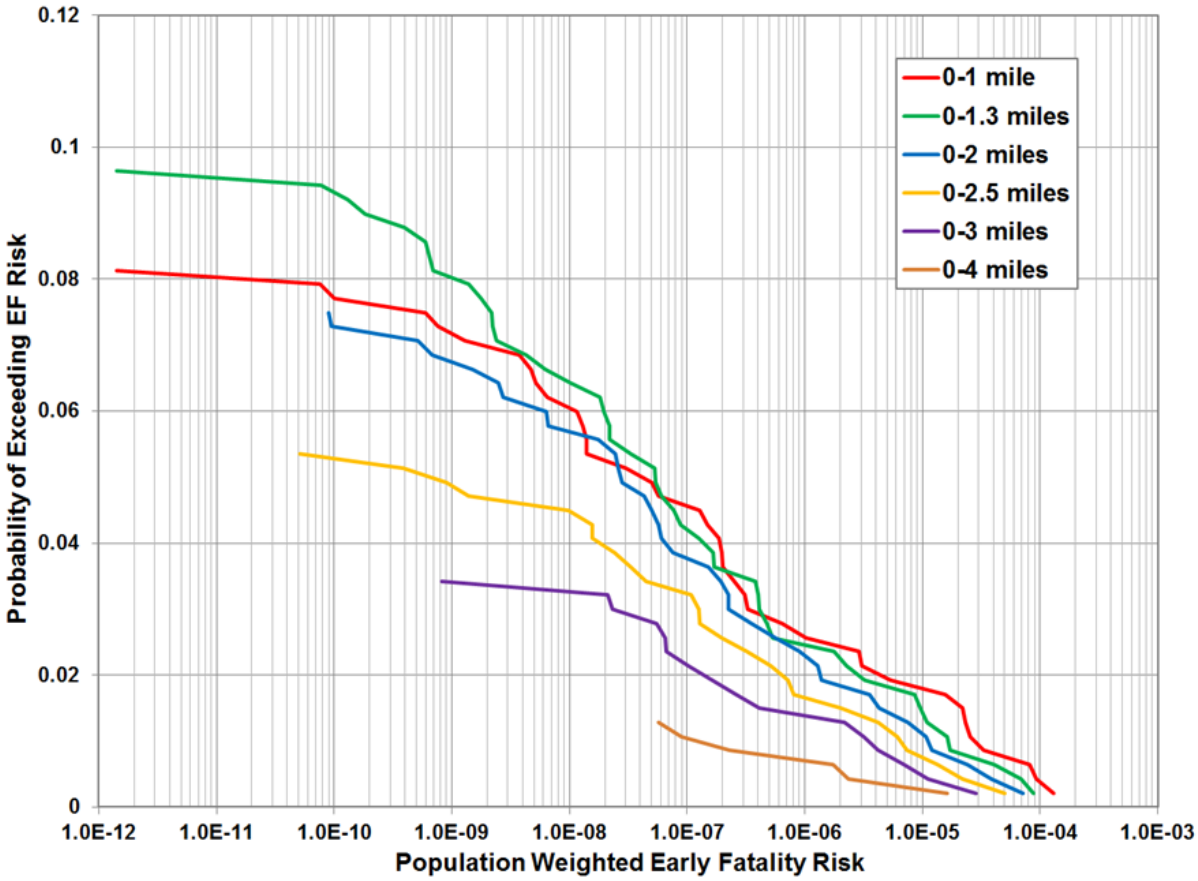

Figure 6-19 Complimentary cumulative distribution function of mean, population-weighted early fatality risk (STSBO w/o random ignition) within six distance intervals centered on Sequoyah

Of the 467 successful MACCS realizations that were evaluated, only 47 realizations (about 10%) had doses high enough to create an early fatality risk to the population within 5 miles. Thus, the small number of nonzero results, a regression analysis to determine which parameters are most important is not included in this report.

6.5 Uncertainty Analysis - STSBO with Random Ignition

6.5.1 Results for LCF Risks

Table 6-15 and Table 6-16 show four statistics (mean, median, 5th percentile, and 95th percentile) for the individual LCF risk conditional on an accident occurring (per event) from the 432 realizations from the MACCS uncertainty analysis. Results are provided at nine spatial intervals centered on Sequoyah. The distances in the table are the inner and outer radii of the areas for the reported LCF risks. The risks are averaged over weather variability. Each of the

statistics in the table represents the overall epistemic (state of knowledge) uncertainty for the groups of MELCOR and MACCS inputs that were treated as uncertain. The results show that mean conditional risks are on the order of 10^{-4} and diminish slightly with distance from the plant.

Table 6-15 Mean, individual STSBO with random ignition LCF risk, conditional on accident (per event) for the MACCS uncertainty analysis for five intervals centered on Sequoyah.

	0-10 Miles	0-20 Miles	0-30 Miles	0-40 Miles	0-50 Miles
Mean	3.1E-04	3.1E-04	3.0E-04	2.7E-04	2.5E-04
Median	2.6E-04	2.5E-04	2.5E-04	2.3E-04	2.1E-04
5th Percentile	7.4E-05	7.7E-05	8.0E-05	7.5E-05	6.9E-05
95th Percentile	6.5E-04	7.2E-04	6.8E-04	6.1E-04	5.5E-04

Table 6-16 Mean, individual STSBO with random ignition LCF risk, conditional on accident (per event) for the MACCS uncertainty analysis for four intervals centered on Sequoyah.

	10-20 Miles	20-30 Miles	30-40 Miles	40-50 Miles
Mean	3.1E-04	2.7E-04	1.8E-04	1.3E-04
Median	2.5E-04	2.3E-04	1.5E-04	1.1E-04
5th Percentile	7.8E-05	7.2E-05	3.8E-05	3.0E-05
95th Percentile	7.5E-04	6.2E-04	4.0E-04	3.2E-04

Figure 6-20 and Figure 6-21 show the complimentary cumulative distribution functions for the same intervals summarized in Table 6-15 and Table 6-16. The points on the curves represent the mean LCF risk over variable weather for each of the 432 realizations representing epistemic uncertainty in this UA and are conditional on the accident occurring. The curves show that the conditional risks span the range of less than 10^{-6} to more than 10^{-3} per event.

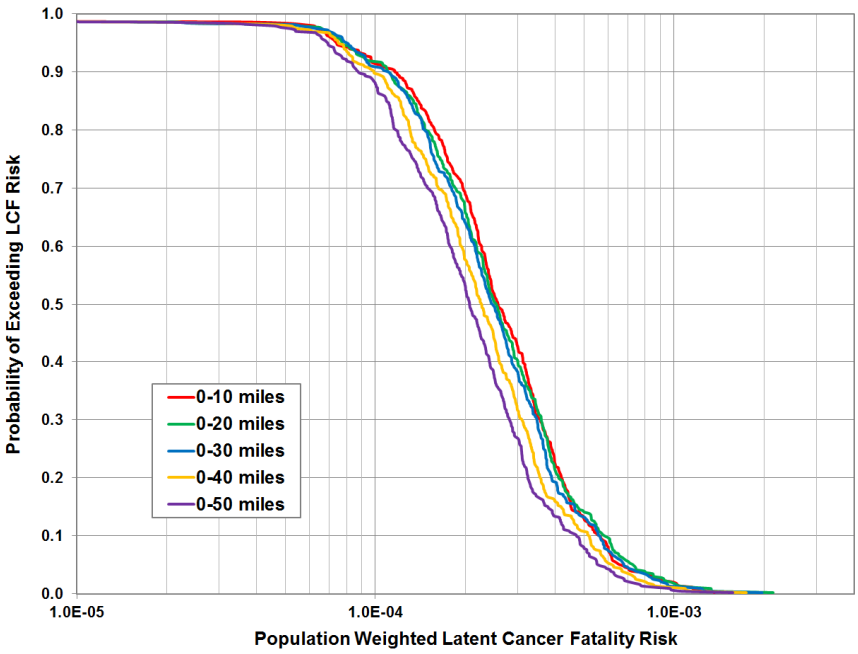

Figure 6-20 Complimentary cumulative distribution function of mean, population-weighted LCF risk (assuming a random ignition source) within five intervals centered on Sequoyah

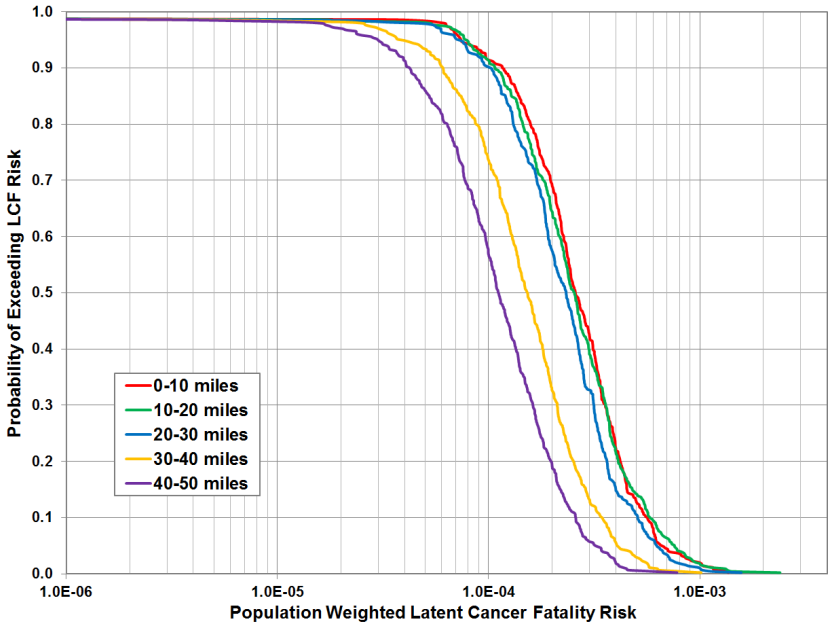

Figure 6-21 Complimentary cumulative distribution function of mean, population-weighted LCF risk (assuming a random ignition source) within five intervals centered on Sequoyah

Figure 6-22 shows the fraction of the total risk from the emergency phase for the set of LCF risk results shown in Figure 6-21.

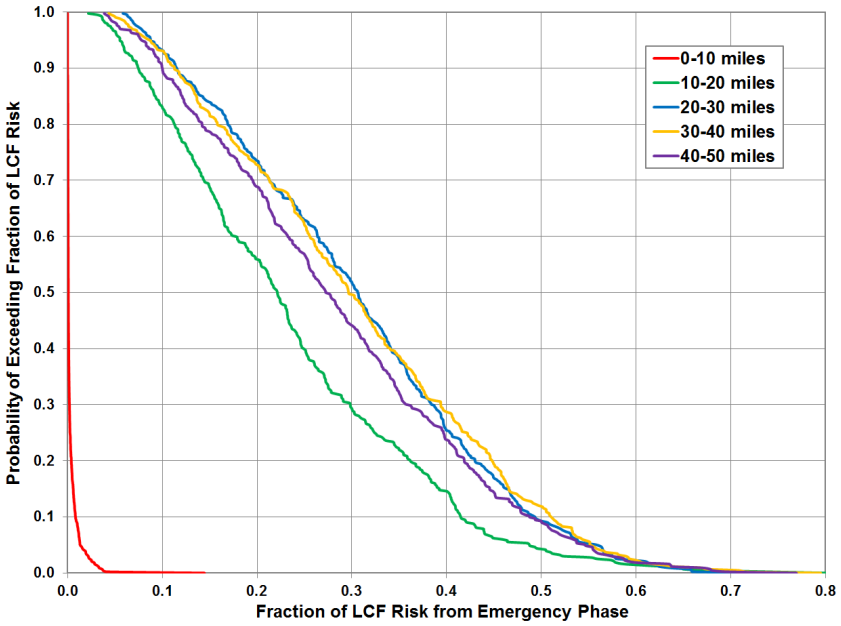

Figure 6-22 Complimentary cumulative distribution function of fraction of mean, population-weighted LCF risk (assuming a random ignition source) from the emergency phase for residents within five intervals centered on Sequoyah

Similar to the results from the STSBO without random ignition, these results show that the contributions from the emergency phase to the individual latent cancer fatality risk are small in comparison to the contributions from the long term phase to the individual latent cancer fatality risk. This is consistent with the results from the deterministic STSBO with random ignition analysis shown in Figure 6-5. Table 6-17 shows the mean contribution of the emergency phase to the overall risk for the STSBO with random ignition scenario, and Table 6-18 shows the fractions of STSBO with random ignition MACCS realizations in which the emergency phase contributions to dose exceeded those of the long term phase.

Table 6-17 Mean contribution of emergency phase to overall risk, STSBO with random ignition.

0-10 miles	10-20 miles	20-30 miles	30-40 miles	40-50 miles
0.3%	24%	31%	31%	29%

Table 6-18 Fraction of STSBO with random ignition MACCS realizations in which the emergency phase contributions to dose exceed those of long term phase.

10-20 miles	20-30 miles	30-40 miles	40-50 miles
4%	10%	12%	9%

As with the results from the STSBO w/o random ignition, the curve for the 0 to 10 mile interval has a very different character than those for the other distance ranges because evacuation is very effective in reducing risk during the emergency phase for the population living within the EPZ. Most of the overall risk within 10 miles is to the 0.5 percent of the public that is assumed to not evacuate; however, some of the risk is to the slowly evacuating cohorts for the realizations with relatively early releases.

6.5.2 Regression Analysis of STSBO with Random Ignition Latent Cancer Fatality Risk

Each of the four regression techniques was applied to the 432 successful realizations that were evaluated for the scenario where random ignition is assumed not to occur. Regression analyses for nine distance intervals were performed: five circular areas with outer radii of 10, 20, 30, 40, and 50 miles and four annuli (rings) from 10 to 20 miles, 20 to 30 miles, 30 to 40 miles, and 40 to 50 miles. However, only the results from 0 to 10, 10 to 20, and 0 to 50 miles are discussed in this report. The trends are similar at the distance intervals that are not discussed.
Table 6-19 through Table 6-21 show the regression results for mean LCF risks from the 432 realizations. The results are based on the LNT dose-response model at three distance intervals from the site: 0 to 10 miles, 10 to 20 miles, and 0 to 50 miles. The word ”mean” is used to indicate a statistical mean over variable weather.

The first two parameters in all three regression tables are CFRISK(8) and SV_frac, although their order is reversed in Table 6-20. Both parameters have large values in the Main Contribution column and also have a significant conjoint contribution. These are the same two parameters that were shown to be most significant in Subsection 6.4.2 and the reasons are the same.

The other important input parameters are mostly the same ones identified in Subsection 6.4.2, namely DDREFA(8), CFRISK(7), and GSHFAC(2), although these appear in a slightly different order than in the previous subsection. Subsets of these parameters are shown to be important for the 10 to 20 and 0 to 50-mile intervals in Table 6-20 and Table 6-21, respectively. The reasons these parameters are important and the general discussion of their role in the consequence analysis is the same as that provided in Subsection 6.4.2.

One new parameter is shown to be significant in Table 6-19 that did not appear in the previous tables, CFRISK(3), which represents the cancer fatality risk factor for breast cancer.

Figure 6-23 through Figure 6-27 show scatter plots for each of the 5 most important parameters shown in Table 6-19. The figures are for the 50-mile circular area. The parameters and the trends are the same as those discussed in section 6.4.2. The difference in source terms with and without random ignition affects the cancer fatality risk, but has only a minor influence on the most important parameters affecting those results.

Table 6-19 Mean, individual, LCF risk regression results within a 0 – 10 mile interval for all realizations based on LNT.

	Rank Regression		Quadratic		Recursive Partitioning		MARS		Main Contribution	Conjoint Contribution
Final R^2	0.62		0.82		0.89		0.76			
Input	R^2 contr.	SRRC	S_i	T_i	S_i	T_i	S_i	T_i		
CFRISK(8)	0.18	0.42	0.28	0.38	0.25	0.54	0.38	0.50	0.230	0.141
SV_frac	0.17	0.37	0.17	0.24	0.21	0.52	0.10	0.15	0.142	0.121
DDREFA(8)	0.07	-0.26	0.06	0.09	0.06	0.26	0.08	0.14	0.058	0.081
CFRISK(7)	0.03	0.22	0.06	0.07	0.01	0.03	0.07	0.09	0.037	0.011
CFRISK(3)	0.03	0.17	0.03	0.11	0.01	0.07	0.05	0.10	0.024	0.052
GSHFAC(2)	0.03	0.20	0.03	0.03	---	---	0.04	0.08	0.020	0.013
rupture	0.03	-0.18	0.02	0.03	0.00	0.01	0.03	0.04	0.018	0.007
CFRISK(4)	0.02	0.14	0.03	0.04	0.01	0.10	0.02	0.04	0.015	0.034
DDREFA(7)	0.02	-0.14	0.01	0.04	0.00	0.02	0.01	0.03	0.010	0.018
CFRISK(6)	0.02	0.12	0.01	0.06	---	---	0.02	0.01	0.008	0.014
priSVcycles	---	---	0.00	0.04	---	---	0.02	0.02	0.005	0.010
Y-91M_ICH(9)	0.00	-0.08	0.01	0.03	---	---	---	---	0.003	0.005
I-134_ICH(9)	0.01	0.09	---	---	0.00	0.04	---	---	0.002	0.013
DLTEVA_7(5)	0.01	-0.09	---	---	0.00	0.02	---	---	0.002	0.004
DLTEVA_7(13)	---	---	0.00	0.02	0.00	0.03	0.00	0.01	0.002	0.018
DDREFA(3)	0.00	-0.06	0.00	0.03	---	---	---	---	0.001	0.008
DLTEVA_7(10)	0.00	0.06	---	---	0.00	0.01	---	---	0.001	0.004
DLTEVA_3(4)	---	---	0.00	0.02	---	---	0.00	0.02	0.001	0.010
EU_melt_T	---	---	---	---	0.00	0.01	---	---	0.000	0.004
DLTEVA_3(1)	---	---	---	---	---	---	0.00	0.01	0.000	0.002
Y-93_ICH(9)	---	---	---	---	0.00	0.03	---	---	0.000	0.010
PR-143_ICH(9)	---	---	---	---	0.00	0.03	---	---	0.000	0.010

** highlighted if main contribution larger than 0.02 or conjoint contribution larger than 0.1*

Table 6-20 Mean, individual, LCF risk regression results within a 10 – 20 mile interval for all realizations based on LNT.

	Rank Regression		Quadratic		Recursive Partitioning		MARS		Main Contribution	Conjoint Contribution
Final R^2	0.59		0.79		0.82		0.71			
Input	R^2 contr.	SRRC	S_i	T_i	S_i	T_i	S_i	T_i		
SV_frac	0.22	0.39	0.16	0.26	0.20	0.55	0.15	0.47	0.154	0.198
CFRISK(8)	0.12	0.36	0.15	0.21	0.14	0.36	0.21	0.26	0.127	0.087
DDREFA(8)	0.05	-0.24	0.06	0.10	0.09	0.36	0.05	0.13	0.052	0.103
CFRISK(4)	0.02	0.14	0.00	0.09	0.01	0.13	0.05	0.35	0.017	0.125
DDREFA(4)	0.01	-0.12	0.02	0.08	0.02	0.12	0.02	0.06	0.016	0.051
CFRISK(5)	---	---	0.06	0.11	0.00	0.03	---	---	0.016	0.021
TIMHOT	0.03	0.15	0.03	0.03	0.00	0.02	0.01	0.04	0.014	0.013
CFRISK(7)	0.02	0.16	0.03	0.06	0.00	0.04	---	---	0.012	0.020
CFRISK(3)	0.02	0.16	0.03	0.07	0.00	0.02	---	---	0.010	0.016
rupture	0.04	-0.20	---	---	0.00	0.03	---	---	0.010	0.008
GSHFAC(2)	0.03	0.18	---	---	---	---	0.02	0.05	0.010	0.008
Y-91M_ICH(9)	0.01	-0.07	0.01	0.03	---	---	0.00	0.04	0.003	0.015
I-134_ICH(9)	0.01	0.09	---	---	0.01	0.06	---	---	0.003	0.014
DDREFA(7)	0.01	-0.09	0.01	0.05	---	---	0.00	0.02	0.003	0.016
DLTEVA_7(5)	0.01	-0.09	---	---	0.00	0.02	---	---	0.003	0.004
EU_melt_T	---	---	0.01	0.04	---	---	---	---	0.002	0.007
DLTEVA_3(4)	---	---	0.01	0.06	---	---	0.00	0.04	0.002	0.022
DLTEVA_2(11)	0.01	-0.08	---	---	0.00	0.03	---	---	0.002	0.008
RH-103M_ICH(9)	---	---	0.01	0.04	---	---	0.00	0.07	0.001	0.027
DLTEVA_7(9)	---	---	---	---	0.00	0.03	0.00	0.09	0.001	0.028
DLTEVA(5)	---	---	---	---	---	---	0.00	0.07	0.001	0.015
priSVcycles	---	---	0.00	0.04	---	---	---	---	0.001	0.010

** highlighted if main contribution larger than 0.02 or conjoint contribution larger than 0.1*

Table 6-21 Mean, individual, LCF risk regression results within a 0 – 50 mile interval for all realizations based on LNT.

	Rank Regression		Quadratic		Recursive Partitioning		MARS		Main Contribution	Conjoint Contribution
Final R^2	0.59		0.78		0.81		0.67			
Input	R^2 contr.	SRRC	S_i	T_i	S_i	T_i	S_i	T_i		
CFRISK(8)	0.14	0.38	0.22	0.28	0.14	0.39	0.30	0.37	0.156	0.099
SV_frac	0.19	0.40	0.15	0.22	0.23	0.55	0.17	0.21	0.153	0.113
DDREFA(8)	0.06	-0.24	0.06	0.10	0.12	0.37	0.10	0.13	0.067	0.083
GSHFAC(2)	0.04	0.21	0.05	0.10	0.00	0.05	0.07	0.09	0.031	0.029
CFRISK(7)	0.03	0.16	0.04	0.07	0.02	0.03	0.05	0.05	0.028	0.011
CFRISK(3)	0.02	0.15	0.03	0.08	---	---	0.04	0.08	0.019	0.020
CFRISK(4)	0.02	0.14	0.03	0.07	0.01	0.09	0.04	0.10	0.018	0.046
DDREFA(4)	0.02	-0.14	0.02	0.05	0.01	0.04	0.04	0.08	0.017	0.025
rupture	0.03	-0.18	---	---	---	---	0.04	0.03	0.014	0.000
shape_fact	0.01	0.09	0.01	0.04	0.00	0.01	0.00	0.01	0.005	0.014
DDREFA(7)	0.01	-0.09	---	---	0.01	0.06	---	---	0.003	0.013
I-134_ICH(9)	0.01	0.10	---	---	0.00	0.04	---	---	0.003	0.011
priSVcycles	---	---	0.01	0.05	0.00	0.02	---	---	0.003	0.016
DLTEVA_7(5)	0.01	-0.09	---	---	---	---	0.00	0.01	0.002	0.001
DLTEVA_2(11)	0.01	-0.08	---	---	0.00	0.02	0.00	0.01	0.002	0.005
GSHFAC_5(1)	---	---	0.01	0.03	---	---	0.00	0.01	0.002	0.008
EU_melt_T	---	---	0.01	0.04	0.00	0.02	---	---	0.002	0.012
BA-140_ICH(9)	---	---	---	---	0.01	0.02	---	---	0.001	0.005
RH-103M_ICH(9)	---	---	---	---	0.01	0.02	---	---	0.001	0.005
Y-91M_ICH(9)	0.01	-0.07	---	---	---	---	---	---	0.001	0.000
CFRISK(5)	---	---	0.00	0.03	---	---	---	---	0.001	0.008
DLTEVA_3(4)	---	---	0.00	0.03	---	---	---	---	0.001	0.007

** highlighted if main contribution larger than 0.02 or conjoint contribution larger than 0.1*

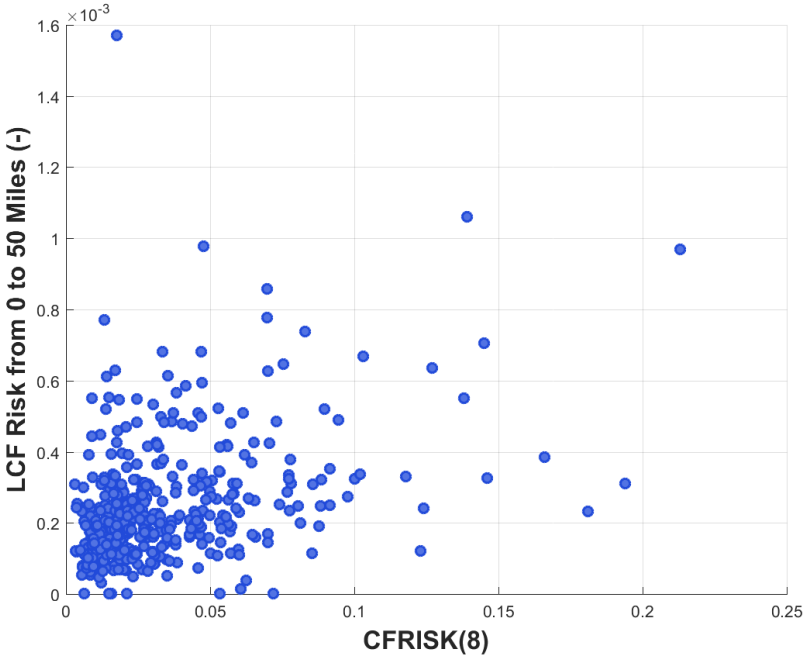

Figure 6-23 Scatter plot of mean, individual, LCF risk within a 0 – 50 mile interval for all realizations versus CFRISK(8), conditional on an STSBO accident occurring

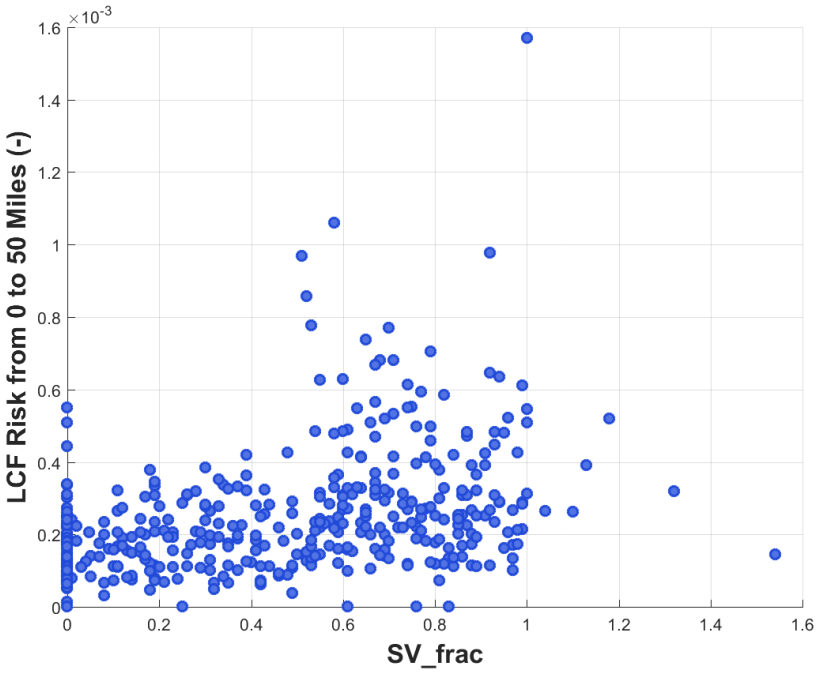

Figure 6-24 **Scatter plot of mean, individual, LCF risk within a 0 – 50 mile interval for all realizations versus safety valve open area fraction, SV_frac, conditional on an STSBO accident occurring**

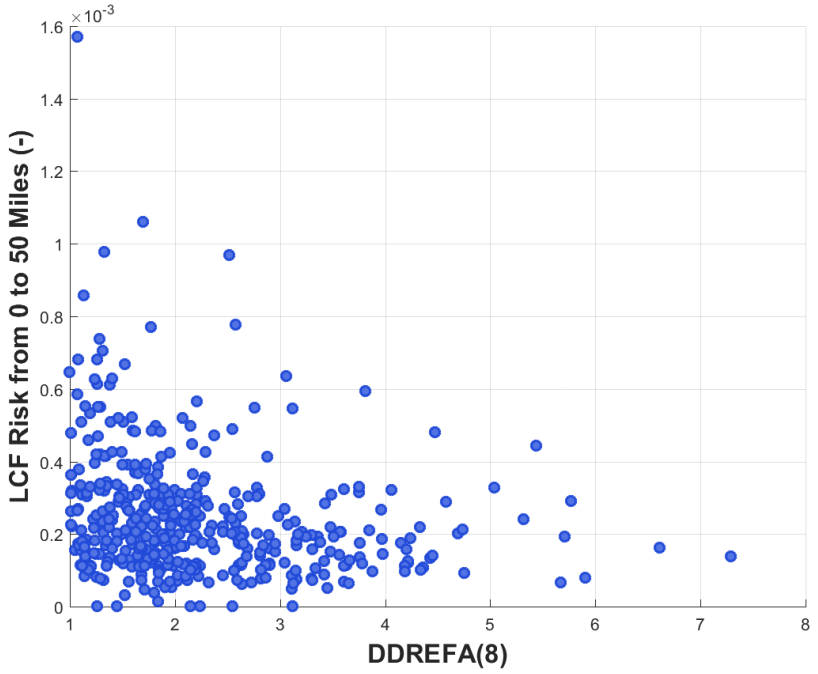

Figure 6-25 **Scatter plot of mean, individual, LCF risk within a 0 – 50 mile interval for all realizations versus DDREFA(8), conditional on an STSBO accident occurring**

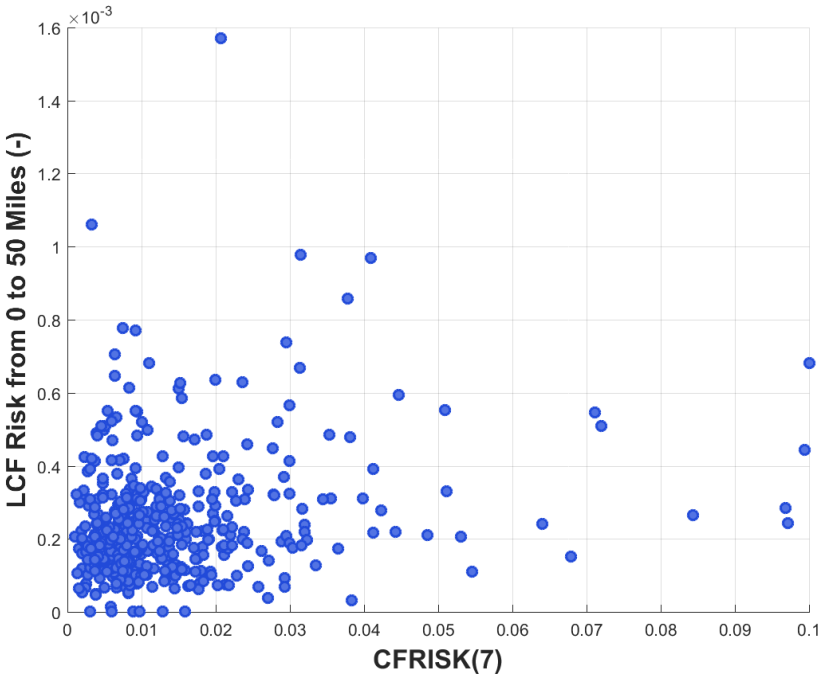

Figure 6-26 Scatter plot of mean, individual, LCF risk within a 0 – 50 mile interval for all realizations versus CFRISK(7), conditional on an STSBO accident occurring

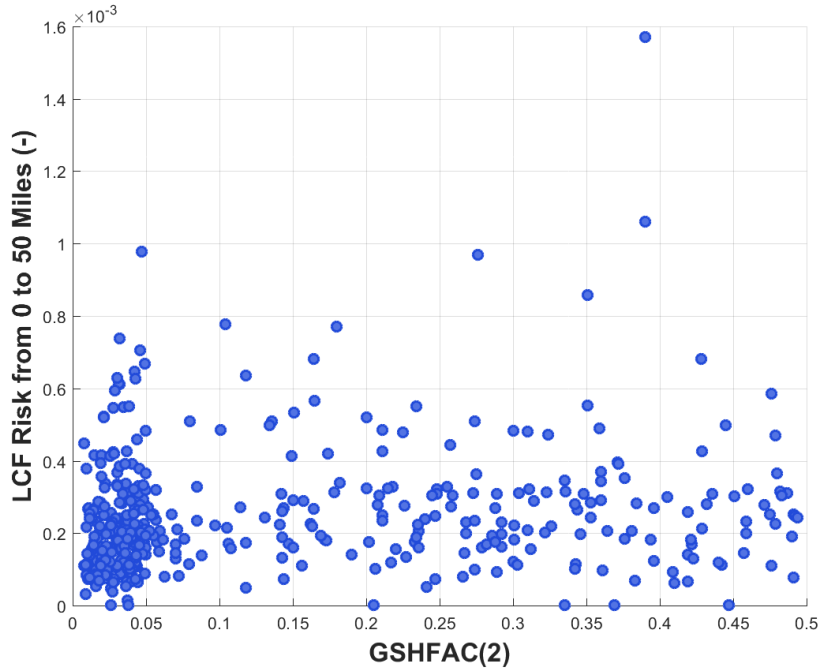

Figure 6-27 Scatter plot of mean, individual, LCF risk within a 0 – 50 mile interval for all realizations versus CFRISK(7), conditional on an STSBO accident occurring

6.5.3 Regression Analysis of Early Fatality Risk Assuming Random Ignition

Table 6-22 shows statistical results for mean individual early fatality risk conditional on an accident occurring (per event) from the MACCS uncertainty analysis at seven spatial intervals representing concentric circles centered on Sequoyah. The distance intervals in the table are the radii of the circular areas and mean indicates that results are averaged over weather variability and within the spatial interval. Each of the statistics in the table represents the overall epistemic (state of knowledge) uncertainty for the groups of MELCOR and MACCS inputs that were treated as uncertain. The results show that mean conditional risks are approximately 10^{-8} and diminish rapidly with distance from the plant. There is no early fatality risk for any of the realizations beyond 5 mi and there are only 12 realizations (less than 3%) with an early fatality risk within 5 mi.

Table 6-22 Mean, individual EF risk with random ignition (STSBO-WRI), conditional on accident (per event) for the MACCS uncertainty analysis for five distance intervals centered on Sequoyah

	0-1.0 miles	0-1.3 miles	0-2.0 miles	0-2.5 miles	0-3.0 miles	0-4.0 miles	0-5.0 miles
Mean	1.2E-08	7.9E-09	1.1E-08	6.8E-09	4.2E-09	2.4E-09	1.2E-09
Median	0.0E+00	0.0E+00	0.0E+00	0.0E+00	0.0E+00	0.0E+00	0.0E+00
5th Percentile	0.0E+00	0.0E+00	0.0E+00	0.0E+00	0.0E+00	0.0E+00	0.0E+00
95th Percentile	0.0E+00	0.0E+00	0.0E+00	0.0E+00	0.0E+00	0.0E+00	0.0E+00

Figure 6-28 shows the complimentary cumulative distribution functions for the same circular areas summarized in Table 6-22. The points on the curves represent the mean LCF risk over variable weather for each of the 432 realizations representing epistemic uncertainty in this UA and are conditional on the accident occurring. The curves show that the conditional risks span the range from 0 to more than 10^{-6} per event.

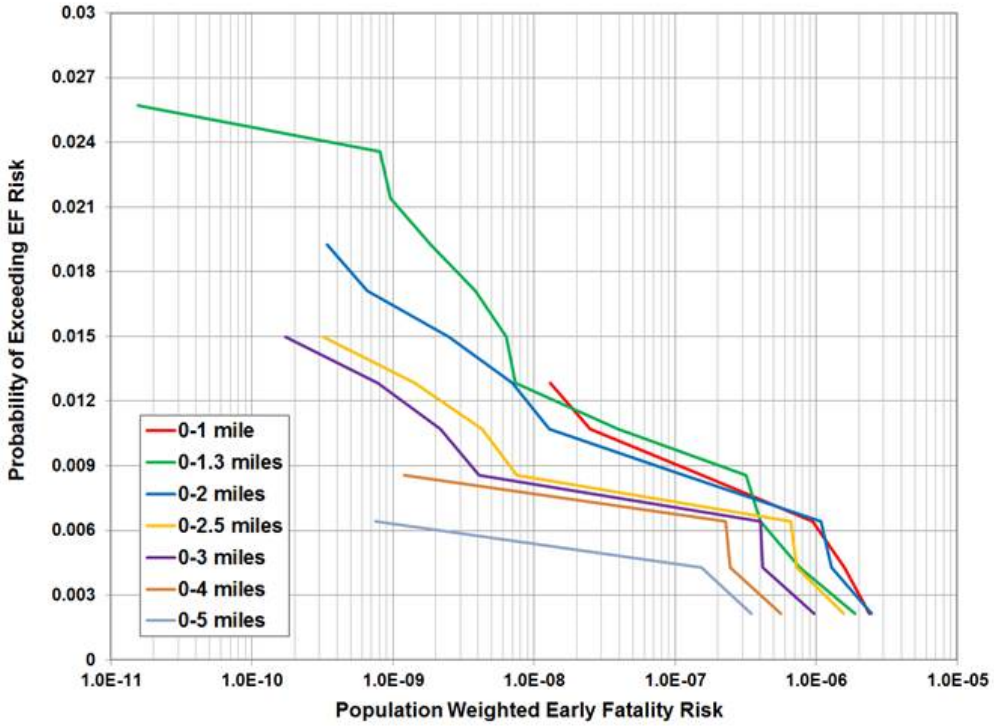

Figure 6-28 Complimentary cumulative distribution function of mean, population-weighted EF risk (with random ignition) within five intervals centered on Sequoyah

Of the 432 successful realizations that were evaluated, only 12 realizations (about 3%) had doses high enough to create an early fatality risk to the population within 5 miles. Thus, a regression analysis to evaluate the most important variables would be essentially meaningless and therefore it was not performed.

6.6 MACCS Results from Selected UA Realizations

This section evaluates three individual UA realizations; two of them happen to be the same realization. The realizations considered are those for the maximum cesium release, the maximum LCF risk, and the maximum EF risk. These correspond to MELCOR realization numbers 110, 232, and 232, respectively, and both realizations are from the UA set without random ignition. Since the maximum LCF and EF risk realizations are the same, the term "maximum risk" is used in several of the figures to denote risks for both LCF and EF.

Because these realizations were not discussed previously, information is provided to put these selected source terms in perspective with the larger set of MELCOR source terms. Cesium and iodine release fraction histories are provided in Figure 6-29 and Figure 6-30. These show that the release timing is very different for the two realizations. The maximum-risk realization has an early and protracted release for both cesium and iodine and has a very large iodine release; the maximum-cesium-release realization has a late but rapid release of both cesium and iodine. The iodine release fraction for the maximum risk realization is larger than for the maximum cesium release realization. Table 6-23 shows that the release fraction for all other chemical groups but cesium is larger for the maximum risk realization. In particular, the large cerium

release (more than 5%) for the maximum risk realization should have a significant contribution to latent cancer fatalities. Also, the barium release of more than 7% should also have a significant contribution because this group contains Sr-90.

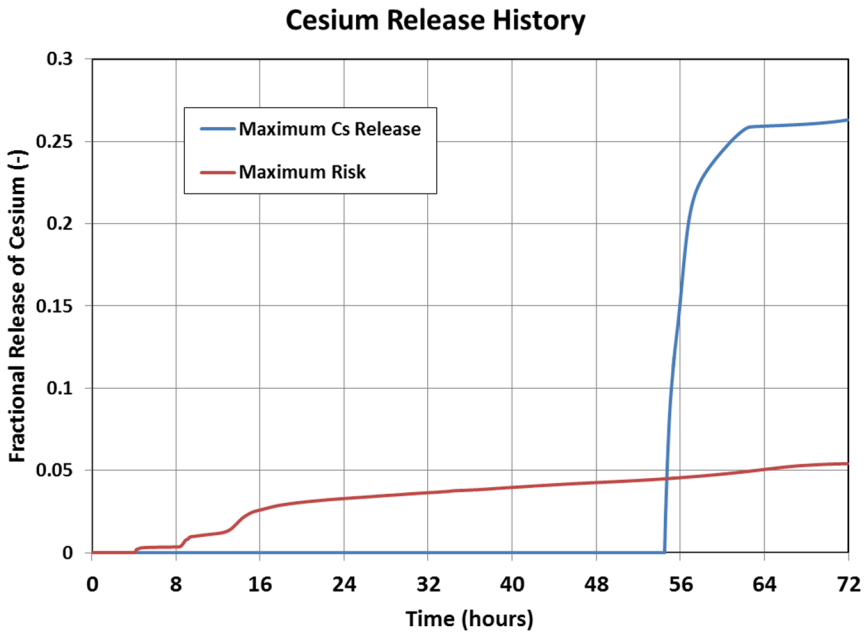

Figure 6-29 Cesium release histories for the maximum cesium release and maximum risk realizations

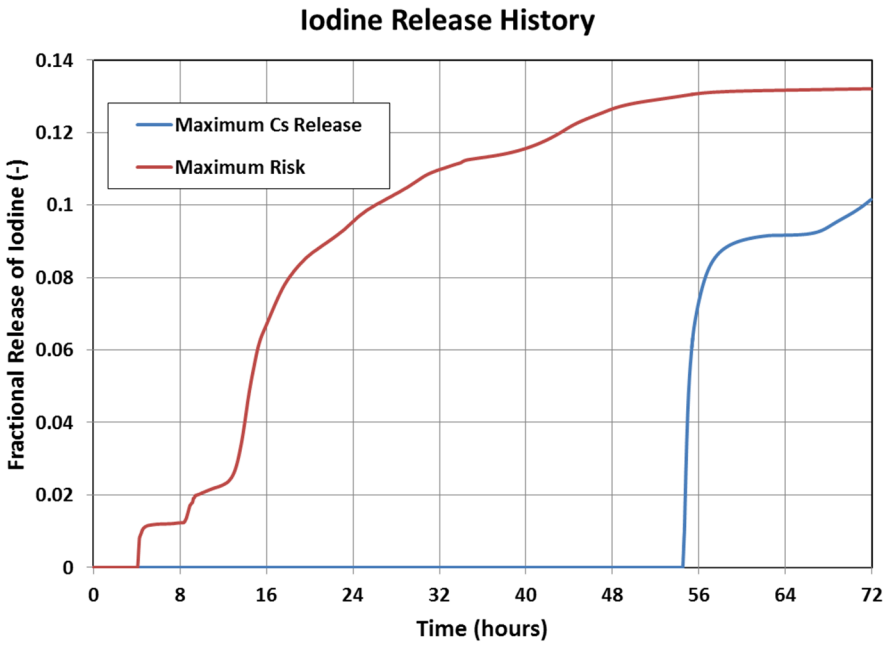

Figure 6-30 Iodine release histories for the maximum cesium release and maximum risk realizations

Table 6-23 Integral release fractions for the maximum cesium release and maximum risk realizations.

	Max Cs Realization	Max Risk Realization
Isotope	Total Fraction Released	Total Fraction Released
Xe	1.0E+00	1.0E+00
Cs	2.6E-01	5.4E-02
Ba	1.4E-04	7.1E-02
I	1.0E-01	1.3E-01
Te	7.2E-03	1.4E-01
Ru	1.9E-07	3.0E-03
Mo	6.4E-02	2.7E-01
Ce	5.7E-06	5.3E-02
La	4.7E-06	3.0E-03

Figure 6-31 and Figure 6-32 show complimentary cumulative distribution functions for LCF risks within circular and annular intervals surrounding the Sequoyah site for the maximum cesium release realization, conditional on the occurrence of an accident. The probabilities shown in the figures represent weather variability. Conditional LCF risks shown in the figures range from about 10^{-4} to almost 10^{-3}. Statistical values, including the mean, for the LCF risks corresponding to these same areas are provided in Table 6-24 and Table 6-25. Early fatality risks are zero for this realization.

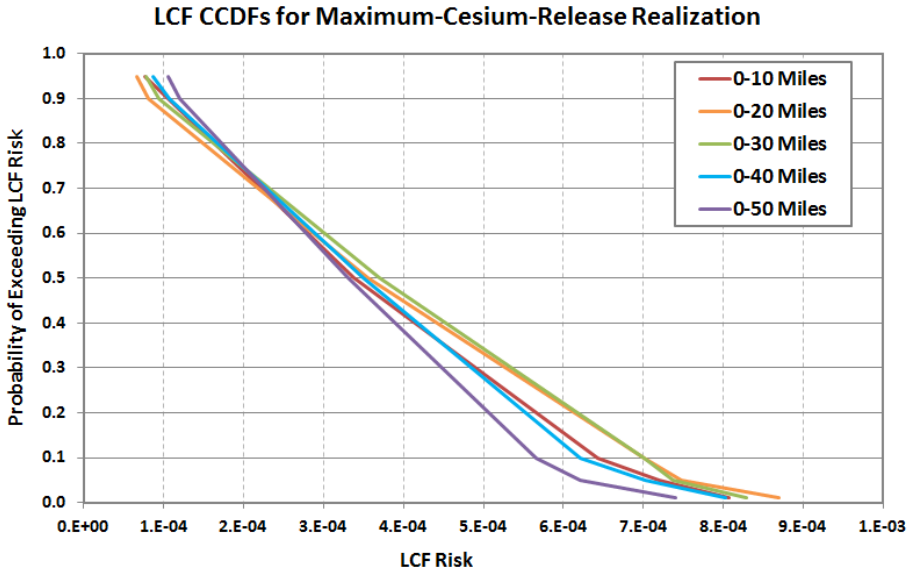

Figure 6-31 Complimentary cumulative distribution function of mean, population-weighted LCF risk (without random ignition source) for the maximum-cesium-release realization within five intervals centered on Sequoyah. Probability represents weather variability.

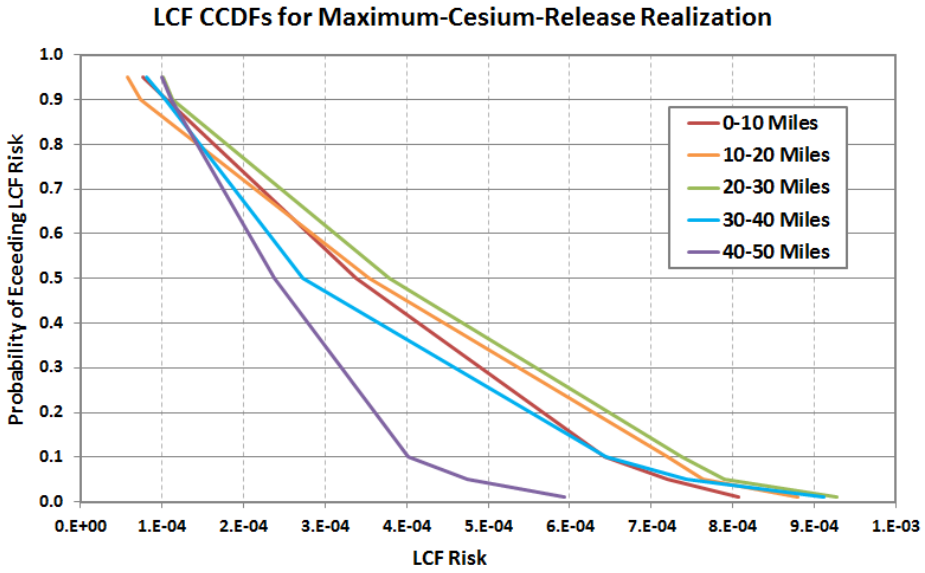

Figure 6-32 Complimentary cumulative distribution function of mean, population-weighted LCF risk (without random ignition source) for the maximum-cesium-release realization within five intervals centered on Sequoyah. Probability represents weather variability

Table 6-24 Mean, individual LCF risks for the maximum-cesium-release realization, conditional on accident (per event) for the MACCS uncertainty analysis for five intervals centered on Sequoyah.

	0-10 Miles	0-20 Miles	0-30 Miles	0-40 Miles	0-50 Miles
Mean	3.7E-04	3.9E-04	4.0E-04	3.8E-04	3.6E-04
Median	3.4E-04	3.6E-04	3.7E-04	3.5E-04	3.3E-04
5th Percentile	7.6E-05	6.7E-05	7.8E-05	8.6E-05	1.1E-04
95th Percentile	7.2E-04	7.5E-04	7.4E-04	7.0E-04	6.2E-04

Table 6-25 Mean, individual LCF risks for the maximum-cesium-release realization, conditional on accident (per event) for the MACCS uncertainty analysis for four intervals centered on Sequoyah.

	10-20 Miles	20-30 Miles	30-40 Miles	40-50 Miles
Mean	3.9E-04	4.2E-04	3.3E-04	2.7E-04
Median	3.5E-04	3.8E-04	2.7E-04	2.4E-04
5th Percentile	5.8E-05	1.0E-04	8.2E-05	1.0E-04
95th Percentile	7.6E-04	7.9E-04	7.4E-04	4.7E-04

Figure 6-33 and Figure 6-34 show complimentary cumulative distribution functions for LCF risks within circular and annular intervals surrounding the Sequoyah site for the maximum-risk realization, conditional on the occurrence of an accident. The probabilities shown in the figures represent weather variability. Conditional LCF risks shown in the figures range from less than 10^{-3} to about 10^{-2}. Statistical values, including the mean, for the LCF risks corresponding to

these same areas are provided in Table 6-26 and Table 6-27. Mean EF risks are approximately 5×10^{-5} within 1.3 miles and 3×10^{-5} within 2 miles of the site for this realization. No early fatality risks exist beyond 3 miles from the site for this realization.

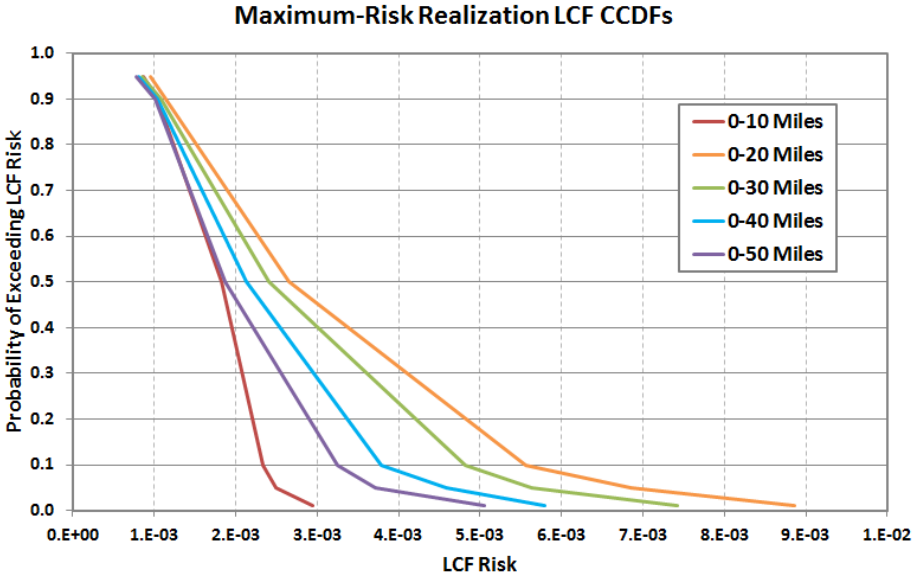

Figure 6-33 Complimentary cumulative distribution function of mean, population-weighted, LCF risk (without random ignition source) for the maximum-risk realization within five intervals centered on Sequoyah. Probability represents weather variability.

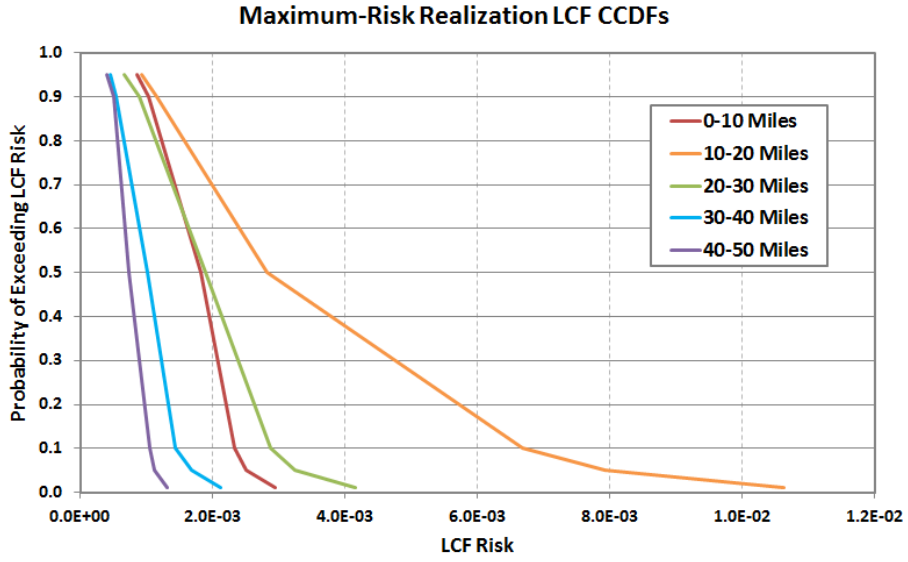

Figure 6-34 Complimentary cumulative distribution function of mean, population-weighted, LCF risk (without random ignition source) for the maximum-risk realization within five intervals centered on Sequoyah. Probability represents weather variability.

Table 6-26 Mean, individual LCF risks for the maximum risk realization, conditional on accident (per event) for the MACCS uncertainty analysis for five circular areas centered on Sequoyah.

	0-10 Miles	0-20 Miles	0-30 Miles	0-40 Miles	0-50 Miles
Mean	1.9E-03	3.2E-03	2.8E-03	2.4E-03	2.1E-03
Median	1.8E-03	2.6E-03	2.4E-03	2.1E-03	1.9E-03
5th Percentile	8.6E-04	9.6E-04	8.6E-04	8.1E-04	7.8E-04
95th Percentile	2.5E-03	6.8E-03	5.6E-03	4.6E-03	3.7E-03

Table 6-27 Mean, individual LCF risks for the maximum risk realization, conditional on accident (per event) for the MACCS uncertainty analysis for four intervals centered on Sequoyah.

	10-20 Miles	20-30 Miles	30-40 Miles	40-50 Miles
Mean	3.5E-03	2.0E-03	1.1E-03	7.8E-04
Median	2.8E-03	1.9E-03	1.0E-03	7.4E-04
5th Percentile	9.3E-04	6.6E-04	4.5E-04	3.9E-04
95th Percentile	7.9E-03	3.2E-03	1.7E-03	1.1E-03

6.7 Sensitivity Analysis

A sensitivity analysis of the STSBO early release scenario was performed to evaluate potential impacts of sheltering in place instead of evacuating. This analysis considers all cohorts within the EPZ. It does not include variations for the shadow evacuees whom reside outside the EPZ and are assumed to evacuate in any event. To facilitate the analysis, the delay to evacuate parameter DLTEVA was set to 604,800 sec (7 days), such that the cohorts considered shelter throughout the entire emergency phase of the accident. Furthermore, the emergency phase normal and hot spot relocation doses, DOSNRM and DOSHOT, were both set to 10,000 rem to prevent residents from relocating. Residents are assumed to stay indoors, so groundshine and cloudshine protection factors for shelter were used. Long term phase parameters were not altered for this analysis.

The strong seismic event that initiates the accident is expected to damage the integrity of some of the homes and facilities within the EPZ. Prediction of which structures could be damaged and to what degree is beyond the scope of this study. It is assumed that the structures are sufficient for occupancy, and that the shielding from radiation outside the structures is unaffected by the accident. However it is reasonable to assume that windows may be damaged and that residents may not be able to repair the damage under the shelter orders allowing increased penetration of outdoor air into the structures.

To account for this, the inhalation and skin protection factors, PROTIN and SKPFAC, were varied between the typical sheltering protection factor of 0.33 to the evacuation protection factor of 0.98. The protection factors PROTIN and SKPFAC are normally assigned the same value. The inhalation protection factor affects LCF risk in the MACCS model whereas the skin protection has no effect on the reported risks. Table 6-28 presents the inhalation and skin

protection factors for each sensitivity analysis. The sheltering protection factor of 0.33 used in the previous cases was taken as in the value for sensitivity 1 to reflect the bounding case of no damage to structures. Sensitivity 2 represents the inhalation and skin protection normally afforded by structures to be 50 percent compromised. Sensitivity 3 assumes that shelters are fully compromised, therefore the protection factors are set to 0.98, which are the same PROTIN and SKPFAC values used for evacuation.

Table 6-28 Inhalation and skin protection factors of the sheltering sensitivity analysis.

STSBO Early Release (Evacuate)	Sensitivity 1 (Shelter)	Sensitivity 2 (Shelter)	Sensitivity 3 (Shelter)
0.33	0.33	0.66	0.98

Figure 6-35 presents the emergency and long term phase LNT, LCF risk results for the 0 - 10 mile interval. The figure shows that the emergency phase LCF risks increase dramatically for sheltering compared with the STSBO ER scenario in which 99.5 percent of the residents evacuate the EPZ. The emergency and long term phase data are shown to indicate the proportions of LCF risk by phase for each sensitivity case. The long term protection factors were not altered for this sensitivity, so the long term LCF risk contributions do not change.

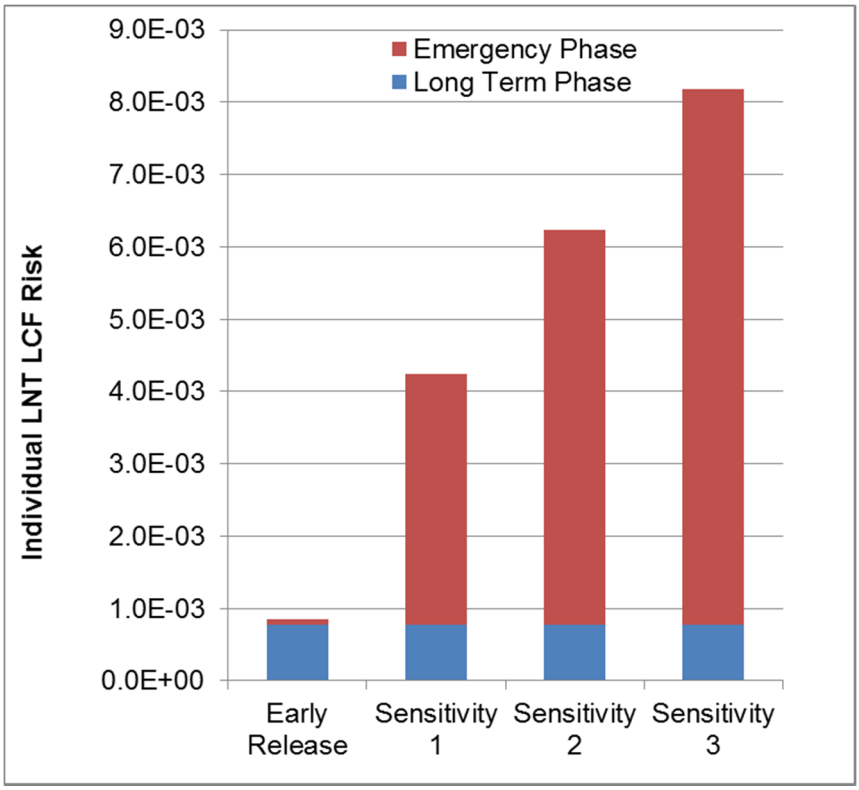

Figure 6-35 Summary of sensitivity analysis long term and emergency phase mean, individual, LNT, LCF risk results for the 0 - 10 mile region

Table 6-29 provides selected results for the 0-10 mile interval, including the emergency phase LCF risk, the fraction of total LCF risk attributed to the emergency phase, and the sensitivity case risk values normalized to the STSBO ER results.

Table 6-29 Sensitivity analysis results for emergency phase LCF risks for the 0 – 10 mile interval, the emergency phase fraction of total LCF risk, and the emergency phase risks normalized to the STSBO early release risk.

Result	Early Release	Sensitivity 1	Sensitivity 2	Sensitivity 3
Emergency Phase LCF Risk	6.7E-05	3.5E-03	5.5E-03	7.4E-03
Emergency Phase Fraction of Total LCF Risk	0.08	0.82	0.88	0.91
Emergency Phase Risk Normalized to STSBO ER	1	52	82	111

These sensitivity cases suggest that sheltering for seven days rather than evacuating for the STSBO ER scenario would result in large increases in the emergency phase doses to the point that they significantly exceed the late phase doses. The emergency phase dose contribution to the total LCF risk was eight percent for the STSBO-ER scenario. The equivalent contribution would increase from eight percent to 82 percent (intact inhalation protection, Sensitivity Case 1) up to 91 percent (completely degraded inhalation protection, Sensitivity Case 3). By normalizing the risk results to the STSBO ER scenario, the emergency phase risk associated with extended sheltering instead of evacuation increases by a factor from 52 to more than 110 times greater with decreasing inhalation protection. Comparing total LCF risk, sheltering increases LCF risks by a factor of approximately six to twelve, increasing with the inhalation protection factor.

The increase in LCF risk is sub-linear with respect to the inhalation protection factor. This is not surprising because the LCF risk during the sheltering period includes dose contributions from groundshine and cloudshine. A linear regression calculation of the emergency phase risk results shown in Figure 6-35 permits determination of the combined groundshine and cloudshine contributions to the emergency phase. The combined contribution to LCF risk is 1.5E-03, which is 30 percent of the emergency phase LCF risk for Sensitivity 1. Under the assumptions of the sensitivity analysis, the risk contributions due to sheltering inhalation protection factor exceeds the risk contributions due to the other exposure pathways.

Table 6-30 shows the early fatality risk results for selected intervals near the plant. The distance interval of 0-1.345 extends one mile beyond the Sequoyah EAB. The STSBO-ER evacuation scenario has zero EF risk results at all intervals, however the sensitivity analysis results in very small but non-zero EF risk values. As expected, the EF risks increase with decreasing inhalation protection. The sensitivity results indicate that the relative maximum EF risk occurs in the 0 – 2 mile distance interval.

The absolute early fatality risk estimated to be on the order of 1E-11 is essentially zero. Overall, this EF risk is negligible even for these sensitivity cases.

Table 6-30 Sensitivity analysis conditional early fatality risk results for selected radial intervals near Sequoyah.

Result	Radius (miles)	Early Release	Sensitivity 1	Sensitivity 2	Sensitivity 3
Early Fatality Risk	0-1	0.0E+00	1.7E-08	2.0E-08	4.6E-08
	0-1.345	0.0E+00	2.3E-06	2.7E-06	3.2E-06
	0-2	0.0E+00	4.7E-06	5.7E-06	6.7E-06
	0-3	0.0E+00	1.4E-06	1.6E-06	1.9E-06
	0-5	0.0E+00	4.7E-07	5.6E-07	6.6E-07

6.8 Summary

The offsite consequence analysis results for Sequoyah SOARCA have been presented as individual LCF and EF risks for both deterministic and probabilistic uncertainty analysis results. In addition, regression techniques were performed on the uncertainty analysis to provide insights as to which parameters or combinations of parameters influence the risk results. Using LNT dose response, the LCF risks of both deterministic and uncertainty analysis range from about 3E-04 to 9E-04 for the 0 – 10 mile region and the LCF risks decrease with increasing distance from Sequoyah. Contributions from the long term phase risks dominate the emergency phase risks for the large majority of the LCF risk results. The EF risks are essentially zero. A sensitivity analysis examines the potential effect of sheltering in place instead of evacuating. The results show that evacuating greatly reduces the emergency phase contributions to risk as compared to sheltering in place, and even more so when structures are damaged from an earthquake.

7. CONCLUSIONS

Through the application of modern analysis tools and techniques, the SOARCA project developed a body of knowledge regarding the realistic outcomes of severe reactor accidents. SOARCA analyses of Peach Bottom and Surry pilot plants revealed insights into the accident progression for important scenarios in a BWR Mark I design and a PWR large dry (subatmospheric) containment design as well as the offsite consequences of potential radioactive releases. This analysis of station blackouts at the third SOARCA pilot plant, Sequoyah, expands on the SOARCA body of knowledge for the next most prevalent containment design in the U.S., the ice condenser. Compared to PWR large dry containments, ice condensers are smaller and have a lower design pressure; therefore, the containment cannot absorb as much energy despite the presence of ice for pressure suppression. Hydrogen combustion has long been known to be a potential challenge to the ice condenser containment. The Sequoyah SOARCA analysis examines phenomenology and modeling unique to the ice condenser design including the behavior of hydrogen and the potential for early containment failure from energetic hydrogen combustion. Beyond expanding the body of knowledge on realistic outcomes of severe accidents, this analysis has complemented and supported NRC's activities to address lessons learned from the Fukushima Dai-ichi accidents, specifically NTTF item 5.2 (reliable hardened vents for containment designs other than Mark I and Mark II) and item 6 (hydrogen control and mitigation inside containment or in other buildings).

The staff used updated and benchmarked standardized plant analysis risk (SPAR) models and available plant-specific external events information to identify the most probable of the very low probability station blackout (SBO) scenario variations for analysis. Similar to the Peach Bottom and Surry analyses, this group of scenarios includes the short-term station blackout (STSBO) and the long term station blackout (LTSBO). Both types of SBOs involve a loss of all AC power. SBO scenarios can be initiated by external events such as a fire, flood, or earthquake. The Sequoyah SOARCA analysis assumes that an SBO is initiated by a low probability severe seismic event because this is an extreme case in terms of timing and equipment failure. For the LTSBO, AC power is lost but the turbine-driven auxiliary feedwater pump (TDAFW) is available until batteries deplete. The contribution to core damage frequency for the LTSBO was estimated at one event per approximately 100,000 years of reactor operation (~1E-5/yr). For the STSBO, AC power is lost and the turbine-driven auxiliary feedwater pump is not available, and therefore the postulated scenario proceeds to core damage more rapidly (hence "short term"). The contribution to core damage frequency for the STSBO is lower, and was estimated at one event per approximately 500,000 years of reactor operation (~2E-6/yr). As a severe accident and consequence analysis, the Sequoyah focus was on the accident progression modeling and offsite consequence modeling coupled with the uncertainty analyses to guide the best selection for parameter inputs and to provide insights on the effects of selected parameters.

SOARCA analyses were performed primarily with two computer codes, MELCOR for accident progression and MACCS for offsite consequences. MELCOR models the thermal-hydraulic response in the reactor coolant system, reactor cavity, containment, and confinement buildings; core heatup, degradation, and relocation; core-concrete attack; hydrogen production, transport, and combustion; fission product transport and release to the environment. MACCS models the atmospheric transport and deposition of radionuclides released to the environment as well as emergency response and long-term protective actions, exposure pathways, dosimetry, and health effects for the affected population. The Peach Bottom and Surry SOARCA studies were comprised of deterministic base case analyses using point estimates for input parameter values,

followed by probabilistic uncertainty analyses (UAs) which sampled distributions representing input uncertainty to generate multiple results to represent the range of potential outcomes. For the Sequoyah SOARCA analysis, staff integrated probabilistic consideration of uncertainty into accident progression and offsite consequence analyses in parallel with deterministic calculations.

Several variations of the STSBO were evaluated. The base case scenario was an evaluation of an unmitigated (i.e., without igniters) STSBO scenario. A sensitivity case of a mitigated STSBO was evaluated in which hydrogen igniters are modeled as operable. Two unmitigated (i.e., igniters are assumed inoperable) STSBO variations were run probabilistically with and without the presence of random ignition sources. Random ignition sources refer to the potential of the accident to lead to sparks possibly caused by structural materials sliding against or falling on other materials, static discharge, etc., but the timing and location of the spark(s) is inherently unknown. The staff modeled hundreds of variations of the STSBO with and without random ignition sources, each of which used different values of important input parameters[40] selected from distributions that account for parameter uncertainty in both accident progression (MELCOR) and offsite consequences (MACCS). For the LTSBO scenario, staff has deterministically analyzed accident progression for a scenario without igniters or random ignition sources, and performed a number of deterministic sensitivity calculations to assess the impact of features including battery duration, hydrogen ignition criteria, and safety valve (SV) behavior. A sensitivity case of a mitigated LTSBO was also evaluated in which hydrogen igniters are modeled as operable.

For the unmitigated STSBO (i.e., igniters inoperable), there are two potential containment outcomes: early failure (~3-12 hours from initiating event) due to hydrogen combustion or late failure (> 30 hours) from more gradual overpressure. If igniters are not available because of the loss of power, containment can fail soon after hot leg rupture or at the time of lower head failure due to hydrogen deflagration. However, if a random spark triggers ignition prior to reactor coolant system breach, the accident is less likely to proceed to early containment failure. An early containment failure can result in the potential for radionuclide release to the environment before the 0-10 mile EPZ population has time to complete evacuation; however, the consequence analysis shows that even under such conditions, health risk to the public is low. Sequoyah SOARCA analyses show that successful use of igniters can control hydrogen accumulation and limit the containment pressure. Hydrogen igniters can help consume oxygen faster leading to less energetic deflagrations and help avert early containment failure.

The unmitigated LTSBO variations fall within the unmitigated STSBO variations in terms of release timing and magnitude, however for the unmitigated LTSBO, there are no cases of early containment failure. For the LTSBO, sensitivity calculations show that hydrogen combustion-induced failure occurs ~18-24 hours after accident initiation. The TDAFW system is very important in extending core cooling and allowing more time for implementation of additional mitigation. The ice is effective at mitigating the containment pressure rise by condensing hot steam and cooling non-condensable gases from the reactor pressure vessel and ex-vessel core concrete interaction. The ice also has the adverse consequence of reducing steam concentrations, which enhances conditions for large burns if the igniters are not available. Even though the benefit is limited because the ice can be completely melted within ~12 hours in the STSBO and ~34 hours in the LTSBO, it can significantly delay the timing of the slow long-term

[40] Because the unmitigated STSBO does not credit human actions, the UA also does not address human actions.

overpressurization failure of the containment. Igniters would delay but not alleviate potential containment overpressure failure following lower head failure if no other mitigation systems are available.

The Sequoyah plant analysis was unique in that it looked at the deterministic and uncertainty analyses in parallel. This allowed identification of important parameters that contribute to the outcome of the accident progression and consequence results. Regression and single-realization analysis results show that uncertain accident progression parameters (of those included in the analysis) most important to release timing are those affecting the timing of the containment failure, which naturally included the containment rupture pressure. An early containment failure was most likely if the hydrogen was distributed throughout the containment prior to the development of a strong ignition source, which was influenced by an early failure of the pressurizer safety valve (low number of safety valve cycles) and a large flow area for failed safety valve. Uncertain accident progression parameters most important to release magnitude (cesium and iodine release fraction) are the ones that affect the timing of the containment failure and events that contribute to fission product revaporization, which included the number of safety valve cycles and the failed safety valve flow area. Uncertain accident progression parameters most important to hydrogen production include the melting temperature of the eutectic formed from fuel (UO_2) and oxidized cladding (ZrO_2), and the parameters that lead to reactor coolant system depressurization (i.e., few pressurizer safety valve cycles before failure and the subsequent flow area of the failed safety valve).

Similar to the results from the Peach Bottom and Surry SOARCA analyses, the Sequoyah analyses show essentially zero individual early fatality risk and a low individual risk of latent cancer fatality for the affected population. Offsite radiological consequences were calculated for each scenario expressed as the average individual likelihood of an early fatality and latent cancer fatality. Even for STSBO variations leading to early containment failure in which the release to the environment begins prior to the completion of the EPZ evacuation, there is essentially zero individual early fatality risk and the individual latent cancer fatality risk is low. Individual LCF risk calculations are generally dominated by long-term exposure to small annual doses (below 2 rem in the year of the accident and below 500 mrem per year in subsequent years corresponding to the habitability criterion) for evacuees and relocated populations returning to their homes after the accident and being exposed to residual radiation over a long period of time.

The use of dose response models that truncate annual doses below certain levels results in a further reduction to the individual LCF risks. Sensitivity calculations using the STSBO early release example source term that consider alternate emergency response actions such as sheltering-in-place instead of evacuating result in larger individual LCF risks (3-6 times higher within 10 miles depending on assumptions for inhalation protection factors).

Regression analysis results show that uncertain input parameters (of those included in the analysis) that show importance to individual LCF risk in the STSBO cases include: failed safety valve flow area (and number of safety valve cycles experienced, in some cases), the cancer

fatality risk factor for the "residual" organ[41] (and sometimes other organs), dose and dose rate effectiveness factor for the "residual" organ, the groundshine shielding factors, and the containment rupture pressure.

In summary, this analysis reinforces the results of past analyses of ice condenser containments showing that successful use of igniters is effective in averting early containment failure. Even for scenarios resulting in early containment failure (radioactive release to the environment prior to completion of evacuation for the 0-10 mile EPZ), resulting individual LCF risks are very small. Although earlier releases were calculated for the Sequoyah SOARCA STSBO than SOARCA Surry STSBO, health risks are projected to be low, with essentially zero individual early fatality risk and conditional individual latent cancer fatality risk results are similar to those calculated for Peach Bottom and Surry SOARCA scenarios. Sequoyah SOARCA results, while specific to Sequoyah, may be generally applicable for other PWRs with ice condenser containments. However, additional work would be needed to confirm this, because differences exist in plant-specific designs, procedures, and emergency response.

41 MACCS uses eight cancer sites (organs), seven of which are specific (lung, red bone marrow, bone, breast, thyroid, liver, and colon) and the last of which ("residual") is used as a surrogate for the remaining soft tissues not explicitly modeled.

8. REFERENCES

[1] 10 CFR 50.54, "Conditions of Licenses," 74 FR 13969, U.S. Code of Federal Regulations, March 27, 2009.

[2] NUREG/CR-2239, "Technical Guidance for Siting Criteria Development," U.S. Nuclear Regulatory Commission, Washington, DC, 1982.

[3] NUREG-1935, "State-of-the-Art Reactor Consequence Analyses (SOARCA) Report," U.S. Nuclear Regulatory Commission, Washington, DC, November 2012.

[4] NUREG/CR-7110, Vol. 1, Rev. 1, "State-of-the-Art Reactor Consequence Analyses Project Volume 1: Peach Bottom Integrated Analysis," U.S. Nuclear Regulatory Commission, Washington, DC, May 2013.

[5] NUREG/CR-7110, Vol. 2, Rev. 1, "State-of-the-Art Reactor Consequence Analyses Project Volume 2: Surry Integrated Analysis," U.S. Nuclear Regulatory Commission, Washington, DC, August 2013.

[6] NUREG/BR-0359, Rev. 1, "Modeling Potential Reactor Accident Consequences," U.S. Nuclear Regulatory Commission, Washington, DC, December 2012.

[7] NUREG/CR-7008, "MELCOR Best Practices as Applied in the SOARCA Project," U.S. Nuclear Regulatory Commission, Washington, DC, August 2014.

[8] NUREG/CR-7009, "MACCS2 Best Practices as Applied in the SOARCA Project," U.S. Nuclear Regulatory Commission, Washington, DC, August 2014.

[9] NUREG/CR-7155, "State-of-the-Art Reactor Consequence Analyses Project: Uncertainty Analysis of the Unmitigated Long-Term Station Blackout of the Peach Bottom Atomic Power Station," U.S. Nuclear Regulatory Commission, Washington, DC, TBD 2016.

[10] SECY-12-0092, "State-of-the-Art Reactor Consequence Analyses – Recommendation for Limited Additional Analysis," U.S. Nuclear Regulatory Commission, Washington, DC, July 2012.

[11] U.S. Nuclear Regulatory Commission, "Proposed Closeout – Generic Safety Issue 189, 'Susceptibility of Ice Condenser and Mark III Containments to Early Failure from Hydrogen Combustion During a Severe Accident,'" Memorandum from Timothy J. McGinty, Director, Division of Safety Systems, Office of Nuclear Reactor Regulation to Edwin M. Hackett, Executive Director, Advisory Committee for Reactor Safeguards, Washington, DC, January 31, 2013 (ML13008A376).

[12] NUREG-1150, "Severe Accident Risks: An Assessment for Five U.S. Nuclear Power Plants," U.S. Nuclear Regulatory Commission, Washington, DC, December 1990.

[13] NUREG/CR-4551, Vol. 5, Rev. 1, Part 1, "Evaluation of Severe Accident Risks: Sequoyah, Unit 1," U.S. Nuclear Regulatory Commission, Washington, DC, December 1990 (ML070540074).

[14] NUREG/CR-6042, Rev. 2, “Perspectives on Reactor Safety,” U.S. Nuclear Regulatory Commission, Washington, DC, March 2002.

[15] NUREG-1350, Vol. 27, “Information Digest, 2015-2016,” U.S. Nuclear Regulatory Commission, Washington, DC, December 2015.

[16] https://www.tva.gov/Newsroom/Watts-Bar-2-Project

[17] U.S. Nuclear Regulatory Commission, “State-of-the-Art Reactor Consequence Analyses Project: Uncertainty Analysis of the Unmitigated Short-Term Station Blackout of the Surry Power Station,” Draft Report. (ADAMS Accession No ML15224A001) 2016.

[18] NUREG/CR-5586, "Mitigation of Direct Containment Heating and Hydrogen Combustion Events in Ice Condenser Plants,” U.S. Nuclear Regulatory Commission, Washington, DC, October 1990.

[19] NUREG/CR-6533, “Code Manual for CONTAIN 2.0: A Computer Code for Nuclear Reactor Containment Analysis,” U.S. Nuclear Regulatory Commission, Washington, DC, December 1997.

[20] “MELCOR Computer Code Manuals, Vol. 1: Primer and Users’ Guide, Version 2.1.6840,” SAND 2015-6691 R, Sandia National Laboratories, August 2015 (ADAMS Accession No. ML15300A479).

[21] “MELCOR Computer Code Manuals, Vol. 2: Reference Manual, Version 2.1.6840,” SAND 2015-6692 R, Sandia National Laboratories, August 2015 (ADAMS Accession No. ML15300A473).

[22] Cardoni, J.A., “Radionuclide Inventory and Decay Heat Quantification Methodology for Severe Accident Simulations,” SAND2014-17667, Sandia National Laboratories, Albuquerque, NM, 2014.

[23] NUREG/CR-6427, “Assessment of the DCH Issue for Plants with Ice Condenser Containments,” U.S. Nuclear Regulatory Commission, Washington, DC, 1999.

[24] NUREG/CR-3653, “Final Report Containment Analysis Techniques A State-of-the-Art Summary,” Prepared by Ames Laboratory, U.S. Nuclear Regulatory Commission, Washington, DC, March 1984.

[25] NUREG/CR-5405, “Failure Due to Hypothetical Elevated-Temperature Pressurization of the Sequoyah Unit 1 Steel Containment Building,” U.S. Nuclear Regulatory Commission, Washington, DC, Prepared by Sandia National Laboratories, February 1990.

[26] NUREG/CR-4551, Vol. 5, Rev. 1, Part 1, “Evaluation of Severe Accident Risks: Sequoyah, Unit 1,” U.S. Nuclear Regulatory Commission, Washington, DC, Prepared by Sandia National Laboratories, December 1990.

[27] NUREG/CR-6706, “Capacity of Steel and Concrete Containment Vessels with Corrosion Damage,” U.S. Nuclear Regulatory Commission, Washington, DC, Prepared by Sandia National Laboratories, February 2001.

[28] NUREG/CR-6920, “Risk-Informed Assessment of Degraded Containment Vessels,” Prepared by Sandia National Laboratories, November 2006.

[29] NUREG-1150 Part II, “Severe Accident Risks: An Assessment for Five U.S. Nuclear Power Plants (Part II: Summary of Plant Results),” U.S. Nuclear Regulatory Commission, Washington, DC, December 1990.

[30] R. K. Kumar, “Flammability of Limits of Hydrogen-Oxygen-Diluent Mixtures,” Journal of Fire Sciences, Vol. 3, July/August 1985.

[31] NUREG/CR-2726, ““Light Water Reactor Hydrogen Manual,” U.S. Nuclear Regulatory Commission, Washington, DC, August 1983

[32] NUREG/CR-2486, “Final Results of the Hydrogen Igniter Experimental Program,” U.S. Nuclear Regulatory Commission, Washington, DC, February 1982.

[33] NUREG/CR-5582, “Lower Head Failure Experiments and Analysis,” U.S. Nuclear Regulatory Commission, Washington, DC, February 1999.

[34] M. T. Farmer et al., “Status and Future Direction of the Melt Attack and Coolability Experiments (MACE) Program at Argonne National Laboratory,” Proceedings 9th International Conference on Nuclear Engineering, Nice, France, April 8-12, 2001.

[35] M. Zhu and A. Lu, “The Counter-intuitive Non-informative Prior for the Bernoulli Family”, *Journal of Statistics Education*, 12:2, 2004.

[36] NUREG/CR-7037, “Industry Performance of Relief Valves at U.S. Commercial Nuclear Power Plants through 2007,” U.S. Nuclear Regulatory Commission, Washington, DC, March 2011.

[37] Hanniet-Girault, N. and G. Repetto, "PHEBUS FPT0 Final Report," Cadarache, France, 1998.

[38] Jacquemain, D., et al., "PHEBUS FPT1 Final Report," Cadarache, France, 2000.

[39] Gregoire, A.C., P. Chapelot, and G. Gregoire, "PHEBUS FPT4 Final Report," Cadarache, France, 2004.

[40] Gregoire, A.C., "PHEBUS FPT2 Final Report," Cadarache, France, 2008.

[41] Pavot, F., et. al., "PHEBUS FPT3 Final Report," Cadarache, France, 2010.

[42] Y. Pontillon, et al., “Lessons learnt from VERCORS tests. Study of the active role played by UO_2–ZrO_2–FP interactions on irradiated fuel collapse temperature,” Journal of Nuclear Materials 344, pp. 265–273 (2005).

[43] Helton, J.C. “Uncertainty and Sensitivity Analysis in the Presence of Stochastic and Subjective Uncertainty” Journal of Statistical Computation and Simulation 197; 57 (1-4): 3-76.

[44] Helton, J.C. Johnson, J.D, Oberkampf W.L. Sallaberry C.J. “Representation of Analysis Results Involving Aleatory and Epistemic Uncertainty” *Sandia Report SAND2008-4379* – Albuquerque, NM: Sandia National Laboratories 2008.

[45] Kasper, G., T. Niida, and M. Yang, “Measurements of viscous drag on cylinders and chains of sphere with aspect ratios between 2 and 50,” J. Aerosol Science, **16** (6), 535-556. Great Britain, 1985.

[46] Hinds, W. C., “Aerosol Technology.” Wiley, 1982.

[47] Brockmann, J. E., et al, Appendix F, “Uncertainty in Radionuclide Release Under Specific LWR Accident Conditions,” in “Range of Possible Dynamic and Collision Shape Factors,” Sandia National Laboratories, Albuquerque, New Mexico, SAND84-0410 Volume 2, 1985.

[48] Kissane, M.P., “On the nature of aerosols produced during a severe accident of a water-cooled nuclear reactor”, Nuclear Engineering and Design, 238, 2792-2800, 2008.

[49] J. Tills, “Hydrogen Control Calculations for the Sequoyah Plant – Reference and Uncertainty Calculations,” March 2003 (ADAMS Accession No. ML031700025).”

[50] Tennessee Valley Authority, “Sequoyah Emergency Preparedness,” Retrieved February 29, 2016 from https://www.tva.gov/Energy/Our-Power-System/Nuclear/Emergency-Preparedness/Sequoyah-Emergency-Preparedness, 2015.

[51] NUREG/CR-6525, Rev. 1, “SECPOP2000: Sector Population, Land Fraction, and Economic Estimation Program,” U.S. Nuclear Regulatory Commission, Washington, DC, 2003.

[52] U.S. Census Bureau, “Annual Estimates of the Resident Population: April 1, 2010 to July 1, 2014,” Washington, DC, March 2015.

[53] U.S. Department of Agriculture, National Agricultural Statistics Service, “CropScape – Cropland Data Layer,” Retrieved February 5, 2016 from https://nassgeodata.gmu.edu/CropScape/, 2015.

[54] Regulatory Guide 1.23, Rev.1, “Meteorological Monitoring Programs for Nuclear Power Plants,” U.S. Nuclear Regulatory Commission, Washington, DC, March 2007.

[55] NUREG/CR-6613, "Code Manual for MACCS2: Volume 1, User's Guide," U.S. Nuclear Regulatory Commission, Washington, DC, 1997.

[56] Regulatory Guide 1.145, “Atmospheric Dispersion Models for Potential Accident Consequence Assessments at Nuclear Power Plants,” U.S. Nuclear Regulatory Commission, Washington, DC, Reissued February, 1983.

[57] ARCADIS, “Evacuation Time Estimates for Sequoyah Nuclear Power Plant Plume Exposure Pathway Emergency Planning Zone,” (TM120006.0001), August, 2013.

[58] Tennessee Valley Authority, “Sequoyah Nuclear Plant – Units 1 & 2 – Emergency Plan Implementing Procedure Revision,” ADAMS Accession No. ML031120394, Chattanooga, TN, 2003.

[59] Storlie, C.B., et al., “Implementation and evaluation of nonparametric regression procedures for sensitivity analysis of computationally demanding models," Reliability Engineering & System Safety, 94(11): p. 1735-1763, 2009.

[60] Sobol, I. “Sensitivity Estimates for Nonlinear Mathematical Models.” Mathematical Modeling and Computational Experiment,” 1, 407-414. 1993.

[61] Helton, J.C., et al., “Survey of Sampling-based Methods for Uncertainty and Sensitivity Analysis," Reliability Engineering & System Safety, 91(10-11): p. 1175-1209, 2006.

[62] MELCOR Computer Code Manuals, Vol. 3: MELCOR Assessment Problems, Version 2.1.7347,” SAND 2015-6693 R, Sandia National Laboratories, August 2015 (ADAMS Accession No. ML15300A476).”

[63] NUREG/CR-6533, “Code Manual for CONTAIN 2.0: A Computer Code for Nuclear Reactor Containment Analysis,” U.S. Nuclear Regulatory Commission, Washington, DC, December 1997.

[64] Nuclear Regulatory Commission, Tills, J., Notafrancesco, A., and Murata, K., “An Assessment of CONTAIN 2.0: A Focus on Containment Thermal Hydraulics (Including Hydrogen Distributions),” SMSAB-02-02, (ML022140438). July 2002.

[65] Storlie, C.B. and J.C. Helton, "Multiple predictor smoothing methods for sensitivity analysis: Description of techniques," Reliability Engineering & System Safety, 93(1): p. 28-54, 2008.

[66] Efron B. and Tibshirani R.J., “An Introduction to the Bootstrap” Monographs on Statistics and Applied Probability 57 - Chapman & Hall/CRC – ISBN 0-412-04231-2, 1993.

[67] M. Zhu and A. Lu, “The Counter-intuitive Non-informative Prior for the Bernoulli Family”, *Journal of Statistics Education*, 12:2, 2004.

[68] NUREG/CR-6823, "Handbook of Parameter Estimation for Risk Assessment,” U.S. Nuclear Regulatory Commission, Washington, DC, 2003.

[69] R.O. Gauntt, N. Bixler, and K.C. Wagner, "An Uncertainty Analysis of the Hydrogen Source Term for a Station Blackout Accident in Sequoyah Using MELCOR 1.8.5 (Draft For Review)," Sandia National Laboratories, Albuquerque, NM, 2003.

[70] Wang X, Zhang L, Moran MD. “Uncertainty Assessment of Current Size-Resolved Parameterizations for Below-Cloud Particle Scavenging by Rain.” Atmospheric Chemistry and Physics 2010; 10(12): 5685-5705.

[71] Sportisse B. A “Review of Parameterizations for Modelling Dry Deposition and Scavenging of Radionuclides.” Atmospheric Environment 2007; 41(13): 2683-2698.

[72] Andronache C. “Estimated Variability of Below-Cloud Aerosol Removal by Rainfall for Observed Aerosol Size Distributions.” Atmospheric Chemistry and Physics 2003; 3(1): 131-143.

[73] Baklanov A, Sorensen JH. “Parameterisation of Radionuclide Deposition in Atmospheric Long-Range Transport Modelling.” Physics and Chemistry of the Earth, Part B: Hydrology, Oceans and Atmosphere 2001; 26(10): 787-799.

[74] NUREG/CR-6244, “Summary of Objectives, Approach, Application, and Results for the Dispersion and Deposition Uncertainty Assessment,” U.S. Nuclear Regulatory Commission, Washington, DC, 1994.

[75] Leadbetter SJ, Hort MC, Jones AR, Webster HN, Draxler RR. “Sensitivity of the Modelled Deposition of Caesium-137 from the Fukushima Dai-ichi Nuclear Power Plant to the Wet Deposition Parameterisation in NAME.” Journal of Environmental Radioactivity 2014; In press.

[76] Saito K, Shimbori T, Draxler R. “JMA's Regional Atmospheric Transport Model Calculations for the WMO Technical Task Team on Meteorological Analyses for Fukushima Daiichi Nuclear Power Plant Accident.” Journal of Environmental Radioactivity 2014; In press.

[77] Brenk HD, Vogt KJ. “The Calculation of Wet Deposition from Radioactive Plumes.” Nuclear Safety 1981; 22(3): 362-371.

[78] McMahon TA, Denison PJ. “Empirical Atmospheric Deposition Parameters: A Survey. Atmospheric Environment - Part A General Topics” 1979; 13(5): 571-585.

[79] NUREG/CR-7161, Rev. 1, "Synthesis of Distributions Representing Important Non-Site-Specific Parameters in Off-Site Consequence Analysis," U.S. Nuclear Regulatory Commission, Washington, DC, 2013.

[80] NUREG/CR-4551, Vol. 2, Rev. 1, Part 7, “Evaluation of Severe Accident Risks: Quantification of Major Input Parameters,” U.S. Nuclear Regulatory Commission, Washington, DC, 1990.

[81] Gregory, J.J., et al., "Task 5 Letter Report: MACCS2 Uncertainty Analysis of EARLY Exposure Results," Sandia National Laboratories, Albuquerque, NM, September 2000.

[82] Eckerman, K., "Radiation Dose and Health Risk Estimation: Technical Basis for the State-of-the-Art Reactor Consequence Analysis (SOARCA) Project," Oak Ridge National Laboratory, Oak Ridge, TN, 2011.

[83] NUREG/CR-6526, “Probabilistic Accident Consequence Uncertainty Analysis, Uncertainty Assessment for Deposited Material and External Doses,” U.S. Nuclear Regulatory Commission, Washington, DC, December 1997.

[84] NUREG/CR-6953, Vol. I, "Review of NUREG-0654, Supplement 3, ‘Criteria for Protective Action Recommendations for Severe Accidents’," U.S. Nuclear Regulatory Commission, Washington, DC, December 2007.

[85] D.J. Pawel, Leggett, R.W., Eckerman, K.F., and Nelson C.B., “Uncertainties in Cancer Risk Coefficients for Environmental Exposure to Radionuclides,” ORNL/TM-2006/583, Oak Ridge National Laboratory, Oak Ridge, TN, 2007.

[86] NUREG/CR-6853, "Comparison of Average Transport and Dispersion Among a Gaussian, a Two-Dimensional, and a Three-Dimensional Model," U.S. Nuclear Regulatory Commission, Washington, DC, October 2004.

[87] International Atomic Energy Agency (IAEA), “Actions to Protect the Public in an Emergency due to Severe Conditions at a Light Water Reactor.” Emergency Preparedness and Response. Vienna, Austria. May, 2013.

[88] NUREG/CR-6864, “Identification and Analysis of Factors Affecting Emergency Evacuations,” U.S. Nuclear Regulatory Commission, Washington, DC, January 2005.

[89] U.S. Department of Labor, Bureau of Labor Statistics, “Consumer Price Index Research Series Using Current Methods (CPI-U-RS),” Washington, DC, August 2015.

[90] Mitchell, Jerry T., et al., “Evacuation behavior in response to the Graniteville, South Carolina, Chlorine Spill,” Quick Response Research Report 178. Boulder, CO: Natural Hazards Center, University of Colorado. 2005.

[91] Wolshon, Brian, J. Jones, and F. Walton. "The Evacuation Tail and Its Effect on Evacuation Decision Making," Journal of Emergency Management. January/February 2010, Volume 8, Number 1. 201.

[92] NUREG/CR-6953 Volume 2, “Review of NUREG-0654, Supplement 3, ‘Criteria for Protective Action Recommendations for Severe Accidents’ Focus Groups and Telephone Survey,” U.S. Nuclear Regulatory Commission, Washington, DC, October 2008.

[93] National Institute of Standards and Technology (NIST). “Performance of Structures During the Loma Prieta Earthquake of October 17, 1989.” U.S. Department of Commerce, Washington, DC, January 1990.

[94] Environmental Protection Agency, “PAG Manual Protective Action Guides and Planning Guidance for Radiological Incidents.” Draft for Interim Use and Public Comment. Washington D.C.: EPA. March 2013.

[95] Federal Emergency Management Agency, “Sequoyah Nuclear Power Plant After Action Report/Improvement Plan,” ADAMS Accession No. ML13085A038, Arlington, VA, January 2013.

[96] Wheeler, T., G. Wyss, and F. Harper, “Cassini Spacecraft Uncertinaty Analysis Data and Methodology Review and Update Volume 1: Updated Parameter Uncertinaty Models for the Consequence Analysis,” SAND2000-2719/1, Sandia National Laboratories, Albuquerque, NM, 2000.

[97] U.S. Nuclear Regulatory Commission, “Update of MACCS Cost Parameters Related to Protective Measures and Decontamination,” ADAMS Accession No. ML15288A523, Draft Report, Washington, DC, 2015

[98] Environmental Protection Agency, “Cancer Risk Coefficients for Environmental Exposure to Radionuclides,” Federal Guidance Report 13, EPA 402-C-99-001, Washington, DC, 2002.

[99] National Council on Radiation Protection & Measurements, Report No. 160, “Ionizing Radiation Exposure of the Population of the United States,” ISBN 978-0-929600-98-7, Bethesda, MD, 2009.

[100] Health Physcis Society, “Radiation Risk in Perspective: Position Statement of the Health Physics Society,” PS010-2, McLean, VA, 2010.

[101] National Academy of Sciences, “Health Effects of Exposure to Low Levels of Ionizing Radiation: BEIR V,” National Research Council, National Academy Press, Washington, DC, 1990.

[102] National Academy of Sciences, “Health Effects of Exposure to Low Levels of Ionizing Radiation: BEIR VII,” National Research Council, National Academy Press, Washington, DC, 2006.

[103] NUREG/CR-7002, “Criteria for Development of Evacuation Time Estimate Studies.” Washington, DC.: NRC. November 2011.

[104] NUREG/CR-6981, “Assessment of Emergency Response Planning and Implementation for Large Scale Evacuations,” U.S. Nuclear Regulatory Commission, Washington, DC, October 2008.

[105] Dow, Kirstin and S. Cutter. “Emerging Hurricane Evacuation Issues: Hurricane Floyd and South Carolina,” Natural Hazards Review, February 2002.

[106] Fu, Haoqiang and C. Wilmot. “A Sequential Logit Dynamic Travel Demand Model for Hurricane Evacuation.” Transportation Research Board 2004 Annual Meeting. Washington DC, January 2004.

[107] 51 FR 30028, “Safety Goals for the Operation of Nuclear Power Plants,” U.S. Nuclear Regulatory Commission, Washington, DC, August 1986

[108] NUREG/CR-4691. Vol. 2. “MELCOR Accident Consequence Code System (MACCS) Model Description,” U.S. Nuclear Regulatory Commission, Washington, DC, February 1990.

[109] Hanna, Steve, and R. Britter, “Wind Flow and Vapor Cloud Dispersion at Industrial and Urban Sites,” Center for Chemical Process Safety of the American Institute of Chemical Engineers, New York, NY, 2002

APPENDIX A UNCERTAINTY QUANTIFICATION AND PROPAGATION

UNCERTAINTY QUANTIFICATION AND PROPOGATION

A.1 INTRODUCTION

The assessment on the influence of the uncertainties relative to key input parameters on the potential consequences follows a single accident at the Sequoyah power plant. The inclusion of uncertainty is an inherent part of any risk analysis of complex systems. The approach chosen for this Sequoyah analysis is based on the methodologies used for the Peach Bottom and Surry UAs [1][2], with some changes implemented based on the lessons learned.

A.1.1 Uncertainty Type

When analyzing a complex system, it is useful to classify the uncertainty under consideration into aleatory uncertainty and epistemic uncertainty. Aleatory (or stochastic) uncertainty refers to the (apparent) inherent randomness in the properties or behavior of the system. This uncertainty is considered to be irreducible and is usually represented via a probability distribution. In classical risk analysis, the consideration of this type of uncertainty will lead to a determination of the risk associated with each output.

Epistemic uncertainty derives from the lack of knowledge about a poorly known, but usually fixed, quantity (or at least a quantity that has a fixed representative value in the context of the analysis). This type of uncertainty is usually reducible by increasing the knowledge about the parameter under consideration. In risk analysis, epistemic uncertainty represents the uncertainty over the risk. The use of a probabilistic framework to characterize lack of knowledge uncertainty is not necessarily the best approach. Over several decades, several mathematical structures were developed to better represent this uncertainty type [3][4]. However, these methods are computationally intensive and lack the clarity of a simple probabilistic approach. Therefore, in this study, epistemic uncertainty is determined by the classical probabilistic approach.

The main reason to separate uncertainty according to these two types is that it brings more insight to decision making. Estimates are made regarding which part of the uncertainty is irreducible and needs to be considered, and which part can be reduced with further study. Regression analyses are used to determine which inputs, amongst those that are uncertain, are driving the output uncertainty, i.e., where to focus future work.

The analysis of complex systems typically requires answering the following four questions:

1. What can happen?
2. How likely it is to happen?
3. What are the consequences if it happens?
4. What is the confidence level in the answers to the first three questions?

The first three questions are referred to as the Kaplan-Garrick ordered triplet [5]. The separation of uncertainty with respect to aleatory and epistemic classifications allows for the definition of a formal mathematical framework in which aleatory uncertainty is used to answer the first two questions (as they deal with randomness in future events and the conditions at the time of the event that may affect the consequences). The third question is answered by the models, which estimate (deterministically) the consequence, given a fixed set of inputs. Epistemic uncertainty answers the fourth (as confidence increases with the state of knowledge that directly depends on epistemic uncertainty).

While it is desirable to keep a separation between epistemic and aleatory uncertainty, this is not always possible in practice. First, the separation requires a simulation to include two embedded loops (see Appendix A Section A.1.3). If high accuracy is necessary for both loops, the number of realizations may quickly become prohibitive. Second, while the definitions of aleatory and epistemic uncertainties are quite unambiguous, the characterization may be much more complex. It is not uncommon to find both an aleatory and an epistemic component in the uncertainty associated with a given input. Finally, some software does not allow for such separation.

When the separation of aleatory and epistemic uncertainty is not feasible, the analysis of the results can still provide a great deal of insight. In the present analysis, when such a separation is not practical, the uncertainty will be represented as epistemic. This decision is driven by the fact that regression analysis (see Section A.2.2) may be applied to epistemically uncertain inputs. Note that it is still possible, once the regression analysis is performed, to separate the inputs into two groups in order to partly estimate how much of the total uncertainty is considered random and how much derives from a lack of knowledge.

A.1.2 Uncertainty Characterization

Each input that is considered uncertain in this analysis has its uncertainty represented with a probability distribution. The process through which the parameters are selected, and the associated uncertainty is represented, (via a probability distribution) is a crucial part of any probabilistic analysis as the results will be strongly affected by the choice. The uncertainty related to each parameter is unique and specific to that parameter. The methodology developed to build the uncertainty distributions can be summarized as follows:

- Data and information was gathered and categorized based on relevance and reliability. For instance, observations and measurements were given more credit to elicitation. In the same spirit, data associated with the same mechanism or from Sequoyah data were considered more representative than proxies.

- Depending on the amount of data available, an appropriate selection of distribution representation was selected. The choice varied from simple distribution fitting when enough observations were available, to Bayesian updating, and to expert elicitation or judgment when no data was available.

- Consequent effort was made to document the rationale and assumptions to demonstrate the depth of the technical basis and because the results are interpreted conditionally upon those assumptions.

A.1.3 Uncertainty propagation for source term and consequence analysis

Monte Carlo methods were developed in the late 1940's [6] as an answer to a specific problem: how can a function of a large number of inputs be estimated numerically. The problem of dimensionality quickly led to an impractical number of runs. The Monte Carlo technique consists of covering the input space by randomly sampling a value in that input space. A dense coverage insures that the approximation of the function is close enough to reality so that the appropriate conclusion can be reached. Demonstrations showed that the Monte Carlo approach will

converge to the true solution as the sample size increases. Thus, the method essentially reduces a multidimensional integral (one dimension per variable) into a mono-dimensional one. The Monte Carlo method is the core of any sampling based approach, notably when the input space represents uncertainty with respect to the system. The original Monte Carlo method is characterized by sampling randomly in each direction, and is sometimes called Simple Random Sampling (SRS).

Latin Hypercube Sampling (LHS), developed in the 1970's [7] improves the Monte Carlo technique by stratifying each distribution in order to insure a dense coverage in each direction of the input space. LHS reduces the variance in each estimate without introducing a bias [8]. One limitation of LHS is that the stratification requires the sample size under consideration to be known at the beginning of the analysis. An additional limitation of this method is that a Latin Hypercube sample cannot be cut into parts because the location of any point is dependent on all other points.

These two limitations of the LHS application preclude its use in the present context. MELCOR is a complex code that requires a change in the time-stepping or discretization for a realization to reach convergence. Some of these refinements are so demanding that they are computationally impractical. Previous uncertainly analyses [1][2] showed that rejecting some of the realizations due to a lack of convergence did not invalidate the coverage of the input space and did not bias the results toward a specific region. Such an analysis is once again necessary considering that it is not possible to have convergence for all realizations. However, the cost of the removal of these non-convergent realizations is that the use of LHS is not recommended and the SRS technique was used. MACCS is not affected by the same problem and each realization leads to a convergent result. Nevertheless, in order to maintain a consistent approach (and mainly in order to use bootstrapping to support stability analysis as will be explained in Section A.2.3) the SRS technique was also used for the MACCS analysis.

The traditional method utilized to distinguish between aleatory and epistemic uncertainty is to use an inner loop for aleatory uncertainty and an outer loop for epistemic. The order of the loops could be reversed in theory, but a preference towards an inner aleatory loop and an outer epistemic loop is derived from what each uncertainty type represents. Aleatory uncertainty associated in the context of risk analysis is perceived intuitively as a probability and is represented as a summary statistic (e.g., mean or median) or a distribution. For a given epistemic set (i.e., for a specific value in the outer loop), risk can be represented conditionally on the assumption that one would have perfect knowledge about the value of the parameter. Epistemic uncertainty is then represented as a distribution on the representative value (e.g., mean or median) or a set of distributions showing confidence in the results given the current state of knowledge. The MACCS code was developed with this strategy in mind, and thus distinguishes between random inputs (mostly weather conditions) and epistemically uncertain inputs. This distinction is preserved and the outputs of interest (latent cancer fatality and prompt fatality at various locations or areas) are estimated as averages (i.e., probabilities).

The MELCOR uncertainty engine considers only one loop and does not allow the separation between aleatory and epistemic uncertainty. The choice is to consider all uncertainties as potentially reducible and therefore epistemic. The distinction between epistemic and aleatory uncertainty can then be done partially at the regression analysis level.

A.2 ANALYZING UNCERTAINTY RESULTS

In the last step of a probabilistic approach, results are statistically analyzed (via uncertainty analysis) and the influence of input parameter uncertainty over the variance of each output under consideration is assessed (via regression analysis). Such analyses help to draw insights with respect to the results. Many techniques have been developed to perform such analyses, several of which are presented in Storlie et al. [9].

A.2.1 Uncertainty Analysis

Uncertainty analysis usually refers to the determination of the uncertainty in the output of interest that derives from the uncertainty in the inputs. Its main purpose is to assess the extent of uncertainty in the results of interest given the uncertainty in the overall system. When a sampling-based approach is used to propagate uncertainty, a sample is generated for each output under consideration. Uncertainty analysis thus corresponds to a statistical analysis of the results of interest.

Graphical representations such as probability density functions (PDF) and cumulative or complementary cumulative distribution functions (CDF and CCDF) are usually used to visualize the extent of the uncertainty under consideration. Statistical measures such as moments (mean, standard deviations) and quantiles (e.g., median, 5th and 95th percentile) are used to summarize the distributions in a more quantitative way.

A.2.2 Regression Analysis

The purpose of the regression analysis was to determine the contributions of individual uncertain inputs to the uncertainty of the analysis results. Several techniques can be used to estimate the influence of each uncertain input on the output uncertainty. Some methods are qualitative while some are more quantitative and can assess the importance of each input relative to the others with respect to uncertainty [11].

The four regression techniques applied in the Peach Bottom and Surry UAs [1][2] were also applied in this analysis to assess quantitatively the importance of uncertain inputs. The results of these four regressions are presented showing the influence of the uncertainty of each input parameter according to each of the techniques. The conclusions of these techniques are supported by the qualitative graphical representations of the relations using scatterplots.

Rank regression, quadratic regression, recursive partitioning, and multivariate adaptive regression splines (MARS) were the four selected regression techniques used in this analysis to estimate the importance of the input parameters on the uncertainty of the outputs. The use of a set of regressions, instead of a single technique, was demonstrated beneficial in the previous analyses [1][2] and was motivated by the fact that there is no perfect regression approach capable of capturing all possible relationships from a given sample. Some regression techniques (such as linear regression) have the advantage of being robust (in the sense that they won't overfit the model and lead to higher artificial R^2 values) but are unable to capture any complex relationship (nonlinear and non-monotonic influences, conjoint influences). Other techniques are more flexible, but may still include some assumptions on the nature of the relationship. Furthermore, such techniques can be less robust and might give importance to spurious relations. In particular, techniques considering conjoint influence can be used to

quickly examine so many possibilities that they find a combination that appears to drive the uncertainty of the output of interest when this is not the case.

Using a suite of regression techniques allows for better coverage of potential relations between input uncertainty and output uncertainty, while also increasing the confidence that an influence is not spurious if it is captured by multiple regressions. The results of each regression were studied by experts in the physical phenomenon under simulation to confirm that the regression results were expected in the physical sense based on the variation of the related input values. Although the use of multiple regression techniques leads to a more complex interpretation of the results, it was considered a necessary step since the application of a single regression technique could lead to a misinterpretation and erroneous conclusions. A short description of each selected technique follows, and more detailed description of the techniques can be found in [12] and [3].

Rank regression

The rank regression technique uses a rank transformation over the input and output variables under consideration. The smallest value of a variable is given a rank of one, the next a rank of two, and so on up to the largest value having a rank of *n* (i.e. sample size). A stepwise linear regression is then applied to the rank-transformed data. The model is linear and additive and is shown in the following form:

$$Y = a_0 + a_1X_1 + a_2X_2 + \cdots + a_nX_n + \varepsilon = a_0 + \sum_{i=1}^{n} a_iX_i + \varepsilon$$

Eq. A-1

Where ε represents (for this regression and the subsequent ones) the amount of uncertainty not explained by the model.

The stepwise approach starts with trying to find the best fit with only one parameter and testing all possible input parameters. It then builds up from this initial fit by selecting the best fit with two parameters, conditional upon keeping the first parameter, and so on. An alpha value, representing the probability for each input effect to be spurious, is selected as a stopping criterion. The default value is set to approximately 15 percent, which means that if there is a 15 percent chance (or more) for the variable to be spurious, it is not included. Rank regression is effective in capturing monotonic relationships between inputs and outputs. The non-parametric aspect makes it less sensitive to outliers. This technique is limited to additive models where no conjoint influences are considered and may perform poorly on non-monotonic relationships.

Three metrics are included for each input variable used to display rank regression results. Two are based on the coefficient of determination, noted conventionally R^2, which represents the amount of variance explained by the regression model. The coefficient of determination is a normalized value which varies between 0 (no variance explained) and 1 (all the variance explained).

- R^2_{inc} gives the cumulative coefficient of determination of the rank regression model when the i^{th} variable has been added (that includes all variables up to the i^{th} for the model).

- R^2_{cont} gives the gain in R^2 when the i^{th} variable has been added compared to the model with $(i-1)$ variables. It is a good indicator of the contribution of this specific variable in explaining the variance of the output in consideration.

- Finally, standardized rank regression coefficients (SRRC) display the rank regression coefficients after they have been standardized to take out the unit influence. The rank regression coefficient is an indication of the strength of the influence. An absolute value close to zero means that the parameter does not have an influence, while an absolute value of one represents a very strong influence. The rank regression coefficient also indicates the positive or negative direction of the influence of this input variable on the considered output. A negative sign represents negative influence in which high values of the input lead to low values of the output and low values of the input lead to high values of the output. A positive sign represents positive influence where high values of input lead to high values of the output and low values of the input lead to low values of the output.

Quadratic regression, recursive partitioning, and MARS techniques

The three additional regression techniques considered (i.e. quadratic regression, recursive partitioning and MARS) are treated differently, as their models do not allow for a direct estimate of the contribution to each individual input to the variance of the output. For each of these models a coefficient of determination (R^2) is estimated and can be used as an indicator of how the regression performed. Once the regression model is available, it can be used to generate a large number of realizations via a variance decomposition technique known as the Sobol decomposition. The Sobol decomposition is a technique that can estimate the contribution of each input and their potential interactions (i.e., conjoint influence) via an integral decomposition of the variance [9]. However, this technique requires a large number of realizations (tens of thousands) to be accurate enough (within a few percentages) and cannot usually be applied directly. However, the regression techniques described below lead to analytical models that can quickly be run a large number of times (over the course of seconds to minutes). Once the Sobol decomposition is applied, the importance of each variable (according to its uncertainty) can be assessed given the regression model. The answer is thus strongly dependent on the quality of the regression model and caution should be applied when the R^2 value is relatively low. In some situations a regression technique (most likely the recursive partitioning) may over-fit and lead to an artificially high R^2. In such case, scatterplots are relied on to confirm whether there is indeed a relation or not.

The Sobol decomposition leads to different metrics than those used in stepwise linear regression. The two metrics selected for this analysis are described below:

- S_i represents the first order sensitivity index and describes how much of the variance of the selected output is explained by the input parameter under consideration by itself (i.e., without conjoint influence). This index therefore estimates the same quantity as R^2_{cont} for the rank regression technique and it is acceptable to compare these two metrics.

- The second metric, labeled T_i , represents the total order sensitivity index and estimates how much of the variance of the selected output is explained by the input parameter alone plus its interaction with the other uncertain parameters (i.e., conjoint influence). It has no analogue in the rank regression model as the additive model does not capture

conjoint influences. The difference between T_i and S_i provides an estimate of the conjoint influence for a single input on the output considered.

Quadratic regression

Quadratic regression techniques apply the same approach as linear regression, including individual input variables, the square of these variables, and second order multiplicative interaction terms. The prediction model is of the form:

$$Y = a_0 + \sum_{i=1}^{n} a_i X_i + \sum_{i=1}^{n} b_i X_i^2 + \sum_{i=1}^{n} \sum_{j=i+1}^{n} c_i X_i X_j + \varepsilon$$

Eq. A-2

Quadratic regression is not solely additive as it can capture second order interactions. It can also capture the parabolic influence measured by the square of variables in the regression model. However, a complex relationship between variables and the output, like asymptotic behavior, may still be hard to capture with this technique and the method remains parametric, making it sensitive to outliers.

Recursive partitioning

Recursive partitioning regression, also known as a regression tree, is a regression method that captures conjoint influences. A regression tree splits the data into subgroups in which the values are relatively homogeneous. The regression function is constructed using the sample mean of each subgroup. This approach results in a piecewise constant function over the input space under consideration. The predictive model is:

$$Y = \sum_{s=1}^{nP} (d_s I_s(X_i))_{i=1,\ldots,n} + \varepsilon$$

Eq. A-3

Recursive partitioning is well adapted to the present study as it strives to capture the effect of thresholds (e.g., a low value for one parameter and a high value for another parameter, or when a certain parameter reaches a threshold value). MELCOR includes many such threshold conditions to initiate some events or processes. One of the drawbacks of this regression is that it considers so many potential relations that it tends to over-fit by capturing spurious correlations. Consequently, checking the relations only found by this regression using scatterplots is recommended and was completed.

Multivariate Adaptive Regression Splines (MARS)

MARS is a combination of (linear) spline regression, stepwise model fitting and recursive partitioning. A regression with a single input starts with a mean-only model and adds basis functions in a stepwise manner while adding the overall linear trend first. A second model using linear regression via least squares is fit to the data. This model is then added to the basis functions in a way that reduces the sum of square error (SSE) between the observations and predictions. A fourth basis function is then added to minimize the SSE again. This process is repeated until *M* (set by default at 200) basis functions have been added.

At this point, the MARS procedure will try to simplify the model using stepwise deletion of basis functions while keeping the y-intercept and linear trend. The $M-2$ candidate leading to the smallest increase of SSE will be selected. This deletion will be applied until regressed to the original linear model.

Stepwise addition and deletion leads to the creation of two different $M-2$ models. The "best" model is chosen using a generalized cross validation score which corresponds to a SSE normalized by the number of basis functions considered. With multiple inputs, the basis functions will consider main effects and multiple-way interactions. The options used for this analysis consider only two-way interactions to avoid the exponential cost of considering more interactions.

MARS usually leads to similar results as linear regression with a greater accuracy, and with the inclusion of non-monotonic effects and conjoint influences. However, it performs poorly with discrete inputs due to the use of splines.

Ranking the variables according to the four regression techniques

A consequence of the use of multiple regressions is that the ranking of the inputs amongst themselves is not obvious when the different regressions disagree. A qualitative approach has been used in the past [1] based on the physics considered in the problem and expert knowledge, but such an approach introduces some subjectivity and is hard to document. A more quantitative approach was implemented for the SOARCA Surry Uncertainty Analysis [Reference 2] and again for the current analysis, due to a strong belief that such a quantitative ranking is only an indicator and should be supported by expert opinion based on the physics of the problem.

Two effects of the uncertainty in the input on the output of consideration are estimated in the present study. The main effect represents the influence of the uncertain input by itself and is estimated with R^2_{cont} in the stepwise regression and S_i for the other three regression techniques. Then the effect of the uncertain input from its interaction with other variables, which is ignored by the stepwise regression as it is an additive regression, is estimated with $T_i - S_i$ for the other three regressions.

The first effect of the uncertainty in the input was considered the most important, and a decision was made to rank the variables according to this main effect. Stepwise regression provides an estimate of the main effect for each variable directly. For the other regressions techniques, the real effect has to be adjusted by the goodness of fit of the model (i.e. the R^2 value from the regression model). In order to accomplish this, each S_i value is multiplied by the R^2 value of the regression model. Finally, if a variable is not included in a given regression, it is supposed that its main effect is null and the corresponding value is set to 0. The four resulting estimates are combined to create a weighted average, represented by:

$$\text{Main influence} = \frac{R^2_{cont} + \sum_{j=1}^{3} R^2_j . S_{i,j}}{4} \qquad \text{Eq. A-4}$$

where R^2_{cont} is from rank regression, j is the index of the three non-linear regression techniques, and R^2_j is the final R^2 for each non-linear technique.

The variables are then sorted according to this 'weighted average' approach in decreasing value, such that the most important variable is listed at the top of the array.

The conjoint influence is captured by estimating $T_i - S_i$ for each of the last three regressions, and adjusted using the R^2 value as a weight. The weighted average is taken again, represented by:

$$\text{Conjoint influence} = \frac{\sum_{j=1}^{3} R_j^2 * (T_{i,j} - S_{i,j})}{3} \qquad \text{Eq. A-5}$$

If the average value is greater than 0.1 (meaning 10 percent of the regression is explained via conjoint influence with this input), the T_i are emphasized to draw attention to a potential important conjoint influence. As the first order indices (i.e., S_i) and total order indices (i.e., T_i) are estimated numerically using a Sobol decomposition, they are approximations. If no conjoint influence is present, it may happen that T_i is estimated slightly lower than S_i. In such situations, the value of $(T_i - S_i)$ was set to 0. These two metrics are added to the summary tables for the four regression results, as an indicator on the importance of the input uncertainty onto the output uncertainty. This represents a best estimate of the input uncertainty influence toward the uncertainty of the output considered.

For the ease of reading the tables, highlighting is applied in the main contribution and conjoint contribution columns to identify the best estimate importance of each input parameters, based on the overall analysis. The cutoff for main contribution effect was set at 0.02, and the cutoff for conjoint effect was set at 0.1. The reason for a difference in the contribution effects is that conjoint contribution influence looks at a larger range of possible interactions (for instance, with 20 inputs variables, the main contribution looks at 20 potential relations while conjoint influence of 2 inputs looks at 190 potential relations) and is more likely to identify spurious correlations. Therefore, an approach that concentrates on the larger contribution was considered appropriate. The threshold values of 0.02 and 0.1 were selected based on the knowledge acquired during Peach Bottom UA [1] and the regressions tables for the present analysis, such that important parameters would be acknowledged and negligible influence would not be highlighted.

Testing for potential over-fitting

Recursive partitioning has a tendency to be more permissive and therefore to overfit. In other words, the regression technique may lead to an artificially high R^2. When only recursive partitioning (or any other technique) finds some strong relation, it is necessary to check for the validity of the relation found. An approach consists in creating a random output for each realization and checking on the result of the regression technique. Two uniform random variables are generated (one continuous and one discrete). The four regression techniques were then used with the same inputs to regress these random outputs. The results can infer whether the selected regression technique can be trusted or not. Tests have shown that recursive partitioning can usually lead to an R^2 of around 0.6 to 0.7 all the time, with mostly conjoint influence captured (no high S_i values, only high T_i values). As a result, for any set of regression leading to only T_i influence, the results of the regression are discarded in the description.

Scatterplots

The use of scatterplots is a qualitative yet powerful technique that completes the suite of regression techniques applied in this analysis. Scatterplots display a set of points, one per realization, whose coordinates correspond to the value of one selected input for the x-axis and of the output considered on the y-axis. It confirms graphically that the relation estimated by any of the regression techniques is indeed present and not spurious.

A.2.3 Stability Analysis

As with any numerical method, Monte Carlo techniques will lead to different levels of accuracy, depending notably on the sample size. The purpose of stability analysis is to assess this level of accuracy and determine if the sample size is big enough or if more realizations may be required.

The notion of stability is hard to capture quantitatively as it is inherently qualitative and often includes subjective judgments. While it can be expressed with a formal approach (for instance, it is not desirable for the confidence interval to be larger than a certain fraction of the standard deviation or a standard error), the ultimate criteria is whether there is enough confidence that the conclusion will not be affected by the accuracy of the Monte Carlo technique used. In order to address this, a decision was made to represent stability as a confidence interval around the statistics of interest and rely on the judgment of experts to conclude whether such an interval is acceptable within the context of this analysis instead of selecting an arbitrary cut-off.

The method selected to estimate these confidence intervals is a classical percentile bootstrap [13]. This method requires the generation of a new sample of the same size (with replacement) from the original output sample. The operation is then repeated a large number of times (1,000 iterations was used) to generate a set of possible output distributions. This leads to a distribution for each statistic (mean and quantiles in the present analysis). A 95 percent confidence interval using percentile bootstrap is obtained by looking at the location of the 2.5 percentile for the lower bound and 97.5 percentile for the upper bound for each of the statistics. A more complete description of the bootstrap technique can be found in [13].

One advantage of the SRS technique is that it is easy to increase the sample size, as any new realization can be added to the existing set. Furthermore, a subset of the sample is a valid sample of the original distribution, which is one of the required assumptions for the use of the bootstrap technique.

This property of SRS can also be used to determine an optimal sample size that will lead to an appropriate stable estimate of one output of interest (within the context of this analysis). Any output data can be split into n groups of samples of size $\frac{M}{n}$ (where M represents the initial sample size). Each sample can then be used to assess the quantity (or quantities) of interest. The operation can be repeated a large number of times by creating different combinations of values within each sample. This technique is equivalent to a bootstrap with the exception that each sample has a size representing a fraction of the initial sample size. With such approach, confidence intervals can be generated for different sample sizes and compared. Since the sample size controls the accuracy of the Monte Carlo techniques (much as grid size controls the spatial accuracy of any numerical method) this approach can be used to estimate when a sample size is big enough to lead to adequate stable results for the selected output of interest (e.g., statistics). Furthermore, if the desired accuracy is not met using the initial sample size,

such technique can be used to extrapolate a potential sample size that should meet the corresponding criterion.

Regression analysis of failed realizations

A certain number of MELCOR calculations fail to converge within a reasonable computational time for various reasons. An analysis is thus completed to determine whether there is a correlation between failed runs and having the realization set in a particular area of the input space. Such a situation would indicate that a particular value for one input (or combination of values for several inputs) would lead to failure, biasing the conclusion that could be drawn by only analyzing the successful runs.

In order to detect a potential relation between input uncertainty and failure, a regression analysis (using the four regressions techniques described above) can be performed, using an indicator function set to 0 when the realization failed to run to completion and 1 when it ran up to the end as the output of interest. These regression results were compared to similar analyses performed on a uniform discrete and a uniform continuous random variable. These regression results were used as a baseline to indicate the ability of the regression techniques to find a relationship between regions of the input space and an unrelated random variable. Similar results between the random variable analyses and the success indicator function analysis would therefore suggest that failed realizations are randomly distributed within the input space.

The regression comparison showed that slightly better models were fit to the realization success indicator than to either of the random outputs. However, none of the realization success indicator regressions resulted in models that suggest a relationship strong enough that it could not be due to random chance; while the regressions generated models, those models were weak. The only parameter indicated as important was priSVcycles, so further study was focused on this parameter.

To determine whether there is a significant relationship between priSVcycles and realization success, two techniques were employed. First the Pearson product-moment correlation coefficient was calculated between priSVcycles and the realization success parameter. The correlation between was approximately 0.20. This suggests a weak relationship between the two parameters. Secondly, separate empirical CDFs for those priSVcycles samples associated with realization success and those samples associated with realization failure were calculated and compared. If a certain range of priSVcycles determined realization success, we would expect the two empirical distributions to be significantly different. The CDFs were compared using a two-sample Kolmogorov-Smirnov test with $\alpha = 0.05$. The test was unable to distinguish between the two distributions, supporting the conclusion that there is not a significant dependence between a region of the sample space and realization success. In combination these tests suggest a small, but questionably significant relationship between priSVcycles and realization completion.

A.2.4 References

[1] NUREG/CR-**7155**, "State-of-the-Art Reactor Consequence Analyses Project, Uncertainty Analysis of the Unmitigated Long-Term Station Blackout of the Peach Bottom Atomic Power Station," U.S. Nuclear Regulatory Commission, Washington, DC, 2016.

[2] "State-of-the-Art Reactor Consequence Analyses Project, Uncertainty Analysis of the Unmitigated Short-Term Station Blackout of the Surry Power Station," Draft Report. ADAMS ML15224A001, U.S. Nuclear Regulatory Commission, Washington, DC, 2016.

[3] Helton, J.C. "Uncertainty and Sensitivity Analysis in the Presence of Stochastic and Subjective Uncertainty" *Journal of Statistical Computation and Simulation* 197; 57 (1-4): 3-76.

[4] Helton, J.C. Johnson, J.D, Oberkampf W.L. Sallaberry C.J. "Representation of Analysis Results Involving Aleatory and Epistemic Uncertainty" *Sandia Report SAND2008-4379* – Albuquerque, NM: Sandia National Laboratories 2008.

[5] Kaplan, S. and B.J. Garrick, "On the Quantitative Definition of Risk," Risk Analysis, 1(1): p. 11-27, 1981.

[6] Metropolis, N. and Ulam S., "The Monte Carlo Method" Journal of the American Statistical Association; 44(247):335-341, 1949.

[7] McKay, M.D., Beckman, R.J., and Conover, W.J., "A Comparison of Three Methods for Selecting Values of Input Variables in the Analysis of Output from a Computer Code" Technometrics 21(2): 239-245, 1979.

[8] Helton J.C. and Davis F.J., "Latin hypercube sampling and the propagation of uncertainty in analyses of complex systems" Reliability Engineering and System Safety 81 (1) 23-69, 2003.

[9] Storlie, C.B., et al., "Implementation and evaluation of nonparametric regression procedures for sensitivity analysis of computationally demanding models," Reliability Engineering & System Safety, 94(11): p. 1735-1763, 2009.

[10] Sobol', I. "Sensitivity Estimates for Nonlinear Mathematical Models." Mathematical Modeling and Computational Experiment," 1, 407-414. 1993.

[11] Helton, J.C., et al., "Survey of Sampling-based Methods for Uncertainty and Sensitivity Analysis," Reliability Engineering & System Safety, 91(10-11): p. 1175-1209, 2006.

[12] Storlie, C.B. and J.C. Helton, "Multiple predictor smoothing methods for sensitivity analysis: Description of techniques," Reliability Engineering & System Safety, 93(1): p. 28-54, 2008.

[13] Efron B. and Tibshirani R.J., "An Introduction to the Bootstrap" Monographs on Statistics and Applied Probability 57 - Chapman & Hall/CRC – ISBN 0-412-04231-2, 1993.

APPENDIX B INPUT PARAMETERS FOR CONSEQUENCE ANALYSIS

;

INPUT PARAMETERS FOR CONSEQUENCE ANALYSIS

The input parameters used for the Sequoyah SOARCA scenarios are shown in this appendix in tabular form. Table B-1 contains the more general ATMOS input parameters used for these scenarios. Table B-2 through Table B-4 contain specific inputs related to the source terms that were extracted from MELCOR results via the MELMACCS code. Table B-5 contains general EARLY input parameters. Table B-6 and Table B-7 contain parameters associated with the population distribution model that was used to treat emergency response. Table B-8 and Table B-9 contain the evacuation direction parameters. Table B-10 contains the CHRONC input parameters. Table B-11 contains the radionuclide inventory.

Table B-1 ATMOS input parameters used in the Sequoyah scenarios.

Variable	Description	STSBO Base Case	STSBO Early	LTSBO
APLFRC	Method of Applying Release Fraction	PARENT	PARENT	PARENT
BNDMXH	Boundary Weather Mixing Layer Height	966	966	966
BNDRAN	Boundary Weather Rain Rate	0	0	0
BNDWND	Boundary Wind Speed	1.66	1.66	1.66
BRKPNT	Breakpoint Time for Plume Meander	3600	3600	3600
BUILDH	Building Height for all Plume Segments	47.2	47.2	47.2
CORINV	Isotopic Inventory at Time of Reactor Shutdown	MELMACCS Data (See Table B-11)	MELMACCS Data (See Table B-11)	MELMACCS Data (See Table B-11)
CORSCA	Linear Scaling Factor on Core Inventory	1	1	1
CWASH1	Linear Coefficient for Washout	1.89E-05	1.89E-05	1.89E-05
CWASH2	Exponential Term for Washout	0.664	0.664	0.664
CYSIGA	Linear Coefficient for sigma-y			
	Stability Class A	0.7507	0.7507	0.7507
	Stability Class B	0.7507	0.7507	0.7507

Variable	Description	STSBO Base Case	STSBO Early	LTSBO
	Stability Class C	0.4063	0.4063	0.4063
	Stability Class D	0.2779	0.2779	0.2779
	Stability Class E	0.2158	0.2158	0.2158
	Stability Class F	0.2158	0.2158	0.2158
CYSIGB	Exponential Term for sigma-y			
	Stability Class A	0.866	0.866	0.866
	Stability Class B	0.866	0.866	0.866
	Stability Class C	0.865	0.865	0.865
	Stability Class D	0.881	0.881	0.881
	Stability Class E	0.866	0.866	0.866
	Stability Class F	0.866	0.866	0.866
CZSIGA	Linear Coefficient for sigma-z			
	Stability Class A	0.0361	0.0361	0.0361
	Stability Class B	0.0361	0.0361	0.0361
	Stability Class C	0.2036	0.2036	0.2036
	Stability Class D	0.2636	0.2636	0.2636
	Stability Class E	0.2463	0.2463	0.2463
	Stability Class F	0.2463	0.2463	0.2463
CZSIGB	Exponential Term for sigma-z			
	Stability Class A	1.277	1.277	1.277
	Stability Class B	1.277	1.277	1.277
	Stability Class C	0.859	0.859	0.859
	Stability Class D	0.751	0.751	0.751
	Stability Class E	0.619	0.619	0.619
	Stability Class F	0.619	0.619	0.619
DISPMD	Dispersion Model Flag	LRTIME	LRTIME	LRTIME
DRYDEP	Dry Deposition Flag	Xe = .FALSE. Other Groups = .TRUE.	Xe = .FALSE. Other Groups = .TRUE.	Xe = .FALSE. Other Groups = .TRUE.
ENDAT1	Control flag indicating only ATMOS is to be run	.FALSE.	.FALSE.	.FALSE.
GRPNAM	Names of the Chemical Classes (Used by WinMACCS)			
	Chemical Class 1	Xe	Xe	Xe

Variable	Description	STSBO Base Case	STSBO Early	LTSBO
	Chemical Class 2	Cs	Cs	Cs
	Chemical Class 3	Ba	Ba	Ba
	Chemical Class 4	I	I	I
	Chemical Class 5	Te	Te	Te
	Chemical Class 6	Ru	Ru	Ru
	Chemical Class 7	Mo	Mo	Mo
	Chemical Class 8	Ce	Ce	Ce
	Chemical Class 9	La	La	La
IBDSTB	Boundary Weather Stability Class Index	5	5	5
IDEBUG	Debug Switch for Extra Debugging Print	0	0	0
IGROUP	Definition of Radionuclide Group Numbers	1 = Xe	1 = Xe	1 = Xe
		2 = Cs	2 = Cs	2 = Cs
		3 = Ba	3 = Ba	3 = Ba
		4 = I	4 = I	4 = I
		5 = Te	5 = Te	5 = Te
		6 = Ru	6 = Ru	6 = Ru
IGROUP		7 = Mo	7 = Mo	7 = Mo
		8 = Ce	8 = Ce	8 = Ce
		9 = La	9 = La	9 = La
INWGHT	Number of Samples for Each Bin Used for Nonuniform Weather Bin Sampling			
	Bin 1	12	12	12
	Bin 2	12	12	12
	Bin 3	23	23	23
	Bin 4	145	145	145
	Bin 5	117	117	117
	Bin 6	64	64	64
	Bin 7	12	12	12
	Bin 8	0	0	0
	Bin 9	97	97	97
	Bin 10	117	117	117

Variable	Description	STSBO Base Case	STSBO Early	LTSBO
	Bin 11	25	25	25
	Bin 12	12	12	12
	Bin 13	83	83	83
	Bin 14	43	43	43
	Bin 15	12	12	12
	Bin 16	0	0	0
	Bin 17	42	42	42
	Bin 18	15	15	15
	Bin 19	18	18	18
	Bin 20	17	17	17
	Bin 21	15	15	15
	Bin 22	12	12	12
	Bin 23	12	12	12
	Bin 24	12	12	12
	Bin 25	12	12	12
	Bin 26	12	12	12
	Bin 27	12	12	12
	Bin 28	7	7	7
	Bin 29	12	12	12
	Bin 30	7	7	7
	Bin 31	7	7	7
	Bin 32	12	12	12
	Bin 33	8	8	8
	Bin 34	11	11	11
	Bin 35	7	7	7
	Bin 36	7	7	7
IRSEED	Seed for Random Number Generator	79	79	79
LATITU	Latitude of Power Plant	35˚ 13' 36"	35˚ 13' 36"	35˚ 13' 36"
LIMSPA	Last Interval for Measured Weather	28	28	28
LONGIT	Longitude of Power Plant	85˚ 5' 28"	85˚ 5' 28"	85˚ 5' 28"
MAXGRP	Number of Radionuclide Groups	9	9	9
MAXHGT	Flag for Mixing Height	DAY_AND_ NIGHT	DAY_AND_ NIGHT	DAY_AND_ NIGHT
MAXRIS	Selection of Risk Dominant Plume	20	1	8
METCOD	Meteorological Sampling Option Code	2	2	2
MNDMOD	Plume Meander	NEW	NEW	NEW

Variable	Description	STSBO Base Case	STSBO Early	LTSBO
	Model Flag			
NAMSTB	List of Pseudo stable Nuclides			
	Isotope 1	I-129	I-129	I-129
	Isotope 2	Xe-131m	Xe-131m	Xe-131m
	Isotope 3	Xe-133m	Xe-133m	Xe-133m
	Isotope 4	Cs-135	Cs-135	Cs-135
	Isotope 5	Sm-147	Sm-147	Sm-147
	Isotope 6	U-234	U-234	U-234
	Isotope 7	U-235	U-235	U-235
	Isotope 8	U-236	U-236	U-236
	Isotope 9	U-237	U-237	U-237
	Isotope 10	Np-237	Np-237	Np-237
	Isotope 11	Rb-87	Rb-87	Rb-87
	Isotope 12	Zr-93	Zr-93	Zr-93
	Isotope 13	Nb-93m	Nb-93m	Nb-93m
	Isotope 14	Nb-95m	Nb-95m	Nb-95m
	Isotope 15	Tc-99	Tc-99	Tc-99
	Isotope 16	Pm-147	Pm-147	Pm-147
NPSGRP	Number of Particle Size Groups	10	10	10
NRINTN	Number of Rain Intensity Breakpoints	3	3	3
NRNINT	Number of Rain Distance Intervals	5	5	5
NSBINS	Number of Weather Bins to Sample	36	36	36
NUCNAM	Radionuclide Names	MELMACCS Data (See Table B-11)	MELMACCS Data (See Table B-11)	MELMACCS Data (See Table B-11)
NUCOUT	Radionuclide Used in Dispersion Print	Cs-137	Cs-137	Cs-137
NUMCOR	Number of Compass Sectors in the Grid	64	64	64
NUMISO	Number of Radionuclides	69	69	69
NUMRAD	Number of Radial Spatial Intervals	29	29	29
NUMREL	Number of Released Plume Segments	40	72	56
NUMSTB	Number of Defined Pseudo	16	16	16

Variable	Description	STSBO Base Case	STSBO Early	LTSBO
	stable Radionuclides			
OALARM	Time to Reach General Emergency Conditions	0	0	0
PDELAY	Plume Release Times	MELMACCS Data (See Table B-2)	MELMACCS Data (See Table B-2)	MELMACCS Data (See Table B-2)
PLHEAT	Plume Heat Contents	MELMACCS Data (See Table B-2)	MELMACCS Data (See Table B-2)	MELMACCS Data (See Table B-2)
PLHITE	Plume Release Heights	MELMACCS Data (See Table B-2)	MELMACCS Data (See Table B-2)	MELMACCS Data (See Table B-2)
PLMDEN	Plume Mass Density	MELMACCS Data (See Table B-2)	MELMACCS Data (See Table B-2)	MELMACCS Data (See Table B-2)
PLMFLA	Plume Mass Flow Rate	MELMACCS Data (See Table B-2)	MELMACCS Data (See Table B-2)	MELMACCS Data (See Table B-2)
PLMMOD	Flag for Plume Rise Input Option	DENSITY	DENSITY	DENSITY
PLUDUR	Plume Segment Durations	MELMACCS Data (See Table B-2)	MELMACCS Data (See Table B-2)	MELMACCS Data (See Table B-2)
PSDIST	Particle Size Distribution by Group	MELMACCS Data (See Table B-3)	MELMACCS Data (See Table B-3)	MELMACCS Data (See Table B-3)
REFTIM	Plume Reference Time Point	0. for first 0.5 for subsequent	0. for first 0.5 for subsequent	0. for first 0.5 for subsequent
RELFRC	Release Fractions of the Source Term	MELMACCS Data (See Table B-4)	MELMACCS Data (See Table B-4)	MELMACCS Data (See Table B-4)
RNDSTS	Endpoints of Rain Distance Intervals			
	Interval 1	2.	2.	2.
	Interval 2	5.	5.	5.
	Interval 3	10.	10.	10.
	Interval 4	15.	15.	15.
	Interval 5	20.	20.	20.
RNRATE	Rain Intensity Breakpoints for Weather Binning			
	Intensity 1	2	2	2
	Intensity 2	4	4	4
	Intensity 3	6	6	6
SCLADP	Scaling Factor	1.0	1.0	1.0

Variable	Description	STSBO Base Case	STSBO Early	LTSBO
	for A-D Plume Rise			
SCLCRW	Scaling Factor for Critical Wind Speed	1.0	1.0	1.0
SCLEFP	Scaling Factor for E-F Plume Rise	1.0	1.0	1.0
SIGYINIT	Initial Sigma-y for All Plume Segments	9.4	9.4	9.4
SIGZINIT	Initial Sigma-z for All Plume Segments	22.2	22.2	22.2
SPAEND	Radial distances for grid boundaries			
	Ring 1	0.09997863	0.09997863	0.09997863
	Ring 2	0.3454824	0.3454824	0.3454824
	Ring 3	0.7499951	0.7499951	0.7499951
	Ring 4	0.9999727	0.9999727	0.9999727
	Ring 5	1.34502	1.34502	1.34502
	Ring 6	2.000007	2.000007	2.000007
	Ring 7	2.500025	2.500025	2.500025
	Ring 8	2.99998	2.99998	2.99998
	Ring 9	4.000015	4.000015	4.000015
	Ring 10	4.999988	4.999988	4.999988
	Ring 11	7.500012	7.500012	7.500012
	Ring 12	9.999975	9.999975	9.999975
	Ring 13	12.5	12.5	12.5
	Ring 14	15.00002	15.00002	15.00002
	Ring 15	20.00001	20.00001	20.00001
	Ring 16	25.	25.	25.
	Ring 17	29.99999	29.99999	29.99999
SPAEND	Ring 18	40.00003	40.00003	40.00003
	Ring 19	50.	50.	50.
	Ring 20	70.00002	70.00002	70.00002
	Ring 21	100.	100.	100.
	Ring 22	150.	150.	150.
	Ring 23	200.	200.	200.
	Ring 24	275.	275.	275.
	Ring 25	350.	350.	350.
	Ring 26	425.	425.	425.
	Ring 27	500	500	500
	Ring 28	750.0001	750.0001	750.0001
	Ring 29	1000	1000	1000
TIMBAS	Time Base for Plume	600	600	600

Variable	Description	STSBO Base Case	STSBO Early	LTSBO
	Expansion Factor			
VDEPOS	Dry Deposition Velocities			
	Aerosol Bin 1	5.0439E-04	5.0439E-04	5.0439E-04
	Aerosol Bin 2	4.629E-04	4.629E-04	4.629E-04
	Aerosol Bin 3	6.0644E-04	6.0644E-04	6.0644E-04
	Aerosol Bin 4	1.0224E-03	1.0224E-03	1.0224E-03
	Aerosol Bin 5	1.9999E-03	1.9999E-03	1.9999E-03
	Aerosol Bin 6	4.0915E-03	4.0915E-03	4.0915E-03
	Aerosol Bin 7	7.8925E-03	7.8925E-03	7.8925E-03
	Aerosol Bin 8	1.2941E-02	1.2941E-02	1.2941E-02
	Aerosol Bin 9	1.6024E-02	1.6024E-02	1.6024E-02
	Aerosol Bin 10	5.1507E-02	5.1507E-02	5.1507E-02
WETDEP	Wet Deposition Flag	Xe = .FALSE. Other groups = .TRUE.	Xe = .FALSE. Other groups = .TRUE.	Xe = .FALSE. Other groups = .TRUE.
XPFAC1	Base Time for Meander Expansion Factor	0.2	0.2	0.2
XPFAC2	Breakpoint for Expansion Factor Model	0.25	0.25	0.25
YSCALE	Scale Factor for Horizontal Dispersion	1	1	1
ZSCALE	Scale Factor for Vertical Dispersion	1.67	1.67	1.67

Table B-2 Plume parameters used in the Sequoyah LTSBO, STSBO Base Case, and STSBO Early scenarios.

SQN LTSBO						
Plume Segment	PDELAY (s)	PLHEAT (J/s)	PLHITE (m)	PLMDEN (kg/m^3)	PLMFLA (kg/s)	PLUDUR (s)
1	8.57E+04	1.039E+07	3.967E+01	8.484E-01	3.009E+00	3.7199E+03
2	8.57E+04	1.414E+07	0.000E+00	8.261E-01	3.904E+00	3.7199E+03
3	8.94E+04	3.007E+07	3.967E+01	1.044E+00	7.724E+00	3.4800E+03
4	9.29E+04	2.794E+07	3.967E+01	1.085E+00	6.688E+00	3.6000E+03
5	9.65E+04	2.498E+07	3.967E+01	1.099E+00	5.976E+00	3.7200E+03
6	1.00E+05	2.402E+07	3.967E+01	1.104E+00	5.796E+00	3.4801E+03
7	1.00E+05	7.042E+05	0.000E+00	1.100E+00	1.707E-01	3.4801E+03
8	1.04E+05	2.320E+07	3.967E+01	1.099E+00	5.855E+00	3.6000E+03
9	1.04E+05	2.416E+05	0.000E+00	1.100E+00	6.118E-02	3.6000E+03
10	1.07E+05	2.142E+07	3.967E+01	1.103E+00	5.510E+00	3.6000E+03
11	1.07E+05	1.033E+06	0.000E+00	1.103E+00	2.656E-01	3.6000E+03
12	1.11E+05	2.095E+07	3.967E+01	1.107E+00	5.367E+00	3.6080E+03
13	1.11E+05	9.867E+05	0.000E+00	1.106E+00	2.531E-01	3.6080E+03
14	1.14E+05	2.093E+07	3.967E+01	1.108E+00	5.317E+00	3.5920E+03
15	1.14E+05	8.951E+05	0.000E+00	1.108E+00	2.274E-01	3.5920E+03
16	1.18E+05	2.227E+07	3.967E+01	1.101E+00	6.038E+00	3.5999E+03
17	1.18E+05	1.238E+06	0.000E+00	1.103E+00	3.389E-01	3.5999E+03
18	1.22E+05	2.766E+07	3.967E+01	1.069E+00	7.520E+00	3.7200E+03
19	1.22E+05	9.766E+06	0.000E+00	1.002E+00	2.623E+00	1.4400E+03
20	1.25E+05	3.426E+07	3.967E+01	1.047E+00	9.102E+00	3.6000E+03
21	1.29E+05	3.813E+07	3.967E+01	1.033E+00	9.556E+00	3.6000E+03
22	1.33E+05	3.995E+07	3.967E+01	1.025E+00	9.842E+00	3.6000E+03
23	1.36E+05	4.107E+07	3.967E+01	1.017E+00	1.008E+01	3.6000E+03
24	1.40E+05	4.199E+07	3.967E+01	1.012E+00	1.025E+01	3.6000E+03
25	1.43E+05	4.261E+07	3.967E+01	1.008E+00	1.038E+01	3.4801E+03
26	1.47E+05	4.031E+07	3.967E+01	1.025E+00	9.659E+00	3.6000E+03
27	1.50E+05	3.953E+07	3.967E+01	1.032E+00	9.409E+00	3.6000E+03
28	1.54E+05	4.045E+07	3.967E+01	1.027E+00	9.650E+00	3.5999E+03
29	1.58E+05	4.207E+07	3.967E+01	1.013E+00	1.011E+01	3.6000E+03
30	1.61E+05	4.275E+07	3.967E+01	1.006E+00	1.031E+01	3.7200E+03
31	1.65E+05	4.264E+07	3.967E+01	1.008E+00	1.027E+01	3.4801E+03
32	1.68E+05	4.217E+07	3.967E+01	1.013E+00	1.012E+01	3.7199E+03
33	1.72E+05	4.206E+07	3.967E+01	1.015E+00	1.008E+01	3.6000E+03
34	1.76E+05	4.209E+07	3.967E+01	1.015E+00	1.008E+01	3.6000E+03
35	1.79E+05	4.246E+07	3.967E+01	1.013E+00	1.016E+01	3.6000E+03
36	1.83E+05	4.284E+07	3.967E+01	1.010E+00	1.026E+01	3.6000E+03
37	1.87E+05	4.177E+07	3.967E+01	1.019E+00	9.957E+00	3.6000E+03
38	1.90E+05	4.185E+07	3.967E+01	1.018E+00	9.969E+00	3.6000E+03
39	1.94E+05	4.200E+07	3.967E+01	1.017E+00	1.000E+01	3.6000E+03
40	1.97E+05	4.217E+07	3.967E+01	1.016E+00	1.004E+01	3.6000E+03
41	2.01E+05	4.232E+07	3.967E+01	1.015E+00	1.007E+01	3.6000E+03

SQN LTSBO						
Plume Segment	PDELAY (s)	PLHEAT (J/s)	PLHITE (m)	PLMDEN (kg/m^3)	PLMFLA (kg/s)	PLUDUR (s)
42	2.05E+05	4.247E+07	3.967E+01	1.014E+00	1.011E+01	3.6000E+03
43	2.08E+05	4.262E+07	3.967E+01	1.013E+00	1.014E+01	3.6000E+03
44	2.12E+05	4.276E+07	3.967E+01	1.013E+00	1.017E+01	3.6000E+03
45	2.15E+05	4.289E+07	3.967E+01	1.012E+00	1.020E+01	3.6000E+03
46	2.19E+05	4.302E+07	3.967E+01	1.011E+00	1.023E+01	3.6000E+03
47	2.23E+05	4.313E+07	3.967E+01	1.010E+00	1.025E+01	3.6000E+03
48	2.26E+05	4.325E+07	3.967E+01	1.009E+00	1.028E+01	3.6000E+03
49	2.30E+05	4.336E+07	3.967E+01	1.009E+00	1.031E+01	3.6000E+03
50	2.33E+05	4.346E+07	3.967E+01	1.008E+00	1.033E+01	3.6000E+03
51	2.37E+05	4.356E+07	3.967E+01	1.007E+00	1.035E+01	3.6000E+03
52	2.41E+05	4.366E+07	3.967E+01	1.007E+00	1.037E+01	3.6000E+03
53	2.44E+05	4.375E+07	3.967E+01	1.006E+00	1.039E+01	3.6000E+03
54	2.48E+05	4.384E+07	3.967E+01	1.005E+00	1.041E+01	3.6000E+03
55	2.51E+05	4.392E+07	3.967E+01	1.005E+00	1.043E+01	3.6000E+03
56	2.55E+05	4.399E+07	3.967E+01	1.004E+00	1.045E+01	3.6000E+03

SQN STSBO Base Case						
Plume Segment	PDELAY (s)	PLHEAT (J/s)	PLHITE (m)	PLMDEN (kg/m^3)	PLMFLA (kg/s)	PLUDUR (s)
1	1.42E+04	4.91E+04	0.00E+00	1.11E+00	1.21E-02	3.60E+03
2	1.78E+04	2.12E+04	3.97E+01	1.11E+00	5.25E-03	3.54E+03
3	1.78E+04	4.23E+04	0.00E+00	1.11E+00	1.05E-02	3.54E+03
4	2.14E+04	1.66E+04	3.97E+01	1.12E+00	4.10E-03	3.60E+03
5	2.14E+04	3.30E+04	0.00E+00	1.12E+00	8.16E-03	3.60E+03
6	2.50E+04	1.49E+04	3.97E+01	1.12E+00	3.68E-03	3.60E+03
7	2.50E+04	2.96E+04	0.00E+00	1.12E+00	7.33E-03	3.60E+03
8	2.86E+04	1.63E+04	3.97E+01	1.11E+00	4.03E-03	3.60E+03
9	2.86E+04	3.24E+04	0.00E+00	1.11E+00	8.01E-03	3.60E+03
10	3.22E+04	1.98E+04	3.97E+01	1.10E+00	4.90E-03	3.60E+03
11	3.22E+04	3.95E+04	0.00E+00	1.10E+00	9.75E-03	3.60E+03
12	3.58E+04	2.12E+04	3.97E+01	1.09E+00	5.23E-03	3.60E+03
13	3.58E+04	4.21E+04	0.00E+00	1.09E+00	1.04E-02	3.60E+03
14	3.94E+04	2.20E+04	3.97E+01	1.09E+00	5.44E-03	3.60E+03
15	3.94E+04	4.38E+04	0.00E+00	1.09E+00	1.08E-02	3.60E+03
16	4.30E+04	2.15E+04	3.97E+01	1.08E+00	5.30E-03	3.60E+03
17	4.30E+04	4.27E+04	0.00E+00	1.08E+00	1.05E-02	3.60E+03
18	4.66E+04	4.14E+04	0.00E+00	1.08E+00	1.02E-02	3.60E+03
19	5.02E+04	4.03E+04	0.00E+00	1.08E+00	9.93E-03	3.60E+03
20	1.87E+05	5.87E+07	3.97E+01	6.69E-01	1.88E+01	3.60E+03
21	1.87E+05	8.49E+07	0.00E+00	6.95E-01	2.62E+01	3.60E+03
22	1.91E+05	5.61E+07	3.97E+01	7.30E-01	1.63E+01	3.60E+03
23	1.94E+05	5.73E+07	3.97E+01	8.12E-01	1.54E+01	3.60E+03
24	1.98E+05	5.70E+07	3.97E+01	8.23E-01	1.52E+01	3.60E+03
25	2.02E+05	5.30E+07	3.97E+01	9.03E-01	1.32E+01	3.60E+03

SQN STSBO Base Case						
Plume Segment	PDELAY (s)	PLHEAT (J/s)	PLHITE (m)	PLMDEN (kg/m^3)	PLMFLA (kg/s)	PLUDUR (s)
26	2.05E+05	5.19E+07	3.97E+01	9.30E-01	1.27E+01	3.60E+03
27	2.09E+05	5.16E+07	3.97E+01	9.34E-01	1.26E+01	3.60E+03
28	2.12E+05	5.15E+07	3.97E+01	9.35E-01	1.25E+01	3.60E+03
29	2.16E+05	5.13E+07	3.97E+01	9.37E-01	1.25E+01	3.60E+03
30	2.20E+05	5.17E+07	3.97E+01	9.33E-01	1.26E+01	3.60E+03
31	2.23E+05	5.13E+07	3.97E+01	9.37E-01	1.25E+01	3.60E+03
32	2.27E+05	5.12E+07	3.97E+01	9.38E-01	1.25E+01	3.60E+03
33	2.30E+05	5.11E+07	3.97E+01	9.39E-01	1.25E+01	3.60E+03
34	2.34E+05	5.11E+07	3.97E+01	9.39E-01	1.25E+01	3.60E+03
35	2.38E+05	5.10E+07	3.97E+01	9.39E-01	1.25E+01	3.60E+03
36	2.41E+05	5.10E+07	3.97E+01	9.40E-01	1.25E+01	3.60E+03
37	2.45E+05	5.09E+07	3.97E+01	9.40E-01	1.24E+01	3.60E+03
38	2.48E+05	5.09E+07	3.97E+01	9.41E-01	1.24E+01	3.60E+03
39	2.52E+05	5.09E+07	3.97E+01	9.41E-01	1.24E+01	3.60E+03
40	2.56E+05	5.08E+07	3.97E+01	9.41E-01	1.24E+01	3.60E+03

SQN STSBO Early						
Plume Segment	PDELAY (s)	PLHEAT (J/s)	PLHITE (m)	PLMDEN (kg/m^3)	PLMFLA (kg/s)	PLUDUR (s)
1	1.28E+04	2.88E+07	3.97E+01	9.79E-01	7.59E+00	3.60E+03
2	1.28E+04	1.66E+07	0.00E+00	8.63E-01	4.46E+00	3.60E+03
3	1.64E+04	2.78E+07	3.97E+01	1.09E+00	6.69E+00	3.66E+03
4	2.01E+04	2.60E+07	3.97E+01	1.10E+00	6.22E+00	3.60E+03
5	2.37E+04	2.32E+07	3.97E+01	1.10E+00	5.54E+00	3.54E+03
6	2.72E+04	2.40E+07	3.97E+01	1.10E+00	5.83E+00	3.60E+03
7	2.72E+04	8.16E+05	0.00E+00	1.06E+00	1.95E-01	3.60E+03
8	3.08E+04	3.29E+07	3.97E+01	1.06E+00	8.40E+00	3.60E+03
9	3.08E+04	1.08E+07	0.00E+00	1.07E+00	2.72E+00	2.58E+03
10	3.44E+04	4.08E+07	3.97E+01	1.02E+00	1.02E+01	3.60E+03
11	3.80E+04	4.42E+07	3.97E+01	9.99E-01	1.09E+01	3.60E+03
12	4.16E+04	4.34E+07	3.97E+01	1.00E+00	1.06E+01	3.60E+03
13	4.52E+04	4.19E+07	3.97E+01	1.01E+00	1.01E+01	3.60E+03
14	4.88E+04	4.22E+07	3.97E+01	1.01E+00	1.02E+01	3.60E+03
15	5.24E+04	4.28E+07	3.97E+01	1.01E+00	1.03E+01	3.60E+03
16	5.60E+04	4.22E+07	3.97E+01	1.01E+00	1.01E+01	3.60E+03
17	5.96E+04	4.19E+07	3.97E+01	1.02E+00	1.00E+01	3.60E+03
18	6.32E+04	4.31E+07	3.97E+01	1.01E+00	1.03E+01	3.60E+03
19	6.68E+04	4.36E+07	3.97E+01	1.01E+00	1.04E+01	3.60E+03
20	7.04E+04	4.29E+07	3.97E+01	1.01E+00	1.03E+01	3.60E+03
21	7.40E+04	4.32E+07	3.97E+01	1.01E+00	1.03E+01	3.60E+03
22	7.76E+04	4.36E+07	3.97E+01	1.01E+00	1.04E+01	3.60E+03
23	8.12E+04	4.38E+07	3.97E+01	1.01E+00	1.05E+01	3.60E+03
24	8.48E+04	4.42E+07	3.97E+01	1.00E+00	1.05E+01	3.60E+03

SQN STSBO Early						
Plume Segment	PDELAY (s)	PLHEAT (J/s)	PLHITE (m)	PLMDEN (kg/m^3)	PLMFLA (kg/s)	PLUDUR (s)
25	8.84E+04	4.42E+07	3.97E+01	1.00E+00	1.05E+01	3.60E+03
26	9.20E+04	4.43E+07	3.97E+01	1.00E+00	1.06E+01	3.60E+03
27	9.56E+04	4.45E+07	3.97E+01	1.00E+00	1.06E+01	3.60E+03
28	9.92E+04	4.47E+07	3.97E+01	9.99E-01	1.07E+01	3.60E+03
29	1.03E+05	4.48E+07	3.97E+01	9.98E-01	1.07E+01	3.60E+03
30	1.06E+05	4.49E+07	3.97E+01	9.97E-01	1.07E+01	3.60E+03
31	1.10E+05	4.51E+07	3.97E+01	9.97E-01	1.07E+01	3.60E+03
32	1.14E+05	4.52E+07	3.97E+01	9.96E-01	1.08E+01	3.60E+03
33	1.17E+05	4.53E+07	3.97E+01	9.95E-01	1.08E+01	3.60E+03
34	1.21E+05	4.53E+07	3.97E+01	9.95E-01	1.08E+01	3.60E+03
35	1.24E+05	4.54E+07	3.97E+01	9.94E-01	1.08E+01	3.60E+03
36	1.28E+05	4.55E+07	3.97E+01	9.93E-01	1.08E+01	3.60E+03
37	1.32E+05	4.56E+07	3.97E+01	9.93E-01	1.09E+01	3.60E+03
38	1.35E+05	4.56E+07	3.97E+01	9.92E-01	1.09E+01	3.60E+03
39	1.39E+05	4.57E+07	3.97E+01	9.92E-01	1.09E+01	3.60E+03
40	1.42E+05	4.57E+07	3.97E+01	9.92E-01	1.09E+01	3.60E+03
41	1.46E+05	4.58E+07	3.97E+01	9.91E-01	1.09E+01	3.60E+03
42	1.50E+05	4.59E+07	3.97E+01	9.91E-01	1.09E+01	3.60E+03
43	1.53E+05	4.69E+07	3.97E+01	9.83E-01	1.12E+01	3.60E+03
44	1.57E+05	4.70E+07	3.97E+01	9.82E-01	1.12E+01	3.60E+03
45	1.60E+05	4.72E+07	3.97E+01	9.80E-01	1.13E+01	3.60E+03
46	1.64E+05	4.70E+07	3.97E+01	9.82E-01	1.12E+01	3.60E+03
47	1.68E+05	4.69E+07	3.97E+01	9.83E-01	1.12E+01	3.60E+03
48	1.71E+05	4.74E+07	3.97E+01	9.79E-01	1.13E+01	3.66E+03
49	1.75E+05	4.76E+07	3.97E+01	9.77E-01	1.14E+01	3.60E+03
50	1.79E+05	4.77E+07	3.97E+01	9.77E-01	1.14E+01	3.60E+03
51	1.82E+05	4.77E+07	3.97E+01	9.76E-01	1.14E+01	3.60E+03
52	1.86E+05	4.78E+07	3.97E+01	9.75E-01	1.14E+01	3.60E+03
53	1.89E+05	4.79E+07	3.97E+01	9.74E-01	1.14E+01	3.60E+03
54	1.93E+05	4.80E+07	3.97E+01	9.74E-01	1.15E+01	3.60E+03
55	1.97E+05	4.80E+07	3.97E+01	9.73E-01	1.15E+01	3.60E+03
56	2.00E+05	4.81E+07	3.97E+01	9.73E-01	1.15E+01	3.60E+03
57	2.04E+05	4.81E+07	3.97E+01	9.72E-01	1.15E+01	3.60E+03
58	2.07E+05	4.81E+07	3.97E+01	9.72E-01	1.15E+01	3.60E+03
59	2.11E+05	4.86E+07	3.97E+01	9.69E-01	1.16E+01	3.60E+03
60	2.15E+05	4.88E+07	3.97E+01	9.65E-01	1.17E+01	3.60E+03
61	2.18E+05	4.87E+07	3.97E+01	9.66E-01	1.17E+01	3.60E+03
62	2.22E+05	4.86E+07	3.97E+01	9.66E-01	1.17E+01	3.60E+03
63	2.25E+05	4.86E+07	3.97E+01	9.66E-01	1.17E+01	3.60E+03
64	2.29E+05	4.86E+07	3.97E+01	9.66E-01	1.17E+01	3.60E+03
65	2.33E+05	4.86E+07	3.97E+01	9.65E-01	1.17E+01	3.60E+03

SQN STSBO Early						
Plume Segment	PDELAY (s)	PLHEAT (J/s)	PLHITE (m)	PLMDEN (kg/m^3)	PLMFLA (kg/s)	PLUDUR (s)
66	2.36E+05	4.86E+07	3.97E+01	9.65E-01	1.18E+01	3.60E+03
67	2.40E+05	4.86E+07	3.97E+01	9.64E-01	1.18E+01	3.60E+03
68	2.43E+05	4.87E+07	3.97E+01	9.64E-01	1.18E+01	3.60E+03
69	2.47E+05	4.87E+07	3.97E+01	9.64E-01	1.18E+01	3.60E+03
70	2.51E+05	4.88E+07	3.97E+01	9.63E-01	1.18E+01	3.60E+03
71	2.54E+05	4.88E+07	3.97E+01	9.62E-01	1.18E+01	3.60E+03
72	2.58E+05	4.89E+07	3.97E+01	9.62E-01	1.19E+01	1.50E+03

Table B-3 Plume parameters used in the Sequoyah LTSBO, STSBO Base Case, and STSBO Early scenarios.

SQN LTSBO										
Class	**Bin 1**	**Bin 2**	**Bin 3**	**Bin 4**	**Bin 5**	**Bin 6**	**Bin 7**	**Bin 8**	**Bin 9**	**Bin 10**
Xe	1.00E-01	1.00E-01	1.00E-01	1.00E-01	1.00E-01	1.00E-01	1.00E-01	1.00E-01	1.00E-01	1.00E-01
Cs	1.94E-01	2.94E-02	5.27E-02	2.15E-01	2.97E-01	1.10E-01	5.75E-02	3.65E-02	7.60E-03	4.56E-04
Ba	2.51E-01	3.95E-02	1.39E-02	5.64E-02	1.02E-01	1.27E-01	2.05E-01	1.66E-01	3.69E-02	2.25E-03
I	1.06E-01	1.86E-02	5.48E-02	2.60E-01	3.98E-01	1.19E-01	2.59E-02	1.39E-02	2.86E-03	1.78E-04
Te	4.20E-02	1.11E-02	8.05E-02	3.44E-01	3.94E-01	9.68E-02	1.86E-02	1.03E-02	2.16E-03	1.30E-04
Ru	4.10E-01	6.67E-02	3.49E-03	9.77E-03	4.29E-02	1.05E-01	1.83E-01	1.46E-01	3.18E-02	1.93E-03
Mo	4.24E-01	5.41E-02	1.85E-02	4.85E-02	7.91E-02	1.13E-01	1.44E-01	9.77E-02	2.04E-02	1.21E-03
Ce	2.96E-01	4.57E-02	1.62E-03	5.42E-03	4.31E-02	1.28E-01	2.39E-01	1.95E-01	4.32E-02	2.63E-03
La	2.61E-01	3.92E-02	1.29E-02	4.46E-02	8.24E-02	1.28E-01	2.17E-01	1.74E-01	3.85E-02	2.34E-03

SQN STSBO Base Case										
Class	**Bin 1**	**Bin 2**	**Bin 3**	**Bin 4**	**Bin 5**	**Bin 6**	**Bin 7**	**Bin 8**	**Bin 9**	**Bin 10**
Xe	1.00E-01	1.00E-01	1.00E-01	1.00E-01	1.00E-01	1.00E-01	1.00E-01	1.00E-01	1.00E-01	1.00E-01
Cs	1.06E-01	2.07E-02	1.06E-01	3.83E-01	3.15E-01	5.84E-02	8.97E-03	2.11E-03	2.98E-04	2.38E-05
Ba	1.13E-01	2.40E-02	1.03E-01	3.14E-01	2.50E-01	1.27E-01	5.87E-02	9.55E-03	9.79E-04	8.21E-05
I	2.10E-01	4.73E-02	1.58E-01	3.20E-01	1.89E-01	5.62E-02	1.51E-02	3.61E-03	5.23E-04	4.68E-05
Te	1.36E-01	2.23E-02	7.07E-02	2.06E-01	1.92E-01	2.06E-01	1.37E-01	2.75E-02	1.80E-03	1.10E-04
Ru	1.85E-01	1.66E-02	7.03E-02	2.20E-01	2.03E-01	1.71E-01	1.08E-01	2.40E-02	2.04E-03	1.58E-04
Mo	2.55E-03	1.42E-03	1.50E-02	5.71E-02	1.69E-01	3.31E-01	2.79E-01	1.24E-01	2.04E-02	9.40E-04
Ce	1.10E-01	2.29E-02	9.03E-02	2.69E-01	2.30E-01	1.55E-01	9.52E-02	2.56E-02	2.91E-03	1.62E-04
La	1.04E-01	2.26E-02	9.13E-02	2.72E-01	2.32E-01	1.55E-01	9.54E-02	2.57E-02	2.91E-03	1.60E-04

SQN STSBO Early										
Class	**Bin 1**	**Bin 2**	**Bin 3**	**Bin 4**	**Bin 5**	**Bin 6**	**Bin 7**	**Bin 8**	**Bin 9**	**Bin 10**
Xe	1.00E-01	1.00E-01	1.00E-01	1.00E-01	1.00E-01	1.00E-01	1.00E-01	1.00E-01	1.00E-01	1.00E-01
Cs	8.98E-02	1.61E-02	6.86E-02	2.26E-01	2.95E-01	1.67E-01	7.11E-02	4.23E-02	2.10E-02	4.50E-03
Ba	3.57E-02	1.11E-02	3.78E-02	1.75E-01	3.16E-01	2.09E-01	9.79E-02	7.05E-02	3.96E-02	7.92E-03
I	8.90E-02	1.22E-02	4.71E-02	1.90E-01	3.27E-01	2.13E-01	7.33E-02	3.06E-02	1.47E-02	3.41E-03
Te	5.07E-02	6.46E-03	2.41E-02	1.38E-01	3.20E-01	2.96E-01	1.18E-01	3.24E-02	1.16E-02	2.47E-03
Ru	1.07E-01	2.59E-02	2.35E-02	5.27E-02	1.03E-01	1.44E-01	1.99E-01	2.06E-01	1.16E-01	2.32E-02
Mo	3.35E-03	1.68E-03	1.57E-02	5.11E-02	1.54E-01	3.43E-01	2.89E-01	1.22E-01	1.85E-02	8.96E-04
Ce	6.75E-02	2.47E-02	2.80E-02	7.59E-02	1.37E-01	1.53E-01	1.78E-01	1.95E-01	1.17E-01	2.36E-02
La	4.34E-02	9.74E-03	4.96E-02	2.15E-01	3.27E-01	1.95E-01	8.48E-02	4.84E-02	2.30E-02	4.28E-03

Table B-4 Release fraction parameters used in the Sequoyah LTSBO, STSBO Base Case, and STSBO Early scenarios.

SQN LTSBO									
Plume Segment	Xe	Cs	Ba	I	Te	Ru	Mo	Ce	La
1	1.345E-01	5.956E-04	5.350E-06	1.945E-03	4.638E-04	3.164E-06	6.541E-05	1.198E-10	1.890E-10
2	1.391E-01	5.276E-04	4.879E-06	1.837E-03	4.345E-04	2.542E-06	5.141E-05	9.824E-11	1.517E-10
3	1.326E-01	7.270E-04	6.198E-06	2.170E-03	5.129E-04	4.403E-06	9.454E-05	1.606E-10	2.596E-10
4	5.511E-03	3.165E-05	1.786E-07	8.271E-05	1.624E-05	1.360E-07	3.935E-06	4.661E-12	7.176E-12
5	7.876E-03	1.437E-04	9.613E-07	3.041E-04	1.189E-04	3.422E-07	1.569E-05	2.239E-11	2.192E-11
6	1.979E-02	4.069E-04	1.686E-05	8.615E-04	5.671E-04	8.022E-06	4.714E-05	2.028E-06	4.039E-08
7	8.360E-04	1.779E-05	4.160E-07	3.759E-05	2.574E-05	4.288E-07	2.117E-06	6.702E-09	1.464E-10
8	8.001E-02	1.874E-03	3.367E-03	3.661E-03	2.461E-03	5.810E-05	2.340E-04	6.771E-04	1.686E-05
9	8.235E-04	1.870E-05	3.842E-05	3.604E-05	2.378E-05	5.740E-07	2.395E-06	7.672E-06	1.950E-07
10	6.833E-02	1.068E-03	2.394E-03	1.838E-03	1.150E-03	2.927E-05	1.566E-04	4.708E-04	1.254E-05
11	3.265E-03	5.003E-05	1.111E-04	8.570E-05	5.357E-05	1.364E-06	7.370E-06	2.184E-05	5.827E-07
12	4.976E-02	5.956E-04	7.265E-04	8.274E-04	4.681E-04	9.711E-06	9.845E-05	1.418E-04	3.955E-06
13	2.410E-03	2.888E-05	3.662E-05	4.053E-05	2.309E-05	4.888E-07	4.748E-06	7.149E-06	1.989E-07
14	3.626E-02	4.666E-04	2.802E-04	5.836E-04	2.917E-04	3.796E-06	8.355E-05	5.442E-05	1.626E-06
15	1.549E-03	1.998E-05	1.197E-05	2.496E-05	1.249E-05	1.622E-07	3.576E-06	2.326E-06	6.950E-08
16	6.600E-02	9.692E-04	2.658E-04	1.233E-03	4.730E-04	3.611E-06	1.639E-04	5.125E-05	1.773E-06
17	4.009E-03	6.435E-05	1.793E-05	7.928E-05	3.162E-05	2.436E-07	1.094E-05	3.456E-06	1.185E-07
18	6.850E-02	6.516E-04	1.131E-04	1.221E-03	2.896E-04	1.629E-06	9.843E-05	2.184E-05	9.414E-07
19	9.442E-03	1.005E-04	1.845E-05	1.732E-04	4.506E-05	2.632E-07	1.557E-05	3.560E-06	1.500E-07
20	5.850E-02	4.014E-04	4.015E-05	1.160E-03	1.803E-04	6.252E-07	4.754E-05	7.799E-06	4.736E-07
21	2.636E-02	1.572E-04	9.173E-06	5.734E-04	8.828E-05	1.401E-07	1.358E-05	1.824E-06	2.013E-07
22	1.585E-02	9.278E-05	2.970E-06	3.693E-04	6.909E-05	4.147E-08	5.651E-06	6.513E-07	1.743E-07
23	1.258E-02	9.285E-05	1.653E-06	3.834E-04	8.222E-05	1.876E-08	3.923E-06	4.423E-07	2.302E-07
24	9.606E-03	1.181E-04	1.059E-06	4.311E-04	8.636E-05	8.993E-09	2.903E-06	3.412E-07	2.426E-07
25	7.480E-03	2.987E-04	7.544E-07	6.920E-04	9.121E-05	4.424E-09	2.218E-06	2.841E-07	2.386E-07
26	2.308E-03	2.472E-04	2.594E-07	5.131E-04	4.260E-05	9.459E-10	6.490E-07	8.789E-08	7.881E-08

SQN LTSBO									
Plume Segment	Xe	Cs	Ba	I	Te	Ru	Mo	Ce	La
27	8.984E-04	4.096E-04	3.260E-07	9.208E-04	7.157E-05	2.183E-10	2.642E-07	3.621E-08	3.454E-08
28	1.536E-03	1.124E-03	1.928E-06	4.437E-03	4.917E-04	2.474E-10	4.970E-07	6.822E-08	6.702E-08
29	3.474E-03	2.336E-03	8.354E-06	1.271E-02	2.276E-03	3.784E-10	1.168E-06	1.618E-07	1.613E-07
30	4.312E-03	2.366E-03	2.275E-05	1.519E-02	6.558E-03	3.347E-10	1.674E-06	2.249E-07	2.266E-07
31	3.506E-03	1.517E-03	3.364E-05	1.010E-02	9.989E-03	2.037E-10	1.656E-06	2.130E-07	2.157E-07
32	2.779E-03	9.217E-04	4.074E-05	6.010E-03	1.218E-02	1.310E-10	1.580E-06	2.051E-07	2.085E-07
33	2.228E-03	5.760E-04	4.365E-05	3.508E-03	1.154E-02	7.276E-11	1.423E-06	2.012E-07	2.048E-07
34	1.964E-03	4.141E-04	4.820E-05	2.324E-03	9.086E-03	4.366E-11	1.352E-06	2.100E-07	2.138E-07
35	1.918E-03	3.420E-04	5.964E-05	1.830E-03	7.053E-03	2.910E-11	1.442E-06	2.389E-07	2.436E-07
36	1.860E-03	3.205E-04	7.128E-05	1.662E-03	5.404E-03	2.910E-11	1.518E-06	2.596E-07	2.646E-07
37	9.388E-04	1.740E-04	4.601E-05	8.538E-04	2.031E-03	0.000E+00	8.512E-07	1.463E-07	1.493E-07
38	8.088E-04	1.609E-04	5.033E-05	7.015E-04	1.308E-03	1.455E-11	8.278E-07	1.388E-07	1.417E-07
39	7.404E-04	1.557E-04	5.718E-05	6.464E-04	9.176E-04	0.000E+00	8.583E-07	1.366E-07	1.393E-07
40	6.818E-04	1.454E-04	6.484E-05	6.755E-04	6.724E-04	0.000E+00	9.085E-07	1.334E-07	1.361E-07
41	6.294E-04	1.467E-04	7.332E-05	7.825E-04	5.243E-04	0.000E+00	9.775E-07	1.296E-07	1.324E-07
42	5.822E-04	1.595E-04	8.271E-05	9.188E-04	4.441E-04	0.000E+00	1.067E-06	1.260E-07	1.286E-07
43	5.397E-04	1.756E-04	9.236E-05	1.070E-03	4.229E-04	1.455E-11	1.178E-06	1.221E-07	1.249E-07
44	5.010E-04	2.085E-04	9.085E-05	1.265E-03	4.655E-04	0.000E+00	1.312E-06	1.186E-07	1.212E-07
45	4.650E-04	1.918E-04	7.585E-05	1.235E-03	5.603E-04	0.000E+00	1.472E-06	1.149E-07	1.175E-07
46	4.307E-04	1.579E-04	5.829E-05	1.138E-03	6.149E-04	0.000E+00	1.654E-06	1.109E-07	1.135E-07
47	3.991E-04	1.234E-04	4.346E-05	8.714E-04	5.927E-04	0.000E+00	1.867E-06	1.072E-07	1.096E-07
48	3.713E-04	9.575E-05	3.268E-05	5.876E-04	6.207E-04	0.000E+00	2.112E-06	1.037E-07	1.061E-07
49	3.446E-04	7.968E-05	2.555E-05	4.010E-04	6.812E-04	0.000E+00	2.376E-06	1.001E-07	1.025E-07
50	3.198E-04	7.176E-05	2.172E-05	2.873E-04	7.117E-04	0.000E+00	2.664E-06	9.686E-08	9.903E-08
51	2.973E-04	6.952E-05	2.054E-05	2.196E-04	7.207E-04	0.000E+00	2.983E-06	9.371E-08	9.588E-08
52	2.760E-04	7.145E-05	2.201E-05	1.808E-04	7.524E-04	0.000E+00	3.334E-06	9.069E-08	9.284E-08
53	2.566E-04	7.717E-05	2.640E-05	1.613E-04	7.084E-04	0.000E+00	3.727E-06	8.813E-08	9.008E-08
54	2.386E-04	8.575E-05	3.187E-05	1.543E-04	6.032E-04	0.000E+00	4.161E-06	8.533E-08	8.748E-08

SQN LTSBO									
Plume Segment	Xe	Cs	Ba	I	Te	Ru	Mo	Ce	La
55	2.217E-04	9.647E-05	3.858E-05	1.560E-04	5.303E-04	0.000E+00	4.639E-06	8.300E-08	8.492E-08
56	2.056E-04	1.101E-04	4.614E-05	1.639E-04	4.840E-04	0.000E+00	5.173E-06	8.044E-08	8.243E-08

	SQN STSBO Base Case								
Plume Segment	Xe	Cs	Ba	I	Te	Ru	Mo	Ce	La
1	2.26E-07	2.64E-09	4.59E-11	4.62E-09	1.80E-09	2.48E-10	3.77E-10	4.40E-15	4.50E-15
2	1.55E-07	1.30E-09	4.13E-11	2.32E-09	1.21E-09	2.13E-10	2.23E-10	4.04E-15	4.08E-15
3	3.09E-07	2.58E-09	8.23E-11	4.62E-09	2.41E-09	4.25E-10	4.44E-10	8.05E-15	8.14E-15
4	1.66E-07	1.42E-09	6.12E-11	2.36E-09	1.29E-09	3.23E-10	2.76E-10	6.25E-15	6.30E-15
5	3.30E-07	2.83E-09	1.22E-10	4.70E-09	2.56E-09	6.43E-10	5.50E-10	1.25E-14	1.25E-14
6	1.90E-07	2.06E-09	1.71E-09	3.15E-09	1.92E-09	6.42E-10	4.49E-10	4.47E-10	1.33E-11
7	3.78E-07	4.10E-09	3.41E-09	6.28E-09	3.82E-09	1.28E-09	8.94E-10	8.90E-10	2.65E-11
8	2.60E-07	2.31E-09	3.20E-09	3.39E-09	1.95E-09	6.34E-10	5.00E-10	8.46E-10	2.63E-11
9	5.17E-07	4.60E-09	6.38E-09	6.74E-09	3.88E-09	1.26E-09	9.95E-10	1.68E-09	5.24E-11
10	3.84E-07	2.42E-09	2.91E-09	3.45E-09	1.76E-09	5.44E-10	5.27E-10	7.62E-10	2.40E-11
11	7.64E-07	4.82E-09	5.79E-09	6.86E-09	3.50E-09	1.08E-09	1.05E-09	1.52E-09	4.78E-11
12	4.85E-07	2.12E-09	2.20E-09	3.19E-09	1.43E-09	3.99E-10	4.59E-10	5.71E-10	1.82E-11
13	9.65E-07	4.21E-09	4.37E-09	6.35E-09	2.85E-09	7.95E-10	9.14E-10	1.14E-09	3.63E-11
14	5.81E-07	1.80E-09	1.59E-09	3.15E-09	1.25E-09	2.83E-10	3.77E-10	4.11E-10	1.33E-11
15	1.16E-06	3.57E-09	3.17E-09	6.27E-09	2.49E-09	5.62E-10	7.49E-10	8.17E-10	2.65E-11
16	6.44E-07	1.44E-09	1.10E-09	3.16E-09	1.02E-09	1.89E-10	2.88E-10	2.80E-10	9.27E-12
17	1.28E-06	2.87E-09	2.18E-09	6.28E-09	2.02E-09	3.75E-10	5.73E-10	5.56E-10	1.84E-11
18	1.40E-06	2.25E-09	1.50E-09	6.41E-09	1.52E-09	2.51E-10	4.29E-10	3.79E-10	1.29E-11
19	1.52E-06	2.06E-09	1.04E-09	7.21E-09	1.16E-09	1.69E-10	3.19E-10	2.59E-10	9.17E-12
20	3.66E-01	6.25E-03	7.79E-05	1.16E-02	2.18E-03	1.94E-08	6.15E-04	3.36E-07	3.31E-07
21	6.27E-01	6.26E-03	1.34E-04	1.61E-02	3.61E-03	2.11E-08	4.36E-04	5.53E-07	5.49E-07
22	4.79E-03	1.04E-02	5.12E-06	4.48E-03	1.99E-04	3.35E-09	2.13E-03	8.21E-08	8.85E-08
23	2.64E-04	1.13E-02	8.68E-06	1.63E-03	8.67E-05	2.15E-10	2.88E-03	1.35E-07	1.47E-07
24	7.65E-05	1.02E-02	1.13E-05	7.58E-04	9.66E-05	5.52E-11	2.72E-03	2.19E-07	2.34E-07
25	1.48E-05	3.67E-03	4.95E-06	2.23E-04	4.55E-05	8.56E-12	9.84E-04	1.11E-07	1.17E-07
26	7.93E-06	2.61E-03	1.24E-05	3.30E-04	5.89E-05	3.22E-12	6.72E-04	9.59E-08	1.01E-07
27	6.82E-06	1.72E-03	1.43E-05	6.63E-04	7.64E-05	2.40E-12	4.13E-04	1.14E-07	1.19E-07
28	6.08E-06	1.14E-03	1.10E-05	7.95E-04	8.98E-05	2.43E-12	2.39E-04	1.31E-07	1.37E-07
29	5.16E-06	8.20E-04	8.97E-06	7.24E-04	1.18E-04	3.50E-12	1.37E-04	1.40E-07	1.46E-07
30	5.39E-06	7.58E-04	8.29E-06	9.44E-04	1.95E-04	4.65E-10	6.49E-02	1.56E-07	1.63E-07
31	6.05E-06	7.13E-04	6.55E-06	1.14E-03	2.49E-04	2.70E-09	6.87E-02	1.37E-07	1.43E-07
32	7.06E-06	8.33E-04	6.67E-06	1.33E-03	4.37E-04	4.45E-09	3.19E-02	1.40E-07	1.46E-07
33	7.78E-06	1.08E-03	9.58E-06	1.64E-03	9.39E-04	6.18E-09	1.62E-02	1.58E-07	1.65E-07
34	8.20E-06	1.24E-03	1.47E-05	2.10E-03	2.00E-03	8.01E-09	8.65E-03	1.81E-07	1.88E-07
35	8.40E-06	1.11E-03	2.27E-05	2.68E-03	3.47E-03	9.57E-09	4.78E-03	2.02E-07	2.11E-07
36	8.58E-06	8.08E-04	3.77E-05	3.32E-03	2.93E-03	1.11E-08	2.70E-03	2.23E-07	2.33E-07
37	8.61E-06	6.18E-04	6.63E-05	3.97E-03	2.00E-03	1.23E-08	1.54E-03	2.39E-07	2.49E-07
38	8.67E-06	5.35E-04	1.06E-04	4.60E-03	1.18E-03	1.26E-08	8.84E-04	2.47E-07	2.57E-07

	SQN STSBO Base Case								
Plume Segment	Xe	Cs	Ba	I	Te	Ru	Mo	Ce	La
39	8.73E-06	5.12E-04	1.55E-04	5.21E-03	6.72E-04	1.29E-08	5.12E-04	2.53E-07	2.64E-07
40	8.67E-06	4.74E-04	2.12E-04	5.11E-03	3.84E-04	1.28E-08	2.97E-04	2.55E-07	2.65E-07

SQN STSBO Early									
Plume Segment	Xe	Cs	Ba	I	Te	Ru	Mo	Ce	La
1	2.07E-01	1.90E-03	3.26E-05	4.82E-03	3.12E-03	3.96E-05	1.68E-04	7.81E-10	8.86E-10
2	1.38E-01	1.32E-03	2.28E-05	3.79E-03	2.42E-03	2.25E-05	9.41E-05	4.48E-10	5.05E-10
3	1.98E-02	1.14E-04	1.93E-06	2.63E-04	1.66E-04	2.89E-06	1.20E-05	5.81E-11	6.52E-11
4	2.63E-03	1.37E-05	2.58E-07	2.73E-05	1.82E-05	6.89E-07	1.95E-06	1.46E-11	1.51E-11
5	3.90E-03	9.07E-05	2.71E-06	1.22E-04	1.07E-04	1.32E-05	2.00E-05	2.47E-10	2.43E-10
6	4.08E-02	1.29E-03	3.32E-05	1.63E-03	1.36E-03	1.71E-04	2.97E-04	3.21E-09	3.17E-09
7	1.27E-03	4.84E-05	1.28E-06	6.09E-05	5.29E-05	6.57E-06	1.11E-05	1.23E-10	1.21E-10
8	2.06E-01	3.01E-03	7.12E-04	4.62E-03	4.19E-03	1.03E-03	7.88E-04	1.07E-04	1.87E-06
9	4.17E-02	8.19E-04	1.32E-04	1.25E-03	1.16E-03	2.71E-04	2.13E-04	1.86E-05	3.20E-07
10	1.53E-01	1.31E-03	2.79E-04	1.87E-03	1.16E-03	3.09E-04	3.30E-04	3.87E-05	1.06E-06
11	8.10E-02	6.93E-04	6.30E-05	1.08E-03	2.98E-04	6.78E-05	1.58E-04	8.92E-06	7.43E-07
12	3.18E-02	3.22E-04	1.01E-05	4.74E-04	1.25E-04	1.00E-05	6.77E-05	1.65E-06	4.38E-07
13	1.30E-02	2.25E-04	2.87E-06	3.62E-04	1.22E-04	2.04E-06	3.18E-05	5.51E-07	3.04E-07
14	9.18E-03	7.84E-04	3.07E-06	1.52E-03	2.42E-04	8.38E-07	2.54E-05	4.91E-07	3.90E-07
15	8.83E-03	3.50E-03	7.75E-06	7.95E-03	7.82E-04	4.95E-07	2.43E-05	5.76E-07	5.08E-07
16	5.91E-03	3.42E-03	1.16E-05	1.16E-02	1.72E-03	2.15E-07	1.52E-05	4.56E-07	4.15E-07
17	4.52E-03	1.78E-03	1.82E-05	7.14E-03	3.82E-03	9.97E-08	9.65E-06	4.02E-07	3.73E-07
18	5.06E-03	1.20E-03	3.86E-05	4.84E-03	9.88E-03	6.75E-08	7.85E-06	4.93E-07	4.63E-07
19	4.48E-03	7.17E-04	6.01E-05	2.75E-03	1.67E-02	3.77E-08	5.01E-06	4.68E-07	4.44E-07
20	2.86E-03	3.80E-04	7.10E-05	1.25E-03	1.38E-02	1.46E-08	2.48E-06	3.28E-07	3.15E-07
21	2.48E-03	4.41E-04	1.03E-04	1.20E-03	8.70E-03	7.80E-09	2.08E-06	3.13E-07	3.03E-07
22	2.18E-03	3.99E-04	1.43E-04	1.68E-03	4.89E-03	4.54E-09	2.18E-06	3.02E-07	2.94E-07
23	1.89E-03	2.88E-04	1.90E-04	1.36E-03	2.71E-03	2.79E-09	2.58E-06	2.91E-07	2.85E-07
24	1.69E-03	2.38E-04	2.54E-04	8.97E-04	1.66E-03	1.75E-09	3.36E-06	2.93E-07	2.87E-07
25	1.40E-03	2.09E-04	2.38E-04	6.36E-04	1.18E-03	1.16E-09	4.10E-06	2.71E-07	2.67E-07
26	1.19E-03	1.99E-04	1.61E-04	5.37E-04	1.23E-03	9.31E-10	5.09E-06	2.61E-07	2.58E-07
27	1.05E-03	2.05E-04	1.01E-04	5.29E-04	1.12E-03	8.15E-10	6.26E-06	2.57E-07	2.54E-07
28	9.17E-04	2.21E-04	6.52E-05	4.89E-04	7.45E-04	8.15E-10	7.53E-06	2.50E-07	2.48E-07
29	8.02E-04	2.32E-04	4.83E-05	4.64E-04	5.51E-04	5.82E-10	8.77E-06	2.43E-07	2.41E-07
30	6.99E-04	2.20E-04	4.36E-05	5.17E-04	4.14E-04	5.82E-10	9.74E-06	2.35E-07	2.34E-07
31	6.11E-04	2.16E-04	4.70E-05	6.47E-04	3.28E-04	5.82E-10	1.03E-05	2.28E-07	2.27E-07
32	5.35E-04	2.20E-04	5.78E-05	6.37E-04	3.19E-04	5.82E-10	1.04E-05	2.21E-07	2.19E-07
33	4.70E-04	2.37E-04	7.37E-05	6.26E-04	3.38E-04	5.82E-10	1.00E-05	2.14E-07	2.13E-07
34	4.11E-04	2.63E-04	9.23E-05	6.53E-04	2.83E-04	5.82E-10	8.67E-06	2.06E-07	2.05E-07
35	3.61E-04	2.99E-04	1.17E-04	7.12E-04	2.56E-04	6.98E-10	6.51E-06	2.00E-07	1.99E-07
36	3.18E-04	3.47E-04	1.45E-04	7.30E-04	2.32E-04	5.82E-10	5.89E-06	1.94E-07	1.93E-07
37	2.80E-04	3.78E-04	1.26E-04	6.74E-04	1.63E-04	8.15E-10	6.42E-06	1.88E-07	1.88E-07
38	2.47E-04	3.29E-04	8.30E-05	6.84E-04	1.18E-04	4.66E-10	7.44E-06	1.83E-07	1.82E-07
39	2.18E-04	2.63E-04	5.32E-05	7.49E-04	9.02E-05	2.33E-10	8.83E-06	1.78E-07	1.78E-07
40	1.93E-04	2.12E-04	3.35E-05	8.48E-04	7.39E-05	2.33E-10	1.04E-05	1.74E-07	1.73E-07
41	1.72E-04	1.87E-04	2.08E-05	9.79E-04	6.51E-05	0.00E+00	1.20E-05	1.71E-07	1.70E-07

SQN STSBO Early									
Plume Segment	Xe	Cs	Ba	I	Te	Ru	Mo	Ce	La
42	1.53E-04	1.82E-04	1.33E-05	1.13E-03	6.03E-05	1.16E-10	1.40E-05	1.70E-07	1.69E-07
43	1.77E-04	2.45E-04	1.13E-05	1.62E-03	7.64E-05	1.16E-10	2.29E-05	2.22E-07	2.22E-07
44	1.54E-04	2.55E-04	7.52E-06	1.58E-03	7.22E-05	0.00E+00	3.00E-05	2.16E-07	2.16E-07
45	1.35E-04	2.60E-04	5.29E-06	1.35E-03	7.10E-05	0.00E+00	3.76E-05	2.16E-07	2.16E-07
46	1.09E-04	2.29E-04	3.63E-06	8.68E-04	6.54E-05	0.00E+00	4.01E-05	1.98E-07	1.97E-07
47	8.87E-05	2.05E-04	2.64E-06	6.01E-04	6.20E-05	0.00E+00	3.99E-05	1.86E-07	1.86E-07
48	8.63E-05	2.26E-04	2.43E-06	5.55E-04	7.21E-05	0.00E+00	4.69E-05	2.10E-07	2.10E-07
49	7.56E-05	2.37E-04	2.16E-06	5.08E-04	7.74E-05	0.00E+00	5.12E-05	2.12E-07	2.11E-07
50	6.43E-05	2.50E-04	1.97E-06	4.75E-04	8.27E-05	0.00E+00	5.57E-05	2.09E-07	2.08E-07
51	5.45E-05	2.59E-04	1.87E-06	3.36E-04	8.95E-05	0.00E+00	6.12E-05	2.06E-07	2.05E-07
52	4.64E-05	2.71E-04	1.84E-06	2.08E-04	9.76E-05	0.00E+00	6.71E-05	2.03E-07	2.02E-07
53	3.93E-05	2.87E-04	1.86E-06	1.36E-04	1.07E-04	0.00E+00	7.32E-05	2.01E-07	2.00E-07
54	3.32E-05	3.08E-04	1.92E-06	9.59E-05	1.17E-04	0.00E+00	7.98E-05	1.99E-07	1.98E-07
55	2.81E-05	3.30E-04	2.04E-06	7.38E-05	1.29E-04	0.00E+00	8.62E-05	1.97E-07	1.96E-07
56	2.37E-05	3.52E-04	2.24E-06	5.83E-05	1.41E-04	0.00E+00	9.28E-05	1.94E-07	1.93E-07
57	1.99E-05	3.71E-04	2.52E-06	4.51E-05	1.53E-04	0.00E+00	9.86E-05	1.92E-07	1.91E-07
58	1.67E-05	3.86E-04	2.87E-06	3.79E-05	1.67E-04	0.00E+00	1.05E-04	1.91E-07	1.90E-07
59	1.56E-05	4.20E-04	3.43E-06	3.77E-05	1.87E-04	4.66E-10	2.36E-02	1.98E-07	1.98E-07
60	1.42E-05	3.95E-04	3.98E-06	3.56E-05	1.61E-04	5.82E-09	5.93E-02	1.73E-07	1.72E-07
61	1.16E-05	3.51E-04	4.59E-06	3.26E-05	1.54E-04	1.06E-08	2.68E-02	1.64E-07	1.64E-07
62	9.66E-06	3.41E-04	5.13E-06	3.30E-05	1.77E-04	1.28E-08	1.27E-02	1.74E-07	1.74E-07
63	8.11E-06	3.54E-04	5.73E-06	3.43E-05	2.14E-04	1.46E-08	6.54E-03	1.90E-07	1.90E-07
64	6.85E-06	3.76E-04	6.46E-06	3.59E-05	2.57E-04	1.64E-08	3.57E-03	2.11E-07	2.11E-07
65	5.84E-06	4.03E-04	7.04E-06	3.78E-05	3.04E-04	1.78E-08	2.02E-03	2.29E-07	2.29E-07
66	5.07E-06	4.30E-04	7.45E-06	3.97E-05	3.52E-04	1.86E-08	1.18E-03	2.42E-07	2.42E-07
67	4.41E-06	4.56E-04	7.62E-06	4.21E-05	4.00E-04	1.87E-08	7.13E-04	2.49E-07	2.50E-07
68	3.76E-06	4.76E-04	7.51E-06	4.40E-05	4.46E-04	1.82E-08	4.55E-04	2.50E-07	2.50E-07
69	3.46E-06	4.85E-04	7.33E-06	4.53E-05	4.92E-04	1.72E-08	3.11E-04	2.47E-07	2.48E-07
70	3.04E-06	4.56E-04	7.14E-06	4.69E-05	5.39E-04	1.59E-08	2.21E-04	2.44E-07	2.45E-07
71	2.80E-06	3.69E-04	7.10E-06	4.97E-05	5.93E-04	1.56E-08	1.52E-04	2.44E-07	2.45E-07
72	1.13E-06	1.24E-04	3.01E-06	2.18E-05	2.64E-04	6.64E-09	4.68E-05	1.03E-07	1.03E-07

Table B-5 EARLY parameters used in the Sequoyah LTSBO, STSBO Base Case, and STSBO Early scenarios.

Variable	Description	LTSBO	STSBO Base Case	STSBO Early
ACNAME	Latent Cancer Effect			
	Cancer Type 1	LEUKEMIA	LEUKEMIA	LEUKEMIA
	Cancer Type 2	BONE	BONE	BONE
	Cancer Type 3	BREAST	BREAST	BREAST
	Cancer Type 4	LUNG	LUNG	LUNG
	Cancer Type 5	THYROID	THYROID	THYROID
	Cancer Type 6	LIVER	LIVER	LIVER
	Cancer Type 7	COLON	COLON	COLON
	Cancer Type 8	RESIDUAL	RESIDUAL	RESIDUAL
ACSUSC	Population Susceptible to Cancer	1.0 for all cancers	1.0 for all cancers	1.0 for all cancers
ACTHRE	Linear Dose-Response Threshold	0	0	0
BRRATE	Breathing Rate (for all activity types)	0.000266	0.000266	0.000266
CFRISK	Lifetime Cancer Fatality Risk Factors			
	Cancer Type 1	0.0111	0.0111	0.0111
	Cancer Type 2	0.00019	0.00019	0.00019
	Cancer Type 3	0.00506	0.00506	0.00506
	Cancer Type 4	0.0198	0.0198	0.0198
	Cancer Type 5	0.000648	0.000648	0.000648
	Cancer Type 6	0.003	0.003	0.003
	Cancer Type 7	0.0208	0.0208	0.0208
	Cancer Type 8	0.0493	0.0493	0.0493
CIRISK	Lifetime Cancer Injury Risk Factors			
	Cancer Type 1	0.0113	0.0113	0.0113
	Cancer Type 2	0.000271	0.000271	2.71E-04
	Cancer Type 3	0.0101	0.0101	0.0101
	Cancer Type 4	0.0208	0.0208	0.0208
	Cancer Type 5	0.00648	0.00648	0.00648
	Cancer Type 6	0.00316	0.00316	0.00316
	Cancer Type 7	0.0378	0.0378	0.0378
	Cancer Type 8	0.169	0.169	0.169
CRIORG	Critical Organ for EARLY Phase	L-ICRP60ED	L-ICRP60ED	L-ICRP60ED
CSFACT	Cloudshine Shielding Factors			

Variable	Description	LTSBO	STSBO Base Case	STSBO Early
	Evacuation Shielding Factor for Cohorts 1&2	1	1	1
	Normal Activity Shielding Factor for Cohorts 1&2	0.31	0.31	0.31
	Sheltering Shielding Factor for Cohorts 1&2	0.31	0.31	0.31
	Evacuation Shielding Factor for Cohorts 3-8	1	1	1
	Normal Activity Shielding Factor for Cohorts 3-8	0.72	0.72	0.72
	Sheltering Shielding Factor for Cohorts 3-8	0.65	0.65	0.65
DCF_FILE	Name of Dose Conversion Factor File	FGR13GyEquivDCF.INP	FGR13GyEquivDCF.INP	FGR13GyEquivDCF.INP
DDREFA	Dose-Dependent Reduction Factor			
	Cancer Type 1	2	2	2
	Cancer Type 2	2	2	2
	Cancer Type 3	1	1	1
	Cancer Type 4	2	2	2
	Cancer Type 5	2	2	2
	Cancer Type 6	2	2	2
	Cancer Type 7	2	2	2
	Cancer Type 8	2	2	2
DDTHRE	Threshold for Applying Dose-Dependent Reduction Factor	0.2	0.2	0.2
DIST_SYMB	Symbol assigned to Population Distribution.	See Table B-5	See Table B-5	See Table B-5
DIST_LABEL	Label assigned to Population Distribution	See Table B-5	See Table B-5	See Table B-5
DLTSHL	Delay from Alarm Time to Shelter			
	Cohort 1	1800	1800	1800
	Cohort 2	0	0	0
	Cohort 3	0	0	0
	Cohort 4	1800	1800	1800
	Cohort 5	9900	9900	9900
	Cohort 6	13500	13500	13500
	Cohort 7	10800	10800	10800
	Cohort 8	1800	1800	1800

Variable	Description	LTSBO	STSBO Base Case	STSBO Early
DLTEVA	Delay from Beginning of Shelter to Evacuation			
	Cohort 1	18000	18000	18000
	Cohort 2	10800	10800	10800
	Cohort 3	16200	16200	16200
	Cohort 4	2700	2700	2700
	Cohort 5	5400	5400	5400
	Cohort 6	10800	10800	10800
	Cohort 7	5400	5400	5400
	Cohort 8	18000	18000	18000
DOSEFA	Cancer Dose-Response Linear Factors	1 for all organs	1 for all organs	1 for all organs
DOSEFB	Cancer Dose-Response Quadratic Factors	0 for all organs	0 for all organs	0 for all organs
DOSHOT	Hot-Spot Relocation Dose Threshold (rem)	5	5	5
DOSMOD	Dose-Response Model Flag	AT	AT	AT
DOSNRM	Normal Relocation Dose Threshold (rem)	1	1	1
DURBEG	Duration of Beginning of Evacuation Phase			
	Cohort 1	4500	4500	4500
	Cohort 2	7200	7200	7200
	Cohort 3	8100	8100	8100
	Cohort 4	1800	1800	1800
	Cohort 5	9000	9000	9000
	Cohort 6	14400	14400	14400
	Cohort 7	2700	2700	2700
	Cohort 8	0	0	0
DURMID	Duration of Middle of Evacuation Phase			
	Cohort 1	9900	9900	9900
	Cohort 2	6300	6300	6300
	Cohort 3	5400	5400	5400
	Cohort 4	9900	9900	9900
	Cohort 5	5400	5400	5400
	Cohort 6	3600	3600	3600
	Cohort 7	2700	2700	2700

Variable	Description	LTSBO	STSBO Base Case	STSBO Early
	Cohort 8	0	0	
EANAM1	Text Describing the EARLY Assumptions	SQN Early (EP 0-10 mile evacuation)	SQN Early (EP 0-10 mile evacuation)	SQN Early (EP 0-10 mile evacuation)
EANAM2	Text Describing the Emergency Response			
	Cohort 1	0-10 Schools	0-10 Schools	0-10 Schools
	Cohort 2	0-10 Special Facilities (Medical)	0-10 Special Facilities (Medical)	0-10 Special Facilities (Medical)
	Cohort 3	0-10 Transit Dependent	0-10 Transit Dependent	0-10 Transit Dependent
	Cohort 4	0-10 Early General Population	0-10 Early General Population	0-10 Early General Population
	Cohort 5	0-10 Middle General Population	0-10 Middle General Population	0-10 Middle General Population
	Cohort 6	0-10 Tail General Population	0-10 Tail General Population	0-10 Tail General Population
	Cohort 7	10-15 Shadow	10-15 Shadow	10-15 Shadow
	Cohort 8	Non-evacuating population (0.005 of 0-10, 0.8 of 10-15, all >15)	Non-evacuating population (0.005 of 0-10, 0.8 of 10-15, all >15)	Non-evacuating population (0.005 of 0-10, 0.8 of 10-15, all >15)
EFFACA	LD50 for Early Fatality Types			
	A-RED MARR (Sv)	5.6	5.6	5.6
	A-LUNGS (Sv)	23.5	23.5	23.5
	A-STOMACH (Sv)	12.1	12.1	12.1
EFFACB	Shape Factor for Early Fatality Types			
	A-RED MARR	6.1	6.1	6.1
	A-LUNGS	9.6	9.6	9.6
	A-STOMACH	9.3	9.3	9.3
EFFACY	Efficacy of the KI Ingestion Threshold or Piecewise for Cohorts 1-8	0.7	0.7	0.7
	Efficacy of KI Ingestion Linear No Threshold of	0.0	0.0	0.0

Variable	Description	LTSBO	STSBO Base Case	STSBO Early
	Cohorts 1-8			
EFFTHR	Threshold Dose to Target Organ			
	A-RED MARR	2.32	2.32	2.32
	A-LUNGS	13.6	13.6	13.6
	A-STOMACH	6.5	6.5	6.5
EIFACA	D50 For Early Injuries			
	PRODROMAL VOMIT	2	2	2
	DIARRHEA	3	3	3
	PNEUMONITIS	16.6	16.6	16.6
	SKIN ERYTHRMA	6	6	6
	TRANSEPIDERMAL	20	20	20
	THYROIDITIS	240	240	240
	HYPOTHYROIDISM	60	60	60
EIFACB	Shape Factor for Early Injuries			
	PRODROMAL VOMIT	3	3	3
	DIARRHEA	2.5	2.5	2.5
	PNEUMONITIS	7.3	7.3	7.3
	SKIN ERYTHRMA	5	5	5
	TRANSEPIDERMAL	5	5	5
	THYROIDITIS	2	2	2
	HYPOTHYROIDISM	1.3	1.3	1.3
EINAME	Early Injury Effect Names and Corresponding Organ			
	PRODROMAL VOMIT	A-STOMACH	A-STOMACH	A-STOMACH
	DIARRHEA	A-STOMACH	A-STOMACH	A-STOMACH
	PNEUMONITIS	A-LUNGS	A-LUNGS	A-LUNGS
	SKIN ERYTHRMA	A-SKIN	A-SKIN	A-SKIN
	TRANSEPIDERMAL	A-SKIN	A-SKIN	A-SKIN
	THYROIDITIS	A-THYROID	A-THYROID	A-THYROID
	HYPOTHYROIDISM	A-THYROID	A-THYROID	A-THYROID
EISUSC	Susceptible Population	1. for all health effects	1. for all health	1. for all health effects

Variable	Description	LTSBO	STSBO Base Case	STSBO Early
	Fraction		effects	
EITHRE	Early Injury Dose Threshold			
	PRODROMAL VOMIT	0.5	0.5	0.5
	DIARRHEA	1	1	1
	PNEUMONITIS	9.2	9.2	9.2
	SKIN ERYTHRMA	3	3	3
	TRANSEPIDERMAL	10	10	10
	THYROIDITIS	40	40	40
	HYPOTHYROIDISM	2	2	2
ENDAT2	Control flag indicating only ATMOS and EARLY are to be run	.FALSE.	.FALSE.	.FALSE.
ENDEMP	Time Duration for the Emergency Phase (day)	7	7	7
ESPEED	Evacuation Speed			
	Initial Evacuation Phase, Cohort 1, 3, 5 (m/s)	1.34112	1.34112	1.34112
ESPEED	Middle Evacuation Phase, Cohort 1, 3, 5	0.89408	0.89408	0.89408
	Late Evacuation Phase, Cohort 1, 3, 5	8.941	8.941	8.941
	Initial Evacuation Phase, Cohort 2	1.34112	1.34112	1.34112
	Middle Evacuation Phase, Cohort 2	1.34112	1.34112	1.34112
	Late Evacuation Phase, Cohort 2	8.941	8.941	8.941
	Initial Evacuation Phase, Cohort 4	2.2352	2.2352	2.2352
	Middle Evacuation Phase, Cohort 4	1.34112	1.34112	1.34112
	Late Evacuation Phase, Cohort 4	8.941	8.941	8.941
	Initial Evacuation Phase, Cohort 6	0.89408	0.89408	0.89408
	Middle Evacuation	1.34112	1.34112	1.34112

Variable	Description	LTSBO	STSBO Base Case	STSBO Early
	Phase, Cohort 6			
	Late Evacuation Phase, Cohort 6	8.9408	8.9408	8.9408
	Initial Evacuation Phase, Cohort 7	8.9408	8.9408	8.9408
	Middle Evacuation Phase, Cohort 7	8.9408	8.9408	8.9408
	Late Evacuation Phase, Cohort 7	8.9408	8.9408	8.9408
	Initial Evacuation Phase, Cohort 8	4.4704E-05	4.4704E-05	4.4704E-05
	Middle Evacuation Phase, Cohort 8	4.4704E-05	4.4704E-05	4.4704E-05
	Late Evacuation Phase, Cohort 8	4.4704E-05	4.4704E-05	4.4704E-05
ESPGRD	Speed Multiplier to Account for Grid-Level Variations in Road Network	Table B-6 Table B-7	Table B-6 Table B-7	Table B-6 Table B-7
ESPMUL	Speed Multiplier Employed During Precipitation	0.8	0.8	0.8
EVATYP	Evacuation Type	NETWORK	NETWORK	NETWORK
GSHFAC	Groundshine Shielding Factors			
	Evacuation Shielding Factor for Cohorts 1&2	0.5	0.5	0.5
	Normal Activity Shielding Factor for Cohorts 1&2	0.05	0.05	0.05
	Sheltering Shielding Factor for Cohorts 1&2	0.05	0.05	0.05
	Evacuation Shielding Factor for Cohorts 3-8	0.5	0.5	0.5
	Normal Activity Shielding Factor for Cohorts 3-8	0.26	0.26	0.26
	Sheltering Shielding Factor for Cohorts 3-8	0.2	0.2	0.2
IDIREC	Direction in Network Evacuation Model	Table B-8	Table B-8	Table B-8
IPLUME	Plume Model Dispersion Code	3-Wind Shift w/o Rotation	3-Wind Shift w/o Rotation	3-Wind Shift w/o Rotation
KIMODL	Model Flag for KI	NOKI	NOKI	NOKI

Variable	Description	LTSBO	STSBO Base Case	STSBO Early
	Ingestion			
LASMOV	Last Ring in Movement Zone	19	19	19
N_POP_DIST	Number of population distributions entered by user	5	5	5
NUMACA	Number of Latent Cancer Health Effects	8	8	8
NUMEFA	Number of Early Fatality Effects	3	3	3
NUMEIN	Number of Early Injury Effects	7	7	7
NUMEVA	Outer Boundary of Evacuation/Shelter Region	14	14	14
NUMFIN	Number of Fine Grid Subdivisions	7	7	7
ORGFLG	Doses to be Calculated for Specified Organ	All TRUE for FGR-13 All TRUE for DOSFAC2 except for A-Lower LI and L-Liver, which are FALSE	All TRUE for FGR-13 All TRUE for DOSFAC2 except for A-Lower LI and L-Liver, which are FALSE	All TRUE for FGR-13 All TRUE for DOSFAC2 except for A-Lower LI and L-Liver, which are FALSE
OVRRID	Wind Rose Probability Override	.FALSE.	.FALSE.	.FALSE.
POP_DIST	Population Distribution assigned to the evacuation grid	Table B-6	Table B-6	Table B-6
POPFLG	Population Distribution Flag	FILE	FILE	FILE
POPFRAC	Population Fraction Ingesting KI	0	0	0
PROTIN [E]	Evacuation Shielding Factor for Cohorts 1&2	0.98	0.98	0.98
PROTIN [N]	Normal Activity Shielding Factor for Cohorts 1&2	0.33	0.33	0.33
PROTIN [S]	Sheltering Shielding Factor for Cohorts 1&2	0.33	0.33	0.33
PROTIN [E]	Evacuation Shielding Factor for Cohorts 3-8	0.98	0.98	0.98

Variable	Description	LTSBO	STSBO Base Case	STSBO Early
PROTIN [N]	Normal Activity Shielding Factor for Cohorts 3-8	0.46	0.46	0.46
PROTIN [S]	Sheltering Shielding Factor for Cohorts 3-8	0.33	0.33	0.33
REFPNT	Reference Time Point (ARRIVAL or SCRAM)	ALARM	ALARM	ALARM
RESCON	Emergency phase resuspension coefficient	0.0001	0.0001	0.0001
RESHAF	Resuspension Concentration Half-Life	182000	182000	182000
RISCAT	Risk by Weather-Category Flag	.FALSE.	.FALSE.	.FALSE.
RISTHR	Risk Threshold for Fatality Radius	0	0	0
SKPFAC [E]	Evacuation Shielding Factor for Cohorts 1&2	0.98	0.98	0.98
SKPFAC [N]	Normal Activity Shielding Factor for Cohorts 1&2	0.33	0.33	0.33
SKPFAC [S]	Sheltering Shielding Factor for Cohorts 1&2	0.33	0.33	0.33
SKPFAC [E]	Evacuation Shielding Factor for Cohorts 3-8	0.98	0.98	0.98
SKPFAC [N]	Normal Activity Shielding Factor for Cohorts 3-8	0.46	0.46	0.46
SKPFAC [S]	Sheltering Shielding Factor for Cohorts 3-8	0.33	0.33	0.33
TIMHOT	Hot Spot Relocation Time (hr)	36	36	36
TIMNRM	Normal Relocation Time (48)	48	48	48
TRAVEL POINT	Evacuee Movement Option	CENTER POINT	CENTER POINT	CENTER POINT
WTFRAC	Weighting Fraction Applicable to this Scenario			
	Cohort 1	0.19283	0.19283	0.19283
	Cohort 2	0.0077	0.0077	0.0077

Variable	Description	LTSBO	STSBO Base Case	STSBO Early
	Cohort 3	0.0015	0.0015	0.0015
	Cohort 4	0.38972	0.38972	0.38972
	Cohort 5	0.31178	0.31178	0.31178
	Cohort 6	0.07794	0.07794	0.07794
	Cohort 7	0.2	0.2	0.2
	Cohort 8	0.005	0.005	0.005
WTNAME	Type of Weighting for Cohorts	SUMPOP	SUMPOP	SUMPOP

Table B-6 SUMPOP distribution labels.

	DIST_SYMB	DIST_LABEL
Population 1	S	0-10 Schools
Population 2	M	0-10 Med Nursing
Population 3	G	0-10 General Pop
Population 4	2	10-15 Shadow
Population 5	3	0-1000 Nonevac

Table B-7 SUMPOP distributions.

Population	Cohort 1 (0-10 Schools)	Cohort 2 (0-10 Special Facilities)	Cohort 3 (0-10 Transit Dependent)	Cohort 4 (0-10 Early Gen Pop)	Cohort 5 (0-10 Middle Gen Pop)	Cohort 6 (0-10 Tail General Pop)	Cohort 7 (10-15 Shadow)	Cohort 8 (Non-Evac)
Population 1: 0-10 Schools (S)	0.3934	0	0.0115	0.2976	0.2381	0.0545	0	0
Population 2: 0-10 Med Nursing (M)	0	0.342	0.0124	0.3228	0.2582	0.0646	0	0
Population 3: 0-10 General Pop (G)	0	0	0.0188	0.4875	0.39	0.0975	0	0.0063
Population 4: 10-15 Shadow (2)	0	0	0	0	0	0	0.2	0.8
Population 5: 0-1000 Nonevac (3)	0	0	0	0	0	0	0	1

Table B-8 Grid-level evacuation speed multipliers used in the Sequoyah LTSBO, STSBO Base Case, and STSBO Early scenarios, cohorts 1-8.

Compass Sector																
Radial Ring	**1**	**2**	**3**	**4**	**5**	**6**	**7**	**8**	**9**	**10**	**11**	**12**	**13**	**14**	**15**	**16**
1	1.1	1.1	1.1	1.1	1.1	1.1	1.1	1.1	1.1	1.1	1.1	1.1	1.1	1.1	1.1	1.1
2	1.1	1.1	1.1	1.1	1.1	1.1	1.1	1.1	1.1	1.1	1.1	1.1	1.1	1.1	1.1	1.1
3	1.1	1.1	1.1	1.1	1.1	1.1	1.1	1.1	1.1	1.1	1.1	1.1	1.1	1.1	1.1	1.1
4	1.1	1.1	1.1	1.1	1.2	1.2	1.2	1.2	1.2	1.2	1.2	1.2	1.2	1.2	1.2	1.2
5	1.1	1.1	1.1	1.2	1.2	1.2	1.2	1.2	1.2	1.2	1.2	1.2	1.2	1.2	1.2	1.2
6	1.2	1.2	1.2	1.2	1.2	1.2	1.2	1.2	1.2	1.2	1.2	1.2	1.2	1.2	1.2	1.2
7	1.2	1.2	1.2	1.2	1.2	1.2	1.2	1.2	1.2	1.2	1.2	1.2	1.2	1.2	1.2	1.2
8	1.2	1.2	1.2	1.2	1.2	1.2	1.2	1.2	1.2	1.2	1.2	1.2	1.2	1.2	1.2	1.2
9	1.2	1.2	1.2	1.2	1.2	1.2	1.2	1.2	1.2	1.2	1.2	1.2	1.2	1.2	1.2	1.2
10	1.2	1.2	1.2	1.2	1.2	1.2	1.2	1.2	1.2	1.2	1.2	1.2	1.2	1.2	1.2	1.2
11	1.2	1.2	1.2	1.2	1.2	1.2	1.2	1.2	1.2	1.2	1.2	1.2	1.2	1.2	1.2	1.2
12	1.2	1.2	1.2	1.2	1.2	1.2	1.2	1.2	1.2	1.2	1.2	1.2	1.2	1.2	1.2	1.2
13	1.2	1.2	1.2	1.2	1.2	1.2	1.2	1.2	1.2	1.2	1.2	1.2	1.2	1.2	1.2	1.2
14	1.2	1.2	1.2	1.2	1.2	1.2	1.2	1.2	1.2	1.2	1.2	1.2	1.2	1.2	1.2	1.2
15	1.2	1.2	1.2	1.2	1.2	1.2	1.2	1.2	1.2	1.2	1.2	1.2	1.2	1.2	1.2	1.2
16	1.2	1.2	1.2	1.2	1.2	1.2	1.2	1.2	1.2	1.2	1.2	1.2	1.2	1.2	1.2	1.2
17	1.2	1.2	1.2	1.2	1.2	1.2	1.2	1.2	1.2	1.2	1.2	1.2	1.2	1.2	1.2	1.2
18	1.2	1.2	1.2	1.2	1.2	1.2	1.2	1.2	1.2	1.2	1.2	1.2	1.2	1.2	1.2	1.2
19	1.2	1.2	1.2	1.2	1.2	1.2	1.2	1.2	1.2	1.2	1.2	1.2	1.2	1.2	1.2	1.2

Compass Sector																
Radial Ring	**17**	**18**	**19**	**20**	**21**	**22**	**23**	**24**	**25**	**26**	**27**	**28**	**29**	**30**	**31**	**32**
1	1.1	1.1	1.1	1.1	1.1	1.1	1.1	1.1	1.1	1.1	1.1	1.1	1.1	1.1	1.1	1.1
2	1.1	1.1	1.1	1.1	1.1	1.1	1.1	1.1	1.1	1.1	1.1	1.1	1.1	1.1	1.1	1.1
3	1.1	1.1	1.1	1.1	1.1	1.1	1.1	1.1	1.1	1.1	1.1	1.1	1.1	1.1	1.1	1.1
4	1	1	1	1	1	1	1	1	1	1	1	1	1	1	1	1.1
5	1	1	1	1	1	1	1	1	1	1	1	1	1	1	1	1
6	1	1	1	1	1	1	1	1	1	1	1	1	1	1	1	1
7	1	1	1	1	1	1	1	1	1	1	1	1	1	1	1	1
8	1	1	1	1	1	1	1	1	1	1	1	1	1	1	1	1
9	1.2	1	1	1	1	1	1	1	1	1	1	1	1	1	1	1
10	1	1	1	1	1	1	1	1	1	1	1	1	1	1	1	1
11	1.2	1	1	1	1	1	1	1	1	1	1	1	1	1	1	1
12	1.2	1	1	1	1	1	1.3	1.3	1.3	1.3	1.3	1.3	1.3	1	1	1
13	1	1	1	1.3	1.3	1.3	1.3	1.3	1.3	1.3	1.3	1.3	1.3	1.3	1.3	1.3
14	1.2	1.2	1.3	1.3	1.3	1.3	1.3	1.3	1.3	1.3	1.3	1.3	1.3	1.3	1.3	1.3
15	1.2	1.3	1.3	1.3	1.3	1.3	1.3	1.3	1.3	1.3	1.3	1.3	1.3	1.3	1.3	1.3
16	1.2	1.3	1.3	1.3	1.3	1.3	1.3	1.3	1.3	1.3	1.3	1.3	1.3	1.3	1.3	1.3
17	1.2	1.3	1.3	1.3	1.3	1.3	1.3	1.3	1.3	1.3	1.3	1.3	1.3	1.3	1.3	1.3
18	1.2	1.3	1.3	1.3	1.3	1.3	1.3	1.3	1.3	1.3	1.3	1.3	1.3	1.3	1.3	1.3
19	1.2	1.3	1.3	1.3	1.3	1.3	1.3	1.3	1.3	1.3	1.3	1.3	1.3	1.3	1.3	1.3

Compass Sector																
Radial Ring	**33**	**34**	**35**	**36**	**37**	**38**	**39**	**40**	**41**	**42**	**43**	**44**	**45**	**46**	**47**	**48**
1	1.1	1.1	1.1	1.1	1.1	1.1	1.1	1.1	1.1	1.1	1.1	1.1	1.1	1.1	1.1	1.1
2	1.1	1.1	1.1	1.1	1.1	1.1	1.1	1.1	1.1	1.1	1.1	1.1	1.1	1.1	1.1	1.1
3	1.1	1.1	1.1	1.1	1.1	1.1	1.1	1.1	1.1	1.1	1.1	1.1	1.1	1.1	1.1	1.1
4	1.1	1.1	1.1	1.1	1.1	1.1	1.1	1.1	1.1	1.1	1.1	1.1	1.1	1.1	1.1	1.1
5	1	1	1	1	1	1	1	1.1	1.1	1.1	1.1	1.1	1.1	1.1	1.1	1.1
6	1	1	1	1	1	1	1	1	1.1	1.1	1.1	1.1	1.1	1.1	1.1	1.1
7	1	1	1	1	1	1	1	1	1.1	1.1	1.1	1.1	1.1	1.1	1.1	1.1
8	1	1	1	1	1	1	1	1	1.1	1.1	1.1	1.1	1.1	1.1	1.1	1.1
9	1	1	1	1	1	1	1	1.1	1.1	1.1	1.1	1.1	1.1	1.1	1.1	1.1
10	1	1	1	1	1	1	1.1	1.1	1.1	1.1	1.1	1.1	1.1	1.3	1.1	1.1
11	1	1	1	1	1	1	1	1.1	1.1	1.1	1.1	1.1	1.1	1.1	1.1	1.1
12	1	1	1	1	1	1	1	1.1	1.1	1.1	1.1	1.1	1.1	1.1	1.2	1.2
13	1.3	1.3	1	1	1	1	1	1	1.1	1.1	1.1	1.1	1.2	1.2	1.2	1.2
14	1.3	1	1	1	1	1	1	1	1.1	1.1	1.1	1.1	1.2	1.2	1.2	1.2
15	1	1	1	1	1	1	1	1	1.1	1.1	1.1	1.1	1.2	1.2	1.2	1.2
16	1.3	1.3	1	1	1	1	1	1	1.1	1.1	1.1	1.2	1.2	1.2	1.2	1.2
17	1.3	1.3	1.3	1.3	1	1	1.1	1.1	1.1	1.1	1.2	1.2	1.2	1.2	1.2	1.2
18	1.3	1.3	1.3	1.3	1	1.1	1.1	1.1	1.1	1.1	1.2	1.2	1.2	1.2	1.2	1.2
19	1.3	1.3	1.3	1.3	1	1.1	1.1	1.1	1.1	1.1	1.2	1.2	1.2	1.2	1.2	1.2

Compass Sector																
Radial Ring	**49**	**50**	**51**	**52**	**53**	**54**	**55**	**56**	**57**	**58**	**59**	**60**	**61**	**62**	**63**	**64**
1	1.1	1.1	1.1	1.1	1.1	1.1	1.1	1.1	1.1	1.1	1.1	1.1	1.1	1.1	1.1	1.1
2	1.1	1.1	1.1	1.1	1.1	1.1	1.1	1.1	1.1	1.1	1.1	1.1	1.1	1.1	1.1	1.1
3	1.1	1.1	1.1	1.1	1.1	1.1	1.1	1.1	1.1	1.1	1.1	1.1	1.1	1.1	1.1	1.1
4	1.1	1.1	1.1	1.1	1.1	1.1	1.1	1.1	1.1	1.1	1.1	1.1	1.1	1.1	1.1	1.1
5	1.1	1.1	1.1	1.1	1.1	1.1	1.1	1.1	1.1	1.1	1.1	1.1	1.1	1.1	1.1	1.1
6	1.1	1.1	1.1	1.1	1.1	1.1	1.1	1.1	1.1	1.1	1.1	1.1	1.1	1.1	1.1	1.2
7	1.1	1.1	1.1	1.1	1.1	1.1	1.1	1.1	1.1	1.1	1.1	1.1	1.1	1.1	1.2	1.2
8	1.1	1.1	1.1	1.1	1.1	1.1	1.1	1.1	1.1	1.1	1.1	1.1	1.1	1.2	1.2	1.2
9	1.1	1.1	1.1	1.1	1.1	1.1	1.1	1.1	1.1	1.1	1.1	1.2	1.2	1.2	1.2	1.2
10	1.1	1.1	1.1	1.1	1.1	1.1	1.1	1.1	1.1	1.1	1.1	1.2	1.2	1.2	1.2	1.2
11	1.1	1.2	1.2	1.2	1.2	1.2	1.2	1.2	1.2	1.2	1.2	1.2	1.2	1.2	1.2	1.2
12	1.2	1.2	1.2	1.2	1.2	1.2	1.2	1.2	1.2	1.2	1.2	1.2	1.2	1.2	1.2	1.2
13	1.2	1.2	1.2	1.2	1.2	1.2	1.2	1.2	1.2	1.2	1.2	1.2	1.2	1.2	1.2	1.2
14	1.2	1.2	1.2	1.2	1.2	1.2	1.2	1.2	1.2	1.2	1.2	1.2	1.2	1.2	1.2	1.2
15	1.2	1.2	1.2	1.2	1.2	1.2	1.2	1.2	1.2	1.2	1.2	1.2	1.2	1.2	1.2	1.2
16	1.2	1.2	1.2	1.2	1.2	1.2	1.2	1.2	1.2	1.2	1.2	1.2	1.2	1.2	1.2	1.2
17	1.2	1.2	1.2	1.2	1.2	1.2	1.2	1.2	1.2	1.2	1.2	1.2	1.2	1.2	1.2	1.2
18	1.2	1.2	1.2	1.2	1.2	1.2	1.2	1.2	1.2	1.2	1.2	1.2	1.2	1.2	1.2	1.2
19	1.2	1.2	1.2	1.2	1.2	1.2	1.2	1.2	1.2	1.2	1.2	1.2	1.2	1.2	1.2	1.2

Table B-9 Evacuation direction parameters used in the Sequoyah LTSBO, STSBO Base Case, and STSBO Early scenarios.

Compass Sector																
Radial Ring	**1**	**2**	**3**	**4**	**5**	**6**	**7**	**8**	**9**	**10**	**11**	**12**	**13**	**14**	**15**	**16**
1	2	2	2	2	2	2	2	2	2	2	2	2	2	2	2	2
2	4	4	4	4	4	4	4	1	1	1	1	2	2	2	2	2
3	4	4	4	4	4	4	4	4	1	1	1	1	1	1	1	1
4	4	4	4	4	1	1	1	1	1	1	1	1	1	1	1	1
5	4	1	1	1	1	1	1	1	1	1	1	1	1	1	1	1
6	2	2	1	1	1	1	1	2	1	4	4	4	4	4	4	4
7	1	1	1	1	1	1	1	4	4	4	4	1	1	1	1	1
8	2	2	2	2	2	2	1	4	4	1	1	1	1	1	1	1
9	1	1	1	1	1	1	1	1	1	1	1	1	1	1	1	1
10	1	1	1	2	2	1	1	2	2	2	2	2	2	1	4	4
11	1	1	1	2	2	1	1	2	2	2	2	1	4	4	4	4
12	1	1	4	2	2	2	1	1	1	1	1	4	4	4	4	4
13	1	1	4	4	1	4	4	4	4	4	4	4	4	4	4	4
14	1	1	1	1	4	4	2	1	4	2	2	2	2	1	1	1
15	1	1	1	1	1	1	4	2	2	2	2	2	1	1	4	4
16	1	2	1	1	4	4	4	2	2	2	1	1	1	4	4	4
17	1	1	1	1	1	4	4	2	2	1	1	1	1	1	1	1
18	1	1	1	1	1	1	1	1	1	1	1	1	1	1	1	1
19	1	1	1	1	1	1	1	1	1	1	1	1	1	1	1	1

Compass Sector																
Radial Ring	**17**	**18**	**19**	**20**	**21**	**22**	**23**	**24**	**25**	**26**	**27**	**28**	**29**	**30**	**31**	**32**
1	2	2	2	2	2	2	2	2	2	2	2	2	2	2	2	2
2	2	2	2	2	2	2	2	2	2	2	2	2	2	2	2	2
3	1	1	1	1	1	1	1	1	1	1	1	1	1	1	1	1
4	1	1	1	1	1	1	1	1	1	1	1	1	1	1	1	1
5	1	1	1	1	1	1	2	1	1	1	1	1	1	1	1	1
6	1	2	2	2	2	2	2	2	1	1	4	4	4	4	4	4
7	1	1	1	1	1	1	1	1	1	1	1	1	1	1	1	1
8	1	1	1	1	1	1	1	1	1	4	4	4	4	4	4	4
9	1	1	2	2	2	2	2	2	2	2	1	4	4	4	4	4
10	4	4	4	4	4	1	2	2	1	4	4	4	4	4	4	4
11	4	2	2	2	2	1	2	2	2	2	2	2	2	2	1	1
12	4	2	2	2	2	1	1	1	1	1	1	1	2	2	1	1
13	4	3	3	1	1	1	1	1	1	1	1	1	1	1	1	1
14	4	4	2	2	1	1	1	1	1	4	4	2	2	1	1	1
15	4	2	2	1	1	4	4	4	2	2	1	1	1	4	4	4
16	4	2	2	1	1	4	1	4	4	2	2	1	1	1	1	1
17	1	4	2	1	1	4	2	1	1	4	2	2	1	1	1	1
18	1	1	1	1	1	1	1	1	1	1	1	1	1	1	1	1
19	1	1	1	1	1	1	1	1	1	1	1	1	1	1	1	1

Compass Sector																
Radial Ring	**33**	**34**	**35**	**36**	**37**	**38**	**39**	**40**	**41**	**42**	**43**	**44**	**45**	**46**	**47**	**48**
1	2	2	2	2	2	2	2	2	2	2	2	2	2	2	2	2
2	2	2	2	2	2	2	2	2	2	2	2	2	2	2	2	2
3	1	1	1	1	1	1	1	1	1	1	1	1	1	1	1	1
4	1	1	1	1	1	2	2	2	2	2	2	1	1	1	1	1
5	1	1	1	1	1	1	1	1	1	1	1	1	1	4	4	4
6	4	4	4	1	1	1	1	1	1	1	1	1	4	4	4	2
7	1	1	1	1	1	4	4	4	2	2	2	1	1	2	2	2
8	4	4	4	4	4	4	4	4	2	2	2	1	1	1	1	1
9	4	4	4	4	4	4	4	2	2	2	2	1	1	1	1	1
10	4	4	4	4	4	4	1	1	1	1	1	1	1	1	1	4
11	1	4	4	4	4	4	4	1	1	1	4	4	4	4	4	4
12	1	1	1	1	1	1	4	1	1	1	1	1	4	1	1	1
13	1	1	1	1	1	1	4	4	1	1	1	1	1	2	2	1
14	1	2	2	1	1	1	1	1	1	2	1	1	1	4	1	1
15	2	2	1	1	1	1	1	1	1	1	4	1	1	1	1	1
16	1	1	1	4	1	1	2	1	1	1	4	2	2	1	1	1
17	4	4	4	1	1	4	2	2	1	1	1	1	1	1	4	4
18	1	1	1	1	1	1	1	1	1	1	1	1	1	1	1	1
19	1	1	1	1	1	1	1	1	1	1	1	1	1	1	1	1

Compass Sector																
Radial Ring	**49**	**50**	**51**	**52**	**53**	**54**	**55**	**56**	**57**	**58**	**59**	**60**	**61**	**62**	**63**	**64**
1	1	1	1	1	1	1	1	1	1	1	1	1	1	1	1	1
2	2	2	2	2	2	1	1	1	1	1	1	4	4	4	4	4
3	1	1	1	1	1	1	1	1	1	1	1	1	4	4	4	4
4	1	1	1	1	4	1	2	1	1	4	4	2	2	1	4	4
5	4	4	4	4	4	4	2	1	1	1	4	4	4	4	4	4
6	2	1	4	4	4	4	1	2	2	1	4	4	3	3	3	2
7	2	1	1	1	1	1	1	1	4	4	4	1	1	4	2	2
8	1	1	1	1	1	1	1	1	1	1	4	4	4	1	2	2
9	1	1	4	4	4	4	4	4	4	4	4	2	2	1	1	1
10	4	4	4	4	4	4	4	4	4	4	4	2	2	2	1	1
11	1	1	1	1	1	1	1	1	1	2	1	1	2	2	1	1
12	1	1	1	1	1	1	1	1	1	1	1	2	2	2	2	2
13	1	1	1	1	1	2	2	1	1	4	4	4	4	2	2	1
14	1	4	4	4	2	2	1	1	4	4	4	4	2	2	2	2
15	1	1	4	4	2	2	1	1	4	1	1	1	4	2	2	2
16	1	1	1	1	4	2	1	1	1	4	4	2	2	1	1	1
17	2	2	1	1	1	4	2	1	1	4	4	2	2	1	1	1
18	1	1	1	1	1	1	1	1	1	1	1	1	1	1	1	1
19	1	1	1	1	1	1	1	1	1	1	1	1	1	1	1	1

Table B-10 CHRONC input parameters used in the Sequoyah LTSBO, STSBO Base Case, and STSBO Early scenarios.

Variable	Description	LTSBO	STSBO Base Case	STSBO Early
CHNAME	CHRONC Problem Identification	SQN	SQN	SQN
CDFRM	Farmland Decontamination Cost ($/ha)			
	Level 1	48800	48800	48800
	Level 2	65300	65300	65300
	Level 3	83100	83100	83100
CDNFRM	Non-farmland Decontamination Cost ($/person)			
	Level 1	7600	7600	7600
	Level 2	24300	24300	24300
	Level 3	43200	43200	43200
CRTOCR	Critical Organ for CHRONC Phase	L-ICRP60ED	L-ICRP60ED	L-ICRP60ED
DPRATE	Property Depreciation Rate	0.2	0.2	0.2
DLBCST	Hourly Labor Cost for Decontamination Worker ($/man-yr)	76000	76000	76000
DPFRCT	Farm Production Dairy Fraction	N/A	N/A	N/A
DSCRLT	Long-Term Phase Dose Criterion	0.5	0.5	0.5
DSCRTI	Intermediate-Phase Dose Criterion (rem)	2	2	2
DSRATE	Societal Discount Rate for Property	0.06	0.06	0.06
DSRFCT	Decontamination Factors			
	Level 1	3	3	3
	Level 2	5	5	5
	Level 3	15	15	15
DUR_INTPHAS	Duration of the Intermediate Phase (yr)	1	1	1
EVACST	Emergency Phase Cost of Evacuation/Relocation ($/person-d)	179	179	179
EXPTIM	Maximum Exposure Time (yr)	50	50	50
FDPATH	COMIDA2 vs. MACCS Food Model Switch	NEW	NEW	NEW

Variable	Description	LTSBO	STSBO Base Case	STSBO Early
FRACLD	Fraction of Area that is Land	N/A	N/A	N/A
FRCFRM	Fraction of Area Used for Farming	N/A	N/A	N/A
FRFDL	Fraction of Decontamination Cost for Labor			
	Level 1	0.35	0.35	0.35
	Level 2	0.35	0.35	0.35
	Level 3	0.35	0.35	0.35
FRFIM	Farm Wealth Improvements Fraction	0.2 in	0.2 in	0.2 in
FRMPRD	Average Annual Farm Production	N/A	N/A	N/A
FRNFIM	Nonfarm Wealth Improvements Fraction	0.72	0.72	0.72
FRNFDL	Nonfarm Labor Cost Fraction			
	Level 1	0.35	0.35	0.35
	Level 2	0.35	0.35	0.35
	Level 3	0.35	0.35	0.35
GWCOEF	Long-Term Groundshine Coefficients			
	Term 1	0.5	0.5	0.5
	Term 2	0.5	0.5	0.5
KSWTCH	Diagnostic Output Option Switch	0	0	0
LBRRATE	Long-Term Breathing Rate	0.000266	0.000266	0.000266
LGSHFAC	Long-Term Groundshine Protection Factor	0.3	0.3	0.3
LPROTIN	Long-Term Inhalation Protection Factor	0.46	0.46	0.46
LVLDEC	Number of Decontamination Levels	3	3	3
NGWTRM	Number of Terms in Groundshine Weathering Equation	2	2	2
NRWTRM	Number of Terms in Resuspension Weathering Equation	3	3	3
POPCST	Per Capita Cost of Long-Term Relocation ($/person)	7750	7750	7750
RELCST	Relocation Cost per Person-Day	143	143	143

Variable	Description	LTSBO	STSBO Base Case	STSBO Early
RWCOEF	Long-Term Resuspension Factor Coefficients			
	Term 1	0.00001	0.00001	0.00001
	Term 2	0.0000001	0.0000001	0.0000001
	Term 3	0.000000001	0.000000001	0.000000001
TFWKF	Fraction Farmland Worker Time in Contaminated Zone			
	Level 1	0.15	0.15	0.15
	Level 2	0.15	0.15	0.15
	Level 3	0.15	0.15	0.15
TFWKNF	Fraction Non-farmland Worker Time in Contaminated Zone			
	Level 1	0.15	0.15	0.15
	Level 2	0.15	0.15	0.15
	Level 3	0.15	0.15	0.15
TGWHLF	Groundshine Weathering Half-Lives			
	Term 1	16000000	16000000	16000000
	Term 2	2.8E9	2.8E9	2.8E9
TIMDEC	Decontamination Times			
	Level 1	364	364	364
	Level 2	364	364	364
	Level 3	364	364	364
TMPACT	Time Action Period Ends (yr)	1	1	1
TRWHLF	Resuspension Weathering Half-Lives			
	Term 1	16000000	16000000	16000000
	Term 2	160000000	1600000000	160000000
	Term 3	1600000000	16000000000	1600000000
VALWF	Value of Farm Wealth	11287	11287	11287
VALWNF	Value of Nonfarm Wealth	3.42714E+05	3.42714E+05	3.42714E+05

Table B-11 Sequoyah radionuclide inventory

Radionuclide	Isotopic Group	Core Activity (Ci)
Kr-85	1	7.85E+05
Kr-85m	1	2.94E+07
Kr-87	1	5.91E+07
Kr-88	1	7.85E+07
Xe-133	1	1.95E+08
Xe-135	1	4.82E+07
Xe-135m	1	3.92E+07
Cs-134	2	9.88E+06
Cs-136	2	2.69E+06
Cs-137	2	7.36E+06
Rb-86	2	1.42E+05
Rb-88	2	7.94E+07
Ba-139	3	1.77E+08
Ba-140	3	1.71E+08
Sr-89	3	1.05E+08
Sr-90	3	5.88E+06
Sr-91	3	1.35E+08
Sr-92	3	1.42E+08
Ba-137m	3	7.01E+06
I-131	4	9.06E+07
I-132	4	1.36E+08
I-133	4	1.93E+08
I-134	4	2.21E+08
I-135	4	1.84E+08
Te-127	5	6.56E+06
Te-127m	5	5.17E+05
Te-129	5	2.13E+07
Te-129m	5	3.11E+06
Te-131m	5	1.53E+07
Te-132	5	1.31E+08
Te-131	5	7.95E+07
Rh-105	6	6.46E+07
Ru-103	6	1.21E+08
Ru-105	6	7.44E+07
Ru-106	6	2.74E+07
Rh-103m	6	1.20E+08
Rh-106	6	3.31E+07
Nb-95	7	1.48E+08
Co-58	7	8.85E+02
Co-60	7	8.09E+04
Mo-99	7	1.77E+08
Tc-99m	7	1.56E+08
Nb-97	7	1.66E+08
Nb-97m	7	1.57E+08
Ce-141	8	1.59E+08

Radionuclide	Isotopic Group	Core Activity (Ci)
Ce-143	8	1.56E+08
Ce-144	8	9.57E+07
Np-239	8	1.29E+09
Pu-238	8	1.52E+05
Pu-239	8	1.78E+04
Pu-240	8	2.12E+04
Pu-241	8	6.05E+06
Zr-95	8	1.59E+08
Zr-97	8	1.65E+08
Am-241	9	6.17E+03
Cm-242	9	1.74E+06
Cm-244	9	1.28E+05
La-140	9	1.75E+08
La-141	9	1.62E+08
La-142	9	1.57E+08
Nd-147	9	6.27E+07
Pr-143	9	1.56E+08
Y-90	9	6.06E+06
Y-91	9	1.32E+08
Y-92	9	1.43E+08
Y-93	9	1.57E+08
Y-91m	9	7.94E+07
Pr-144	9	9.67E+07
Pr-144m	9	1.57E+06

APPENDIX C ROADWAY CAPACITY ANALYSIS

ROADWAY CAPACITY ANALYSIS

C.1 Approach

Evacuation routes are dispersed throughout the emergency planning zone (EPZ) such that addressing the infrastructure issues by quadrant provided a reasonable approach for determining evacuation time estimates (ETEs) which account for damage to bridges. All bridges within the EPZ were assumed to fail due to the earthquake. The roadway network was reviewed using aerial mapping to determine available routes to exit the EPZ, and the capacities of these routes were calculated. Topography of the area was reviewed using United States Geological Service mapping to identify low lying areas to also assess the potential for roadway impacts due to flooding should the upstream Watts Bar dam fail. From the ETE study, the number of vehicles exiting different areas of the EPZ was identified. Using the number of vehicles and capacity at the exit points of the EPZ, an estimate of the evacuation time was calculated. A description of the bridge locations, alternate routes, and evacuating vehicles is provided below.

Data from the 2013 Sequoyah ETE
SQN ETE 5 highest volume roadways
SR 58 SB – 12,046 vehicles
SR 319 SB – 10,976 vehicles
US27/SR29 NB – 7,709 vehicles
I-75 SB – 5,317 vehicles
SR 58 NB – 3,351 vehicles

Table 3-4 of the ETE study provides the following for the winter day scenario
Total vehicles = 50,894
Population = 127,883 (includes general public, schools, and transients)

C.2 Major Roadways within the EPZ

SR 58
Bridge over Harrison Bay

- Includes Harrison Bay State Park.
- Alternate routes are Ooltewah Georgetown Road and SR 312 south to exit EPZ.
- This bridge location is very near the location in the ETE report where an analysis of the road closure was performed. The results of the ETE road closure analysis increased the 90 percent ETE by 1.5 hours and the 100 percent ETE by 3.5 hours. Similar results would be expected if this bridge is assumed to fail. The increase in ETE only affects the eastern side of the EPZ because the roadway network on the western side of the Chickamauga Lake is independent of the east side.

I-75
Due to limited access and bridge failures below, I-75 is assumed to be unavailable within the bounds of the EPZ.

Bridge on I-75 near Green Gap.

- I-75 passes under roadway crossing. Assume failure causes I-75 to close.

- Alternate routes include frontage road south to exit EPZ.

Interchange on I-75 just north of Ooltewah near south limit of EPZ.
- I-75 passes over roadway crossing. Assume failure.

- Affected area is mostly EPZ pass through traffic. There is only one interchange from SR64 onto I-75 and this is located along the eastern EPZ boundary near Cleveland.

- Alternate routes include frontage road south to exit EPZ.

Bridge on I-75 crossing Bancroft Road.
- I-75 passes over Bancroft Road. Assume bridge failure.

- Alternate routes include Bancroft Road south to exit EPZ.

- Population north of I-75 would need to travel north along residential roads to SR 312 to exit the EPZ.

SR 312
No bridges or crossings assumed to fail

SR 60
No bridges or crossings assumed to fail

SR 306/Freewill Road NW
No bridges or crossings assumed to fail

Ooltewah Georgetown Road
No bridges or crossings assumed to fail

West side of Chickamauga Lake
SR 319
Bridge at Dockside
- Bridge over water inlet. Assume failure.

- Alternate routes exist north and south of bridge. There should be a minor effect of less than 10 minutes extra travel to exit this area.

Bridge over railroad near Hixon on EPZ boundary.
- Roadway bridge crosses over railroad, assume failure.
- Considerable area affected.
- Alternate route is residential street a quarter mile north of bridge.
- Reduced roadway capacity on alternate route, but additional travel distance is minimal.

US 27
Due to multiple assumed bridge failures below, assume entire length of road is unusable.
- Interchange at SR 153
- Interchange at Thrasher Pike
- Interchange at Harrison Lane
- Interchange at SR 153

- Bridge over Daisy Dallas Road
- Bridges over CR 2158
- Bridge over Card Road
- Interchange with SR 319
- Bridge between SR 319 and Dayton Pike crossing
- Bridge crossing Dayton Pike
- Interchange with SR 111
- Bridge over Possum Creek

Using the ETE Table 3-4 data for vehicles by evacuation sector, an estimate of the vehicle evacuation routing was performed. The EPZ is split by Lake Chickamauga such that evacuation routing on each side of the lake is independent of the other side. For the analysis, the EPZ was divided into approximate quadrants with the lake serving as the north/south centerline. Next, the routing was reviewed with respect to the postulated damaged infrastructure. The following vehicles were then assigned to each quadrant. From data provided in the ETE study, vehicles were summed by EPZ quadrant as follows:

- NW quadrant: 7,100

- NE quadrant: 2,100

- SE quadrant: 22,500 (Approximately 1,300 vehicles from Sector C-5 and part of C-3 evacuate separately and 21,200 vehicles exit the along the south boundary of the EPZ)

- SW quadrant: 19,200 (this section includes the Middle Valley and Hixon area bounded by the lake, SR 27, the north edge of Sector A-1, and A-3, and the south edge of the EPZ.

Total: 50,900 vehicles

C.3 Capacity Analysis

MACCS allows input of speeds for each cohort and then allows the analyst to adjust the speed at the grid element level. Therefore, one section of the EPZ was used as the control section where the speed multiplier is 1.0 and sectors that have higher or lower speeds were then adjusted from the base speed.

C.3.1 Southwest Half of the EPZ

The large population in the SW EPZ quadrant controls the evacuation time for the west side of Lake Chickamauga. SR 27 bisects this quadrant and the west side of the EPZ. The ETE study converts population to vehicle count and shows approximately 16,800 evacuating vehicles for the area between SR 27 and Lake Chickamauga in the area of Middle Valley and Hixon. The EPZ is divided into alpha numeric sectors. Sectors A-1 and A-3 would typically evacuate to the north using SR 27; however, the bridges along SR 27 are assumed to fail in this area eliminating the use of the evacuation route and forcing evacuation in the southerly direction. Approximately 2,400 vehicles from these sectors could be affected. Thus, the total number of vehicles evacuating south from this area is 19,200. The area north and west of SR 27 is lightly populated and the exit routes have not been impacted.

The ETE study provides estimates for the SSW area in Table 6-3 when wind is from the NNE-NE. The SSW area includes Middle Valley and Hixon. From the ETE study, the evacuation time

for this area is approximately 3.75 hours for 90 percent of the public and 5 hours for 100 percent of the public. After the seismic event, the most likely roadways accessible to evacuees from the area of Middle Valley and Hixon include Hamill Road, Old Hixon Pike, Grubb Road, Lake Resort Drive, and Dayton Boulevard. These roadways do not have bridge crossings in this area and would provide alternate routes out of this section of the EPZ.

Each of these routes is a single lane roadway with a capacity of 1,200 pc/h, which is developed from a base capacity of 1,600 pc/h with Highway Capacity Manual (HCM) adjustments for peak hour (0.88), heavy vehicles (0.86) and terrain (0.99). It is assumed this includes 10 percent heavy vehicles (trucks, buses, trailers, etc.). With approximately 19,400 vehicles, the exit time would be about 3.25 hours (rounded to quarter hour) using the exit capacity of these 5 locations. However, additional time is needed for evacuees to identify their current route is blocked, travel the rural backroads to find an unobstructed alternative route, and travel in congested traffic until they exit the EPZ. An additional 2 hours is assumed to address these actions, and to reflect additional capacity reduction which occurs in oversaturated roadways. The mobilization time of 2.5 hours is added, which is in the upper range of the Figure 5-1 mobilization curve in the ETE study, but is reasonable to reflect delay due to the seismic event. The combined time of 7.75 hours is used as the ETE for this section of the SW quadrant of the EPZ. This time would begin after the sirens for General Emergency.

Dayton Pike, also called Dayton Boulevard near the south limit of the EPZ, is a 2 lane (one lane each direction) roadway that runs parallel to US 27 throughout the EPZ. Near the north and south limits of the EPZ, Dayton Pike crosses US 27 and would be assumed unavailable at these two points. Evacuees from the southwest quadrant of the EPZ would need to travel local routes for about the last mile to exit the EPZ to the south. Evacuees from the northwest quadrant of the EPZ would need to travel local routes for about the last 3 miles to exit the EPZ to the north. There is a low lying area around Dallas Bay where a review of the topography shows the elevations in this area could be susceptible to flooding making additional local roadways impassible. The larger roadways in the area were already removed from the analysis due to assumed bridge failures.

C.3.2 Northwest Quadrant of the EPZ

CR 1126 and Poe Road are identified as evacuation routes and do not have bridges, thus are assumed unobstructed. US 27 is assumed unavailable due to bridge failures, but there are at-grade crossings that will allow evacuees to travel unobstructed out of the EPZ. Because there is a relatively small population in this area and there are multiple evacuation options, even with the loss of US 27, the travel speeds for this quadrant are assumed to be 20 percent faster than the speeds established for the SW EPZ quadrant. This is consistent with the ETE study which shows under normal conditions, the ETE for 100 percent of the population of this area is 20 percent shorter than the SW quadrant. This increase was applied through the use of speed multipliers in MACCS. There is a low lying area near the north end of Soddy Daisy along the stretch of Dayton Pike that passes near the Lake Chickamauga inlet. Review of the topography shows the elevations in this area are relatively flat and may be subject to flooding making additional local roadways inaccessible.

C.3.3 Eastern Half of the EPZ

The ETE study identifies a large population that will exit the SE quadrant of the EPZ, and this controls the evacuation time for the east side of the Lake Chickamauga. SR 58 runs north/south through the eastern side of the EPZ. Bridges on SR 58 and Snow Hill Road cross a lake finger and are assumed to fail. These failures will necessitate rerouting of traffic to southern EPZ exit points. Multiple bridges on US 74/I-75 are assumed to fail, and this prevents vehicles

from evacuating east, with the exception of Sector C-5 and part of Sector C-3 (in the ETE) which are located east of US 74/I-75. Hickory Valley Road would remain accessible, but serves a very small population and in this analysis is not assumed to contribute to the evacuation.

There are approximately 21,200 vehicles that would be rerouted to evacuate south out of the EPZ on the portion of the two-lane (each direction) SR 58 that is open, and on single lane (each direction) roadways of South Hickory Valley Road and Webb Road. This provides 4 lanes of outbound traffic from the SE quadrant of the EPZ. There is a low lying portion of Harrison Bay Road, immediately north of the bridge on SR 58, that appears likely to flood if the upstream dam were to fail. However, the traffic near the potentially flooded area is already assumed to travel north and would not be impacted if flooding occurred in this location. Snow Hill Road has a few low lying areas, but investigation found these appear elevated sufficiently such that they would not likely flood. Using the same roadway capacity data above, it would take about 4.5 hours to evacuate 21,200 vehicles. An additional 2 hours is added for evacuees to identify their current route is blocked, travel the rural backroads to find an unobstructed alternate route, and travel in congested traffic until they exit the EPZ. Mobilization time of 2.5 hours is also added as described earlier. The total evacuation time for the SE quadrant is 9 hours and begins after the sirens for General Emergency.

Consistent with guidance in NUREG/CR-7002, the ETE study includes a roadway impact analysis. The study evaluated SR 58 as though it was completely closed, and evacuees were re-routed to accessible roadways. SR 58 bisects the EPZ on the east side of the lake and is the most heavily travelled evacuation route within the EPZ. The ETEs increased from 3.5 hours to about 5 hours for the 90 percent evacuation and from 5 hours to about 8.5 hours for the 100 percent evacuation. This evacuation time compares well with the capacity analysis above. The capacity analysis also assumes bridge fail on I-75; but, because I-75 has limited access points within the EPZ, the SR 58 roadway closure generally represents the effects of the seismic event on evacuation of the eastern half of the EPZ.

C.4 MACCS Input

MACCS allows the input of speeds for the beginning, middle, and late phases of the evacuation. Speeds are provided for each cohort. The speeds identified above were used throughout the EPZ and were adjusted through the use of speed multipliers. Following the approach described above, speeds are established for the eastern half of the EPZ and were adjusted at the grid level using MACCS speed multipliers. Figure C-1 shows assumed bridge failures and low lying areas within the EPZ.

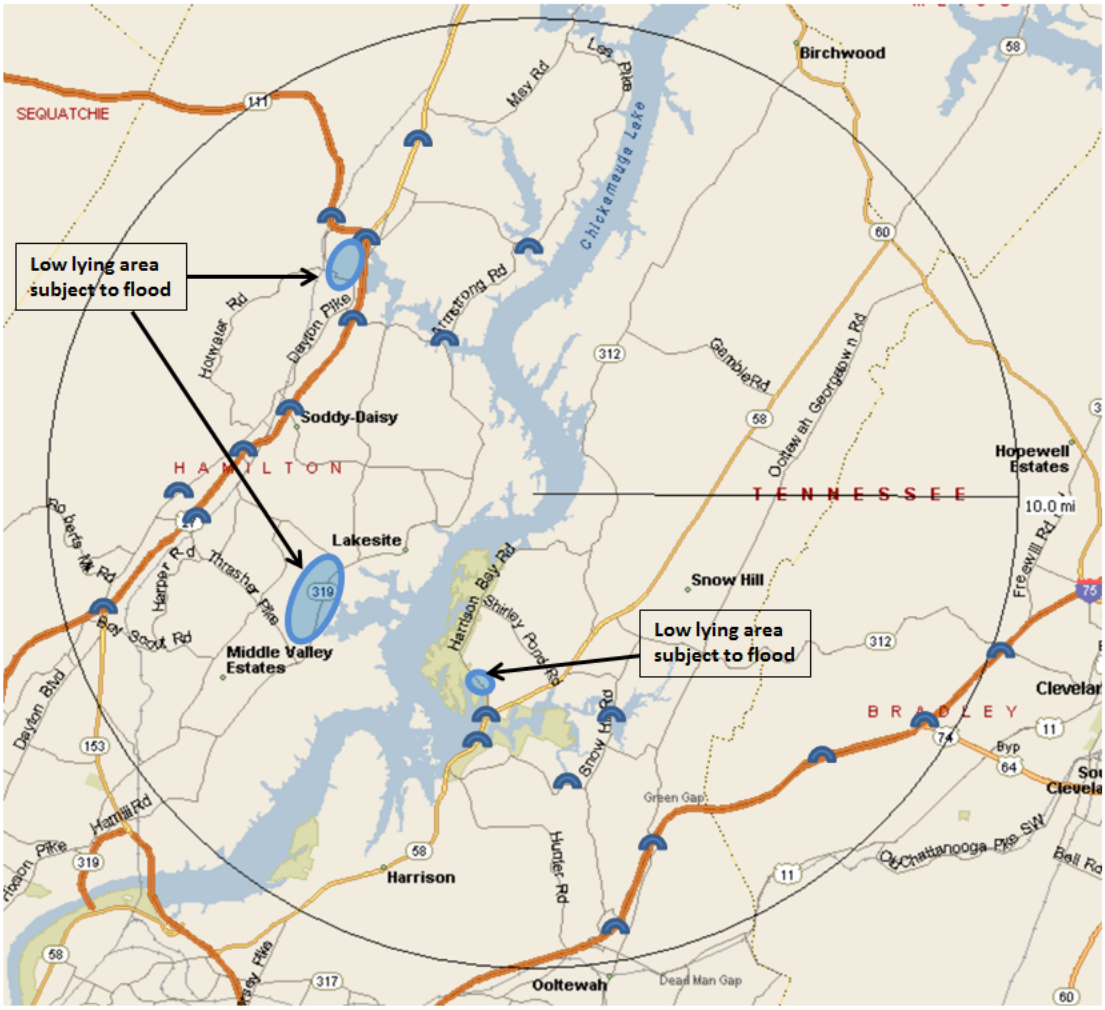

Figure C-1 Assumed bridge failures and low lying areas within the EPZ